REVIEW OF THE VKI DOCTORAL RESEARCH

2011 - 2012



von Karman Institute for Fluid Dynamics

Covert art : *Pictures taken from the articles written by Delphine Laboureur (front cover[1]) and Davide Masutti (back cover[2]) who have been attributed the best presentation award during the symposium.*

©2012 by the von Karman Institute for Fluid Dynamics

Waterloosesteenweg 72, B-1640 Sint-Genesius-Rode
To order: https://www.vki.ac.be

ISBN 978-2-87516-031-7

D/2012/0238/593, T. Magin, Editor-in-Chief

The contents of this book are the property of the von Karman Institute for Fluid Dynamics. No part of this book may be reproduced or distributed in any form of by any means, or stored in a database or retrieval system, without the prior written permission from the Publisher.

[1] Velocity field from high-speed images, processed by using the LS-PIV technique, that represent the flame enlargement induced by the water sub-layer boiling in a Boilover phenomenon
[2] Isolated roughness induced transition on a sharp 7 degree half-cone at Mach 6

PREFACE

The third Symposium on the doctoral research of the von Karman Institute for Fluid Dynamics took place during the period March 5 to 7, 2012. The doctoral students have presented the progress of their research work carried out in the three departments: Aeronautics and Aerospace, Environmental and Applied Fluid Dynamics, Turbomachinery and Propulsion. The first year students have presented a poster on their research plans and some preliminary results, while the most advanced students have proposed a twenty minute presentation followed by a session of questions.

This event was attended by the faculty of the von Karman Institute as well as by some colleagues from universities and industrial partners. The Symposium was open to external attendees free of charge. In addition to the presentations of the PhD candidates, we had the pleasure to welcome prominent keynote lecturers who have opened each day the Symposium:

- Jérôme Anthoine from ONERA, "***Hybrid chemical propulsion for space transportation***"
- Cam Tropea from Technische Universität Darmstadt, "***Can we expect novel developments in spray diagnostics?***"
- Yannick Le Maoult from Université de Toulouse, "***Thermoreflectometry and phosphors thermometry applied to materials science***"

This year, the best presentation award has been attributed on an equal footing to **Delphine Laboureur** for her research on ***Experimental characterization and modeling of hazards (BLEVE) and Boilover (small scale Boilover experiments)*** and to **Davide Masutti** for his research on ***Natural and Induced Transition on a 7 degree Half-Cone at Mach 6***. We would like to congratulate them on their achievement. The illustrated cover art of these proceedings is based on their research results.

This proceedings volume contains 43 papers which are divided into the following topics: Transition from Laminar to Turbulent Flow, Plasma Flow, CFD and Modeling for Re-entry Flow, Flow during Industrial Hazard, Atmospheric Flow, Multiphase Flow and Heat and Mass Transfer Flow, Aeroacoustics, Flow in Turbines, Flow in Compressors, Engine Analysis and Improvements, Multidisciplinary Optimization in Turbomachinery, Static and Dynamic Stability of Re-entry Vehicle.

We would like to emphasize that this publication serves as a tool for communication and aims to enhance exchange between the doctoral candidates and the faculty and external attendees. The annual publication of their results in proceedings is of crucial importance to research at the VKI providing a thorough review of the different activities within the three departments.

As such, the doctoral candidate students of the VKI play a key role in strengthening the expertise in experimental and numerical/physical modeling of the Institute. In addition to basic research, works carried out at the Institute often leads to implementation of real life industrial applications critical to the fluid dynamics community.

The present proceedings are registered under an ISBN number and may be referred to in any further publication.

Jésus Garicano Mena Jérôme Sans Phd Representatives and Symposium co-Chairs	Patrick Rambaud Associate Professor Symposium Chair	Jean Muylaert VKI Director

The contribution of all VKI members who helped with this event is deeply acknowledged in particular the faculty, library and printing office.

TABLE OF CONTENTS

Editorial notes i

Table of contents iii

Transition from Laminar to Turbulent Flow

Henny Bottini 3
Qualification of a supersonic test section in a compression-tube wind tunnel

Jayson Babajee 13
Modeling and analysis of the laminar to turbulent transition in a low-pressure turbine

Davide Masutti 25
Natural and Induced Transition on a 7deg Half-Cone at Mach 6

Guillaume Grossir 37
A free-stream and boundary layer characterization of the Longshot contoured hypersonic nozzle

Bart Van Hove (first year doctoral summary) 49
Trajectory and atmospheric reconstruction for entry vehicles

Gennaro Serino (first year doctoral summary) 51
Development of advanced hypersonic models for transition to turbulence: uncertainty quantification of transition prediction

Sebastian Scholl (first year doctoral summary) 57
Conjugate heat transfer using large eddy simulation in rib roughened cooling channels

Francesco Baldani (first year doctoral summary) 59
Heat transfer in high subsonic velocity environments behind the fan of a gas turbine

Flow in Compressors

Fatma Ceyhun Sahin 73
Passive vortex generators as end-wall flow control elements

Jérôme Sans 83
The effect of solidity on compressor performance and stability

Michael Joly 93
Accelerated optimization for multi-disciplinary design of transonic and contra-rotating turbomachinery components

Engine Analysis and Improvements

Laura Villafañe 105
Aero-thermal analysis and characterization of fine wire thermocouple probes

Victor F. Villacé 117
Simulation of a variable-combined-cycle engine for dual subsonic and supersonic cruise

Static and Dynamic Stability in Transonic Flow

Sebastien Paris 133
Experimental determination of the dynamic derivatives of a reentry capsule in transonic supersonic regime

Multiphase Flow

Marcos Lema 147
Multi-phase fluid hammer: modeling, experiments and simulations

Bart Janssens 157
Numerical modeling and experimental investigation of fine particle coagulation and dispersion in dilute flows

Evangelos Bacharoudis 163
Flow visualization and Planar Laser Induced Fluorescence (PLIF) measurements on horizontal shear-driven liquid films at the edge of a plate

Imre Horváth (first year doctoral summary) 175
Development and application of the Multi Wavelength Light Extinction technique for the characterization of nano- and microparticles

Jorge Pinho (first year doctoral summary) 177
Experimental study and modeling of two-phase flow cavitation and flashing through complex valves

Chiara Spaccapaniccia (first year doctoral summary) 179
Experimental study of buoyant plume and thermal stratification in a liquid metal nuclear reactor

Pierre Schrooyen (first year doctoral summary) 181
Development of a numerical simulation tool for the aerothermal flow through an ablative Thermal Protection System for atmospheric entry

Atmospheric Flow

Boris Conan 187
Experimental parametric study of the influence of an idealized upstream ridge on the flow characteristics over Alaiz mountain

Domingo Muñoz Esparza 195
Mesoscale modelling and on-site measurements of the offshore boundary layer in the North Sea

Flow with important heat transfer and/or combustion

Delphine Laboureur 205
Experimental characterization and modeling of hazards: BLEVE and Boilover: small scale Boilover experiments

Anthony Delmas 217
Shape and temperature field distortions induced by convective effect on hot object in the visible, near infrared and infrared bands

Aeroacoustics

Péter Tóth 231
Beamforming in Non-ideal Acoustic Environments
(Grid Adaptation for L_1 Norm Generalized Inverse Beamforming)

Korcan Kucukcoskun 239
Prediction of free and scattered acoustic fields of low-speed fans: scattering of tonal fan noise by a rigid corner

Leandro Dantas de Santana 247
Unsteady panel code for airfoil turbulence interaction computation

Plasma Flow

Damien Le Quang 255
Investigation of high enthalpy plasma flow

Bernd Helber 265
Methodology for ablation investigations of innovative ablators in the VKI Plasmatron facility including first results on a carbon fiber preform

Silvânia Lopes 275
Modeling of inductively coupled plasma reactor for nanoparticles production

Alessio Cipullo 285
Ground testing methodologies improvement in plasma wind tunnels using optical emission diagnostics

Numerical Approach for Hypersonic Flow

Erik Torres 299
Direct Simulation Monte Carlo in reentry flows

Işıl Şakraker (first year doctoral summary) 311
In-flight experiment design and ground testing of a re-entry Cubesat

Thorsten Scholz (first year doctoral summary) 313
Mission analysis and design of a CubeSat network

James B. Scoggins (first year doctoral summary) 317
Development of multiphysics numerical methods to study coupled flow, radiation, and ablation phenomena for planetary entry vehicles

Lasse Mueller (first year doctoral summary) 321
Multidisciplinary gradient-based optimization of turbomachinery components using CAD parameterization

Gilles Bailet (first year doctoral summary) 323
Re-entry platform for in-flight demonstration and in-situ measurement

Alessandro Munafo 327
Multiscale models and computational methods for aerothermodynamics

Khalil Bensassi 337
Arbitrary Lagrangian-Eulerian simulation of a moving piston in hypersonic ground test facility

Jesús Garicano Mena 343
Residual Distribution methods for atmospheric entry aerothermodynamics

Julien De Mûelenaere 349
Stagnation line approximation for ablation thermochemistry

Development of Advanced CFD

Stefano D'Angelo 361
A generalized framework for adjoint error estimation of PG method applied to linear problems

Martin Vymazal 371
High-order RDS and p-multigrid solution algorithms for compressible flow

TRANSITION FROM LAMINAR TO TURBULENT FLOW

Qualification of a Supersonic Test Section in a Compression-tube Wind Tunnel

Henny Bottini

Turbomachinery and Propulsion Department, von Karman Institute for Fluid Dynamics, Belgium, bottini@vki.ac.be

Supervisor: Guillermo Paniagua

Associate Professor, Turbomachinery and Propulsion Department, von Karman Institute for Fluid Dynamics, Belgium, paniagua@vki.ac.be.

Abstract

The qualification of a reduced-noise test section for supersonic transition experiments at different Mach numbers is presented. The low-disturbances environment was analyzed by both hot-wire measurements and the assessment of the boundary layer status along the wind-tunnel walls. Maps of the flow static pressure around and downstream of a single roughness element were made by the use of Pressure Sensitive Paint with the lifetime and the intensity methods.

Keywords: Supersonic flow, wind tunnels, mass-flow fluctuations, boundary-layer, Pressure-Sensitive Paint, wall shear stress quantification, thin oil film

1. Introduction

In air-breathing engines, the status of the boundary layer along the intake surface dictates the aerothermal performance. This paper presents the qualification of a quiet wind tunnel to study roughness induced boundary layer transition in an adjustable supersonic regime (M_∞ from 1.5 to 2.2) with Reynolds varying from 3 to $4.6 \cdot 10^7$ m^{-1}.

At the intake where pressure gradients and shocks appear the boundary layer should be adequately predicted and controlled. A turbulent boundary layer is more robust than a laminar one, but the higher aerothermal losses must be properly accounted for in the combined vehicle-engines design.Consequently, transition experiments are required to identify the transition onset and the driving physical phenomena. This kind of experiments, however, requires a facility that does not interfere with the transition process on the test article. At the considered supersonic Mach numbers, the facility must not produce strong pressure fluctuations. Namely, the RMS in pressure should be less than 1% of p_∞ [1]. In order to extrapolate the wind tunnel data towards real flight conditions, also the wind tunnel fluctuations should be bounded [2]. Harvey in [3] proved that the main cause of pressure fluctuations inside the test section of a supersonic wind tunnel is the turbulent boundary layer on the test section walls, which radiates pressure disturbances onto the test article. Therefore, the solution for having meaningful transition experiments is to keep the boundary layer laminar on those walls, that is, to have a ”quiet wind tunnel”. The present paper presents results by an oil-dot technique to assess the boundary layer status on the facility internal walls, and by hot-wire measurements to quantify the intensity of the free-stream mass-flow fluctuations.

The first test campaign in the qualified supersonic wind tunnel aimed at mapping the pressure field produced by a single three-dimensional roughness in a supersonic boundary layer. These maps are produced by Pressure Sensitive Paint applied all around the roughness element. Its capabilities were exploited with two different methods, the lifetime method and the intensity method. Both are presented in their main aspects and with their results, along with the paint calibration method and process.

2. Wind Tunnel Qualification

The first tests of this new wind tunnel have been dedicated to its qualification. Firstly the correctness of the wind tunnel starting, i.e. the presence of a shock-free supersonic expansion in the divergent, has been verified experimentally. Secondly, the tests focused

on measurement of the wind tunnel noise, i.e. they assessed the wind tunnel degree of quietness.

2.1. Practical Mach range achievable

The result of the first wind tunnel qualification campaign is the Mach range achievable in practice. The tests of this campaign were run without test article in the test section. The absence of the shock was verified by the use of fifteen pressure taps drilled on the ends of the two ramps that constitute the divergent of the nozzle (ten taps on the upper ramp and five on the lower ramp). They measured the static pressure at the wall along an axial length of 36 *cm* from the location of the test article leading edge to the very end of the nozzle. The measurements were then compared with pressure and Mach number axial evolutions by a quasi-1D calculations of the supersonic shock-free expansion corresponding to the same total quantities as those of the run. The comparison between the calculations and the measurements is illustrated by Fig. 1 for the static pressure and by Fig. 2 for the Mach number.

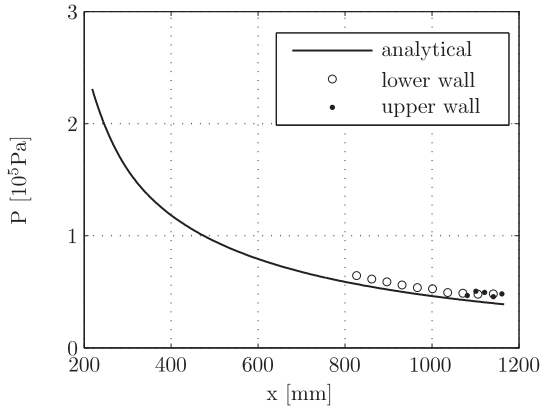

Figure 1: Typical static pressure axial evolution throughout the whole nozzle divergent (p_0=4.2 bar)

Figure 1 and 2 show how the measured pressure and Mach number evolution along the divergent matches very satisfactorily the theoretical evolution. This means that no shock wave is present in the divergent, that is the wind tunnel is correctly started by the total pressure value selected for the test. At this point Table 1 presents the Mach-number range achievable by the wind tunnel along with the corresponding unit Reynolds numbers, test times, and total pressures of the tests. Note that as test Mach number is considered the one reached by the flow in the divergent at the axial position of 80 *cm* from the throat.

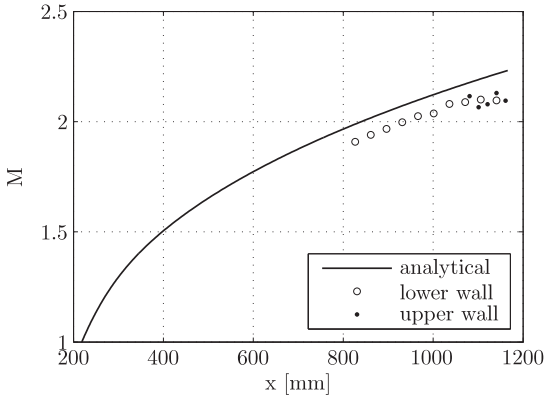

Figure 2: Typical Mach number axial evolution throughout the whole nozzle divergent (p_0=4.2 bar)

Table 1: Mach number range, unit Reynolds numbers and test times of the wind tunnel

Mach number	unit Re 10^7 m^{-1}	test time [ms]	p_0 [bar]
1.55	3	600	3
1.72	3	800	3
1.93	4	750	4.2
2.12	4.6	1100	5

2.2. Assessment of wind-tunnel noise

As stated in the preceding, a quiet wind-tunnel must generate very low disturbances and these are mainly due to the turbulent boundary layer along the wind tunnel walls. However, also free-stream fluctuations play a role at supersonic Mach numbers and they are generated in the most upstream parts of the facility. Here are presented the results of the experiments made to assess the boundary layer status on the wind tunnel walls and the intensity of free-stream turbulence for different Mach numbers.

2.2.1. Assessment of the boundary-layer state on the wind-tunnel walls

One of the major features of a quiet wind tunnel should be a laminar boundary layer along the test section wall. If this is not possible throughout the entire test section, at least it should go as far downstream as not to radiate turbulence noise directly onto the test article. As stated in the introduction, the bleeding slots at the throat have been designed for this purpose. Then we had to assess the effectiveness of this design by looking at the state of the boundary layer on the

wind tunnel walls. This was done by measuring the shear stress on the tunnel walls using a novel technique, the thin oil film method [4].

The thin oil film method relies on the principle that the rate at which oil thins along a surface flown by a fluid is function of the wall shear stress due to the flow. This principle, in turn, relies on the thin-film theory which, thence, represents the mathematical foundation of the technique here tried.

Squire, one of the principal contributors to thin-film theory, demonstrated that oil flows in the direction of the boundary layer skin friction, except near separation. (In this latter case, in fact, it tends to indicate separation earlier than in the absence of oil.) His model of the motion of the thin film in two dimensions is

$$\frac{\partial h}{\partial t} + \frac{\partial h U_c}{\partial x} + \frac{\partial h W_c}{\partial z} = 0 \tag{1}$$

with h the oil film thickness, and U_c and W_c the oil velocities averaged along the x and z directions. Expression for U_c and W_c were derived from the momentum equations in the same way. Here this derivation is presented for U_c.

The convection (inertial) term in the momentum equation of the oil moving under the effect of the flow, and the velocity gradients in the directions other than the normal to the surface are neglected. The resulting simplified equation is integrated twice with the boundary conditions that oil velocities are equal to those in the boundary layer at the surface of the oil, that the viscous stresses in the oil and the air are equal at the oil/air surface, and that at the body surface the oil is stationary. The results is this expression for oil velocity

$$u = \frac{1}{\mu}\left(\frac{\partial P}{\partial x} - \rho g_x\right)\left(\frac{y^2}{2} - hy\right) + \frac{\tau_w}{\mu} y \tag{2}$$

The oil velocity then becomes function of: the pressure gradient and the volume forces in the direction of the oil motion; viscosity and the wall shear stress; and film thickness, h, along with the height above the surface $y \in [0 \div h]$. Now taking the average over y of the velocity one obtains an expression without dependency on y, i.e. for U_c

$$U_c = \frac{\tau_{w,x} h}{2\mu} - \frac{h^2}{3\mu}\left(\frac{\partial P}{\partial x} - \rho g_x\right) \tag{3}$$

Repeating the same analysis for the z-direction yields

$$W_c = \frac{\tau_{w,z} h}{2\mu} - \frac{h^2}{3\mu}\left(\frac{\partial P}{\partial x} - \rho g_z\right) \tag{4}$$

Introducing both Eqs. 3 and 4 in Eq. 1 one obtains the equation

$$\frac{\partial h}{\partial t} + \frac{\partial}{\partial x}\left[\frac{\tau_{w,x} h^2}{2\mu} - \frac{h^3}{3\mu}\left(\frac{\partial P}{\partial x} - \rho g_x\right)\right] + \frac{\partial}{\partial z}\left[\frac{\tau_{w,z} h^2}{2\mu} - \frac{h^3}{3\mu}\left(\frac{\partial P}{\partial x} - \rho g_z\right)\right] = 0 \tag{5}$$

which, considering that the effects of pressure gradient and volume forces are often negligible, finally reads

$$\frac{\partial h}{\partial t} + \frac{\partial}{\partial x}\left[\frac{\tau_{w,x} h^2}{2\mu}\right] + \frac{\partial}{\partial z}\left[\frac{\tau_{w,z} h^2}{2\mu}\right] = 0 \tag{6}$$

Tanner, afterwards, completed the theory and made it more usable by assuming that the oil film profile depends only on the shear stress variation in x [4, and refs. therein] as

$$h = \frac{\mu}{t\sqrt{\tau_w}} \int_0^x \frac{dx}{\sqrt{\tau_w}} \tag{7}$$

here h is the height of the oil film at x and time t. This equation then becomes trivial if the shear stress at the wall can be considered constant in x varying from 0 to L:

$$h = \frac{\mu L}{t\tau_w} \tag{8}$$

It is thus possible to deduce τ_w from the slope of the oil surface because Eq. 8 will hold near the leading edge of the moving film for any shear stress distribution. Finally, small distributed oil droplets, instead of a uniform film over the entire surface, allow to consider the wall shear stress constant so to comply with the assumption at the basis of Eq. 8.

Since the measurements are done on one part of the nozzle divergent, the boundary layer flow is subject to a non-negligible favorable pressure gradient, thus a check of the above derived equations validity with this new term accounted for was in need. An order-of-magnitude analysis of Eq. 5 confirmed that, despite the pressure gradient term increased its relative weight, it was still one order of magnitude lower than the wall shear-stress term. This means that the equation of the thin film theory is still valid and can be applied also for the wall shear stress measurement on the current case.

In practice, every test consisted in putting dots on the surface of the lower ramp constituting a part of the

divergent of the nozzle, and recording their deformation by means of a high-speed camera viewing from one side into the facility (Fig. 3). In every test a variable number of dots arranged on one or two rows was layered.

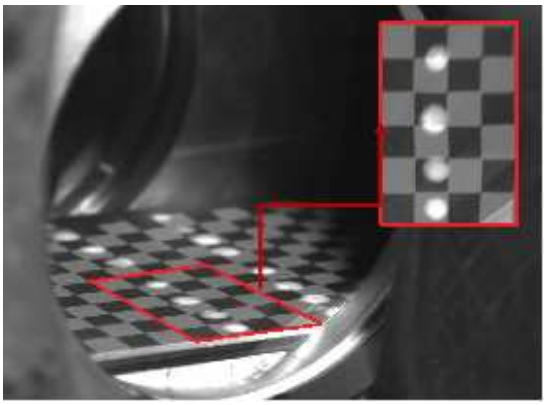

Figure 3: Oil dots on a checkered area for the reference image

In order to accurately analyze the recorded temporal evolution of the dots, an algorithm was developed in Matlab®. It reads the high-speed-camera video frame by frame, implements a correction to the images distorted by the non-orthogonal view, selects a specific dot on the initial frame, and computes the deformation of that dot throughout all the frames, i.e. in time, up to the test end. In this way Eq. 8 can be applied to extract the wall shear stress value.

To obtain the area and the longitudinal deformation of the dot in S.I. units a reference image with a chessboard over the surface is used (Fig. 3). It also served for the image correction mentioned above.

A total of six tests was performed and the main results are presented in Fig. 4

Here, one sees the experimental results for each dot on a row (+) and their average over the row (o) compared with CFD laminar calculations of the flow in the divergent of the nozzle. ε is the difference between the average value and the CFD reference value for the same position along the nozzle. It is evident that the measurements lay always below the computed laminar values so to allow the conclusion that the boundary layer is not turbulent, i.e. it is laminar. This result was found also for M_∞ equal to 2 and 2.2. The oil-dot technique then proves itself a simple yet useful way to assess the boundary layer status, but not yet a technique for shear stress measurements because of the still high inaccuracy shown by Fig. 4. In the end one can conclude that this serious source of noise is avoided in the present supersonic facility, and it was

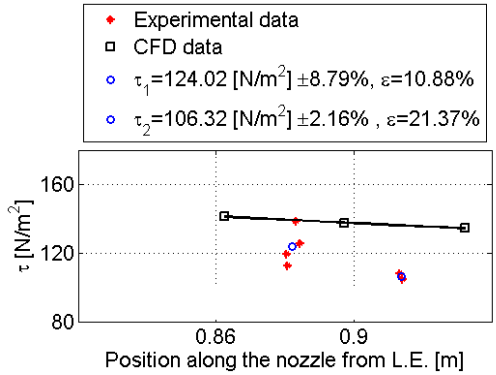

Figure 4: Measured shear/stress values at two different locations (M_∞ = 1.9)

only left to measure the other important one: the free-stream turbulence intensity. This is presented in the next subsection.

2.2.2. Hot-wire measurements of free-stream turbulence intensity

The free-stream turbulence measurements consisted in the measurements of the mass-flow fluctuations, and were made by a double hot-wire probe mounted on a boom on the axis of the test section (see Fig. 5). The hot-wires were of the constant-temperature type, Platinum-coated, 3-mm long, and had a diameter of 9 μm. Only the wire with the highest over-heating ratio (R_w/R_a = 1.6) was used for the measurements. The hot-wire electronics allowed a maximum frequency resolution of 20 kHz. A total of seven tests was performed.



Figure 5: The double hot-wire in the test section

The hot-wire calibration was made *in situ*, i.e. at the

same time as the measurements. The mean flow quantities in each test were calculated from p_0, p and T_0 measurements, and time intervals in which they were mostly constant were singled out of the entire test duration. Then, the mean values of ρU were plotted against the corresponding hot-wire voltage outputs so to have a calibration curve of the type $E^2 = A + B(\rho U)^{0.5}$ for each test. From this calibration function, the inverse function $(\rho U) = f(E)$ was obtained and applied to the time-dependent hot-wire output to get the values of the mass-flow fluctuations $\rho U'$.

The upper limit of the fluctuations frequency range, as stated in the preceding, was set by the electronics used at 20 *kHz*, whilst for the lower limit some considerations had to be done. It has been soon evident that the entire facility vibrated during each test, and so did the boom hosting the hot-wire. These low-frequency mechanical vibrations were however recorded by the hot-wire as flow fluctuations and thus they had to be removed from the hot-wire measurements during the signal post-processing. An estimation of the range of these vibrations has been possible thanks to some previous tests made with a flat plate mounted as a cantilever in the test section and equipped with an accelerometer (Figs. 6 and 7). The frequency spectrum of the plate mechanical vibrations is reported in Fig. 8. Even if the mechanical system composed by the plate and its supporting beams differed from that comprised of the boom and its support (the attachment to the wind tunnel was the same, instead), we considered the accelerometer data still as a good estimation of the mechanical vibrations suffered by the hot-wire.

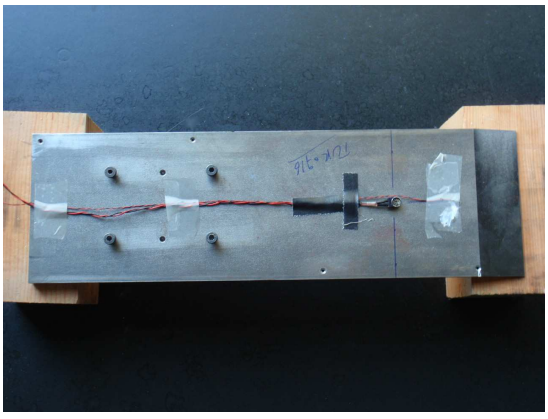

Figure 6: The accelerometer used for mechanical-vibrations measurements glued on the flat plate

One can see that the strongest vibrations occur for a frequency less than 700 *Hz*, thus this value has been used as the lower limit of the $\rho U'$ frequency range.

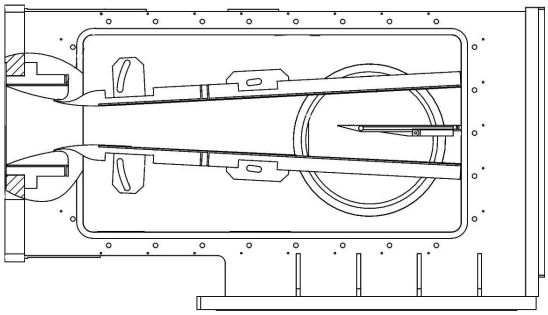

Figure 7: The flat plate with the accelerometer in the test section

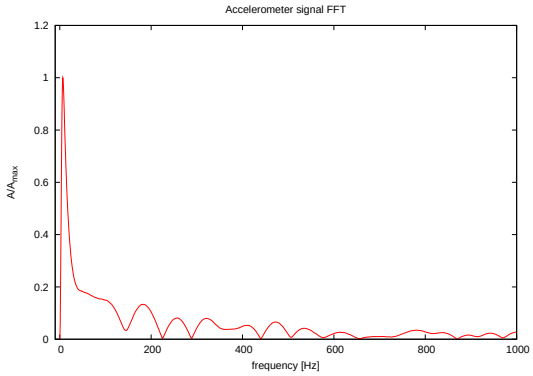

Figure 8: Frequency spectrum of mechanical vibrations of a flat plate in CT2

In conclusion, the free-stream mass-flow intensities measured in the frequency range [700÷20000] *Hz* are reported in Table 2 for two different Mach numbers. These values are reported in Fig. 9 where they can

Table 2: Free-stream mass-flow fluctuations

M_∞	unit Re 10^7 m^{-1}	$\rho U'$ $\frac{RMS}{\rho U}$
1.72	3	0.63%
1.93	4	1.14%

be compared with data form other supersonic facilities. Here are shown (linked by lines) data measured in the 1960' in a JPL supersonic quiet wind tunnel as reported in [5], plus additional data about free-stream mass-flow disturbances in the Russian ITAM wind tunnels T313 and T325. The JPL wind-tunnel features a 1%-turbulence settling chamber with four screens and one air filter; the ITAM T325 features a settling chamber with honeycomb, ten screens, and

a not-further-detailed noise–reduction system, whilst the T313 is reported as conventional.

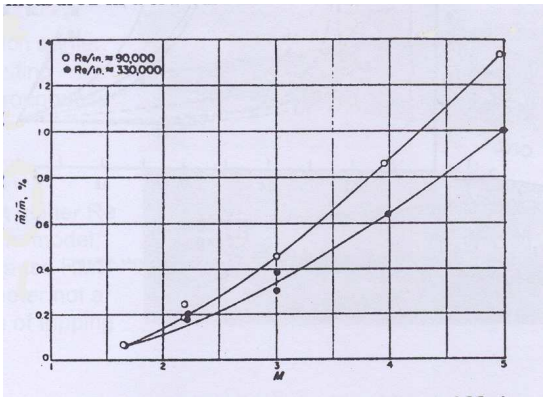

Figure 9: Variation of mass-flow fluctuations with free-stream Mach number, [5]

Regarding the JPL data, the curve of interest for the comparison is that for the unit Reynolds number equal to $(1.3 \cdot 10^7 m^{-1})$ that features an interpolated value of about 0.1% for the Mach numbers tested in the present work. This means that the values measured are six to ten times those of this quiet wind tunnel. These values are typical of non-quiet wind tunnels, like confirmed by the value from the ITAM T313, even if at a higher Mach number, and by the values of the T325 used at transonic conditions; in this latter case, the T325 resulted noisier than as operated at supersonic conditions. In effect such a result does not come as a surprise: in the present wind tunnel there are none of the low-turbulence-level characteristics of the JPL and ITAM facilities.

The modifications to the facility general layout needed to implement these characteristics, in fact, would affect the compression tube itself, its air inlet from the high-pressure supply system, and its outlet to the test section, so that the entire structure of the wind tunnel would be heavily changed. This change could then conflict with the actual primary purpose of the wind tunnel, which is turbo-machinery air-foil testing, and for this reason has not been implemented so far.

3. Pressure-Sensitive-Paint measurements: pressure field around a roughness in a supersonic boundary layer

The first test campaign to be performed in the qualified wind tunnel aimed at proving the capabilities of a rather interesting non-intrusive pressure-field measurement technique: the Pressure Sensitive Paint, [6]. This technique consists in laying on the surface, whose pressure is to map, a special paint that consists of luminescent molecules in an oxygen-permeable binder. During the measurement these molecules are excited by an external pulsing light source (e.g., lasers, LEDs, or a gas discharge lamp) and start emitting light at a wavelength larger than that of the excitation. The physical phenomenon that makes the pressure measurement possible is that the intensity and luminescent lifetime of the emitted light are sensitive to the ambient concentration of Oxygen, which is proportional to the Oxygen partial pressure, which in turn is proportional to the local static pressure of the flow. Therefore, one can recover the local static pressure on each point of the PSP-coated surface by detecting the emitted light (by photomultiplier tubes or digital cameras) and by using the following Sterner-Volmer equation to relate its intensity or lifetime to static pressure and values taken at a reference condition

$$\frac{I_{ref}}{I} = \frac{\tau_{ref}}{\tau} = A(T) + B(T)\frac{p}{p_{ref}} \qquad (9)$$

In Eq.9 I is the light intensity, τ the lifetime, and p the static pressure. A and B are the Sterner-Volmer coefficients and must be obtained by the calibration of the paint. They both depend on the paint temperature because of the *"Oxygen quenching"* that alters the paint response as the temperature increases. This effect consists in the luminophore molecule returning to the un-excited state by colliding with an Oxygen molecule instead of by emitting light. The intensity of this quenching is directly proportional to the concentration of Oxygen in the paint binder, which in turn is directly proportional to the binder permeability to Oxygen. This finally is directly proportional to paint temperature according to an Arrhenius relationship [6, and reference therein].

The intensity method is the most straightforward. A continuous illumination excites the paint, and a camera records the intensity of the paint emission. The camera has a filter to avoid the mixing of the light emitted and the light just reflected by the paint. This technique requires a normalization of each image with a "wind-o" reference in order to compensate variations in the local paint properties, e.g. thickness or luminophore concentration.

The lifetime technique is more complex and only recently has became attractive because of the improvements in camera sensitivity and dynamic range. In practice, lifetime measurements are (often) carried

out using a pulsed illumination and a gated CCD camera that acquires at least two subsequent images, some (one) during and some (one) after the excitation. Each image is an integration of the paint emission intensity over the camera gate time. The intensity ratio computed from the image taken after the excitation and that taken during is proportional to the emission lifetime, thus to the static pressure as from Eq. 9.

During the present investigation both the intensity and lifetime techniques were investigated, so the binary PtTFPP/FIB PSP paint, by Innovative Scientific Solutions Inc. (ISSE), was calibrated for both of them.

3.1. PSP calibrations for the lifetime and the intensity methods

The calibration setup consisted of five pulsed high-power LEDs as light source; two long-pass optically-filtered LaVision Imager Intense CCD cameras as a detector (during the first calibrations);and the sample model painted with the PSP . The latter was equipped with electric heaters and a thermocouple to calibrate in the temperature range $T \in [0 \div 60]\ ^0$C. This range was selected by accounting for the maximum recovery temperature of the flow during the supersonic tests of the paint, i.e. the maximum temperature experienced by the paint during the short-duration tests. The sample was placed in a vacuum chamber instrumented with a pressure tap and with an inlet from an air pump to set the pressure values for the calibration (Fig. 10).

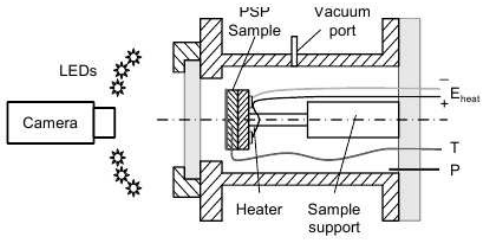

Figure 10: Sketch of the calibration setup

Two samples with twelve and fifteen layers of paint were used to assess paint thickness effect. Pressures ranging from about 10^4 *Pa* to ambient pressure were tested. Twenty pairs of images were taken for each calibration point.

In case of the lifetime calibration and in order to nd the optimum timing for the cameras a large number of gate combinations and durations were tested. The best results were obtained for a rst exposure of 400 μs that was started 100 μs after the beginning of the LED light pulse. The illumination was switched o after 500 μs. At this moment the exposure of the second camera began. In order to integrate over the complete exponential decay, the length of exposure two was set to 200 μs.Selected data sets and the mean calibration curve obtained with the life-time technique are shown in Fig. 11

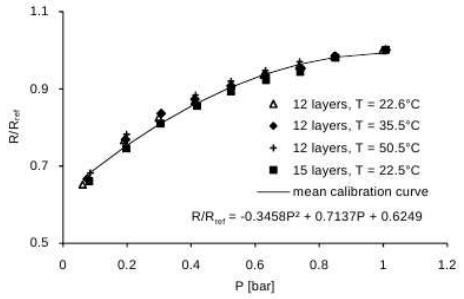

Figure 11: Calibration of binary PSP for dierent sample temperature and paint thickness(lifetime method)

The ratio *R* between the image taken before and that taken after the paint excitation was normalized with the ratio at 1 *bar*, R_{ref}. Figure 11 shows that neither a variation of the sample temperature nor a change of the paint thickness lead to a meaningful discrepancy between the mean calibration curve and the data points.

In case of the intensity calibration the results are summarized by Fig. 12. Now the two sets of data points illustrate the good reproducibility of the calibration. The higher intensities of these images lead to a better signal-to-noise ratio, hence to a fair agreement with the mean calibration curve. A quadratic least square fit was applied resulting in a regression coefficient, *R*2, of 0.9985.

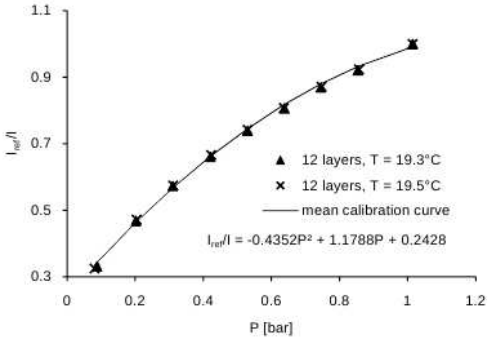

Figure 12: Calibration of binary PSP for dierent sample temperature and paint thickness(intensity method)

3.2. PSP test results

The tests consisted in mapping the pressure field generated by a single roughness element ($h \times w \times l = 5 \times 4 \times 4\ mm^3$) glued onto the lower nozzle-wall and invested by a $M_\infty = 1.8$ flow (Fig. 13). The pressure sensitive paint was applied around and downstream of the roughness by the use of an airbrush. Thin layers of paint were alternately applied in left-right and up-down passes until a uniform layer was achieved. The pressure taps were not covered in order to maintain a smooth surface. Since very thin layers of paint were applied, the inlets of the static pressure taps were only very slightly aected and could still serve efficiently for obtaining the static pressure evolution along the nozzle. One pressure tap was equipped with fast reference pressure transducers to allow assessing the paint temporal response to the pressure drop at the beginning of the test.

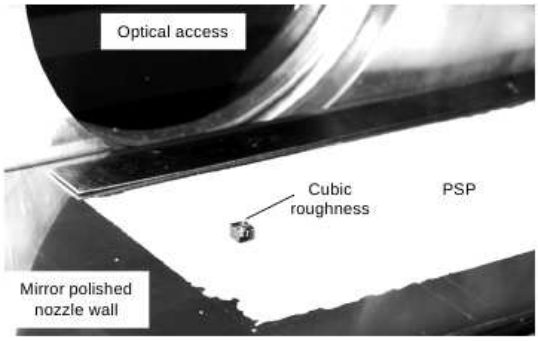

Figure 13: The PSP applied around a cubic roughness

Figure 14 shows the pressure map by the intensity method and Fig. 15 that by the lifetime method.

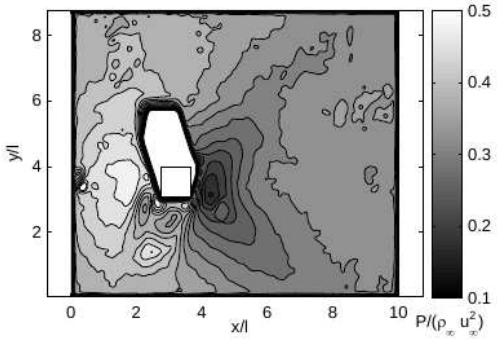

Figure 14: PSP map of the static pressure field around a single roughness element in a $M_\infty = 1.8$ flow, $l = 4\ mm$ (intensity method)

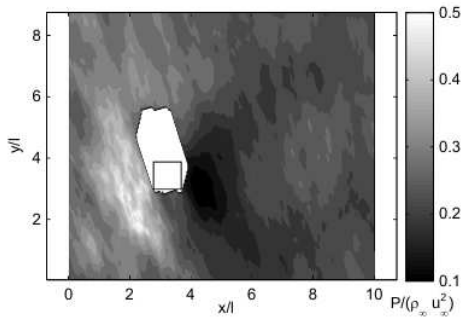

Figure 15: PSP map of the static pressure field around a single roughness element in a $M_\infty = 1.8$ flow, $l = 4\ mm$ (lifetime method)

In both pictures the static pressure values are expressed relatively to the dynamic pressure. The image of the roughness looks very elongated because of the geometrical correction needed by the non-orthogonal angle of view of the cameras; the square drawn at the basis of this white zone signals the right position of the roughness respect to the pressure field.

In Fig. 14 the pressures range from approximately 250 *mbar* in the wake of the roughness to about 1000 *mbar* in the stagnation region upstream of the cuboid. The high pressure region has a semi-circular shape most likely due to the detached bow shock in front of the roughness. The triangular low pressure branches emanating at an angle of approximately 45 deg from the rear corners of the cuboid are likely related to an expansion into the wake. That is, the flow is displaced by the roughness and its wake, because as the streamlines go around the cuboid they acquire a convex curvature that leads to an expansion. Further downstream they turn to a concave curvature tending to the centreline and turning in the stream-wise direction of the mean flow-field. This in turn leads to a compression of the flow. Throughout this compression the pressure increases gradually and adapts to the mean static pressure downstream of the roughness. The low pressure regions get narrower with span-wise distance from the centreline because the displacement effect of the roughness, and hence the curvature of the streamlines, is weaker and weaker. Finally, the very low pressure at the back of the roughness indicates the typical recirculation zone to be expected in that position.

The same qualitative pattern as in Fig. 14 is observed in the pressure map shown in Fig. 15. Although the spatial resolution can be considered still good, camera sensitivity had to be sacrificed. This led

to a reduced signal-to-noise ratio that caused less distinctive pressure contours and an underestimation of the overall pressure levels if compared to the intensity measurements. However, in the end the stagnation region upstream and the low pressure footprint downstream of the rectangular roughness, i.e. the major features of the flow, can still be identified.

The difference in the results from the two methods is because the experiments were performed with the same hardware. For the intensity based method, long, i.e. hardware-wise less-demanding, camera exposures, were required and the hardware was capable of a good signal to noise ratio. For the lifetime method, instead, shorter exposures were needed and the hardware performed with a lower signal to noise ratio.

The intensity method allows a longer time during which the camera can integrate the paint luminescence and, in the end, yield a higher signal levels, thus a better pressure resolution. The lifetime method, instead, requires (kept the hardware, i.e. the camera, the same) a stronger conditioning of the data in the post-processing of the images. This consisted in a more important *"binning of the pixels"*, that is, the combination of the signal from some adjacent pixels into one single signal. For the intensity method combining four pixels was enough, while for the lifetime method thirty two had to be combined. This explains then the coarser aspect of the pressure map by the lifetime method.

4. Conclusions & future work

The supersonic wind tunnel has been qualified and its performance, state of the boundary layer, and free-stream turbulence levels assessed. In this process and in the first test campaign it demonstrated the possibility of multiple Mach numbers in the range of unit Reynolds number $[3 \div 4.6] \cdot 10^7\ m^{-1}$. The boundary layer on the ramps constituting the lower and upper part of the nozzle divergent was found laminar, which indicates that noise will not radiate from them. Conversely, the free-stream mass-flow fluctuations were found high for the strict quiet-wind-tunnel standards, but in the same range as a normal, non-quiet one.

The good optical access onto the wind tunnel has made possible Pressure Sensitive Paint measurements, which gave noticeable results just limited by the hardware at disposal in case of the lifetime technique.

Future work will still focus on supersonic testing of the single roughness effects on a supersonic boundary layer but using different measurement techniques. Thin-films will be used for heat-flux measurements and piezoelectric-electric sensors (PCBs) for unsteady-pressure measurements. Both of these measurements will be performed at different wall temperatures and for roughness of different height.

Acknowledgments

The work here presented would have been much harder and longer without Mr. Peter Schreivogel taking care of the PSP experimental campaign, Mr. Glauco Bonfanti taking care of the development of the oil-dots experiments, Dr. T. Yasa setting up the hot-wire experiments, and, finally, Mr. Pierre Londers taking care of the wind-tunnel mounting and operations.

This work was performed within the Long-Term Advanced Propulsion Concepts and Technologies II project investigating high-speed transport, LAPCAT II, coordinated by ESA-ESTEC, and supported by the EU within the 7th Framework Program, Theme 7 TRANSPORT, Contract no.: ACP7-GA-2008-21 1485.

References

[1] S. V. Murthy, F. W. Steinle, On boundary layer transition in high subsonic and transonic flow under the influence of acoustic disturbances and free-stream turbulence, in: AIAA 85-0082, 1985.

[2] S. R. Pate, Effects of wind tunnel disturbances on boundary-layer transition with emphasis on radiated noise: A review, in: 11th Aerodynamic Testing Conference, Colorado Springs, Colorado/March 18-20, 1980.

[3] W. Harvey, Influence of free-stream disturbances on boundary-layer transition, Tech. rep., NASA (1978).

[4] G. Bonfanti, Development of oil-dot visualization technique for wall shear stress measurements, Research Master project 2011-07, von Karman Institute for Fluid Dynamics (2011).

[5] S. Schenider, Survey of boundary-layer transition for hypersonic applications, 2011.

[6] P. Schreivogel, G. Paniagua, H. Bottini, Pressure sensitive paint techniques for surface pressure measurements in supersonic flows, Experimental Thermal and Fluid Science in publication (in publication) in publication.

Modeling and Analysis of the Laminar to Turbulent Transition in a Low-pressure Turbine

Jayson Babajee

Turbomachinery and Propulsion Department, von Karman Institute for Fluid Dynamics, Belgium, jayson.babajee@vki.ac.be

Supervisor: Tony Arts

Professor, Head, Turbomachinery and Propulsion Department, von Karman Institute for Fluid Dynamics, Belgium, arts@vki.ac.be

University Supervisor: Francis Leboeuf

Professor, LMFA (Laboratoire de Mécanique des Fluides et d'Acoustique), France, Francis.Leboeuf@ec-lyon.fr

Abstract

The present study focuses on the assessment and the validation of the Langtry-Menter γ-$\widetilde{Re}_{\theta t}$ correlation-based transition model, recently implemented in the RANS code elsA from ONERA. The test cases are two Low-Pressure Turbine (LPT) rotor blades, with the same compressible Zweifel loading coefficient but different load distributions. The corresponding experimental results are provided by the von Karman Institute. The outlet isentropic Reynolds number, based on blade chord and outlet isentropic velocity, ranges from 60000 to 250000 in order to investigate the complex separation-induced transition phenomenon occurring at low Reynolds number cruise condition. The turbulence intensity is the natural freestream turbulence of the facility (0.9%). The numerical test campaign provides good predictions, particularly when accurately tailoring the trailing edge and wake regions of the mesh. The numerical mass-averaged kinetic losses are in good agreement with the experimental ones. Moreover, the flow topology parameters (the transition onset, the transition end and the separation) show good agreement in comparison to the experimental results and correlations from the open literature. One is even able to detect separation-induced transition with reattachment before the trailing edge at the lowest Reynolds number. However, the authors stress the turbulence Reynolds number effect on the prediction of separation-induced transition for strong diffusion LPT blades and particularly when the flow is subjected to a long bubble or even an open separation.

Keywords: Low-Pressure Turbine, Separation-Induced Transition, Reynolds number, Turbulence, Correlation

Nomenclature

Acronyms

AGS	Abu-Ghannam and Shaw transition criterion
HL	High-Lift
H&W	Hatman and Wang
LPT	Low-Pressure Turbine
RANS	Reynolds-Averaged Navier-Stokes
TD	Extrapolated "S1" decay of turbulence

Symbols

c	Chord
E	Destruction term of transport equation
g	Pitch
H	Shape factor
k	Turbulent kinetic energy
k_l	Laminar kinetic energy
$l.e.$ / LE	Leading edge
M	Mach number
P	Production term of transport equation
P_0	Total Pressure
R	Radius
Re	Reynolds number
Re_t	Turbulence Reynolds number
Re_θ	Momentum thickness Reynolds number
$Re_{\theta c}$	Critical momentum thickness Reynolds number

$\widetilde{Re}_{\theta t}$	Local transition onset momentum thickness Reynolds number (transported variable)
Re_v	Vorticity Reynolds number
s	Curvilinear abscissa
s_0	Suction side TE curvilinear abscissa
t	Time
T	Period
$t.e.$ / TE	Trailing edge
Tu	Turbulence intensity [in %]
U / V	Velocity
x	Axial coordinate
y	Wall distance

Greek symbols

β	Flow angle (referred to axial direction)
γ	Intermittency
ζ	Mass-averaged kinetic losses [in %]
θ	Momentum thickness
λ_θ	Pressure gradient parameter
μ	Molecular viscosity
μ_t	Turbulent eddy viscosity
ρ	Density
σ_f	γ-transport equation diffusion coefficient
$\sigma_{\theta t}$	$\widetilde{Re}_{\theta t}$-transport equation diffusion coefficient
τ_{wall}	Wall shear stress
Ψ	Compressible Zweifel loading coefficient
ω	Specific turbulence dissipation rate
Ω	Rotational speed
ΔH	Total enthalpy variation across the rotor blade
ΔV_θ	Tangential velocity variation across the rotor blade

Subscripts

ax	Axial
eff	Effective
end	End of transition
is	Isentropic
$onset$	Onset of transition
sep	Separation
γ	Intermittency
θt	Momentum thickness at transition onset
1	Inlet condition
2	Outlet condition

1. Introduction

The main topic of this study is to analyze the laminar to turbulent transition mechanisms that occur in a LPT. For this purpose, one can evaluate the work done on the rotor in a pure axial machine with the turning of the flow from the Euler's momentum equation:

$$\Delta H = \Omega \cdot R \cdot \Delta V_\theta \tag{1}$$

A standard LPT is usually made of several stages (4 stages in the case of the CFM56-7B). LPTs commonly operate at an outlet Mach number in the range from 0.6 to 0.9 and weight 20% to 30% of the overall mass of the engine [1]. Thus, the aim is not to manufacture more powerful and heavier aero-engines such as an industrial gas turbine but to get the most efficient one in terms of power with respect to weight and losses mainly. At a first sight, one solution is inevitably to reduce the weight of the LPT by reducing the number of blades. This implies an increase of the pitch-to-chord ratio (g/c). This entails a more important loading per blade in order to compensate for the lower number of working blades for a given stage loading. As a consequence, the velocity suction peak will be higher as well as the diffusion over the rear part of the suction side. Nevertheless, one has to be aware, for this study, of the separation and transition phenomena. This conveys the importance of the Reynolds number (Re) since the current LPT operating Reynolds number is below 100000 at cruise conditions and more than 400000 at take-off. This shows the wide operating conditions of a LPT and above all the changing flow conditions as highlighted by Hourmouziadis [2]. This is why the study of the transition mechanisms is of interest because in the case of open separation, the flow topology is not as the one predicted by standard ideal model.

Therefore, the main aim of this work will be to assess the γ-$\widetilde{Re}_{\theta t}$ transition model of Langtry and Menter [3] on two HL-LPT rotor blades (where "HL" stands for "High-Lift" and is mainly characterized by the tendency to decrease the number of blades per row and consequently to increase the loading per blade).

2. Transition and Separation Phenomena in LPT

Transition occurs due to the amplification of instabilities in the boundary layer. The main factors to consider are the Reynolds number, the turbulence intensity, the turbulence scales and the pressure gradient.

2.1. Steady Transition

Even though a LPT environment is rather unsteady, one still needs to define the fundamental physics behind steady transition since most of cascade investigations in wind tunnels are carried out under steady

conditions. There are four kinds of transition (the natural transition, the by-pass transition, the separation-induced transition and the reverse transition (relaminarization)).

In LPT cases, the last three cases are of interest since natural transition only occurs at very low turbulence levels (below 0.1%). In the by-pass transition, transition occurs due to disturbances that lead directly to the formation of turbulent spots by by-passing the growth of Tollmien-Schlichting waves. Basically, those disturbances are characterized by a high turbulence level. In the separation-induced transition, the flow is subjected to a separation bubble which is mainly caused by an adverse pressure gradient and depends on the Reynolds number as well. Then, at low Reynolds numbers and with a strong diffusion (which is the case of HL-LPT), the laminar boundary layer separates and the transition process occurs in the free shear layer. However, depending on the Reynolds number and on the turbulence intensity and scales, the reattachment process may not happen, leading to an open separation which is the worst case in terms of losses. There are three separated flow modes according to the work of Hatman and Wang [4]. Those are the transitional separation mode, the laminar separation/short bubble mode and the laminar separation/long bubble mode. At last, the reverse transition is typically a way back from a turbulent flow to a laminar one which occurs in region of very strong acceleration such as the rear part of the blade pressure side.

2.2. Multimode Transition

This type of transition is an unsteady phenomenon. It is a realistic illustration of the turbomachinery environment where the wakes from a blade row impinge on the following blade row while triggering the transition or inhibiting separation. Actually, the growth of turbulent spots, after the impingement of a wake on the suction side of a blade, implies the occurrence of calmed regions which are less sensible to disturbances. They present the advantages of the laminar and turbulent regions without their respective drawbacks [5]. The effectiveness of these calmed regions was illustrated in [6; 7]. This region follows the turbulent region at a lower velocity as shown in the work of Schubauer and Klebanoff [8]. They highlighted that the flow starts to be very stable and no breakdown seems to occur from the spot tail. Moreover, the interest of this calmed region is seen in the distance-time diagram (Fig. 1). The difference between the leading and trailing edge velocities of this region insures the development of a laminar look-alike region.

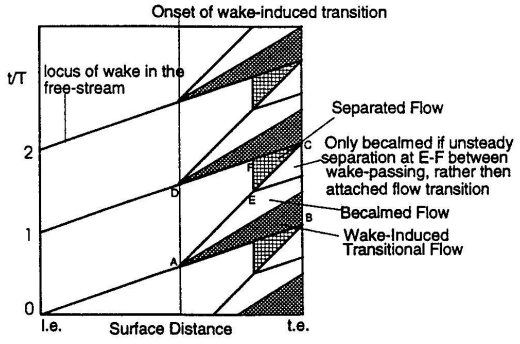

Figure 1: Time-space diagram of the turbulent spots (Schulte and Hodson [9])

2.3. Parameters Affecting Transition and Separation

At this point of the review, the most important factors affecting transition are the Reynolds number, the turbulence scales, the pressure gradient and the unsteady features of the incoming wakes. However, Mayle [10] depicted the existence of other factors which are less significant in terms of turbulent spot production rate than the pressure gradient such as the surface roughness. Moreover, other designs [11; 12; 13; 14] might be of interest such as transversal roughness elements, jets and plasma actuators.

3. Numerical Approach

To understand the phenomenon of separated-flow transition, one should get a large database in order to assess the findings on each configuration in the aim of making a universal model. However, it could demand a lot of effort since each configuration may be one of a kind and consequently will not infer the principle of universality. That is why data-driven correlations are still useful in predictive models based on trends. The cornerstone of those correlations is the momentum thickness Reynolds number (Re_θ). It is based on the momentum thickness (θ) which quantifies the portion of momentum flux loss due to the presence of the wall. It means that the momentum thickness will behave differently according to the nature of the flow in the boundary layer. That might be an explanation for the perpetual use of this parameter in the correlations. However, one drawback is its complicated assessment in a cascade configuration. Then, one sees the interest of the numerical approach to get more information about this critical parameter.

3.1. Transition Modeling

Most of the transition criteria are based upon empirical correlations [10; 15]. Those criteria are made non-local as they take into account the history of the boundary layer with the freestream information (turbulence intensity and pressure gradient). When the transition criterion is met, the so-called "intermittency weighting function" is switched on from 0 to 1 (like a step) and consequently triggers the production of the turbulent kinetic energy. However, despite its numerical definition, it still keeps the same qualitative meaning of the intermittency coefficient which is the fraction of time during transition for which the flow is turbulent. Besides, this kind of methodology implies the need for the boundary layer thickness calculation from the integration of the velocity profiles. Instead of triggering transition by a switch (via the intermittency weighting function), the transition process should be handled locally with a gradually evolving intermittency weighting function. That is why new methods for the computation of transition founded on transport equations (using local quantities) are of interest such as the γ-$\widetilde{Re}_{\theta t}$ model of Langtry and Menter [3]. Another transport equation transition model based on the laminar kinetic energy approach [16; 17] seems promising.

3.1.1. Correlation-Based Transport Equation Model

The γ-$\widetilde{Re}_{\theta t}$ model central idea is the van Driest and Blumer's vorticity Reynolds number concept [18]. It allows to link the transition onset momentum thickness Reynolds number to the local boundary layer quantities. The concept is depicted in Eqns. 2 and 3.

$$Re_v = \frac{\rho \cdot y^2}{\mu} \cdot \left|\frac{\partial u}{\partial y}\right| = \frac{\rho \cdot y^2}{\mu} \cdot S \tag{2}$$

$$Re_\theta = \frac{\max\left(Re_v\right)}{2.193} \tag{3}$$

In fact, this model gets rid of the integration of the boundary layer velocity profile along "computation lines" based on the wall mesh lines. Those velocity profiles were used to determine the onset of transition according to non-local transition criteria (such as the Abu-Ghannam and Shaw correlation [15]) in the sense that they are based on the turbulence intensity and the pressure gradient parameter estimated at the edge of the boundary layer.

The transport equation for the numerical intermittency (γ) is:

$$\begin{aligned}\frac{\partial(\rho\gamma)}{\partial t} + \frac{\partial\left(\rho U_j \gamma\right)}{\partial x_j} = \\ P_\gamma - E_\gamma + \frac{\partial}{\partial x_j}\left[\left(\mu + \frac{\mu_t}{\sigma_f}\right)\frac{\partial\gamma}{\partial x_j}\right]\end{aligned} \tag{4}$$

In their first publication, Menter et al. [19] did not disclose all their functions and particularly the F_{length} and the $Re_{\theta c}$ functions. At this time, it was known they were function of the transition onset momentum thickness Reynolds number ($\widetilde{Re}_{\theta t}$). That is why several groups throughout the world focused on the determination of these functions [20; 21; 22; 23]. At last, the originators of this transition model published their own version of these missing functions [3]. However, in this study, the CFD code elsA relies on the calibrations of those functions performed by Content and Houdeville [23].

The transport equation for the transition onset momentum thickness Reynolds number ($\widetilde{Re}_{\theta t}$) is:

$$\begin{aligned}\frac{\partial\left(\rho\widetilde{Re}_{\theta t}\right)}{\partial t} + \frac{\partial\left(\rho U_j \widetilde{Re}_{\theta t}\right)}{\partial x_j} = \\ P_{\theta t} + \frac{\partial}{\partial x_j}\left[\sigma_{\theta t}\left(\mu + \mu_t\right)\frac{\partial\widetilde{Re}_{\theta t}}{\partial x_j}\right]\end{aligned} \tag{5}$$

The purpose of this equation is to transform the non-local empirical correlation into a local quantity in order to compute the transition length function (F_{length}) and the critical momentum thickness Reynolds number ($Re_{\theta c}$), necessary for the numerical intermittency equation (Eqn. 4).

Then, when Re_θ (cf. Eqn. 3) exceeds locally $Re_{\theta c}$ (which is a function of $\widetilde{Re}_{\theta t}$), γ equals one due to the activation of P_γ in Eqn. 4. After, a function defines the effective intermittency γ_{eff} by the maximum value between γ and γ_{sep}. This latter separation intermittency coefficient (γ_{sep}) is part of a separation-induced transition correction that allows the local intermittency to exceed one. At last, γ_{eff} imposes the laminar regions locally and triggers the transition mechanism by turning on the production term of the turbulent kinetic energy transport equation because this transition model is coupled to the SST k-ω turbulence model. Besides, γ_{eff} affects the destruction term of the turbulent kinetic energy transport equation. The mentioned separation-induced transition correction is to let k to grow more rapidly once the boundary layer separates. This is the reason why it exceeds one.

3.1.2. Phenomenological Transport Equation Model

This laminar kinetic energy (k_l) model is based on the laminar fluctuation energy in the pre-transition region of the boundary layer as first introduced by Mayle and Schulz [24]. Their starting point was the fact that the laminar fluctuations preceding transition are primarily caused by the work of the imposed fluctuating free-stream pressure forces on the flow in the boundary layer. This framework has led several research groups to focus on this concept [16; 17]. Lardeau et al. [17] highlighted that the pre-transitional fluctuations leading to bypass transition are due to the presence of low-frequency/low amplitude streamwise vortices in the boundary layer. It turned out that the kinetic energy of the laminar fluctuations (k_l) can be described by a transport equation similar to the transport equation for the turbulent kinetic energy (k). The objective is to model the pre-transitional fluctuations with the k_l equation. Once a parameter including the kinetic energy is greater than some threshold level, the energy from the streamwise fluctuations k_l is transferred to the turbulent fluctuations [25]. Besides, the transition process is defined by a transfer of energy from k_l to k via the pressure-strain mechanism [16]. It is called "energy redistribution".

4. Results

In this section, the investigations of two HL-LPT rotor blades (T108 and T106C) are presented in terms of numerical methodology, comparison with experimental results and assessment of the γ-$\widetilde{Re}_{\theta t}$ model. A linear cascade configuration as well as the high speed, low Reynolds number VKI S1 wind tunnel facility are documented in Michálek et al. [26]. The main characteristics of the blades are provided in Tab. 1.

Table 1: Blades Characteristics

Blade	T108	T106C
c (mm)	98.42	93.01
c_{ax} (mm)	81.23	79.97
Pitch-to-chord ratio, g/c	0.90	0.95
β_1 (deg)	33.2	33.2
$\Psi{=}2 \cdot \frac{g}{c_{ax}} \cdot \frac{\lvert\rho V_\theta V_x\rvert_2 - \lvert\rho V_\theta V_x\rvert_1}{\rho_2 V_2^2}$	1.22	1.24
Configuration	Front-loaded	Aft-loaded
Diffusion Rate, D_R $D_R{=}\frac{\frac{V_{peak}-V_{2,is}}{V_{2,is}}}{\left\lvert\frac{s_{peak}-s_0}{s_0}\right\rvert}$	0.41	0.58
Velocity Ratio, $\frac{V_{peak}}{V_{2,is}}$	1.31	1.30
$M_{2,is}$	{0.5 ; 0.6}	0.65
$Re_{2,is}$ ($\times 10^3$)	[60 ; 160]	[80 ; 250]
$Tu_{l.e.}(\%)$	0.9	0.9
$Re_t = \frac{\rho k}{\mu \omega}$	[4.8 ; 12.7]	[6.7 ; 22.2]

4.1. Computational Methodology

In this paper, three-dimensional CFD simulations are carried out with the in-house ONERA code elsA (ensemble logiciel de simulation en Aérodynamique). The elsA software package is based on a cell-centered finite volume method for solving the Navier-Stokes equations. The space discretization relies on multi-block structured meshes. It allows the simulation of steady or unsteady flows, inviscid or viscous fluids, in fixed or moving frames. However, in this study, only RANS simulations with the Menter k-ω SST turbulence model are considered, coupled with the γ-$\widetilde{Re}_{\theta t}$ transition model. The use of the particular single-step case of the Runge-Kutta method for time integration, known as the "Backward Euler" time integration scheme is used. This scheme is coupled with a LU implicit phase technique. The space discretization scheme is a second order Roe scheme. The mesh topology is a periodic standard O4H with High Staggered corrections since the geometries are defined by high values of deviation (Fig. 2). The central O-mesh is around the blade and has at least 41 points in the perpendicular direction away from the blade surface. In the streamwise direction around the blade, the number of nodes is above 225 in order to get a good discretization of the suction side of the blade. The extension of the mesh in the spanwise direction is restricted to 5 layers and consequently symmetry

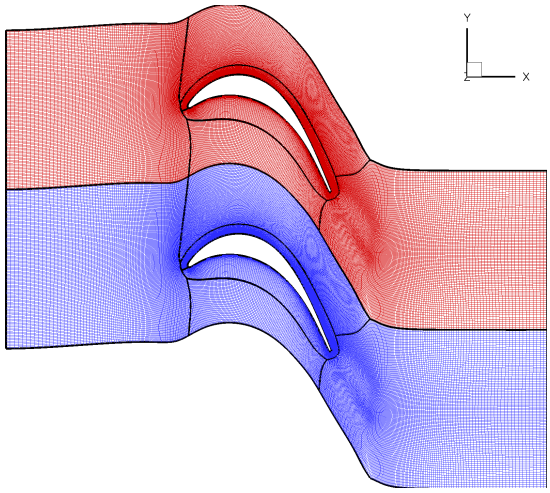

Figure 2: Mesh topology of T106C ($\Psi = 1.24$)

boundary conditions are used to define the pseudo-hub and -shroud. This saves a lot of computation time by focusing on the middle of the blade in order to apply convergence acceleration methodologies. As the study focuses on LPT blades which have high aspect-ratios, it is possible to avoid the calculation of the endwall regions. This is to mimic the experimental configuration where the measurements were taken at midspan. This methodology is referred as "2.5D". Thus, the aforementioned steady RANS "2.5D" γ-$\widetilde{Re}_{\theta t}$ model methodology is meant to be a prediction tool which could be used with an industrial prospect for blade design.

Before starting these test campaigns, a study of the mesh (not presented here for a lack of space) was carried out in order to assess the influence of the wake treatment. It turned out that the wake prediction could be too wide and not deep enough with respect to the experimental wakes (and consequently the mass-averaged kinetic losses). In fact, the cells downstream of the trailing edge of the blade should follow the flow direction. From this mesh strategy, the number of nodes for both configurations is 46605 in one streamwise layer. Moreover, y^+ values are below 1 through the Reynolds number ranges.

Concerning the computational inlet conditions for distant boundaries, one needs to provide turbulence and transition variables. About the transition ones, γ is set to 1.0 and $\widetilde{Re}_{\theta t}$ is determined by a correlation [3]. The turbulence variables (turbulent kinetic energy k and specific turbulence dissipation rate ω), at those inlet conditions, are incompletely known according to Spalart and Rumsey [27]. However, the decay of turbulence, ahead of the cascade, is available from the test campaign carried out at the von Karman Institute [26] where it was assessed behind a turbulence grid in the S1 facility. This "S1" decay law was compared to a decay law from Chassaing [28]. He described two phases of the decay of turbulence. The initial phase is defined as the prevalence of the eddies in the decay of turbulence (in the region downstream the turbulence grid). The final phase is defined as the prevalence of the dissipation in the decay of turbulence (far downstream the turbulence grid). In Fig. 3, one can see the good agreement between the two sets of decay of turbulence (the "S1" one and the initial phase one from Chassaing [28]). Then, since the turbulence intensity measured without any grid of turbulence (0.9%) is in between the initial and final phases but closer to the initial phase, an extrapolation of the "S1" decay law was done in order to get the input values (and particularly the dissipation rate) for the inlet boundary conditions. Thus, from this extrapolated "S1" decay law,

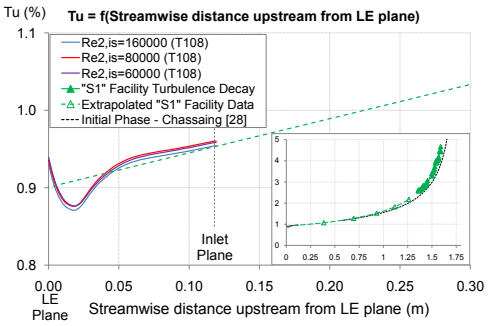

Figure 3: "S1" Decay of turbulence ahead of the cascade

it is possible to set the inlet boundary conditions according to the desired values at the leading edge plane. When assessing the CFD predictions of the turbulence evolution ahead of the cascade at several outlet isentropic Reynolds number ($Re_{2,is}$), one can see that the inlet boundary condition inputs enable the CFD predictions to match the experimental trends (Fig. 3). Then, this methodology for imposing the dissipation rate at the inlet boundary condition is adopted for this study. To give an order of magnitude, the Kolmogorov length scale for the T106C blade at $Re_{2,is} = 120000$, $M_{2,is} = 0.65$ and $Tu_{l.e.} = 0.9\%$ is 4.10^{-4} m for the CFD calculation whereas Michalek et al. [2010], who carried out the experimental investigation of this configuration, had 5.10^{-4} m.

Finally, a comparison between the well-used non-local transition criterion of Abu-Ghannam and Shaw (AGS) [15] and the newly implemented transition

transport equation model γ-$\widetilde{Re}_{\theta t}$ [3] was carried out in order to show the superiority of this transport equation model since both approaches are correlation-based but differ from the way the information is treated (non-locally or locally). Figure 4 shows this superiority with the isentropic Mach number (M_{is}) distribution along the suction side of the T108 blade. Besides, it has to be reminded that the correlation of Abu-Ghannam and Shaw [15], which is part of the framework behind the correlation used in Langtry and Menter transition model [3], is based upon experimental data which pressure gradient parameter (λ_θ) is between ±0.1. In the current study, the two HL-LPT rotor blades have a λ_θ that can be lower than −0.1.

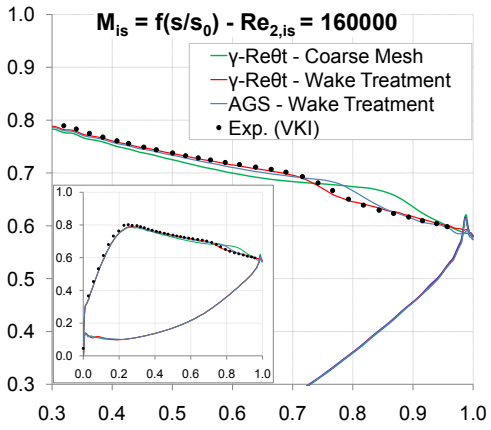

Figure 4: T108 comparison of γ-$\widetilde{Re}_{\theta t}$ model and AGS criterion at $Re_{2,is}$ = 160000, $M_{2,is}$ = 0.6 and Tu_1 = 0.9% (abscissa: s/s_0, ordinate: M_{is})

4.2. T108 Cascade

After setting up the methodologies of the study, one can focus on the T108 blade and the comparison with other research groups using different transition models and/or different methodologies. Corral and Gisbert [29] worked on this geometry with the γ-$\widetilde{Re}_{\theta t}$ model coupled with the RANS solver Mu^2s^2T. Their model features a $\widetilde{Re}_{\theta t}$-transport equation diffusion coefficient ($\sigma_{\theta t}$) equals to 10 and a s_1 function (which controls the reattachment location [30]) depending upon $\widetilde{Re}_{\theta t}$ and the distance to the wall. They performed 2D computations with a very fine unstructured mesh of 70000 points. Pacciani et al. [31] used the laminar kinetic energy concept coupled with the Wilcox k-ω turbulence model. They performed 2D computations with a non-periodic single-block O-type mesh of 57521 nodes. Benyahia et al. [32] used the RANS code elsA developed by ONERA. They worked on the implementation of the γ-$\widetilde{Re}_{\theta t}$ transition model and used it coupled with the Menter k-ω SST turbulence model. They performed 3D computations with a O4H structured mesh of 14545 points in one spanwise layer. The difference between Benyahia et al. [32] γ-$\widetilde{Re}_{\theta t}$ model and the one used in the present work is the value of the diffusion coefficient ($\sigma_{\theta t}$=10 in Benyahia et al. [32] and $\sigma_{\theta t}$=2 in the present work, value recommended by Langtry and Menter [3]). At last, the VKI experimental results [33] are provided.

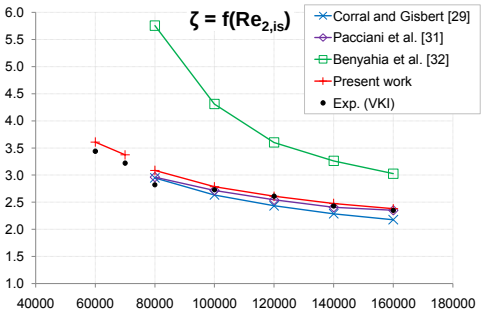

Figure 5: T108 mass-averaged kinetic losses (abscissa: $Re_{2,is}$, ordinate: ζ)

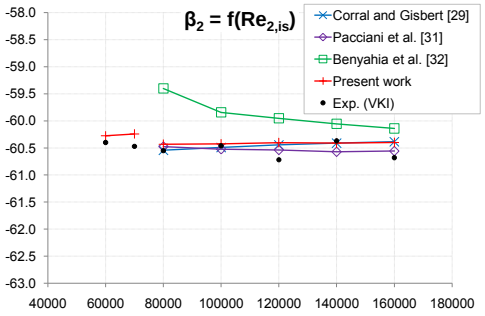

Figure 6: T108 mass-averaged outlet flow angle (abscissa: $Re_{2,is}$, ordinate: β_2)

The comparisons, in terms of mass-averaged kinetic losses (ζ) and outlet flow angle (β_2), are depicted in Figs. 5 and 6. From these figures, one can see that the present study predictions are in good agreement with the experimental measurements over the full $Re_{2,is}$ range. As a remark, the break in the $Re_{2,is}$ range is intentional since the two lowest $Re_{2,is}$ were performed in the facility at a lower outlet isentropic Mach number ($M_{2,is}$=0.5 instead of 0.6). From those trends, the similarity between the correlation-based transition model (Corral and Gisbert [29] and the present study) is remarkable even though the calibration parameters are not the same (such as $\sigma_{\theta t}$ and s_1). This could be a reason why an offset in the

trends is noticeable. However, this might be due to the different values of the turbulence Reynolds number ($Re_t = \mu_t/\mu = (\rho k)/(\mu\omega)$) used between the two groups to compute the dissipation rate at the inlet boundary condition. The quality of the mesh in both studies does not seem to imply any mesh dependency. This last point leads to the comparison between the present study predictions with the ones of Benyahia et al. [32]. Their predictions overestimate the experimental results, even though they got good predictions of the M_{is} distribution over the blade suction side. The reason is a question of mesh dependency since they used the coarsest mesh among all the presented studies and there is no apparent wake treatment or refinement in the wake vicinity. At last, the comparison with Pacciani et al. [31] predictions leads to a good matching. Since their laminar kinetic energy approach is intented to be based on more physical models, one can conclude on the reliability of the correlation-based transition model, used in this study, for this HL-LPT blade configuration. Moreover, the M_{is} distribution

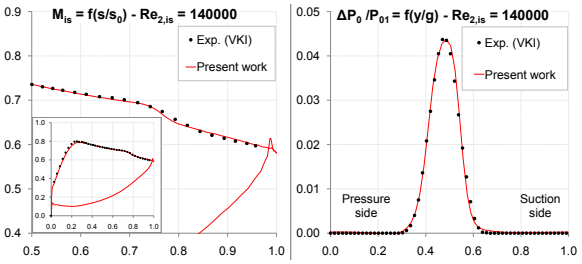

Figure 7: T108 isentropic Mach number distribution and wake profile at $Re_{2,is} = 140000$ (left abscissa: s/s_0, left ordinate: M_{is}, right abscissa: y/g, right ordinate: $\Delta P_0/P_{01}$)

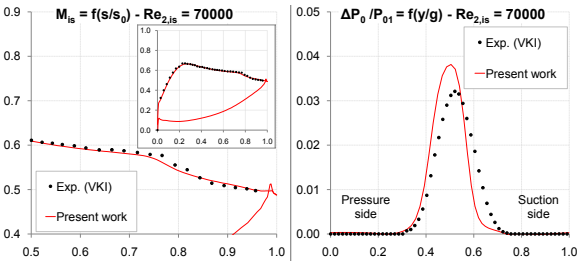

Figure 8: T108 isentropic Mach number distribution and wake profile at $Re_{2,is} = 70000$ (left abscissa: s/s_0, left ordinate: M_{is}, right abscissa: y/g, right ordinate: $\Delta P_{01}/P_{01}$)

over the suction side of the blade as well as the wake profile, extracted at $0.5 \cdot c_{ax}$ downstream the trailing edge, of two $Re_{2,is}$ (140000 and 70000) are provided (Figs. 7 and 8). From these plots, one can assess the fairly good wake predictions in terms of width and depth. The M_{is} distributions are pretty good as well in terms of pressure plateau, reattachment and Mach number level.

4.3. T106C Cascade

After the results of a front-loaded blade (T108) with a mild diffusion rate (Tab. 1), the study of an aft-loaded blade (T106C) with a strong diffusion is presented below. Like the former section, the same research groups worked on the T106C blade with the same methodology and numerical approach, except Benyahia et al [32] who used for the T106C a finer mesh with a wake treatment. Once again, the comparisons in terms of ζ and β_2 are illustrated (Figs. 9 and 10). This time, the ζ are well predicted up to

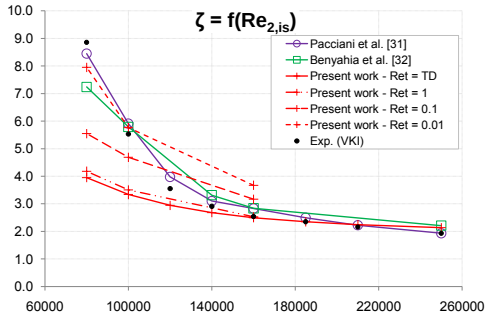

Figure 9: T106C mass-averaged kinetic losses (abscissa: $Re_{2,is}$, ordinate: ζ)

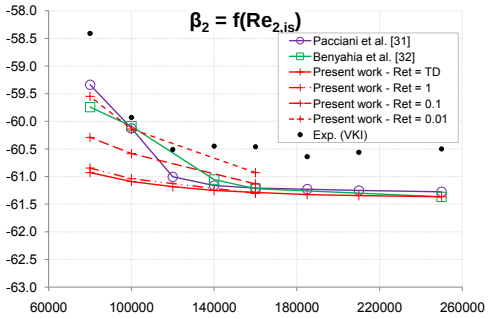

Figure 10: T106C mass-averaged outlet flow angle (abscissa: $Re_{2,is}$, ordinate: β_2)

$Re_{2,is} = 140000$. For lower values, one can observe the underprediction of the "TD" trend which corresponds to the value extracted from the extrapolated "S1" decay law. Apparently, the values of Re_t used by the other research groups are lower than the one used in the 'TD" trend (Tab. 1). In fact, Pacciani et al. [31] used a ratio of turbulence length scale over the

axial chord of 2.5×10^{-3} which represents a value of Re_t of approximately 0.93. Benyahia et al. [32] used a value of 0.1. Since the predictions seem to be Re_t-dependent, a study of this Re_t was carried out. From Figs. 9 and 10, one can see the improvements of the predictions (particularly at low $Re_{2,is}$) by lowering Re_t (up to 0.01). Concerning the other research groups, they are able to catch the bursting of the bubble (i.e. when the topology of the bubble changes from a short one to a long one and when the pressure distribution is clearly affected [34]) and even an open separation.

Let's have an insight at the level of turbulence across the cascade in the "freestream" region (between two blades) for $Re_{2,is} = 80000$. From Fig. 11, one can see that for $Re_t = 0.01$, the level of turbulence is really low (around 0.1%). This behavior is close to a pseudo-laminar case or an external flow configuration. Moreover, it does not follow the extrapolated "S1" decay law. This conclusion is applicable to $Re_t = 0.1$ as well whereas $Re_t = 1$ seems close to the extrapolated "S1" decay law. In fact, when checking the M_{is} distribution, one can notice the proximity of the $Re_t = 1$- and $Re_t = TD$-cases (Fig. 12). In addition, from the experimental data, one would expect an open separation. This is predicted by the two lowest Re_t (0.1 and 0.01) where the M_{is} distributions are affected by this open separation phenomenon as illustrated by a lower peak Mach number as well as a more upstream position of it [34]. Morever, it is followed by a longer pressure plateau. In addition, the wake profile (Fig. 12), extracted at $0.5 \cdot c_{ax}$ downstream the trailing edge, illustrates the correct prediction done by the lowest Re_t. The wake profile is wider and deeper (which confirms the influence of the open separation on the size of the boundary layer and consequently the velocity deficit). The investigation of a higher inlet turbulence level (1.7%) illustrates the preponderance of the dissipation at low Re_t on the turbulent kinetic energy level (Fig. 11).

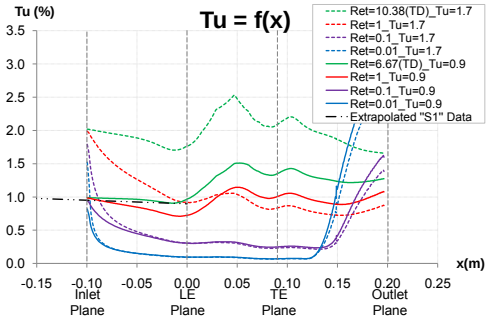

Figure 11: Turbulence across T106C cascade at $Re_{2,is} = 80000$ with the influence of the Re_t

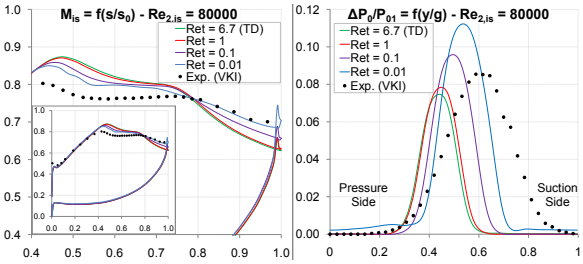

Figure 12: T106C isentropic Mach number distribution and wake profile with Re_t effect at $Re_{2,is} = 80000$ (left abscissa: s/s_0, left ordinate: M_{is}, right abscissa: y/g, right ordinate: $\Delta P_{01}/P_{01}$)

4.4. *Validation of the γ-$\widetilde{Re_{\theta t}}$ Transition Model Implemented in elsA: Assessment of the Flow Topology Parameters*

In this last section, a focus on the flow topology parameters is illustrated. These parameters are the transition onset, the transition end and the separation locations. One can extract them from both the numerical and experimental data. However, Re_θ is only accessible via the numerical predictions. Then, one can compare those information with correlations of the open literature.

To get those flow topology parameters, one can rely on the effective intermittency (γ_{eff}), the turbulent/laminar viscosity ratio (μ_t/μ), the shape factor (H) and the wall shear stress (τ_{wall}). γ_{eff} is the output of the correlation behind the transition model. While scanning the boundary layer from the wall to the edge, one can use this parameter when it suddenly increases to 1 and then decreases. The sudden increase might be defined as the transition onset. This position is considered as the moment where the intermittency first starts to grow [30]. Besides, there is a correlation between $Re_{\theta c}$ and $\widetilde{Re_{\theta t}}$ which defines the lag between the first rise of intermittency and the moment where the skin friction starts to increase [30]. For μ_t/μ, one can assess the transition onset when it exceeds 1. This criterion is defined by the ratio of the eddy viscosity and the molecular viscosity. Thus, when this ratio exceeds 1, it means the turbulence patterns are preponderant. For H, one can assess the transition onset when it is maximum before any sudden decrease. Indeed, it is well-known that the shape factor of a laminar incompressible boundary layer ($H \approx 2.6$) is higher than a turbulent one ($H \approx 1.3$) in a flat plate configuration. Moreover, the shape factor is influenced by the adverse pressure gradient in those HL-LPT con-

figurations. Thus, it allows to assess the position of a possible separation point when H exceeds 3.5. For τ_{wall}, one will notice a sudden increase of it close to its minimum value. When τ_{wall} starts to stabilize at a constant value and even to decrease in order to follow the trend of the fully turbulent case, then this position is defined as the transition end. When τ_{wall} is negative, this indicates a separation. When τ_{wall} exceeds zero after being negative, one can define a reattachment. About the experimental information, one can assess the flow topology parameters with the combination of the M_{is} distribution over the blade [5] and the pseudo-wall shear stress [26].

From Fig. 13, one can see the evolution of the transition onset location with $Re_{2,is}$. For the T108 case, the movement of the transition onset towards the trailing edge as $Re_{2,is}$ decreases is well captured by the flow topology parameters, except γ_{eff} which predicts earlier transition onsets. In fact, this was expected since γ_{eff} defines the moment when $Re_{\theta c}$ is reached and where γ first starts to grow [30]. One can draw the same conclusion about the T106C blade except that at low $Re_{2,is}$, the flow is prone to long bubble and open separation bubble topologies which affect the positions of separation and transition onset significantly [5]. From both the T106C experimental data and numerical predictions, the trend of the transition onset to travel downstream as $Re_{2,is}$ decreases is respected. However, when decreasing more $Re_{2,is}$, the Re_t effect is clearly visible. Thus, the expected upstream movement of the transition onset is not predicted in the extrapolated "S1" decay law Re_t-case whereas it is predicted when Re_t is extremely low (0.01, depicted by the plain symbols in Fig. 13). Concerning the separation point (Fig. 15), its upstream movement as $Re_{2,is}$ decreases is respected from both the experimental and numerical data. Once again, the Re_t effect is noticeable in the T106C case. About the transition end position (Fig. 14), its downstream movement as $Re_{2,is}$ decreases is predicted by the numerical approach while it seems pretty constant for the experimental predictions through the $Re_{2,is}$ range. The reason, which is also applicable to the experimental transition onsets, is the low spatial resolution of the pseudo-wall shear stress measurements. There are 15 hot-film gauges, spread over the suction side. They are regularly spaced in the deceleration part (~5 mm in the curvilinear axis). At last, Fig. 16 illustrates the relationship between the momentum thickness Reynolds number at separation ($Re_{\theta,sep}$) and $Re_{2,is}$ for both blades. In addition to the numerical predictions, the criteria proposed by Hatman and Wang [4] are depicted. As expected, the higher $Re_{2,is}$ are situated in the "Laminar Separation - Short Bubble" region of the plot. Then, the bursting $Re_{2,is}$ for the T108 blade is considered to be around 115000 (even though no clear bursting is visible from ζ and β_2 experimental trends in Figs. 5 and 6). Likewise, the T106C bursting $Re_{2,is}$ is assessed with Fig. 16 and is considered to be around 160000, which is overestimated according to ζ as well as β_2 experimental trends (Figs. 9 and 10).

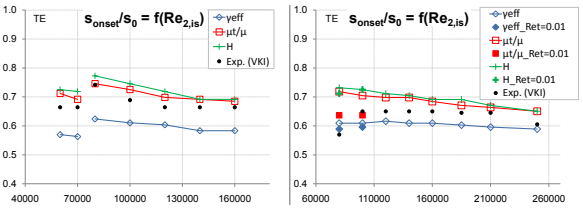

Figure 13: Transition onset through the $Re_{2,is}$ range for T108 (left) and T106C (right) (abscissa: $Re_{2,is}$, ordinate: s_{onset}/s_0)

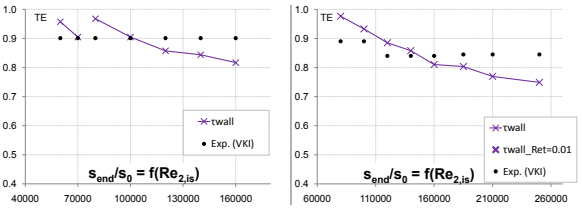

Figure 14: Transition end through the $Re_{2,is}$ range for T108 (left) and T106C (right) (abscissa: $Re_{2,is}$, ordinate: s_{end}/s_0)

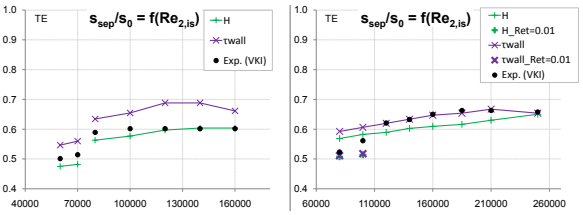

Figure 15: Separation through the $Re_{2,is}$ range for T108 (left) and T106C (right) (abscissa: $Re_{2,is}$, ordinate: s_{sep}/s_0)

5. Conclusions

A new and promising transport equation transition model [3], recently implemented in elsA [23] (one equation for γ and other one for $\widetilde{Re}_{\theta t}$), was assessed on two HL-LPT rotor blades (T108 and T106C). Since those blades are prone to separation-induced transition, they form a good sample group for the model validation as a prediction tool.

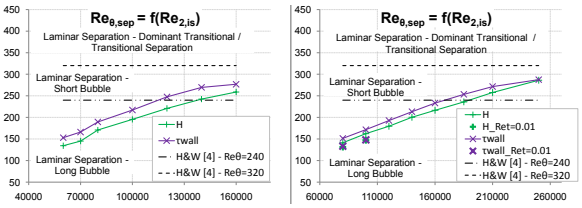

Figure 16: $Re_{\theta,sep}$ through the $Re_{2,is}$ range for T108 (left) and T106C (right) (abscissa: $Re_{2,is}$, ordinate: $Re_{\theta,sep}$)

In the present work, the authors focused on the importance of the turbulent variables boundary conditions which are commonly defined by Re_t. It was concluded, from the experimental decay law, that one can predict the state of the boundary layer, and consequently ζ for mild diffusion HL-LPT rotor blades (T108). For more harsh diffusion HL-LPT rotor blades (T106C), the boundary layer state predictions are satisfactory for mid-$Re_{2,is}$ but are underestimated in the low-$Re_{2,is}$ range where long bubble and open separation topologies are encountered. In fact, an investigation of Re_t has illustrated the influence of this parameter on the boundary layer state predictions. Thus, by lowering more and more this parameter, and as a consequence increasing the dissipation rate, it was possible to predict the expected flow topologies. However, this high dissipation rate does not fulfill the requirements of the experimental decay of turbulence as the flow in the cascade is defined by really low levels of turbulence ($\sim$0.1%). Therefore, this low-Re_t approach lacks predictive behavior as a tuning seems necessary. Nevertheless, an investigation of the diffusion of the turbulent variables into the boundary layer might be of interest in order to understand how it affects the position of separation. Indeed, it seems this position impacts the onset of transition according to the Re_t-investigation (the upstream movement of separation point induces an upstream movement of the transition onset at low $Re_{2,is}$ whereas it induces a downstream movement at mid $Re_{2,is}$). Besides, one has to remember the correlation for the onset of transition in the adverse pressure gradient region is basically meant for attached flows [15; 19] and ranges up to $\lambda_\theta = \pm 0.1$ (λ_θ can be lower than -0.1 for the HL-LPT blade cases of the present work).

Concerning those flow topology parameters, their assessment reveals to be in good agreement with the experimental results.

At last, this steady RANS approach using this new transition model exhibits its robustness in predicting separation-induced transition for mild diffusion HL-LPT rotor blades but needs to be carefully used if strong diffusion HL-LPT configurations are intended for investigation. In fact, more work on the calibration process is expected in order to extend the applicability of this promising model on strong diffusion HL-LPT blades.

6. Acknowledgments

The experimental results reported in this work were obtained within the European research project TATMo "Turbulence and Transition Modelling for Special Turbomachinery Applications" (AST5-CT-2006-030939).

The authors would like to thank SNECMA for the permission to publish this paper. They are also grateful to Jan Michálek (VKI) and Abdelkader Benyahia (ONERA) for the constructive discussions.

References

[1] H. P. Hodson, R. J. Howell, The Role of Transition in High Lift Low Pressure Turbines, von Karman Institute for Fluid Dynamics Lecture Series 2005-03.

[2] J. Hourmouziadis, Aerodynamic Design of Low Pressure Turbines, AGARD Lecture Series 167.

[3] R. B. Langtry, F. R. Menter, Correlation-Based Transition Modeling for Unstructured Parallelized Computational Fluid Dynamics Codes, AIAA Journal 47 (12) (2009) 2894–2906.

[4] A. Hatman, T. Wang, A Prediction Model for Separated-Flow Transition, ASME Journal of Turbomachinery 121 (3) (1999) 594–602.

[5] T. Coton, Unsteady Wake-Boundary Layer Interaction on Advanced High Lift Low Pressure Turbine Airfoils, Ph.D. thesis, Université Libre de Liège (December 2003).

[6] H. Pfeil, R. Herbst, Transition Procedure of Instationary Boundary Layers, in: ASME Gas Turbine Conference and Exhibit and Solar Energy Conference, no. 79-GT-128, San Diego, California, USA, 1979.

[7] H. Pfeil, R. Herbst, T. Schröder, Investigation of the Laminar-Turbulent Transition of Boundary Layers Disturbed by Wakes, ASME Journal of Engineering for Power 105 (1) (1983) 130–137.

[8] G. B. Schubauer, P. S. Klebanoff, Contributions on the Mechanics of Boundary-Layer Transition, Technical Note 3489, National Advisory Commitee for Aeronautics (September 1955).

[9] V. Schulte, H. P. Hodson, Prediction of the Becalmed Region for LP Turbine Profile Design, ASME Journal of Turbomachinery 120 (4) (1998) 839–846.

[10] R. E. Mayle, The Role of Laminar-Turbulent Transition in Gas Turbine Engines, ASME Journal of Turbomachinery 113 (4) (1991) 509–537.

[11] C. G. Himmel, H. P. Hodson, Modifying Ultra-High Lift Low Pressure Turbine Blades for Low Reynolds Number Applications, in: 12th International Symposium on Unsteady Aerodynamics, Aeroacoustics & Aeroelasticity of Turbomachines (ISUAAAT12), no. I12-S7-3, Imperial College London, UK, 2009.

[12] C. G. Himmel, H. P. Hodson, Passive Air Jets for Loss Reductions in High Lift Low Pressure Turbines, in: ISABE, no. 1295, 2009.

[13] R. J. Volino, O. Kartuzova, M. B. Ibrahim, Experimental and Computational Investigations of Low-Pressure Turbine Separation Control Using Vortex Generator Jets, in: ASME Turbo Expo 2009: Power for Land, Sea and Air, no. GT2009-59983, Orlando, Florida, USA, 2009.

[14] J. Huang, T. C. Corke, F. O. Thomas, Plasma Actuators for Separation Control of Low-Pressure Turbine Blades, AIAA Journal 44 (1) (2006) 51–57.

[15] B. J. Abu-Ghannam, R. Shaw, Natural Transition of Boundary Layers - The Effects of Turbulence, Pressure Gradient and Flow History, Journal Mechanical Engineering Science 22 (5) (1980) 213–228.

[16] D. K. Walters, D. Cokljat, A Three-Equation Eddy-Viscosity Model for Reynolds-Averaged Navier-Stokes Simulations of Transitional Flow, ASME Journal of Fluids Engineering 130 (12) (2008) 121401.1–121401.14.

[17] S. Lardeau, N. Li, M. A. Leschziner, Large Eddy Simulation of Transitional Boundary Layers at High Free-Stream Turbulence Intensity and Implications for RANS Modeling, ASME Journal of Turbomachinery 129 (2) (2007) 311–317.

[18] E. R. van Driest, C. B. Blumer, Boundary Layer Transition: Freestream Turbulence and Pressure Gradient Effects, AIAA Journal 1 (6) (1963) 1303–1306.

[19] F. R. Menter, R. B. Langtry, S. R. Likki, Y. B. Suzen, P. G. Huang, S. Völker, A Correlation-Based Transition Model Using Local Variables - Part I: Model Formulation, ASME Journal of Turbomachinery 128 (3) (2006) 413–422.

[20] W. Piotrowski, W. Elsner, S. Drobniak, Transition Prediction on Turbine Blade Profile with Intermittency Transport Equation, in: ASME Turbo Expo 2008: Power for Land, Sea and Air, no. GT2008-50796, Berlin, Germany, 2008.

[21] P. Malan, K. Suluksna, E. Juntasaro, Calibrating the γ-Re_θ Transition Model, in: ERCOFTAC Bulletin 80, 2009, pp. 53–57.

[22] W. Elsner, W. Piotrowski, P. Warzecha, Transition Modelling with Intermittency Transport Equations, in: ERCOFTAC Bulletin 80, 2009, pp. 49–52.

[23] C. Content, R. Houdeville, Application of the γ-R_θ laminar-turbulent transition model in Navier-Stokes computations, in: AIAA 40th Fluid Dynamics Conference and Exhibit, no. AIAA 2010-4445, Chicago, Illinois, USA, 2010.

[24] R. E. Mayle, A. Schulz, The Path to Predicting Bypass Transition, ASME Journal of Turbomachinery 119 (3) (1997) 405–411.

[25] E. Dick, Eddy Viscosity Models for Turbulence and Transition, von Karman Institute for Fluid Dynamics Lecture Series 2009-08.

[26] J. Michálek, M. Monaldi, T. Arts, Aerodynamic Performance of a Very High Lift Low Pressure Turbine Airfoil (T106C) at Low Reynolds and High Mach Number with Effect of Free Stream Turbulence Intensity, in: ASME Turbo Expo 2010: Power for Land, Sea and Air, no. GT2010-22884, Glasgow, UK, 2010.

[27] P. R. Spalart, C. L. Rumsey, Effective Inflow Conditions for Turbulence Models in Aerodynamic Calculations, AIAA Journal 45 (10) (2007) 2544–2553.

[28] P. Chassaing, Turbulence en mécanique des fluides - Analyse du phénomène en vue de sa modélisation à l'usage de l'ingénieur, 1st Edition, Cépaduès-Editions, 2000.

[29] R. Corral, F. Gisbert, Prediction of Separated-Induced Transition Using a Correlation-Based Transition Model, in: ASME Turbo Expo 2010: Power for Land, Sea and Air, no. GT2010-23239, Glasgow, UK, 2010.

[30] R. B. Langtry, A Correlation-Based Transition Model using Local Variables for Unstructured Parallelized CFD codes, Ph.D. thesis, Universität Stuttgart (May 31 2006).

[31] R. Pacciani, M. Marconcini, A. Arnone, F. Bertini, A CFD Study of Low Reynolds Number Flow in High Lift Cascades, in: ASME Turbo Expo 2010: Power for Land, Sea and Air, no. GT2010-23300, Glasgow, UK, 2010.

[32] A. Benyahia, L. Castillon, R. Houdeville, Prediction of Separation-Induced Transition on High Lift Low Pressure Turbine Blade, in: ASME Turbo Expo 2011: Power for Land, Sea and Air, no. GT2011-45566, Vancouver, British Columbia, Canada, 2011.

[33] J. Michálek, A. Ilikan, T. Arts, A Comparison of High and Low Speed Aerodynamic Performance of a Very High Lift Low-Pressure Turbine Airfoil (T108) at Low Reynolds Numbers: Experimental Analysis and Numerical Prediction, in: 9th European Conference on Turbomachinery Fluid Dynamics and Thermodynamics, Istanbul, Turkey, 2011.

[34] W. B. Roberts, A Study of the Effect of Reynolds number and Laminar Separation Bubbles on the Flow through Axial Compressor Cascades, Ph.D. thesis, Université Libre de Bruxelles (May 1973).

Natural and Induced Transition on a 7deg Half-Cone at Mach 6

Davide Masutti

Aeronautics and Aerospace Department, von Karman Institute for Fluid Dynamics, Belgium, masutti@vki.ac.be

Supervisor: Olivier Chazot

Associate Professor, Aeronautics and Aerospace Department, von Karman Institute for Fluid Dynamics, Belgium, chazot@vki.ac.be

University Supervisor: Fulvio Scarano

Professor, Department of Aerospace Engineering, TU Delft, The Netherlands, F.Scarano@TUDelft.nl

Abstract

Pressure fluctuations caused by instabilities in the boundary layer are among the causes which lead to transition on a space vehicle during atmospheric re-entry. The knowledge of these unsteady fluctuations could help to identify the mechanisms which take part into the transition process and better predict them. With this target and in support of the EXPERT PL4/PL5 post-flight analysis, surface pressure measurements have been performed in the VKI H3 Hypersonic Wind Tunnel. A 7deg half-angle cone with exchangeable nosetip was equipped with a streamwise array of high frequency pressure transducers (PCB 132A31). Instabilities in the boundary layer have been investigated on a smooth surface and behind an isolated roughness element. The results provided on a simplified ground test model, show the growth of second mode waves under a laminar boundary layer and their break down to turbulence as a function of Reynolds number and streamwise location. Moreover the effect of an isolated roughness element on the boundary layer has been characterized in terms of generated instabilities.

Keywords: hypersonic, turbulence, boundary-layer transition, roughness, pressure measurements, infrared thermography

Nomenclature

δ^*	Displacement thickness of the nozzle walls
ρ_∞	Free-stream density
c_p	Heat capacity at constant pressure
$C_{F_{II}}$	Turbulent mean boundary layer parameter
k	Roughness height
Q_w	Heat flux
T_0	Total temperature
T_w	Wall temperature
u_∞	Free-stream velocity

1. Introduction

Laminar-to-turbulent transition during atmospheric re-entry is a major issue for vehicle design. The process of boundary layer transition is accompanied by an increase in surface heat transfer and skin friction on the vehicle. ESA EXPERT project addresses the testing of critical re-entry technologies, leading in particular, to a more accurate design and effective development of thermal protection and boundary layer transition control systems. In this frame, VKI is contributing to the project with a payload for induced transition studies. Pressure fluctuations in the boundary layer are among the causes which lead to instabilities and after to the turbulent breakdown in the boundary layer, the determination of these unsteady fluctuations is helping to identify the mechanism which takes part in the transition process. With this target, surface pressure measurements have been performed in the VKI H3 Hypersonic Wind Tunnel. A 7deg half-

angle cone with exchangeable nose was equipped with a stream-wise array of high frequency pressure transducers (PCB 132A31). The use of these peculiar ultra high frequency sensors demand a dynamic calibration which has to be addressed in a shock tube. Instabilities in the boundary layer are also investigated, with respect to the tunnel noise influence and the induced laminar-to-turbulent transition mechanism. The results provided on standard ground test model, representative of the conical EXPERT's wall, are helping to enhance the understanding of the boundary layer transition characteristics for the forthcoming post-flight analysis on the EXPERT vehicle.

2. Experimental Setup

2.1. VKI H3 Mach 6 Hypersonic Wind Tunnel

All experiments have been performed in the H3 Hypersonic Wind Tunnel of the von Karman Institute for Fluid Dynamics. The VKI H3 test facility is a conventional noisy blow-down to vacuum type wind tunnel. It can provide a uniform axisymmetric jet with a diameter of 12 cm at Mach 6. Dried air is supplied from a 40 bar reservoir, which can deliver stable stagnation pressures ranging from 6 to 30 bar. Air is heated up in pebble-bed heater to a total temperature of 500K to avoid condensation in the test section. The unit Reynolds number of the flow can be varied between 6E6 1/m and 28E6 1/m. The wind tunnel is provided with a model injection mechanism to avoid blockage of the wind tunnel and also to avoid excessive heating of the model itself during the start-up. The test chamber is vacuumed prior to the test using a supersonic ejector. The model is injected into the hypersonic free-jet with a model injection arm, once the Mach 6 flow is fully established in the test chamber. The noise level (normalized Pitot pressure fluctuations) of the facility is approximately 1.6% and a turbulence level of 0.8% (more information can be found in Masutti and Spinosa [1].

2.2. Models

The wind tunnel model used for the pressure measurements is a stainless-steel/Plexiglas 7deg half-cone, 265mm long. Sharp (0.55mm radius) and blunt (2.5mm radius) nose tips were used in this test campaign. The model is composed by half cone made in steel and half cone made in Plexiglas; the singularity of this assembly allows simultaneous measurements with the high frequency pressure transducers and the infrared thermo camera. A sketch of the stainless-steel side of the cone and the location of the sensors are given in Fig. 1.

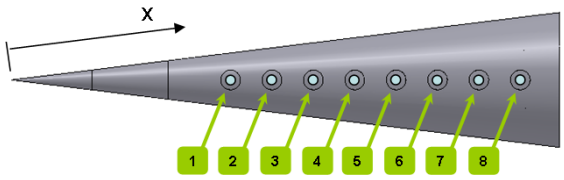

Figure 1: 7deg half-cone (side view)

Number	x [mm]	Sensor type
1	106	none
2	126	PCB132
3	146	none
4	166	PCB132
5	186	PCB132
6	206	Kulite XCE-093-50A
7	226	PCB132
8	246	PCB132

Table 1: PCB location on the 7deg half-cone

2.3. Instrumentation and data acquisition

Pressure fluctuations measurements and the instabilities investigation are performed on the cone model using PCB132A sensors. These sensors already prove their successful capabilities identifying and characterizing boundary layer instabilities [2; 3; 4; 5]. The PCB132A is a time-of-arrival sensor with a piezoelectric design. Because of its ability to detect very high frequency pressure fluctuations, the sensor is designed to have a bandwidth between 11 KHz and 1 MHz, therefore the mean pressure value information is not available. The PCB132A sensor, thanks to its very high resonant frequency (above 1MHz) is suitable to study boundary layer instabilities and their breakdown to turbulence. The sensor itself is a cylinder of 3.18 mm diameter and 7 mm length, although the real sensitive area (on top of the cylinder) is reduced to 1.6 mm^2. The diagonal of a 1.6 mm^2 square is equal approximately to 1.8 mm, this length can be considered as the spatial resolution of the sensor itself. Since the sensor was meant to be used to detect shock/pressure waves it has not yet been accurately calibrated for the purpose of investigating boundary layer instabilities. Different ways of calibrating the PCB sensors are in use or under investigation (see Beresh et al.[6] and

Berridge [5]). In this framework a new type of calibration has been investigated but since the results are still in the preliminary phase, the factory calibration is used to post-process the results analyzed from here on.

All the PCB132 sensors are powered by a PCB 482C05 signal conditioner (unity gain) which provides a constant-current excitation of 4mA to the piezoelectric sensing element. The signal conditioners are connected to a VKI custom made 40dB low-noise amplifier with a build-in 900 KHz Butterworth six-poles low-pass filter. The amplified signals are then digitally sampled at 2 MHz/channel by a 14-bit National Instruments PXI-6133. The power spectral densities of the PCBs' signal were calculated using the 'Power Welch Method' on 0.25 sec of samples. The evaluation of the power spectra was done with a 500 points Blackman window with 50% overlap and a frequency resolution of 4 kHz. The sensors location for the 7deg half-cone is defined in Table 1.

Infrared Thermography is used to provide a quantitative measure of heat transfer and is useful for quantifying increased surface heating due to laminar-to-turbulent transition. The radiation emitted by an object is a function of its surface temperature. Taking into account the emissivity of the surface, the reflected ambient radiation and the absorption in air or through optical elements [7], the Infrared Thermography can accurately measure the temperature of a body. For the latter reason, the IR technique is very suitable to study high-speed aerothermodynamics and atmospheric entry problems [8]. To capture the wall temperature evolution on the model, a FLIR ThermaCAM SC-3000 Infrared Camera has been used. The camera records a 320 x 240 pixels image at a max sampling frequency of 50Hz. The detector of the camera is cooled internally to 70K by a Stirling cycle. To assure a high IR transmissivity between the model surface and the IR camera, a germanium optical window is used. Despite the high transmissivity of germanium some residual reflections are present; this effect is then mitigated during the data reduction with a background subtraction procedure. The calibration is performed on a black body to relate the measured IR intensity to the model surface temperature.

$$St_{mod} = \frac{Q_w}{\rho_\infty u_\infty c_p (T_0 - T_w)} \quad (1)$$

The modified Stanton number (Santarelli and Charbonnier [9]) multiplied by the cubic root of the Reynolds number (Eq. 1) is used to display the status of the boundary layer on the cone.

3. Results

3.1. Natural Transition

The power spectral density (PSD) of five different PCB132A sensors mounted on the 7deg half-cone is computed to investigate the behavior of the instabilities taking part in the transition process. To represent the PSD of the pressure fluctuations measured by the PCB132A and compare the fluctuation amplitudes between them at different freestream conditions, the pressure fluctuations are normalized by the wall pressure [4] at the corresponding sensor location. Since the PCB132A sensor does not provide the mean value of the pressure, but only its fluctuations, the wall pressure for the 7deg half-cone has been computed using the freestream measured condition with the Taylor-Maccoll equation for supersonic/hypersonic cones at zero angle of attack [10]. The results are reported in Fig. 2, where the PSD of normalized pressure fluctuations on a smooth 7deg half-cone are investigated at different Reynolds number ranging from 6.75E6 1/m to 27.1E6 1/m. Instabilities at very high frequency can be seen in the PSD of the pressure fluctuations (Fig. 2). Those instabilities in the boundary layer were already identified by Tollmien and Schlichting in the '30s, then this early stability theory was revised and completed by Mack [11] in 1984. Mack demonstrated that the most dominant instabilities on a cone at zero angle of attack under hypersonic edge Mach numbers are second modes waves (called also Mack waves in his name). These instabilities are acoustic-like waves contained and reflected within the boundary layer, their frequency scales with the inverse of the boundary layer thickness itself as seen by Stetson and Kimmel [12] and Chokani [13]. Initially these second mode waves grow linearly before the location of transition and then they become nonlinear prior to the breakdown to turbulence.

Fig. 2(a) shows the initial amplitude of second mode waves growing with increasing downstream location, while their frequencies (represented by the peak frequency in the PSD) are decreasing downstream. The first PCB132A sensor, located at x = 126 mm from the nosetip, shows that the measured frequency for second mode waves is around 550 kHz. The second PCB132 at a location x=166mm is measuring the most unstable second mode waves at a peak frequency near 500 kHz. For the other locations at x = 186 mm, x = 226 mm and x = 246 mm, the second modes are measured around 450 kHz, 400 kHz and 370 kHz respectively. The fifth PCB132 at x = 246 mm also shows a weak harmonic of the second mode

wave at a frequency around 750 kHz. Comparing the evolution of the second mode waves from Fig. 2(a) to Fig. 2(c) no wave breakdown and therefore no natural transition were detectable at a freestream Reynolds number below 14.1E6 1/m on the 7deg half-cone.

In the case of a freestream Reynolds number of 18E6 1/m (Fig. 2(d)), the first three PCB sensors are measuring second mode waves at a frequency respectively of 620 kHz, 520 kHz and 490 kHz, while the fourth PCB at x = 226mmm location shows a appreciable non-linear amplitude growth respect to the upstream sensors. The fifth sensor, x = 246 mm, is affected by a fully turbulent develop boundary layer although some instabilities are left over with a very

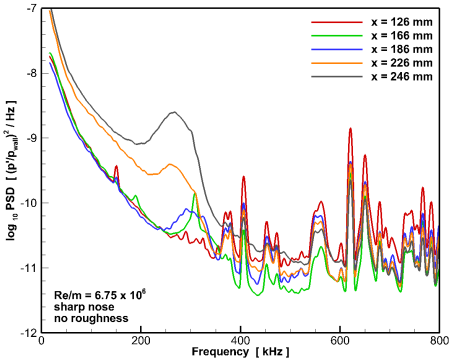

(a) PCB132 power spectral density for 7deg half-cone, Re/m = 6.75E6, no roughness

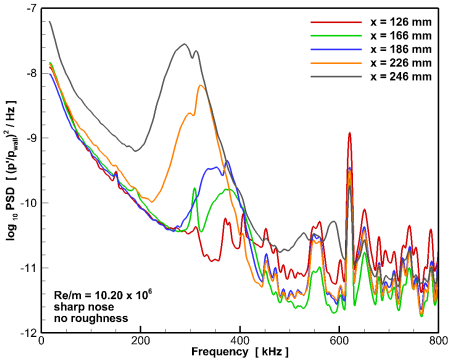

(b) PCB132 power spectral density for 7deg half-cone, Re/m = 10.2E6, no roughness

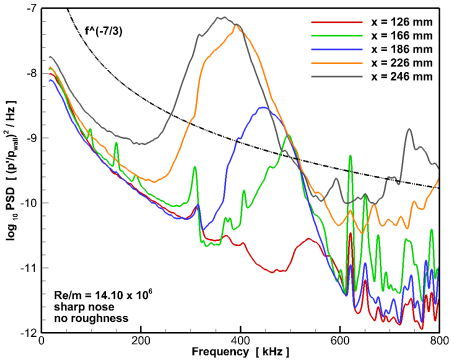

(c) PCB132 power spectral density for 7deg half-cone, Re/m = 14.1E6, no roughness

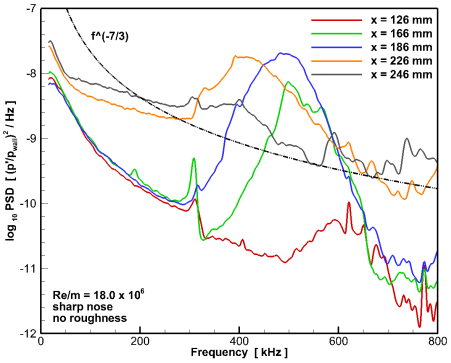

(d) PCB132 power spectral density for 7deg half-cone, Re/m = 18.0E6, no roughness

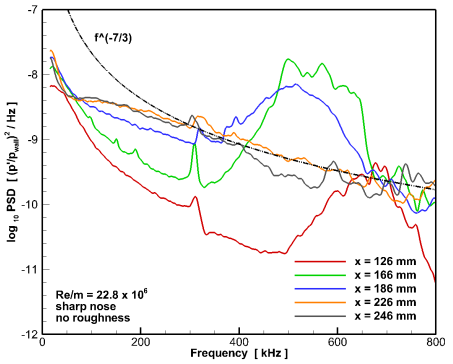

(e) PCB132 power spectral density for 7deg half-cone, Re/m = 22.8E6, no roughness

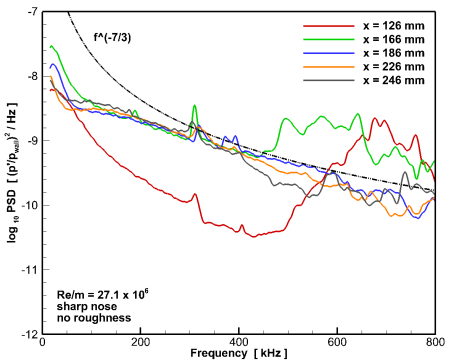

(f) PCB132 power spectral density for 7deg half-cone, Re/m = 27.1E6, no roughness

Figure 2: Second mode instabilities on a 7deg half-cone

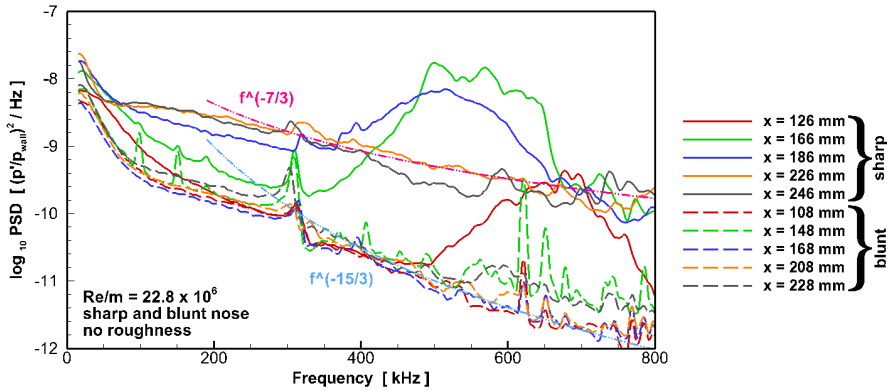

Figure 3: Nose bluntness effect on second modes

small amplitude. One can consider that the location of transition is somewhere between x = 226 mm and x = 246 mm for this Reynolds number. Increasing further the freestream Reynolds number, the natural transition front is moving upstream and more sensors are drowned in a turbulent boundary layer. In Fig. 2(e) the first two sensors are able to measure instabilities near frequencies of 670 kHz and 550 kHz, while the third one at x = 186 mm shows already a non-linear amplitude growth. The last two sensors, x = 226 mm and x = 246 mm, are measuring a fully developed boundary layer turbulent decay which is collapsing on a $f^{-7/3}$ curve. The $f^{-7/3}$ is the scale for turbulent decay of pressure for high wavenumbers [14], it differs from the classical Kolmogorov law of $f^{-5/3}$ because there is no directly dissipation of pressure with respect to velocity.

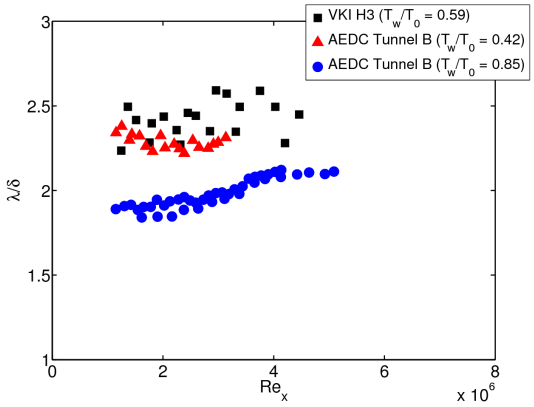

Figure 4: Approximate wavelength of second modes (replotted from Stetson and Kimmel [12])

Using a cross-correlation function on the signals from two adjacent sensors is possible to identify the velocity of the wave packets traveling downstream. The information on the velocity is then useful to compare with the boundary layer thickness and to compute the approximate wavelength of second modes. In Fig. 4, the wavelength of the second modes computed on a 7deg half-cone in VKI H3 conditions (T_w/T_0=0.59) are compared with results from Stetson and Kimmel [12] on a similar cooled and un-cooled 7deg half-cone in the AEDC Tunnel B at Mach 8 (T_w/T_0=0.42 and T_w/T_0=0.85). Fig. 4 shows that the ratio between the wavelength of the second mode waves and the boundary layer thickness on the cone is around 2.5, in good agreement with experimental measurements by Stetson and Kimmel. The nosetip bluntness effect on instabilities has also been investigated. In Fig. 3 are given the power spectral densities of pressure fluctuations on both a sharp (solid lines) and a blunt 2.5 mm cone (dashed lines). Measurements for the same Reynolds number of 22.8E6 1/m show how the second mode waves and the non-linear growth effects are suppressed by using a blunt nose on the cone. The origin of this phenomenon, extensively treated in the literature by Stetson [15; 16] and Singh et al. [17], is due to a layer of high specific entropy and strong entropy gradients in the inviscid flow.

This layer, simply known as entropy layer, is a region of high temperature and low density gas created by the large entropy due to the strong bow shock at the blunt nosetip [18]. The characteristics of the entropy layer, its thickness and its persistence in affecting the downstream boundary layer are a function of the bluntness of the vehicle and the freestream conditions [17]. The entropy layer, before being swallowed by the boundary layer, promotes changes of the flow

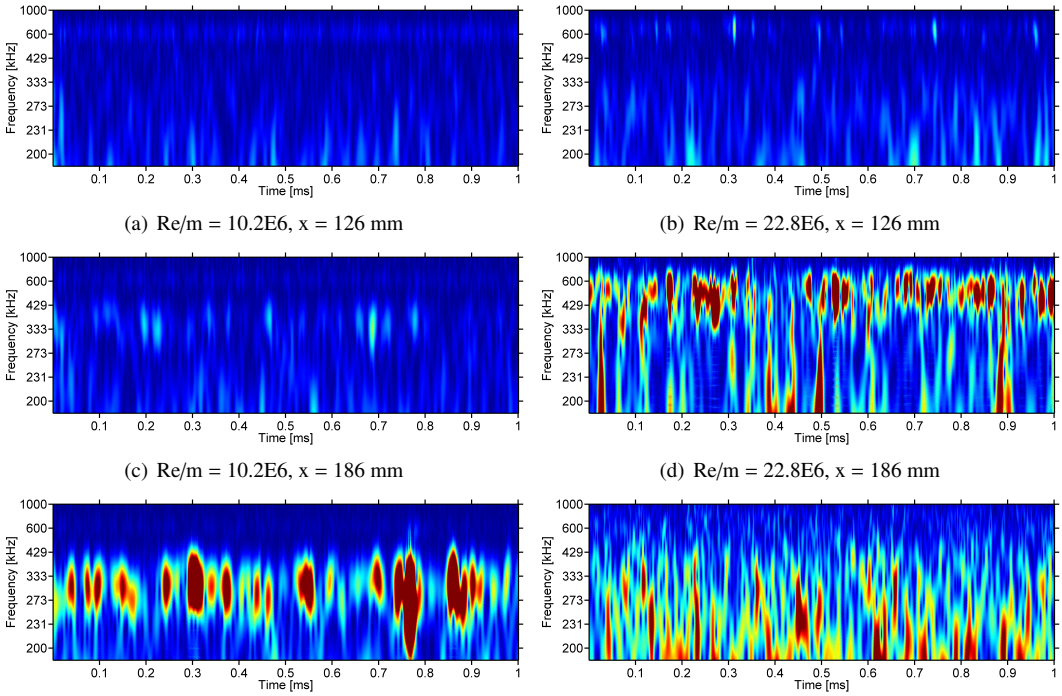

(a) Re/m = 10.2E6, x = 126 mm

(b) Re/m = 22.8E6, x = 126 mm

(c) Re/m = 10.2E6, x = 186 mm

(d) Re/m = 22.8E6, x = 186 mm

(e) Re/m = 10.2E6, x = 246 mm

(f) Re/m = 22.8E6, x = 246 mm

Figure 5: Wavelet analysis for different Reynolds number and sensors location

properties in the boundary layer itself. More precisely it induces a growth of the viscous layer, it changes the Mach number at the edge of the boundary layer and it also change the local Reynolds number. Because of these induced effects, the entropy layer helps to stabilize the boundary layer and moves backward the point in which transition occurs [19; 20]. From Fig. 3 can be observed how the PSDs of the pressure fluctuations on a blunt 7deg half-cone at VKI H3 conditions lie on a $f^{-15/3}$ curve, which is typical for a laminar boundary layer. One has to remember that in relation to the blunt body paradox, analyzed by Reshotko [21], a great increase of nose bluntness would generate a reversal in the transition front, bringing suddenly the natural transition front close to the nose. This latter behavior is also known in the literature as the 'transition-reversal phenomenon' (Rosenboom [20]) and its characterization is still an open issue.

3.1.1. Wavelet Analysis

A wavelet analysis has been applied to the signal of the PCB sensors for different Reynolds number and different locations. The analysis has been performed using a complex Morlet mother wavelet over a millisecond portion of the signal with 500 ns time resolution. Fig. 5 includes the analysis for two different Reynolds number 10.2E6 1/m and 22.8E6 1/m, at three different locations of 126 mm, 186 mm and 246 mm. Comparing the results given in Fig. 5(a), 5(c) and 5(e) for the same Reynolds number and increasing downstream distance, the second mode waves are increasing amplitude and decreasing frequency.

Second mode waves can be identified as wave packets traveling in the boundary layer at a random repetition rate. Through the wavelet analysis these wave packets can be cross-correlated and the computed velocity shows similar results as in Fig. 4. Considering a higher Reynolds number (Fig. 5(b), Fig. 5(d) and Fig. 5(f)), second mode instabilities appear at a higher frequency around 650 kHz at the location x = 126mm, in agreement with the PSD estimation shown in Fig. 2(e). Increasing the downstream location at x =186mm, the second mode waves are visible with a frequency around 500kHz. In this location the boundary layer in still not fully turbulent as from the PSD in Fig. 2(e) and is affected by an early stage of the breakdown to turbulence. This early breakdown process is visible in Fig. 5(d), where second mode wave packets are coexisting with turbulence traces (represented as red vertical lines in the wavelet analysis). At the end

of the cone x = 246mm the boundary layer is fully turbulent, in Fig. 5(f) the second modes are completely disappeared and the wavelet analysis shows a chaotic trace.

3.1.2. Natural Transition Correlation

To characterize and compare natural transition onset location on a 7deg half-cone in VKI H3 conditions, the pressure fluctuations rms normalized by the computed Taylor-Maccoll mean wall pressure and the modified Stanton number (Eq. 1) from the infrared measurements are presented in Fig. 6. The modified Stanton number in Fig. 6 has been normalized by the cubic root of the Reynolds number. Experimental results as a function of the Reynolds number are compared with the Eckert theory for laminar and fully turbulent boundary layer. The results from the experiments show a visible boundary layer transition for unit Reynolds number of 27.1E6 1/m, 22.8E6 1/m and 18E6 1/m with the onset of natural transition respectively at 133mm, 150mm and 184mm. In the cases with Reynolds number of 14.1E6 1/m and 10.2E6 1/m no transition is visible because of the short length of the cone.

Moreover it is possible to compare the transition location on a 7deg half-cone in VKI H3 conditions with the Pate's transition correlation [22]. During the 70's, Pate conducted extensive research into transition in different conventional hypersonic wind tunnel. Pate firstly discover how freestream noise dominates the transition process on cones and flat plates, his work is still considered as a masterpiece. The correlation developed by Pate predicts the natural transition location on cones and flat plates at zero angle of attack. The correlation itself is based on tunnel noise parameters like the tunnel turbulent mean boundary layer parameter $C_{F_{II}}$ [23], the displacement thickness of the nozzle walls δ^* and the test section circumference. All the parameters and the correlation are described in detail in Pate's original manuscript [22].

In this analysis the transition locations obtained with the transition correlation at different unit Reynolds number of 27.1E6 1/m, 22.8E6 1/m 18E6 1/m and 14.1E6 1/m are respectively 152mm, 170mm 198mm and 233mm (values shown in Fig. 6 as vertical dashed line). Again Fig. 6 shows also the normalized pressure fluctuations for different sensor locations as a function of the freestream unit Reynolds number. A threshold of the normalize pressure fluctuations around a value of 0.02-0.025 represents the freestream noise level (see Masutti and Spinosa [1]) below which the boundary layer on the cone can be considered laminar. Streamwise pressure fluctuations during a laminar-to-turbulent transition process are characterized by the presence of a peak that occurs near the end of the transition process [22]. This peak can be observed in Fig. 6 for Reynolds number cases of 27.1E6 1/m, 22.8E6 1/m and 18.0E6 1/m. The last two PCB pressure sensors (226mm and 246mm) at unit Reynolds number of 14.1E6 1/m and 10.2E6 1/m, are affected by an anomalous recirculation phe-

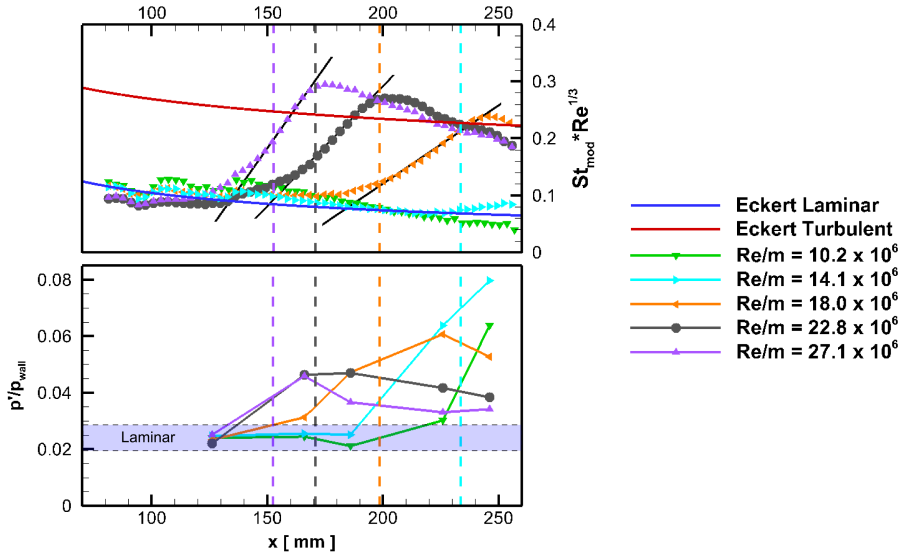

Figure 6: Natural transition and Pate correlation

nomena, so the peak in the normalized pressure fluctuations is not considered to be related to any transition in the boundary layer. The same anomalous recirculation has been observed also using the Infrared Thermography technique, but its effect was small if compared with the heat flux measured at the wall in a turbulent boundary layer.

Comparing in Fig. 6 the experimental results obtained and the Pate's transition correlation for cones, there is a fairly good agreement in the natural transition location. In particular, the location of transition inferred by the Infrared technique is always upstream of about 7-14% if compared with both the Pate correlation and the pressure fluctuation measurements. If pressure fluctuation and Pate correlation are analyzed, the peak of pressure fluctuations is generally downstream of the predicted transition location. The uncertainty of the transition location inferred by the PCB sensors is large because of the poor spatial resolution.

3.2. Roughness Induced Transition

To investigate the isolated roughness induced transition on a 7deg half-cone, a combination of measurements techniques has been used. The results obtained from fast pressure transducers, infrared thermography and oil visualization bring a set of complementary information. The use of infrared thermography alone is not enough to determine the status and the topology of the boundary layer. An infrared image at the model's wall could hide the vortex structures and moreover bring to an incorrect interpretation of the results. Fast pressure transducers at the wall, could add the unsteady information missing from the infrared technique and the oil flow can highlight the small vortex structure at the wall. Looking at Fig. 7 it is possible to see the effect on boundary layer transition of an isolated roughness element (ramp k=0.3mm placed at x=70mm). The group of images shows the effect of Reynolds number and nose bluntness on induced transition. Comparing Fig. 7(a) and Fig. 7(b) the effect of the Reynolds number can be observed on a sharp cone. The apex of the turbulent wedge [24], recognized as the transition location, is moving upstream closer to the isolated element as the Reynolds number increase. Moreover with a unit Reynolds number of 18E6/m natural transition is also present on the cone (Fig. 7(b), so induced and natural transition are coexisting.

On the other hand, with the blunt nose the effectiveness of the roughness element is decreasing. Comparing Fig. 7(a) and Fig. 7(c) the stabilizing effect of the entropy layer on the induced transition becomes clear. On a sharp cone, at a relatively low Reynolds number 7E6 1/m, the wake of the ramp is visible and characterized by a possible turbulent wedge at the end of the cone (Fig. 7(a)), while with a blunt nose the boundary layer on the cone is unperturbed and no wake is visible (Fig. 7(c)). Analyzing the effect of the nose at a higher Reynolds number around 18E6 1/m (Fig. 7(c) and 7(d)) the nose bluntness is stabilizing the natural transition (as discussed previously on Fig. 3) without any apparent interference on the induced turbulent wedge. Carefully observing the turbulent wedge in

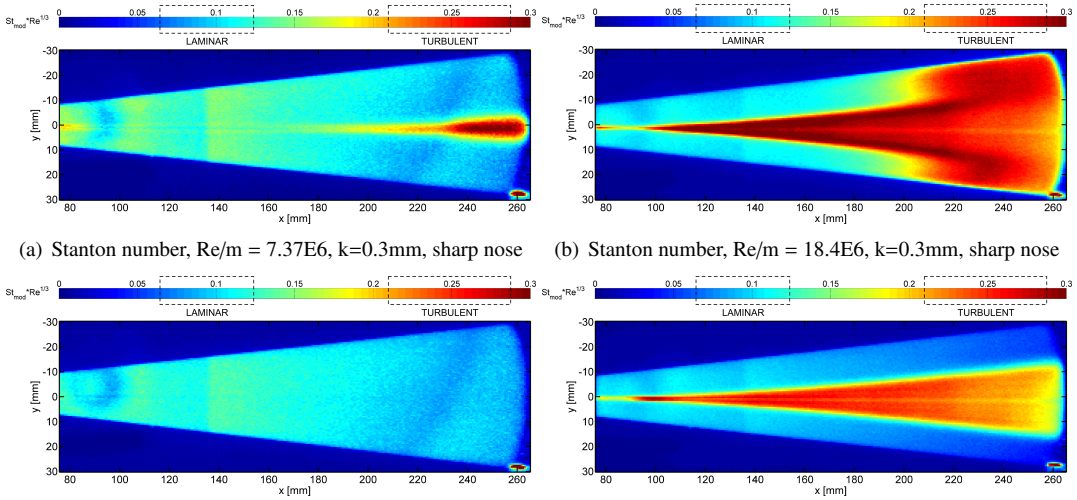

(a) Stanton number, Re/m = 7.37E6, k=0.3mm, sharp nose (b) Stanton number, Re/m = 18.4E6, k=0.3mm, sharp nose

(c) Stanton number, Re/m = 7.04E6, k=0.3mm, blunt nose (d) Stanton number, Re/m = 18.8E6, k=0.3mm, blunt nose

Figure 7: Infrared images on a 7deg half-cone

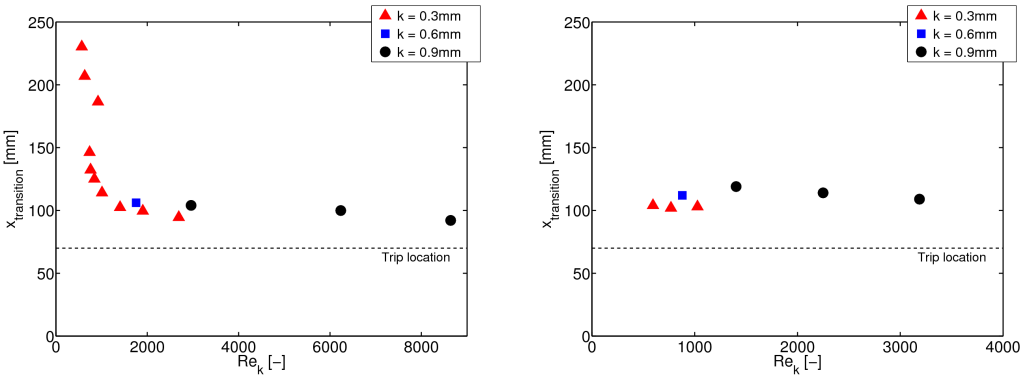

(a) Sharp cone (b) Blunt cone

Figure 8: Roughness transition location vs Reynolds number

Fig. 7(d), it is possible to distinguish some vortical structure in the boundary layer. A big colder line is present along the cone in the middle of the turbulent wedge, this line represent the accumulation line of the two big primary vortices created at the tip of the ramp element and flowing downstream attached to the wall. In addition to the two big vortices, are visible also four secondary colder line (two by side in a symmetric pattern), representing some secondary structures induced by the primary vortices. More details on these specific structures are provided on a flat plate in Tirtey [25].

The plots in Fig. 8 show the roughness induced transition location on a sharp and blunt 7deg half-cone as a function of the Re_{kk} parameter. As can be observed for the sharp nose in Fig. 8(a), the transition location moving closer to the location of the roughness element as soon as the Re_{kk} parameter is increasing. The transition location is approaching rapidly to the roughness element reaching an asymptote determined by the minimum incubation length for the development of the laminar-to-turbulent process in the boundary layer. Similar results are validated by observations of van Driest and McCauley [26] and Schneider [27] in both noisy and quiet wind tunnels. Fig. 8(b) represents similar results on a blunt 2.5mm nose, where only the asymptote of the minimum incubation length is obtained. Unfortunately with the test performed the downstream shift of the transition location was not observed therefore no comparison can be done.

3.2.1. Oil flow visualization

The oil visualization technique has been used to highlight some of the structure hiding in the boundary layer. These structures are mainly primary and secondary vortices created in the wake of an isolated roughness element. Fig. 9 shows the experimental results obtained with the oil flow technique on a 0.9 mm height ramp at a Reynolds number of 18E6/m for different nose bluntness. A detailed sketch of the vortex topology is given in Fig. 10. A primary set of vortices is created from the sides of the roughness element because of the pressure gradient resulting from the shape of the ramp itself. This pressure gradient is thus generating a pair of contra-rotating vortices which are flowing downstream attached to the wall. Right at the back of the ramp there is a so called 'dead-air region' characterized by a recirculation zone downstream the backward facing step of the ramp. Following the 'dead-air region' from Fig. 10 an accumulation line is observed, where the residual oil on the surface is pushed by the contra-rotating vortices. To maintain the momentum balance in the flow, every primary vortex is coupled with another contra-rotating vortex on the side (see the bird tail footprint of the primary couple of vortices in Fig. 10). Following downstream the wake of the roughness, a pair of new vortices (secondary couple of vortices) are induced by the momentum of the primary ones. These secondary vortices are visible in the sketch of Fig. 10 and in the experimental results in Fig. 9. Can be observed that these new secondary vortices are separated from the primary ones by an accumulation line of oil.

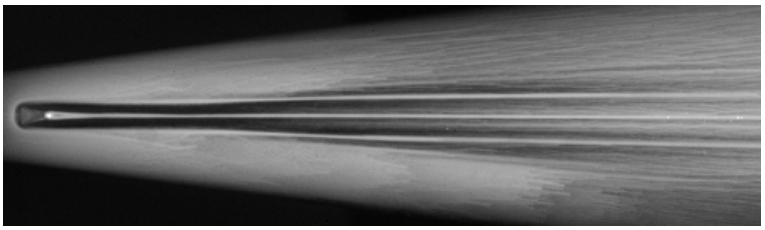

(a) Oil visualization on a sharp cone, ramp k=0.9mm, Re=18E6/m

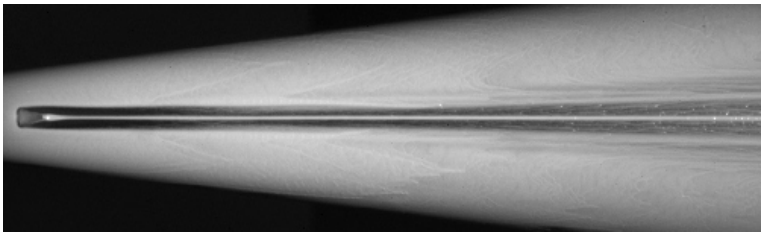

(b) Oil visualization on a blunt 2.5mm cone, ramp k=0.9mm, Re=18E6/m

Figure 9: Oil visualization

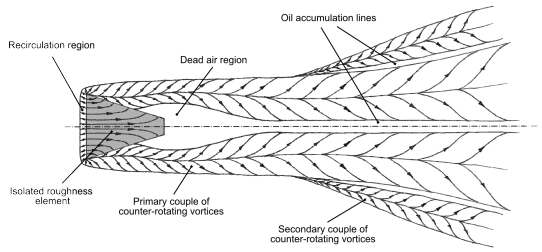

Figure 10: Vortex topology

Generally all these vortices tend to diverge because of the conical nature of the flow around the model. Comparing Fig. 9(a) and 9(b) can be observed the effect of the nose bluntness. In particular, the two pictures 9(a) and 9(b) differ from each other not only by the footprint of the induced wake but also by a visibly different background on the cone surface. This background in Fig. 9(a) is typical of a reduced oil thickness due to the increased skin friction in a turbulent boundary layer, while the same background in Fig. 9(b) in clearly not affected by any transition and the oil surface is smooth all along the cone. The main conclusion is that the nose bluntness is apparently changing the topology of the vortex, the same pair of primary contra-rotating vortices are present in both cases. Carefully observing Fig. 9(b) also the secondary vortices are present, but their appearance is delayed downstream with respect to the sharp nose case. This phenomenon is probably linked to the entropy layer developing from the blunt nose of the cone.

4. Conclusions

Second mode waves have been measured in the VKI H3 Hypersonic Wind Tunnel. Initial growth of second mode modes has been confirmed on a smooth 7deg sharp half-cone. Frequency of second modes is decreasing with increasing downstream measurement location. Moreover, frequency of second modes are also increasing with the increasing Reynolds number and the thinning of the boundary layer since instabilities frequencies are scaling with the inverse of boundary layer thickness. Second mode breakdown has been observed starting from a Reynolds number of 18E6 1/m on the rear part of the 7deg half-cone. With the increasing Reynolds number, several sensor locations were affected by breakdown to turbulence validating the upstream movement of the onset of natural transition. The effect of nose bluntness has been also characterized, showing that a strong entropy layer created by the bow shock is able to change the boundary layer characteristics, like Mach number at the edge, stabilizing the boundary layer itself and damping all the instabilities. From these typical results, on standard models, it appears that the transition phenomenon is strongly linked to the characteristic of the boundary layer. Considering this last statement further investigations are necessary for a more accurate flight extrapolation in the perspective of the EXPERT post-flight analysis.

References

[1] D. Masutti, E. Spinosa, Disturbance Level Characterization of a Hypersonic Blow-Down Facility, in: 41th AIAA Fluid Dynamics Conference, Honolulu, June 2011, AIAA-2011-3887.

[2] K. Fujii, Experiment of the Two-Dimensional Roughness Effect on Hypersonic Boundary-Layer Transition, Journal of Spacecraft and Rockets 43 (4) (2006) 731–738.

[3] M. Estorf, R. Radespiel, S. P. Schneider, Surface-Pressure Measurements of Second-Mode Instability in Quiet Hypersonic Flow, in: 46th AIAA Aerospace Sciences Meeting and Exhibit, Reno, January 2008, AIAA-2008-1153.

[4] K. M. Casper, Hypersonic Wind-Tunnel Measurements of Boundary-Layer Pressure Fluctuations, in: 39th AIAA Fluid Dynamics Conference, San Antonio, June 2009, AIAA-2009-4054.

[5] D. C. Berridge, Measurements of Second-Mode Instability Waves in Hypersonic Boundary Layers With A High-Frequency Pressure Transducer, Master's thesis, Purdue University (2010).

[6] S. J. Beresh, J. F. Henfling, R. W. Spillers, , B. O. M. Pruett, Measurement of Fluctuating Wall Pressures Beneath a Supersonic Turbulent Boundary Layer, 48th AIAA Aerospace Sciences Meeting.

[7] T. Arts, H.-L. Boerrigter, J.-M. Buchlin, M. Carbonaro, G. Degrez, Introduction to Measurement Techniques in Fluid Dynamics, von Karman Institute for Fluid Dynamics, 2001.

[8] C. O. Asma, J. Thoemel, S. Paris, O. Chazot, Utilization of infrared thermography to investigate atmospheric entry aerothermodynamics of space vehicles at von Karman Institute, in: QIRT 2008, 9th International Conference on Quantitative Infrared Thermography, Krakow, July 2008.

[9] P. Santarelli, J. Charbonnier, Heat Transfer Data Reduction User Guide for the VKI-H3 Wind Tunnel, Tech. rep., von Karman Institute (February 1999).

[10] J. D. Anderson, Modern Compressible Flow, McGraw-Hill Science, 2002.

[11] L. H. Mack, Boundary-Layer Linear Stability Theory, Tech. rep., Jet Propulsion Laboratory (1984).

[12] K. F. Stetson, R. L. Kimmel, On Hypersonic Boundary-Layer Stability, in: 30th Aerospace Sciences Meeting & Exhibit, Reno, January 1992, AIAA 92-0737.

[13] N. Chokani, Nonlinear evolution of Mack modes in a hypersonic boundary layer, Physics of Fluids 17-1 (January 2005) doi:10.1063/1.1825471. doi:10.1063/1.1825471.

[14] W. K. George, P. D. Beuther, R. E. A. Arndt, Pressure spectra in turbulent free shear flows, Journal of Fluid Mechanics 148 (1984) 155–191, doi:10.1017/S0022112084002299. doi:10.1017/S0022112084002299.

[15] K. F. Stetson, Nosetip bluntness effects on cone frustrum boundary layer transition in hypersonic flow, in: 16th AIAA Fluid and Plasma Dynamics Conference, Danvers, July 1983, AIAA-83-1763.

[16] K. F. Stetson, Comments on Hypersonic Boundary-Layer Transition, Tech. rep., Wright Research & Development Center (September 1990, WRDC-TR-90-305 7).

[17] D. J. Singh, A. Kumar, S. N. Tiwari, Effect of Nose Bluntness on Flow Field Over Slender Bodies in Hypersonic Flows, in: 27th AIAA Aerospace Sciences Meeting, Reno, Janaury 1989, AIAA-89-0270.

[18] J. D. Anderson, Hypersonic and High Temperature Gas Dynamics, American Institute of Aeronautics & Astronautics, August 2000.

[19] K. F. Stetson, E. Thompson, J. Donaldson, L. Siler, Laminar Boundary Layer Stability Experiments on a Cone at Mach 8, Part 2: Blunt Cone, in: 22nd AIAA Aerospace Science Meeting, Reno, January 1984, AIAA-84-0006.

[20] I. Rosenboom, S. Hein, U. Dallmann, Influence of Nose Bluntness on Boundary-Layer Instabilities in Hypersonic Cone Flows, in: 30th AIAA Fluid Dynamics Conference, Norfolk, June 1999, AIAA-99-3591.

[21] E. Reshotko, Roughness-Induced Transition Transient Growth in 3-D Supersonic Flow, Tech. rep., RTO/NATO (2008, RTO-EN-AVT-151-12).

[22] S. R. Pate, Dominance of Radiated Aerodynamic Noise on Boundary Layer Transition in Supersonic-Hypersonic Wind Tunnels, Tech. rep., Arnold Engineer Development Center (March 1978, AEDC-TR-77-107).

[23] E. van Driest, The Problem of Aerodynamic Heating, Aeronautical Engineer Review (1956) 26–41.

[24] A. Fiala, R. Hillier, Aerothermodynamic of Turbulent Spots and Wedges at Hypersonic Speed, in: 5th European Symposium on Aerothermodynamics for Space Vehicles, November 2004.
URL http://articles.adsabs.harvard.edu//full/2005ESASP.563..615F/0000615.000.html

[25] S. Tirtey, Characterization of a Transitional Hypersonic Boundary Layer in WindTunnel and Flight Conditions, Ph.D. thesis, ULB (2009).

[26] E. R. van Driest, W. D. McCauley, The effect of controlled three-dimensional roughness on boundary layer transition at supersonic speeds, Tech. rep., North American Aviation, Inc. (November 1958).

[27] S. P. Schneider, Effects of Roughness on Hypersonic Boundary-Layer Transition, School of Aeronautics and Astronautics, Purdue University.

A Free-stream and Boundary Layer Characterization of the Longshot Contoured Hypersonic Nozzle

Guillaume Grossir

Aeronautics and Aerospace Department, von Karman Institute for Fluid Dynamics, Belgium, grossir@vki.ac.be

Supervisor: Patrick Rambaud

Assistant Professor, Aeronautics and Aerospace Department, von Karman Institute for Fluid Dynamics, Belgium, rambaud@vki.ac.be.

University Supervisor: Herman Deconinck

Professor, Université Libre de Bruxelles, Belgium, deconinck@ulb.ac.be.

Abstract

A flow characterization of the VKI Longshot contoured hypersonic nozzle is performed using a static pressure probe and a boundary layer pitot rake. Static pressures larger than expected are recorded denoting a possible non-isentropic flow expansion. Turbulent boundary layers are measured at three different locations from the nozzle exit up to half the nozzle length. Turbulence intensities are determined at the nozzle exit and show levels expected for a conventional noisy wind tunnel. Direct flow visualization is used for further characterization of the flow into the test section. It reveals an unexpected excited test gas during the flow establishment followed by a bright flash around the hypersonic jet during testing time. This deeper characterization of the flow will allow for future boundary layer transition experiments to be performed in a better known environment.

Keywords: Hypersonic, Mach number, Reynolds number, Longshot, wind-tunnel, boundary layers, laminar, turbulent, transition, nozzle, non-isentropic, free-stream, noise levels, turbulence intensities.

Nomenclature

Symbols

C_p	pressure coefficient, -
d	distance to the nozzle wall, mm
D	static pressure probe diameter, mm
f	frequency, Hz
M	Mach number, -
p	flow pressure, Pa
r	radial distance from nozzle center line, mm
Re	Reynolds number, -
t	time, ms
T	flow temperature, K
x	distance from nozzle exit, mm
γ	specific heat ratio, -
ρ	flow density, kg/m^3
τ	response time, ms
$\varnothing$	diameter, mm

Subscripts/Superscripts

0	stagnation conditions in nozzle reservoir
e	at boundary layer edge
$exit$	based on nozzle exit diameter
in	based on probe inlet diameter
lam	laminar
unit	based on a 1 m reference length
res	resonance
$static$	static quantity
t_2	total conditions after a normal shock wave
∞	free-stream value
$'$	perturbation

Abbreviations

B.L.	boundary layer
fps	frames per second

1. Introduction

Transition to turbulence phenomenon in hypersonic flows is known to be very sensitive to the quality of the upstream environment among numerous other parameters. The free-stream noise levels are of particular interest as reported in [1; 2; 3] and the largest levels promote earlier transition on models located within the test section as clearly shown in Fig. 1.

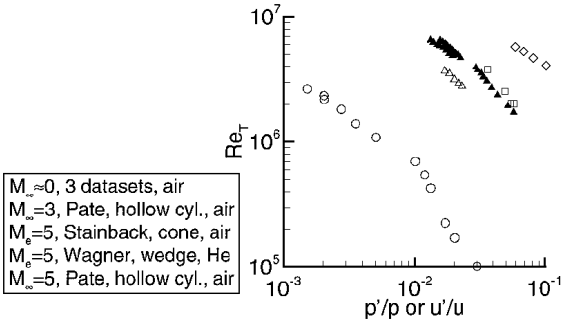

Figure 1: Transition Reynolds number data plotted as a function of the measured disturbance levels ([4])

The origin of disturbances in the free-stream can be divided into three contributions: vorticity fluctuations (turbulence), entropy variations (temperature spottiness) and sound waves (pressure fluctuations) ([5; 6]), each of them issuing from various sources shown in Fig. 2. Ideally, a complete characterization of each type of the disturbances in an hypersonic facility is required. However, for Mach numbers larger than 2.5, pressure fluctuations may be the dominant source as shown by [5]. These are pressure radiations from the turbulent boundary layers developing along the nozzle walls and these noise levels are proportional to the amount of nozzle wall covered by a turbulent boundary layer ([7]). Moreover, these pressure fluctuations are proportional to the fourth power of the free-stream Mach number [1; 3] thus increasing significantly for high Mach numbers facilities.

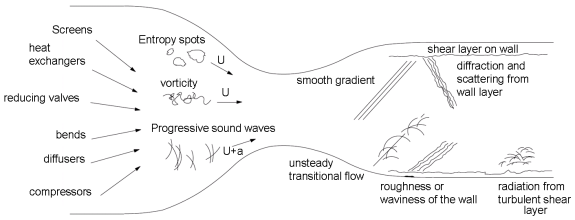

Figure 2: Free-stream disturbances in supersonic wind tunnels ([3])

Therefore, in agreement with the recommendations stated in [8] for any turbulence studies in hypersonic flows, it is first required to determine with accuracy the surrounding environment before attempting any transition characterization on given geometries. The purpose of the experimental campaign reported herein was to characterize the flow of the VKI Longshot hypersonic facility which will be used for future boundary layer transition studies.

This paper focuses on the characterization of nozzle wall boundary layers and on the determination of the free-stream noise levels. Free-stream static pressure measurements are also conducted along the nozzle in order to determine with a better accuracy the free-stream Mach numbers. Finally, flow characterization is supported by flow visualization.

2. Experimental setup

2.1. Probes and instrumentation

2.1.1. Free-stream static pressure probe

A recently manufactured free-stream static pressure probe (shown in Fig. 3) was designed to better characterize the free-stream and to reconstruct with a better accuracy the different flow quantities such as free-stream Mach or Reynolds numbers. A Kulite XCQ-093 with a range of 14000 Pa is used for the static pressure measurements. The first results reported in [9] showed a poor reliability of the probe whose measurement was repeatedly lost after few ms into each experiment. Nevertheless, a first analysis of the recorded pieces of data showed Mach numbers surprisingly lower than expected in the free-stream. These results were to be improved and confirmed by more accurate measurements which will now be reported in section 3.

2.1.2. Boundary layer stagnation pressure rake

A newly designed boundary layer stagnation pressure rake has been used to characterize the boundary layers developing along the nozzle walls and to determine the free-stream noise levels. In order to perform measurements of free-stream disturbances, the frequency-response of the probe must be sufficiently high. The best solution is to use pressure sensors directly exposed to the flow so that no cavities can introduce either fluctuation damping or response delays. However, the VKI Longshot facility is known to be seeded by particles issuing from upstream diaphragms and other elements. Direct exposition of the sensors

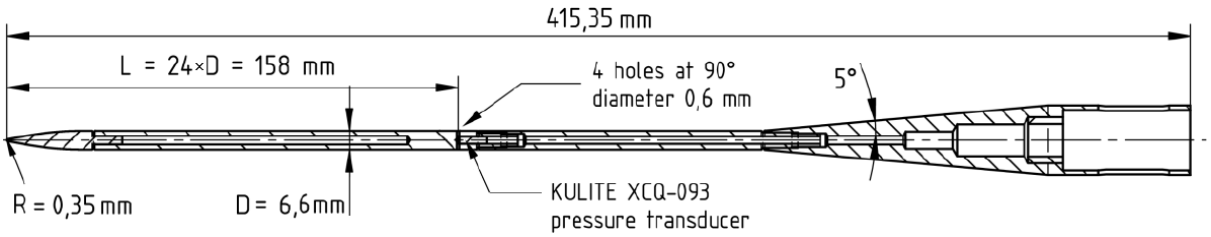

Figure 3: Static pressure probe following the design of Nagamatsu ([9])

to the flow presents large risks of destroying them and therefore sensors must be protected.

The mounting of each pressure sensor together with its protective elements is shown in Fig. 4. The pressure sensor is mounted at the end of a thin tube and a thick screen (drilled with four holes with $\varnothing = 0.5$ mm) is located in front of it, held by a cap. The inlet diameter of the cap is $\varnothing_{in} = 1.5$ mm. The chicane introduced should reduce the risks of direct particle impact on the membrane of the sensor. The volume of the cavities and tubes introduced is 8.5 mm^3 which influences the frequency response of the sensors. From shock tube calibration, the response time is $\tau \approx 14\mu s$, and the resonance frequency of the system is $f_{res} \approx 20$ kHz.

A total of 7 fast-response Kulite XCE-093 with a range of 100000 Pa sensors are installed in a rake support shown in Fig. 5.

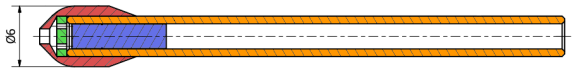

(a) Design (cap, screen, tube and sensor)

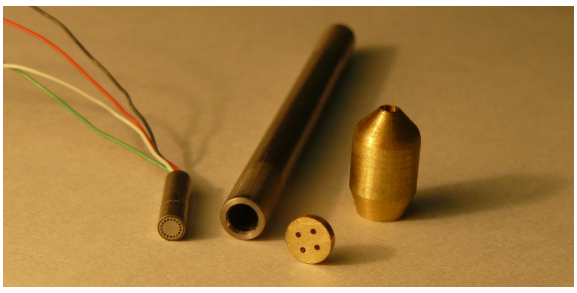

(b) Exploded view

Figure 4: Pitot tube

2.2. Facility

The VKI Longshot hypersonic facility is used with a 3 m long contoured nozzle having an exit diameter of $\varnothing_{exit} = 426$ mm. It is designed to attain Mach

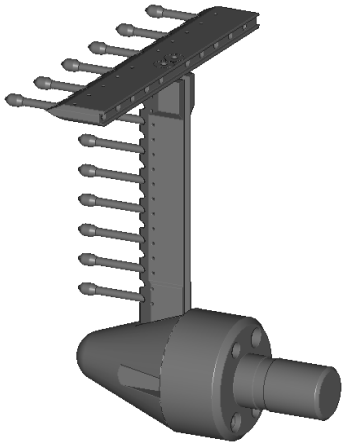

(a) Pressure rake design

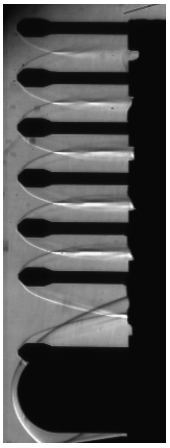

(b) Schlieren of the rake (additional probes in the view)

Figure 5: Pressure rake for boundary layer characterization

14. Test gas is N_2. The test section is located into a closed tank of 15 m^3 initially vacuumed to $p \approx 0.1$ Pa. The structure of the jet changes from under-expanded at the beginning of an experiment to over-expanded at the end of the experiment due to the decreasing stagnation conditions with time and rising pressure into the test section.

2.3. Test matrix

The experiments reported here are all using a "Low" Reynolds number condition (varying with time between $9.5 \times 10^6 \gtrsim \mathrm{Re}_{\mathrm{unit}} \gtrsim 5.5 \times 10^6$/m, 2500 K $\gtrsim T_0 \gtrsim$ 1000 K, 1200 bar $\gtrsim p_0 \gtrsim$ 200 bar). This is the lowest Reynolds number conditions achievable by the facility and it was chosen in order to delay boundary layer transition along the nozzle walls and thus decrease free-stream noise levels.

Test times are of the order of $t \approx 20$ ms at the nozzle exit and $t = 0$ is chosen as the time where the

measured reservoir pressure reaches half of its peak amplitude.

Boundary layer characterization using the pressure rake has been performed at three locations along the nozzle axis: at the nozzle exit ($x = 0$ mm) and inside the nozzle ($x = -750$ and -1500 mm) as shown in Fig. 6 where the background colors are representing the total pressure after a shock wave p_{t_2}. Measurements have been performed from the nozzle center line up to 9.5 mm to the wall.

Static pressure measurements were performed only at $x = 0$ and -750 mm, both at $d \approx 130$ mm and within the uniform Mach 14 core according to available laminar CFD computations.

2.4. Data acquisition

Data were acquired at 500 kS/s using a 16-bit PXI-6123 module for the static pressure probe (signal was amplified by 500 using a Fylde amplifier (FE-351-UA)), and at 2.5 MS/s for the boundary layer rake using a 14-bit PXI-6133 module. Both modules were mounted on a National Instruments PXI-1045 chassis.

3. Longshot free-stream measurements

3.1. Modifications to the static pressure probe

The cause of initially poor signal quality (see [9]) has been identified as being due to a sensitivity of the static pressure sensor to mechanical vibrations induced by the flow. The probe has been stiffened and mounted directly onto a sting instead of using lateral supports.

Also, the previous design of the probe was using 4 tapered holes connected to one single chamber for the static pressure measurement. Their inlet diameter was 0.8 mm but the influence of the tapered shape on the measurements was questionable ([H. Olivier, priv. comm.]). Thus, the probe has been modified by fitting precision tubes inside the existing holes, reducing the inlet diameter to 0.6 mm but allowing to fill with a compound the tapered inlet. The surface has then been polished until it matched the surrounding shape. This is shown in Fig. 7. According to the results presented in [10], the reduced inlet diameter may increase slightly the viscous effects in the tubes and lead to measured pressures about 2-3% larger than previously.

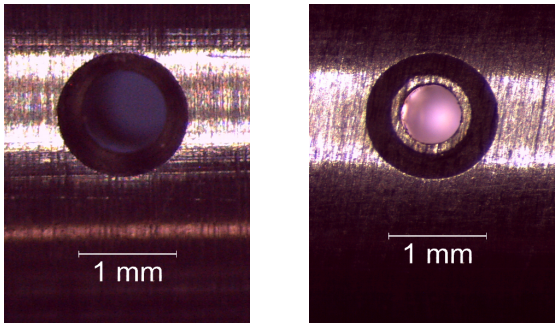

(a) Old design with tapered holes, $\varnothing_{in} = 0.8$ *mm*

(b) New design with straight holes, $\varnothing_{in} = 0.6$ *mm*

Figure 7: Inlet holes of the static pressure probe

The influence of viscous effects increasing the static pressure along the probe cannot be checked with the present design and one had to rely on CFD results to determine the static pressure measurement location. A second probe is being manufactured with several sensors at different locations from the nosetip in order to evaluate the influence of these viscous effects along the probe and to confirm the present results.

3.2. Results

The free-stream static pressure measured at the nozzle exit and at $x = -750$ mm inside the nozzle and using tapered or straight holes is reported in Fig. 8. The decay measured follows the typical decay of the

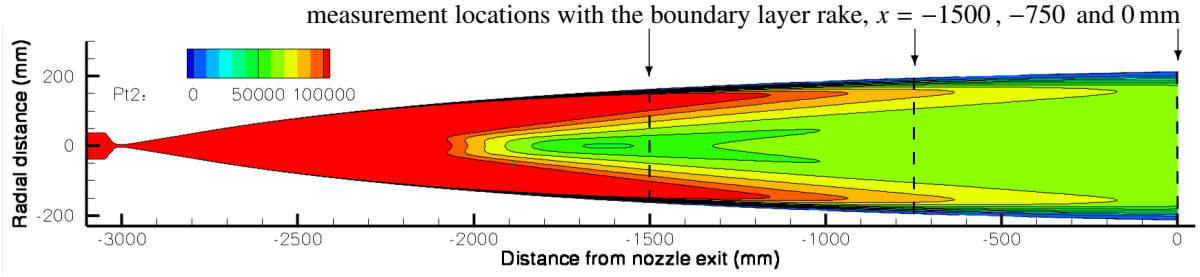

Figure 6: Measurement locations along the nozzle on top of CFD prediction of stagnation pressure p_{t_2} for t=0 ms

reservoir conditions of the wind-tunnel. The quality of the measurements has been improved with respect to previous tests by reducing the amplitude of the oscillations. Since the probe stiffening, measurements could be performed over the whole test duration for every single test.

The steady calibration of the probe lead to measurements uncertainties about 5.4%. Additionally, the sensor used has a combined linearity, hysteresis and repeatability uncertainty of ±15 Pa according to manufacturer specifications which shows the poor accuracy achievable when compared to the free-stream pressure range of few hundreds of Pa. The oscillations measured by the probe are within these uncertainty limits and may simply be related to the sensor capabilities. It is clear that the high-frequency free-stream static pressure fluctuations that could be used as an indicator of the free-stream noise levels cannot be retrieved with this probe due to design limitations.

The modification of the inlet holes shape does not seem to influence strongly the measurements performed at $x = -720$ mm inside the nozzle. The repeatability is excellent and the influence of the reduced diameter of the probing holes (inducing larger viscous effects) is within the uncertainty of the probe.

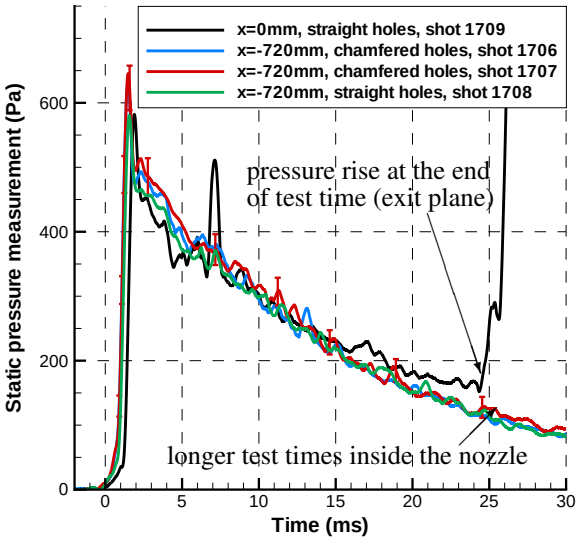

Figure 8: Measured static pressure

The trend of the decaying static pressure at the nozzle exit is different from measurements inside the nozzle and other measurements are being performed to confirm this trend. The pressure recorded in the nozzle is slightly larger than at the exit at the beginning of an experiment. The peak recorded at the nozzle exit at $t \approx 7$ ms is likely to be an external perturbation ans should be disregarded. The tendency is then inverted at $t \approx 12$ ms due to a difference in the decay trends of the measurements at these two locations. Larger static pressures at the exit of a nozzle than inside have already been reported in other hypersonic facilities and may be due to various non-isentropic flow phenomena in the nozzle.

For instance, vibrational freezing followed by relaxation of the heated test gas coming from the reservoir of the nozzle [11; 12] or flow condensation enhanced by impurities seeding the flow and acting as nucleation sources [13; 14; 15; 16] must be investigated. In both cases, heat would be progressively released into the free-stream, rising the free-stream static temperature and changing other related free-stream properties such as the Mach number. The static pressure is directly affected by such process and is an excellent way to detect non-isentropic flow expansions. Other phenomena such as the relaxation time of specific heats or the presence of shock waves inside the nozzle due to imperfections along the nozzle walls need to be examined.

3.3. Free-stream Mach number determination

The free-stream Mach number can be rebuild using various measurements. Ratios of test section stagnation pressure to reservoir stagnation pressure p_{t_2}/p_0 and static pressure to test section stagnation pressure p_{static}/p_{t_2} will be used here. The second method using p_{static}/p_{t_2} leads to free-stream Mach numbers much lower than the ones expected from the design of the nozzle and the ones rebuild using p_{t_2}/p_0 (Fig. 9). The uncertainties on the Mach numbers do not even overlay each other. This mismatch is mainly due to a measured static pressure being about twice larger than expected and is likely to be due to a non-isentropic flow phenomenon to be identify further. This could also be due to viscous effects along the probe much larger than predicted by CFD and fooling the measurements.

Static pressure measurements inside the nozzle lead to increasing free-stream Mach number during the experiments with a repeatable trend. This is not observed for the experiment at the nozzle exit although there is also a slope change at $t = 7$ ms. This trend is coming from the static pressure measurements reported in Fig. 8. Although the reason has not yet been identified precisely, it could be due to less severe vibrational mode relaxation with the decaying reservoir temperature. Flow condensation would be expected to increase during an experiment due to the decaying

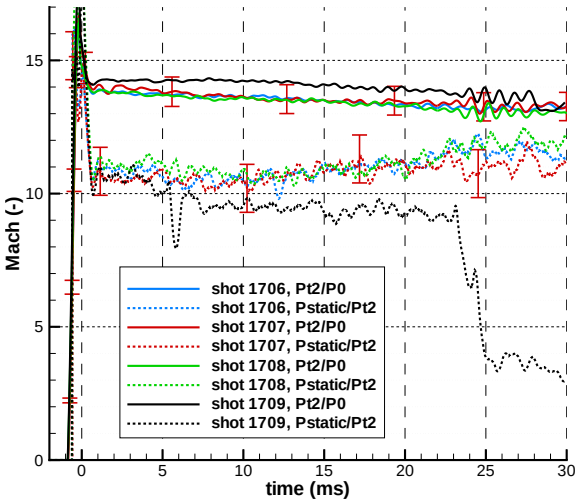

Figure 9: Free-stream Mach number determined from p_{t_2}/p_0 and p_{static}/p_{t_2}

flow static temperature. This should lower further the Mach number which is not observed here.

4. Boundary layers characterization

4.1. Purposes

Boundary layers along the 3 m long contoured nozzle have not yet been characterized despite two decades of regular tests. A turbulent nozzle wall boundary layer would strongly influence the free-stream environment by rising the noise levels. Regarding the length of the nozzle, it is believed that the boundary layers are turbulent in the exit plane. However, since the nozzle uses a contoured design, there is a cone of uniform flow inside the nozzle as shown in Fig. 10 and thus if transition is appearing far enough downstream the nozzle throat, it would be possible to have a small but useful "quiet" core. In this zone, the noise radiated by the nozzle wall boundary layers would remain relatively low and be closer to the conditions encountered in real flight. To assess this possibility, measurements inside the nozzle are required to characterize the boundary layers and to determine the free-stream noise levels. From CFD computations, the uniform part of the flow inside the contoured nozzle starts at $x \approx -1.5$ m. By following a characteristic line, the critical location for the boundary layer transition radiating noise into the free-stream is at $x \approx -1.8$ m .

4.2. Boundary layer profiles

4.2.1. Mean values

Successive measurements were performed with the few sensors available at the nozzle exit in order to obtain complete profiles of the stagnation pressure across the nozzle. This procedure was then repeated at several locations along the nozzle. The stagnation pressure (at various time instants during the test time) is plotted in Fig. 11 where the decay is again due to the decreasing reservoir conditions with time.

Nozzle wall boundary layers are clearly visible and are about 100 mm thick.

The large peak at the end of the test time is due to the closure of the hypersonic jet. This time mainly depends upon the location across and along the nozzle and only slightly with test conditions. The latter characterization will be developed in section 4.2.4.

The free-stream noise levels are slightly visible as fluctuating stagnation pressure and will be analyzed further in section 4.2.5.

4.2.2. Dimensionless profiles

Boundary layer profiles have been extracted at different time instants for the three measurements locations along the nozzle. In order to improve the comparison between different experiments and to compare

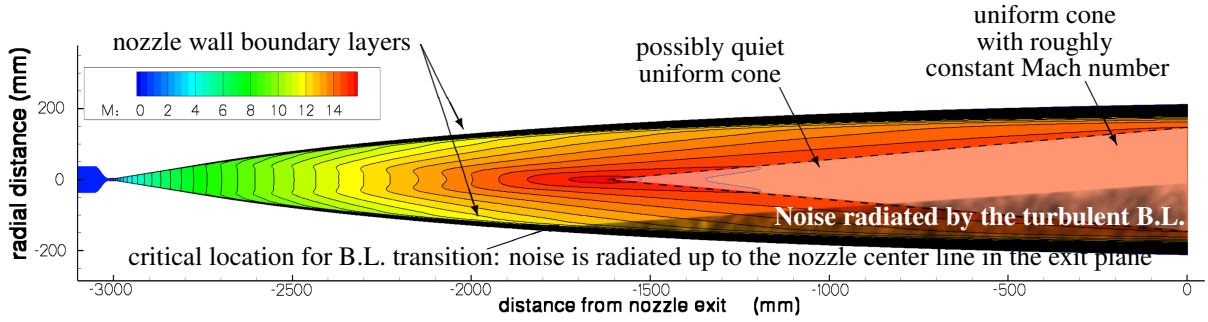

Figure 10: CFD prediction of Mach number in the nozzle and sound radiation by the boundary layers

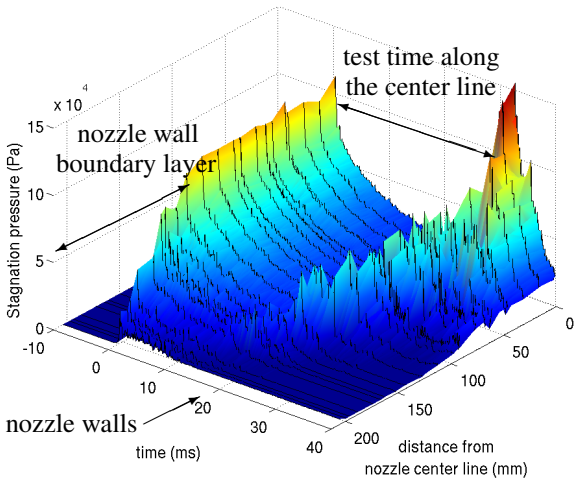

Figure 11: Stagnation pressure profile as a function of time at the nozzle exit for experiments at "Low" Reynolds (using N_2)

profiles considered at different time instants, the stagnation pressure p_{t_2} profiles have been normalized. A local reference stagnation pressure belonging to the boundary layer profile was preferred to the reservoir stagnation pressure located upstream. The location chosen along the profile is in such a way that all the experiments used had one sensor at that position. Precise locations are $r = 91\,\text{mm}$, $r = 90\,\text{mm}$ and $r = 59\,\text{mm}$, respectively for profiles at $x = 0\,\text{mm}$, $x = -750\,\text{mm}$ and $x = -1500\,\text{mm}$. The results are presented in Fig. 12 for the three locations along the nozzle. For each of these pictures, several boundary layer profiles (in color) are plotted at different time instants. The mean value of these profiles is plotted with a thicker plain black line. The time considered is limited to the beginning of the experiment up to 12 ms when the jet starts closing itself at the nozzle exit and pollutes measurements close to the wall.

The measurements at the nozzle exit show a thick boundary layer with some larger disturbances in the profiles at $r \approx 155\,\text{mm}$ and a lower pressure close to the nozzle center line. Larger pressures are recorded in the wall vicinity where the closest probing location was at $d = 9.5\,\text{mm}$. Shock waves from Schlieren flow visualization (Fig. 5b) were still observed at that location hence the flow is still supersonic. However, the generated shock and the probe itself may locally disturb the boundary layer and change the flow topology. This is the reason for the larger stagnation pressure for the closest wall measurement.

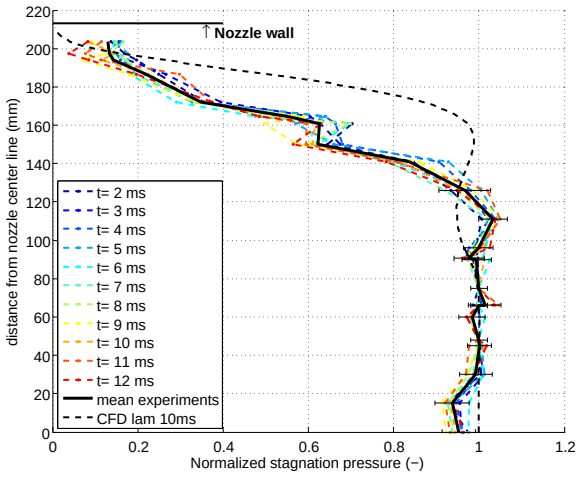

(a) at the nozzle exit

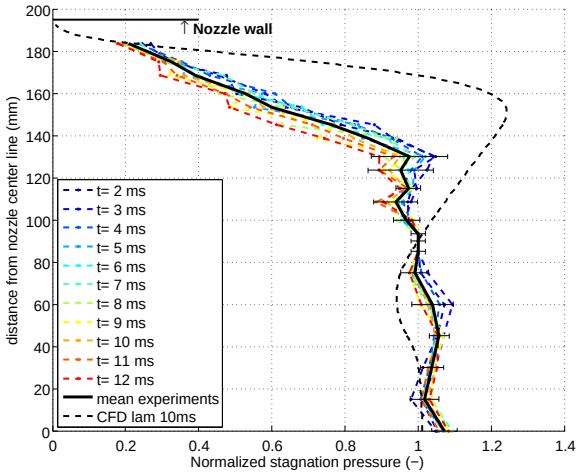

(b) at 750mm inside the nozzle

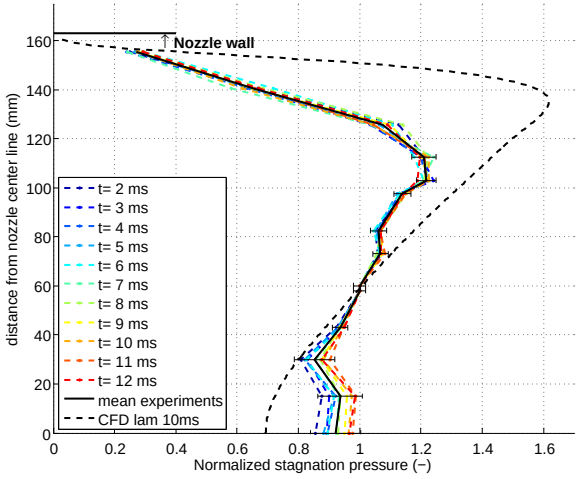

(c) at 1500mm inside the nozzle

Figure 12: Normalized stagnation pressure profiles across the boundary layer

The free-stream Reynolds number is decreasing during an experiment and the boundary layer thickness along the nozzle walls was thus expected to increase. This is not observed clearly in Fig. 12a where boundary layer profiles are well superimposed, showing a similar boundary layer state and a similar boundary layer thickness.

Inside the nozzle, at $x = 750\,\text{mm}$ (Fig. 12b), the recorded stagnation pressure profile is still relatively flat in the center part with relatively thick boundary layers.

Further inside the nozzle, at $x = 1500\,\text{mm}$ (Fig. 12c), the shape of the profile is seen to be very different from the previous ones with a larger peak at the edge of the boundary layer and decreasing towards the nozzle axis. These profiles are very well superimposed and suffer from much lower disturbances except along the nozzle center line. This might be due to a changing flow topology better illustrated by Fig. 13 where boundary layer profiles have been considered for a much longer time before the end of the test time at that location. A flattening of the profiles is clearly observed but its precise origin is not yet known.

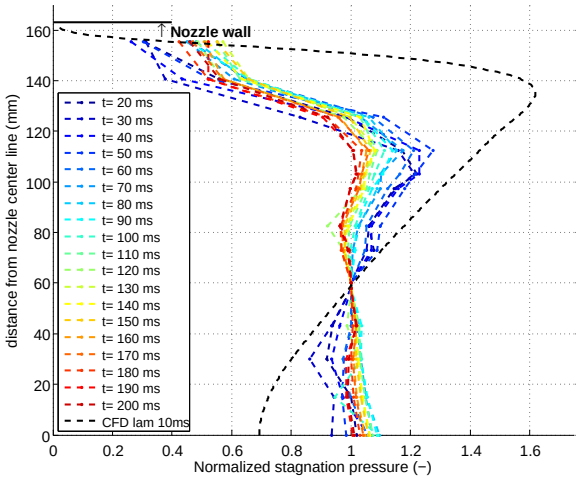

Figure 13: Unsteady normalized stagnation pressure profile at $x = -1500\,\text{mm}$

Mean profiles obtained after normalization have been converted back to a stagnation pressure using the reference stagnation pressure p_{t_2} measured at $t = 10\,\text{ms}$ and plotted in Fig. 14. The nozzle is composed of several sections assembled together with smoothed joints. If these were introducing disturbances into the flow, perturbations could be tracked from one location to another. Characteristic lines are represented here for Mach 12 following the uncertainties shown in section 3.3. The exit profile exhibits a strong disturbance close to the wall. Visual inspection of the nozzle has not revealed either steps or gaps at these locations. Disturbances occurring close to the center line can be followed by analyzing the profiles at successive locations. Disturbances along the center line at $x = -750\,\text{mm}$ may be followed up to the nozzle exit plane but intermediate measurements would be required for definitive conclusions.

4.2.3. Comparison with CFD results

A stagnation pressure profile issuing from CFD results is also given for comparison in each plot of Fig. 12. These laminar steady computations were performed with Longshot free-stream conditions corresponding to $t = 10\,\text{ms}$ ($p_0 = 5.84 \times 10^7\,\text{Pa}$, $T_0 = 1800\,\text{K}$) and using a perfect gas law to describe the gas behavior.

The stagnation pressure (determined from Eq. 1) is normalized using the local value at the same locations as used for experimental results (see section 4.2.2).

$$p_{t_2} = p_\infty \left[\frac{(\gamma+1)\,M_\infty^2}{2} \right]^{\frac{\gamma}{\gamma-1}} \left[\frac{\gamma+1}{2\gamma M_\infty^2 - (\gamma-1)} \right]^{\frac{1}{\gamma-1}} \quad (1)$$

At $x = 0$, $-750\,\text{mm}$ and $-1500\,\text{mm}$, the predicted stagnation pressures p_{t_2} are respectively 28315 Pa, 28440 Pa and 32203 Pa. The measurements at the same locations previously lead respectively to 35730 Pa (+ 21%), 39220 Pa (+ 27%) and 42150 Pa (+ 24%). Moreover, even normalized, the shape of the profile appears to be very different from the ones measured experimentally. The reason is a different boundary layer state which likely was turbulent in the experiments due to the long nozzle used. The apparent fuller profiles of laminar boundary layers have already been reported at lower Mach numbers in [17; 18] and may explain the present mismatch of stagnation pressure p_{t_2} profiles.

Additional computations performed with a more accurate equation of state and turbulent boundary layers will improve the comparison.

4.2.4. Available test time

The time of arrival of the test gas in the nozzle depends on the location considered. Along the center line, the test gas arrives at $t = 0.62\,\text{ms}$, 0.95 ms and 1.3 ms, respectively for $x = -1500$, $x = -750$ and $x = 0\,\text{mm}$.

The larger stagnation pressure observed by the end of the test time in Fig. 11 is due to the closure of the

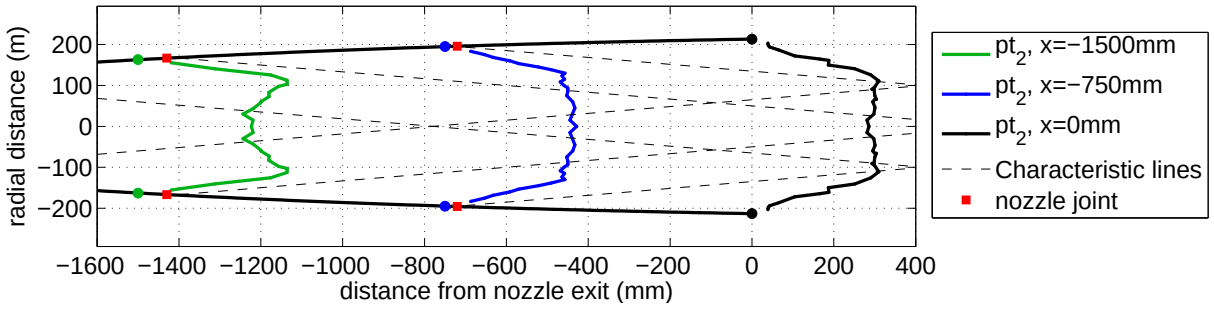

Figure 14: Boundary layer profiles through the nozzle with characteristic lines at Mach 12

hypersonic jet. The time at which it occurs is a function of both r and x. The values reported here are in agreement with other values measured previously at the exit and at $x = 250$ mm (dashed lines). The local closure time is plotted in Fig. 15. It appears clearly that the test times available are much longer inside the nozzle. Thus, for future transition measurements on models, it is suggested to use long geometries partially located inside the nozzle. This will allow to reach large local Reynolds numbers required for boundary layer transition and will avoid the short test time at the exit due to the early jet closure.

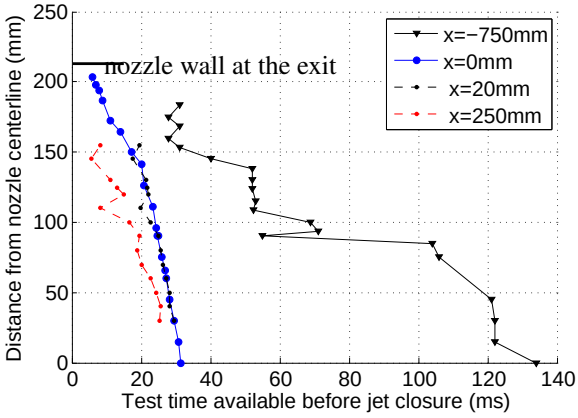

Figure 15: Jet closure time for various locations along the nozzle

4.2.5. *Free-stream noise levels*

The flow of most hypersonic facilities is seeded by high-velocity particles issuing from various upstream elements. This usually prevents the use of sensors directly exposed to the flow and reduces hopes for a complete description of the flow noise levels of hypersonic facilities. Nevertheless, a first approximation of the free-stream noise levels can be obtained by analyzing pitot pressure measurements and their fluctuations.

A pressure coefficient can be expressed at each measurement location according to the classical definition:

$$C_p = \frac{p - p_\infty}{\frac{1}{2}\rho_\infty u_\infty^2} \tag{2}$$

which in the hypersonic limit, using N_2, and for stagnation points reduces to $C_p = 1.839$.

Neglecting the low free-stream pressure when compared to the pitot pressure, Eq. 2 can be rewritten as $p_{t_2} = \frac{1.839}{2}\rho_\infty u_\infty^2$. Then, neglecting density fluctuations (although they may be important, no probe could differentiate them during the present measurements) and second order terms, the velocity fluctuations can be linked to the pressure fluctuations through Eq. 3.

$$u'_\infty = \frac{p'_{t_2}}{1.839\,\rho_\infty u_\infty} \tag{3}$$

The RMS of the pitot pressure signal was considered over 0.2 ms windows, with a 50% overlap. The local velocity fluctuations have then been non-dimensionalized with the mean free-stream velocity along the center line at that time instant. Results are shown in Fig. 16 in terms of u'/u_∞. As one expects, the largest levels of disturbances are recorded within the turbulent boundary layer (up to 20-25% in the outer part of the nozzle boundary layer). This turbulent motion of eddies into the boundary layer radiates noise into the free-stream and leads to noise levels measured about $3.8\% \pm 1.1\%$. The influence of the normal shock wave in front of the sensor is likely to increase the noise levels according to the numerical work of [19]. Despite this amplification, the noise levels in the free-stream would remain 2 to 3 orders of magnitude larger than what they are in real flight conditions. Therefore,

the Longshot facility is a conventional "noisy" hypersonic wind tunnel and transition experiments will strongly be influenced as shown in Fig. 1.

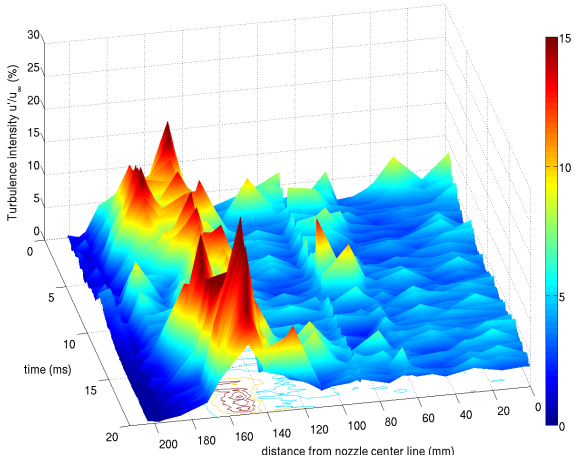

Figure 16: Turbulence intensities at the nozzle exit

4.2.6. Measurements further inside the nozzle

The boundary layer profiles measured are believed to be turbulent even at $x = -1500\,\text{mm}$ when compared to CFD predictions although pitot pressure fluctuations are much lower inside the nozzle (Fig. 12c). Measurements further inside the nozzle with the rake are not possible with the sensors currently used and rake support vibrations would become an issue. The instrumentation of the walls of the nozzle should be considered as an interesting workaround to detect the transition location closer to the throat of the nozzle. Temperature measurements are suggested since thermocouples sensors are more robust and not subject to nozzle vibrations as would be pressure sensors.

5. Flow visualization

In order to support the current flow investigation and identify possible sources of non-isentropic flow phenomena, a flow visualization has been conducted in the test section of the facility. It is known for decades that during an experiment, a brief bright light is observed in the test section although nothing is known about its source, nature nor even its duration and precise location. The first direct flow visualization is reported hereafter. A Phantom v.7 high-speed camera was used to record frames as the ones presented in Fig. 17 at 4796 fps with an exposure time of 195 μs in a complete darkness environment.

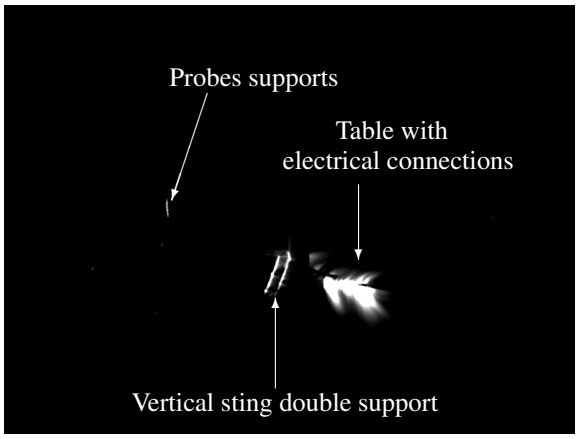

(a) Excited gas at stagnation point of probes and supports, $t = 0.5\ ms$

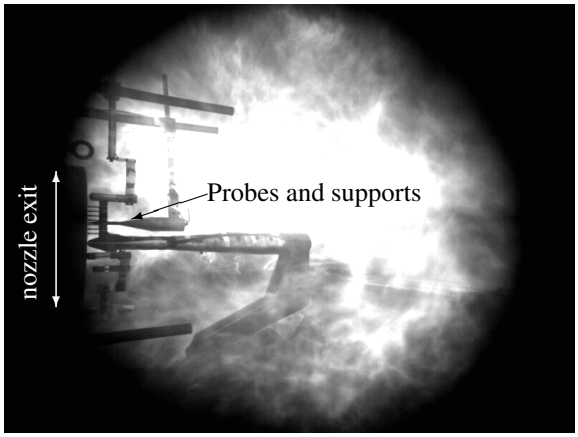

(b) Identical view angle, diffuse light around the hypersonic jet, $t = 27\ ms$

Figure 17: Light emission from the Longshot facility captured by a high-speed camera using a wide-angle objective

Two clearly distinct phenomena are distinguished. At first, a bright flow is observed around the stagnation point of probes and supports following the shape of the shock waves around these bodies. These are identified as real gas effects with excitation of N_2. This lasts only for a brief period about 1 ms during which the high enthalpy test gas can be tracked successively from the stagnation probes at the nozzle exit towards the end of the dump tank where a bright light is observed as similarly mentioned in [20].

Secondly, a different and even brighter feature slowly appears before gradually fading away (Fig 17b). It appears about $t \approx 4$ ms while the initial test gas has reached the end of the test chamber and starts to recirculate around the hypersonic jet. This correlates well well with the rise of static pressure beside the jet at $t \approx 4$ ms. The diffuse light is observed all around the high velocity jet without having a clearly defined structure and lasts for 25 to 30 ms. The jet itself does not appear to be bright with an apparent shear layer on some frames. It has been recorded for many successive experiments using different points of view, and even shorter exposure times. Whether this light has an influence on the measurements remains to be evaluated. The possible excitation/deexcitation of the test gas by high velocity seeding particles should also be investigated.

Despite various spectroscopy measurements using an intensified camera and optical fibers pointing across the jet, on stagnation probes, at the back of the test section, along the jet boundaries and in the test section, no significant measurement could be obtained and no conclusion drawn regarding the frequency content of the emitted light. Thus, additional experiments are required to identify the precise nature of these features.

6. Conclusions

The static pressure probe has been significantly improved and the influence of the inlet tapered holes on the higher measured static pressure has been ruled out. The influence of the viscous effects on the probe remains unknown and will be the purpose of a coming test campaign. The different behavior of the decaying trend for the measured static pressure between early and end of an experiment also requires additional experiment to explain the rising trend observed for the free-stream Mach numbers. The lower Mach numbers deduced from these measurements could be explained by a non-isentropic flow expansion although it requires deeper analysis of the possible flow phenomena.

Nozzle boundary layers have been characterized at three locations along the nozzle. Comparison with laminar CFD shows a poor agreement, depicting a likely turbulent boundary layer even at $x = -1500$ mm into the nozzle. The precise location where transition to turbulence occurs in the nozzle has not yet been determined but, in the present configuration, the Longshot facility is unlikely providing a quiet core even for this "Low" Reynolds number condition. Turbulent CFD results should support the present conclusions.

Advantages of using long models fitted into the nozzle have been reported in order to benefit from larger local Reynolds numbers and avoid early jet closure.

The noise levels measured at the nozzle exit are about 3.8% in the uniform part of the hypersonic jet which confirms the Longshot facility is effectively a conventional "noisy" facility not directly representative of flight conditions. The source of these large levels is due to the turbulent boundary layers along the nozzle walls where much larger fluctuations have been recorded.

The emission of light into the test section has been observed for the entire test duration and is partially issuing from an initial excited test gas visible at the stagnation point of all probes. It is then followed by a much longer diffuse but still bright light source which might be due to test gas excitation by seeding particles.

The present results are providing a better knowledge of the flow in the hypersonic contoured nozzle of the Longshot facility which can already be used for boundary layer transition experiments. From the analysis of the present results, new unknowns are also rising such as possible non-isentropic flow phenomena, unsteady boundary layers inside the nozzle or the origin of the light emission in the test section. These all require to be the object of subsequent investigations within the facility.

Acknowledgments

I gratefully acknowledge FRIA (Fonds pour la formation à la Recherche dans l'Industrie et dans l'Agriculture) for the financial support of this project. I am also thankful to K. Bensassi and D. Le Quang for their respective help in providing CFD results and support for the application of spectroscopy techniques.

References

[1] J. Laufer, Sound radiation from a turbulent boundary layer, Technical Report TR-32-119, Jet Propulsion Laboratory, California Institute of Technology, Pasadena, California (November 1961).

[2] J. Laufer, Some statistical properties of the pressure field radiated by a turbulent boundary, Physics of Fluids 7 (8) (1964) 1191–1197.

[3] S. P. Schneider, Development of hypersonic quiet tunnels, Journal of Spacecraft and Rockets 45 (4) (2008) 641–664.

[4] S. P. Schneider, Effects of high-speed tunnel noise on laminar-turbulent transition, Journal of Spacecraft and Rockets 38 (3) (2001) 323–333.

[5] S. R. Pate, C. J. Schueler, Radiated aerodynamic noise effects on boundary layer transition in supersonic and hypersonic wind tunnels, AIAA Journal 7 (3) (1969) 450–457.

[6] S. R. Pate, Effects of wind-tunnel disturbances on boundary-layer transition with emphasis on radiated noise: a review, in: AIAA (Ed.), 11th Aerodynamic testing conference, no. 80-0431, 1980.

[7] J. M. Kendall Jr., Supersonic boundary-layer transition studies, in: JPL Space Programs Summary, Vol. 3, Jet Propulsion Laboratory, 1970, pp. 43–47.

[8] E. Reshotko, Boundary layer stability and transition, Annual Review of Fluid Mechanics 8 (1976) 311–349.

[9] B. Van Hove, Free stream measurements and related data reduction methods for the Longshot hypersonic wind tunnel, Project report 2011-31, von Karman Institute (June 2011).

[10] H. Olivier, H. Kindl, Development of a static pressure probe (progress report), Tech. Rep. HT-PR-E34-711-RWTH, Shock Wave Laboratory RWTH Aachen (December 1995).

[11] A. H. Boudreau, Characterization of hypersonic wind tunnel flow fields for improved data accuracy, in: AGARD-CP-429, AGARD, 1987.

[12] A. H. Boudreau, Methodology of hypersonic testing, in: von Karman Institute (Ed.), Lecture Series, no. LS 1993-03, 1993.

[13] P. D. Arthur, Effects of impurities on the supersaturation of nitrogen in a hypersonic wind tunnel, Ph. d. thesis, Calif. Inst. of Technol., Pasadena, California (1952).

[14] P. P. Wegener, L. M. Mack, Condensation in supersonic and hypersonic wind tunnels, in: H. L. Dryden, T. von Kármán (Eds.), Advances in applied mechanics, Vol. 5, Academic Press Inc., 1958, Ch. 7, Condensation in supersonic and hypersonic wind tunnels, pp. 307–447.

[15] H. G. Stever, Condensation phenomena in high speed flows, in: Fundamental of Gas Dynamics, Princeton University Press, 1958, Ch. F, pp. 526–573.

[16] M. Lederer, W. Yanta, W. Ragsdale, S. Hudson, W. Griffith, Condensation in hypersonic nitrogen wind tunnels, in: AIAA 16th aerodynamic ground testing conference, no. 1990-1392, Seattle, WA, 1990.

[17] P. C. Stainback, J. B. Anders, W. D. Harvey, A. M. Cary, J. Harris, An investigation of boundary layer transition on the wall of a Mach 5 nozzle, in: AIAA 12th Aerospace and Sciences meeting, no. 1974-136, 1974.

[18] W. D. Harvey, P. C. Stainback, J. B. Anders, A. M. Cary, Nozzle wall boundary layer transition and free-stream disturbances at Mach 5, AIAA Journal 13 (3) (1975) 307–314.

[19] H. S. Ribner, Spectra of noise and amplified turbulence emanating from shock-turbulence interaction, AIAA Journal 25 (3) (1987) 436–442.

[20] T. J. McIntyre, H. Kleine, A. F. P. Houwing, Optical imaging techniques for hypersonic impulse facilities, The Aeronautical Journal 111 (2007) 1–16.

Trajectory and Atmospheric Reconstruction for Entry Vehicles

Bart Van Hove

Royal Observatory of Belgium, Reference Systems and Geodynamics, Belgium, bartvh@observatoire.be

Supervisor: Chazot Olivier

Associate Professor, Aeronautics and Aerospace department, von Karman Institute for Fluid Dynamics, Belgium, chazot@vki.ac.be

University Supervisor: Lacor Chris

Full Professor, Department of Mechanical Engineering, Vrije Universiteit Brussel, Belgium, Chris.Lacor@vub.ac.be

University Co-Supervisor: Özgür Karatekin

Royal Observatory of Belgium, Reference Systems and Geodynamics, Belgium, ozgur.karatekin@oma.be

Abstract

Reconstruction of the hypersonic entry of planetary capsules has mainly focused on engineering trajectories (position/velocity). However, development of sophisticated on-board experiments and demand for in-situ atmospheric profiles by the climate modeling community, require accurate atmospheric conditions.

Keywords: trajectory, atmosphere, reconstruction, FADS, flow characterization, uncertainty quantification.

1. Introduction

Reconstruction of the hypersonic entry of planetary capsules has mainly focused on the engineering trajectory (position, velocity). The interpretation of accurate on-board experiments (e.g. EXPERT) and a demand for in-situ atmospheric profiles by the planetary climate modeling community, require accurate reconstruction of also the atmospheric conditions. Currently, this is typically limited to +/-15% [ref 1]. Atmospheric profiles from hypersonic entry are especially interesting on planets where in-situ measurements are scarce, such as Mars [ref 2].

Figure 1 is a simplified representation of the reconstruction process. The set of available measurements almost always includes accelerometers; sometimes also gyroscopes, nose surface pressures (for use in a Flush Air Data System) and Doppler shifts in the radio link signal are included. Additional information going into the reconstruction can include an aerodynamic database built from CFD simulations or wind tunnel experiments, a planetary gravity model and even uncertainty estimates of the above (including the measurements). This additional information is listed under the catch-all term 'database' indicating prior knowledge. A sophisticated, accurate database is preferable to a very simple set of assumptions. Finally, the processing consists of the integration of equations of motion and optionally some method to combine multiple measurements. These range

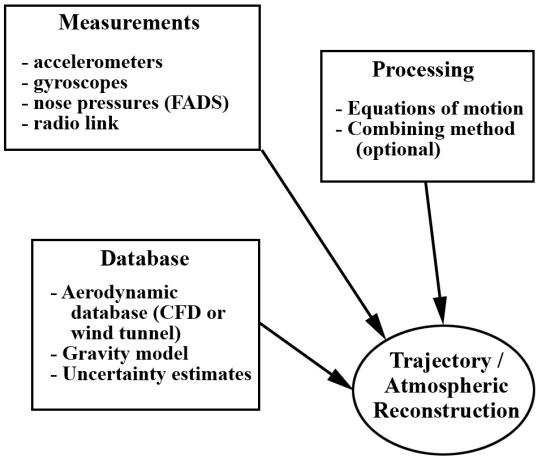

Figure 1: Simplified reconstruction process

from simple comparative calculations to stochastical Kalman filters that produce weighted averages based on uncertainty estimates in the database. Such a filter also produces uncertainty estimates on the results.

2. Approach

We will investigate several of the above elements to determine which are crucial to the atmospheric reconstruction effort. Resulting atmospheric profiles can be compared to each other and climate models. Available datasets include ARD on Earth, Phoenix, Pathfinder, MER on Mars and Huygens on Titan. NASA's Mars Science Laboratory (MSL) will land in August 2012. MSL is the best equipped Mars entry vehicle to date, including nose pressures for FADS and heat flux measurements.

Currently, we use the Phoenix dataset as a test case for estimating atmospheric reconstruction accuracy and sensitivity to measurements and database elements. The result will be a versatile reconstruction code including simple uncertainty quantification (UQ) analysis. We can incorporate existing work such as the VKI 6-DOF trajectory code, the Royal Observatory's radio Doppler code and a publically available Inertial Measurement Unit reconstruction code [1].

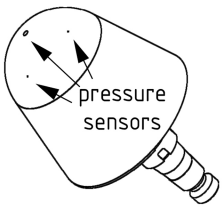

Figure 2: FADS sensors on wind tunnel probe

MSL will be the first opportunity to use a FADS system on Mars for separating aerodynamic and atmospheric uncertainties. Reconstruction code using the pressure measurements has been developed at NASA Langley [2]. At VKI we are currently building the basic FADS expertise, as well as investigating the incorporation of state-of-the-art UQ methods and heat flux measurements to improve FADS accuracy. In broad strokes, this consists of CFD simulations with associated UQ, carried out by the team of T. Magin, and wind tunnel testing (Figure 2) with associated flow characterization by the team of O. Chazot, including the PhD candidate. Specifically, we are developing a static pressure probe (Figure 3) to more accurately determine the Longshot flow conditions.

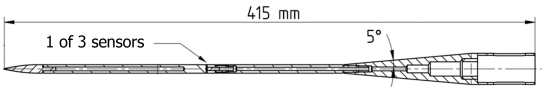

Figure 3: Nagamatsu hypersonic static pressure probe

We will use the Phoenix dataset and the reconstruction tool to produce synthetic datasets for a hypothetical FADS system, and similarly for the MSL dataset when it becomes available in August 2012. The objective is to identify design and processing features that constrain or benefit the accurate calculation of atmospheric profiles such as the free stream density. Inverse problem UQ and wind tunnel results should quantify the state-of-the-art accuracy and point out methodologies for improvement.

3. Conclusion

Reconstruction of atmospheric conditions (i.e. static pressure and density) during hypersonic entry has received little attention compared to reconstruction of the basic trajectory. More accurate atmospheric conditions have direct applications to lifting-entry vehicle control, interpretation of in-flight experiments and climate modeling (especially on non-Earth planets such as Mars). Our aim is to improve that accuracy with a comprehensive approach including CFD, wind tunnel testing, UQ tools and various processing techniques depending on the available sensor information.

Acknowledgments

Candidate supported by Royal Observatory of Belgium (ROB), collaboration with VKI who are involved in projects to improve the accuracy of Flush Air Data Systems.

References

[1] P. Withers, M. C. Towner, B. Hathi and J. C. Zarnecki, Analysis of entry accelerometer data: A case study of Mars Pathfinder, Journal of Planetary and Space Science 51 (1) (2003) 541–561.

[2] S. Dutta and R. D. Braun, Mars Entry, Descent and Landing Trajectory and Atmosphere Reconstruction, Ph.D. thesis, Guggenheim School of Aerospace Engineering, Georgia Institute of Technology (2010).

Development of Advanced Hypersonics Models for Transition to Turbulence: Uncertainty Quantification for Transition Prediction

Gennaro Serino

Aeronautics and Aerospace Department, von Karman Institute for Fluid Dynamics, Belgium, gennaro.serino@vki.ac.be

Supervisors: Thierry Magin[♣] & Patrick Rambaud[♠]

[♣]*Assistant Professor* & [♠]*Associate Professor, Aeronautics and Aerospace Department, von Karman Institute for Fluid Dynamics, Belgium, magin@vki.ac.be., rambaud@vki.ac.be*

University Supervisor: Vincent E. Terrapon

Professor, Aerospace and Mechanical Engineering Department, Université de Liège, Belgium, vincent.terrapon@ulg.ac.be.

Abstract

Transition has a crucial role in hypersonic applications. During an atmospheric reentry, transition increases the aerodynamic heating of the space vehicle thus compromising the integrity of the heat shield.
A new method for transition prediction is proposed by using Uncertainty Quantification (UQ) in numerical simulations. UQ aims at simulating a system by taking into account all the uncertainties due to its physical variability and to the hypothesis used in the mathematical models.
Preliminary results on a Mach 6 flat plate shows good agreement with experimental transition location detected via the heat flux distribution.

Keywords: Laminar to turbulent transition, Hypersonic, Uncertainty Quantification (UQ), Computational Fluid Dynamics (CFD)

1. Introduction

Simulations of aerospace applications are challenging problems involving many complex physical phenomena ; for instance, predicting the response of thermal protection materials to extreme reentry conditions involve flow transition from laminar to turbulent and aerothermochemistry. Reliable predictions of such complex systems require sophisticated mathematical models to represent the physics and phenomena such as transition. A systematic and comprehensive validation, including the quantification of uncertainties inherent in such models, is required.
Conventionally, engineers resort to safety factors to account for uncertainty parameters and to determine the quantities of interest, such as the heat shield thickness. These factors allow to avoid space mission failure and ensure safety of the astronauts and payload, but this is at the expense of reduced mass of embarked payload. Uncertainty Quantification (UQ) is a systematic approach to establish "error bars" on quantities of interest, such as the heat flux, yielding to the design of the heat shield with more confidence. At the interface of physics, mathematics and statistics, UQ tools are still in constant development in computational science. These tools aim at developing rigorous methods to characterize the impact of "limited knowledge" on the quantities of interest.
We propose to develop a UQ methodology to study transition from laminar to turbulent in hypersonic flows. Moreover, the methodology that we propose to develop will be general and can be applied to many other research topics such as flow transition in turbo machinery.

2. Objectives

The project general goal is to propose a new approach in transition prediction. In order to achieve this goal, it will be necessary to also improve

our understanding of transition mechanisms in hypersonic flows. A variety of tools will be used to model turbulence (DNS, RANS, e^N, PSE) and coupled with UQ in order to yield a reduced model suitable for engineering applications. All uncertainties and errors will be taken into account in order to define the design margins for space vehicles. The uncertainties will comprise the free stream conditions (Mach number, pressure, temperature, turbulence intensity), surface parameters (roughness element height), transition model parameters and wall chemistry models, in order to investigate a wide range of cases including natural and bypass transition.

3. State of the art

One of the most critical tasks in the design of space vehicle is the prediction of transition from laminar to turbulent flow. Transition depends on several parameters and, in particular, it is promoted by the presence of surface unevenness as roughness, steps, gaps and ramps (Fig.1). A sound transition model valid in the hypersonic regime is still lacking.

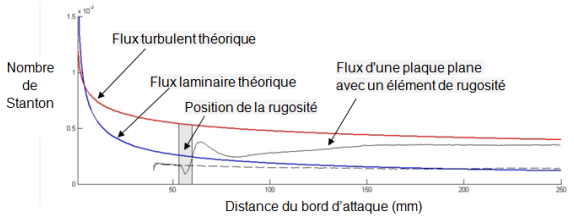

Figure 1: Theoretical(blue and red lines)-experimental(black line) comparison of the heat flux on a flat plate with a ramp roughness element (P_0 = 31 Bar, T_0 = 500 K, M = 6) [29].

Experimental investigations in hypersonics are quite expensive and they can be only be performed in short times and for limited operating conditions. CFD allows to simulate a wide range of conditions even if there are difficulties to model and predict transition at high Mach number. Models include Wilcox's procedure to use the low-Reynolds number $k-\epsilon$ model, reported in [4], as a transition region model where a roughness strip is used to fix the transition point. Schmidt and Patankar's production term modifications for low-Reynolds number $k-\epsilon$ models is an attempt to solve the problems these models have in simulating the transition region. Moreover, Warren, Harris and Hassan [5] developed a one equation turbulence model that accounts for the first and second mode disturbances in the transition region. Other models that can be considered include the algebraic transition region model of ONERA/CERT and the linear combination model of Dey and Narashima [6]. An interesting approach is the eddy viscosity-intermittency transition model ($R-\gamma$) which is based on the work of Ryong Cho and Kyoon Chung [7]. The model exploits the transport equation for the eddy viscosity (R) of Goldberg's one-equation turbulence model reported in [8] that is similar in form to the model of Spalart-Allmaras shown in [9]. The model was applied in [10] by the author for roughness induced transition prediction in hypersonic flows. The model was able to correctly predict the onset of transition even though all the physical processes (vortices and flow topology) were not completely reproduced.
In conclusion, these methods fail because of 3 reasons: conditions vary for each particular mission, random nature of transition (uncertainty in free stream turbulence, surface unevenness), simple models do not reflect all the physical processes. UQ is the strategy which aims to investigate the effects of those uncertainties in numerical simulations with a probabilistic approach.

4. Scientific strategy

4.1. Role of Uncertainty Quantification in predictive simulation

UQ allows to simulate a system by taking into account all uncertainties regarding the boundary, initial conditions and the model parameters.
All the uncertainties are modeled with a distribution which resembles the expected behavior of the considered variable. Each distribution is then modulated with a transfer function to obtain the output quantity of interest. We will calculate how the quantities of interest are influenced when the random variables describing the sources of uncertainties take different values. We therefore study how the uncertainties "propagate" through the simulations.
The most common approaches in propagation are the Monte Carlo method and the polynomial chaos method [12]. With respect to conventional sensitivity approaches, UQ offers the possibility to take into account the effect of statistical distributions in numerical simulations.

4.2. Methodology

The novelty of the approach consists in using UQ in numerical transition prediction. Simulations will be carried out with a case-dependent random parameter which, for instance, will mimic the uncertainty of the disturbance spectrum. The probabilistic distributions as well as the range of variations of the variables will be based on experimental data. Once these parameters will be selected, numerical simulations will be performed and a quantity of interest will be computed to evaluate the effects of the parameters. This quantity can be the stream wise location of increase in skin friction or in heat transfer, which may be regarded as representative of the transition location. Several independent simulations will be performed in order to use, for example, a Monte-Carlo sampling to build the response approximately, as an interpolant of a response surface (the collocation points), using a Lagrange polynomial. Several research codes developed at the VKI will be used in the proposed research.

- Simulations will be carried out with a Reynolds Average Navier Stokes (hereafter RANS) and a Linear Stability Theory (hereafter LST) codes. UQ on LST codes [24] will be used to investigate the onset of transition. UQ on RANS codes will be used to determine both the onset of transition and the successive turbulent flow. Turbulence models based on different transport equations will be used in order to obtain different transfer functions. This will contribute to complete the lack of knowledge derived by using such approximations and to reduce the uncertainties due to the models.

- Direct Numerical Simulations (DNS) will be used to investigate some interesting cases highlighted with the RANS/LST simulations. For instance, RANS models predict transition by switching the solution from laminar to turbulent flow. Experimental results showed that, when transition occurs, the skin friction and the heat flux distribution are characterized by an overshoot immediately following its onset (Fig.1). RANS models are not capable of reproducing such an overshoot so that a further investigation is necessary by performing DNS on limited zone of interest with the codes mentioned in [20] and [21].

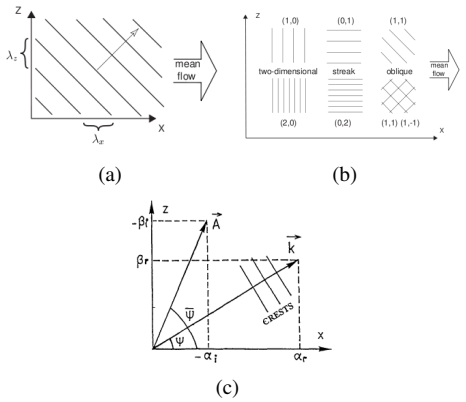

Figure 2: (a)Wave propagating in the mean flow with streamwise wave number λ_x and spanwise wave number λ_z, (b)Examples of notation for wave disturbances[13], (c) Notation for the oblique waves

- The strategy and the conclusions derived by test cases will be used for the final validation case and for the eventually application of the inverse problem. This will be the EXPERT re-entry vehicle configuration. A wide experimental database based on wind tunnel tests is available which will give important contribution to investigate real flight conditions with the proposed methodology.

5. Application

The methodology is currently applied in transition prediction for the oblique breakdown mechanism occurring in supersonic boundary layers. In this case, the LST code VESTA, developed at the VKI by Pinna [24], is used to compute the linear amplification of oblique waves on a Mach 6 flat plate. The code is used to compute the N factor for the e^N transition prediction method in order to detect the transition location on the flat plate to be compared with experimental data. The linear stability is coupled with the UQ which consists in assigning an uncertain spectrum, that is a probability density function (pdf), to the frequency and to the propagation angle of the oblique waves traveling inside the domain(Fig. 2).

Then, the quantity of interest, that is the N factor, is computed at each location as a 2D function dependent on both the frequency and the wave angle. Results of the LST are then sampled by using a Monte Carlo method to compute the main statistical moments of the quantity of interest. The criterion for transition is the N factor experimentally determined in the facility where the test has been carried out. Finally, the probability of transition is computed at each station on the

flat plate as the probability of having the computed N factor exceeding the threshold value given by experimental results as represented in Fig.3.

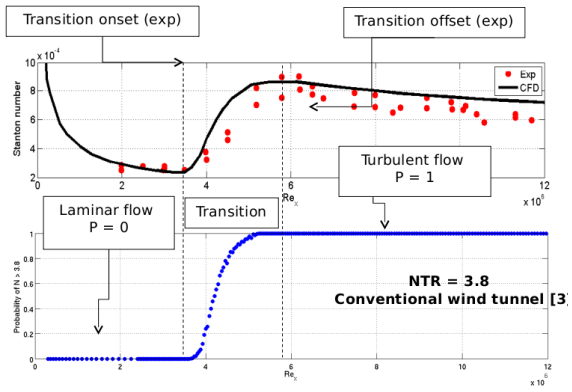

Figure 3: Comparison between experimental data (red dots), RANS solver (black line) and probability of transition (blue dots) for the Mach 6 flat plate test case in [27]

6. Conclusions

A probabilistic transition prediction methodology is proposed by combining numerical simulations and Uncertainty Quantification. Results on test case concerning a hypersonic flat plate demonstrates the agreement with experiments in terms of transition onset location. Good agreement was achieved on the transition point but the prediction of transition offset occurs slightly before experimental value thus the numerical transition length is shorter than in the experiments. Comparison is made between the probability of transition (N-factor greater than the threshold value for transition) and the experimental/computed heat flux distribution. It is possible to infer a parallel between the computed probability and the intermittency since the range of variability is the same [0,1] and also the physical meaning, since the intermittency is defined as the turbulent-laminar time ratio. Further investigation will involve a second test case on a 5° sharp and blunt cone. Preliminary results are promising and it will be interesting to determine in future work the impact of the methodology on simulations of higher complexity as RANS, with transitional models, and DNS.

Acknowledgments

The author gratefully acknowledges the “Fonds de la Recherche Scientifique” for the FRIA fellowship which is financing the current doctoral research.

References

[1] H. Schlichting, Boundary Layer Theory, Springer, 1995.

[2] Anderson J.D., Hypersonic and High Temperature Gas Dynamics, AIAA, 1986.

[3] R.D. McDaniel, R.P. Nance and H.A. Hassan, Transition Onset Prediction for High-Speed Flow, Journal of Spacecraft and Rockets, vol. 37 n3, 2000.

[4] Wilcox David C., Turbulence Modeling for CFD, DCW Industries, 1993.

[5] Warren E., Harris J. and Hassan H., A Transitional Model for High Speed Flow, AIAA-94-1851-CP, 1994.

[6] Narashima R., The Laminar Turbulent Transition Zone in the Boundary Layer, Progress in Aerospace Science,vol.22, pages 29-82, January 1985.

[7] Ryong Cho Ji, Kyoon Chung M., A $k-\epsilon$ Equation Turbulence Model, Journal of Fluid Mechanics, vol.237, pages 301-322, 1992.

[8] Goldberg U., Turbulence Closure with a Topography-Parameter-Free Single Equation Model, International Journal of Computational Fluid Dynamics, vol. 17. pages 27-38, 2003.

[9] Spalart,P.R., Allmaras,S.R., A one equation turbulence model for aerodynamic flows, American Institite of Aeronautics and Astronautics (AIAA), vol. 92-0439, 1992.

[10] Serino G., Numerical prediction of transition in hypersonic flow, von Karman Institute for Fluid Dynamics, DC report 2011.

[11] Malik, M. R., Hypersonic flight transition data analysis using parabolized stability equations with chemistry effects, Journal of Spacecraft and Rockets 40 (3), 332, 2003.

[12] G. Iaccarino, T. Chantrasmi, A. Doostan, Towards Uncertainty Quantification in High-Speed Turbulent Flow Simulations, Stanford PSAAP Center - UQ Workshop - July 2008.

[13] Berlin, S., *Oblique Waves in Boundary Layer Transition*, Doctoral Thesis, Stockholm, 1998.

[14] Marco Panesi, Kenji Miki, E. Prudencio, Serge Prudhomme, Quantification of Uncertainty in Hypersonic Flows, RTO-AVT-VKI short course on Uncertainty Quantification, Stanford University, California, 2010.

[15] Ioana Cozmuta, Uncertainty Quantification and Statistical Engineering for Hypersonic Entry Applications, RTO-AVT-VKI short course on Uncertainty Quantification, Stanford, CA, 2011.

[16] Ren Pecnick, Jeroen A.S. Witteveen, and Gianluca Iaccarino, Uncertainty quantification for laminar-turbulent transition prediction in RANS turbomachinery applications, AIAA 2011-660, Orlando, Florida, 49th AIAA Aerospace Sciences Meeting including the New Horizons Forum and Aerospace Exposition 4 - 7 January 2011.

[17] S.C.Tirtey, O.Chazot, L.Walpot, Characterization fo hypersonic roughness-induced boundary-layer transition, PhD Thesis, von Karman Institute for Fluid Dynamics, 2010.

[18] Magin, T. E., A model for inductive plasma wind-tunnels, Ph.D. thesis, von Karman Institute for Fluid Dynamics, Rhode-Saint-Genese, 2004.

[19] Marxen, O., Iaccarino, G. & Shaqfeh, E., Disturbance evolution in a Mach 4.8 boundarylayer with 2-D roughness-induced separation and shock, Journal of Fluid Mechanics, in press, 2009.
[20] Marxen O., Iaccarino G., Shaqfeh S.G., Boundary-layer transition via spatially growing oblique waves, Center for Turbulence Research, Stanford University, Under consideration for publication in Journal of Fluid Mechanics, 2009.
[21] Marxen O., Iaccarino G., Shaqfeh S.G., Uncertainty quantification for linear and weakly non-linear supersonic boundary-layer instability, Center for Turbulence Research, Stanford University, Annual Research Briefs 2009, 2009.
[22] Marxen O., Iaccarino G., Instabilities in supersonic boundary layers in the presence of uncertainty, Center for Turbulence Research, Stanford University, 2009.
[23] Iaccarino G., Magin T., Prudhomme S., Abgrall R., Bijl H., RTO-AVT-VKI Short Course on Uncertainty Quantification, Bruges BE, May 13-14, 2011.
[24] Pinna F., Numerical study of stability and transition of flows from low to high Mach number, von Karman Institute for Fluid Dynamics, Universitá "La Sapienza" di Roma, PhD thesis, 2012.
[25] Arnal D.,Special Course on Progress in Transition Modeling, AGARD report 793, 1993.
[26] Horvath T.J., Berry S.A., Hollis B.R., Chang C.L. and Singer B.A., Boundary layer transition on slender cones in conventional and low disturbance Mach 6 wind tunnels, NASA Langley Research Center, AIAA 2002-2743.
[27] Dilley A.D.,Evaluation of CFD turbulent heating prediction techniques and comparison wit hypersonic experimental data, NASA/CR-2001-210837.

Conjugate Heat Transfer using Large Eddy Simulation in Rib Roughened Cooling Channels

Sebastian Scholl

Turbomachinery and Propulsion Department, von Karman Institute for Fluid Dynamics, Belgium, sebastian.scholl@vki.ac.be

Supervisor: Tom Verstraete

Assistant Professor, Turbomachinery and Propulsion Department, von Karman Institute for Fluid Dynamics, Belgium, tom.verstraete@vki.ac.be.

University Supervisor: Wolfgang Schröder

Professor, RWTH Aachen, Aerodynamisches Institut, office@aia.rwth.de.

Abstract

In this work, computations will be performed to study the flow and the conjugate heat transfer in rib roughened cooling channels of turbine blades. Turbulence will be simulated and modeled via Large Eddy Simulation. The computation will be validated through the comparison with existing experimental data for the cooling channel flow.

Keywords: Conjugate Heat Transfer, Large Eddy Simulation, Gas Turbines, Turbine Blade, Cooling Channels

1. Introduction

The Turbomachinery industry tries to comply with both the claims for environmental awareness and the rising use of energy. Hence, the requirements for performance and efficiency of gas turbines increase. One method to improve the cycle performance of gas turbines is to increase the turbine inlet fluid temperature. Although improvements of the temperature resistance of the materials have been made over the last decades, the turbine inlet temperature exceeds the melting temperature of the material in modern gas turbines (see figure 1). Hence, the turbine blades have to be cooled. Since life of a turbine blade is reduced by half with an increased temperature of 30 Kelvin [2], engineers have to predict the local heat transfer coefficients and temperatures accurately. Furthermore, the pressure drop should be as low as possible and at the same time, the cooling efficiency as high as possible. Therefore, cooling channels are turbulated, for instance by obstacles such as ribs. Thus, the complexity of the flow field increases and it is not possible to predict the wall temperature a priori.
To gain reliable results for efficient thermal design of turbine blade cooling, both the heat conduction in the solid and the convection have to be taken into account simultaneously, which is called a conjugate heat transfer (CHT) problem.
Although CHT is a coupled problem, many studies compute the solid and the flow field separately. It

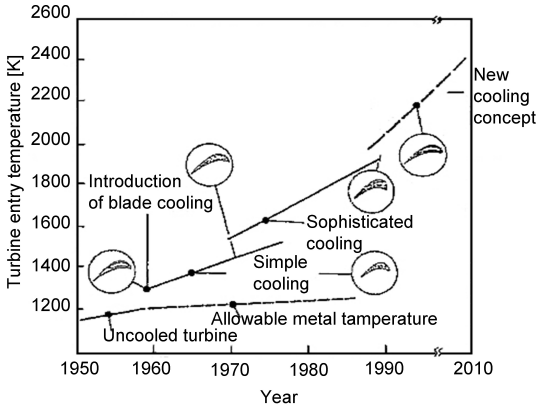

Figure 1: Variation of turbine entry temperature and the allowable metal temperature over several decades[1].

could be shown that this approach does not lead to satisfactory results in comparison with experimental investigations [3]. Besides the attempt to calculate CHT uncoupled, there are mainly two different approaches to solve CHT problems in a coupled manner as described by Verstraete [4] and summarized as follows. The first approach, the conjugate method, computes both the fluid domain and the solid domain at each time step simultaneously. For the conjugate method, one monolithic solver for both fields is used.
However, a major problem in CHT is that the characteristic time scale in the solid is usually about orders of magnitude larger than in the fluid. Due to the computation of both fields at a small time step, the conjugate method is computationally less efficient than the second approach, the coupled method. In this method, the fluid and the solid field are solved by separate solvers. The fluid field is solved and interrupted after some time steps in order to renew the boundary conditions at the interface to the solid domain which is computed by a steady state approach. By using two different solvers for the solid and the fluid, the coupled method provides an opportunity to treat the different appearing time scales computationally more efficient, although an iterative procedure is needed between the fluid and the solid solvers.
The complex, unsteady flows in cooling channels affect the heat transfer coefficient. Reynolds Averaged Navier-Stokes (RANS) methods are not able to reproduce those complex flow conditions. Large Eddy Simulations (LES), which resolve a part of the turbulent spectrum, provide more accurate results to predict the heat transfer [5].

2. Objectives

After reviewing literature and the state of the art, we aim to solve the CHT problem in cooling channels with a coupled approach using LES for the flow computation in order to achieve more accurate results in comparison with RANS simulations. Since LES are more expensive than RANS, we aim to accelerate the process of the coupled computations by developing a method which takes the different characteristic time scales of the solid conduction and the flow convection into account.
Finally, after validating our numerical approach with analytical solutions and existing experimental investigations [6], we aim to study rib roughened cooling channels and the influence of different parameters of the turbulators on the heat efficiency and the pressure drop.

Acknowledgments

The research leading to these results has received funding from the European Community's Seventh Framework Programme (FP7, 2007-2013), PEOPLE programme, under the grant agreement No.FP7-290042 (COPAGT project).

References

[1] B. Lakshminarayana, Fluid Dynamics and Heat Transfer of Turbomachinery, John Wiley & Sons, Inc., Hoboken, NJ, USA, 2007.

[2] J.-C. Han, S. Dutta, S. Ekkad, Gas turbine heat transfer and cooling technology, Taylor & Francis, 2001.

[3] A. Heselhaus, A hybrid coupling scheme and stability analysis for coupled solid /fluid turbine blade temperature, in: ASME, International Gas Turbine & Aeroengine Congress & Exhibition, 43rd, Stockholm, Sweden, 1998.

[4] T. Verstraete, Multidisciplinary Turbomachinery Component Optimization Considering Performance, Stress, and Internal Heat Transfer, Ph.D. thesis, Universiteit Gent (2008).

[5] F. Duchaine, F. Wlassow, G. Leroy, N. Gourdain, Advanced nmerical simulation dedicated to the prediction of heat transfer in a highly loaded turbine guide vane., in: Proceedings of ASME Turbo Expo: Power for Land, Sea and Air, 2010.

[6] L. Casara, T. Arts, Experimental investigation of the aerothermal performance of a high blockage rib-roughened cooling channel, ASME Journal of Turbomachinery 127 (2005) 580–588.

Heat Transfer in High Subsonic Velocity Environments behind the Fan of a Gas Turbine

Francesco Baldani

Mechanics Department, Belgium Royal Military Academy, Belgium, francesco.baldani@rma.ac.be

Supervisor: Tony Arts

Professor, Head, Turbomachinery and Propulsion Department, von Karman Institute for Fluid Dynamics, Belgium, arts@vki.ac.be.

Supervisor: Walter Bosschaerts

Professor, Head, Mechanics Department, Belgium Royal Military Academy, Belgium, Walter.Bosschaerts@rma.ac.be

University Supervisor: Souad Harmand

Professor, Head, Fluid Dynamics and Heat Transfer Department of the TEMPO Lab, Valenciennes and Hainaut-Cambresis University (France), Souad.harmand@univ-valenciennes.fr

Abstract

The aim of the project is to propose a methodology to retrieve the heat flux through a finned heat exchanger placed downstream of the fan of a turbine jet engine. The core of the Ph.D. study is the solution of the so called Inverse Heat Conduction Problem (IHCP). To solve the IHCP the surface temperature of the heat conducting body has to be used as boundary condition of the problem. The Infra Red thermography is used to measure the heat exchanger surface temperature. The experiments are performed at low speed and at high subsonic speed, the latter in a blow-down wind tunnel capable to reach Mach numbers of the order of 0.75. The flow field in the blow-down wind tunnel test section is characterized by exploiting the Constant Temperature Anemometry (C.T.A.) technique. In order to be able to perform multi-point measurements, an 'ad-hoc' hot-wire probes support has been conceived and manufactured.

Keywords: Inverse Heat Conduction Problem, High Subsonic Speed, Infra Red Thermography, Constant Temperature Anemometry, hot-wire probes support

1. Introduction

The improvements in the manufacturing techniques as well as in the available materials push the aero-thermal engineers to find better solutions in order to improve engine performance. Indeed, improving turbine engine performance for military and civil purposes has a deep impact on thermal efficiency, fuel consumption, life-time and consequently allows the new environmental, noise and emissions standards to be met.

The aim of the project is to study the heat transfer from a hot surface to a cold flow under conditions similar to those encountered by aircraft turbine engines, hence using the main flow of the engine to study a heat exchanger placed just downstream of the fan. The main part of the research project deals with the solution of the "inverse heat conduction problem" which consists of imposing the object surface temperature as boundary condition and computing via numerical methods the resulting heat flux. The heat transfer coefficient is to be studied both locally and globally, since a global study of h is fundamental in the preliminary design phase while a local study of h is useful to understand the effects of the geometry on the local flow conditions (i.e. the turbulence intensity level) and on the achievable heat exchange.

We should remind that in the case of forced convection the flow is influenced by the amount of heat injected and that the flow rate versus the heat power in-

jected is one of the major triggers for the flow that develops. On top of this the conduction within the plate adds up with the heat convection from the surface.
It should also be clear that in order to deepen the understanding of the heat transfer occurring in installations such as finned heat exchangers one always has to consider that a simple superposition of the heat exchange phenomena is not enough. Indeed, one should rather talk of "conjugate" heat transfer, which is the actual coupled interaction of conduction and convection. Neglecting the effect of the wall conduction, for instance, will result in imposing unrealistic thermal boundary conditions at the solid-fluid interface since this greatly affects the temperature distribution. This leads to wrong heat transfer rates and coefficients.
For all these reasons the characterization of the wind tunnel test section flow field is a crucial issue. This is why the C.T.A. technique is chosen to characterize the flow field obtainable in the wind tunnel.

2. Conjugate Heat Transfer Concept

Since the studies conducted by Perelman[1] the importance of imposing correct boundary conditions when dealing with heat transfer problems involving a solid submerged in a flowing fluid is well known. Indeed, it is proven that in the presence of large thermal gradients (in space) and if the fluid encounters obstacles (rib, fin, etc..) the thermal boundary conditions imposed (uniform T_{surf}, uniform heat flux) in the classical study (purely convective) are unrealistic.It is therefore very important imposing the correct boundary conditions at the solid-fluid interface. The theory of choice is the conjugate heat transfer theory. It is based on the concept that the effects of the solid domain conduction have to be coupled with the convection phenomenon happening over the solid surface. The idea is to perform surface temperature measurements of the finned heat exchanger under analysis with the I.R. thermography technique after having characterized the wind tunnel test section flow field exploiting the C.T.A. technique and/or the P.I.V. technique in order to be able to impose the correct boundary conditions for computing the surface heat flux distribution (via commercial FEM solvers or as proposed hereafter via a numerical solution of the so obtained Inverse Heat Conduction Problem)[2; 3; 4].

3. Transient Inverse Heat Conduction Problem

Determining local convection coefficients accurately or performing accurate local heat flux measurements is a hard and expensive task but for many cases the heat flux distribution is an indispensable parameter. For finned heat exchangers this task is particularly challenging [5; 6; 7]. Indeed heat transfer measurements at the fin base would introduce a thermal resistance between the primary surface and the fin due to the presence of the measurement device. Therefore the heat fluxes at the fin base have to be determined indirectly by measuring the heat fluxes through the extended surface and the primary surface. Among the available techniques to perform such measurements (heat flux sensors, local temperature measurements) the inverse heat conduction technique is probably the most suitable for our study. It is mainly used to estimate temperatures or heat fluxes at surfaces that are inaccessible for measurements. The advantage of this method is that the experimental studies can be performed under similar conditions and similar environment as during the operation. To solve an inverse heat conduction problem, a mathematical optimization method is required, which uses temperature measurements as input. Based on surface temperatures of a solid object, heat fluxes on one or more surfaces of the object can be estimated, so the need for internal temperature measurements can be omitted. Depending on the temperature measurement technique, the disturbance of the local temperature fields and heat flux distribution is limited or even absent. It also has the advantage that the temperature field in the whole object can be reconstructed based on surface temperature measurements, together with the coupled heat flux distribution. The proposed code allows the determination of the local convective heat exchange coefficient h(x,y,t), taking into account the conductive flux in the heated plate. In general the heat flux can rise and fall abruptly and can be both positive and negative where negative values indicate heat losses from the surface. According to Beck, Blackwell and St.Clair [8] the source of heating is immaterial to the IHCP procedures. Mathematically the IHCP (for the 1-D case) can be described as in the set of equations 1 to 4.

$$\frac{\partial}{\partial x}\left(k\frac{\partial T}{\partial x}\right) = \rho c\frac{\partial T}{\partial t} \tag{1}$$

Where the thermal conductivity k, the density ρ and the specific heat c are postulated to be known functions of temperature.

$$T(x,0) = T_0(x) \tag{2}$$

$$\frac{\partial T}{\partial x} = 0 \; at \; x = L \tag{3}$$

One can rewrite the temperature at the first location at one time as in equation 4.

$$T\left(x_1, t_i\right) = Y_i \tag{4}$$

The objective is to estimate the surface heat flux at discrete times, t_i, from

$$q\left(t_i\right) = -k \left.\frac{\partial T\left(x, t_i\right)}{\partial x}\right|_{x=0} \tag{5}$$

After the paper by Beck, Blackwell and Haji-Sheikh [9], where a review of some inverse heat conduction methods can be found, the chosen method to solve the IHCP is the so called 'function specification method' (FSM). The FSM has the advantage to be simple in concept and to not change the physics of the problem since the intrinsic parabolic nature of the problem is unchanged. The FSM is sequential in nature and thus computationally efficient and moreover the measurements in the distant future do not affect the 'present' estimates as for other methods [9]. The FSM can be used for linear and nonlinear problems and finite differences, finite elements or numerical convolution can be used. The method itself consists in minimizing, with respect to the heat flux q_M the sum of squares function as described by Eq. 6[9]. The equations 6 to 11 refer to measurements acquired by one sensor over multiple time steps.

$$S_M = \sum_{i=1}^{r} = \left(Y_{M+i-1} - T_{M+i-1}\right)^2 \tag{6}$$

which involves the times t_M, t_{M+1}, ..., t_{M+r-1}. Hence 'future' information is used to obtain q_M. Some functional form for $q\left(t\right)$ for t_M to t_{M+r-1} is selected, the simplest being

$$q_{M+1} = q_M, \;\; i = 1, 2, \ldots, r \tag{7}$$

The calculated temperature T_{M+i-1} is expanded in a Taylor series for q_M obtaining

$$T_{M+i-1} = T_{M+i-1}|_{\hat{q}_M} + X_{M+i-1,M}\left(q_M - \hat{q}_M\right) \tag{8}$$

where $X_{M+i-1,M}$ is the sensitivity coefficient defined by

$$X_{M+i-1,M} = \frac{\partial T_{M+i-1,M}}{\partial q_M} \tag{9}$$

the resulting algorithm after minimizing Eq. 6 with respect to q_M is

$$\hat{q}_M = \hat{q}_{M-1} + \frac{\sum_{i=1}^{r}\left[Y_{M+i-1} - T_{M+i-1}|_{q_M=\cdots\simeq\hat{q}_M}\right] X_{M+i-1,M}}{\sum_{i=1}^{r} X_{M+i-1,M}^2} \tag{10}$$

Only $\hat{q}_M$ is retained for time t_M, and M is increased by one and the procedure is repeated. The iterative regularization method minimizes the whole domain function

$$S_M = \sum_{i=1}^{I} = \left(Y_i - T_i\right)^2 \tag{11}$$

where I is the total number of measurements. It should be noticed that in our analysis we use multiple sensors (i.e. surface temperature cartography $T(x, y, t)$ measured by the I.R. camera). Anyway this does not affect the exposed solution methodology but just the mathematical formalism.

3.1. IHCP Solution Validation

One can validate the proposed solution methodology for a flat plate of very thin thickness in a laminar flow. The validity of the proposed solution can be checked by solving twice the direct model via a CFD software (*Fluent*© in our case). We compute first the heating phase with equations 17 to 22. In Eq. 17 the heat transfer coefficent h is computed from the Nusselt correlation (see equations 12 to 16).

$$Nu = 0.332 \cdot Re^{1/2} \cdot Pr^{1/3} \tag{12}$$

Equation 12 can be rewritten as follows to take into account for the Nusselt number evolution along the plate:

$$Nu(x) = \frac{0.332 \cdot Re(x)^{1/2} \cdot Pr^{1/3}}{\left[1 - \left(\frac{x_0}{x}\right)^{3/4}\right]^{1/3}} \tag{13}$$

If we take $x_0 = 0$ then the equation 13 reduces to:

$$Nu(x) = 0.332 \cdot Re(x)^{1/2} \cdot Pr^{1/3} \tag{14}$$

Since fluid properties (such as viscosity, diffusivity, etc.) can vary significantly with temperature, there can be some ambiguity as to which temperature one should use to select property values. The recommended approach is the use of the average of the wall and free-stream temperatures, defined as the film temperature $T_{film} = \dfrac{T_{surface} + T_{air}}{2}$.

Now recalling that the Nusselt number can be also expressed as reported in equation 15 we will be able, once $Nu(x)$ is known, to compute $h(x)$ as from equation 16.

$$Nu(x) = \frac{h(x) \cdot x}{k_{air}} \tag{15}$$

$$h(x) = \frac{Nu(x) \cdot k_{air}}{x} \tag{16}$$

The equation 12 holds for a laminar, isothermal, local situation with $Pr > 0.6$ which is the situation we will deal with imposing a flow velocity (U_∞) of 10 m/s and a flow bulk temperature (T_∞) of 18° C.

$$(dzdxdy)\,\lambda\left(\frac{\partial^2 T}{\partial x^2} + \frac{\partial^2 T}{\partial y^2}\right) + P\,(dzdxdy) \quad = \quad \rho c_p \frac{\partial T}{\partial t}\,(dzdxdy) + hdxdy\,(T - T_\infty) \tag{17}$$

with as initial condition

$$T\,(x, y, 0) = T_0 \tag{18}$$

and as boundary conditions

$$-\lambda \left.\frac{\partial T}{\partial x}\right|_{x=0} = 0 \tag{19}$$

$$-\lambda \left.\frac{\partial T}{\partial x}\right|_{x=L} = 0 \tag{20}$$

$$-\lambda \left.\frac{\partial T}{\partial y}\right|_{y=0} = 0 \tag{21}$$

$$-\lambda \left.\frac{\partial T}{\partial y}\right|_{y=H} = 0 \tag{22}$$

The result of this first direct simulation is the surface 'hot' reference temperature cartography $T\,(x, y, t_1) = T_1$. The second direct simulation is performed to compute the cooling phase and therefore to retrieve the surface 'cold' reference temperature cartography $T\,(x, y, t_2) = T_2$ (exploiting Eq. 23 and equations 18 to 22).

$$(dzdxdy)\,\lambda\left(\frac{\partial^2 T}{\partial x^2} + \frac{\partial^2 T}{\partial y^2}\right) \quad = \quad \rho c_p \frac{\partial T}{\partial t}\,(dzdxdy) + hdxdy\,(T - T_\infty) \tag{23}$$

It is now possible to use T_1 and T_2 as boundary conditions for the solution of the IHCP. The obtained result is reported in Figure 1.

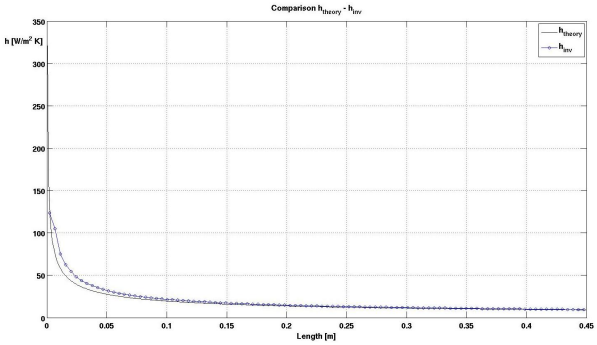

Figure 1: Theory - IHCP solution Comparison

4. Experimental Facilities and Set-up

The facility used for the high speed experiments is a blow-down wind tunnel where the air coming from a pressurized tank can be heated.
A velocity $U_{mean} \approx$ 30-230 *m/s* with a flow temperature $T_{mean} \approx$ 290-320 *K* are flow conditions that can be considered satisfying the similarity rules to those appearing at the inlet of an aircraft engine during various flight conditions. See Figure 2 for the working scheme of the installation. The test section sketch and the installation of the measuring tools are sketched in Figure 3.

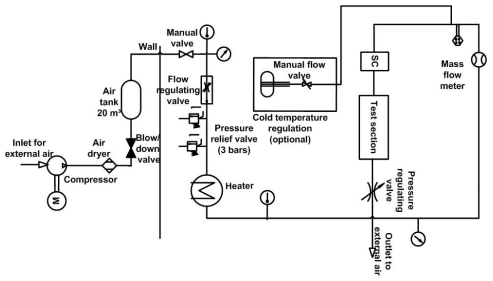

Figure 2: Facility Working Principle Diagram (Courtesy of ULB)

The experimental set-up for the low speed experiments is shown in Figure 4. In the picture it is possible to see the I.R. camera used to acquire the surface thermographs, a hot-wire rake used to check the test section velocity and the heating resistance together with its power supply.

5. Experimental Campaigns and Data Analysis

The following sections summarize the sets of experimental campaigns that have been conducted in order to characterize the high speed wind tunnel test section

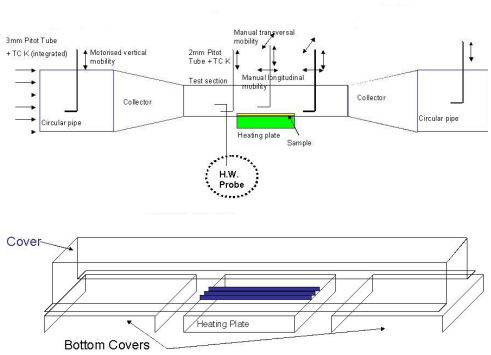

Figure 3: Test Section and Measuring Tools Installation Sketch (Courtesy of ULB)

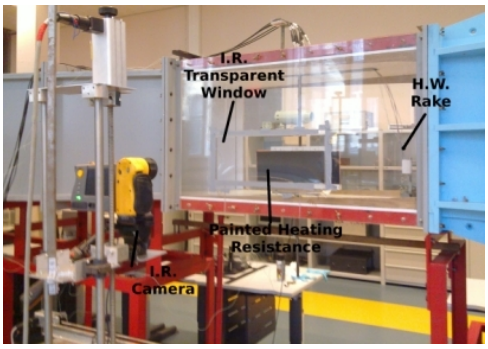

Figure 4: I.R. Low Speed Experiments setup

flow field and to validate the inverse heat conduction problem solution method.

5.1. High Speed Experimental Campaign

The aim of the high speed experimental campaign is to characterize the blow-down wind tunnel flow field via the C.T.A. technique. Using hot-wire probes five different regimes of interest are investigated. A second experimental campaign is performed to measure the velocity profile and the effect of the presence of a finned heat exchanger in the section. A third series of experiments is performed to test the capabilities of a manufactured hot-wire probes rake.

5.1.1. Mean Flow Field Measurements

The tests are performed with a plane bottom wall. The five investigated regimes classified according to the velocity and the mean total temperature of the fluid in the test section are summarized in table 1.

5.1.2. Traverses Experiments

This experimental campaign is performed with the finned heat exchanger placed in the test section but

Regime #	U_{mean}	T_{total}
1	230 m/s	315 K
2	160 m/s	305 K
3	130 m/s	300 K
4	60 m/s	295 K
5	30 m/s	295 K

Table 1: Tested Regimes

with no heat injection (i.e. no heat exchange between the finned surface and the flow) during the measurements. The experiments consist in hot-wire probe traverses in order to measure the velocity profiles before and after the prototype. The sketch in Figure 5 shows the positions and the locations where the experiments are performed.

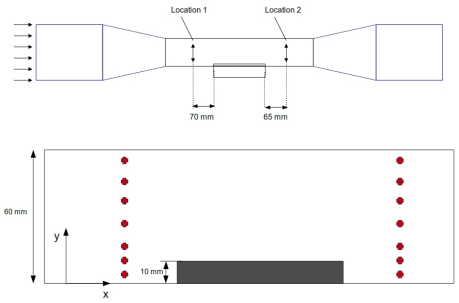

Figure 5: H-W. Traverses Experiments

According to the frame of reference shown in Figure 5 the positions analyzed for the two locations are: y = 6-11-16-26-36-46-56 *mm*. The measurements in the two locations are performed during two different experiments.

5.1.3. Hot-wire Rakes

A major issue while performing the traverses experiments is to keep the flow conditions perfectly constant in order to let the moving probe face the same flow field. To overcome this problem a design for a hot-wire probes rake is proposed, so that the velocity could be measured in different positions at once.

The designed support is based on a well known *NACA* 4 digits symmetrical wing. The manufactured 3 probes support installed in the test section can be seen in Figure 6. The reasons why after some preliminary studies a symmetrical wing based on a NACA-0025 airfoil is chosen are reported next. The support has to be inserted in a high velocity environment, which



Figure 6: Manufactured 3 Probes Support

means that important forces could occur. Therefore, to greatly reduce the forces acting on the rake, and consequently the need for stout holders any kind of shape creating important drag forces should be avoided. The area facing the flow should be as small as possible to reduce the blockage and consequently the interference with the free flow. Additionally when dealing with velocities of the order of 230 *m/s* reducing the vibrations of the support becomes also very important. The adopted solution besides satisfying the above mentioned requirements allows also to minimize the wake size drastically reducing the interference effects on other measuring tools installed behind the rake itself. After the validation of the 3 probes support we decided to manufacture a 5 probes support that could grant the vertical velocity profile measurement of the whole test section at once.

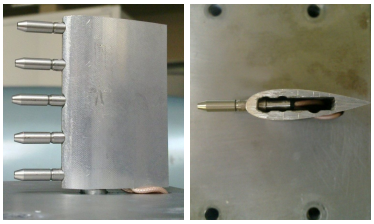

Figure 7: Manufactured 5 Probes Support

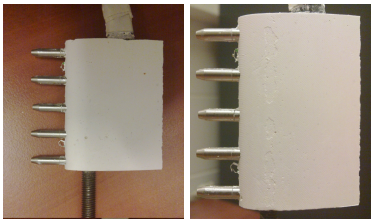

Figure 8: Manufactured 5 Probes Support (Plaster)

In the rake shown in Figure 7 the probes are installed at a distance of 12.5 *mm* from each other. In Figure 8 we can see the last version of the H.W. rake, prepared with molding plaster and where two thermocouples have been embedded in the support. This probe support has been tested only at low speed.

5.2. C.T.A. Data Analysis

When dealing with signals like those obtainable with the C.T.A. one can perform mainly three kind of analysis:

1. Descriptive static statistic analysis:
    - averaged values
    - skewness, kurtosis
    - variance, standard deviation
2. Spectral analysis
3. Signal correlation analysis
    - autocorrelation
    - cross-correlation

Since the C.T.A. technique is an indirect measurement technique a calibration law is required. Calibration units are available for this purpose, letting us associate to a known velocity the voltage measured by the hot-wire probe [10]. But this procedure cannot be exploited to analyze the data when the temperature varies during the measurements. Since the environment in which the hot–wire probe is placed is characterized by rather significant temperature variations, 6/7 *K* during the same regime and from 320 *K* to 295 *K* from the beginning to the end of a complete run, rather than a calibration curve a calibration surface with the temperature as additional variable would be required. The biggest issue to obtain such a calibration surface is that a dedicated wind tunnel is needed, where both the velocity and the flow temperature can be controlled. The one available at the Royal Military School can reach a maximum velocity of 30 *m/s* under controlled temperature conditions but during the experiments the velocity ranges between 40 *m/s* and 230 *m/s*. Therefore an alternative calibration procedure is needed. The "in-situ" calibration proposed consists in extracting the measured voltage, velocity and temperature for each investigated flow regime. The raw voltages are then corrected in temperature according to equation 25 and an iterative procedure implemented in *Matlab*© computes simultaneously the *"reference King's Law coefficients"*. The basic idea is to retrieve a "unique" calibration law that can be used even if the temperature is changing, the scheme in Figure 9

presents the strategy to obtain the proposed calibration curve.

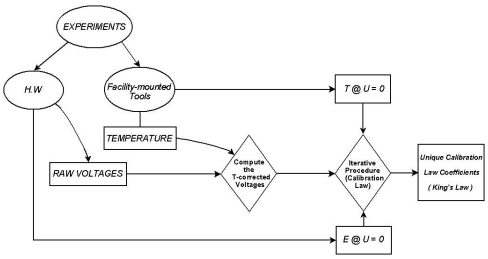

Figure 9: Unique Calibration Law Procedure Logical Scheme

In this way it is possible to perform experiments and exploit the acquired data to obtain a calibration law that is corrected in temperature. Equation 24 shows the King's law while in equation 25 the correction applied before linearization of the data is reported [11].

$$E_{corr}^2 = A_{ref} + B_{ref} \cdot U^{n_{ref}} \tag{24}$$

$$E_{corr} = E_{meas} \cdot \left(\frac{T_w - T_{ref}}{T_w - T_a} \right)^{0.5 \cdot (1 \pm m)} \tag{25}$$

where T_w is the wire temperature, T_{ref} is the reference temperature (in this case the temperature in the test section immediately before the experiment), T_a is the ambient temperature, measured by the facility mounted instrumentation. The parameter m is called *"Temperature Loading Factor"* and is suggested by Dantec for temperature correction purposes, it should be kept between 0.2 and 0.3 and added or subtracted depending on whether T_a is bigger or smaller than T_{ref} respectively. An example of the resulting "unique" calibration law is reported in Figure 10.

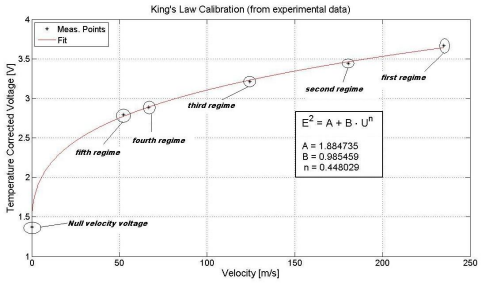

Figure 10: Unique Calibration Law Example

5.2.1. Correction for Fluid Temperature Drift

To obtain the actual velocities the reference King's law coefficients are "tuned" according to the measured fluid temperature. The corrected King's law coefficients are computed as described by the set of equations 26.

$$\begin{cases} A_{corr} = \left(\dfrac{T_w - T_a}{T_w - T_0} \right)^{(1 \pm m)} \cdot \dfrac{K_{f_a}}{K_{f_0}} \cdot \left(\dfrac{Pr_{f_a}}{Pr_{f_0}} \right)^{0.2} \cdot A_{ref} \\ B_{corr} = \left(\dfrac{T_w - T_a}{T_w - T_0} \right)^{(1 \pm m)} \cdot \dfrac{K_{f_a}}{K_{f_0}} \cdot \left(\dfrac{Pr_{f_a}}{Pr_{f_0}} \right)^{0.33} \cdot \\ \qquad \cdot \left(\dfrac{\rho_{f_a}}{\rho_{f_0}} \right)^{n} \cdot \left(\dfrac{\mu_{f_a}}{\mu_{f_0}} \right)^{-n} B_{ref} \end{cases} \tag{26}$$

The physical air properties in equation 26 are computed at the temperatures T_{f_a} and T_{f_0} respectively the ambient and reference film temperatures obtainable as follows:

$$\begin{cases} T_{f_a} = \dfrac{T_w + T_a}{2} \\ T_{f_{ref}} = \dfrac{T_w + T_{ref}}{2} \end{cases} \tag{27}$$

So after the correction the King's calibration law should be rewritten as follows:

$$E^2 = A_{corr} + B_{corr} \cdot U^n \tag{28}$$

Eventually the velocity in the wind tunnel test section is computed as reported by the expression in equation 29.

$$U = \left(\frac{E^2 - A_{corr}}{B_{corr}} \right)^{\frac{1}{n}} \tag{29}$$

5.3. Low Speed Experimental Campaign: I.R. Analysis

The aim of the low speed experimental campaign is to validate the methodology and the tools to be used to solve the IHCP. In a low speed wind tunnel a quasi-2D heating resistance has been placed in the test section and surface thermographs are recorded [12] in order to exploit a numerical procedure capable to compute the heat conduction coefficient. The analysis of the requirements and of the constraints led to the conception of the experimental model as sketched in Figure 11.

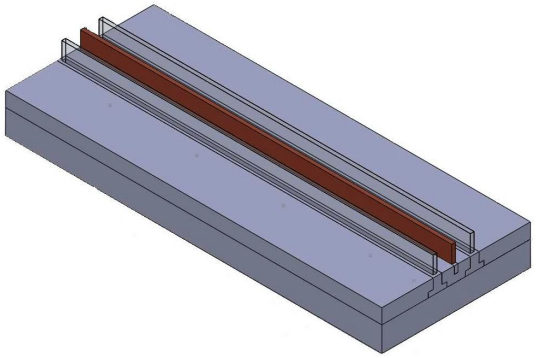

Figure 11: Experimental Model Conception Sketch

The real heat exchanger is reproduced by means of a central fin, made of copper and acting as heating resistance. On the two sides of this central fin is placed a set of two fins made of I.R. transparent material (CaF_2 for instance). The idea is to exploit the prototype symmetry in order to simplify its testing model. Additionally using a heating resistance as central fin allows us to know and control the heat injected.
According to the mentioned needs the proposed procedure to perform the experiments can be summarized as follows:

1. Heat the central fin up to the maximum allowed temperature
2. Open the facility valve in order to reach a stabilized velocity
3. Increase the heating power injected in the fin according to the velocity increase in order to keep the heating resistance at a constant temperature
4. Once the velocity and the fin T_{surf} are stabilized acquire a reference surface thermograph (hot surface)
5. Switch off the heating resistance
6. Record the fin T_{surf} evolution with the I.R. camera (cold surface)
7. Solve the IHCP via the numerical calculation

For what concerns the experiments presented in this work one should remind that the configuration proposed in Figure 11 has been replaced by a stand alone very thin (0.25 mm) but with a bigger surface (170 x 450 mm) heating resistance for a sake of simplicity. The heating resistance is of the order of 20Ω and it is fed with 12 $Volts$. The flow velocity in the wind tunnel test section is 10 m/s. The above mentioned procedure is then applied as described.

5.4. I.R. Experiments Data Analysis

The code exploited to solve the IHCP needs to be fed with a matrix of data representing the thermograph acquired by the I.R. camera. Therefore once recorded, the images must be prepared in order to be used as boundary conditions for the numerical method proposed. The rebuilding procedure could be summarized as follows:

1. An I.R. image where the color map palette is present is needed in order to be able to know the color levels to be linked to the temperature levels (see Figure 12).
2. Retrieve a vector able to translate the R(ed)-G(reen)-B(lue) data contained in the I.R. images into a matrix containing the surface temperature.
3. Pick up conveniently a frame from the recorded I.R. video, this will be the cold surface and fix the time step for the numerical solution (see Figure 13).
4. Translate the image into a $Matlab^{©}$ exploitable matrix.
5. Crop the image in order to contain only the surface of interest (i.e. only the flat plate and not the supports, etc. . . .), see Figure 14.

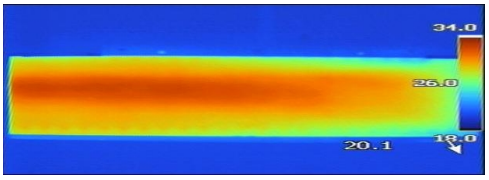

Figure 12: Color Vs. Temperature Levels

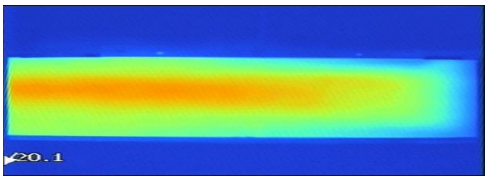

Figure 13: Cold Surface I.R. Image

Once prepared the I.R. images for the analysis one should just insert the right surface dimensions, time step and material characteristics in the script and feed the script with the hot surface and the cold surface informations matrices [13].

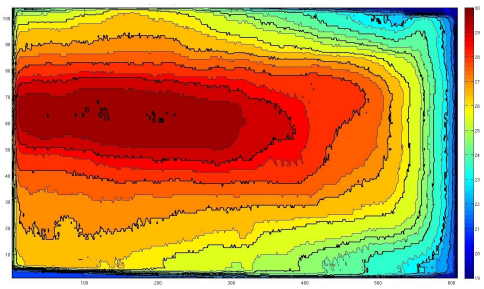

Figure 14: Cropped and Translated Image Example

6. CFD Low Speed Simulation

The purpose of these simulations is to check the behavior of the hot-wire probes support when inserted in the flow field. For this work the calculations have been used also to define the distance at which should be placed the heating resistance used for the I.R. experimental campaign. Indeed it is important to reduce at the maximum the influence of the wake released by the probe rake so that the recorded I.R. images depict the actual situation of a "hot" object submerged by an undisturbed "cold" flow. In Figure 15 is reported the geometry used to perform the simulations, it is possible to notice that the probe prongs and the wires are not modeled.

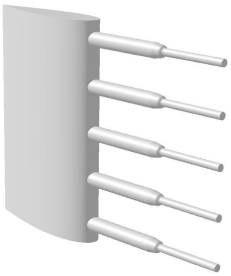

Figure 15: H.W. Rake Model

The model is created with the open source software K-3D ($http://www.k-3d.org/$) while the mesh is produced with the automatic mesher $HEXPRESS^{TM}/Hybrid$. The calculations have been performed with the commercial solver $Fluent^{©}$. The domain reproducing the R.M.A. wind tunnel test section ($60\ cm\ x\ 60\ cm\ x\ 120\ cm$) is of about two millions cells. The 3-D steady state simulations have been performed using a standard $k-\epsilon$ turbulence model and the $Fluent^{©}$ enhanced wall treatment option enabled. The discretization schemes used are the $Fluent^{©}$ standard scheme for the pressure and the first order upwind scheme for the momentum, the turbulent kinetic energy and the turbulent dissipation rate. The velocity used for the simulation is the same as the one used for the I.R. test, $10\ m/s$.

7. Results

In this section the obtained results are presented. The flow field analysis of the blow-down wind tunnel are presented first. The low speed I.R. analysis experiment are only partially presented as they are performed for validation purposes and the whole methodology could not be fully discussed in this article. Eventually are presented the numerical simulations of the H.W. rake behavior performed at low speed.

7.1. Mean Flow Field Results

It is of crucial importance to characterize the turbulence in the testing chamber, the size of the turbulent scales and the frequency content. In the following table the results of the static statistic analysis and of the autocorrelation analysis are summarized [14; 15; 16; 17; 18]. The results for each flow regime are resumed in Table 2.

Table 2: EXPERIMENTAL CAMPAIGN RESULTS RESUME

Regime	***1***	***2***	***3***	***4***	***5***
U_{meas} $[m/s]$ (Pitot)	226.29	180.65	126.35	72.33	45.33
U_{comp} $[m/s]$ (H.W.)	234.19	170.57	123.10	71.04	47.26
Uncertainty $[m/s]$	±4.47	±4.44	±4.08	±0.99	±0.35
Uncertainty %	1.91	2.60	3.32	1.39	0.74
Re_d	42.25	31.25	22.81	13.31	8.91
Mach number	0.66	0.49	0.35	0.21	0.14
T_{mean} $[K]$	≈ 315	≈ 307	≈ 301	≈ 296	≈ 293
R.M.S.	5.615	3.398	2.846	1.753	1.267
Variance	31.523	11.549	8.098	3.072	1.604
Turbulence Intensity %	2.397	1.992	2.312	2.467	2.680
Skewness	-0.695	-0.506	-0.320	-0.314	-0.286
Kurtosis	3.655	3.791	3.483	3.565	3.512
Int. Length Scale $[mm]$	37.897	38.572	41.617	20.740	19.330
Taylor Micro Scale λ $[mm]$	6.795	4.855	4.163	2.739	2.468
Dissipation Rate ϵ $[m^2/s^3]$	283.83	200.56	189.11	163.86	104.82
Kolmogorov Length Scale η $[mm]$	0.0931	0.1003	0.1010	0.1038	0.1155

The frequency analysis is performed exploiting the F.F.T. (Fast Fourier Transform) algorithm of Matlab which uses a special version of the discrete Fourier transform to filter the data. The error analysis for the presented results is performed according to the error propagation theory (the Kline-McClintock approach) always using a confidence interval of the 95%.

7.2. Hot-wire Traverses Results

The measures, coupled with pressure measurements, allow computing the pressure losses caused by

the presence of the heat exchange. The test conditions repeatability being one of the main issues, the results presented cannot be retained as quantitatively precise. This is especially true since the traverses at the two locations have been performed during two different tests. However the experimental campaign gives meaningful information about the general flow field behavior [19].

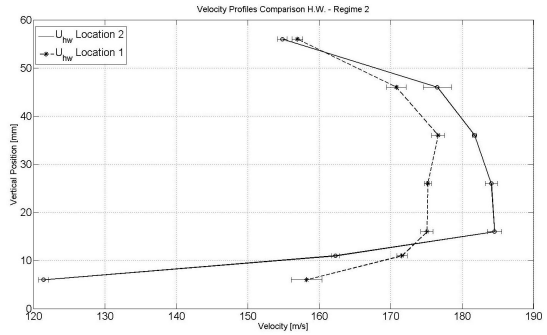

Figure 16: Velocity Profiles - H.W. Measures

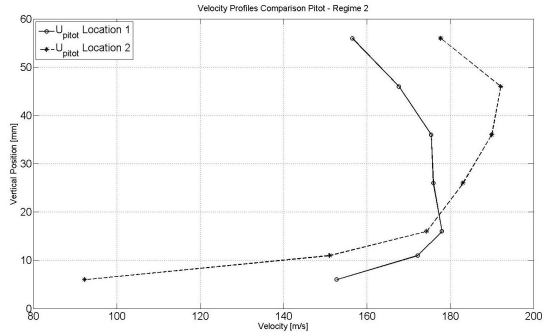

Figure 17: Velocity Profiles - Pitot Measures

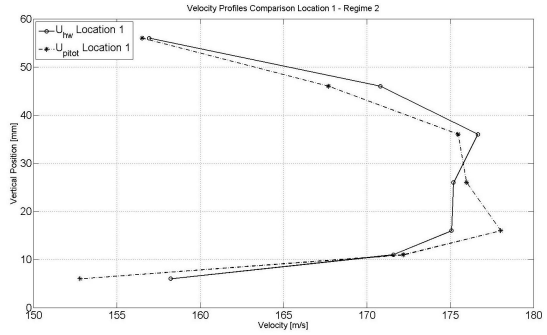

Figure 18: Velocity Profiles - Location 1, H.W. - Pitot Comparison

From Figure 18 and Figure 19 we can notice a discrepancy between the measurements performed with

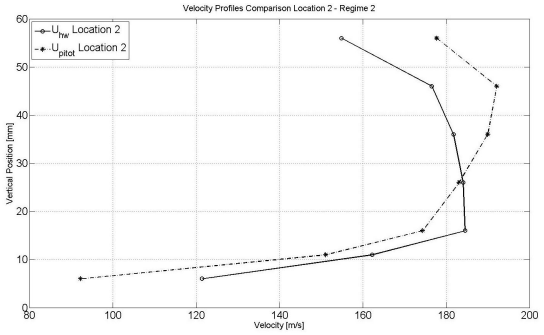

Figure 19: Velocity Profiles - Location 2, H.W. - Pitot Comparison

the hot-wire and the Pitot tube that seems to be mainly due to the fact that the wind tunnel is a blow-down facility. In facts with such facilities one of the biggest issues is to be certain to have exactly the same flow conditions for enough time to perform a full traverse analysis. If we compare these results with the results in table 3 it is clear that performing multi-point measurements gives much more reliable measurements since we are certain that the flow conditions will be the same.

7.3. Hot-wire Rake Results

Since the wind tunnel is exploited in parallel by ULB and some modifications have been performed on it the results obtained with the hot-wire rakes should not be compared with above reported results. The main purpose of the performed experiments is to validate the manufactured rakes.

Regime	***Position***	U_{meas} Pitot	U_{meas} H.W.
1	1	$\approx 205.04\ m/s$	$\approx 205.64\ m/s$
	2	$\approx 207.01\ m/s$	$\approx 207.95\ m/s$
	3	$\approx 201.64\ m/s$	$\approx 203.40\ m/s$
2	1	$\approx 177.59\ m/s$	$\approx 171.01\ m/s$
	2	$\approx 173.34\ m/s$	$\approx 173.70\ m/s$
	3	$\approx 169.77\ m/s$	$\approx 170.78\ m/s$
3	1	$\approx 120.89\ m/s$	$\approx 121.88\ m/s$
	2	$\approx 124.40\ m/s$	$\approx 125.97\ m/s$
	3	$\approx 119.61\ m/s$	$\approx 124.54\ m/s$

Table 3: H.W. Rake 3 Probes Vs. Pitot

In table 3 are reported the velocities measured with the 3-probes support and a Pitot tube at the same positions but at a different distance from the test section inlet during the same test. It is easy to understand as the possibility to simultaneously measure the whole velocity profile drastically reduce the uncertainty linked

to the capacity of maintaining exactly the same flow conditions for a long period of time. Therefore the accuracy of the velocity profiles measured with the rake is much higher and the profile shape gives indications on the actual test section flow field being not linked to the wind tunnel working parameters controlled by the operator.

7.4. CFD Simulation Results

In Figure 20 is plotted the computed velocity profile along the x-axis extracted from the wing trailing edge to the end of the numerical domain.

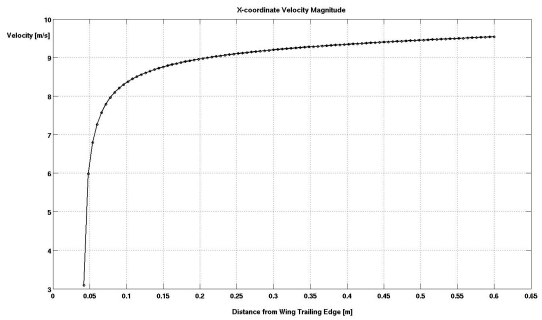

Figure 20: X-coordinate Velocity Plot

It is possible to notice that after 35 cm the influence of the rake wake starts being negligible, this why the heating resistance used for the I.R. experiment has been placed at about 40 cm from the probe support.

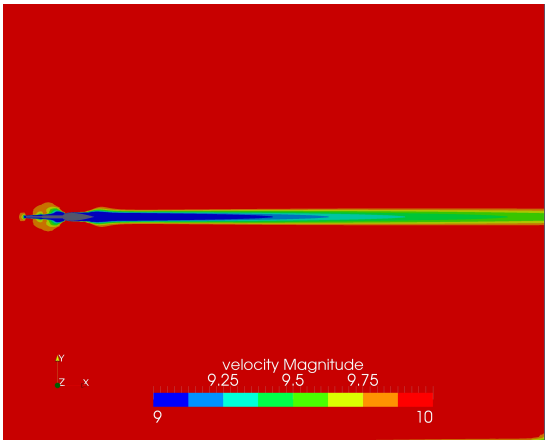

Figure 21: CFD-computed Velocity Contour Plot

From the contour plot reported in Figure 21 it is possible to see the influence of the presence of the rake in the whole domain. The results obtained could be used for comparison with oil flow visualization. This will be more interesting when moving to the high velocity case as the oil visualization allows to clearly see if the transition to supersonic occurs and where the flow in case detach from the wing surface.

8. Conclusions

The analysis performed to check the flow field quality makes us assume that modifications should be performed on the wind tunnel. Indeed the very low turbulence level, together with the almost parabolic velocity profiles measured, let us assume that flow could probably not be fully developed when entering the test section. Though the absence of spectral peaks lets us deduce that the turbulence in the flow field is homogeneous and no frequency correlated structures are present (no vortex shedding or other phenomena). This leads to the conclusion that performing minor modifications should be enough to improve the flow field quality. The coupling of Pitot tube and hot-wire probe traverse measurements shows that the general behavior of the flow field is maintained almost constant. Nevertheless it also testifies that the wind tunnel is not able to reproduce exactly the same conditions (p_{tot} profile, U profile, etc..) for two consecutive tests. The tests performed with the hot-wire probes rake show the quality of the chosen support design in order to overcome the main issue affecting a blow-down facility: maintain exactly the same working conditions for a long period of time. Indeed the rake allowed us to measure the velocity at five different positions instantaneously without affecting significantly the flow field itself. The obtained results have been taken into account by the U.L.B. engineers while conceiving a revised version of the facility that is now under construction. The flow field of this new wind tunnel will be investigated in the next months.
For what concerns the numerical solution of the IHCP the validation test performed gave encouraging results. Though the lesson learned from the preliminary test performed is that one has to carefully prepare the experimental setup in order to reduce as much as possible the heat losses (very high thermal insulation on the sides and on the back face of the fin). Furthermore, preparing the experimental setup to work with a finned heat exchanger at high subsonic velocity will be even more challenging. Nevertheless the task to validate the methodology and develop a consistent approach to this kind of analysis can be considered as accomplished. The simulations performed over the H.W. probe rake have been very helpful to correctly

prepare the I.R. low velocity experimental setup. Additionally the geometry and the meshing procedure are now well established so that it will be easier to move to high subsonic velocity case.

9. Future Developments

One of the main and more imminent tasks will be to check the flow field quality in the revised version of the blow-down wind tunnel. Besides this task the capabilities of the H.W. rake made in plaster should be validated, indeed CFD simulations and flow oil visualization at high speed are scheduled in order to accomplish the task. The I.R. experiments proposed methodology and the proposed algorithm to solve the IHCP should be validated at low speed. Furthermore the procedure needs to be optimized for a flow reaching $M \approx 0.7$ where possible issues could be the very small amount of time to grab I.R. images, the flow stabilization, the fin temperature stabilization, etc ...

Acknowledgments

I would like to thankfully acknowledge the "TEMPO Laboratory" of the University of Valenciennes guided by Professor Souad Harmand for giving me the opportunity to exploit their knowledge on the IHCP.

I also would like to sincerely thank the ULB research engineer Nicolas Heintz for the months of work performed together and the availability he showed.

References

[1] T. Perelman, On conjugated problems of heat transfer, International Journal of Heat Mass Transfer (Vol. 3, pp. 293-303).

[2] F. Kreith, Principles of Heat Transfer, second revised edition Edition, International Text Books in Mechanical Engineering, International Textbook Company Ltd, 158 Buckingham Palace Road London, 1965.

[3] P. H. Groeber, D. S. Erk, Fundamentals of Heat Transfer, third revised edition by dr. u. grigull Edition, McGraw-Hill Series in Mechanical Engineering, McGraw-Hill Book Company, INC., 1962.

[4] F. Coletti, A. Armellini, T. Arts, C. Scholtes, Aero-thermal investigation of a rib-roughened trailing edge channel with crossing jets - part ii: Heat transfer analysis, ASME paper No. GT2008 - 50695.

[5] A. Willockx, Using the inverse heat conduction problem and thermography for the determination of local heat transfer coefficients and fin effectiveness for longitudinal fins, Ph.D. thesis (2009).

[6] B. Cukurel, T. Arts, C. Selcan, Conjugate heat transfer characterization in a ribbed cooling channel, Conference Proceedings (ISAIF10-161).

[7] F. Coletti, Coupled flow field and heat transfer in an advanced internal cooling scheme, Ph.D. thesis (2010).

[8] J. Beck, B. Blackwell, C. S. C. Jr., INVERSE HEAT CONDUCTION - Ill-posed Problems, first edition Edition, International Text Books in Mechanical Engineering, Wiley Interscience Publication, 1985.

[9] J. Beck, B. Blackwell, A. Hoji-Sheikh, Comparison of some inverse heat conduction methods using experimental data, International Journal of Heat Mass Transfer (Vol. 39, pp. 3649-3657).

[10] Various, Measurement Techniques in Fluid Dynamics - An Introduction, second revised edition Edition, VKI Lecture Series, von Karman Institute, 2001.

[11] F. E. Jorgensen, How to measure turbulence with hot–wire anemometers, Dantec Dynamics, Tonsbakke 16-18, DK-2740 Skovlunde, Denmark, 2005.

[12] G. Cardone, T. Astarita, G. Carlomagno, Wall heat transfer in static and rotating 180 degrees turn channels by quantitative infrared thermography, Re. Gén. Therm. (37, 644-652).

[13] F. Baldani, W. Bosschaerts, R. Wagemakers, High velocities wind tunnel flow field investigation and heat exchanger infrared analysis. part 1: Experimental set-up, experiments and first results, Conference Proceedings (ISAIF10-11).

[14] H. Bruun, Hot–wire Anemometry, Principles and Signal Processing, Oxford University Press Inc., 1995.

[15] D. Hanson, K. Horan, Turbulence/cascade interaction: spectra of inflow, cascade response and noise (A98-30871).

[16] AIAA, Turbulence in Complex Flows: A Selected Review, AIAA, Reno, NV, 1992.

[17] AIAA, Preliminary Measurements of Velocity, Density and Total Temperature Fluctuations in Compressible Subsonic Flow, AIAA, Reno, NV, 1983.

[18] P. Stainback, K. Nagabushana, Review of hot-wire anemometry techniques and the range of their applicability for various flows, Electronic Journal of Fluids Engineering, Transactions of the ASME.

[19] F. Baldani, W. Bosschaerts, Turbulence measurements in a high subsonic non-isothermal flow field. turbine engines inlet conditions analysis, Conference Proceedings (ISABE-2011-1815).

FLOW IN COMPRESSORS

Passive Vortex Generators as End-Wall Flow Control Elements

Fatma Ceyhun Sahin

Turbomachinery and Propulsion Department, von Karman Institute for Fluid Dynamics, Belgium, sahinc@vki.ac.be

Supervisor: Jean-François Brouckaert

Associate Professor, Turbomachinery and Propulsion Department, von Karman Institute for Fluid Dynamics, Belgium, brouckaert@vki.ac.be

University Supervisor: Tony Arts

Professor, IMMC, EPL, UCL, Belgium, arts@vki.ac.be

Abstract

Low profile vortex generators (VGs), selected with the aid of preliminary numerical simulations, are included into a compressor cascade and their effects are observed in terms of exit plane total pressure and velocity distributions. The orientation of VGs can be optimized according to their possibility of decreasing the global loss or improving the exit angle. Several VG configurations are presented in this study.

Keywords: vortex generator, 5-hole probe, compressor cascade measurements

1. Introduction

The present contribution focuses on losses through a compressor cascade. Preliminary numerical simulations of the investigated blade profile showed that the secondary flows dominate the passage and decrease the performance of compressor dramatically [1]. Independent simulations of the flow around low profile VGs [2] guided the selection of geometrical and location parameters for a VG which is supposed to provide a minimum increase in the boundary layer thickness, and hence the associated loss.
Compressor blades and low profile VGs are combined in the C1 facility. The cascade performance is investigated in terms of total pressure, flow velocity and exit angle. The orientation of a VG in a passage is defined according to the results of a numerical investigation [2] and selected sizes of VGs, considering two different wetted area cases, are tested. VGs are promising when they are at a correct location. According to the numerical simulations, the pressure loss behind the VGs increases with increasing wetted area and also incidence angle [2]. That unavoidable increase in loss is expected and it is not considered in selecting the VGs to be tested.
Even though the initial numerical simulation for low profile VGs were not considering neither the blades, nor the adverse pressure gradient in the flow, the experimental validation shows that they were still useful in selecting a correct incidence angle, since the simulations were evaluated in a comparison base.
Considering the application of VGs in a real turbomachinery passage will not allow symmetry as long as the VGs are implemented inside the passage. Different VGs are also tested at the inlet section of the cascade.

2. Experiments

Behind compressor cascade, 5-hole probe measurements are conducted, half a blade chord downstream of the trailing edge. That is in Fig. 1. Knowing that the flow is symmetricaly in the facility, a plane extending from the cascade end-wall up to half a span length distance from the end-wall is scanned. The inlet stagnation condition is set at 45 mm H_2O relative pressure and the exit of the cascade is at atmospheric pressure. The calibration procedure and the resulting calibration maps for the 5-hole probe were presented in [2].
5-hole probe measurements provide both total pressure and flow direction information. Hence, loss in stagnation pressure as well as the velocity field in the

measurement plane are easily obtained but velocity gradients can only be obtained in pitch-wise and span-wise directions. If vorticity is calculated in order to obtain more information on the flow field, the result is only in the axial direction, $(\frac{\partial v}{\partial z} - \frac{\partial w}{\partial y})\hat{i}$. That value neglects the main flow but includes only secondary flow information. In order to observe the flow separation from the cascade end-walls and from the blade surface, 3-D velocity field information is required. For that purpose, measurements are extended to +/- 5% of the chord length on either side of the principal measurement plane, which is also depicted in Fig. 1. The resulting vorticity is a 3-D vector field,

$$(\frac{\partial v}{\partial z} - \frac{\partial w}{\partial y})\hat{i} + (\frac{\partial u}{\partial z} - \frac{\partial w}{\partial x})\hat{j} + (\frac{\partial u}{\partial y} - \frac{\partial w}{\partial x})\hat{k} \quad (1)$$

where the $\hat{j}$ component is pitch-wise vorticity which will give the information on the axis-span plane and the $\hat{k}$ component will give information on the blade to blade plane since it is the span-wise vorticity.

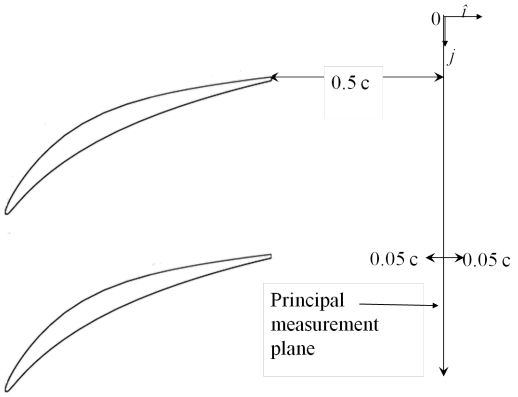

Figure 1: One passage of the cascade and the measurement plane behind it.

3. Configuration of VGs

Low profile VGs altering in terms of geometrical shape are tested. Triangular VGs, having two different sizes, are installed inside the passage and rectangular VGs are installed upstream of the blade leading edge.

3.1. Inside the Passage

A preliminary pressure measurement behind the cascade, installing the triangular VGs at a distance of 1/3 chord behind the leading edge [3] resulted in an increase of the global loss and the flow visualisations in the same study showed that flow separation on the corner was not as early as expected but it was closer to the trailing edge. Hence, for that new study which is focusing on increasing the number of configurations tested, in order to optimize the VG geometry and their positioning, a position which is supposed to have a more positive effect on the corner separation is preferred. Inside the passage, the leading edge of the triangular VG is fixed at a distance of 2/3 chord from the blade leading edge. The distance of a triangular VG from the blade suction surface is always equal to the height of the VG. The orientation of the VG is defined with respect to the inlet flow angle. The positioning of a triangular VG inside the passage is detailed in Fig. 2.

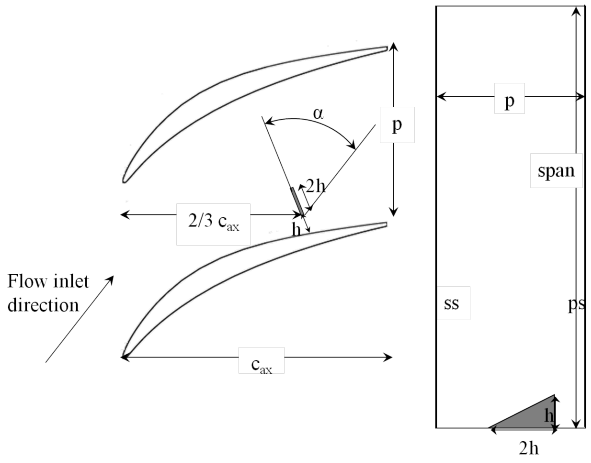

Figure 2: Triangular VG configuration inside the passage.

3.2. Upstream of the Leading Edge

Rectangular VGs are always tested at the inlet section of the passage, 11% of the chord upstream of the leading edge. The angle between the inlet flow and the VG is fixed at 20° and the position of the VG is changed in the pitch-wise direction. That distance is also referred to the blade leading edge and non-dimensionalised with the pitch length.The rectangular VG configuration at the passage inlet is in Fig. 3.

3.3. Types of VGs

Two different sizes of triangular VGs, h=5 mm and h=10 mm are tested at different incidence angles. Each configuration is named with respect to the VG height as well as the incidence angle. Triangular VGs will be referred as 't', followed with the VG height, h and 'a' will stand for 'angle' followed by the angle

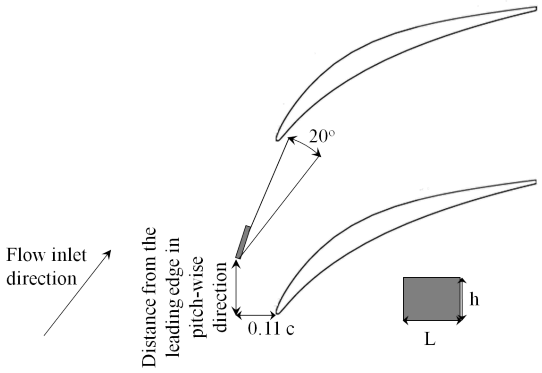

Figure 3: Rectangular VG configuration before the leading edge.

value. For instance, t5a30 will refer to a triangular VG having a height of 5 mm and oriented at 30° with respect to the cascade inlet flow.
Rectangular VGs, which are referred with an 'r', have a fixed length, L, defined as 10% of the chord. Two different heights, 6.5 mm and 8 mm are tested. 6.5 mm corresponds to 1/3 of the fully developed upstream end-wall boundary layer thickness of the facility and 8 mm corresponds to 1/10 of the blade chord length. The distance of an rVG in the pitch-wise direction from an axial line tangent to the blade leading edge ranges between 0 and 20% of the pitch-length. Hence, an rVG is named like r*hpd* which means r6p10 is a rectangular VG having height of 6.5 mm, at a distance of 10% of the pitch from the leading edge.

4. Measurements

4.1. Stagnation Pressure

The exit stagnation pressure, P_{o_2}, is measured by means of the kiel head of the five hole probe and the corresponding calibration map is used for the incidence correction, which is necessary especially at high angles.

4.2. Total Pressure Losses Behind the Cascade

The chamber pressure, which is the inlet stagnation pressure of the cascade (P_{o_1}), is set at 45 mm H_2O above atmospheric pressure and any possible variation in that level because of the blockage at the exit by the 5-hole probe is checked before each measurement. The stagnation pressure loss behind the cascade is defined as

$$(P_{o_1} - P_{o_2})/(P_{o_1} - p_1) \tag{2}$$

The inlet static pressure, p_1 is calculated according to the calibration of the wind tunnel [3].
The loss value of Eq. 2 is also mass averaged through pitch in order to observe the global effects of the VGs on the flow and also compare those effects at different span-wise positions.

4.3. Flow Angles

The tubes of the 5-hole probe are meant to measure the flow angle within two perpendicular planes. Mass averaging of the angles is also considered to deliver a more robust comparison between different control cases.

4.4. Velocity Field Behind the Cascade

The output of the 5-hole probe, interpreted with four calibration maps, allows obtaining the three components of the velocity in the measurement planes. Subtracting the mean value defined across one pitch allows defining the velocity vectors related to the secondary flow phenomena.

4.5. Vorticity Vectors

The mathematical curl of the velocity vector field, as defined in Eq. 2, defines the vorticity vector field and the components of that vector field are interpreted separately.

4.6. Shape Factor

The characteristics of the boundary layer, developing on the cascade end-wall are obtained considering the axial and span-wise components of the velocity vectors. The shape factor is defined as the ratio of displacement thickness and the momentum thickness [4] where displacement thickness is a discrete integral in that case,

$$\delta^* = \int_0^\delta (1 - u/U)\, dy. \tag{3}$$

As well as the momentum thickness

$$\theta = \int_0^\delta (u/U)(1 - u/U)\, dy. \tag{4}$$

Hence, the shape factor is

$$H = \delta^*/\theta \tag{5}$$

5. Experimental Results

5.1. Base Flow

5.1.1. Total Pressure Losses Behind the Cascade

The base flow total pressure loss as defined in Eq. 2 is depicted in Fig. 4 in terms of a colour map as well as a span-wise distribution of mass average through one pitch. The loss coefficients of the span-wise distribution are non-dimensionalized by the value obtained at mid-span. In the vicinity of the cascade wall, the loss is about 75% of the mid-span loss and it drops to its minimum level, which is almost the half of the loss at the mid-span, about 18 mm away the wall and then the loss starts increasing because of a probable separation from the blade suction side.

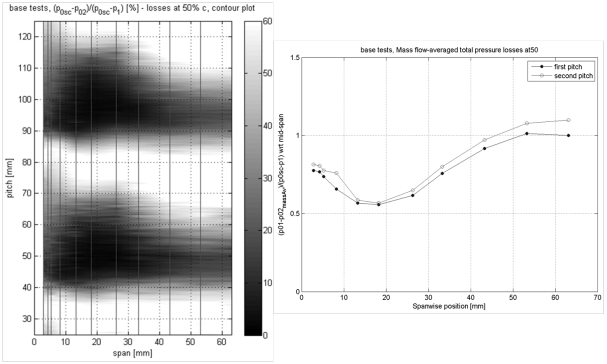

Figure 4: Total pressure loss behind the cascade in case of base flow.

5.1.2. Flow Angles

Mass averaged total pressure loss for base flow case is depicted in Fig. 5 with the averaged pitch angle distribution in order to observe any relation between pressure loss and pitch angle. The pitch angle is also normalized (in terms of a difference) with respect to the value at the mid-span. At the span-wise position where the loss is minimum, the pitch angle has its maximum value and the angle distributions converge approaching to the mid-span. End-wall effects on that angle distribution are dropping the pitch-angle in the vicinity of the end-wall. It is acceptable to consider a passage vortex effect which diverts the flow to the suction side of the neighbouring blade according to that lower angle region observed in Fig. 5.

5.1.3. Velocity Field Behind the Cascade

The secondary velocity vector field for the base flow case is shown in Fig. 6. The blade trailing edge is located at ∼ 81 mm in the pitch-wise direction as

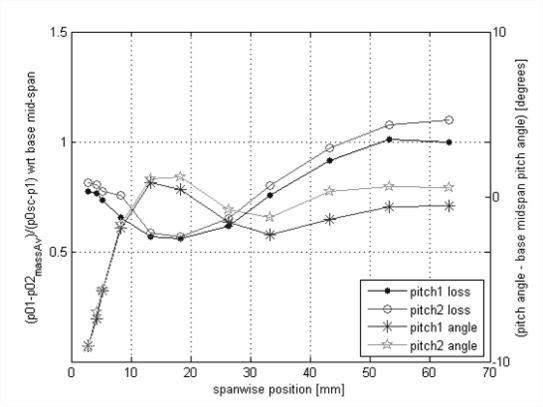

Figure 5: Span-wise distribution of averaged pressure loss and pitch angle.

well as 48.8 mm (=pitch) farther (∼ 130 mm). That reference will be considered in interpreting the figures on the controlled (with VGs) cases. Two components

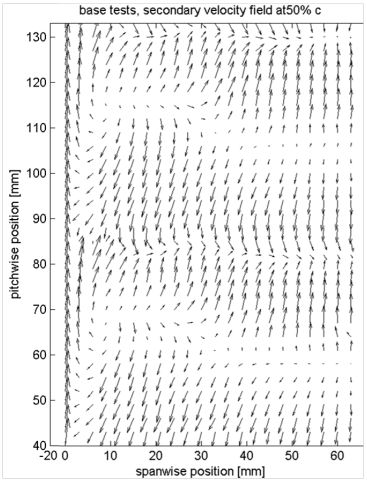

Figure 6: Secondary velocity vector field for base flow.

of the vorticity, from Eq. 1, on the principal plane of measurements are shown in Fig. 7 and Fig. 8, respectively. The position of trailing edge, that corresponds to the maximum loss on that plane, is indicated in those figures as horizontal lines. Fig. 7 includes also the shape factor of the boundary layer developing on the cascade end-wall. The highly viscous region close to the end-wall is easily observed in Fig. 7. The shape factor indicates an unstable boundary layer behaviour besides a probable separation in the wake. In Fig. 8, vortices are observed in couples where the positive signed ones are at a pitch-wise position corresponding to the pressure side of the blade and the negative

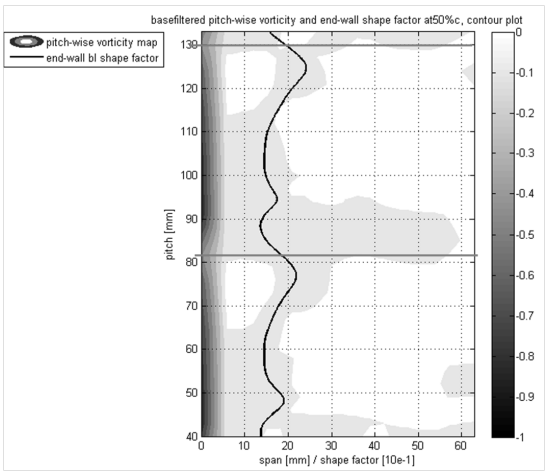

Figure 7: Pitch-wise vorticity map and end-wall shape factor for the base flow.

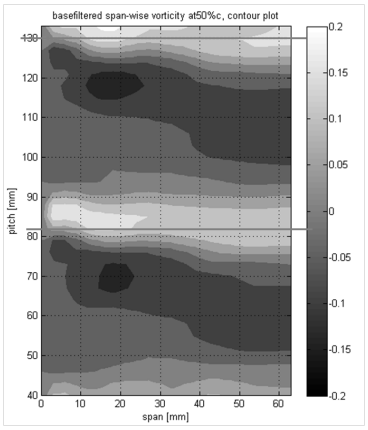

Figure 8: Span-wise vorticity map for the base flow.

signed ones are on the suction surface and they extend up to counter-rotating component of the adjacent vortex closer to the mid-span which also corresponds to the high loss region for the stagnation pressure.

5.2. Controlled Flow

5.2.1. Triangular VGs

Triangular VGs are implemented in the facility according to the configuration defined in Fig. 2.
The triangular VG with a height of 5 mm, VG5, is tested at three different incidence angles with respect to the inlet flow of the cascade. Total pressure loss distributions are shown in Fig. 9 respectively for VGs incidence angle of 20°, 30° and 53° with respect to the cascade inlet flow angle. Those figures are not easy to be distinguished from each other. In the following figure, Fig. 10, the averages over one pitch, normalized with the loss coefficient of the base flow at mid-span, are compared with the base flow case and the effect of VGs are easier to be observed. The integral of the losses are also on the figure. A very clear observation before calculating the integral is that the VG incidence angle 20° case is the only case which is promising to provide a loss reduction. After varying

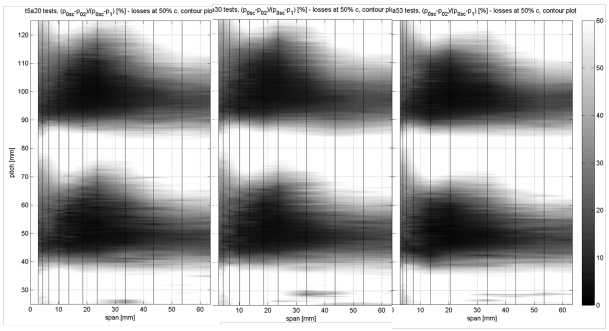

Figure 9: Total pressure loss maps behind the cascade controlled with VG5.

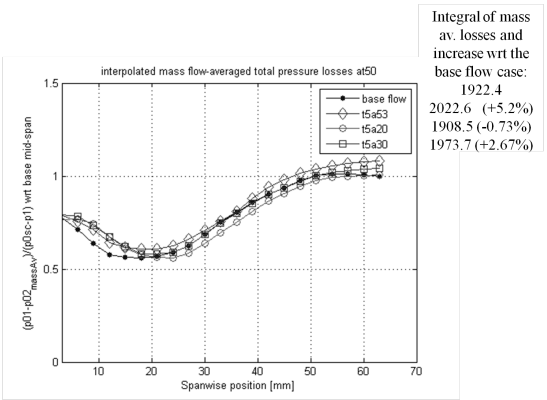

Figure 10: Mass flow rate averaged pressure loss behind cascade with VG5.

the VG incidence angle, the VG height is also varied and in Fig. 11 pressure loss maps for VG incidence angles of 20° and 53°, respectively, are depicted. Since VG10 has a wetted area four times larger than the one of the previous case, different effects of it according to the incidence angle are observed on those maps. When the VG incidence angle is low, the disturbance from VG10 is more quickly suppressed approaching the mid-span. Instead of comparing two VG10 cases with the base flow, they are also compared with VG5 cases at the same VG incidence angle. The integral under the mass averaged curves of Fig. 12 shows that at low incidence angle, it is possible to reduce the to-

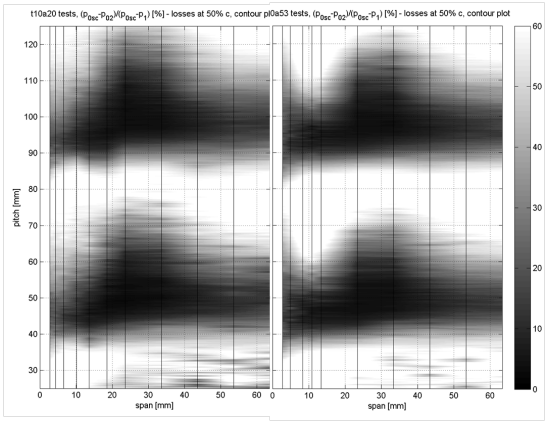

Figure 11: Total pressure loss maps behind the cascade controlled with VG10.

tal pressure loss regardless of the VG height and although larger VG drops it more after 22 mm from the end-wall, local increase behind VG10 results with less global reduction. The comparison of mass averaged losses behind VGs at 53°, in Fig. 13 shows that global loss increases are unavoidable behind a large VG at large incidence angle. The comparison of the av-

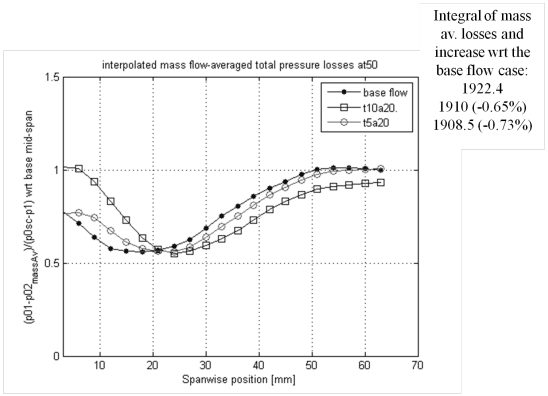

Figure 12: Mass flow rate averaged pressure loss behind cascade with triangular VGs at 20°.

eraged pitch angles is in Fig. 14. Distributions are once more shown as the difference from the base flow mid-span value. The lower incidence angles of VG5 have no effect on the pitch angle up to a distance of 40 mm from the end-wall and then their effect is increasing the pitch angle slightly. On the other hand, the high VG incidence angle cases decrease the pitch angle constantly up to 30 mm from the end-wall and then its decreasing effect is stronger. The mass average values of pitch angles are compared for a given incidence angle behind different heights of triangular VGs in

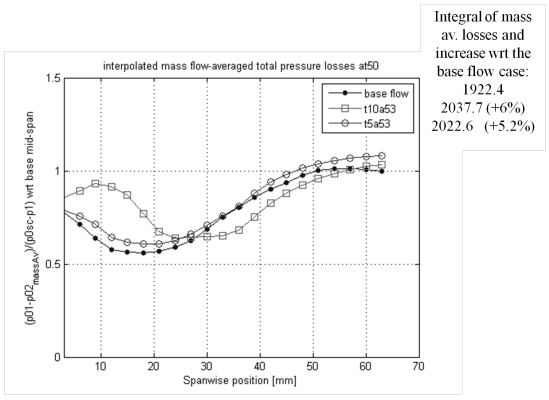

Figure 13: Mass flow rate averaged pressure loss behind cascade with triangular VGs at 53°.

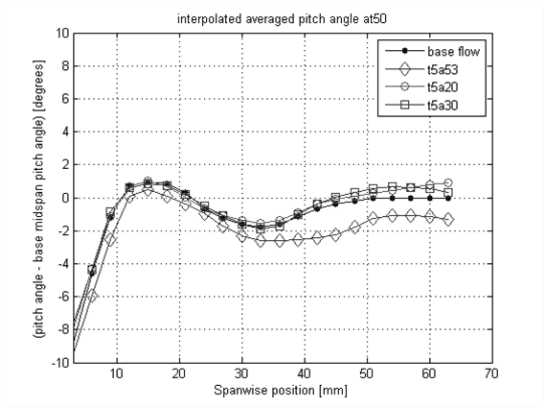

Figure 14: Pitch angle behind cascade with VG5 averaged thorough one pitch.

Fig. 15 and Fig. 16. The lower incidence angle cases are in Fig. 15. The triangular VG10 is useful in avoiding the significant drop in pitch angle in the end-wall vicinity, also recalling that global pressure loss drops behind it. If regions closer to mid-span are considered, VG10 is still more beneficial compared to VG5, considering the effect on the pitch angle. A higher incidence angle for VG10 causes the most significant drop in pitch angle, closer to mid-span, Fig. 16. The pitchwise component of the vorticity vectors, $\frac{\partial u}{\partial z} - \frac{\partial w}{\partial x}$, is depicted in Fig. 17 for VG5 controlled cascade cases, respectively for 20°, 30° and 53°. The shape factor of the cascade end-wall boundary layer is also plotted on top of the vorticity maps. The shape factor value near the blade increases compared to the base flow case and the maximum shape factor location is shifted closer to the suction surface of the blade with low incidence angle. The secondary peak of the shape factor distribution through the pitch is decreased at lower incidence

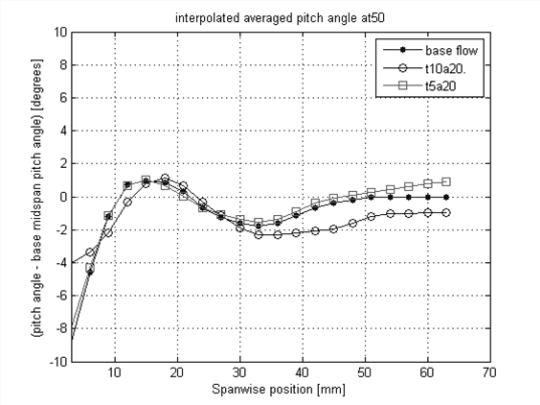

Figure 15: Pitch angle behind cascade with triangular VGs at 20° averaged thorough one pitch.

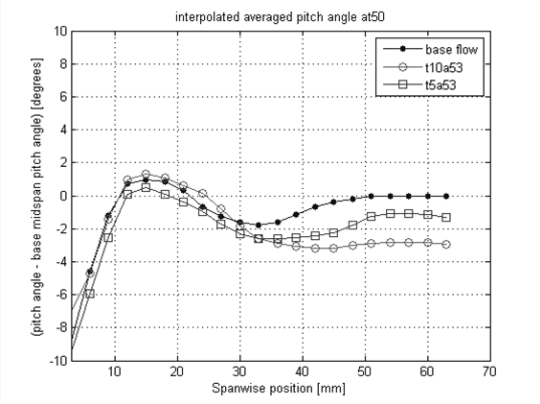

Figure 16: Pitch angle behind cascade with triangular VGs at 53° averaged thorough one pitch.

angles.

The span-wise vorticity, $\frac{\partial u}{\partial y} - \frac{\partial v}{\partial x}$ component for the VG5 controlled cases are shown in Fig. 18. A couple of stronger counter-rotating vortices are observed in the end-wall vicinity, where the effects of VGs still exist. The pitch-wise and span-wise vorticity distributions for VG10 are depicted in Fig. 19 and Fig. 20, respectively, with the corresponding shape factors. The secondary peak of the end-wall boundary layer shape factor is dropped by VG10 at 20° significantly and the increase of shape factor behind the blade is less than the one for the VG5 tests. It also worth to recall that t10a20 is able to provide a decrease in both global loss and mid-span pitch angle. Weaker span-wise vortices seen in Fig. 20 compared to Fig. 18 might be a sign of an earlier merge of vortices generated by VG10.

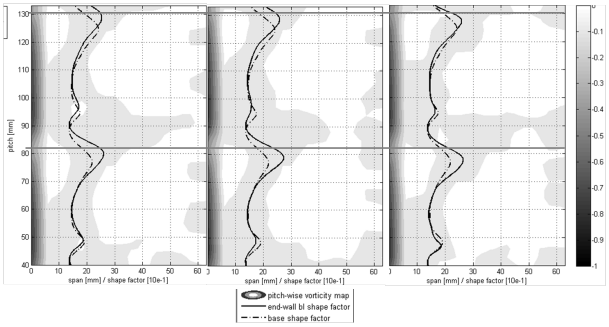

Figure 17: Pitch-wise vorticity map and shape factor for the cascade end-wall behind the cascade controlled with VG5.

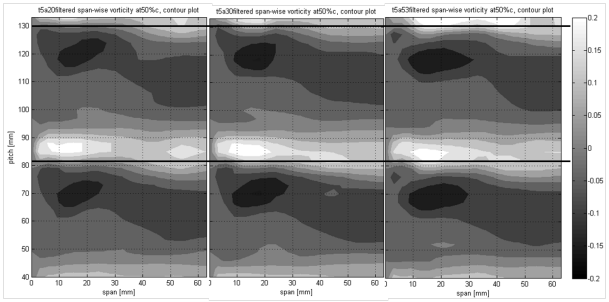

Figure 18: Span-wise vorticity map behind the cascade controlled with VG5.

5.2.2. Rectangular VGs

Since the VGs are implemented on both end-walls, the symmetry of the cascade flow is perfectly kept. However, in real application of VGs inside compressor passages, it is not possible to have VGs larger than the gap between casing and the blade tip. Hence, if the symmetry of the passage needs to be kept, a better position to start controlling the flow should be upstream of the blades. For that configuration, rectangular VGs are suggested. Rectangular VGs are fixed in the upstream section according to Fig. 3. Initially, three different positions through the pitch are tested. Those are, VGs aligned with the leading edge, at a distance of 10% and 20% of the pitch away from the suction side reference of the blade. The distributions of total pressure loss for r6p0, r6p10, r6p20, respectively are shown in Fig. 21. When the VG is aligned with the trailing edge, the generated loss is higher than the one in the other cases. Mass averaged results are compared in Fig. 22. As the distance of 10% pitch length gives the minimum increase of global loss, there must be an optimum pitch-wise position of the rectangular VG on that axial position. Also square VGs are tested at 10% pitch position. The loss distribution is plotted

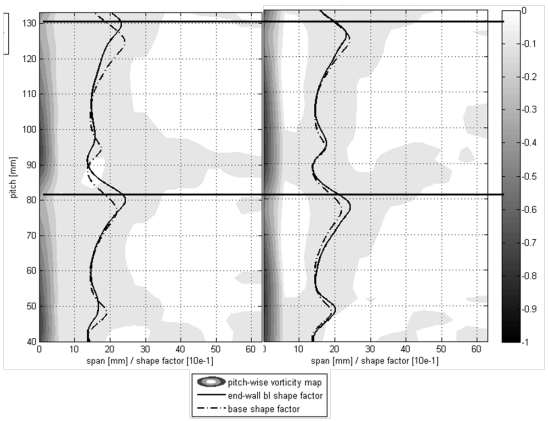

Figure 19: Pitch-wise vorticity map and shape factor for the cascade end-wall behind the cascade controlled with VG10.

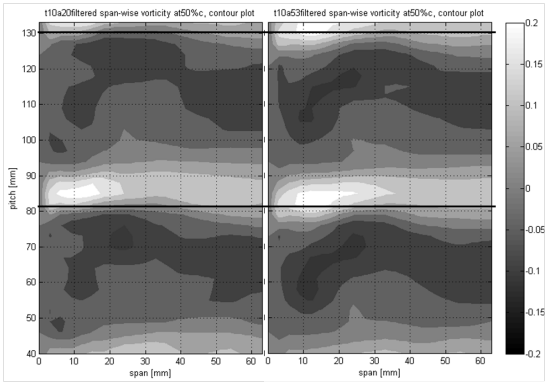

Figure 20: Span-wise vorticity map behind the cascade controlled with VG10.

in Fig. 23 and compared with r6p10 case in Fig. 24. The repeatability of those measurements have to be satisfied before claiming that VG geometry should be described with respect to the blade geometry rather than flow properties. The effects of the rectangular VG on the pitch angle are compared in Fig. 25. Among the cases presented in Fig. 25, r6p0 is the only one which provides a constant drop of the pitch angle, through span. On the other hand, as VG6 is further to the pressure side of the adjacent blade, it constantly increases the pitch angle distribution and $\sim$ 25% VG height difference have an insignificant effect on the pitch angle despite the unexpected effect on the mass averaged loss distribution. The effect of rectangular VGs in pitch-wise and span-wise vorticity are shown in Fig. 26 and Fig. 27, respectively. The distance of 10% of the pitch from the suction surface is candidate to be an optimum position in dropping the local end-wall boundary layer shape factor as well as for

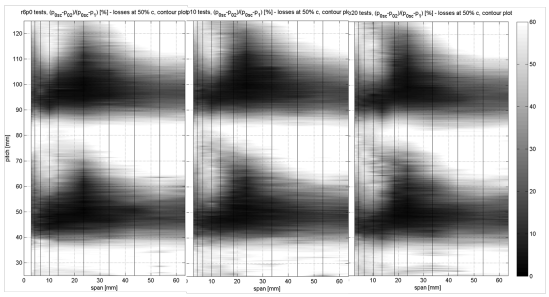

Figure 21: Total pressure loss maps behind the cascade controlled with VG6.

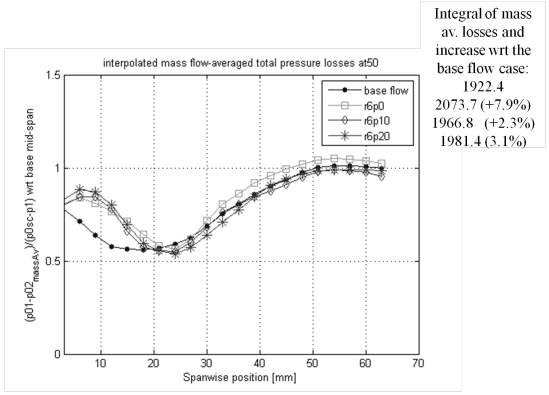

Figure 22: Mass flow rate averaged pressure loss behind cascade with VG6.

global mass averaged loss. Since the generation of vortices are much earlier than that by VGs located inside the passage, span-wise vortices are weaker in the measurement plane, compared to the previous plots. The results behind the cascade controlled with square VG8 are shown in Fig. 28 and Fig. 29. An expected result of increasing the VG height is observed in Fig. 28 such that the decreasing effect of r6p10 on the shape factor disappears.

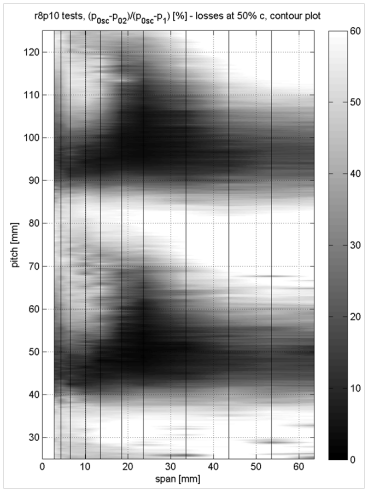

Figure 23: Total pressure loss map behind the cascade controlled with VG8.

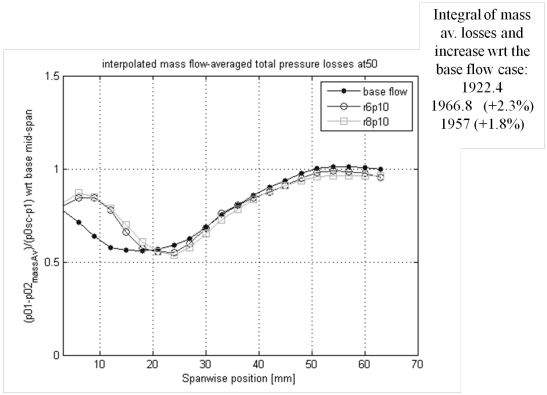

Figure 24: Mass flow rate averaged pressure loss behind cascade with rVGs at 10% of the pitch.

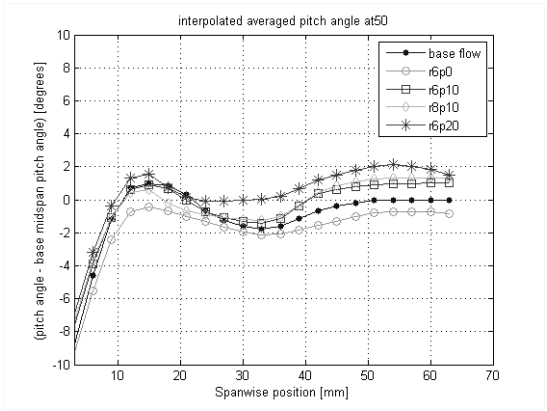

Figure 25: Pitch angle behind cascade with rVG averaged thorough one pitch.

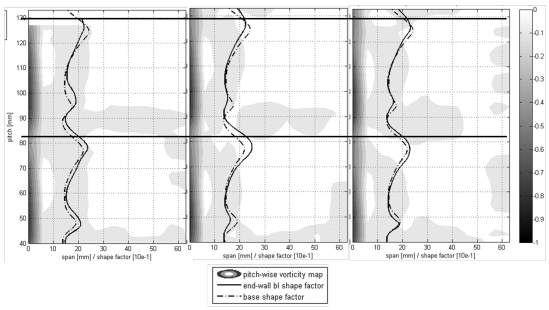

Figure 26: Pitch-wise vorticity map and shape factor for the cascade end-wall behind the cascade controlled with VG6.

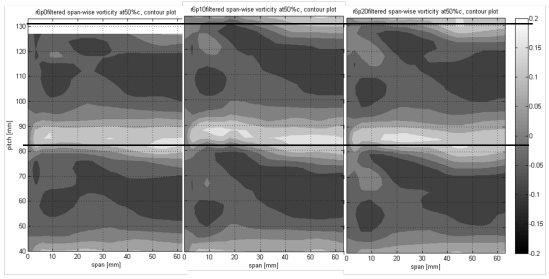

Figure 27: Span-wise vorticity map behind the cascade controlled with VG6.

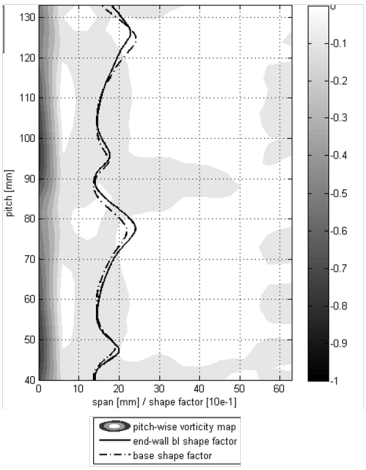

Figure 28: Pitch-wise vorticity map and shape factor for the cascade end-wall behind the cascade controlled with VG8.

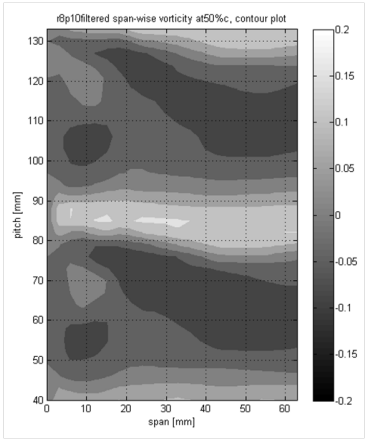

Figure 29: Span-wise vorticity map behind the cascade controlled with VG8.

6. Conclusion

If the design parameter is only the global loss behind the cascade, triangular VGs inside the passage, at a relatively low incidence angle are useful in dropping the loss in total pressure although they cause local increase in the level behind themselves.
Another important parameter should be related to the end-wall boundary layer. If the shape factor from the cascade end-wall is considered, rectangular VGs before the blade leading edge are able to provide a local decrease of end-wall shape factor, where increase of that value behind the blades is unavoidable in any case. VG10 at 20° gives the minimum local end-wall boundary layer shape factor. Another case which provides such a local drop in end-wall shape factor is the rectangular VG6 at a distance of 10% of the pitch length from the blade suction surface.
The effect of VGs on mass averaged pitch angle is contradictory with their effect on the mass averaged total pressure loss, except t10a20 case.
Considering the three parameters, total pressure loss, shape factor and pitch angle, among the tested control cases, triangular VG10 at 20° is the best candidate to be focused on as a secondary flow control device.

7. Future Plans

In order to figure out optimum pitch-wise position for rVG6, 15% of the pitch length will be tested as a control location.
The trend of pressure loss is decreasing as the incidence angle of tVG is decreased. However, instead of a continuous decrease with the incidence angle, an optimum angle is expected. Hence, lower incidence angle between the inlet flow and the VG cases will be tested.
Although the repeatability of base flow is verified after each controlled case measurement, none of the controlled cases are ensured in that term. The tests for randomly selected cases will be repeated on the main measurement plane at certain span-wise positions.

References

[1] Sahin, F.C., Boundary Layer Separation Control on a Compressor Blade, in: Summaries of VKI's Doctoral Candidate Research 2009-2010, Sint-Genesius Rode, Belgium, 2010.
[2] Sahin, F.C., Design of a Compressor Cascade for Flow Control Tests, in: Summaries of VKI's Doctoral Candidate Research 2010-2011, Sint-Genesius Rode, Belgium, 2011.
[3] Albiero, A., Aerodynamic Performance of End-Wall Flows, SR 2011-05, von Karman Institute for Fluid Dynamics (May 2011).
[4] Kiock, R., Boundary Layers on Turbomachinery Blades, CN 118, von Karman Institute for Fluid Dynamics (1983).

The Effect of Solidity on Compressor Performance and Stability

Jérôme Sans

Turbomachinery and Propulsion Department, von Karman Institute for Fluid Dynamics, Belgium, sans@vki.ac.be

Supervisor: Jean-François Brouckaert

Associate Professor, Turbomachinery and Propulsion Department, von Karman Institute for Fluid Dynamics, Belgium, brouckaert@vki.ac.be

Co-Supervisor: Tony Arts

Professor, von Karman Institute of Fluid Dynamics, Turbomachinery and Propulsion Department, Belgium, arts@vki.ac.be

University Supervisor: Philippe Chatelain

Professor, Université Catholique de Louvain, Institute of Mechanics, Materials and Civil Engineering, Belgium, philippe.chatelain@uclouvain.be

Abstract

The solidity in a compressor is the ratio of the aerodynamic chord over the pitch. The following PhD project aims at investigating numerically and experimentally the effect of the solidity on both compressor performance and stability. A low-pressure compressor stage designed and manufactured by TechSpace Aero and representative of a state-of-the-art booster helps to support the study. Existing compressor correlations are reviewed to extract the influence of solidity on deviation, incidence and losses. The issue of the optimum solidity is also covered. Then, the effect of solidity is assessed by CFD thanks to FINE/Turbo of NUMECA International. Rotor and stator blade numbers of TechSpace Aero's booster are varied independently to generate different compressor stages. The performance of all the configurations are assessed from choke to stall. The effect of solidity on pressure ratio, efficiency and stall limit is discussed.

Keywords: Compressor, solidity, pitch, chord, blade number

Nomenclature

Roman symbols

c	[m]	Aerodynamic chord length
s	[m]	Pitch
t	[m]	Blade thickness
M	[-]	Mach number
p	[Pa]	Pressure
V	[m/s]	Absolute velocity
W	[m/s]	Relative velocity
Z	[-]	Blade number
D	[-]	Diffusion factor
D_{eq}	[-]	Equivalent diffusion ratio
C_p	[-]	Static pressure coefficient

Greek symbols

β	[°]	Flow angle
γ	[°]	Stagger angle
δ	[°]	Deviation angle
ϕ	[°]	Camber angle
θ	[m]	Momentum thickness
σ	[-]	solidity
ρ	[kg/m^3]	Density
ω	[-]	Total pressure losses
Ψ_a	[-]	Zweifel coefficient

Acronyms

DCA	Double circular arc
LP	Low pressure
MCA	Multiple circular arc
VKI	von Karman Institute

Subscript

0	Stagnation condition
1	Upstream condition
2	Downstream condition
s	Static condition
i	Ideal condition
θ	Tangential direction

1. Introduction

The solidity is the ratio of the aerodynamic chord over the peripheral distance between two blades also called the pitch. This parameter must be selected early in the design process and the important role played by the solidity in the loading assessment makes its choice a crucial step that should be regarded with great care. Despite some spurious attempts to define an optimum solidity in terms of loading or efficiency, no general rule exists to guide the designer in this choice.

In the last decades, a constant increase of solidity in engine compressors has been noticed (Fig. 1). This reflects the need for the engineer to satisfy more and more severe high loading requirements that can only be achieved with high solidity. As shown in Fig. 2, the solidity trend observed over the last 50 years is mainly explained by the use of long-chord blades (i.e. low aspect ratio[1]) which brought many experimental evidences of stability enhancements and a better behaviour with respect to secondary flows [2] (A. J. Wennerstrom, 1989). However, this chord enlargement is limited by the axial extent of the compressor which is imposed by mechanical requirements. Some improvements might still emerge by looking at the pitch effect that is directly linked to the blade number.

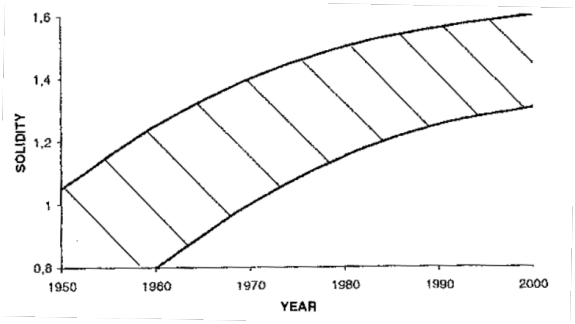

Figure 1: Evolution of the solidity in engine compressors over the last years [1] (T. Obrecht, 2006).

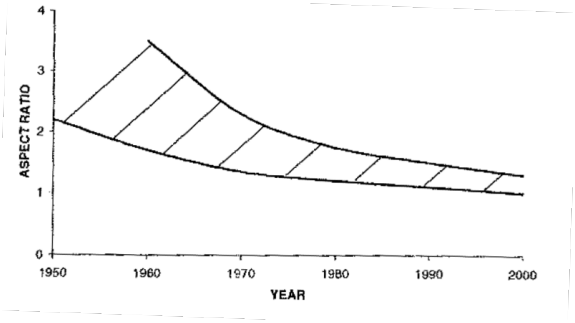

Figure 2: Evolution of the aspect ratio in engine compressors over the last years (T. Obrecht, 2006).

Unfortunately, even though either a chord extension or a blade number increase allows to work at higher loading, both methods present the undeniable disadvantage of increasing the engine weight, meaning a higher fuel consumption and pollutant emissions. It is therefore essential to fully understand the benefits and the drawbacks when adjusting those parameters. In that prospect, the following PhD project aims at investigating numerically and experimentally the effect of the solidity on both compressor performance and stability. As a support to this investigation, the low-pressure compressor stage studied at VKI within the framework of the DREAM project is considered. The stage has been designed and manufactured by TechSpace Aero and is representative of a state-of-the-art booster. Its performance has been assessed both numerically with the CFD software FINE/Turbo^{TM} from Numeca International and experimentally in the VKI R4 facility.

The first part of the work covers all the existing

[1]The aspect ratio is defined as the ratio of the blade height over the aerodyamic chord.

compressor cascade correlations and tries to characterize the influence of solidity on deviation, incidence and losses. The role played by solidity on the blade loading is addressed and existing optimum solidity criteria are presented.

After reviewing the literature, the effect of solidity is assessed through CFD. The study is achieved in 3D using the complete geometry and design conditions of the baseline booster of the DREAM project. Different stage configurations are analyzed by changing the blade number of both rotor and stator. The focus is set on the impact on pressure and efficiency as well as the stability margin.

2. Literature review

Two main issues are addressed in this section. Firstly, correlations from cascade tests are reviewed. Despite the fact that the flow in axial compressors is mainly governed by three-dimensional effects, cascade theory allows to shed some light on the physical phenomena taking place in the three-dimensional machine. These correlations essentially come from the 1960's and may have been corrected since then by engine manufacturers. However, all compressor designers once dealt with those data. Secondly, the question of the optimum solidity is studied.

2.1. Cascade correlations

The geometrical definitions given in Fig. 3 are the NASA-SP36 conventions used in the rest of the document ([3], 1965). The angles are referred to the axial direction and usually given in degrees.

- β_1 relative inlet flow angle;
- β_2 relative outlet flow angle;
- κ_1 inlet blade metal angle;
- κ_2 outlet blade metal angle;
- ϕ camber angle;
- i incidence angle;
- δ deviation angle;
- γ stagger angle;
- c aerodynamic chord;
- s pitch.

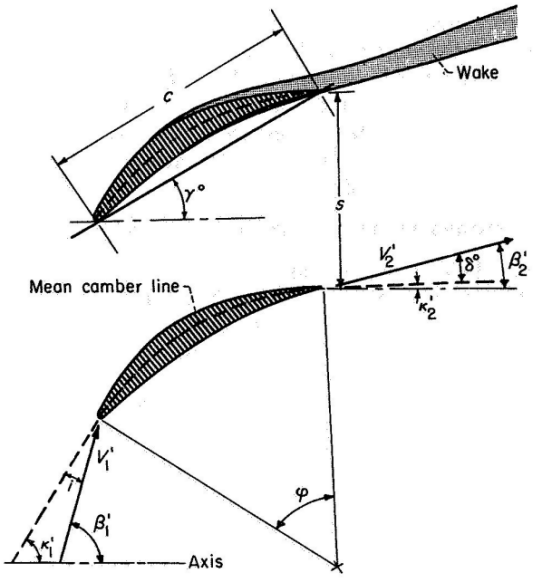

Figure 3: Geometrical configuration and angle definition in a compressor cascade

The three parameters commonly used to characterize the performance of compressor cascades are the incidence, the deviation and the pressure losses. The angles are defined in Fig. 3 while the losses are given by Eq. 1.

$$\bar{\omega} = \frac{p_{02} - p_{01}}{p_{01} - p_{s1}} \tag{1}$$

The minimum loss incidence is considered as the reference incidence and is illustrated in Fig. 4. For NACA65 and DCA blades, cascade performance has been studied at low Mach number ($M < 0.3$) and for various solidities as well as different thicknesses, camber angles and inlet flow angles[2].

Knowing the type of blade (NACA65 or DCA), the turning to be achieved, the maximum thickness and the solidity, the designer is able to calculate the minimum loss incidence and deviation. For an arbitrary blade and design requirement (for example, a DCA blade and design angle of $\beta_1 = 50°$) and applying NASA's correlation, Fig. 5 and Fig. 6 show that varying the camber or the maximum thickness to chord ratio, deviation always decreases with solidity.

This highlights the guidance role of the solidity in cascade: the higher the solidity, the better the flow

[2] All the results are available in the NASA design book [3] but are not copied here for the sake of clarity.

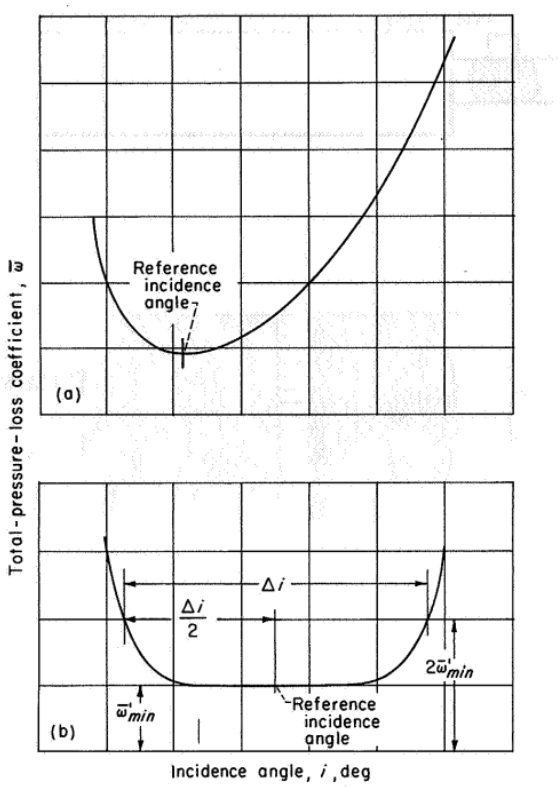

Figure 4: Definition of the reference incidence angle:(a) minimum loss angle clearly defined; (b) minimum loss angle taken as the mean of the incidence angle range defined by the angles where the losses reach twice its minimum value.

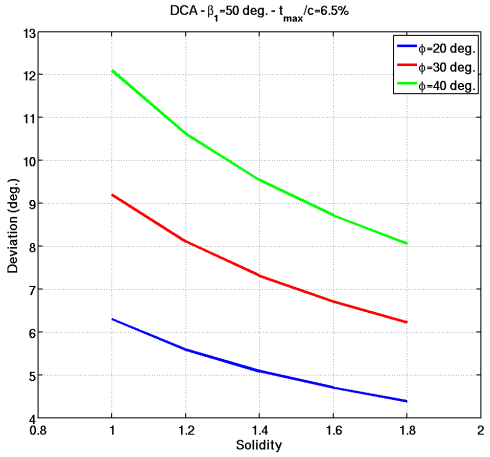

Figure 5: Deviation at minimum loss incidence following NASA SP36 correlations for a DCA blade: $\beta_1 = 50°$ constant maximum thickness to chord ratio of 6.5% and varying camber angle.

follows the blade and the lower is the deviation. This had already been pointed out by Carter ([4], 1949).

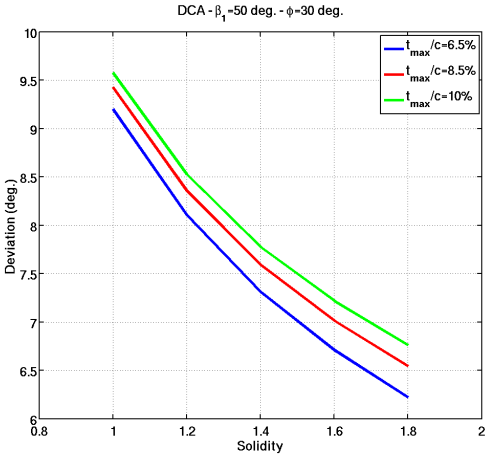

Figure 6: Deviation at minimum loss incidence following NASA SP36 correlations for a DCA blade: $\beta_1 = 50°$ constant camber angle of 30° and varying maximum thickness to chord ratio.

Indeed, the famous Carter's rule, given by Eq. 2, relates the deviation to the camber and the solidity, and allows to establish the same conclusion.

$$\delta = m\phi\sqrt{\frac{1}{\sigma}} \tag{2}$$

The empirical coefficient m of Eq. 2 has been tabulated by Carter [4]. In practise, Carter's rule is still used but, nowadays, NASA's correlation are considered as more reliable, more accurate and more systematic.

The solidity also plays an important role in the blade loading. The loading assessment is essential to characterize in which conditions the blade is operating and how far it is from stall.

The first attempt in characterizing the loading comes from Zweifel in 1945 [5]. He compared the lift of the blade to a reference lift based on the outlet velocity. After arrangement, the Zweifel coefficient Ψ_a is given below:

$$\Psi_a = \frac{\Delta V_\theta (V_1 + V_2)}{\sigma V_2^2} \tag{3}$$

To establish this coefficient, Zweifel relied on different cascade tests from turbines and compressors. Surprisingly, this coefficient has the remarkable property that for many different blades the minimum drag-lift ratio is independent on the inlet and outlet

air angles β_1 and β_2 and always lies between $\Psi_a = 0.9$ and $\Psi_a = 1$. This is illustrated in Fig. 7.

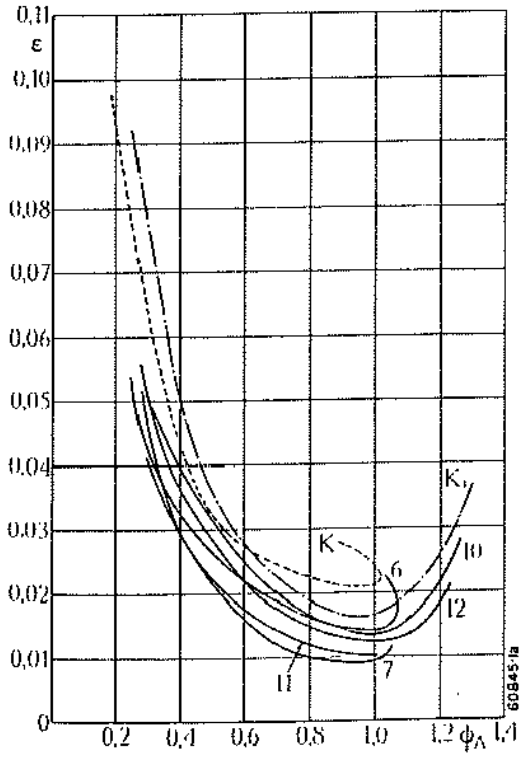

Figure 7: Drag-lift ratio in function the Zweifel loading factor Ψ_a for different type of blading [5] (O. Zweifel, 1945).

This makes it possible to define an optimum pitch distance to operate at maximum lift-drag ratio for given β_1 and β_2. Hence, given upstream and downstream flow angles and velocities, the optimum pitch distance required for maximum lift-drag ratio (i.e. $\Psi_a = 0.9$) can be determined. The data used by Zweifel mainly come from turbine cascade tests but his method can be trusted to select an optimum pitch -at least as a first guess- in compressor blade design. Eck ([6], 1973), Wallis ([7], 1983) or Dixon ([8], 1998) refer to Zweifel's optimum pitch distance when designing optimum fan blades. This parameter is also mentioned by T. Obrecht in [1] to address the loading of compressor blades.

Regarding the assessment of the loading and the stability limit of cascades, the greatest advancement comes from Lieblein and his diffusion factor in 1953 [9]. It was admitted that the suction side boundary layer, facing an adverse pressure gradient, was responsible for the limiting pressure rise and turning of the flow. Therefore, Lieblein linked the suction side deceleration of the flow to a local diffusion factor:

$$D_{loc} = \frac{V_{max} - V_2}{V_2} \tag{4}$$

where V_{max} is the peak suction side velocity and V_2 the outlet velocity. Under the form of Eq. 4, the calculation of the diffusion factor was very time-consuming and not practical. A simplified diffusion factor was then defined to assess the loading of the blades:

$$D = (1 - \frac{V_2}{V_1}) + \frac{\Delta V_\theta}{2V_1\sigma} \tag{5}$$

This simplification brings up the outlet-inlet velocity ratio, the tangential velocity difference as well as the solidity. Then, Lieblein put the wake momentum thickness in relation with the diffusion factor for many various types of blading as illustrated in Fig. 8 from [3]. The wake momentum thickness starts

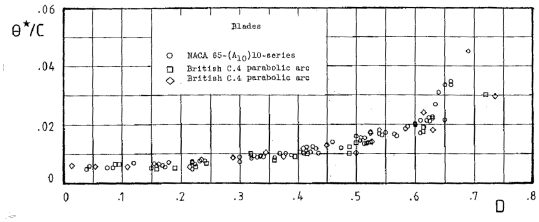

Figure 8: Variation of the wake momentum thickness with diffusion factor [3] (W. H. Robbins, R. J. Jackson, S. Lieblein, 1965).

to rise more steeply for diffusion factors above 0.6. Therefore, a diffusion factor of 0.6 has been selected as the inception of blade stall.

However, because the measurement of the blade momentum thickness is not always realizable, Lieblein proposed to use loss parameters which would mainly rely on the total pressure losses and flow angles and which would closely approach the wake momentum thickness. Those are given by:

$$\frac{\theta}{c} \approx \frac{\omega \cos(\beta_2)}{2\sigma} \tag{6}$$

$$\frac{\theta}{c} \approx \frac{\omega \cos(\beta_2)}{2\sigma} \left(\frac{\cos(\beta_2)}{\cos(\beta_1)}\right)^2 \tag{7}$$

All Lieblein's results are gathered on Fig. 9 using the loss parameters of Eq. 6 and Eq. 7. Plotted in function of the diffusion factor, the two curves of Fig. 9 offer good approximations of Fig. 8.

The loss parameter of Eq. 6 is the most common one (because it is easier to measure) and the most widely quoted in the literature. It remains more or less constant and close to 0.007 until a diffusion level of 0.6 is reached. However, the second loss parameter of Eq. 7 looks to be a better indicator of stall.

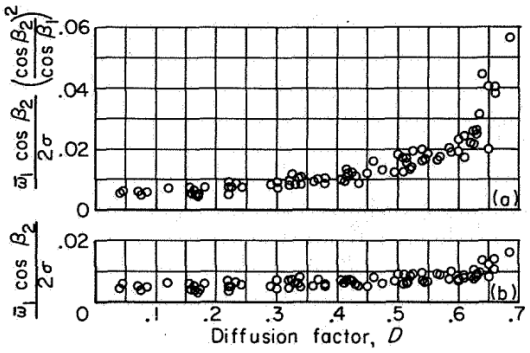

Figure 9: Variation of downstream losses in function of the diffusion factor [3] (W. H. Robbins, R. J. Jackson, S. Lieblein, 1965).

The work of Lieblein allows to shed light on the role played by the solidity in the appraisal of the loading and the losses. An increase of solidity allows to reduce the diffusion factor but gives more total pressure losses. It also helps to lower the diffusion ratio and, then, to delay the stall emergence. When the solidity decreases, the losses follow. However, if the diffusion ratio approaches its limit, high diffusion losses appear and the flow may separate completely. The designer is thus confronted to a trade-off between low losses (choosing low solidity) and high stability (choosing high solidity).

Later, Lieblein provided new correlations of momentum thickness (and loss parameter) in terms of an equivalent diffusion ratio [10]. This equivalent diffusion ratio expresses the ratio of the maximum suction side velocity to the inlet velocity. This approach encountered a great support and has been used and adapted by many as Koch and Smith ([11], 1976) or Wright and Miller ([12], 1991). It is widely accepted that Koch's data are the most complete and accurate. However, in the prospect of this paper, Lieblein's data are more convenient to understand the role played by the solidity in the loading assessment and the loss development.

The influence of the Mach number must also be mentioned. Heilmann et al. ([13], 1968) showed that the effect of solidity is not independent of Mach number. It seems that going to slightly supersonic Mach numbers, it is better to keep the solidity as high as possible to avoid important shock losses.

2.2. The optimum solidity

It has been shown in the previous section that higher solidities go with higher losses while lower solidities induce higher diffusion and then higher losses. Somewhere in between those two extreme situations sits an optimum solidity. As presented on Fig. 7, research from Zweifel already exposed an optimum loading sitting between $\Psi_a = 0.9$ and $\Psi_a = 1.0$. For given inlet and outlet velocity triangles, this suggests that an optimum solidity can be selected using Eq. 8.

$$\sigma_{\text{opt}} = \frac{\Delta V_\theta (V_1 + V_2)}{\Psi_{a_{\text{opt}}} V_2^2} \tag{8}$$

where $\Psi_{a_{\text{opt}}}$ must be chosen between $\Psi_a = 0.9$ and $\Psi_a = 1.0$. The same manipulation could be done with Lieblein's diffusion factor but no criterion which defines an optimum diffusion factor exist.

Another method had already been offered by Howell in the 1940's ([14]). He observed that the nominal tangential deflection was only depending on the solidity and he found out that the best solidity could be calculated using Eq. 9.

$$\tan(\beta_1) - \tan(\beta_2) = \frac{1.55}{1 + \dfrac{1.5}{\sigma}} \tag{9}$$

Even though Howell's work is considered as a reference and was used for a long time, nowadays, it is considered not to be reliable anymore.

More recently, in 1988, A. B. McKenzie published an quite appealing method to get the optimum solidity ([15]). According to his results the solidity which leads to the best efficiency is linked to an ideal static pressure rise given by:

$$C_{p_i} = \frac{p_{s_2} - p_{s_1}}{1/2\, \rho_1 w_1^2} = 1 - \frac{\rho_2}{\rho_1} \left(\frac{w_2}{w_1} \right)^2 \tag{10}$$

As plotted in Fig. 10, the optimum pitch-chord ratio (in terms of maximum efficiency) appears to be a linear function of the ideal static pressure rise Eq. 11.

$$s/c = 9(0.567 - C_{p_i}) \tag{11}$$

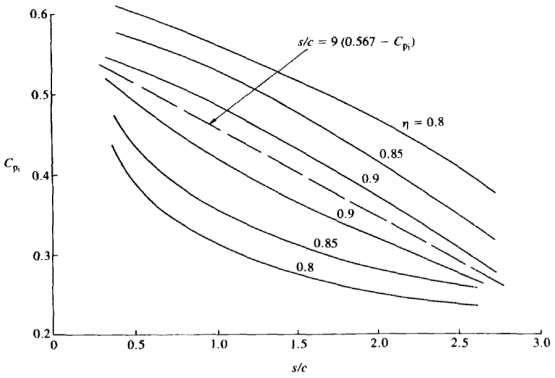

Figure 10: Efficiency contours in function of pitch-chord ratio s/c and ideal static pressure rise C_{p_i} [15] (A. B. McKenzie, 1988).

Considering the case of the DREAM project booster and its rotor inlet and outlet conditions available in Table 1, the different methods have been compared to each other and to the actual solidity of the booster. The results are presented in Table 2. Only Zweifel's method gives realistic solidities.

	Span location	β_1	β_2	w_1	w_2
Velocity	Hub	49°	18°	263 m/s	207 m/s
Triangle	Mid	48°	28°	255 m/s	197 m/s
Data	Tip	49°	38°	252 m/s	192 m/s

Table 1: Rotor inlet and outlet velocity triangles of the DREAM project booster

Optimum solidities					
	Span location	Howell	Zweifel $\Psi_a = 0.9$	McKenzie	State-of-the-art
σ	Hub	1.76	1.63	0.54	1.52
	Mid	0.90	1.25	0.61	1.28
	Tip	0.49	0.98	0.59	1.26

Table 2: Solidity recommendations from Howell's, Zweifel's, and McKenzie's methods

The issue of the optimum solidity can also be approached by considering the loss correlation: for given inlet and outlet velocity triangles there exists only one solidity that produces the minimum amount of losses. Indeed, knowing the upstream and downstream velocity triangles the diffusion factor is only a function of the solidity. Hence, whatever loss parameter is used, the total pressure losses also become a function of one single variable being the solidity. Finally, the solidity which gives the minimum loss is the solution of the minimization problem summarized below:

$$\left.\begin{matrix}\beta_1\\ \beta_2\\ V_1\\ V_2\end{matrix}\right\} \rightarrow D = g(\sigma) \rightarrow \omega = f(\sigma)$$

Then,

$$\sigma_{opt} =: \left\{\sigma \text{ such as } \frac{d\omega}{d\sigma} = 0\right\}$$

The method has been applied using Lieblein's correlations of Fig. 9(b). Hearsey ([16], 1986) gives a reliable polynomial fit of this correlation given by Eq. 12.

$$\frac{\omega\cos(\beta_2)}{2\sigma} = 0.004 + 0.004722\,D + 0.095679\,D^3 \quad (12)$$

Using the mid-span velocity triangle data of Table 1, Fig. 11 presents the losses as a function of the solidity. Lines of constant diffusion factor are also available in Fig. 11. The minimum loss solidity sits around 0.8. This corresponds to a diffusion factor higher than 0.45. This method could be applied with more accurate loss correlation as Koch and Smith provided in [11]. However, as no constraint is set on the loading it will always result in very low solidities which have high diffusion and offer very poor stability margins.

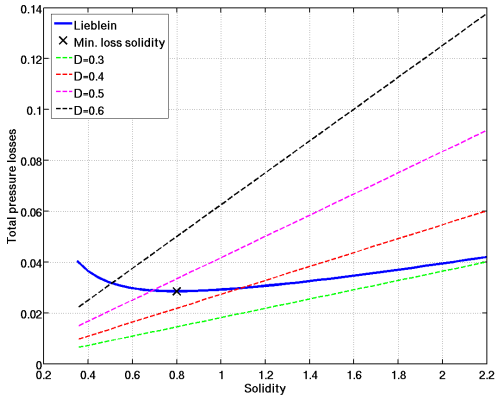

Figure 11: Evolution of losses in function of solidity using correlation of Fig. 9(b) and mid-span data of Table 1.

3. Numerical investigation

Two investigations have been performed. The first one studies the effect of rotor blade number while the second looks at the influence of stator blade number. Both are based on the DREAM project booster. This LP compressor is a 1.5 stage composed of inlet guide vanes, a rotor and a stator. The compressor has been studied at VKI both numerically with the commercial software FINE/Turbo of NUMECA International and experimentally in the high-speed R4 facility[3]. A 3D view of the 1.5 stage is available in Fig. 12.

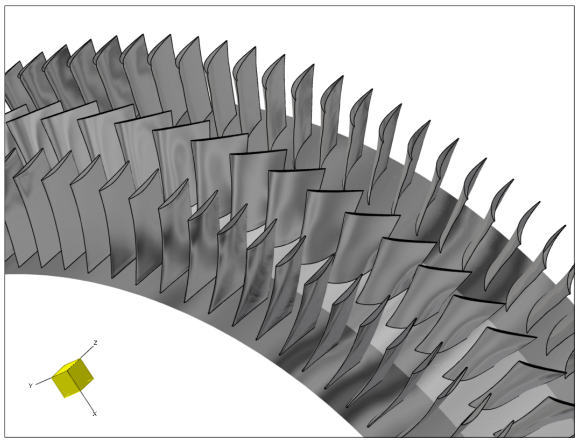

Figure 12: Three-dimensional view of the 1.5 stage (inlet guide vanes, rotor, stator).

3.1. Set-up

The whole 1.5 stage is considered but the rotor and stator blade numbers are varied independently. For each different blade number a new mesh has been created. The mesh of baseline and its properties are extensively described in [17]. In order to optimize the post-processing the number of points and configuration of the meshes remain constant and only the blade periodicity is varied from one case to another.

The boundary conditions are part of the specifications of TechSpace Aero as well as the turbulence model that is the low Re Yang Shih k-ϵ model. The compressors have been throttled by increasing the static pressure at stator outlet and always ensuring the radial equilibrium. Approaching the stall region the back-pressure has been raised iteratively to find the last stable conditions. This point has been considered as the stall point.

The booster has been designed in a way that the stall starts from the rotor hub (between 20% and 40% of the blade height from the hub). This may unfortunately compromise the stability analysis of the compressor.

3.2. Influence of rotor blade number

The performance of three different rotors have been assessed from choke to stall. The corresponding blade numbers are indicated in the Table 3. The rotor

Tested rotor solidities				
	Blade number	σ_{hub}	σ_{tip}	Relative to design (%)
Design	66	1.32	1.09	-15%
	76	1.52	1.26	-
	86	1.72	1.43	+15%

Table 3: Tested rotor blade numbers and solidities

pressure ratio and efficiency are plotted in Fig. 13 and Fig. 14. Looking at Fig. 13, it appears that the high

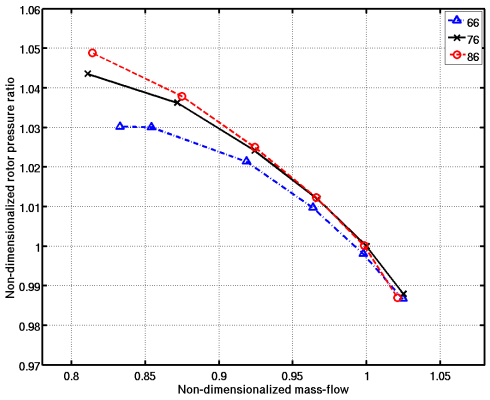

Figure 13: Rotor pressure ratio versus mass-flow for 66, 76 and 86 rotor blades on DREAM compressor.

solidity rotor achieves the highest pressure ratio. This is in agreement with cascade theory or Carter's rule (Eq. 2) which predicts that the deviation is reduced when the solidity increased. As the deviation is lower, the flow turning increases and more pressure rise is achieved. However, the situation is not so obvious at choke.

[3]The experimental results have not been published yet while the whole numerical investigation can be found in [17].

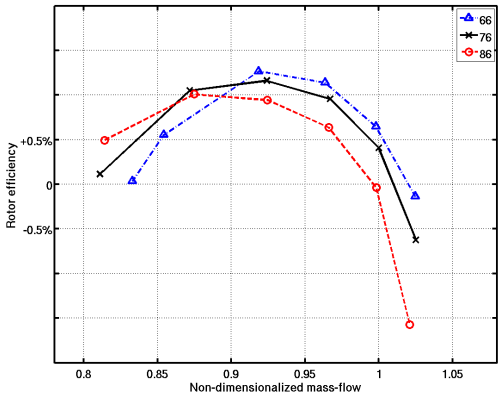

Figure 14: Rotor efficiency versus mass-flow for 66, 76 and 86 rotor blades on DREAM compressor.

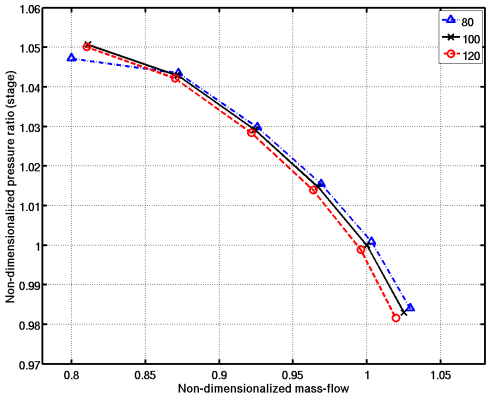

Figure 15: Stage pressure ratio versus mass-flow for 80, 100 and 120 stator blades on DREAM compressor.

The effect on the maximum efficiency is clear and the lowest solidity shows the best efficiency. This is rather expected as cascade correlations predict less losses for low solidity. Nonetheless, the trend does not remain the same on the whole operating range. The low solidity rotor is the less stable. This is most probably coming from a very high diffusion on the blades. No improvement appears between the mid and the high solidity rotors which is quite unexpected and requires a deeper analysis.

3.3. Influence of stator blade number

The influence of stator solidity has also been studied by changing the number of vanes. The tested stator solidities are available in the Table 4. In terms

Tested stator solidities				
	Blade number	σ_{hub}	σ_{tip}	Relative to design (%)
Design	80	1.47	1.46	-20%
	100	1.83	1.82	-
	120	2.20	2.19	+20%

Table 4: Tested stator blade numbers and solidities

of efficiency and pressure ratio, the effect of stator solidity is more straighforward than for the rotor. Removing blades improve both pressure ratio (Fig. 15) and efficiency (Fig. 16). When there is no work addition, a blade row only represents a source of friction losses that decrease the total pressure. Then, the same temperature rise is achieved whatever the number of blades while less pressure losses are encountered when less stator vanes are present. It results in

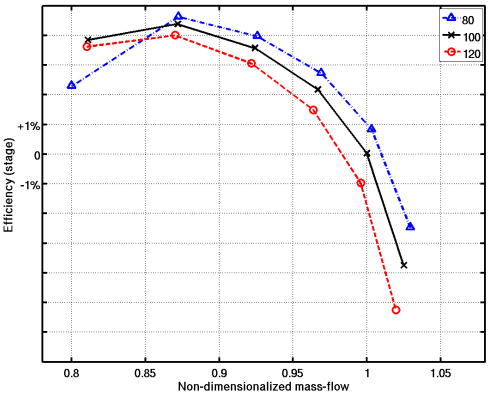

Figure 16: Stage efficiency versus mass-flow for for 80, 100 and 120 stator blades on DREAM compressor.

a higher pressure ratio and a higher efficiency. The opposite happens when adding some blades. These conclusions are in agreement with cascade correlations. Between the stages with 100 and 120 stator blades no difference appears in terms of stability. The low solidity stator stalls before the others. Although reducing the stator blade number might have transposed the stall inception in the stator, a complete three-dimensional analysis of the flow is required to understand the stall behaviour of the stage.

4. Conclusion

The solidity effect has been reviewed in the literature and some existing optimum solidity criteria have been presented. A numerical investigation

has been performed in order to see some effect on the booster designed and manufactured by Techspace Aero within the framework of the European DREAM project. Both rotor and stator blade numbers have been varied independently to analyze their impact on the compressor performance. It appeared that:

- the higher the solidity, the lower the deviation and the better the guidance;
- the higher the solidity, the higher the losses (and the lower the efficiency).

For a rotor, the better guidance results in a higher turning and consequently, to a higher pressure ratio. A stator only sees a higher solidity as a source of higher losses. This is reflected in both lower efficiency and pressure ratio.

To be complete, this study must be extended to different types of blades and different compressors. A blade generator has already been implemented at VKI in order to generate through CFD a more extensive database than the one of the 1960's NASA correlations. This blade generator is able to create NACA65 (A10-series), DCA, MCA or wedge profiles. They all have their own range of application and definitely have different behaviours regarding solidity variations. For each type of blade, incidence, turning, inlet Mach number and solidity must be varied. A cascade configuration will be set up and solved in FINE/Turbo. Some examples of the blade generator capabilities are plotted in Fig. 17.

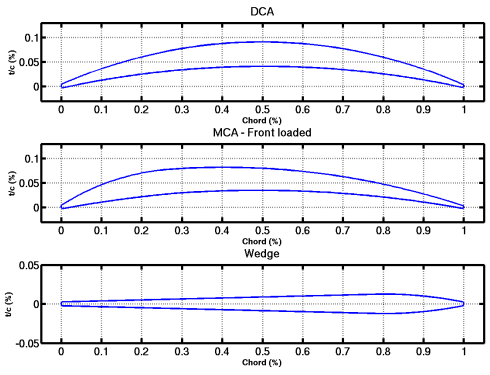

Figure 17: Profiles generated with the VKI blade generator.

Other three-dimensional test cases may be investigated. Until now, only Techspace Aero's booster has been considered. A fan stage which presents slightly supersonic tip regions could highlight the influence of Mach number on the effect of solidity. This could support previous work from Heilmann et al. [13].

The final validation of this study will be cascade tests in the C3 high-speed facility of VKI. This experimental part would focus on the validation of the CFD database.

Acknowledgments

This research is supported by TechSpace Aero.

References

[1] T. Obrecht, HP compressor preliminary design, in: Advances in axial compressor aerodynamics, von Karman Institute for Fluid Dynamics Lecture Series, Belgium, 2006.
[2] A. J. Wennerstrom, Low aspect ratio axial flow compressors: why and what it means, Journal of Turbomachinery 111 (4) (1989) 357–365.
[3] W. H. Robbins, R. J. Jackson, S. Lieblein, Aerodynamic design of axial-flow compressors, NASA SP-36 (1965).
[4] A. D. S. Carter, The low-speed performance of related aerofoils in cascades, A.R.C. Tech. Report, NGTE (September 1949).
[5] O. Zweifel, The spacing of turbo-machine blading, especially with large angular deflection, The Brown Boveri Review.
[6] B. Eck, Fans, Pergamon Press, 1973.
[7] R. Wallis, Axial flow fans and ducts, John Wiley & Sons, Inc., 1983.
[8] S. Dixon, Fluid mechanics, thermodynamics of turbomachinery, 4th Edition, Butterworth-Heinemann, 1998.
[9] S. Lieblein, Diffusion factor for estimating losses and limiting blade loadings in axial-flow compressor blade elements, Tech. rep., NACA, Lewis Flight Propulsion Laboratory, Cleveland, Ohio (June 1953).
[10] S. Lieblein, Loss and stall analysis of compressor cascades, Journal of Basic Engineering 81 (4) (1959) 387–400.
[11] C. C. Koch, L. H. J. Smith, Loss sources and magnitudes of axial flow compressors, Journal for Engineering for Power.
[12] P. I. Wright, D. C. Miller, An improved compressor performance prediction model, in: Proceedings of Institution of Mechanical Engineering, 1991.
[13] W. Heilmann, H. Starken, H. Meyer, Cascade wind tunnel tests on blades designed for transonic and supersonic compressors, Tech. rep., Institut fuer Luftstrahlantriebe, AGARD-CP-34 (1968).
[14] A. R. Howell, Fluid dynamics of axial compressors, in: Proceedings of Institution of Mechanical Engineering, Vol. 153, 1945.
[15] A. B. McKenzie, Fluid dynamics of axial compressors, in: Proceedings of Institution of Mechanical Engineering, Vol. 202, 1988.
[16] R. M. Hearsey, Practical compressor aerodynamic design, in: Adanced topics in turbomachinery technology, 1986.
[17] J. Sans, Numerical investigation of a single stage axial compressor, PR 2010-10, von Karman Institute for Fluid Dynamics (2010).

Accelerated Optimization for Multi-Disciplinary Design of Transonic and Contra-Rotating Turbomachinery Components

Michael Joly

Turbomachinery and Propulsion Department, von Karman Institute for Fluid Dynamics, Belgium, joly@vki.ac.be

Supervisor: Tom Verstraete

Assistant Professor, Turbomachinery and Propulsion Department, von Karman Institute for Fluid Dynamics, Belgium, verstraete@vki.ac.be

Supervisor: Guillermo Paniagua

Associate Professor, Turbomachinery and Propulsion Department, von Karman Institute for Fluid Dynamics, Belgium, panigua@vki.ac.be

University Supervisor: Paul Cizmas

Professor, Aerospace Engineering Department, Texas A&M University, cizmas@tamu.edu

Abstract

Optimization techniques offer promising perspectives for the design of complex turbomachinery components. To limit the weight of current and future aero-engine configurations, the number of stages tends to be reduced and more power output is expected from each blade row. The design of highly-loaded components is subsequently multi-disciplinary, with concurrent objectives in terms of aerodynamic efficiency and structural integrity. To speed up the process of an aero-mechanical optimization, the implementation of Computational Fluid Dynamics (CFD) solvers on Graphics Processing Units (GPU) is investigated in a first part. Turbines operating in the transonic regime experience shock waves. To limit the mechanical stress induced by the vane-rotor shock interaction, it is proposed in a second part to optimize the vane geometry to attenuate its downstream distortion. The impact on the stage will be evaluated by computing the unsteady forcing on the following rotor. In a third part, the design of contra-rotating fans is investigated in order to produce compact and highly-loaded configurations. The proposed methodology enables one to achieve a complete design, from the flow path definition to the aero-mechanical characterization of the fan.

Keywords: Multidisciplinary Optimization, GPU Accelerated CFD, Transonic Turbine, Contra-Rotating Fan

1. Introduction

The design of innovative turbomachinery components for compact high-speed propulsion flight vehicle or for limited fuel burns of current aircrafts requires to reduce the number of stages to save weight. A reduction of the size of the machine leads to an increase of the load on each single components. The related design challenges are inherently multidisciplinary. Trade-offs between aerodynamic efficiency and structural integrity have to be found and optimization strategies provide promising perspectives.

Compared to traditional design strategies, optimization techniques, such as Evolutionary Algorithms, are able to augment the explored design space and to consider simultaneously several conflicting objectives. To speed up the most expensive Computational Fluid Dynamics (CFD) evaluation of an aero-mechanical design problem, parallel computations could be performed, typically using several Central Processing Units (CPU). Alternatively, much work has recently been focused on Graphics Processing Units (GPU) and applications of GPU in aerospace highlighted the potential acceleration of computing time from 10 to 20 times faster [1, 2]. The present project proposes in a first part to investigate GPU-accelerated CFD.

Optimization techniques are then applied to inves-

tigate innovative design methodologies for turbomachinery configurations involving demanding fluid and solid requirements. In particular, high-pressure turbines operate in the transonic regime leading to strong shock interactions between the vane and the rotor blades. To limit the risk of high-cycle fatigue on the rotor, the vane could be designed for limited downstream distortion. A design approach with steady-state evaluations to reduce the shock waves propagation downstream of the vane is proposed. The impact on the stage will be evaluated by computing the unsteady forcing on the following rotor.

The design of transonic fans reveals also strong compromises between aerodynamic and structural considerations. While conventional fans produce a pressure ratio of about 1.6, many research trends focus on much higher loads. A design methodology to achieve highly-loaded fan is investigated in this project. As an alternative to traditional 1-D parametric studies, an optimization of the flow path is performed to initiate the aerodynamic design of the fan. To by-pass any two-dimensional sub-optimal results, a three-dimensional optimization is directly processed, including several section profiles along the span, as well as lean and sweep. High-fidelity CFD and Finite Element structural analysis are employed to guaranty the aerodynamic efficiency and the structural integrity of the finalized design. This methodology will be extended to the design of contra-rotating fans.

2. Implementation of GPU Accelerated CFD for Optimization of Turbomachinery Components

The present project targets the development of a CFD solver with GPU capacities, aiming at the integration of fast and robust Navier-Stokes evaluations into aero-mechanical design-optimization strategies.

2.1. Implementation of a Multi-Block CFD solver

In preparation prior to implementation on GPU, a multi-block viscous solver is implemented on conventional CPU. Both H and O4H mesh topologies are considered (See O4H topology in Figure 1). The class orientation of the C++ language is extensively used to make the code as generic as possible, making an adaptation to other topology very practical. The structured mesh is initialized by an algebraic grid and then smoothed with an elliptic method.

In the present status, an Euler solver has been implemented. The convective fluxes are computed with the Roe flux-difference splitting scheme. A

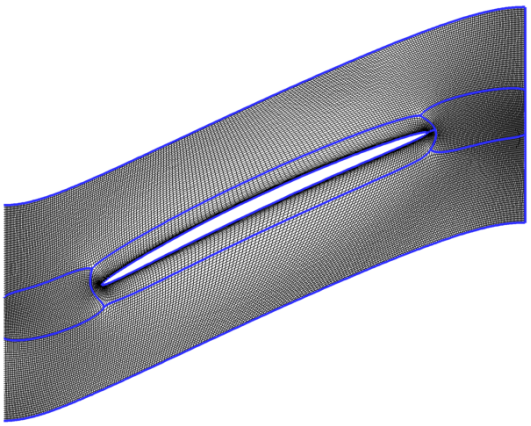

Figure 1: O4H MESH TOPOLOGY

Runge-Kutta time-stepping scheme is employed to obtain a steady-state solution. Boundary conditions of solid wall, inlet and outlet complement the solver. The solver is applied to the geometry of a channel with a bump (bump height = 10% of channel height). Using atmospheric conditions (Pa=101300Pa and Ta=288K), values of total pressure and temperature are fixed at the inlet considering an inlet Mach number. The inlet flow is imposed to be in the axial direction. The back pressure is imposed to be equal to the atmospheric pressure. For the transonic with an inlet Mach number of 0.9, the solution has a shock and is therefore strongly dependent on the grid size. With more refinement, the location of the shock system appears more precisely (See Figure 4). In the present case, the interaction between the shock system and the outlet subsonic boundary leads to some instabilities observed in the convergence history.

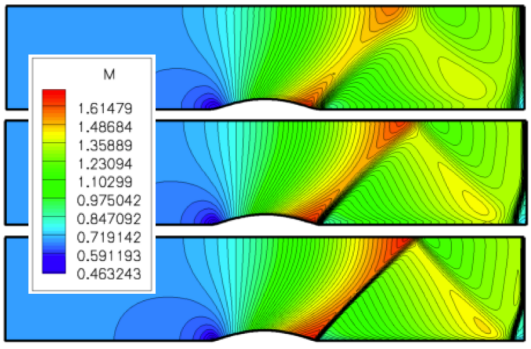

Figure 2: MACH NUMBER FIELD IN A CHANNEL FOR THREE DIFFERENT GRID REFINEMENTS (UP : $130 * 30$, $MIDDLE$: $250 * 60$, $BOTTOM$: $400 * 120$)

2.2. Implementation of CFD solver on GPU

After completion of the multi-block solver, this one would be implemented on Graphics Processing Units (GPUs). A GPU is a processor that exhibits higher level of parallelism than conventional CPUs (higher rate of floating-point operations per second) and has the strong potential to accelerate scientific computing. Extensive parallelism within GPU accelerated CFD requires however significant changes to the implementation of the underlying code. NVIDIA provides in this concern an extension to the C programming language called CUDA [3], in which the developer can set up a large number of threads that are grouped into thread blocks. Each block is then associated with one of the multi-processors of the GPU, where the threads could be scheduled and synchronized to handle memory concerns.

3. Attenuation of Vane-Rotor Shock Interaction in a High-Loaded Transonic Turbine Stage

Turbines operating in the transonic regime experience shock waves. Giles [4] highlighted strong shock interactions between the vane and the rotor. Sieverding et al. [5] described the aerodynamics of the trailing-edge shock system within transonic turbine vanes. On the suction side a left running shock travels downstream in a direct manner towards the rotor (hereafter, direct shock on Figure 3). On the pressure side, a right running shock impinges onto the adjacent vane suction side, generating a hereafter called reflected shock that propagates to the following blade row. Hence, the pressure field in the vane/rotor gap is characterized by two strong static pressure gradients in the pitch-wise direction, related to the passage of direct and reflected shock waves.

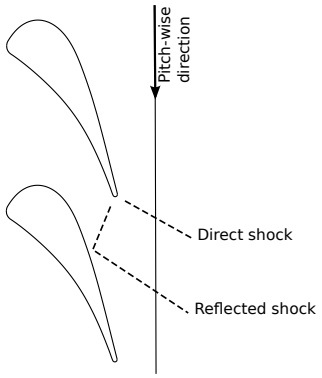

Figure 3: SHOCK SYSTEM DOWNSTREAM OF A TRANSONIC TURBINE VANE

3.1. Objectives

Within the present work, the evolutionary optimization design tool for turbomachinery component, developed at the von Karman Institute [6], is applied to conceive original transonic two-dimensional vanes with limited vane downstream distortion and reduced losses. Aerodynamic performances are evaluated by a steady-flow Navier-Stokes solver.

The distortion downstream of the vane section is assessed by the the standard deviation of the downstream pitch-wise static pressure distribution (eq.1). The region of interest is located 35% of the axial chord, downstream of the stator trailing edge, where the rotor leading edge should be located.

$$\sigma = \sqrt{\int_{y_0}^{y_0+pitch} \frac{(p(1.35 * \lambda, y) - \bar{p})^2}{pitch}.dy} \qquad (1)$$

The second objective is to ensure high efficiency; the kinematic loss coefficient (eq. 2) ought to be minimized [**?**].

$$\xi = 1 - \eta = 1 - \frac{V_2^2}{V_{2is}^2} \qquad (2)$$

3.2. Parametrization and Evaluation

The definition of the parametrization is a crucial step in any optimization problem, since it defines the optimal geometry that can be represented. Each parameter should have a clear impact on the geometry definition, to ease the identification of the optimal set of parameters. Moreover, the design space defined by ranges for each parameter accounts for the available shape variety; if the optimal shape cannot be represented, it will not be found by the optimizer.

Two-dimensional airfoil sections are defined starting from the definition of the camberline by the following set of parameters: axial chord, stagger angle, inlet metal angle and outlet metal angle. The suction and pressure side curve are defined by Bézier curves, for which the control points are specified relative to the camber line. High-pressure turbines are characterized by the passage ducted by two adjacent airfoils and this parametrization enables a detailed control of the throat region (See Figure 4).

The mesh generation is parametrized and can therefore be executed in an automated manner independently of the blade shape. A H-type periodic non-matching mesh is used and particular care is addressed to the meshing of the throat area and the non-matching

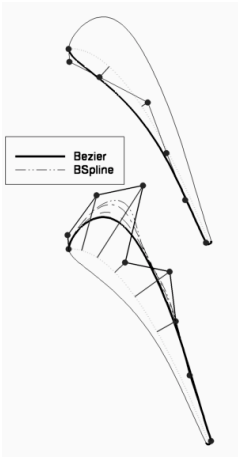

Figure 4: CONTRACTION CHANNEL PARAMETRIZATION

boundaries. The performances of each individual are evaluated with the Navier Stokes sovler TRAF [7]. The Reynolds-Averaged Navier-Stokes equations are solved using a Runge-Kutta time integration and a discretization based on finite volumes with a cell-centered scheme. The two-layer mixing length model of Baldwin and Lomax is used to compute the boundary layer as fully turbulent. The solver shows good agreements with experimental results obtained in the CT3 test facility of the von Karman Institute (See Figure 5).

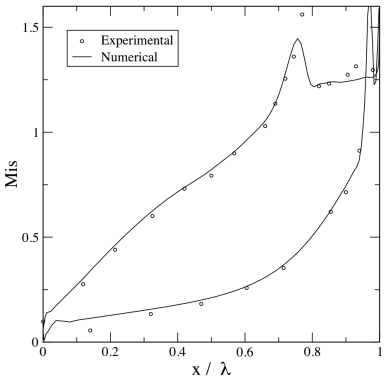

Figure 5: MACH NUMBER DISTRIBUTION ON CT3 VANE

3.3. Optimization

An optimization run with 200 generations of 60 individuals is performed and the evolution of the process is illustrated in Fig. 6. Through the optimization process, the individuals of each population are progressively satisfying the constraints. Hereafter the objective value is minimized. The best candidate obtained with the single-point strategy provides a reduction of 43.2% of the downstream pitchwise static pressure standard deviation. The loss coefficient is 1.4% lower than the baseline, the outlet flow angle 0.02 degree larger and the mass flow increased by 0.3%.

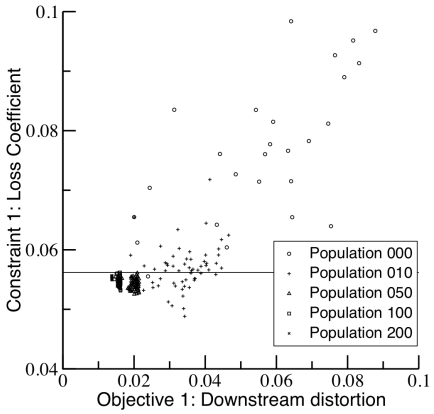

Figure 6: OPTIMIZATION ITERATIONS

On density gradient fields (See Figure 7), the left running shock, i.e. direct shock, clearly appears with lower intensity for the optimized airfoil. By contrast, the right running shock has a stronger intensity than the baseline. Its reflection on the adjacent blade suction side, i.e. reflected shock, appears with higher intensity. A strong impingement on the suction side of the adjacent vane is also observed on the Mach number distribution (See Figure 8, left). With a similar suction side and increased thickness on the pressure side, the contraction channel of the optimized airfoil is narrower than the baseline's. The channels are choked and therefore sonic sections impose the mass flows. For the baseline, the sonic section is located at the end of the convergent channel and coincides with the geometric throat. On the other hand, the channel resulting from the optimized airfoil is convergent-divergent. The sonic section moved upstream and is inclined (See Figure 7). This explains how similar mass flows could be reached with different geometric throats. The convergent-divergent shape of the optimized contraction channel over-accelerates the flow downstream of the sonic line, increasing the Mach number levels on the rear pressure side and mid suction side. With a faster flow within the contraction channel, the trailing edge shock system is modified and the propagation of shock waves downstream is remarkably attenuated (See Figure 8, right).

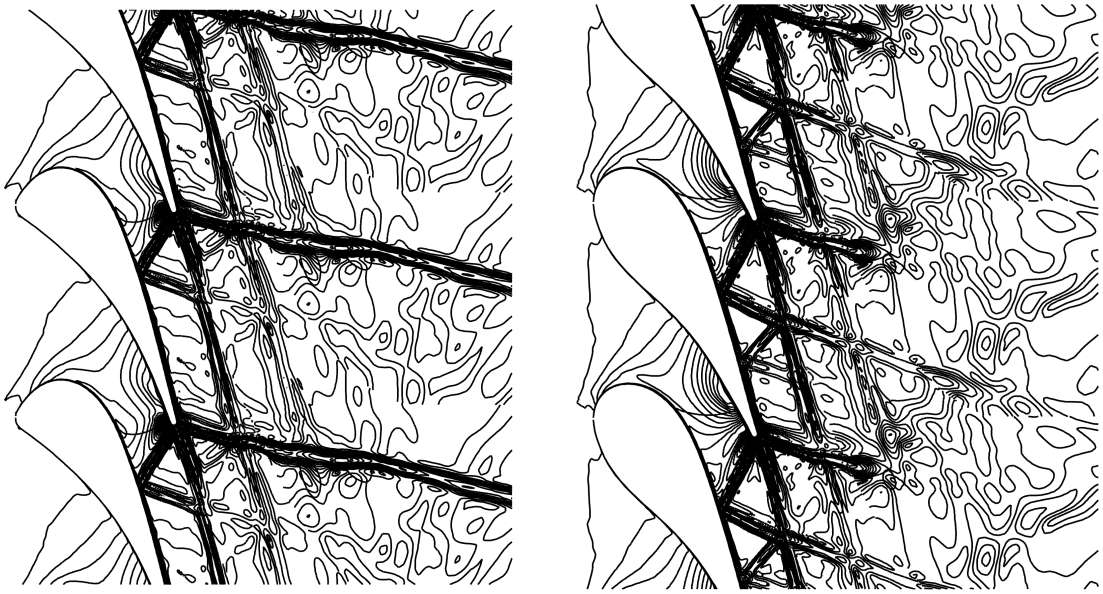

Figure 7: DENSITY GRADIENT FIELDS AND SONIC LINES FOR BASELINE (LEFT) AND OPTIMIZED (RIGHT) GEOMETRIES

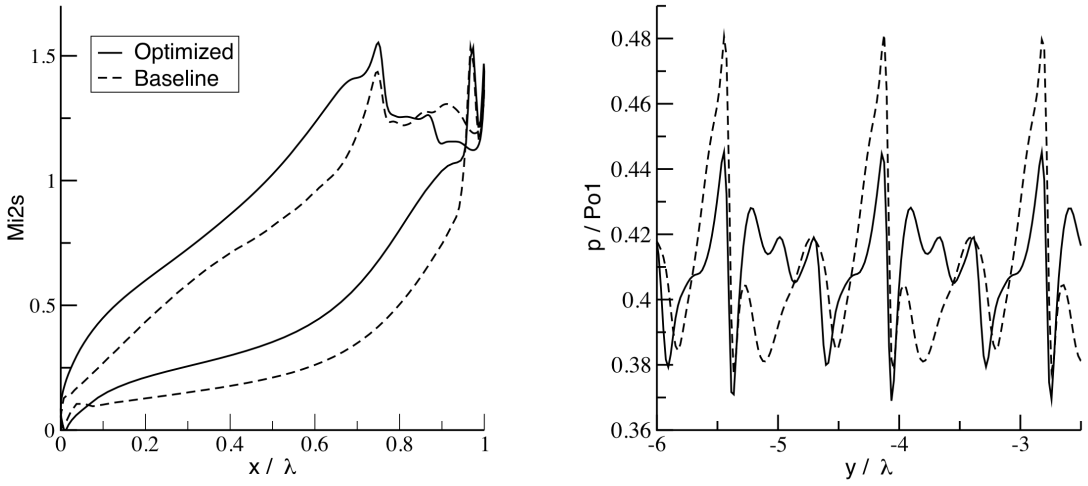

Figure 8: MACH NUMBER ALONG PROFILE AND DOWNSTREAM PITCH-WISE PRESSURE DISTRIBUTIONS

4. Full-Design of Compact Transonic Fan with Optimal Aero-Mechanical Performances

4.1. Design Methodology

The traditional design strategy for transonic fans consists of four successive steps [8]. A preliminary design is achieved with low-fidelity models such as through-flow techniques. Subsequently a blade-to-blade two-dimensional CFD and quasi-three dimensional computations are performed to generate a three-dimensional geometry. Then, a fully three-dimensional viscous optimization is applied to improve the performance considering three-dimensional effects, such as end-bends and secondary losses, introducing sweep and lean to the geometry but without section profiles adaptation. A finite element structural analysis is ultimately performed to assess the geometry.

The main drawback of the traditional fan design strategy is the parametric study employed during the preliminary design phase based on through-flow modeling. Such an approach is not capable of extensively exploring the whole design space. Secondly, the two-dimensional optimization that generates section profiles considers only limited three-dimensional flow patterns, ignoring for example end-walls and secondary flows. The obtained "sub-optimal" profiles then remain constant during the three-dimensional optimization, and the flow angles prescribed by the through-flow model are therefore not optimized during the optimization with the high-fidelity solver. Using this method, through-flow codes, despite being limited in physical modeling, generally fix 80% to 90% of the final fan design.

An improved design methodology is proposed and employs multi-objective optimization at every design steps to achieve the complete aero-mechanical design of a highly loaded axial flow fan. It aims to smooth the intermediate steps between the preliminary design and the three-dimensional aero-structural optimization of the geometry. The through-flow model is first integrated in an optimization loop to enlarge the design space of the preliminary design. It is crucial to consider a wide range of candidates at this early stage of the design, where the end-walls, the blade count, flow angles, and the wheel speed are selected. Through-flow computations, however, do not include any information about blade geometry; only the solidity (i.e. pitch/chord ratio) is considered through correlations. It is then proposed to directly initiate a three-dimensional optimization based on the preliminary design results. Three-dimensional fan rotor geometries are generated from the stacking along the span of chord-wise camber angle and thickness distributions. Possible values of incidence and deviation angles are estimated to define feasible ranges of inlet and outlet metal angles at different radii. The performances of each three-dimensional candidates are assessed simultaneously with fluid and structure evaluations. A viscous flow solver computes the pressure ratio and adiabatic efficiency of the fan, while a finite element solver evaluates its structural integrity.

4.2. Single-Stage Highly Loaded Fan

The methodology is demonstrated for the design a highly loaded axial flow fan. The aim is to produce a compact fan that achieves a similar pressure ratio compared to the NASA rotor 37 (PR=2.1) but with a subsonic inlet relative Mach number at the hub. The expected benefit is an enlarged operating range, allowing the shock system to adapt itself better along the span as the machine is throttled.

A first optimization of the flow path configuration is performed. The through-flow model solves the streamline curvatures and radial gradients at inter-row positions based on the radial equilibrium principle. Losses on the Euler work are introduced based on profile losses and shock losses [9, 10]. The objectives of the through-flow optimization, written in their minimization form, are:

- *1-η*: Maximize the predicted efficiency
- *Tip radius*: Minimize the machine size, considering the end-wall tip radius parameter as a objective
- *for* $M_{1ri} > 1.0$, $max(\beta_{2i}-\beta_{1i})$: Minimize the highest value of relative flow turning over the spans of supercritical profiles, limiting the risk of boundary layer separation at the shock impingement on the adjacent blade suction side

Figure 9 shows Pareto fronts as a result of the through-flow optimization. It can be observed that a higher tip radius allows a higher efficiency and a limited relative flow turning over the span of supercritical profiles. Nonetheless, our interest remains in a reduced radius to achieve maximum compactness. The selected candidate is denoted by a diamond in Figure 9. The configuration obtained is a transonic fan with a subsonic inlet relative Mach number of 0.58 at the hub and a supersonic value of 1.42 at the tip.

The three-dimensional optimization is constrained to produce fan geometries achieving a pressure ratio

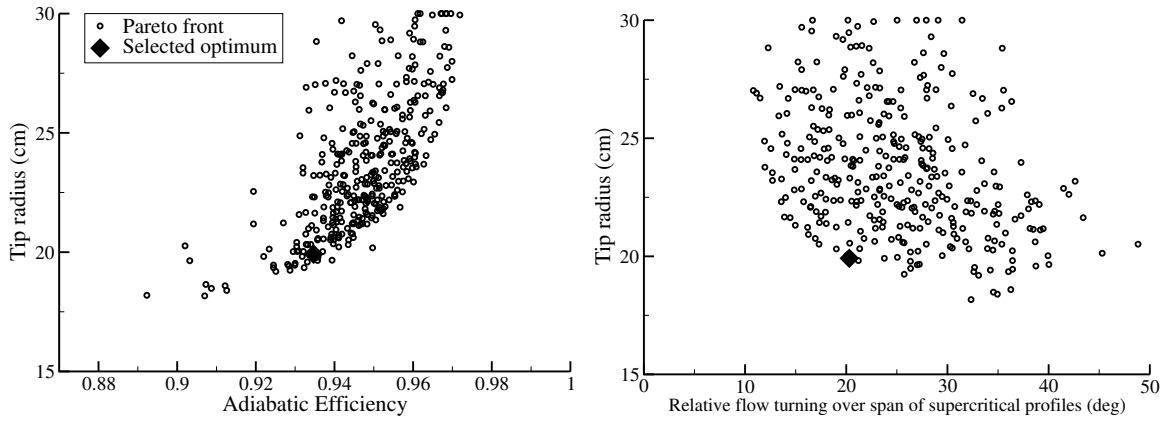

Figure 9: THROUGH-FLOW OPTIMIZATION PARETO FRONT

between 2.1 and 2.2 with a minimum required mass flow rate of 20.2 kg/s at the design point. The objective is to maximize the design-point adiabatic efficiency. The achieved fan geometry provides a pressure ratio of 2.11 with an efficiency of 89% (See Figure 10).

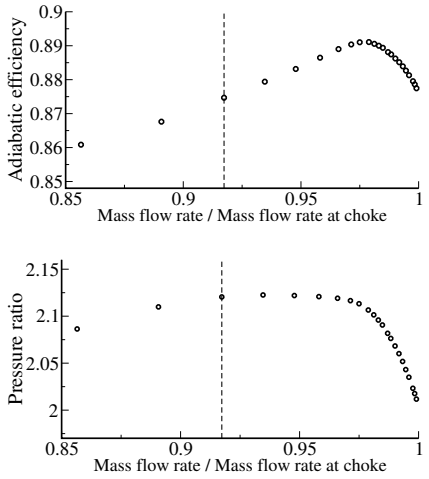

Figure 10: OPTIMAL FAN PERFORMANCES

In transonic fans, a shock system impinges the suction side at higher spans. The high rotational speed of the blade makes the section profiles at high radius reach supersonic speeds. Consequently, a shock originates at the leading edge, with a right-running part hitting the suction side of the adjacent blade and a left-running part propagating upstream (See Figure 11). The flow in the region close to the front suction side is supersonic, and its inclination is therefore influenced by the shape of the suction side surface. The Mach number upstream of the profile and the inlet flow angle are not independent of each other. There is one particular incidence, the unique incidence [11], at which operation is possible.

Considering off-design operations, this shock system at the higher spans changes as the machine is throttled. At the choke point (lower back pressure and higher mass flow rate than design point, see Fig. 12, left), a double shock system occurs in the throat with a weak shock attached to the leading edge followed by a strong passage shock. At the design point (See Fig. 11), the oblique shock and the passage shock merge into a single shock. This is the optimal loss configuration. As the back pressure increases, the shock system moves ahead of the leading edge, eventually leading to stall (See Fig. 12, right).

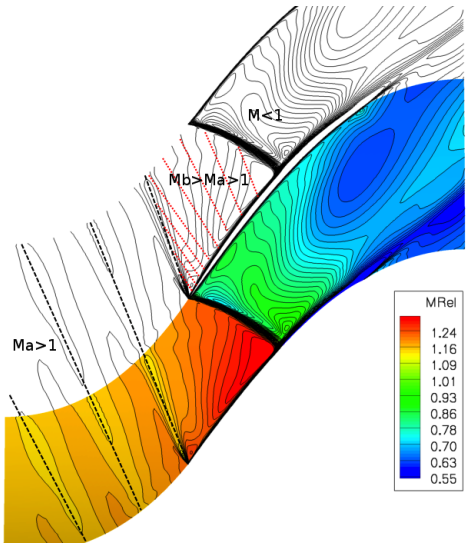

Figure 11: DENSITY FIELD AND MACH NUMBER LEVELS AT DESIGN POINT, 80% SPAN

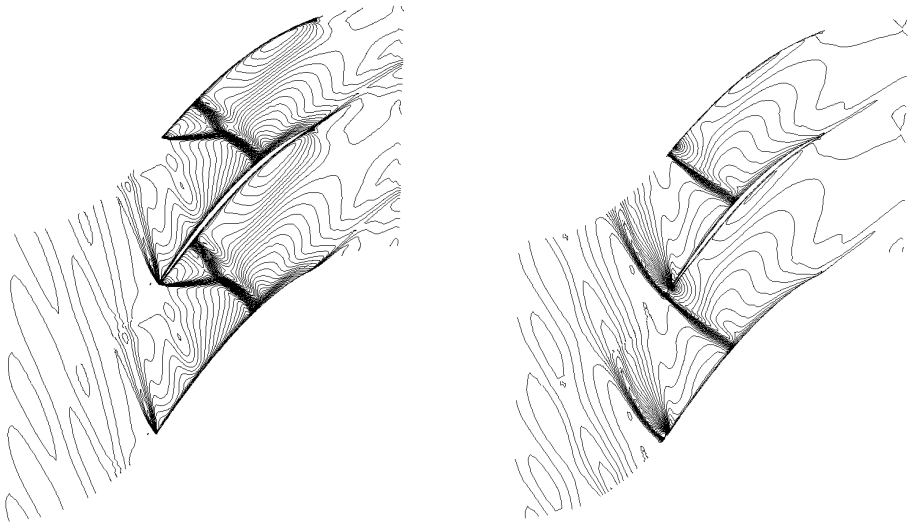

Figure 12: DENSITY FIELD AT CHOKE POINT (LEFT) AND NEAR STALL POINT (RIGHT), 80% SPAN

4.3. Aero-Mechanical Optimization

To guarantee the structural integrity of the fan rotor, a multi-disciplinary optimization is performed with the simultaneous evaluation of aerodynamic and mechanical performances. The blade geometry generated for the fluid evaluation is adapted to integrate a root that would be fastened to the disk, as well as a hub fillet radius. The solid geometry is then discretized using a finite element grid to enable the computation of the stresses.

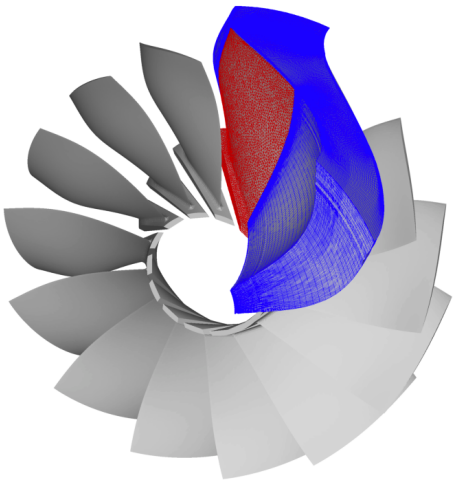

Figure 13: FLUID AND SOLID GRIDS

The solver Calculix [12] is used to compute the von Mises stresses in the blade. The following boundary conditions are applied:

- Centrifugal force
- Fixed translational degrees of freedom on the root faces
- Flow pressure load on both sides of the blade

Flow pressure values from the fluid solution are considered during the structure analysis, which follows the fluid computation for the performance evaluation of each design candidate. At each FEM node on both suction and pressure sides, the flow pressure value is interpolated from the fluid evaluation results with an inverse distance-weighted method. The interpolation is therefore influenced most by the nearby points and less by the more distant points. The FEM elements sharing a face on the blade sides are retrieved, and a pressure value is assigned to the face on the side, computed as the average of the values on its three corners. Figure 14 shows the pressure field on the suction side as a CFD result (left) and after interpolation on the FEM grid (right).

The von Mises stress evaluation reveals that the aero-optimal geometry exceeds the titanium yield strength limit by 109% (maximum stress of 1972 Mpa with a limit of 940Mpa). The stresses are distributed along the whole chord and span of the geometry (See Figure 15,left). Stress peaks are understood to originate from brutal camber change along the span. Figure 16 (left) illustrates a superposition of hub and tip section profiles projected on the circumferential plane. Even though very little contribution of lean and sweep is observed, severe spanwise evolution of the leading-

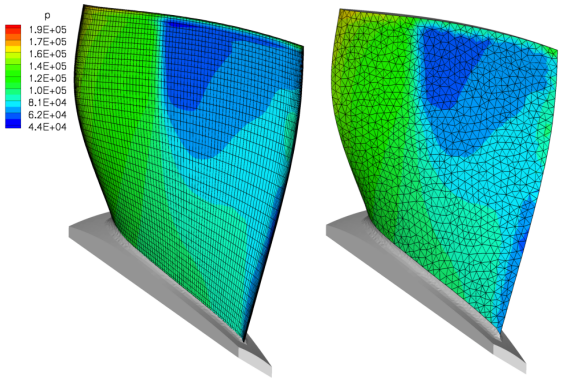

Figure 14: FLOW PRESSURE ON SUCTION SIDE OF CFD (LEFT) AND FEM (RIGHT) GRIDS

and trailing-edge position are shown with the curve linking the two profiles. The aero-mechanical optimal design exhibits a maximum stress of 639 Mpa, which represents a 65% reduction compared to the aerodynamic optimal design with only 1% loss in aerodynamic efficiency. The stress attenuation is understood as an effect of the smoother spanwise change of camber and a larger profile thickness at the hub.

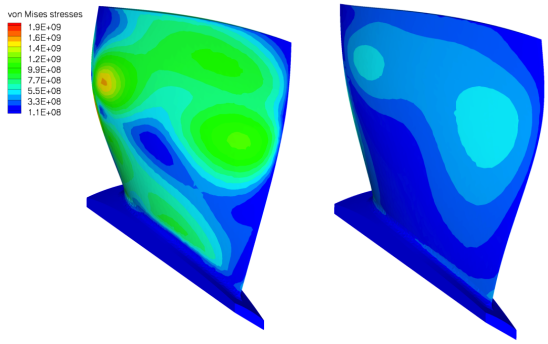

Figure 15: VON MISES STRESS ON SUCTION SIDE FOR AERO (LEFT) AND AERO-MECHANICAL (RIGHT) DESIGNS

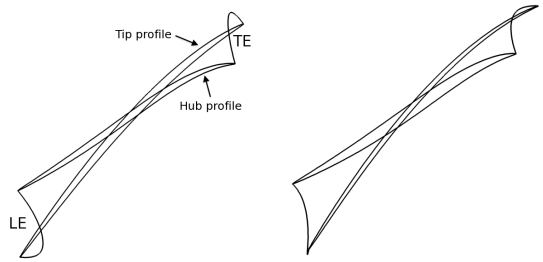

Figure 16: SECTION PROFILES STACKING FOR THE AERO (LEFT) AND AERO-MECHANICAL (RIGHT) DESIGNS

5. Conclusion

This paper presents the current status of the doctoral work entitled "Accelerated Optimization for Multi-Disciplinary Design of Transonic and Contra-Rotating Turbomachinery Components". The three main topics of investigation have been initiated and consists of: implementation of GPU-acceleration CFD, attenuation of shock interaction in transonic turbine, design and optimization of contra-rotating fan. The first part would result in the speed up aero-mechanical optimizations and will take place with progressive steps of implementation. In a second part, an optimized vane design for reduced downstream distortion has been achieved, providing a 43.2% reduction of downstream pitch-wise static pressure standard deviation. The unsteady interaction with the downstream rotor remains to be evaluated. In a third part, a methodology to design compact single-stage highly loaded axial flow fans has been proposed. Based on this, the simultaneous design of the two rotors of a contra-rotating fan is now targeted, considering both aerodynamic and mechanical performances.

References

[1] E. Elsen, P. LeGrelsey, E. Darve, "Large calculation of the flow over a hypersonic vehicle using a GPU", Journal of Computational Physics, 227(24), pp. 10148-10161, 2008

[2] T. Brandvik, G. Pullan, "An Accelerated 3D Navier-Stokes Solver for Flows in Turbomachines", ASME GT2009-60052, 2009

[3] NVIDIA, "NVIDIA CUDA Programming Guide", Version 3.1.1, 2010

[4] M.B. Giles, "Stator/Rotor Interaction in a Transonic Turbine", Journal of Propulsion, Vol.6, No.5, pp.621-627, 1990

[5] C. Sieverding, M. Stanislas, J. Snoeck, "The base pressure problem in transonic turbine cascades", Journal of Engineering for Power, Vol. 102, pp. 711718, 1980

[6] T. Verstraete, "CADO, a Computer Aided Design and Optimization Tool for Turbomachinery Applications", 2nd International Conference of Engineering Optimization, 2010

[7] A. Arnone, "Viscous Analysis of Three-Dimensional Rotor Flow Using a Multigrid Method", Journal of Turbomachinery, Vol. 116, pp. 435-445, 1994

[8] W. Calvert, R. Ginder, "Transonic Fan and Compressor Design", Journal of Mechanical Engineering Science, Vol. 213, N. 5, pp. 419-436, 1999

[9] S. Lieblein, F. Schwenk, F. Broderick, "Diffusion Factor for Estimating Losses and Limiting Blade Loadings in Axial Flow Compressor Blade Elements", NASA Research Memorandum AD011178, 1953

[10] G. Miller, G. Lewis, M. Hartmann, "Shock Losses in Transonic Rotor Rows", Journal of Engineering for Power, Vol. 83, pp. 235-242, 1961

[11] H. Lichtfuss, H. Starken, "Supersonic Cascade Flow", Progress in Aerospace Sciences, Vol. 15, pp. 37-149, 1974

[12] G. Dhondt, "The Finite Element Method for Three-Dimensional Thermomechanical Applications", Wiley, 2004

ENGINE ANALYSIS AND IMPROVEMENTS

Aero-thermal Analysis and Characterization of Fine Wire Thermocouple Probes

Laura Villafañe

Turbomachinery and Propulsion Department, von Karman Institute for Fluid Dynamics, Belgium, laura.villafane@vki.ac.be

Supervisor: Guillermo Paniagua

Associate Professor, Turbomachinery and Propulsion Department, von Karman Institute for Fluid Dynamics, Belgium, paniagua@vki.ac.be.

University Supervisor: Jose María Desantes

Full Professor, Máquinas y Motores Térmicos, Universitat Politècnica de València, Spain

Abstract

Thermocouple probes for accurate gas temperature measurements require specific designs optimized for a given application and precise characterization of the probe performances. In the present investigation a numerical procedure is proposed that outperforms previous experimental approaches to analyze the thermocouple response and the different sources of temperature error. Results from conjugate heat transfer simulations on different shielded thermocouples are presented, that provide information of the influence of the design parameters on the error sources.

Keywords: thermocouples, conjugate heat transfer (CHT), recovery factor, conduction effects, response time, transfer function

1. Introduction

Innovative finned heat exchangers are being studied in the bypass of gas turbine engines to improve their thermal management. In this context, high fidelity temperature measurements are needed along the three dimensional transonic flow within an intermittent facility, interacting with an array of fins.

In the present investigation numerical simulations are performed to study the steady and unsteady heat fluxes within a temperature probe. A numerical procedure to analyze the response of thermocouple probes is proposed. Its application to shielded thermocouples allows investigating the distinct contributions that deviate the measurement from the real gas temperature, and their evolution with time.

Multiple attempts to provide correction factors for standard thermocouple designs can be found in the literature [1; 2; 3]. It is a common practise to report over-all recovery factors experimentally determined as an indicator of the temperature error of a thermocouple. While useful in comparing probe designs, they account for the total effect of radiation, conduction and convection on the probe on a given flow environment, within a correction coefficient in which not all the temperature errors have the same weight under different experimental conditions. The variability of the heat fluxes with the environment and probe design, requires each thermocouple to be carefully designed and calibrated. However, precise corrections from experimental probe calibrations are impractical. During calibration not only the flow conditions need to be replicated but also the thermal interactions between the probe and the test bench. Furthermore, the precision to reproduce and to characterize the calibration environment determines the accuracy of the corrections.

The numerical characterization of the probes excells previous experimental experiences in accuracy and simplicity. The presented numerical methodology allows understanding and quantifying the design parameters required to achieve precise gas temperature measurements. Adiabatic recovery factors, conduction error estimations and response time characteris-

tics are determined for a shielded probe with different values of wire diameter, thermocouple wire properties and boundary conditions at the thermocouple wire support. The present numerical approach may be coupled with optimizers to facilitate and improve the design of a probe for a certain application.

2. Thermocouple Probe Design

2.1. Application

To study a heat exchanger to be mounted downstream of the engine's inlet fan, a measurement test bench was prepared. A transonic wind tunnel with a distorted annular sector, helicoidal test section was manufactured. Total flow temperature measurements are to be performed in this intermittent wind tunnel discharging to the atmosphere from a pressurized vessel. The flow temperature decreases during a test run due to the flow expansion in the reservoir. Flow temperature traverses are to be recorded along the test section of transversal area about 0.013 m^2. High-frequency response is required in order to allow fast traverses. A rake of temperature probes allows to maximize the measurement locations in a test. Precise characterization of the probe response is necessary to synchronize all readings, as well as to accurately analyze the heat exchanger efficiency.

2.2. Pre-existent design rules

The temperature of a thermocouple junction is the result of the energy balance including the convective heat flux between the junction and the surrounding gas, radiation to the surrounding walls, and conductive flux to the wire. The balance is different for each probe and each condition. The measured temperature would be equal to the total flow gas temperature in the absence of radiative heat fluxes, conductive flux to the thermocouple support and dissipation of kinetic energy in the boundary layer.

General design rules provide advises to reduce the temperature error sources. A shield is recommended in order to decrease the error caused by the dissipation of kinetic energy in the boundary layer around the junction (often called velocity error). The shield also provides structural resistance in high velocity flows and reduces radiation effects. However decreasing the velocity of the flow decreases the convective heat transfer, penalizing the conduction error and the response time. Thus, the internal velocity must be kept as high as allowable. The internal velocity is function of the vent hole to inlet ratio. The junction position within the shield is a compromise between non-aligned entrance flow effects, and flow alteration due to convective heat transfer to the shield. Recommended values are given by Rom and Kronzon [2], Saravanamuttoo [4] and Glawe et al. [1]. The wires within the shield can be placed parallel or perpendicular to the flow. In the first case, the length of the wires is limited to prevent wire bending. In the second, the length is limited by the shield diameter.

Conduction errors can be estimated from the simplified solution of the 1D energy equation for a wire element dx, (Eq.1), considering symmetry boundary condition $\partial T/\partial x = 0$ at the junction ($x = 0$), and isothermal temperature $T_w = T_{sp}$ at the support of the wire ($x = l$). Eq. 2 provides a simplified solution particularized for the junction. The assumption of constant gas temperature and constant convection coefficient h, neglects the effect of the real flow temperature differences along the wire.

$$h(T - T_g)\pi d_w dx = k\frac{\partial^2 T}{\partial x^2}\pi\frac{d_w^2}{4}dx \tag{1}$$

$$T_{ad} - T_j = \frac{T_{ad} - T_{sp}}{\cosh(l\sqrt{\frac{4h}{k_w d_w}})} = \frac{T_{ad} - T_{sp}}{\cosh(l/l_c)} \tag{2}$$

Let us consider the total temperature of the gas T_g, equal to the junction recovery temperature T_{ad}, namely the total temperature in the absence of velocity error. Design rules derived from this simplified solution recommend to have high values of h (high velocities), high l/d_w ratios, low conductivity wire materials, and support temperatures close to gas temperature. Petit et al. [5] suggest that the ratio l/l_c should not be smaller than 5.

The contribution of the error due to radiation is generally important at high flow temperatures. The simplified relationship (Eq.3) considering the most adverse conditions with unity view factor and equal conductive and radiative areas yielded a negligible error, lower than $4 \cdot 10^{-4}$%, about 1 mK.

$$T_0 - T_j = \frac{K_R\sigma\epsilon A_R(T_j^4 - T_W^4)}{hA_c} \tag{3}$$

In flow temperature transients the energy balance at the thermocouple junction or on a dx at any position along the wire can be expressed by Eqs. 4. As in the steady case, T_g is considered equal to T_{ad} in the absence of velocity errors.

$$S_j h_j (T_g - T_j) + \frac{\pi}{2} d_w^2 k_w \left(\frac{\partial^2 T_w}{\partial x^2}\right)|_{x=0} = \rho_j C_{p,j} V_j \frac{\partial T_j}{\partial t}$$
$$h_w (T_g - T_w) + \frac{d_w}{4} k_w \left(\frac{\partial^2 T_w}{\partial x^2}\right) = \rho_w C_{p,w} \frac{d_w}{4} \frac{\partial T_w}{\partial t} \quad (4)$$

In the case of uniform temperature on the junction, constant heat transfer coefficient independent with time, and no heat transfer by conduction between the junction and the adjacent wire, the thermocouple response to a temperature step is a first order system, Eq. 5. The assumption of first order system would be also valid for the assembly wire and junction if their diameters are identical, there are no radial or longitudinal temperature gradients, no conductive heat transfer to the supports, and the heat transfer coefficient is constant in time and along the length of the wire. Eq. 5, provides the time constant.

$$T_g = T_j + \tau \frac{\partial T_j}{\partial t}, \quad \text{with} \quad \tau_j = \frac{\rho_j C_{p_j} V_j}{h_j S_j}; \quad \tau_w = \frac{\rho_w C_{p_w} d_w^2}{4 k_g N u_w} \quad (5)$$

2.3. Shielded probe design

The temperature probe consists of a rake of five shielded thermocouples. Minimization of blockage effects given the small transversal area of the test section is considered, while preserving the structural resistivity of the whole rake. The geometric characteristics of the temperature probe heads are sketched in Fig. 1.

A type T thermocouple (copper-constantan) is placed perpendicular to the flow with a total length equal to the internal shield diameter, 2 mm. This wire configuration is intended to avoid wire bending at high velocities. Ratios $(l/d)_w$ of 79 are obtained with wires of 25.4 μ m diameter. The ratio weld-bead to wire diameter measured after probe manufacturing is about 2.7. The shield diameter is a compromise between the blockage minimization, wire structural resistivity and limitation of conduction errors. The shield is made of polycarbonate, chosen for its low conductivity. In agreement with the values recommended in the literature [1], [2], [4], the inlet/outlet area ratio is 4 and the junction is placed at 1/2 internal shield diameters from the entrance.

3. Methodology of the aerothermal study.

The transfer function of a thermocouple probe can be obtained by evaluating the response to a temperature step. Experimentally, the accuracy of the temperature corrections requires a precise control of the gas temperature excitation and test conditions.

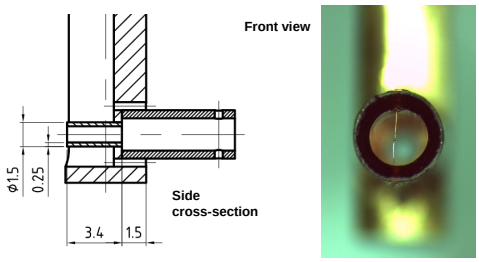

Figure 1: Shielded thermocouple probe.

At the transonic conditions of interest, the characteristic time for the flow to develop around the thermocouple is two orders of magnitude smaller than the characteristic time of the thermal transient in the thermocouple wires. This allows to perform simulations in two stages. First of all, a steady simulation is solved to establish the flow around the probe considered isothermal. This steady solution is referred as the reference case. Secondly a conjugate heat transfer (CHT) simulation is initiated from the reference solution, solving also the energy balances within the solid domains of the thermocouple. This second stage is ran in steady or transient state depending on whether the interest is focused on the steady temperature errors or on the transient behavior. In the latter case, the result is the response of the thermocouple to a temperature step. The decomposition in two stages highly reduces the computational cost.

This methodology allows the analysis of the heat fluxes within the thermocouple and the influence of the flow environment, probe geometry and wire materials.

4. Numerical Tools.

4.1. Computational domain and solver

The shielded thermocouple head is modeled in a 3D domain constituted by a quarter of a cylinder thanks to the existence of two symmetry planes on the probe geometry. The grid extends 6 shield diameters in the radial direction and in the axial direction upstream of the probe, and 10 diameters downstream. The three solid parts (shield , wire and junction) are meshed independently and concatenated to the gas domain mesh in the NS solver used. The gas hybrid 3D mesh composed by about 1.75 million cells is shown in Fig. 2.

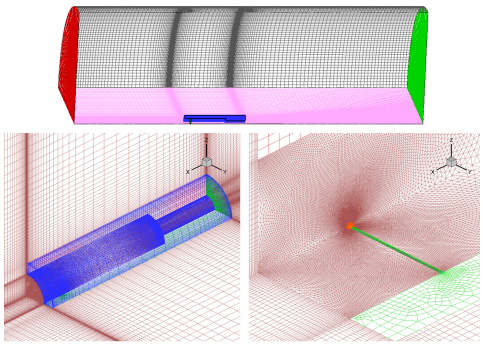

Figure 2: Computational domain. Left: TC shield view. Right: TC wire and junction.

The grid is refined along the walls of the solid parts and specially around the thermocouple wire and junction.

The Reynolds Averaged Navier Stokes solver employed was CFD++ (v.8.1). The k-epsilon turbulence model was considered, with initial values of k and epsilon estimated as a function of the free stream nominal velocity, with a free-stream turbulence level of 1% and a turbulence length scale based on the tube inner diameter. Values of y^+ in the vicinity of the thermocouple junction are lower than 0.3, and lower than 0.5 along the wire. For the steady simulations convergence is achieved after 1000 iterations , 5.5 hours CPU time in 8 parallel Intel Core 2 Quad Q9400 (2.66 GHz) machines. For the transient simulations the temperature of the solids is released by changing the boundary conditions to CHT. The integration time step is adjusted as function of the temperature gradients starting from 0.1ms. The CPU time required to reach steady junction temperature when CHT is activated in all the solid domains, varies depending on the wire conductivity. Approximately 1000 iterations with different time steps are required in a low conductive material, involving 51 hours CPU time running in 8 parallel machines, while up to 6000 iterations are required for a high conductive wire.

4.2. Numerical test conditions

Nominal flow conditions for the simulations correspond to inlet boundary conditions $T_s = 273.22K$, $P_s = 101325Pa$, $V_\infty = 231.12m/s$, and $P_s = 101325Pa$ at the domain outlet. Different Mach and Reynolds numbers were tested for the geometrical configuration corresponding to the design geometry.

Three geometrical configurations were analyzed (Table. 1), the reference design is henceforth referred

Table 1: Probe geometric configurations.

	Geom 1	*Geom 2*	*Geom 3*
$l, [mm]$	1	1	1
$d_w, [mm]$	0.0254	0.0508	0
$d_j, [mm]$	0.07	0.14	0.07

Geom 1. The shield is the same in the three cases. The modified parameter is the wire diameter, doubled in *Geom 2* where the ratio junction to wire diameter has been kept constant. *Geom 3* refers to the study of a spherical junction with infinitely thin wires.

Heat loss through the wires to the support is function of the wire dimensions, material conductivity, support temperature and convective heat transfer along the wire. In order to study the so called conduction effects different wire materials and boundary conditions at the support are analyzed for the configurations *Geom 1* and *Geom 2*. In all cases the shield material is polycarbonate and the junction properties are an average of the two materials of type T thermocouple (copper and constantan). Two other materials are also considered in the study: Nicrosil and an ideal material with low conductivity, referred as Ideal (Table 2). The different support boundary conditions tested were:

(a) The shield-support behaves as an adiabatic solid,
(b) the shield is isothermal at 300 K,
(c) CHT on the shield.

5. Steady Temperature Effects

5.1. Global Temperature Correction

The junction temperature results as the balance between the convective heat fluxes between gas-junction and gas-wire, and the conductive flux between junction and wire influenced at the same time by the conductive heat flux between the wire and its support. If those effects were decoupled, individual error equations could be used to estimate the deviation of the measured temperature. However, in practical applications the junction temperature must be evaluated by the simultaneous solution of the different heat flux rates [6].

The overall recovery factor Z (Eq. 6), indication of the difference between the measured temperature (T_j) and the total temperature of the gas (T_0), can be decomposed into several contributions. The first term

Table 2: Material properties of thermocouple wires. Evaluated at 23°C.

	Copper	Constantan	Nicrosil	Ideal	Polycarbonate
K, [W m^{-1} K^{-1}]	401	19.5	13	1	0.2
ρ, [kg m^{-3}]	8930	8860	8530	8860	1210
C_p, [J kg^{-1} K^{-1}]	385	390	460	390	1250

(a) is the velocity error, related to the adiabatic recovery factor. The second term (b), takes into account the temperature error due to conduction and convection of heat in the wire in contact with the junction, for a given temperature of the support-shield (T_{sp}). The last term (c) collects the adiabatic recovery factor of the shield and the conduction effects between the shield, the probe stem, and the external probe support. The numerical method applied allows analyzing separately each contribution.

$$(1-Z) = \frac{T_0 - T_j}{T_0 - T_\infty} = \overbrace{\frac{T_0 - T_{ad}}{T_0 - T_\infty}}^{a} + \overbrace{\frac{T_{ad} - T_j}{T_{ad} - T_{sp}}}^{b} \cdot \overbrace{\frac{T_{ad} - T_{sp}}{T_0 - T_\infty}}^{c} \tag{6}$$

5.2. Velocity error

Temperature probes are intended to measure the gas total temperature, i.e. the temperature that the gas would attain if it is brought to rest through an isentropic process. However, in real gases (where the Prandtl number differs from one), frictional heat is generated within the boundary layer, hence the conversion of kinetic energy into thermal enthalpy is not perfect. The recovery factor, Eq. 7, represents the amount of kinetic energy recovered by the gas, where T_{ad} is the temperature of the surface of the junction in case it would behave as an adiabatic body, and V is the reference flow velocity upstream of the junction. The recovery factor is function of the geometry of the immersed body and the Prandtl number of the fluid. Experimental values of adiabatic recovery factor determined by different authors [7; 8; 9] were collected by Moffat [10] for bare wires parallel and normal to the flow.

$$r = \frac{T_{ad} - T_s}{V^2/2C_p} = 1 - \frac{T_0 - T_{ad}}{V^2/2C_p} \tag{7}$$

For shielded thermocouples behaving as adiabatic bodies, the term (a) in Eq. 6 represents an overall adiabatic recovery factor, related to r as expressed by Eq.8. The velocity upstream of the junction within the shield (V) is different from the free stream flow velocity (V_∞).

$$Z_a = \frac{T_{ad} - T_s}{V_\infty^2/2C_p} = 1 - \frac{T_0 - T_{ad}}{V_\infty^2/2C_p} = 1 - (1-r)(V_{int}^2/V_\infty^2) \tag{8}$$

Experimental determination of recovery factors is impractical since the junction temperature needs to be measured with great accuracy, and ensuring negligible influence of conduction along the wires to the supports, so that the junction behaves as an adiabatic body. Steady simulations at different flow velocities allow determining both r and Z_a and their sensibility to flow Mach and Reynolds numbers. Wire and shield are considered adiabatic solids in the computations and CHT is solved at the junction, which temperature is considered T_{ad}.

Computations have been also performed considering all the solid boundaries adiabatic, junction included. The average temperature on the junction adiabatic surface $T_{ad,m}$ has been compared with the junction temperature derived when CHT is solved on it, for the same flow conditions. Temperature differences observed, lower than 0.004 % ($T_{ad,m} - T_{ad}/T_{ad,m}$), are explained by the junction heat capacity of the small junctions considered.

Figure 3(a) shows the evolution of the recovery factor r and the overall recovery factor Z_a, for three different Mach numbers at constant Reynolds number based on the wire diameter. The adiabatic recovery factor slightly increases when the flow Mach number, and thus the velocity within the shield (about six times slower than the external flow), increases. The results are in good agreement with the recovery values compiled in the work of Moffat [10]. The effect of increasing Reynolds number at constant Mach number is also indicated. For the same probe geometry *Geom 1*, at constant temperature and Mach number, an increase in the Reynolds number is due to an increase in static pressure, and its consequence is to slightly decrease the recovery factor. For the nominal flow conditions, increasing the diameter of the thermocouple wire and junction *Geom 2*, yields to an increase of the Reynolds number, and analogously a slight decrease of the recovery factor. The overall recovery factor presents the same tendency while being less sensitive to Mach and

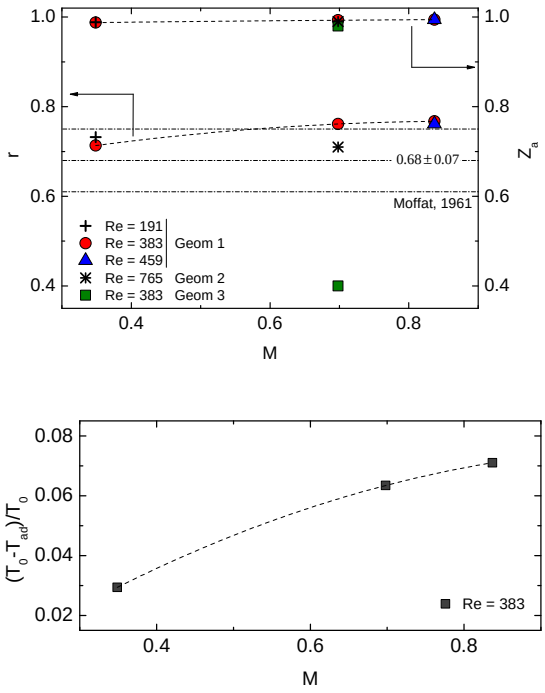

Figure 3: a) Recovery factors for different probe geometries, Mach and Reynolds numbers, b) Temperature error due to no isentropic flow deceleration

Reynolds variations.

Recovery factors have been computed likewise for *Geom 3*, providing lower values. The flow behavior around a sphere is clearly not similar to that around a thermocouple junction, neither to the flow parallel to a cylinder [10]. Comparison of the flow fields around the junction for *Geom 1* and *Geom 3*, shows a stronger flow deceleration in the first case forced by the presence of the wires. The thermal boundary layer around the junction in the presence of the wires is substantially thicker, and the transformation of the flow kinetic energy into thermal energy is more efficient.

Although the recovery factor increases with the Mach number, the kinetic velocity rises in a higher amount, thus the temperature error represented in Fig. 3(b) for the nominal flow conditions, also increases with velocity.

5.3. Conduction error

Free of velocity errors, the difference between the real junction temperature and the total temperature is the temperature error due to conduction, namely the product of terms (b) and (c) in Eq.6. In a well designed thermocouple, the junction temperature should be little sensitive to the support temperature, what is true when (b) is close to zero. In that case the overall contribution to the temperature error due to conduction would be negligible whatever the contribution of the term (c). In real applications term (b) is different to zero.

Term (b) reflects the influence of the conduction effects along the wire and those to the support, on the junction temperature. Its contribution can be expressed by the solution of the one dimensional energy equation, Eq.2. Thus, it decreases exponentially as the parameter l/l_c increases (for x$\geq$ 5, cosh x $\simeq$ 0.5e^x). Term (c) indicates the strength of the potential heat transfer between the thermocouple and the support. The lower temperature of the shield/support with respect to the total gas temperature in the absence of velocity error, $T_{ad} - T_{sp}$, drives the conduction to the wire. In the case the support would be perfectly isolated from external sources, it is function of the recovery factor of the complete shield/support. In reality, it is also function of the depth of immersion of the support on the flow, its geometry and thermal properties, and the external boundary condition of the probe.

The values of the parameter l/l_c for each material and each of the two geometries considered are indicated in Tab. 3. For the computation of l/l_c, Eq. 9, air conductivity is evaluated at the gas total temperature

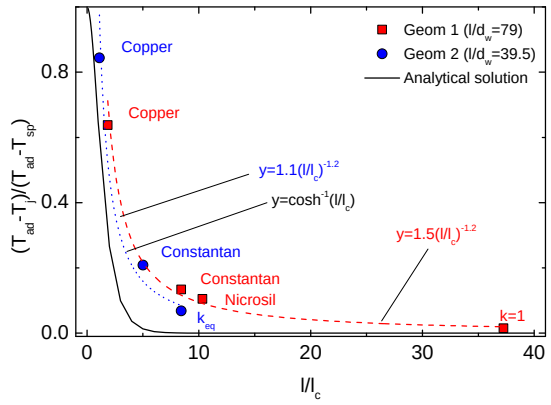

Figure 4: Ratio junction to support temperature deviations with respect to total temperature in function of the parameter l/l_c. Results from CHT simulations

[6], and the Nusselt number is derived from a correlation valid for wires perpendicular to the flow [10]: $Nu = (0.44 \pm 0.06)Re^{0.5}$.

$$\frac{l}{l_c} = l\sqrt{\frac{4h}{k_w d_w}} = \frac{2l}{d_w}\sqrt{\frac{Nuk_g}{k_w}} \tag{9}$$

Fig. 4 shows the non-dimensional conduction temperature error corresponding to term(b) in Eq.6. All results correspond to complete CHT simulations. The temperatures difference ratio is plotted versus the parameter l/l_c, which for a given probe geometry is only varied by a change in the wire material. The error decreases as the parameter l/l_c increases indicating that the junction temperature is less influenced by the conduction effects. The results show two slightly distinct trends for each l/d_w case that are best fitted by power laws with a common exponent coefficient of -1.2. The equivalent material, k_{eq}, corresponds to an hypothetical material with a conductivity such that the l/l_c value for $Geom2$ is equal to the l/l_c value for constantan wire and $Geom1$ ($k_{eq} = k_{const}\sqrt{2}/4$). At this l/l_c value (8.43), the contribution of conduction of term (b) is slightly smaller for $Geom2$. The analytical prediction (Eq.2) underestimates the results when compared with the numerical results. This discrepancy can be explained by the simplifications introduced in the analytical solution, especially the assumption of homogeneous gas temperature and heat transfer coefficient along the wire, and equal to the conditions at the junction. The parameter l/l_c is a good estimator of the conduction error, but inappropriate to establish a unique relation with the temperature error.

Figure 5(a) represents the global contribution to the conduction error computed for the reference probe ge-

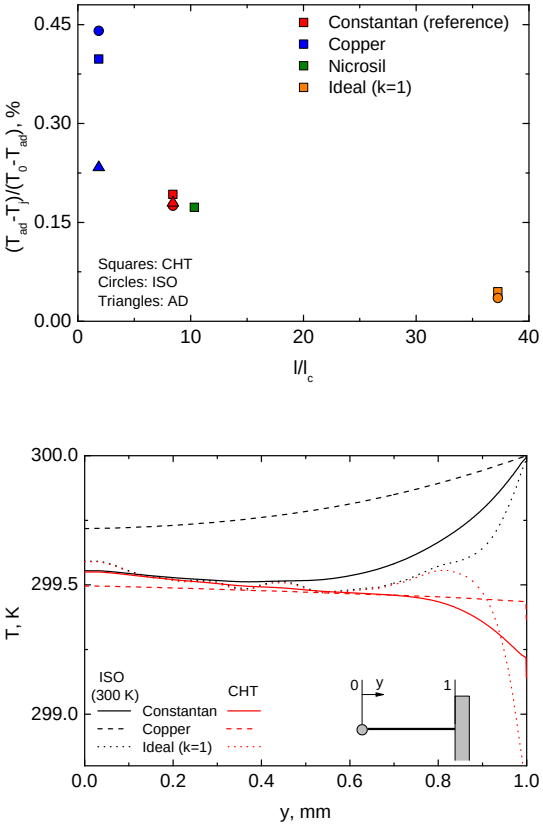

Figure 5: a)Overall temperature errors due to conduction in function of l/l_c, b)Wire temperature distributions

Table 3: Material parameters of thermocouple wires affecting conduction.

	Constantan	Copper	Nicrosil	Ideal	Equivalent
k, [kW m^{-1} K^{-1}]	19.5	401	13	1	6.89
l/l_c (Geom 1)	8.43	1.86	10.33	37.24	
l/l_c (Geom 2)	5.01	1.11	n.a.	n.a.	8.43

ometry (*Geom*1) for different materials. The figure compares for a given wire material and geometry, thus a given l/l_c, the variability of the temperature error due to the conditions at the shield/support. Fig. 5(b) displays the temperature distribution along the wire in the same conditions for three of the materials and two of the boundary conditions, adiabatic support and CHT within wire and support. The junction temperature ($y = 0$) is the same for the ideal wire ($l/l_c = 37$) independently of the conduction at the shield, with an overall conduction error about 0.04 %. The temperature at each position along the wire is less affected by the longitudinal conduction, hence by the shield temperature, and more by the convective heat flux. Thus the temperature distribution is able to reflect the non homogeneity of the gas temperature around the wire. The junction is only influenced by the wire temperature adjacent to it, and the effect of the shield temperature penetrates until the last 20% of the wire. In the case of constantan wire the temperature along the wire is affected by conduction to the shield to a higher extent. However, the temperature at the junction converges to almost the same value for the different boundary conditions. Overall conduction errors vary between 0.18 and 0.19 %. In the copper wire case, with a l/l_c about 2, conduction with the support influences the junction temperature in a higher degree. Errors vary between 0.23 and 0.45% depending on the support conditions.

The reference adiabatic temperature considered for the analysis of the conduction errors is that of the junction. However, due to the strong flow deceleration taking place around the wire in the vicinity of the junction, there is a less efficient flow deceleration in this region. Thus, the temperature recovered is lower when compared to the junction. This effect can be observed in Fig. 5(b) for the ideal wire distribution in which the temperatures at 10 to 20 % from the junction are slightly lower than at the junction. It explains also the slight difference between the junction temperatures for constantan and ideal material wires. The higher conductivity of constantan forces the junction to stabilize at the lower temperature of the wire in the vicinity, while for the ideal material the temperature at the junction rises to almost the adiabatic temperature.

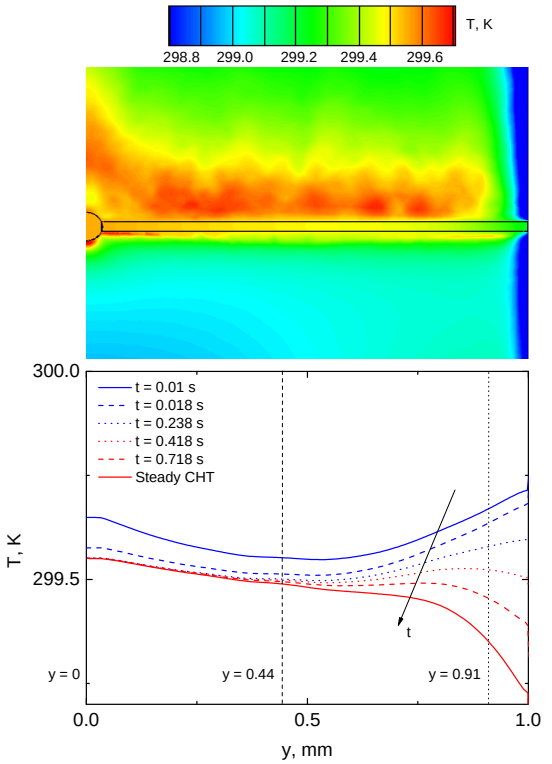

Figure 6: a)2D temperature contour, steady conditions. b) Evolution of constantan wire temperature distribution. CHT result

6. Transient Temperature Effects

The diffusive characteristics of the heat fluxes within the probe introduce a temperature lag on the junction temperature. The properties and geometry of the thermocouple wires affect the junction temperature evolution.

The numerical methodology applied in this study allows analyzing the temperature evolution on the complete probe in response to a temperature step. All the results correspond to the reference flow conditions and the initial temperature of the probe is T_i=300 K.

The temporal evolution of the temperature along the constantan wire for *Geom*1 is displayed in Fig.6. At

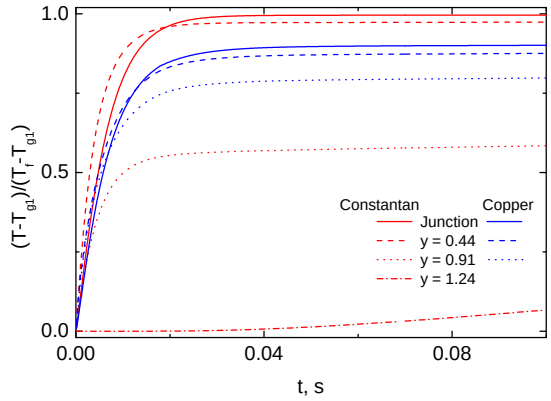

Figure 7: Temperature evolution at four control points on constantan and copper wires

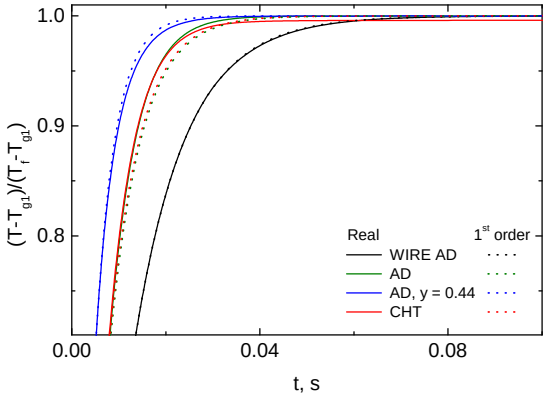

Figure 8: Comparison junction temporal evolutions with the correspondent first order.

each position along the wires, the rate of temperature change is different. The response time of the shield is much higher than that of the junction or wire due to its larger thermal inertia and lower thermal diffusivity a. Thus the part of the wire closer to the junction $y = 0$ reaches the final temperature faster than the part of the wire close to the shield/support due to its influence by conduction. Figure 7 shows the time temperature history at three wire positions and a point within the shield, for constantan and copper materials. The temperature traces are made non dimensional with their steady value in order to compare the response times, not taking into account the differences on the final temperature achieved.

All the temperature distributions, except that of the shield, show a fast initial temperature change, followed by a slower evolution. The fast initial temperature rise is dictated by the inertia of the junction or wire elements. The slow down is accentuated by the influence of the support at a certain position. In the constantan case the junction overpasses the conventional threshold of the 63.2 % of the response in 6.5 ms, and achieved the 90% of the final temperature in 18 ms. The temperature at $y = 0.44$mm shows a faster initial rise due to the lower thermal inertia of a wire element when compared with the junction, of bigger volume. However the convergence to the final temperature takes longer than in the junction due to the influence of the evolution of the shield at this point. The same behavior is observed at $y = 0.91$, but influenced in a higher degree by the shield temperature evolution.

The comparison of the temperature evolutions in the copper wire case, is analogous. When compared with the constantan results, the initial response of the copper is slightly slower, and the temperature evolutions at the different points closer in terms of the temperature rate evolution. It is explained by the higher conductivity of the copper, that implies higher diffusivity along the wire, and thus smoother temperature gradients between the different positions. Whereas in the constantan case, the effect of the support is little felt close to the junction but greatly affecting the opposite wire extreme.

In the ideal case of no existence of conductive heat between junction and wire, or if equal wire and junction diameters and no conduction flux with the support, the response of the thermocouple would be that of a first order system, Eq. 5. The characteristic would be the time required to complete 63.2 % of its response to a gas temperature step. None of the wire temperature evolutions represented in Fig.7 corresponds to a first order response due to the influence of the support.

Non dimensional junction temperature evolutions are represented in Fig. 8 for the ideal case of adiabatic wire, and constantan wire with two different support conditions: CHT and adiabatic. For each evolution the time to reach 63.2% of the final temperature was used to evaluate the corresponding first order response. When the wires are considered adiabatic, the junction evolution collapses to the first order response. The presence of the wires modifies the temperature response whatever the condition at the support. When no flux occurs between shield and wires the junction reaches the final temperature without the delay caused by the support but it does not correspond to a first order. This result is in agreement with the works of Yule [11] and Petit [5]. The influence of the wires causes an acceleration of the junction response if compared

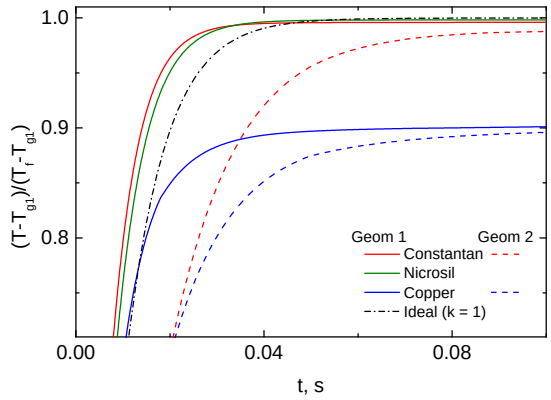

Figure 9: Junction temporal evolution. CHT simulations

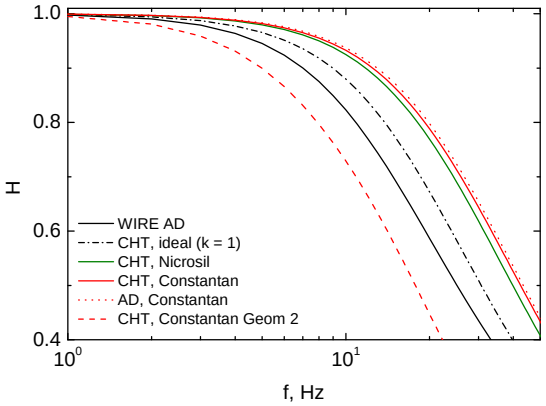

Figure 10: Transfer functions for different wire materials, wire diameter, and support conditions

with the adiabatic wire result. It is instigated by conductive effects from the faster response of a wire element. The evolution at $y = 0.44$ is included in the graph for comparison. A simple decomposition in two first order systems expressing the response of the wire and support as done in cold wires [12] does not accurately reproduce the junction response in the presence of conductive effects.

Figure 9 displays the non dimensional junction temperature evolutions for different wire materials and the two wire diameters (*Geom*1 and *Geom*2). All cases correspond to complete CHT simulations with the consequent possible influence of the slower response of the support. For the cases in which the conductive effects on the junction are not too noticeable ($l/l_c \geq 5$), the higher the wire conductivity the faster the response of a wire element and therefore the faster the response of the junction. Increasing the wire and junction diameters introduces a delay in the response due to the increase of the thermal inertia, and a decrease of the parameter l/l_c, hence an increase of the conductive fluxes.

Assuming the response of a thermocouple can be expressed as linear system model of m-order, the transfer function of the thermocouple in the Z domain can be expressed by the ratio of two m-order polynomials, Eq. 10. A digital procedure [13] was used to determine the invariant transfer function that reproduces better the junction response in each case.

$$H(z) = \frac{b_0 \cdot z^{-d} + b_1 \cdot z^{-1-d} + \ldots + b_m \cdot z^{-m-d}}{1 + a_1 \cdot z^{-1} + a_2 \cdot z^{-2} + \ldots + a_m \cdot z^{-m}} \quad (10)$$

A first order response was found for *Geom*1 with adiabatic wires and for *Geom*3, in accordance with the temporal analyses. A second order system fitted the junction response when the support is adiabatic. A second order system represented likewise the complete CHT simulation in the case of the ideal wire material, where the conductive effects are negligible. For the case of the nicrosil wire, a third order response was found. The higher the effect of the support, the higher the order of the system found to represent the transfer function. The response was found to be that of a 5th order system, for both *Geom*1 and *Geom*2 and constantan wire. For copper wires the response could be considered 5th or 6th order, although the fitting was less accurate. The transfer functions representing the junction responses for several test cases are shown in Fig. 10. The faster response corresponded to constantan wires with cutting frequencies slightly higher than 10 Hz.

7. Conclusions

Gas temperature measurements with thermocouples are to be performed in a transonic flow interacting with finned heat exchangers. Accurate and fast response temperature probes are required.

A new methodology was proposed to numerically resolve temporal evolution of the heat transfer balances within a thermocouple probe. It has been applied to a shielded type thermocouple, providing valuable information of the effect of the design parameters on the different error sources. This procedure overcomes the experimental complexities and inaccuracies providing detailed information of the performances of a given probe in the range of flow conditions of interest.

Results from conjugate heat transfer simulations were analyzed at different values of the main non di-

mensional parameters driving the heat flux within the thermocouple probe. This approach dissects the commonly described experimental "recovery factor" into two steady error sources: flow velocity effects and conductive-convective errors. Radiation effects were shown to be negligible for the flow environment of interest.

Recovery factors for the shielded probe were computed at different Mach and Reynolds numbers. The temperature error increase due to velocity effects is shown, and thus, the benefit of shield designs against bare thermocouples.

Temperature errors due to conduction were analyzed for different wire diameters, wire materials and support temperature conditions. The influence of conductive errors on the junction temperature is mainly dictated by parameter l/l_c, which collects the effects of the wire conductivity, length and diameter and flow convective heat transfer. The decrease of the temperature error with increasing values of l/l_c is reported. If high values of the parameter l/l_c cannot be achieved the conductive temperature error is dominated by the wire support. Results are shown for different support conditions.

Time resolved CHT simulations allowed analyzing the temporal temperature evolution within the probe. The effect of the different heat sources on the response time has been shown. The present numerical approach allowed computing the transfer function of the probe, and analyzing the effects of the temperature errors on the response order.

References

[1] G. E. Glawe, R. Holanda, L. N. Krause, Recovery and Radiation Corrections and Time Constants of Several Sizes of Shielded and Unshielded Thermocouple Probes for Measuring Gas Temperature, Tech. rep., Lewis Research Center, Cleveland, Ohio (1978).

[2] J. Rom, Y. Kronzon, Small shielded thermocouple total temperature probes, Tech. rep., Institute of Technology, Israel (1967).

[3] T. M. Stickney, Recovery and time-response characteristics of six thermocouple probes in subsonic and supersonic flow, NACA TN 3455, Tech. rep., Lewis Flight Propulsion Laboratoty, Cleveland Ohio (1955).

[4] H. I. H. Saravanamuttoo, Recommended practices for measurement of gas path pressures and temperatures for performance assessment of aircraft turbine engines and components, Advisory Report 245, AGARD Advisory Report No. 245 (1990).

[5] C. Petit, P. Gajan, J. C. Lecordier, P. Paranthoen, Frequency response of fine wire thermocouple, J. Phys. E: Sci. Instrum 15 (1982) 760–764.

[6] M. D. Scadron, I. Warshawsky, Experimental determination of time constants and Nusselt numbers for bare wire thermocouples in high velocity air streams and analytic approximation of conduction and radiation errors. NACA TN 2599, Technical Note 2599, Lewis Flight Propulsion LAboratory, Cleveland, Ohio (1952).

[7] C. H. H, A. Kalitinsky, Temperature measurements in high velocity air streams, Trans. ASME 67 (1945) A–25.

[8] F. S. Simmons, Recovery Corrections for Butt Welded stright wire thermocouples in high velocity, high temperature gas streams, Tech. rep., NACA RM-E54G22a (1954).

[9] G. Glawe, F. S. Simmons, T. M. Stickney, Radiation and recovery corrections and time constants of several chromel-alumel thermocouple probes in high temperature high velocity gas streams, Tech. rep., NACA TN-3766 (1956).

[10] R. J. Moffat, Gas temperature measurement.

[11] A. J. Yule, D. S. Taylor, N. A. Chigier, Thermocouple Signal Processing and On-Line Digital Compensation, Journal of Energy 2, No 4 (1978) 223–231.

[12] R. Dnos, C. Sieverding, Assessment of the cold wire resistance thermometer for high speed turbomachinery applications, Journal of Turbomachinery 119, N0 1 (1997) 140–148.

[13] G. Paniagua, R. Dnos, Digital compensation of pressure sensors in the time domain, Experiments in Fluids 32, No 4 (2002) 417–424.

Simulation of a Variable-Combined-Cycle Engine for Dual Subsonic and Supersonic Cruise

Víctor Fernández Villacé

Turbomachinery and Propulsion Department, von Karman Institute for Fluid Dynamics, Belgium, villace@vki.ac.be

Supervisor: Guillermo Paniagua

Associate Professor, Turbomachinery and Propulsion Department, von Karman Institute for Fluid Dynamics, Belgium, paniagua@vki.ac.be.

University Supervisor: José L. Montañés

Professor, Aerothermodynamics and Propulsion Department, Universidad Politécnica de Madrid, joseluis.montanes@upm.es

Abstract

Novel propulsion concepts need to be developed for a feasible sustained high speed flight. To that end, the Scimitar engine benefits from the thermal integration of the cryogenic fuel through a complex combined cycle. This paper presents the numerical model of the Scimitar engine while in air-turbo-rocket configuration, the development of an analysis procedure based on the exergy concept and the engine operational envelope together with its performance figures while flying a determined trajectory between Mach 2.5 and 5.

Keywords: Air-Breathing Engine, Combined Cycle, Exergy, High Speed Propulsion, Numerical Modeling, Variable Cycle.

1. Introduction

The Scimitar engine is a hydrogen-fueled propulsive plant for the aircraft A2, a concept proposed by Reaction Engines Ltd., for the project Long-Term Advanced Propulsion Concepts and Technologies II (LAPCAT II). Scimitar is a variable cycle engine that combines a turbofan-based cycle with an air-turbo-rocket cycle (Fig. 1). The turbofan-based cycle operates from take-off to Mach 2.5. It is augmented with an afterburner (A/B) during the acceleration phase only, having the capability of maintaining a "dry" subsonic cruise regime at Mach 0.9. Between Mach 2.5 and Mach 5 the engine operates as an air-turbo-rocket with a ramjet burner in the bypass. At Mach 5 the vehicle cruises and the cycle is that of a gas generator air-turbo-rocket engine [1]. From take off to Mach 2.5 the core flow is diverted towards the hub turbine (HT) that drives the fan (F); then it is mixed with the air from the by-pass duct. From Mach 2.5 to Mach 5 the core flow is fed into the core main combustion chamber and nozzle and the fan windmills, whose speed is brought down as the by-pass nozzle is progressively closed. In this regime the by-pass acts as a ramjet with an annular exhaust around the core jet.

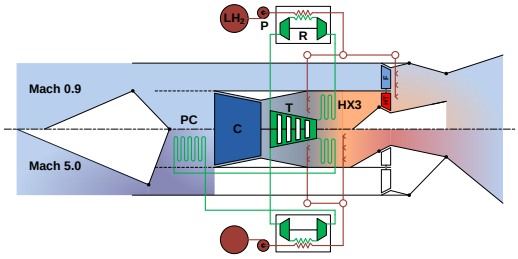

Figure 1: Turbofan (upper half) and air-turbo-rocket (lower half) configurations of Scimitar.

During the supersonic operation, the by-pass nozzle throat is adjusted to provide an optimum matching of the intake and the compressor that minimizes the air spillage. At supersonic cruise regime, the by-pass nozzle is fully closed completing the contour of the core nozzle. The intake has variable geometry: its throat is wide open at low subsonic speeds and closes progressively towards the supersonic regime. Table 1

shows the schedule of each working mode in function of the flight speed: subsonic acceleration, SbA; subsonic cruise, SbC; supersonic acceleration, SpA; supersonic cruise, SpC.

Mach Range	Regime	Mode
0.0 - 0.9	SbA	Turbofan A/B
0.9	SbC	Turbofan
0.9 - 2.5	SpA	Turbofan A/B
2.5 - 5.0	SpA	Ramjet + ATR
5.0	SpC	ATR

Table 1: Variable cycle schedule of Scimitar.

The engine core consists of a compressor that supplies air to the combustion chamber. It is driven by an helium turbine, which is not fluid-dynamically coupled to the compressor as in the conventional turbofan configuration. In this manner the turbine can be constantly operated at high efficiency for the wide operational range of the air compressor. The helium follows a closed Brayton cycle and flows through the precooler (PC) during the supersonic cruise (above Mach 3.1) in order to recuperate the thermal energy of the incoming air. Cryogenic hydrogen acts as heat sink in the loop, which allows the conversion of the recuperated thermal energy into useful work to drive the turbine. The energy interchange between helium and hydrogen is done through a complex recuperator (R) (shown simplified in Fig. 1). The heat exchanger HX3 behind the first injection ramp of the core combustor provides the complementary energy demanded by the helium cycle. Fig. 2 shows the cycle with its corresponding station numbering.

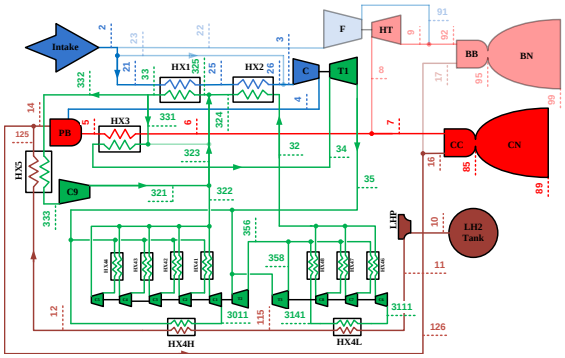

Figure 2: Cycle stations numbering.

During the conceptual design phase of an engine, the numerical model can give an indication about important quantities, e.g. net/gross thrust, specific consumption, specific thrust, which are fundamental when several propulsive concepts are compared. But it is also used to check the proper coupling of the engine modules for off design operations. This is of remarkable importance in the engine Scimitar, which has a novel configuration that combines three different propulsive concepts (turbofan, air-turbo-rocket and ramjet) into the same combined cycle. The proper matching of the major modules: intake, engine core and by-pass duct is to be analyzed to detect penalties on the overall cycle performance at any point of the operational range. The present work explores the performance of Scimitar in the air-turbo-rocket configuration finding its operational limits along the trajectory of the A2 aircraft.

2. Numerical Model

The numerical model is programmed in the symbolic simulation environment EcosimPro by assembling together the engine modules: compressors, turbines, heat exchangers, combustion chambers, nozzles and intake. When available, real geometry and cycle design parameters are used. When they are not, a number of engineering hypotheses are taken to accomplish the design cycle. Finally, the set of differential-algebraic-equations that describe the model behavior is integrated with the differential-algebraic system algorithm DASSL [2].

The model is constructed upon the set of libraries of the European Space Propulsion System Simulation (ESPSS), which integrates the components and functionalities needed for the simulation of propulsive systems. The libraries are being developed under the supervision of the European Space Agency and are intended to become a standard in Europe. Additional ad-hoc elements (heat exchangers and turbomachinery components) have been developed based on and as a complement to the ESPSS set. Here it follows a brief description of the libraries. For a more in dept explanation the reader is encouraged to refer to the user manual [3].

The physical formulation inside each component is time-dependent. The joining elements (manifolds, volumes, valves and junctions) as well as the turbomachinery elements and the intake lack of a spatial discretization. Manifolds and volumes apply the conservation equations, given a characteristic volume, to compute the state variables pressure and enthalpy (p, h). Valve and junction elements make use of their reference cross sectional area to compute the flow variables mass flow and enthalpy flow $(\dot{m}, \dot{H})$ across it ,

accounting for the possible sonic blockage of the section. The dimension of the turbomachinery components is provided indirectly by the scaling factors applied to the characteristic map of a real machine. The ducts in the heat exchangers and the combustors implement the 1D governing equations in their conservative form:

$$\frac{\partial \vec{\omega}}{\partial t} + \frac{\partial \vec{f}(\vec{\omega})}{\partial x} = \vec{\Omega}(\vec{\omega}), \tag{1}$$

where the conservative variables, flux and source terms are respectively:

$$\begin{aligned} \vec{\omega} &= A \left\{ \begin{array}{c} \rho \\ \rho v \\ \rho e \end{array} \right\}; \; \vec{f}(\vec{\omega}) = A \left\{ \begin{array}{c} \rho v \\ \rho v^2 + p \\ \rho v (e + p/\rho) \end{array} \right\}; \\ \vec{\Omega}(\vec{\omega}) &= \left\{ \begin{array}{c} 0 \\ -0.5 \xi \rho v |v| A + p(dA/dx) \\ \dot{q} \end{array} \right\}, \end{aligned} \tag{2}$$

where A is the flow area. The closure relations are provided by the state and calorific equations of the fluid and each expressions for the heat transfer $\dot{q}$ and the friction factor ξ.

The state and calorific description of helium and hydrogen are implemented in ESPSS by a look up routine in the corresponding fluid tables from the NIST database [3]. The hydrogen temperature ranges from 20 K, at the pump exit, to about 1000 K at the preburner inlet and it is considered to be in a normal composition, this is 75% ortho-hydrogen and 25% para-hydrogen, because its properties are available for a wider range (up to 700 K) than for ortho-hydrogen. However, the usage of para-hydrogen would be beneficial for the cycle because of its higher heat absorption capability. In the range $700-1000\ K$ the hydrogen termodynamic behavior can be approximated by that of a semi-perfect gas. Air and the combustion gases inside the combustor components are described as perfect mixtures of semi-perfect gases. The state and calorific relations of the semi-perfect gas are:

$$p = \rho R_g T \tag{3}$$

$$h = h_0 + \int_{T_0}^{T} C_p(T)\, dT, \tag{4}$$

where h_o is the reference for the enthalpy at T_0. The gas exhausting the combustors, flowing into the nozzle or the heat exchanger $HX3$, is characterized as a perfect gas: the specific heats C_p, C_v equal those values computed at the combustor exit and does not vary with the temperature.

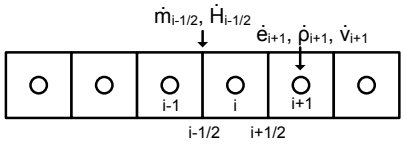

Figure 3: Staggered grid.

The heat addition per unit of length, $\dot{q}$, is computed by means of:

$$\dot{q} = h_c\, \Gamma\, (T_w - T), \tag{5}$$

where Γ is the wet perimeter of the duct under consideration and T_w is the wall temperature. An appropriate correlation for Nusselt number depending on the flow characteristics is used to compute the convective heat transfer coefficient, h_c:

$$h_c = Nu\ k/D_h; \qquad Nu = f(Re, Pr). \tag{6}$$

The friction factor ξ accounts for the pressure loss per unit of length of the duct. It is provided by a correlation valid for laminar, turbulent and transient flows [4]:

$$\xi = k_f\, f/D_h \tag{7}$$

$$f = 8 \cdot \left(\left(\frac{8}{Re} \right)^{12} + (A + B)^{-3/2} \right)^{1/12} \tag{8}$$

$$A = \left(2.457 \cdot ln \frac{1}{(7/Re)^{0.9} + 0.27 \cdot \epsilon/D_h} \right)^{16} \tag{9}$$

$$B = (37530/Re)^{16} \tag{10}$$

The correction coefficient k_f serves to adjust the pressure loss along the fluid vein to the required design value.

Eq. 1 is solved with a centered scheme in a staggered mesh, where the state variables (e_i, ρ_i, v_i) are computed at the cell nodes and the fluxes $(\dot{m}_i, \dot{H}_i)$ at the cell interfaces, Fig. 3.

2.1. Combustion chambers and nozzles

During the combustion process the composition of the combustion gases is an additional dependent variable. Under the hypothesis of chemical equilibrium, the equilibrium composition is that one which minimizes the Gibbs energy for the current state (p, T) of the mixture. For each of the grid nodes, at each time step, the minimization problem is solved in an iterative manner together with the conservation Eqs. 1.

Along the nozzle following the combustor, the flow is supposed to be frozen, the compositions being the

same as calculated in the outlet cell of the combustor. Despite that the software offers the capability of computing the equilibrium composition of the flow, this calculation was discarded to speed up the simulations. Also with this same purpose, a one- and two-nodes spatial discretizations were chosen respectively for the preburner and the main combustor chamber. For the combustion of air with hydrogen, 19 reacting species, with the elements H, N, O, are considered in the equilibrium calculation. The geometry is characterized by the distribution of cross-sectional area along the axis, $A(x)$, in (Eq. 2).

Some of the heat generated in combustor is transfered to the fuel and the oxidizer in their respective manifolds. But, apart from this, the preburner surface is supposed to be adiabatic. However, the nozzle is cooled by radiation to the environment, whose temperature varies along the vehicle trajectory accordingly to the International Standard Atmosphere (ISA) model. A uniform view factor of one is considered on the external surface of the nozzle to compute the radiated heat as predicted by the law of Stefan-Boltzmann. For the heat transfer on the internal surface of the nozzle, the convective heat transfer coefficient h_c is computed from the correlation of Bartz [5] and the law of Stefan-Boltzmann for the radiated heat. The heat flux from the fluid inside each cell is then:

$$\dot{q}_{wall\ i} = h_{c\ i}\,\Gamma_{wall\ i}\,(T_{wall\ i} - T_{a\ i}) \quad (11)$$

$$+ \sigma\,A_{wall\ i}\,(T^4_{wall\ i} - T^4_i), \quad (12)$$

where $\Gamma_{wall\ i}$ is the wet perimeter of the ith cell, with bulk and solid wall temperatures of T_i and $T_{wall\ i}$, σ is the Stefan-Boltzmann constant. The adiabatic wall temperature $T_{a\ i}$ is approximated by:

$$T_{a\ i} = T_i\,(1 + Pr_i^{0.33}\,(\gamma_i - 1)\,0.5\,M_i^2), \quad (13)$$

being Pr_i, M_i and γ_i the Prandtl and Mach numbers and the ratio of specific heats in the ith-cell. The correlation of Bartz provides the expression of the film coefficient:

$$h_c = 0.026\,\mu_i^{0.2}\,(k/\mu)_i^{0.6}\,Cp_i^{0.4}\cdot \quad (14)$$

$$\cdot\ \dot{m}_{th}^{0.8}/A_i^{0.9}\,(0.25\,\pi\,D_{th}/R_c)^{0.1}, \quad (15)$$

where $\dot{m}_{th}$, D_{th} and R_c are respectively the throat mass flow, diameter and curvature radius; k_i, μ_i and Cp_i are the thermal conductivity, viscosity and specific heat at constant pressure of the combustion gases at the grid position i and A_i is the cross area of the section i. In the equations above, the temperature dependent gas properties (Pr_i, k_i, μ_i and Cp_i) are evaluated at a temperature in between the bulk and the wall temperatures.

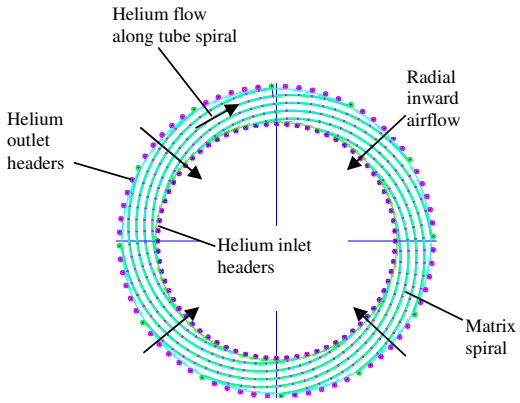

Figure 4: Frontal view of one precooler module showing the spiral of tubes [6].

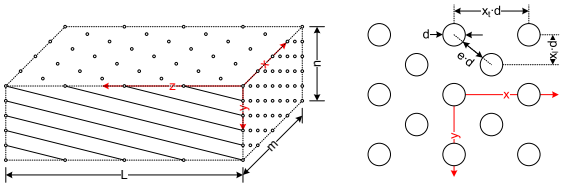

Figure 5: Equivalent matrix of tubes in cross-flow.

The flow in the nozzle is solved from Eq. 1-2 disregarding the unsteady and viscous (ξ) terms. A 5-node discretization is taken.

2.2. *Heat exchangers*

Three different models of heat exchanger were developed to simulate the Scimitar precooler (HX1 and HX2), reheater (HX3) and the regenerator modules (HX4L, HX4H, HX5, and the He-He regenerators). They are based on the existing capabilities of the ESPSS libraries. The fluid flow is computed as described in the above paragraphs, being only the geometry and heat transfer behavior characteristic to each one of them.

2.2.1. *Precooler*

The precooler contains two modules consisting of a number of tubes with $d = 0.96$ mm external diameter tangentially mounted in a spiral around the engine axis. The air flows radially inwards across the tubes and the helium inside the tubes follows the spiral path from the internal to the external headers, Fig. 4. The

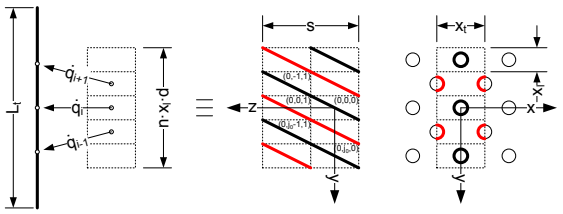

Figure 6: Equivalent computational domain of the periodic flow field. The perimeter of the section Γ in Eq. 5 is equal in every cell of the staggered arrangement (bold contours in the rightmost figure).

low temperature module HX2 is placed coaxially inside the high temperature module HX1, both sharing a common manifold. Because the ratio of the module diameter to the tube size is in the order of 10^3, the curvature effect on the flow field can be discarded. The planar equivalent bank of staggered tubes in crossflow is shown in Fig. 5. The transversal and longitudinal pitches are respectively of 2 and 1.5 tube diameters (x_t, x_l), which results in a passage minimum width of 0.8 tube diameters.

Under the assumption of uniform boundary conditions at the matrix inlet and outlet surfaces the flow is periodic. The dimensions of the periodic domain in the transversal plane XZ are $x_l \times s/2$, being s the tangential tube pitch, Fig. 6. The thermal field in the domain along the Y-direction through the cell $(i, j, k) = (0, 0, 0)$ is T_{0j0} with $j = 1, n$ and i, j, k the indexes in x-, y-, z-directions respectively and n the number of nodes. The temperature distribution seen by the helium pipe passing through this cell is T_{0jk}, with $j = 1, n$ and $k = -j$. Because the temperature field is periodic in z-direction: $T_{ijk} = T_{ij0}$, $\forall j = 1, n$, the helium pipe through $(0, 0, 0)$ sees the same temperatures as those along the periodic domain. In consequence, the flow is solved by applying the 1D conservation equations Eq. 1 to a single helium pipe and to the periodic domain, having both the same nodal temperatures in a counter flow disposition. The heat capacity of the tube wall is also taken into account by the balance of heat fluxes in the wall:

$$\dot{q}_{air\ j} + \dot{q}_{hel\ n-j} = -\frac{(m \cdot C)_{wall}}{n} \cdot \dot{T}_{wall\ n-j} \qquad (16)$$

$$j = 1, n \qquad (17)$$

being $(m \cdot C)_{wall}$ the heat capacity of the wall of one single pipe.

The mass flow and heat flux through the overall matrix equal the contribution of one single domain times the total number of tubes in the matrix. The number of discretization nodes is $n = 20$, equally spaced. The helium pipe has the same internal diameter and length as the tubes of the real module. The air duct cross sectional area is smaller than that of the periodic domain and equals the passage minimum area of the matrix:

$$\frac{A_{min}}{A} = \frac{2 \cdot e \cdot d \cdot L}{x_t \cdot d \cdot L} \qquad (18)$$

$$= \frac{2}{x_t}\left(\sqrt{x_t^2/4 + x_l^2} - 1\right) \approx 0.803, \qquad (19)$$

being A the surface of matrix perpendicular to the flow.

The distributed pressure loss in both the helium and air sides is computed from Eq. 10, with some adjustment of the correction coefficient k_f to match the module design pressure loss.

The length of the interface helium-air for the calculation of the heat flux, Γ in Eq. 5, is the pipe external perimeter. The Nusselt number on the helium side is computed with the following extension of the Dittus-Boelter correlation [3], valid from laminar through transitional to turbulent regimes:

$$Nu = (Nu_{lam}{}^{16} + Nu_{tur}{}^{16})^{1/16} \qquad (20)$$

$$Nu_{tur} = 0.023 \cdot Re^{0.8} \cdot Pr^{0.4} \qquad (21)$$

$$Nu_{lam} = 4, \qquad (22)$$

with the Reynolds number based on the hydraulic diameter D_h.

With respect to the heat transfer on the air side, Fig. 7(a) summarizes the survey carried out on previous works on heat transfer through a bank of staggered tubes in crossflow. The results shown are for the heat transfer in a square bank ($x_t = x_l = 2$) under the hypothesis of isothermal boundary condition. The analytical correlation of Khan for steady flow is close to the empirical results by Hausen. The steady quasi-3D numerical calculations of Nakayama where obtained over a bank of square tubes. The results for the unsteady fully developed flow calculations by Beale show that the staggered configuration is naturally unstable without any external excitation, hence the averaged Nusselt number is nearly the same in both cases: with and without the external stimulus. Finally it is the expression provided by Khan [7] the one used in the present application for being conservative respect to the numerical results and because it retains the influence of the matrix geometry in an analytical expression:

$$Nu = C \cdot Re^{1/2} Pr^{1/3} \qquad (23)$$

$$C = \frac{0.61 x_t{}^{0.091} x_l{}^{0.053}}{1 - 2 \cdot exp(-1.09 x_l)}, \qquad (24)$$

where the Reynolds number is based on the average speed in the passage minimum area and the external diameter of the tube.

Fig. 7(b) compares the values of Nusselt number by Khan and Hausen for the geometry and operational range ($Re \approx 300 - 600$) of the Scimitar precooler. The analytical expression of Khan for a single row of tubes in cross flow (blockage ratio $b = 0.55$) shows values very close to those of Hausen.

2.2.2. *Reheater*

The reheater (HX3) is located downstream of the preburner (PB) with the purpose of maintaining a constant inlet temperature to the helium turbine (T1) during any flight condition. It is composed by an inner and outer cylindrical shrouds with a number of plates N_p radially disposed between them. The gas from the preburner flows along the axis whereas the helium does it radially inward, from the outer to the inner shroud and through the plates, Fig. 8(a). The ratio of the passage span to its mean diameter is 2:5 but because the passage slenderness is very high (1:120) the curvature of the inner/outer shroud is deprecated and the passage assumed to be rectangular. Each plate is divided into a number n_z of strips, each one having a number N_t of square channels with a cross section of 1.5 x 1.5 mm^2. The helium streams flow along these channels in the direction of $r < 0$ and the gas flows along the direction $z > 0$ between the plates. The tangential pitch s_i is the one measured at the inner shroud in the real reheater, minor (hence critical) than the one at the outer shroud, Fig. 8(b).

Under the hypothesis of uniform boundary conditions on the gas inlet and outlet planes, only one fluid passage is discretized, being the total flow and heat flux N_p times that of a single passage. With the same assumption done for the helium, only one plate is representative of the whole reheater. The flow in the helium channels is solved with a pseudo-2D discretization of the plate in the *RZ*-plane: the flow inside each channel of the same strip is solved with a 1D discretization along the r-direction and n_z strips are considered along the z-direction. The thermal connectivities between the $n_z + 1$ fluid veins are established assuming that the wall temperature along the strip is constant and equal to the gas bulk temperature for each axial position: $T_{wall\ i,k} = T_{gas\ k}$ with $i = 1, n_r$ and $k = 1, n_z$, Fig. 8(c). The thermal capacity of the wall is taken into account when applying the energy

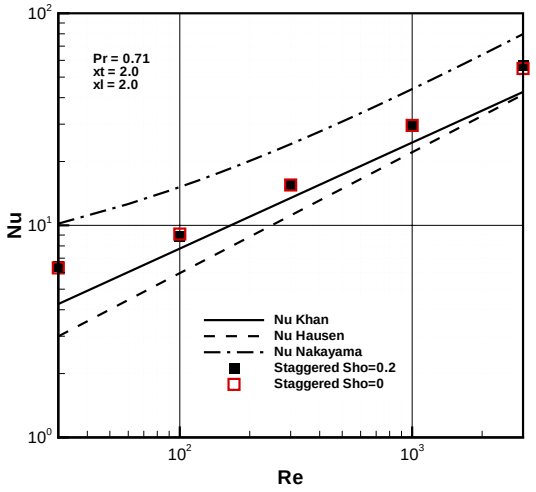

(a)

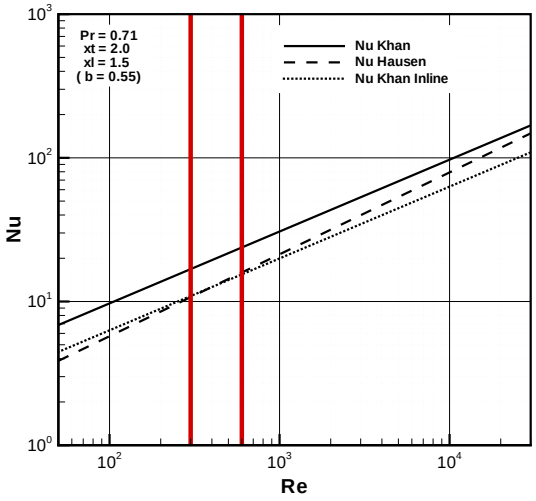

(b)

Figure 7: (a) Comparison of the Nusselt predictions by Hausen [8], Khan [7], Nakayama [9] and Beale [10] for the staggered square tube bank. The calculations of Beale were done with ($Sh_o = 0.2$) and without ($Sh_o = 0$) initial perturbation. (b) Comparison of the Nu predictions on the geometry of the precooler by Khan (Eq. 24) and Hausen [8]. The results of Khan for the single row in crossflow (Khan inline) [11] are shown as well. Scimitar operational range is shown between the red lines.

balance to the wall:

$$\dot{q}_{gas\ k} + \sum_{i=1}^{n_r} \dot{q}_{hel\ ik} = -(m \cdot C)_{wall} \cdot \dot{T}_{wall\ k} \qquad (25)$$

$$k = 1, n_z \qquad (26)$$

being $(m \cdot C)_{wall}$ the heat capacity of the wall of a single strip.

A discretization in $n_r = 5$ and $n_z = 10$ nodes is used respectively for the helium and gas flows. In the calculation of the heat flux into the helium and the combustion gas $\dot{q}$, in Eq. 5, the convective heat transfer coefficient is computed using the previous Eqs. 20-22, in which the Reynolds number is based on the hydraulic diameter:

$$D_h = 2s_i(D_o - D_i)/(2s_i + D_o - D_i). \qquad (27)$$

2.2.3. Regenerator

The regenerator comprises two types of units: helium-to-helium (HX41-44 and HX46-48) and helium-to-hydrogen (HX4H, HX4L and HX5), both of them are modeled as alternatively stacked layers of heating and cooling channels characteristic of the compact plate / channel micro heat exchangers [12]. Each unit contains a number M of modules circumferentially disposed around the engine axis. As in the previous cases, curvature effects can be disregarded as the ratio of the channel height to its radial position from the engine centerline is in the order of 10^{-4}. Each module has N rows of respectively M_h and M_c heating and coolant channels each being, the total number of channels per regenerator M x N x M_h x M_c. The channels are embedded in the same base material and the rows are disposed in counterflow, Fig. 9. The purpose of this geometry is twofold: firstly laminar regime can be achieved along the full length of the channels which minimizes the pressure drop. Secondly the cooling performance is significantly improved by the large increase of the heat exchange area, in the order of 10^4 m^2 per unit. Both heating and coolant channels have a cross section of 50 x 50 μm^2 and are count in a number of $\approx$ 10^7 per module, hence the 1D fluid field along any two hot and cold channels is representative of the overall module.

The energy equation applied to the wall is the same Eq. 17, for which now the air and helium flows refer to the heating and coolant channels respectively and $(m \cdot C)_{wall}$ is the thermal capacity of the complete matrix, the number of nodes being $n = 30$. The convective heat transfer coefficient in Eq. 5 is obtained by

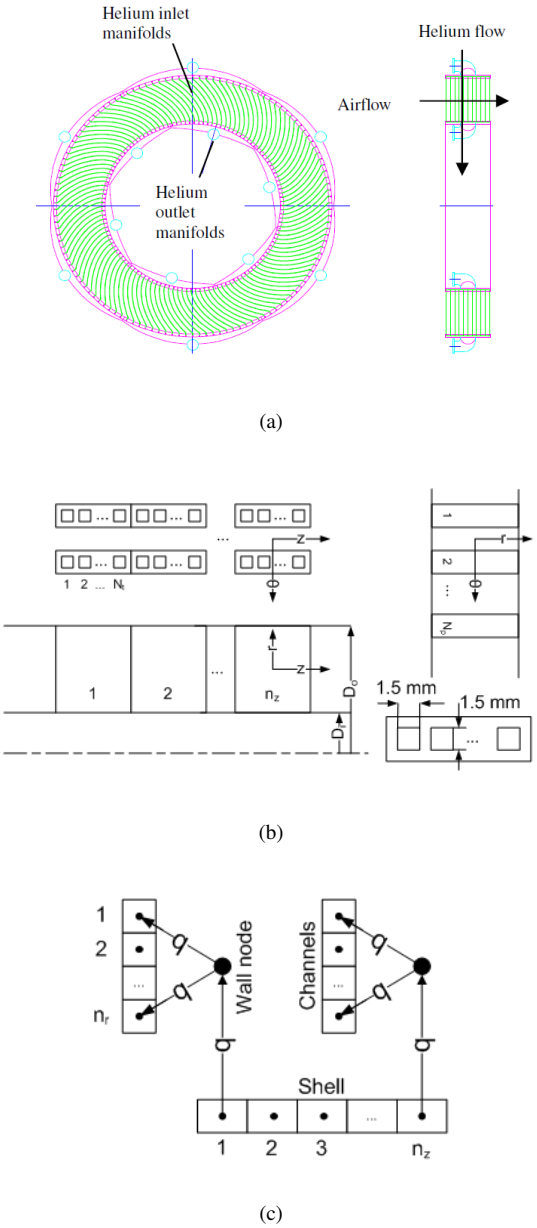

Figure 8: Reheater module: (a) frontal and side view [6], (b) geometrical definition of the numerical model and (c) thermal connectivities between gas and helium channels.

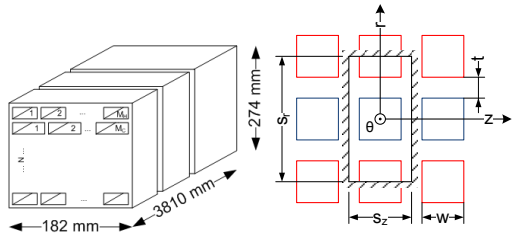

Figure 9: Geometry of the regenerator modules.

assuming a constant Nusselt number of 10 along the channels for both hot and cold streams.

2.3. Turbomachinery

They make use of steady experimental characteristics to predict the machine off-design performance in terms of its pressure ratio π, mass flow rate $\dot{m}$ and adiabatic efficiency η. The characteristic maps are given as functions of the corrected speed $\tilde{N}$ and the β-parameter:

$$\pi(\tilde{N},\beta)\,; \qquad \tilde{\dot{m}}(\tilde{N},\beta)\,; \qquad \eta(\tilde{N},\beta) \tag{28}$$

$$\tilde{N} = \frac{\Omega/N_d}{\sqrt{\theta}} \cdot \frac{30}{\pi_n} \tag{29}$$

$$\tilde{\dot{m}} = \dot{m} \cdot \sqrt{\theta_{in}}/\delta_{in} \tag{30}$$

In order to fulfill the performance at the design point, the turbomachine is resized applying constant factors to the characteristic map $(\Pi, \tilde{M}, H)$ of a known machine:

$$\pi = 1 + K_\pi \cdot (\Pi(\tilde{N},\beta) - 1) \tag{31}$$

$$\tilde{\dot{m}} = K_{\dot{m}} \cdot \tilde{M}(\tilde{N},\beta) \tag{32}$$

$$\eta = K_\eta \cdot H(\tilde{N},\beta) \tag{33}$$

The map of the helium turbine (T1) was computed from a CFD off-design analysis [13] of the counter rotating machine designed for Scimitar during the previous project LAPCAT I [14].

The maps of the air compressor and the other units in the regenerator are selected from the map database elaborated by Kurzke [15]. The compression stages of the regenerator are supposed to perform like a single stage mixed flow compressor, whose characteristics [16] are rescaled for each unit (C1-C8). The turbines T2 and T3 are based on the characteristics of the first stage of a highly loaded axial turbine [17]. In these helium machines, the correction for the working fluid is done by means of the parameter θ in Eqs. 29, 30:

$$\theta = R_{hel} T_{in}/(RT_{in})_{std}, \tag{34}$$

with R_{hel} the gas constant of the helium and in the denominator, the gas constant of the air and the standard total inlet temperature for which the map was obtained. The map of the air compressor corresponds to that of an axial high pressure core compressor [18].

The task of the helium recirculator (C9) is to increase the cooling through the precooler while flying at high speed for a short range of Mach numbers. Because it only overcomes the pressure loss through the high temperature module (HX1) and the regenerator (HX5), its consumption is very low ($\approx$ 100 kW) in comparison with the compression stages, which is ten times larger. Consequently its power is not accounted for in the engine evaluations. Moreover it is supposed to work continuously at an efficiency $\eta = 0.9$, no matter the mass flow or pressure ratio. This simplifies the engine model and accelerates the calculations. The liquid hydrogen pump (LHP), whose power is of the same order as that of the recirculator, is not included in the model for the same reason.

The energy balance yields that the mechanical power in the shaft equals the power to the fluid side:

$$P = \dot{m} \cdot \Delta h_t \tag{35}$$

$$P = T \cdot \Omega \tag{36}$$

$$\frac{\Delta h_{t,s}(p_{t_{in}}, T_{t_{in}}, p_{t_{out}})}{\Delta h_t} = \begin{cases} \eta; & (turb.) \\ 1/\eta; & (comp.) \end{cases} \tag{37}$$

In Eq. 37, $\Delta h_{t,s}$ is the total enthalpy change of an isentropic evolution from inlet to outlet status.

The excess of torque $T_{sh} - T$ accelerates the rotor, with inertia I:

$$T_s(\Omega; t) - T = I \cdot \dot{\Omega}, \tag{38}$$

This equation relaxes the mechanical constraint by allowing a difference between the torque applied on the shaft T_{sh} and the torque that the rotor transfers to the fluid T. In a similar way the constraint on the machine discharge duct is relaxed:

$$\dot{m} - \dot{m}' = \tau \cdot \ddot{m}', \tag{39}$$

being $\dot{m}$ the flow rate read from the map, $\dot{m}'$ the actual flow rate passing through the machine and $\ddot{m}'$ its time derivative. The time τ is a measure of the convective characteristic time in the duct of the turbomachine:

$$\tau \approx \frac{l_{c_{in}} + l_{c_{out}}}{2 \cdot a_{in}}, \tag{40}$$

where $l_{c_{in/out}}$ is the characteristic length of the inlet/outlet ducts and a_{in} the speed of sound computed

at the inlet of the machine. The solution of this differential equation must satisfy the constraint imposed by the discharge duct:

$$\dot{m}'(\dot{m}, \tau, t) = f(\pi; t), \tag{41}$$

where f is the characteristic of the discharge duct.

The combination of Eq. 28-38 establishes the form of the mechanical constraint on the operating point, $I_\Omega \equiv 0$; whereas Eq. 28, 30-32, 39 and 41 determine the constrain imposed by the discharge duct, $I_{\dot{m}} \equiv 0$. The solution of the system of equations:

$$\begin{cases} I_\Omega(\tilde{N}, \beta; K_\pi, K_{\dot{m}}, K_\eta, N_d, T_s, \vec{B}, \vec{P}; t) = 0 \\ I_{\dot{m}}(\tilde{N}, \beta; K_\pi, K_{\dot{m}}, f, \vec{B}, \tau; t) = 0 \end{cases} \tag{42}$$

$$\vec{B} = (\delta_{in}, \theta_{in}); \ \vec{P} = (\Omega_0, I) \tag{43}$$

is the transient operating line of the turbomachine $\tilde{N}(t), \beta(t)$ which, for a given machine size $\{K\}_{\pi,\dot{m},\eta}, N_d$, is determined by the inlet conditions $\vec{B}$, the discharge characteristic f and the mechanical constraint T_s. The integration constant Ω_0 is the initial shaft speed.If $\dot{\Omega} = \dot{m}_{out} = 0$, the previous system for the steady operating line is:

$$\begin{cases} I_{\Omega_0}(\tilde{N}_0, \beta_0; K_\pi, K_{\dot{m}}, \vec{B}, T_s \cdot N_d, \eta_0 \quad) = 0 \\ I_{\dot{m}_0}(\tilde{N}_0, \beta_0; K_\pi, K_{\dot{m}}, \vec{B}, f \qquad\qquad\quad) = 0 \end{cases} \tag{44}$$

Normally the turbomachine is linked to other fluid components like pipes, manifolds or heat exchangers and mounted on the same spool than other $m-1$ machines. The steady state of this assembly cannot be known a priori. However the stagnation pressures and temperatures in the fluid components can be approximated by those of the design cycle. These provide the inlet conditions $\vec{B}$ and the value f. The speed N_d, operating point $(\tilde{N}_0, \beta_0)$ and efficiency η_0 are design values. The size of the machines is then determined by m equations like Eq. 44 and the closure equation introduced by the common spool: $\sum_{i=1}^{m} T_{s_i} = 0$. Fig. 10 shows the input data and design values required for the matching of a compressor with a turbine on the same shaft.

3. Results

The performance of Scimitar in the air-turbo-rocket configuration is evaluated in the Mach range from Mach 2.5 to supersonic cruise at Mach 5. Understanding the behavior of this configuration is crucial as it constitutes the propulsive core of the engine, being the

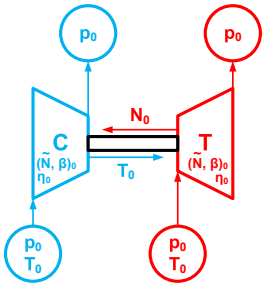

Figure 10: Input data to size the compressor-turbine matching.

turbofan and ramjet configurations subtle variations of it.

Exergy is the potential work that can be extracted from a system that interacts with the environment in a reversible manner. It is a measure of the quality of the energy contained by a system or transfered by a process in relation with the environment. It will serve to establish a common definition of the efficiency that can be applied without distinction to the overall engine as to its subcomponents.

The combination of the First and the Second Principle of Thermodynamics yields the expression of the exergy balance [19] in a control volume (CV):

$$\dot{E}_{CV} = (1 - T_0/T)\dot{Q}_T + \dot{W} + \tag{45}$$

$$+ \sum_i (\dot{m}\epsilon)_i - \sum_o (\dot{m}\epsilon)_o - \dot{I}, \tag{46}$$

where $\dot{E}_{CV}$ is the unsteady accumulation of exergy in the control volume and the terms in the right hand side account respectively for the availability transfer due to heat, work and mass exchange through the boundaries. The last term is the exergy destruction or irreversibility associated to the process taking place in the control volume. It is proportional to the entropy production $(\dot{\sigma}_p)$ and the environmental temperature (T_o) through the Gouy-Stodola theorem: $\dot{I} = T_o \dot{\sigma}_p$. The procedure to evaluate the specific exergy ϵ of the incoming (i) and outgoing (o) fluid streams is explained in Annex A. The specific exergy at each engine station is shown in Table 2. They are evaluated from the standard reference environment at $T_o = 288.15\ K$, $p_o = 1\ atm$ and relative humidity $\phi_o = 46\ \%$, which corresponds to a molar content of $7750 ppm$ of water in dry air at standard conditions [20].

Table 2 also shows the pressures, temperatures and mass flow rates corresponding to different stations of the Scimitar engine during cruise at Mach 5 and 25 km altitude. In this condition the by-pass duct is closed, hence the fan (F), hub turbine (HT), by-pass burner

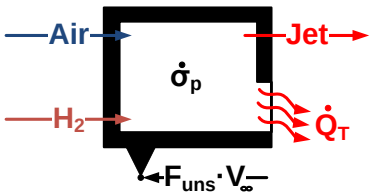

Figure 11: Control volume used in the effectiveness calculation.

(BB) and nozzle (BN) are not in operation (shadowed components in Fig. 2). The corresponding station numbering is shown in Fig. 2.

Applying Eq. 46 to the control volume in Fig. 11, which represents the engine, and considering stationary regime yields:

$$\underbrace{F_u\, v_\infty}_{\dot{W}_u} = \underbrace{(\dot{m}\epsilon)_{air} + (\dot{m}\epsilon)_{H_2}}_{\dot{W}_a} - \tag{47}$$

$$\underbrace{-T_0\dot{\sigma}_p + (1 - T_0/T)\dot{Q}_T - (\dot{m}\epsilon)_{jet}}_{-\dot{I}}, \tag{48}$$

where $\dot{W}_u$ is the useful propulsive power of the uninstalled thrust F_u at the flight speed V_∞ and $\dot{W}_a$ is the available power computed from the exergy inflow of air (station 0) and hydrogen (station 11). The rightmost term $\dot{I}$ is the irreversibility incurred by the system, composed by the internal energy waste, the heat released across the non adiabatic boundaries and the exergy lost with the exhaust jet (station 89). The non-adiabatic boundary is the nozzle wall, which is cooled by radiation to the ambient. The exergy lost with the jet is the inherent cost of generating thrust in the reaction engine. The uninstalled thrust is computed as:

$$F_u = \dot{m}_{jet} v_{jet} - \dot{m}_{air} v_\infty + (p_e - p_{atm}) A_e, \tag{49}$$

with v_∞ the flight speed, p_e and A_e the static pressure and cross area at the nozzle exit section and p_{atm} the atmospheric pressure at the given flight altitude. Based on the exergy balance of Eq. 48 a "second-law efficiency" or effectiveness can be defined as the ratio of useful to available power:

$$\eta_\epsilon = \frac{\dot{W}_u}{\dot{W}_a} = 1 - \frac{\dot{I}}{\dot{W}_a} = 34.3\% \tag{50}$$

Taken as a reference, the effectiveness computed by Etele for a turbojet cruising at Mach 0.8 ranged from 15% to 17.5% [21]. Scimitar doubles this effectiveness thanks to the thermal integration of the fuel in the cycle showing its enormous potential for very high speed fight.

The engine is a system with two degrees of freedom. The first one is the pair of values for the stagnation inlet temperature and pressure of the air, which are determined for the given ascent trajectory of the vehicle. The second is the fuel inflow or engine throttle, which directly acts on the engine thrust. Additional four engine variables are governed by control laws that set the engine off-design performance during throttling and acceleration towards supersonic cruise. They are the helium turbine inlet temperature, the air flow rates across both bypasses of the precooler modules and the helium flow in the recirculator loop.

Fig. 12 shows the regulation of the engine mass flows by these control laws while the engine accelerates from Mach 2.5 to Mach 5 for a constant mixture ratio of 43. The inlet temperature of the helium turbine is maintained at a constant value of $1000K$ by diverting fuel from the main combustion chamber (CC) towards the preburner (PB). The engine designer establish $635K$ as the maximum inlet temperature of the air compressor [1]. To fulfill this requirement the air from the intake starts flowing through the precooler (PC) at Mach 3 as the bypass (BP PC) closes gradually. The precooler reaches full operation above Mach 3.5. With respect to the regulation of the precooler temperatures, at Mach numbers less than 3.8, only the second precooler module (HX2) is needed to cool down the incoming air and the first module (HX1) is bypassed. Above Mach 4.8 the circulator (C9) and the additional regenerator module (HX5) increase progressively the flow of cool helium through the first precooler module (HX1) in order to maintain its temperature below $1000K$.

Fig. 13 shows the operational envelope of the Scimitar core. The flight Mach number and altitude are related through the A2 vehicle trajectory. The uninstalled thrust, effectiveness and specific thrust (defined as the ratio of uninstalled thrust to fuel mass flow) at each flight condition and fuel inflow values are shown. The domain of operating points is bounded by the turbomachinery operational limits, set by their respective characteristic maps as the maximum / minimum allowed values of the parameter β and the corrected speed.

4. Conclusions

Based on the existing capabilities of the European Space Propulsion System Simulation, appropriate models of the heat exchanger modules and the turbomachinery elements have been developed to better represent their physical behavior and therefore the

	Design point at Mach 5			
Station	$P\ [bar]$	$T\ [K]$	$\dot{m}\ [kg\ s^{-}]$	$\epsilon\ [kJ\ kg^{-}]$
0	14.1	1247	176.5	862
2	3.4	1247	176.5	744
25	3.1	853	176.5	416
3	2.8	633	176.5	255
4	12.1	971	176.5	612
11	18.0	20	4.05	129993
115	17.7	289	4.05	121872
12	16.7	832	4.05	125276
125	14.3	978	4.05	126569
14	14.3	978	0.04	126569
16	14.3	978	4.01	126569
5	10.3	995	176.5	642
6	10.2	997	176.5	643
CC	9.0	2615	180.6	-
PB	10.4	993	176.5	-
89	0.02	704	180.6	3569
3011	128.7	302	11.1	2940
3111	47.3	32	11.1	4351
3141	47.6	295	11.1	2317
32	199.1	587	33.3	3753
321	198.2	849	10.0	4507
322	198.2	849	55.1	4507
323	198.2	849	65.1	4507
324	198.1	842	33.3	4483
33	197.2	1001	97.4	5046
34	196.6	1000	88.4	5039
35	129.2	859	88.4	4269
356	48.4	596	22.2	2839
358	48.4	614	11.1	2856

Table 2: Cruise cycle at Mach 5. The corresponding stations can be seen in Fig. 2. The values of pressure and temperature are for stagnation conditions except for *CC*, *PB* and 89, which refer respectively to the values inside the combustion chamber, preburner and nozzle exit section.

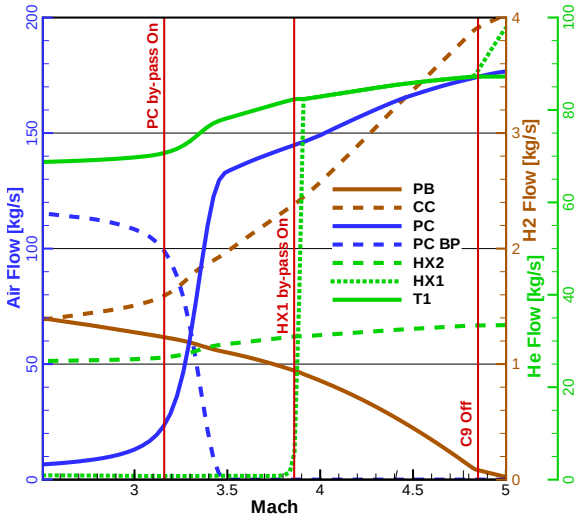

Figure 12: Engine mass flow rates during acceleration from Mach 2.5 to cruise at Mach 5 at a constant mixture ratio of 43.

model accuracy. The simulation of Scimitar in its air-turbo-rocket configuration provides the foreseen performance during supersonic cruise and that of the engine core during acceleration from Mach 2.5 to Mach 5 as well as its operational envelope. The dynamic nature of the model allows the introduction of control laws in a natural way.

Finally, the exergetic analysis provides a meaningful definition of the efficiency or effectiveness of the system, which is an indication of the engine degree of thermal integration within its environment. A crucial issue for high speed propulsion.

Acknowledgments

This work was performed within the Long-Term Advanced Propulsion Concepts and Technologies II project investigating high-speed air-breathing propulsion. LAPCAT II, coordinated by ESA-ESTEC, is supported by the EU within the 7th Framework Programme, Transport, Contract no.:ACP7-GA-2008-21 1485.

References

[1] F. Jivraj, R. Varvill, A. Bond, G. Paniagua, The scimitar precooled mach 5 engine, in: 2nd European Conference for Aerospace Sciences, EUCASS, Brussels, Belgium, 2007.

[2] L. R. Petzold, DASSL: Differential Algebraic System Solver, Tech. rep., Sandia National Laboratories, Livermore, California (1983.).

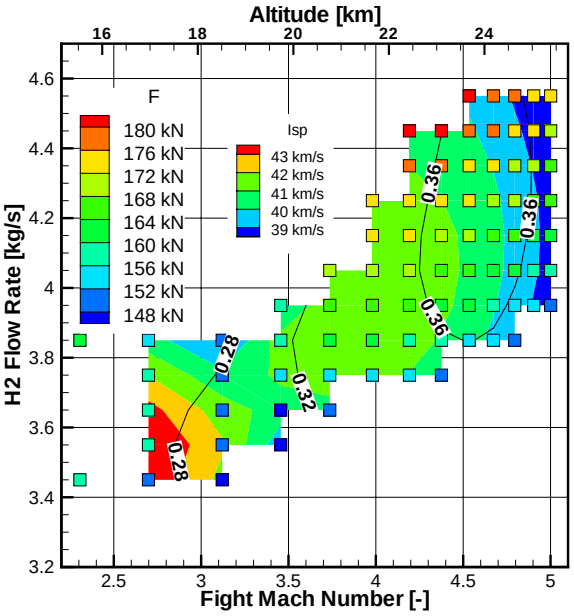

Figure 13: Scimitar core operational envelope. The filling color of each square indicates uninstalled thrust , the colored contours indicate the specific impulse and the effectiveness is shown by the contour lines.

[3] ESA, Astrium-Bremen, Cenaero, Empresarios Agrupados Int. and Kopoos, ESPSS EcosimPro Libraries User Manual, Tech. Rep. TN-4140, European Space Agency, version 2.0 (May 2010).

[4] S. W. Churchill, Friction-factor equation spans all fluid-flow regimes, Chemical Engineering 84 (24) (1977) 91–92.

[5] D. R. Bartz, Turbulent boundary-layer heat transfer from rapidly accelerating flow of rocket combustion gases and of heated air, Advances in Heat Transfer 2 (1965) 1–108.

[6] R. Varvill, Heat exchanger development at reaction engines ltd, in: 59th International Astronautical Congress, IAC-08-C4.5.2, International Astronautical Federation, IAC, Glasgow, Scotland, 2008.

[7] W. A. Khan, J. R. Culham, M. M. Yovanovich, Convection heat transfer from tube banks in crossflow: Analytical approach, International Journal of Heat and Mass Transfer 49 (2006) 4831–4838.

[8] H. Hausen, Heat Transfer in Counterflow, Parallel Flow and Cross Flow, McGrawHill, New York, 1983.

[9] A. Nakayama, F. Kuwahara, T. Hayashi, Numerical modelling for three-dimensional heat and fluid flow through a bank of cylinders in yaw, Journal of Fluid Mechanics 498 (2004) 139–159.

[10] S. B. Beale, D. B. Spalding, A numerical study of unsteady fluid flow in in-line and staggered tube banks, Journal of Fluids and Structures 13 (1999) 723–754.

[11] W. A. Khan, J. R. Culham, M. M. Yovanovich, Fluid flow and heat transfer from a cylinder between parallel planes, Journal of Thermophysics and Heat Transfer 18 (2004) 395–403.

[12] H. Webber, S. Feast, A. Bond, Heat exchanger design in combined cycle engines, in: 59th International Astronautical Congress, IAC-08-C4.5.1, International Astronautical Federation, IAC, Glasgow, Scotland, 2008.

[13] R. Bontempo, Performance analysis of a contrarotating turbine, Stagiaire Report VKI SR 2010-11, Von Karman Institute for Fluid Dynamics (June 2010).

[14] G. Paniagua, S. Szokol, H. Kato, G. Manzini, Contrarotating turbine aerodesign for an advanced hypersonic propulsion system, Journal of Propulsion and Power 24 (6) (2008) 1269–1277.

[15] J. Kurzke, Component map collection 2 (2004).

[16] Tech. Rep. 21-4460-2.3, Air Force Mixed-Flow Compressor Garrett Turbine Engine Company (1982).

[17] R. G. Stabe, W. J. Whitney, T. P. Moffitt, Performance of a high-work low aspect ratio turbine tested with a realistic inlet radial temperature profile, Technical Memorandum NASA-TM-83655, NASA (June 1984).

[18] N. Cumpsty, Jet Propulsion - A simple guide to the aerodynamic and thermodynamic design and performance of jet engines, Cambridge University Press, 1997, fig. 11.5, p.115.

[19] M. J. Moran, H. N. Shapiro, Fundamentals of engineering thermodynamics, 5th Edition, 2004.

[20] G. P. Anderson, S. A. Clough, F. X. Kneizys, J. H. Chetwynd, E. P. Shettle, Afgl atmospheric constituent profiles (0-120km), Scientific Interim AFGL-TR-86-0110, Air Force Geophysics Laboratory, Hanscom Air Force Base (1986).

[21] J. Etele, M. A. Rosen, Sensitivity of exergy efficiencies of aerospace engines to reference environment selection, Exergy, An International Journal 1 (2) (2001) 91 – 99.

A. Exergy Calculation

The exergy of a pure species X_k has two contributions: the physical exergy and the chemical exergy. The first one is due to changes in its thermo-mechanical state (p, T, v) with respect to the reference environment $(p_0, T_0, 0)$, which in a molar basis can be stated as:

$$\bar{\epsilon}_k^{ph} = \bar{h}_k(p,T) - T_0\bar{s}_k(p,T) + \quad (51)$$

$$+ \quad v^2 \cdot M_k/2 - \bar{g}_k(p_0,T_0). \quad (52)$$

The chemical exergy, in the case of species behaving as semi-perfect gas that are not necessarily present in the environment but produced from the chemical reaction of species present in it, takes the form:

$$\bar{\epsilon}_k^{ch} = \bar{g}_k(p_0,T_0) - \sum_i \nu_{ki}\,\bar{g}_i(y_i^0 \cdot p_0, T_0). \quad (53)$$

In the above expression y_i^0 is the molar fraction of species X_i^0 in the environment and ν_{ki} are the stoichiometric coefficients of the decomposition reaction of one mol of species X_k into the species of the environment $\left\{X_i^0\right\} = \{N_2, O_2, H_2O, Ar\}$:

$$\begin{gathered} N_a O_b H_c Ar_d \longrightarrow a/2 \cdot N_2 + \\ +(b/2 - c/4) \cdot O_2 + c/2 \cdot H_2O + d \cdot Ar \end{gathered} \quad (54)$$

$$[\nu_{ki}] = \begin{bmatrix} a_1/2 & b_1/2 - c_1/4 & c_1/2 & d_1 \\ \vdots & \vdots & \vdots & \vdots \\ a_k/2 & b_k/2 - c_k/4 & c_k/2 & d_k \end{bmatrix} \quad (55)$$

The species of the environment and their possible reaction products are at gaseous state, hence the exergy contribution by a possible phase change of the substance to its phase at the current utilization state is accounted by $\bar{\epsilon}_k^{ph}$; the Gibbs potential $\bar{g}_k(p_0, T_0)$ is evaluated for pure gaseous species.

If the fluid stream at pressure p and temperature T consists of an ideal homogeneous mixture of species with molar fractions y_k, then the total exergy can be written as:

$$\bar{\epsilon} = \sum_k y_k \bar{\epsilon}_k^{ph}(y_k \cdot p, T) + \sum_k y_k \bar{\epsilon}_k^{ch} \tag{56}$$

For a constant reference environment, different gas models can be used to evaluate respectively the physical and chemical contributions to the exergy if both provide the same values of enthalpy and entropy at the environmental state (p_0, T_0). It is the case while evaluating the exergy of hydrogen for the present analysis. The chemical contribution is computed from the CEA reference whereas the physical contribution is provided by the more accurate NIST real fluid database. Because the helium does not mix with any other fluid stream, there is no need of computing its chemical exergy, the values shown in Table 2 are the physical exergy contribution. For the air and combustion gases, which are modeled as semi-perfect gases, both exergy contents are evaluated from the CEA reference.

B. Reference Environment

The environment contains the main atmospheric constituents: nitrogen, oxygen, argon and water vapor. Its composition is computed supposing that it behaves as a mixture of steam and dry air such that the volumetric fractions of its constituents are:

$$y_k = (1 - y_w) y_k^{dry};\ k \in \{N_2, O_2, Ar\}, \tag{57}$$

where y_k^{dry} are the mols of N_2, O_2 and Ar per mol of dry air and y_w are the mols of water per mol of dry air. The composition of the dry air is kept constant as the atmospheric conditions p_o, T_o and water content vary: 78.12%, 20.96% and 0.92% in volume of respectively N_2, O_2 and Ar. The water content y_w is specified by means of the relative humidity ϕ, that relates p_o and the saturation pressure of the water at the given environmental temperature T_o:

$$y_w = p_w^v(T_o)/p_o \cdot \phi. \tag{58}$$

STATIC AND DYNAMIC STABILITY IN TRANSONIC FLOW

Experimental Determination of the Dynamic Derivatives of a Reentry Capsule in Transonic Supersonic Regime

Sébastien Paris

Aeronautics and Aerospace Department, von Karman Institute for Fluid Dynamics, Belgium, paris@vki.ac.be

Patrick Rambaud

Associate professor, Aeronautics and Aerospace Department, von Karman Institute for Fluid Dynamics, Belgium, rambaud@vki.ac.be

University Supervisor: Gérard Degrez

Professor, Université libre de Bruxelles, Belgium, gdegrez@ulb.ac.be

Abstract

Aerodynamic damping is investigated in the subsonic and transonic regimes for re-entry vehicles. Static moment, free oscillations and forced oscillations experiments are carried out on replica models in the von Karman Institute (VKI) S-1 supersonic-subsonic wind tunnel. The frequency of oscillations induced in wind tunnel is made to match the reduced frequencies of flight vehicles based on their natural frequencies. In free oscillation mode, the inertia of the vehicle is adjusted for the same reason. Recent results on this vehicle with a sting as support are compared with existing data in literature and with a previous campaign carried out in the VKI-S1 with a transversal support on a different experimental set-up. It shows significant effects of the support on the static and dynamic measurement. Proper validation of the methods should give better confidence into the results for the dynamic characterization of the vehicles.

Nomenclature

Symbols

α	Angle of attack, rad
θ	Pitch angle, rad
C_D	Drag cofficient, -
C_L	Lift coefficient, -
C_m	Pitching moment coefficient, -
$C_{m_q} + C_{m_{\dot{\alpha}}}$	Pitching moment derivatives, rad^{-1}
q_∞	Dynamic pressure, Pa
ρ_∞	flow density, kg/m^3
St	Strouhal number, -

Abbreviations

CG	Center of Gravity
CTV	Crew Tranport Vehicle
SLA	Stereolithography

1. Introduction

Entry capsules provide an attractive option for planetary exploration missions. Designed to survive during early phases of atmospheric entry, these vehicles often become dynamically unstable at low altitudes. Proper characterization of aerodynamic damping can allow drogue chute deployment at lower Mach number. Such findings may permit smaller drogue chute designs, thus enabling a payload volume and weight increase as well as a vast decrease in drag penalties.

The aerospace vehicle is exposed to unsteady flow fields that may have significant effects on its characteristics of motion. As a result, the dynamic stability information, considered of rather lesser importance for a number of years, has became an object of relatively high interest. The reason is obvious: in the past, for aircrafts at low angles of attack, most of the dynamic stability parameters were relatively easy to predict analytically. It had only a relatively insignificant or at least, a relatively constant effect on the resulting flight characteristics of the vehicle. With the

advent of flight at high angles of attack at high speeds, all that has drastically changed. The dynamic stability parameters are now found to depend strongly on the non-linear effects and can no longer be calculated using relatively simple linear analytical methods as in the past and new methods are needed. Since the non-linear instability phenomena are not well known for the moment, it is in general difficult to simulate them using CFD. Thus, the experimental techniques in wind tunnels are certainly the best way to obtain dynamic stability information at realistic Reynolds and Mach numbers.

2. Objective

The objective of this project is to develop the experimental tools for the study of the dynamic stability in the subsonic and supersonic range. The wind tunnel S1 was selected for this purpose. Different experimental technique need to be implemented in it. The free oscillation technique consists in releasing the model in a given position and observing the model oscillating around its axis. It gives directly the behavior of the model. The forced oscillation technique does not give directly the characteristic of the model. Oscillations are forced by a crankshaft mechanism and the pitching moment is measured during the oscillations thanks to a balance. These techniques have been developed and used with various reentry vehicle and need to be properly validated in order to assess the uncertainty of the methods.

3. Theory

3.1. Motion equations

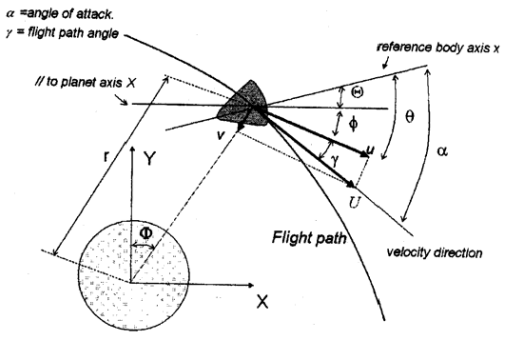

Figure 1: Space vehicle entering the atmosphere [2]

The motion of a space capsule during planetary reentry can be seen, by classical mechanics, as a combination of translation and rotation around its center of gravity. The classical equations of motion of the vehicle are obtained using a fixed system of coordinates, and assuming the vehicle to be rigid. Then one can deduce the six equations governing the movement of the object in the three dimensions. However since the system obtained is quite complex to solve (impossible analytically), one usually makes some assumptions: the displacement is made in two dimensions, the rotation of the earth is neglected and the gravity force is constant.

In the wind tunnel, the angle of attack and the pitch angle are equals:

$$\theta = \alpha \Leftrightarrow \gamma = 0 \tag{1}$$

A set of three equations governing the movement of the vehicle in two dimensions can be obtained:

$$m\frac{dU_x}{dt} = q_\infty S C_D \tag{2}$$

$$m\frac{dU_z}{dt} = q_\infty S C_L - mg + m\frac{U^2}{r} \tag{3}$$

$$I\ddot{\theta} = q_\infty S C_m D \tag{4}$$

This third equation represents the rotation of the capsule around his pitch axis. The pitching moment coefficient can be rewritten depending on the other parameters:

$$C_m = \frac{\partial C_m}{\partial \alpha}(\alpha - \alpha_0) + C_{m_q}\frac{D}{2U}\dot{\theta} + C_{m_\alpha}\frac{D}{2U}\dot{\alpha} \tag{5}$$

C_m may be separated into two parts (recalling that α and θ are equivalent here):

- a static one: $\frac{\partial C_m}{\partial \alpha}(\theta - \theta_0)$
- and a dynamic one: $\left(C_{m_q} + C_{m_{\dot{\alpha}}}\right)\frac{D}{2U}\dot{\theta}$

Hence the equation 4 can be written:

$$I\ddot{\theta} = q_\infty S C_{m_\alpha} D(\theta - \theta_0) + q_\infty S \frac{D^2}{2U}\left(C_{m_q} + C_{m_{\dot{\alpha}}}\right)\dot{\theta} \tag{6}$$

This equation describes the motion of the model around its pitching axis. The C_{m_α} coefficient is the static coefficient which can be known thanks to the static measurement of the pitching moment.

The aim of the present activities is to determinate the dynamic coefficient: $C_{m_q} + C_{m_{\dot{\alpha}}}$.

3.2. Similarity parameters

The experiment conditions are based on the similarity with flight data. The similarity can be made on several parameters, but it is usually impossible to make all of them respected in the same time. As a consequence, one has to choose which ones are of primary importance. Geometry of the model is of course one of them and means that the model should be a scaled representation of the vehicle outer shape. In order to reproduce correctly the movement, the CG location of the flight vehicle should correspond to the center of rotation of the wind tunnel model. Another important parameter to match while performing experiments in transonic and supersonic regime is the Mach number. Here, the experiments deal only with Mach numbers high enough not to neglect the compressible effects, and hence the Mach number similarity has to be applied. Finally, the third parameter to match for the similarity concern is the oscillations reduced frequency. This non-dimensional number is very similar to a Strouhal number, but is based on the frequency of the model oscillations and not on a frequency relating to the flow. It is assumed that this parameter should be matched in order to obtain the same aerodynamic behavior as in flight. The reduced frequency matching depends on the test technique that is used and its computation is presented below. It is worth to mention that the Reynolds number similarity, which is very often a major concern in fluid dynamics experiments, cannot be fulfilled in the classical facilities: it is in fact much lower for the experiments than for the flight due to the large scaling factor, while the other parameters do not changed a lot. However, it is usually admitted that the stability phenomena are affected by the flow regime (meaning laminar or turbulent), and not much by the exact matching of the Reynolds number. For the similarity of this study, the flow in flight is certainly fully laminar and as the Reynolds number reached during experiments is much lower than the one of flight, one can assume that the flow is completely laminar for experiments as well as for the flight.

3.3. Reduced Frequency (Strouhal Number)

The reduced frequencies of both the model and the flight vehicle for the forced oscillation tests should be maintained to equate the dissipation or input of energy from the surrounding flow field (aerodynamic influences) on the model during testing with the flight vehicle. It is defined by the Strouhal number (St). Oscillations occur at the natural frequencies of the actual flight vehicle upon atmospheric re-entry condition. Thus, during free and forced oscillations tests on the models, the Strouhal number based on the natural frequency and characteristic length of the flight vehicle is used. The general formulation is given by:

$$St = \frac{fD}{U_\infty} \tag{7}$$

Extraction of the natural frequency f of the flight vehicle is obtained from the 'spring' and 'damping' constant in equation 6.

$$f_{flight} = \frac{1}{2\pi}\left(\sqrt{\underbrace{\frac{q_\infty S\, D\, |(\partial C_m/\partial\theta)|}{I}}_{static\ restoring\ moment} - \underbrace{\left(\frac{q_\infty S\, D\left(C_{m_q} + C_{m_{\dot\alpha}}\right)}{2I}\right)^2}_{aerodynamic\ damping}}\right)_{flight} \tag{8}$$

The aerodynamic damping can be neglected due to its magnitude relative to the static restoring moment contribution. Thus, the Strouhal number of the flight vehicle becomes:

$$\begin{aligned}(St)_{flight} &= \left(\frac{fD}{U_\infty}\right)_{flight} \\ &= \left(\sqrt{\frac{\rho_\infty S\, D^3\, |(\partial C_m/\partial\theta)|}{8\pi^2 I}}\right)_{flight}\end{aligned} \tag{9}$$

ρ_∞ is the free stream density. The respect of the similarity provides the value of the inertia and of the driving frequency respectively for the free and forced oscillations:

$$I_{experiment} = \left(\frac{I}{\rho_\infty D^5}\right)_{flight} \times \left(\rho_\infty D^5\right)_{experiment} \tag{10}$$

$$f_{experiment} = \frac{1}{2\pi}\left(\sqrt{\frac{\rho_\infty S\, D^3\left(-\frac{\partial C_m}{\partial\alpha}\right)}{2I}}\right)_{flight} \times \left(\frac{U_\infty}{D}\right)_{experiment} \tag{11}$$

4. The free oscillations technique

For this technique, the model is free to rotate around an axis passing by the CG location. It is release in a position different of the trim angle. The model is then free to oscillate around the trim angle. The incidence angle is recorded over time. In order

to simplify the writing of the equation of motion, it is replaced by a more general form:

$$\ddot{\theta}(t) + a\dot{\theta}(t) + b\theta(t) = 0 \tag{12}$$

where a and b are two coefficients

One can obtain the damping in pitch parameter from the resolution of this equation with:

$$C_{mq} + C_{m\dot{\alpha}} = -\frac{I\alpha}{q_\infty S D \frac{D}{2U_\infty}} \tag{13}$$

4.1. Envelope Method

The method used for the resolution of the differential equation and the extraction of the damping in pitch parameter is the envelope method. It consists in using only the maximum or the minimum value of the signal for each oscillation, and in computing the logarithmic decrement between two extrema. For a theoretical second order signal, the oscillations damping is computed by:

$$a = \frac{2}{nT} \ln\left(\frac{x_2}{x_1}\right) \tag{14}$$

T is the period of the signal x_1 and x_2 are two extreme values separated by n periods.

In computing the damping over the whole signal (either by using the first and the last extremum or by making an envelope fitting of the whole signal), a single value is found for the damping in pitch parameter. However, due to the large variation of the oscillations amplitude during the tests, it appeared that this method is too global and does not take into account the possible changes in the damping term: it is not satisfactory.

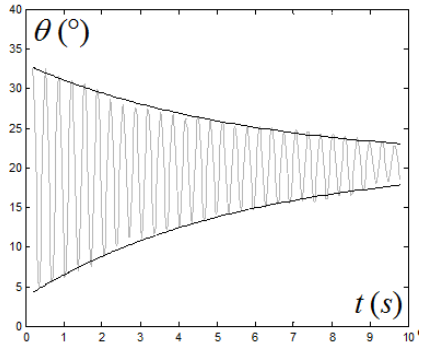

Figure 2: Envelope curves

On the opposite, by calculating the damping value between each two consecutive maxima or minima, the experimental uncertainty has a large influence on the results, which are therefore very scattered and not usable properly. As a consequence, what it seems to be the best technique is a compromise between the two: the use of about seven oscillations of the signal to perform the average damping over them gives results of a quite accuracy and without a large scattering.

5. The forced oscillations technique

Models oscillate with one degree of freedom over a fixed range of oscillation angles in a periodic pattern. The forced oscillations induce moments on the model in addition to the aerodynamic loads. Moments and incidence angles are recorded over time. Contrary to the free oscillations equation of motion, the equation for forced oscillations cannot be solved directly for the damping in pitch parameter because of the mechanical moments, which cannot be evaluated independently from the actual experiments. However, in performing the so-called no flow measurements (which consist in forcing the oscillations of the model, with the wind tunnel not working), one gets the following equation of motion (like the equation 5 without the aerodynamic terms):

$$I\ddot{\theta}(t) - c\dot{\theta}(t) - k\theta(t) = M_{nf}(t) \tag{15}$$

$M_{nf}(t)$ is the external forcing moment as a function of time in no flow conditions. Then, in computing the difference between the equation 15 with flow and without flow, one finds:

$$q_\infty S D \frac{D}{2U_\infty}\left(C_{mq} + C_{m\dot{\alpha}}\right)\dot{\theta}(t) + q_\infty S D C_{m\alpha}\theta(t) = M_{nf}(t) - M_f(t) \tag{16}$$

$M_f(t)$ is the external forcing moment as a function of time in flow conditions In a more general form, it gives:

$$A\dot{\theta}(t) + B\theta(t) = \frac{\Delta M(t)}{qS D} \tag{17}$$

The mechanical moments as well as the inertial part of the original equation of motion do not appear anymore for the resolution of the problem. However, the use of the two sets (with and without flow) of experiments requires absolutely the equality in the evolution of the angle of attack ($\theta_f(t) = \theta_{nf}(t)$ at every instant). One can obtain the damping in pitch parameter from the resolution of this equation with:

$$C_{mq} + C_{m\dot{\alpha}} = A\frac{2U}{D} \tag{18}$$

The principle of the energy resolution consists in integrating the work absorbed by the system (corresponding to amplification) or dissipated (corresponding to damping) during one oscillation cycle. In fact, since the mechanical friction is not null in the driving system, some energy injection is always necessary to compensate the losses. The energy is injected by the power supply. Depending on the loop direction (see figure 3), one can deduce if the system oscillations would be amplified or damped while subjected to free oscillations. The first case is represented by a counter clockwise loop associated to a dissipation of energy, whereas the second situation is associated to a clockwise loop associated to an input of energy.

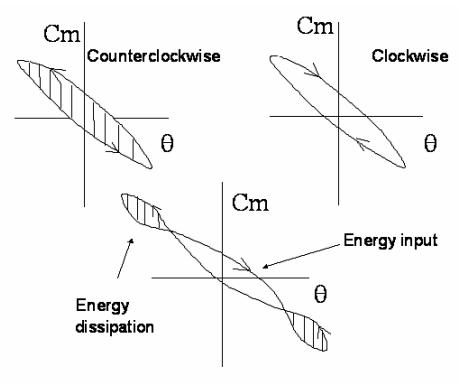

Figure 3: Energy method representation

The general expression of the damping in pitch parameter is the following [2]:

$$C_{m\dot{\alpha}} + C_{mq} = \frac{\oint C_m d\theta}{\int_T \dot{\theta}^2 dt}\frac{2U}{D} \tag{19}$$

One can notice that, as the graphical representation has shown it, the damping in pitch parameter (about which it has been said that a negative value means dynamic stability) and the pitching coefficient integral are of the same sign.

6. Equipment

6.1. Supersonic / Transonic S-1 Wind Tunnel

The VKI supersonic/transonic wind tunnel S-1 is a continuous closed circuit facility of the Ackeret type, driven by a 615 kW axial flow compressor. Two 40 cm x 36 cm test sections are used: a contoured nozzle with M = 2.0 and a slotted transonic section with variable Mach number, from 0.4 to 1.05. The tunnel is equipped with scani-valves for pressure distribution measurements, multi-component strain gage balances, and a free-to-tumble mounting system for investigations of dynamic stability of aerospace vehicles.

Mach	P_0	p_∞	$Re_{L_{ref}}$	T_0	ρ_∞	U_∞
-	Pa	Pa	-	$°C$	$kg.m^{-3}$	$m.s^{-1}$
0.5	26685	22514	169306	26	0.2755	168.72
0.6	26681	20891	198116	32	0.2558	203.42
0.69	26772	19421	223702	40	0.2374	234.54
0.8	26695	17565	247673	48	0.2151	269.50
0.89	27710	16248	262591	56	0.2000	299.32
2.0	9430	1193	875900	25	0.0249	519.25

Table 1: Typical Flow conditions

6.2. Experimental setup

Several experimental setups have been designed and build over the years for the static and for the dynamic measurement.

6.2.1. Static experiments

First configuration

The first experimental setup was built during the CTV phase A and one of the purposes was to cover the full domain of interest for the AEDB (360°). The figure 4 shows the next setup where a stepping motor was added in order to rotate the model during the test. The reference length is 50mm, the diameter of the capsule . Static force and moment measurements are now possible in a range of [-225;+225°]. Axial and normal forces are measured by two strain gage balances implemented in the arms. The stepping motor and the angle measurement digital device are mounted on this balance so that all aerodynamic efforts are applied on the balances.

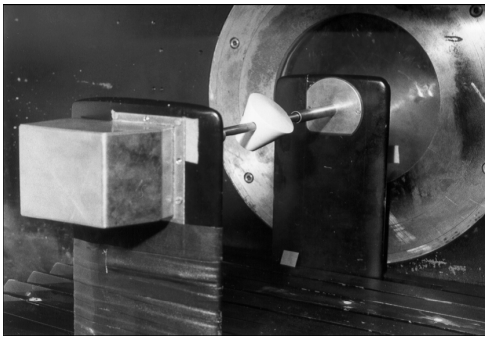

Figure 4: Experimental setup for the static test(improved)

The main interest of this setup was the possibility to measure the aerodynamic effort for any angle of attack but the presence of the transversal support interferes with the flow and can introduce significant error.

Second configuration

The second configuration is similar to the first one but the balance and the driving mechanism are not in the wind tunnel but outside. The setup designed for the dynamic testing (see figure 8) was used for this purpose.

Last configuration

For the recent testing, the support is now a sting. The model for the static measurement is made in Ureol; a light material easy to machine. The reference length is 77mm in order to install the equipment inside (balances, encoder, oscillating mechanism). The balance was designed to fit into the model along the symmetry axis. The center of reduction of the balance is close to the center of mass for a better sensitivity (figure 5 and figure 6).

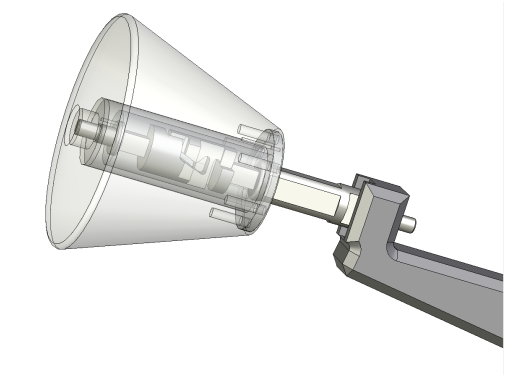

Figure 5: Model for the static tests with the balance

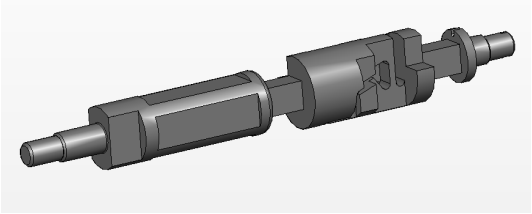

Figure 6: Balance for the static measurement

6.2.2. Dynamic experiments

Old configuration

The free to tumble setup used for the first campaign was developed during a previous study and modification was done in order to improve the quality of the angular measurement. The encoder is now able to give the angular position with 0.18° of accuracy. The picture (Figure 7) gives a general view of the set-up in the wind tunnel. The rod is mounted on two ball bearings and linked to the encoder in one side and to the release system on the other side. It is possible with this technique to know the exact angular position for an infinite range. When the center of gravity is not on the axis of symmetry, it is necessary to add a mass to equilibrate the model. Otherwise, the trim position is influenced by the actual position of the center of gravity and do not depend only of the aerodynamic characteristic. The model is made of foam and resin and the reference length is 50mm.

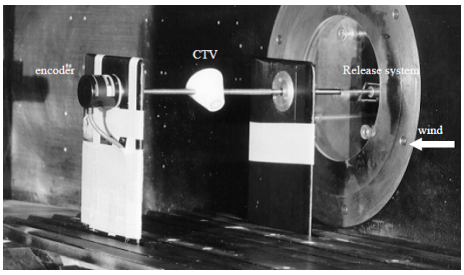

Figure 7: First Set-up for free to tumble test

Second configuration

A new setup was developed for the VKI S1 wind tunnel to support a model by a transversal rod. This rod is linked to a mechanism able to supply an oscillating movement or it is free to tumble. In this last case, an effort was made to limit the friction of the bearing to a minimum level. For this purpose, ceramic ball bearings were used because friction is very low when they are used without lubrication. A magnetic encoder will measure the angular position with high accuracy (4096 steps/revolution). In order to adjust the inertia of the model, a mass can be add on the support but the complete system must be as light as possible to reach the lowest value of inertia. For this purpose, particular care will be taken in the choice of material for the oscillating elements.

The previous experience shows problems in releasing system. It was not fast enough and it was difficult to adjust accurately the initial position. A new system was designed to allow fast and accurate

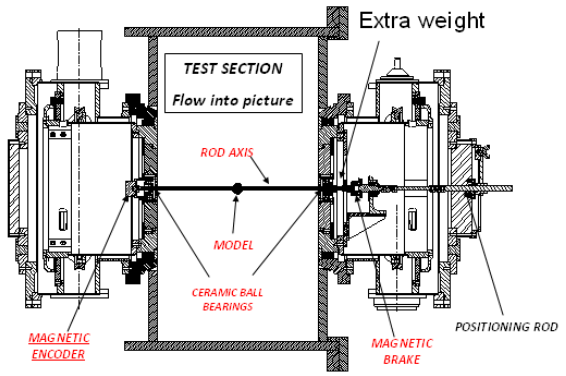

Figure 8: Experimental setup for free oscillations testing

angular release position. It is made of a small disk attached to the transversal rod and an electromagnet. This one can be operated by the operator thanks to a secondary axe passing through the wind tunnel.

New configuration

Like for the static efforts, when using a transversal support, the support disturbs the flow topology and produce significant error on the pitching moment measurement. The new setup was designed in order to produce the oscillations of the capsule through a sting. Since the aim of the study is to measure the forces applied on the capsule while oscillating. The setup is rather complicated (figure 9, 10 and 11):

- A big electrical motor is fixed outside the wind tunnel. It drives the model with the required frequency and amplitude.
- The rotation of the motor is transformed into oscillations thanks to an eccentric system.
- A secondary sting is then animated of periodic forward / backward translation movement inside of the main sting.
- The diameter of the main sting is selected to avoid excessive flexion during the tests campaign.
- Inside of the model, a static piece supports the encoder and the axis of the model.
- This axis is oscillating thanks to a crankshaft system and the balances are fixed on the axis.
- Interfaces between the balances and the model are adjusted together and should give a perfect trim position of the model.
- One optical encoder is fixed inside the model.
- For these dynamic measurements, the center of gravity is very important. It means that the center of rotation of the capsule should correspond to the center of gravity.

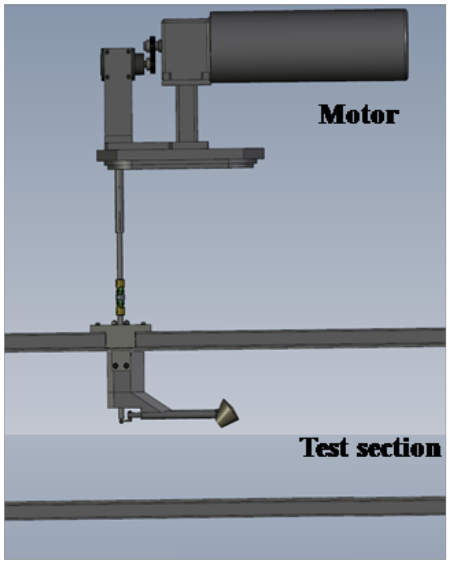

Figure 9: Overview of the dynamic set up

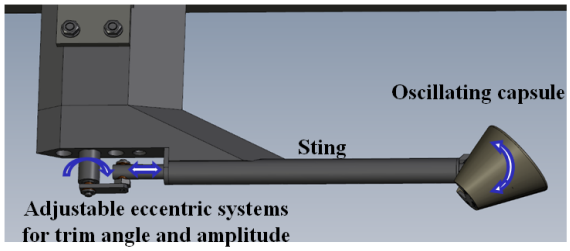

Figure 10: Zoom in on the oscillating system

The model is constructed in several parts which are then assembled on the balances which are fixed on the axis. The figure 11 gives a view of the different pieces composing the model.

To obtain the forces applied on the model during the experiments, an aerodynamic balance was designed (balance VKI3822). Two of them are placed inside the model for a better symmetry and so, a higher accuracy.

The four arms of the balance behave like four beams. The arm distortions are followed by the different distortion gauges stuck at different places on each arm. The center of reduction of the balance is located

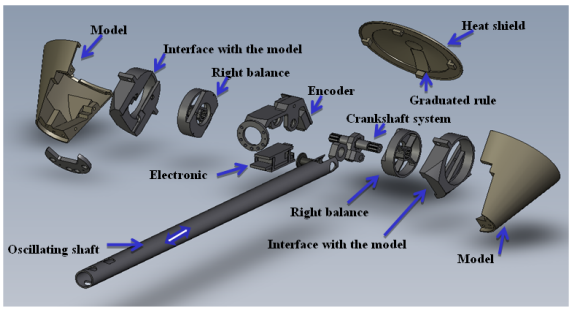

Figure 11: different pieces constituting the model

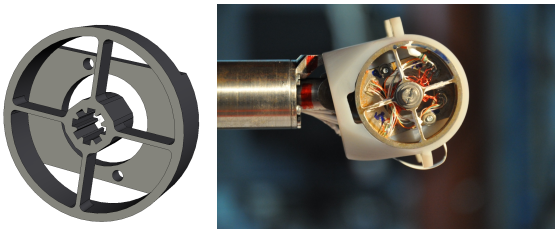

Figure 12: Dynamic balance

on the axis of rotation. The balance allows also the measurement of the axial and normal force in order to compensate for interferences.

7. Models manufacturing

As mentioned before, the model has to be light whatever the technique used. In case of free to tumble model, the model is light in order to respect the similitude and when the forced oscillation technique is used, the mass is reduced as much as possible in order to decrease the inertial part of the moment and increase the accuracy. Over the years, the technique used to build the model has changed. First models were built from foam and resin and the shape was obtained by casting. The problem of the casting was the accuracy of the shape of the model. Then, SLA prototyping was used because of the complexity of the model but this technique does not allow to control the shape of the model and the location of the CG. The last improvement consists in mixing the SLA for the complexity and the classical machining for the quality. It is the more precise way to build a model but improvements are still needed to decrease the uncertainty in CG location.

8. Results

Many results have been obtained over the years. This part gives typical results obtained with the CTV model.

8.1. Static tests

During the first campaign, the moment can be measured over a large range of angle of attack and the model is supported by a transversal rod. The results are given in the figure 13. The figure 14 shows the same measurement with the new setup. The range of angle of attack is limited to 15°. The slope is similar but the trim angle is very different ($\alpha \approx -40°$ for the first campaign and $\alpha \approx -17°$ for the second). These last measurements have been compared with literature data and good agreement is found (see figure 15). It clearly indicates the strong influence of the support for this kind of measurement.

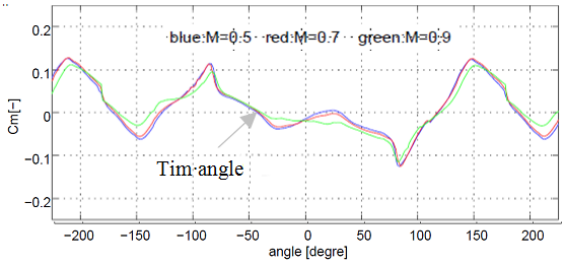

Figure 13: Pitching moment on CTV in transonic regime (first Setup)

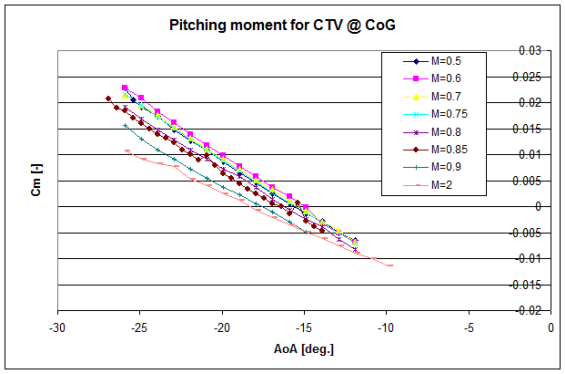

Figure 14: Pitching moment coefficient on the CTV capsule (new setup)

8.2. Dynamic tests

The dynamic test carried out during the first campaign consisted in qualitative measurement. The purpose of the tests was to measure the trim angle (figure

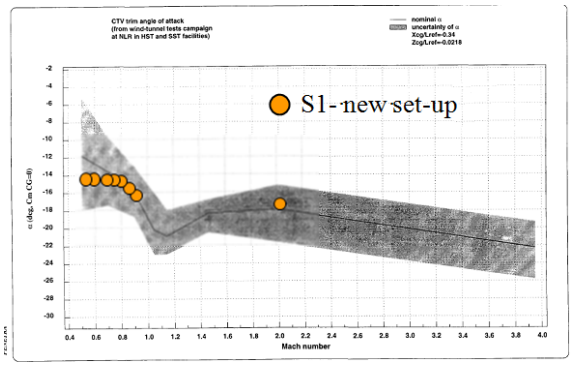

Figure 15: Trim angle of the CTV capsule (new set-up versus literature)

15) and to estimate the range of angle of attack for which the model is dynamically stable (see figure 16 and table 2). It can be noted that the dynamic trim angle is the same than the static one. The support was the same and produced the same effect. The phase diagram indicates clearly if the model is stable or not and it can be compared with static result. The trim points found by static experiments are confirmed with the dynamic setup and each of these points is stable.

model Mach # release angle	CTV Heavy 0.5 final angle	0.7 final angle	0.9 final angle
10	42.2 / 42.4	42.3 / 42.4	39.8 / 39.9
55	42.5 / 42.3 / 42.4	42.4	39.9
80	42.4	42.5	40.1
100	42.8 / 42.4 / 42.5	42.5 / -30.7	40.1 / 40.2
130	42.4 / 42.5 / LO / >>	42.6 / -30.7	40.2
155	42.4	42.5 / 42.4 / -30.7 / LO / >>	170.7
180	42.4 / LO / >>	171.4	40.3 / 40.4
200	42.4 / -34 / LO / >>	42.5 / -31.1 / LO / >>	40.3
225	>>	>>	>>
245	>>	>>	40 / 39.9 / LO / >>
270	43.6 / -34 / -33.8	42.5 / -31.1	40.2 / 38.9
310	42.3 / 42.4 / -33.8	42.5	40.1 / 40.2
330	-33.9 / -33.8	-31	40.3 / 40.2 / 39.6
0			

>> full rotation
LO : continuous Large Oscillation

Table 2: Final position of the CTV Capsule

The more recent dynamic experiments were performed with the forced oscillating mechanism supported by a sting. Experiments are carried out for various frequencies of oscillation in order to assess the sensitivity of this parameter. The damping parameter is computed using the energy method described before. For the CTV, the results are given in the figure 17. It shows the domain of similitude between 0.002 and 0.003. In this range, $C_{mq} + C_{m\dot{\alpha}} \approx$

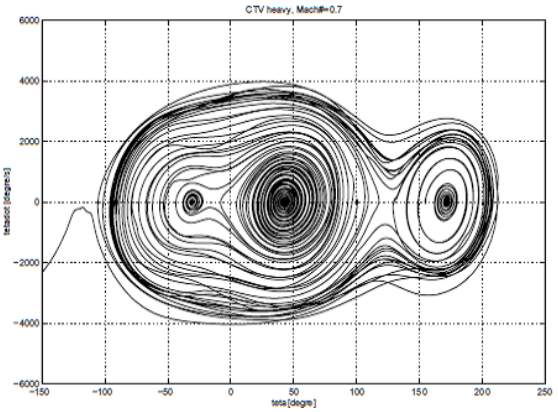

Figure 16: Phase diagram of the CTV capsule at Mach=0.7

+0.7. That means the vehicle is dynamically unstable. It is noted that for higher Strouhal number, the damping parameter is suddenly increasing. It happens for Strouhal =0.003 at Mach number of 0.9 and for Strouhal =0.006 at Mach number of 0.5.

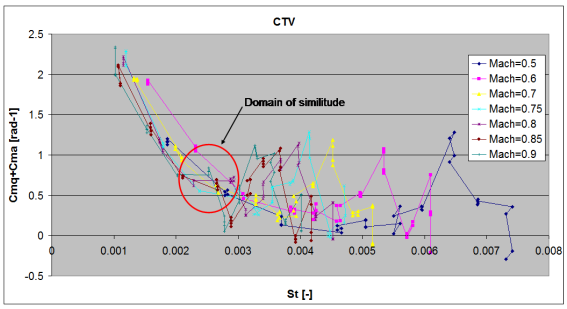

Figure 17: Damping parameter for the CTV capsule in subsonic regime

Dynamic results are given in the figure 18 for supersonic flow. For the CTV capsule, in the range of similitude, the damping parameter is clearly negative indicating stable behavior. A stable capsule in supersonic regime becoming unstable in subsonic is usual and not surprising. The phase diagram (only available for the subsonic regime) was showing opposite behavior, the vehicle was stable between Mach =0.5 and Mach=0.9

9. Error analysis

It is now clear that the transversal support introduced error. The recent experiment, carried out with a sting seems to give results of higher quality. Many aspect of the uncertainty have been studied. The error due to the balance is proportional to the one on

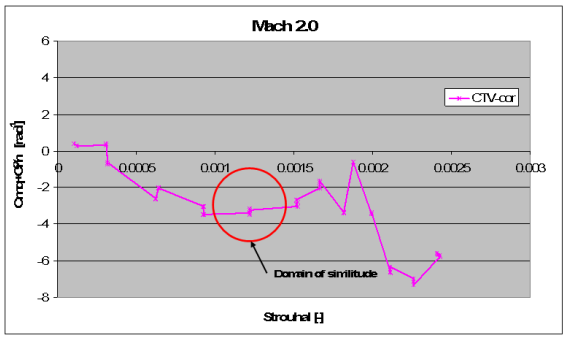

Figure 18: Damping parameter for the CTV capsule in supersonic regime

the damping coefficient (2.3%). The repeatability is good and the flow properties are very accurate. The more critical sources of uncertainty are coming from the CoG location, the balance stiffness, and the support effect. Many efforts have been done to respect the CoG and error is expected to be relatively small (err<0.1mm). For the balance stiffness, a small shift in angle can happen between angle deduced from the rotation of the main driving shaft and the real angle. Under the maximum load of the balance, its flexure does not exceed 0.07° which corresponds to a shift on the main shaft of a bit less than 1°. The associated error on the damping parameter is deduced to be less than 35 %. It is not possible to quantify the effect of the support because the reference value is not known.

10. Lesson learnt

During this project, models were designed and machined for static and dynamic experiments. In the last campaign, the static model was supported from the base through a balance. Due to the high sensitivity of the CoG location, very special care has to be taken to locate the center of reduction of the balance on the CG. An error of positioning of 0.1mm in the y direction produces a significant error on the trim angle. The model for the dynamic testing was much more complex as it must include the oscillating mechanism, two balances and the encoder. The fast prototyping technique allows producing light model with complex shape but results in not extremely accurate model. For this project, the outer shape of the model was further machined after assembly of all the elements with classical machining. At the end of this second step, some errors are still present in the positioning and it is suggested to investigate more on the way to produce the model for future campaign.

The forced oscillation mechanism allows adjusting the amplitude and the frequency of the model up to the required frequency to respect the similitude. The main difficulty came from gaps between pieces. The bronze bearing should be replace by ball bearing or needle bearing in order to guaranty the movement with minimum friction and minimum gap for every couple of piece. The sting itself was big compare to the capsule. A significant part of the base of the model was removed to allow the passage of the sting. It is known that the sting introduce error in the force measurement but it should be minimize as much as possible. The design was made with such big sting to avoid the flexion. Our experience from this campaign let us believe that the diameter can be further reduced.

The instrumentation for the static measurement is limited to the balance and the encoders used to measure the angle of attack. The balance should of course be correctly calibrated and special measurement must be taken in order to define precisely the location of the center of reduction. As explained before the definition of the trim angle of attack is very sensitive to the location of the center of reduction. For the dynamic experiment, two balances are used. The purpose of using two balances was to keep a good symmetry in the efforts, so that the interferences are limited. Possible improvements for the balance are the size and the stiffness. It is evident that the space in the capsule being limited, a smaller balance would help in the integration phase. Due to the strong oscillations during experiment and the gap between pieces, the balance must withstand high angular acceleration and deflection can be observed. A possibility is to increase the stiffness of the balance or to take it into account in the post-processing. The measurement of the angle of attack during the oscillating tests was initially expected to be measured by an encoder inside the model. It was finaly decided to use an encoder outside the wind tunnel on the driving mechanism but the gaps between pieces introduced significant error and should be corrected by a correct modelisation of all the interfaces. If possible, the angle of attack should be measured as close as possible of the capsule in order to avoid the multiple corrections.

The results for the static effort are in agreement with reference data for CTV. When compared to the measurement performed in the past at VKI with a transversal support, a large deviation is observed on the trim angle of attack. The transversal support is suspected to induce perturbation in the wake and to influence the measurement. Difference on the trim angle was about 20°. In the field of another ESA contract,

same kind of conclusion was done for the EXPERT vehicle. Both static and dynamic results are different depending on the support used (sting or transversal).

The CTV was already tested in the past with the transversal support and with the free to tumble technique. First of all, as already mentioned before, the trim angle was very different from the one obtained in the present campaign. Secondly, the dynamic behavior of the capsule was clearly stable over a large range of angle while it is now unstable. It is difficult to give a clear conclusion at that point about this difference. Possible source of error were discussed in the section 9. The support is one of the sources of uncertainty but the error cannot be assessed in the field of the present experiment.

The interference of the support on the flow has been shown by comparison between the present results and a previous campaign on CTV. This problem has also been demonstrated with the EXPERT vehicle by comparing the results from VKI and result from ITAM and SibNIA [17] on the same geometry but with a different supporting device. In both case the difference is significant for the static and dynamic testing. More investigation should be done to assess the support effect. As it is not possible to make experiment in wind tunnel without any support, it is proposed to investigate this effect with numerical tools. The first step consists in static computation in order to assess the effect of the supports and how they can affect the flow. In a second step, unsteady computation should be done on a static model. Comparison with existing experimental results should help in a better understanding the support effect and the topology of the flow. The final objective is to perform unsteady CFD on an oscillating capsule. Damping parameters can then be calculated with the same technique than the one used in wind tunnel.

11. Future work

Many results have been obtained with different experimental techniques. These results can be very different from one technique to another one and need to be properly validated. That will be the last part of this work. The purpose is to impose on the model a damping perfectly known when forced oscillations are applied. The method to deduce the damping parameter can then be used and results can be compared with the reference. Eddy current break was selected to impose a well-known damping. The advantage is to be able to vary the coefficient and eventually to impose a damping function of the angle of attack. This validation will give more confidence into the method used to found the dynamic derivative. As explained before, the support plays an important role in the results. CFD tools will be used to assess the effect of the support. Better understanding of the flow around the model and the sting should help in choosing the best configuration to be used in wind tunnel to found the dynamic derivative.

12. References

[1] S. Paris and J.M. Charbonnier, "Aerodynamic force and moment measurements and dynamic characterization of an Apollo capsule in the VKI S-1 wind tunnel", VKI, Internal note, 1997

[2] O. Karatekin, "Aerodynamics of a planetary entry capsule at low speeds", VKI, PhD thesis, 2002

[3] J. Yunis, "Analysis of forced oscillation, sting and tare force tests of subsonic and supersonic reentry vehicles", VKI, Stagiaire report, 2007 [4] E.S. Hanff, "Direct forced oscillation techniques for the determination of stability derivatives in wind tunnels", AGARD lecture series n°114 "Dynamic stability parameters", 1981

[5] G.E. Burt and J.C. Uselton, "Effect of sting oscillations on the measurement of dynamic stability derivatives", Journal of aircraft, Vol.13 n°3, 1976 [6] "Experimental determination of dynamic stability parameters", VKI, Lecture series 2008-02 , 2008

[7] R. Fail, "Experimental determination of stability and control aerodynamic characteristics", VKI, Lecture series 80 "Aircraft stability and control", 1975

[8] D.M. Tang and E.H. Dowell, "Experimental investigation of three dimensional dynamic stall model oscillating in pitch", Journal of aircraft, Vol.32 n°5, 1995

[9] S. Paris, J. Ouvrard and B. Torgler, "Free and forced oscillation testing of Apollo, Pares and Expert capsules", VKI, Contract report, 2008

[10] D.I. Greenwell, "Frequency effects on dynamic stability obtained from small amplitude oscillatory testing", Journal of aircraft, Vol.35 n°5, 1998

[11] F.Y. Wang, O. Karatekin and J.M. Charbonnier, "Low speed aerodynamics of a planetary entry capsule", Journal of spacecraft and rockets, Vol.36 n°5, 1999

[12] E.S. Hanff and C.O. O'Leary, "Oscillatory test techniques", AGARD report n°776 "Special course on aircraft dynamics at high angles of attack: experiments and modelling", 1991

[13] L.E. Ericsson and J.P. Reding, ”Review of support interference in dynamic tests”, AIAA Journal, Vol.21 n°12, 1983

[14] K. Orlik-Rckemann, ”Review of techniques for determination of dynamic stability parameters in wind tunnels”, AGARD lecture series n°114 ”Dynamic stability parameters”, 1981

[15] B.L. Uselton and F.B. Cyran, ”Sting interference effects as determined by measurements of dynamic stability derivatives, surface pressure, and base pressure for Mach numbers 2 through 8”, AEDC-TR-79-89, 1980

[16] L.E. Ericsson, ”Support interference”, AGARD lecture series *n*°114 ”Dynamic stability parameters”, 1981

[17] S.Paris, A. Karitonov, J. Ouvrard SR 4000-VKI. Tool for the study of dynamic stability of reentry vehicle in the transonic/supersonic regime. Determination of aerodynamic damping coefficient of the Expert vehicle in transonic regime. Sept. 2010.

MULTIPHASE FLOW

Multi-Phase Fluid Hammer: Modeling, Experiments and Simulations

Marcos Lema

Environmental and Applied Fluid Dynamics Department, von Karman Institute for Fluid Dynamics, Belgium, lema@vki.ac.be

Supervisor: Patrick Rambaud

Associate Professor, Environmental and Applied Fluid Dynamics Department, von Karman Institute for Fluid Dynamics, Belgium, rambaud@vki.ac.be

Supervisor: Jean-Marie Buchlin

Associate Professor, Environmental and Applied Fluid Dynamics Department, von Karman Institute for Fluid Dynamics, Belgium, buchlin@vki.ac.be

University Supervisor: Fernando López Peña

Professor, Naval and Oceanic Engineering Department, University of A Coruña, Spain, flop@udc.es

Abstract

The operation of spacecraft propulsion systems is regularly faced with adverse fluid hammering effects during the priming phase. This manoeuvre is done by fast opening of an isolation valve and the classical water hammer taking place involves multiphase phenomena, such as cavitation and absorption/desorption of a non-condensable gas. Due to the lack of experimental studies modelling the spacecraft's hardware, the physical models implemented in the numerical codes cannot be validated properly when computing the corresponding overpressures during priming with a multiphase flow. Hence, a new experimental facility reproducing all the physical phenomena taking place in the propellant lines during the priming has been built, and the experimental data is used to validate the physical models. Two CFD codes are used to model the flow configuration and the numerical results presented as X-t diagrams reveal a complex multilayer configuration prior to the fluid hammer occurrence, which certainly affects the speed of sound in the fluid and changes the pressure surge produced during priming.

Keywords: Multi-phase flow, fluid hammer, water hammer, cavitation, absorption, desorption, priming, spacecraft propulsion.

1. Introduction

When a satellite is launched to the space, its propulsion system is initially inactive, with the liquid propellant confined in the tanks and isolated from the nozzles and catalyst beds by three valves, as sketched in figure 1. Once the spacecraft has been ejected from the launcher vehicle, the evacuated propellant lines are filled with pressurized liquid propellant. This maneuver is called "priming" and is carried out by the fast opening of a pyrotechnic isolation valve. This induces a fluid hammer pressure front that may turn out to be critical if the corresponding overpressures are not correctly taken into consideration in the pipe line and sub-system dimensioning. Furthermore, since the propellant lines are initially vacuum pumped or filled with a non-condensable gas (NCG) at low pressure, the classical water hammer includes various multiphase phenomena, such as cavitation and boiling front. Finally, the driving pressure gas can be absorbed into the liquid propellant during storage and can desorb during the priming process.

Due to the complexity of these multiphase phenomena occurring in spacecraft hardware, there are very few literature references describing experiments with all the specifications of the above configuration, and which are necessary for a proper validation of the physical models implemented in the CFD codes.

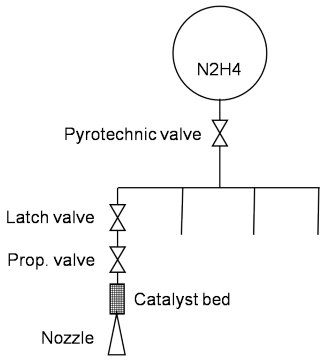

Figure 1: Monopropellant propulsion system configuration

Nowadays, various numerical codes are able to accurately predict the liquid compressibility effects when computing a single-phase fluid hammer but they still need to be extended and calibrated for cases with cavitation and two-phase flows. Furthermore, the numerical treatment of a dissolved NCG in the liquid phase needs to be improved. In both cases, the existence of a well documented experimental database is mandatory for the improvement and validation of these physical models. Even if it is possible to find numerous studies dedicated to the fluid hammer, the references dealing with the priming process are not so numerous and the data available is not sufficient for validation purposes.

A first group of reference deals with the explosive decomposition of hydrazine due to the adiabatic compression produced at the liquid propellant front. In these studies, such as Briels and Hollenbaugh[1], [2], Hutchinson and Schmitz[3] and Bunker et al.[4], the purpose was not to study priming directly, but the adiabatic compression that may be a consequence of it. In fact, liquid hydrazine is known to undergo exothermic decomposition when the liquid is heated under quasistatic conditions. These studies used both U-shaped tubes or fast opening valves to create the pressure raise compressing the hydrazine, but the test conditions have been poorly described. Bunker et al.[4] used, to our knowledge, high speed imaging for the first time to visualize the hydrazine liquid front, capturing the formation of foam at the gas-liquid interface. The authors described this foam as nitrogen bubbles surrounded by thin layers of liquid hydrazine. When the foam experiences a compression due to the accelerated liquid column, the nitrogen bubbles are heated adiabatically and the generated heat is transferred to the hydrazine layer.

A second group of references are specifically dedicated to the analysis of flow transients during the priming process, using both experimental and theoretical/numerical approaches, on simplified test configurations or the whole propulsion system, where the authors tried to evaluate the risk of adiabatic detonation or the integrity of the piping system facing water hammer pressure surges. In this category we can list the studies from Yaggy [5], Prickett et al.[6] Molinsky[7], Martin et al.[8], Joh et al.[9] and Morgan[10]. The main conclusions of these studies are: unsteady friction plays an important role, the two-phase phenomena are directly linked to the pressure surge amplitude and water can replaced MMH (monomethylhydrazine) as test fluid, producing pressure surges higher than the MMH and is, therefore, conservative. Several authors attempted to model the priming process using dedicated numerical tools, such as Lin and Baker[11], Navickas et al.[12], Ounougha and Colozzi[13], Leca et al.[14] and Hern[15]. In most of the cases, the simulations have been done with 1D simulations where two-phase phenomena were not taken into account.

Finally, two references are closely related to the present study, Gibek and Maisonnneuve[16] and Lecourt and Steelant[17], where the main objective were to model experimentally the priming process taking place in satellites and to create an experimental database for validation purposes. Gibek and Maisonnneuve used both real propellants and water, while Lecourt and Steelant used only inert fluids. The authors of these studies concluded the existence of a boiling front from the start, resulting in a local two-phase mixture of vapour and liquid. Furthermore, the NCG initially present in the test pipe get compressed when the valve opens and the liquid front travels downstream. Since this compression occurs very fast, it is mainly adiabatic at the boundaries, producing an intense mixing and heat transfer at the multiphase liquid-vapour/NCG front. Lecourt and Steelant[17] also studied in detail the evolution for the first pressure peak, where a multiple step evolution before reaching the maximum pressure value was observed, and gave some hypothesis to explain this behaviour.

2. Objectives

The aim of this work is to study the fluid hammer phenomenon in a confined environment with both experimental and numerical approaches. The experimental results come to complete the data already available in the literature, but using an experimental set-up which can reproduce all the physical phenomena taking place in the propellant lines during prim-

ing. The numerical investigation is done with 1D and 3D CFD codes and their results are compared against the experimental data. This comparison will allow the improvement and validation of the physical models implemented in the codes.

3. Experimental facility

A new experimental facility has been built at the von Karman Institute and includes all the elements of a satellite propulsion system directly involved in the fluid hammer occurrence: a pressurized liquid tank, a fast opening valve (FOV) and a given length of pipe line. The main objective during the design phase was to conceive a facility without singular elements such as elbows and T-junctions upstream the FOV, and with the same inner diameter in every flow conduction. It is well known that these geometrical singularities create secondary pressure waves, which complicate the general pressure measurements interpretation. Furthermore, the absence of these elements simplify considerably the numerical modelling of the facility and, thus, the results validation.

The facility layout is shown in figure 2, which is intended to be clamped on a vertical wall. The main components are a pressure vessel, a fast opening valve (FOV) and a given length of the propellant line, referred to as "test element" hereafter. Three test element configurations are used: straight, 90° elbow and T-bifurcation. The test elements are made with the same titanium tube of $1/4''$ and following the same construction rules used for aerospace applications. The facility also includes a vacuum system to set the test conditions (test element initially vacuum pumped or filled with a NCG gas at low-pressure). The characterization of the wave front induced by the fluid hammer is achieved through interchangeable measurement modules attached to the bottom end of the test element. Two types of measurement modules are proposed in this study: an instrumented module with unsteady pressure and temperature transducers and a transparent module made out of quartz for flow visualization with high speed imaging. The test vessel is a spherical accumulator that can mount an elastic membrane and it is equipped with an ultrasonic transducer to measure the speed of sound in the liquid. The purpose of the membrane is to avoid the absorption of the NCG during the liquid pressurization, allowing to run experiments with "pure" liquid. These test results provide very useful information to understand how the dissolved gas affects the fluid hammer mechanism. Furthermore, since the working liquid is already saturated with air in standard conditions during storage, the fluid needs to be deaerated to run experiments without any dissolved gas. The liquid deaeration is done by means of a depressurization process using a second accumulator, called deareation vessel, connected to the vacuum pump. The dissolved gas is removed by keeping the liquid in a low-pressure atmosphere. This facility allows to work with inert fluids and nitrogen as driving pressure gas.

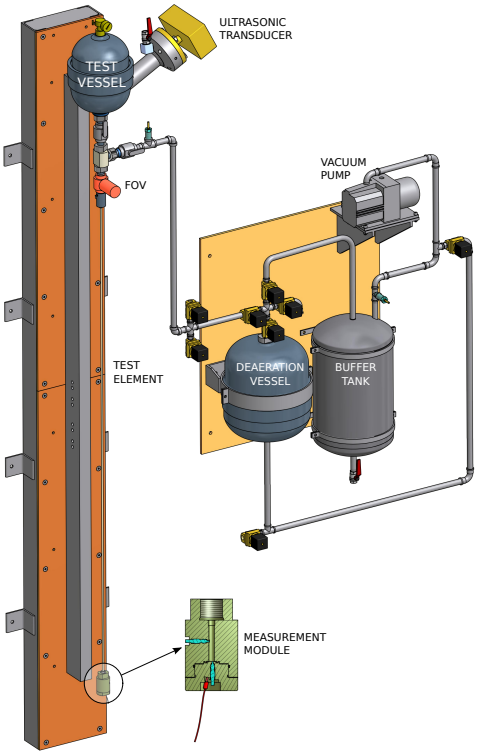

Figure 2: Experimental facility layout

4. Numerical tools

The numerical study is carried out with two commercial codes: EcosimPro/ESPSS and CFD-ACE+. EcosimPro is a 1D simulation tool, object-oriented and capable of computing steady state and transient physical processes. The code employs the European Space Propulsion System Simulation (ESPSS) library [18], which is needed to model all aspects of a functional propulsion system. This is achieved by four

libraries: **Fluid_properties** library, a database with the properties of most of the fluids used for aerospace applications, **Fluid_flow_1d** library, which allows 1D transient simulation of two-fluid, two-phase flows, and **Tanks** and **Turbo_Machinery** library, to model tanks, pumps, turbines and compressors. Based on the simplified facility, the schematic view shown in figure 3 was done in EcosimPro with generic elements from the ESPSS library. The model configuration is quite straightforward with this code, where the main parameters that the user needs to set are the initial conditions of pressure and temperature in every flow element, the mass fraction of NCG dissolved in the liquid and the valve opening law.

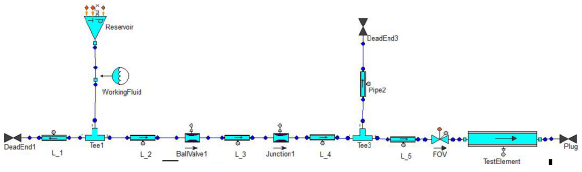

Figure 3: Schematic view of the simplified facility under EcosimPro

The second numerical code used in this study is CFD-ACE+, a general 3D computational fluid dynamics and multiphysics solver. This commercial code has been updated with a full cavitation module, which allows to work with a homogeneous mixture of liquid, vapour and NCG (with absorption and desorption), to model non-isothermal flows and liquid compressibility for fluid hammer simulations. In this module, cavitation is solved with a method where turbulence is taken into consideration in the bubble growth and collapse computation [19]. Regarding the liquid compressibility, the module proposes several models for different liquids. There are two models for water compressibility: Rouleau [20] and Elansary [21], one model for oil by Rouleau, and two models proposed by Onera for ethanol and MMH.

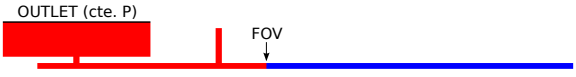

Figure 4: 2D domain and initial conditions configuration for the CFD computations

The numerical simulations with CFD-ACE+ are carried out on a 2D domain shown in figure 4, which includes the liquid tank and the geometry of the piping network. The test conditions are set separately upstream and downstream the valve, as sketched in figure 4, where red colour represents the pressurized liquid, and blue colour the vacuum pumped test element. The valve opening process is done using the grid deformation capability of the code.

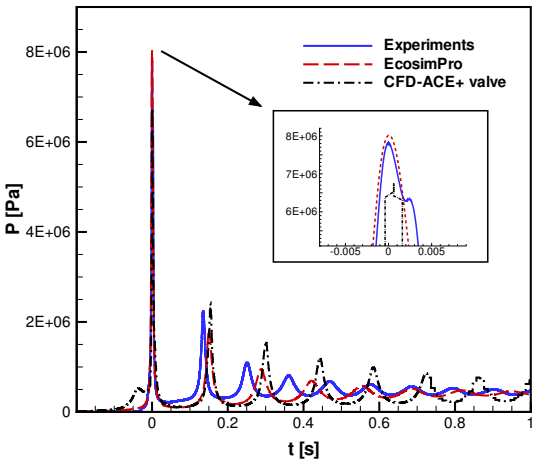

Figure 5: Experimental and numerical results comparison with test conditions $P_t = 0.4\,MPa$ and $P_p = 10\,kPa$

Figure 5 shows the comparison of preliminary experimental measurements with the data obtained with the numerical codes EcosimPro/ESPSS and CFD-ACE+ modelling the same set-up. The comparison with EcosimPro/ESPSS results gives a reasonably good agreement for the first pressure peak, although the computed pressure level is slightly higher. Furthermore, even if the successive pressure spikes are always higher in the experiments, the damping of the successive pressure peaks is also very consistent with the experimental data. The CFD results show a slightly lower first pressure surge but higher successive pressure peaks. On the other hand, the time delay between peaks computed numerically with both codes is rather similar. The fact that the numerical codes are not consistent with the pressure level estimation, and looking to the frequency of the peaks , it looks like the liquid velocity is predicted too low. This might be due to the difficulty of evaluating the friction for an accelerated, multiphase flow. On top of that, the speed of sound modeling a liquid/gas mixture needs to be improved in both codes, since this value looks over-predicted. Anyway, these first results show that both codes are already able to compute the fluid hammer phenomenon during priming, providing a good estimation of the first pressure surge.

5. 2D presentations of the results: X-t diagrams

Although the numerical codes are not yet fully validated when modelling the priming operation, they are already powerful tools to analyse the fluid hammer phenomenon. Therefore, EcosimPro/ESPSS has been chosen to validate the facility design. In this case, the test conditions are set to $P_t = 2\,MPa$ and $P_p = 1\,kPa$, using water and nitrogen as working fluids in the $2\,m$ straight test element configuration. Since the pipe flow can be assumed one-dimensional, the numerical results can be presented using X-t diagrams. These diagrams allow temporal and spatial representation of the flow in the same graph, where the x-axis corresponds to the position along the test element, and the time is plotted in the y-axis. Figure 6 shows the X-t diagram obtained with the EcosimPro results, where the colour levels represent the pressure amplitude. The pressure evolution at the bottom end of the test element P_{wh} is plotted at the right side of the figure for a better understanding.

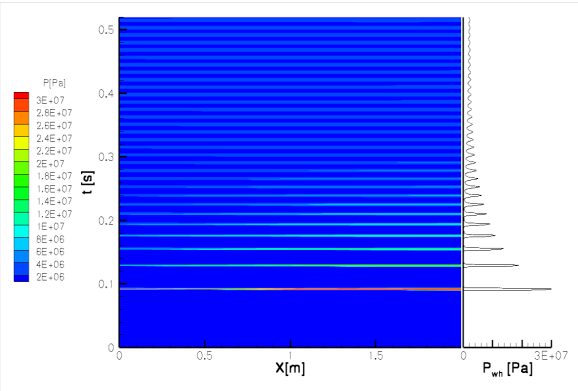

Figure 6: X-t diagram for the pressure variable

According to the Joukowsky equation, the kinematic energy is converted into pressure, leading to a pressure peak of $30\,MPa$. In the X-t diagram the pressure raise produced by the fluid hammer appears as parallel stripes, whose thickness is equivalent to the pressure spike bandwidth at each location of the test element. The stripes colour intensity decreases as one moves upwards on the diagram (in time), which shows, as in the 1D pressure evolution diagram, that the pressure spikes are damped in time until its complete attenuation. On the other hand, the pressure amplitude also decreases from right to left (in space), showing that the pressure raise decreases while travelling along the pipe. Thus, the 2D map is a valuable tool of analysis, providing information that can not be obtained with a 1D history recording.

6. Multiphase behaviour of the liquid front

The fluid hammer produced in the present flow configuration involves several multiphase phenomena, including vaporous and gaseous cavitation. Vaporous cavitation occurs when the local pressure drops below the vapour pressure and gaseous cavitation occurs when the local pressure drops below the saturation pressure of the NCG dissolved in the liquid[22]. That is why the most complex features taking place occur when the liquid front faces the vacuum conditions in the test element, i.e between the opening of the FOV and the arrival of the liquid front at the bottom end. In order to identify the physical phenomena involved, two parameters are proposed: the void fraction, α, which expresses the fraction of the gaseous phase (vapour and NCG) in a given volume of fluid, and the NCG mass fraction, x_{nc}.

$$\alpha = \frac{V_{gas}}{V_{total}} \tag{1}$$

$$x_{nc} = \frac{m_{nc}}{m_{total}} \tag{2}$$

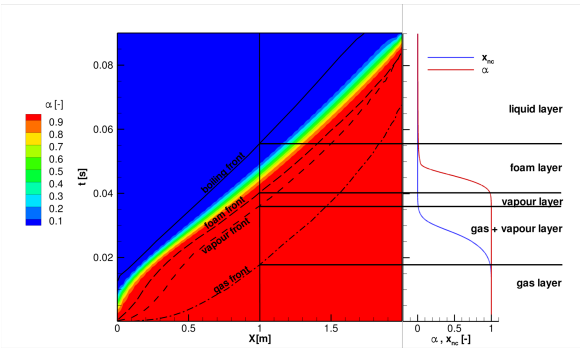

Figure 7: X-t diagram for the void fraction before the first impact

In equation 2, m_{nc} refers only to the NCG in evolved state. Therefore, when $\alpha = 1$, the volume is full of gas (vapour or NCG) and when $x_{nc} = 1$ the volume is full of NCG in gaseous state.

Figure 7 shows the X-t diagram coloured with the void fraction, together with a side graph with the void fraction and the NCG mass fraction history obtained at half-length of the test element ($X = 1\,m$). The time interval represented in this diagram goes from the opening of the FOV until the impact of the liquid front at the bottom end ($0 < t < 0.09\,s$). According to this

graph, five different layers can be distinguished when moving upstream in the graph at $X = 1\,m$. Initially, there is only the presence of NCG ($x_{nc} = 1$), creating the **gas layer**. Later, a thick **gas+vapour layer** appears, where the NCG is gradually evacuated and replaced by the vapour phase ($\alpha = 1$ and $x_{nc} < 1$). The third layer contains only vapour: **vapour layer** ($\alpha = 1$ and $x_{nc} = 0$). In the fourth layer, droplets of liquid start to appear ($\alpha < 1$), generating the **foam layer**. Finally, in the fifth layer there is only liquid phase ($\alpha = 0$), named **liquid layer**. As the liquid layer approaches the bottom end, the pressure increases, which makes the vapour condensate and the NCG dissolve into the liquid.

This multi-layer structure with variable composition basically reflects the consecutive multi-phase flow phenomena taking place during priming. The sudden exposure of the liquid to vacuum initiates its vaporization or boiling as it falls suddenly below the vapour line. The vaporization process takes place over a finite layer thickness where the liquid transforms gradually towards a pure vapour. Within this layer, liquid and vapour coexist and form a foam. Due to their large density ratio, the vapour is expelled upstream of the foam front where it eventually mixes up with the NCG. This does not happen immediately at the foam front but slightly upstream of it, at the vapour layer front. The priming or gas front indicates the most downstream location of the upcoming water hammer effect.

7. Fluid hammer mechanism during priming

Since the first impact of the liquid front is in the origin of the pressure surge, the understanding of the first pressure spike may give insight in the wave propagation and dissipation mechanism. To do so, the pressure evolution in the 50 nodes in which the test element was discretized during the computations with EcosimPro/ESPSS has been plotted in a single graph, and zooming in the first pressure spike ($0.09 < t < 0.094$), as shown in figure 8. The corresponding pressure raise for node 1, 25 and 50 has been highlighted with thicker lines for the sake of clarity, where node 1 is situated right after the FOV, node 25 is at half-length of the test element and node 50 gives the highest pressure surge obtained at the forward end.

When the FOV opens, the liquid front travels along the pipe, arriving at $t = 0.09\,s$ at the bottom end. Since the test element has a length of $2\,m$, the average travelling velocity of the liquid front is $22.22\,m/s$. The front velocity drops to zero after the impact and the kinetic

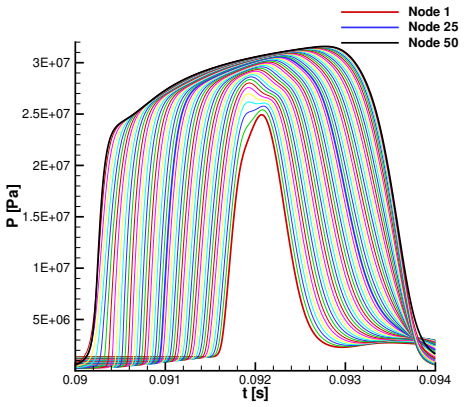

Figure 8: First pressure peak recorded in the 50 nodes of the test element

energy of the flow is converted into pressure energy. In order to estimate the pressure raise, let us assume that the density and the sound velocity in the liquid are constant and equal to $998\,kg/m^3$ and $1482\,m/s$ respectively (distilled water at $20°C$). With these values, the Joukowsky equation gives a pressure raise equal to $\Delta P = 32.8\,MPa$. This value is consistent with the one obtained numerically, $P_{wh} = 31.3\,MPa$, recorded at the bottom end during the first pressure peak. This flow information, pressure raise and null flow velocity, is now transmitted upstream at the speed of sound as a pressure wave ("PW1"). One can observe that, according to figure 8, there is a time delay of approximately $\Delta t_1 = 0.0014\,s$ between the pressure raise at the bottom end (thick black line) and the one produced at the valve location (thick red line). Taking into account that the test element is $2\,m$ long, this gives a velocity of $1429\,m/s$, which is also consistent with the theoretical value.

Figure 8 also shows that the pressure raise produced has two slopes. First, there is an abrupt, quasi-instantaneous, pressure augmentation until $P_{wh} = 23\,MPa$. Front this point, the pressure continues increasing at a lower rate, with the peak at $P_{wh} = 31.3\,MPa$. An attempt to explain this behaviour may be offered with figure 9, which shows the liquid front velocity in each node. As it was already said, around $t = 0.09\,s$, when the liquid front reaches the bottom end, the flow velocity drops to zero, and the water hammer taking place increase the liquid pressure. The pressure wave starts travelling upstream given the new flow information to the liquid flow, i.e. null velocity and P_{wh}. But while this is happening, there is part of the liquid column that is still travelling downstream,

which explains the continuous pressure increase at the bottom end. In other words, since upstream pressure is always greater than downstream pressure before the impact, the surge pressure will continuously increase in order to bring fluid flow to rest[11].

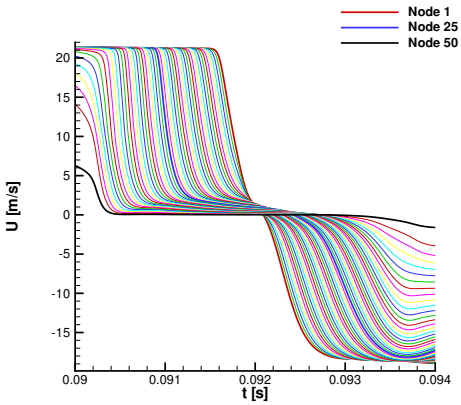

Figure 9: Liquid front velocity computed during the first pressure peak

At $t = 0.092\,s$ the pressure wave reaches the FOV and shortly after the tank. This fact imposes a new pressure condition to the flow, which is P_t. Such a change occurs because the tank has an infinite volume compared to the one of the test element. The pressure condition set by the tank travels now downstream as a expansion wave ("EW1"). Under these circumstances, and before EW1 arrives to the bottom end, there is a high pressure gradient in the fluid (P_t <<< P_{wh}), which makes the liquid column to move towards the tank for $t > 0.092\,s$, as it is observed in figure 9 (negative velocity values due to the upstream direction). This is possible because the liquid has an elastic behaviour with variable density, as figure 10 shows, causing a higher negative velocity in the fluid particles close to the valve, around $-19\,m/s$, than those close to the bottom end. Furthermore, this difference is more pronounced after node 25, showing in the last node a maximum negative velocity of nearly $-2\,m/s$.

While the liquid column starts to move upstream, the pressure starts to drop and, approximately at $t = 0.0928$, the fluid particles at the bottom end start moving upstream. The movement of the whole liquid column is possible due to the growing of the void fraction downstream. In fact, the liquid column leaves a foam pocket behind, which is clearly identified in figure 12. The colour map of this X-t diagram represents the void fraction and, according to the side graph plotted in the same figure, the foam pocket consists of a mixture of only liquid and vapour, as no trace of NCG is predicted after the arrival of EW1. Based on the X-t diagram of figure 12, we observe that this first foam pocket reaches the coordinate $X = 1.3\,m$ during the EW1 reflection.

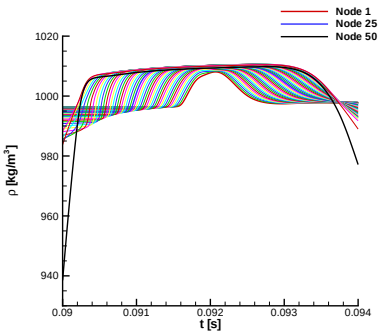

Figure 10: Liquid front density computed during the first pressure peak

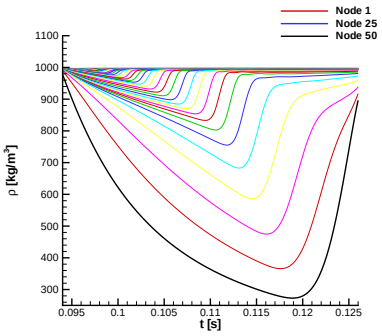

Figure 11: Liquid front density computed after the arrival of EW1

The density variation after the first peak shown in figure 11 is also related to the foam pocket, where the density value shows a pronounced decrease in the nodes affected by the pocket growth. Finally, between $0.11\,s < t < 0.12\,s$ the fluid density starts to increase (figure 11) and the void fraction to decrease until the collapse of the foam pocket. This phenomenon generates a new impact of the liquid column against the bottom wall, producing a second pressure raise "PW2", and the whole process starts all over again. Each pressure spike is attenuated due to viscous dissipation, driving to the complete extinction of the fluid hammer phenomenon after $0.8\,s$.

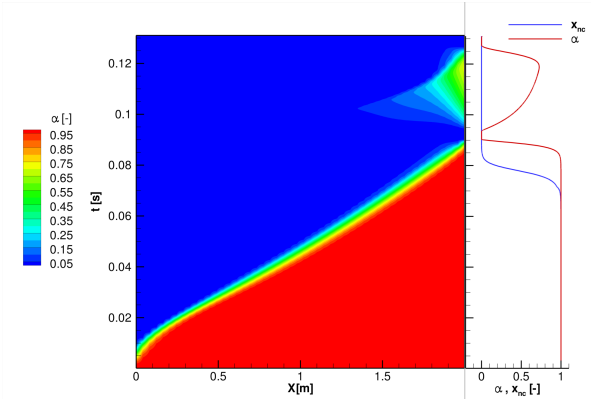

Figure 12: X-t diagram: foam pocket formation during the first expansion reflection

8. Summary

This work describes both experimental and numerical approaches to study the priming process taking place in satellites. The experimental facility proposed in this study reproduces the fluid hammer produced during priming, which consists of a pressurized liquid tank, a fast opening valve and a given length of propellant line, which is vacuum pump before launching a test.

Two numerical codes are used for the numerical approach: EcosimPro and CFD-ACE+. Both codes have been updated respectively with the ESPSS library and the full cavitation module, which allow the modelling of fluid compressibility with a homogeneous mixture of liquid, vapour and NCG. The comparison of the experimental and the numerical results has shown a reasonable good prediction of the first pressure peak. On the other hand, some effort is still needed in the prediction of the second and successive peaks with both codes.

The X-t processing has shown the multiphase nature of the liquid front, with the generation of multiple layers at the liquid front before the impact at the bottom end. A detailed analysis of the speed of sound is now necessary in each layer, and needs to be taken into account to model correctly the pressure peak level and the time delay between successive peaks.

Finally, the analysis of the fluid hammer mechanism has shown a complex behaviour of the flow and the pressure waves during the first pressure peak. The displacement of the liquid column upstream, the generation of a foam pocket at the bottom end and the collapse of this pocket is in the origin of the successive pressure peaks produced in the flow.

Acknowledgments

This study is supported by the European Space Agency through the GSTP activity AO/1-6210/09/NL/CP.

References

[1] O. M. Briles, R. P. Hollenbaugh, Adiabatic compression testing of hydrazine, in: AIAA/SAE 14th Joint Propulsion Conference, Las Vegas, USA, 1978.

[2] O. Briles, D. Hagemann, F. Benz, T. Farkas, Explosive decomposition of hydrazine due to rapid gas compression, Tech. rep., White Sands Test Facility (1985).

[3] F. E. Hutchinson, H. D. Schmitz, Adiabatic compression phenomena in hydrazine propulsion systems, in: 20th AIAA/SAE/ASME joint propulsion conference, 1984.

[4] R. L. Bunker, D. L. Baker, J. H. S. Lee, Explosive decomposition of hydrazine by rapid compression of a gas volume, Tech. rep., Johnson Space Center, White Sands Test Facility (1990).

[5] K. L. Yaggy, Analysis of propellant flow into evacuated and pressurized lines, in: 20th AIAA/SAE/ASME Joint Propulsion Conference and Exhibit, 1984.

[6] R. P. Prickett, E. Mayer, J. Hermal, Water hammer in a spacecraft propellant feed system, Journal of Propulsion and Power 8 (3) (1992) 592–597.

[7] J. Molinsky, Water hammer test of the seastar hydrazine propulsion system, in: 33rd AIAA/ASME/SAE/ASEE Joint Propulsion Conference & Exhibit, 1997.

[8] T. Martin, L. Rockwell, C. Parish, Test and modeling of the mars '98 descent propulsion system waterhammer, in: 34rd AIAA/ASME/SAE/ASEE Joint Propulsion Conference & Exhibit, 1998.

[9] C. Y. Joh, K. D. Park, Pressure surge analysis and reduction in the kompsat propellant feed system, in: Proceedings KORUS 2000. The 4th Korea-Russia International Symposium on Science and Technology, 2000.

[10] M. J. Morgan, Pressure transient characterization test for star-2 propulsion system fuel manifold, in: 40th AIAA/ASME/SAE/ASEE Joint Propulsion Conference and Exhibit, 2004.

[11] T. Y. Lin, D. Baker, Analysis and testing of propellant feed system priming process, Journal of Propulsion and Power 11 (3) (1995) 505–512.

[12] J. Navickas, W. C. Rivard, A. R. Porter, D. L. Baker, K. A. Rathgeber, Structural pressures developed during fill of evacuated systems, in: AIAA, Fluid Dynamics Conference, 1996.

[13] L. Ounougha, F. Colozzi, Correlation between simulations and experiments on water hammer effect in a propulsion system, in: Proceedings of Second Eurpean Spacecraft Propulsion Conference, 1997.

[14] C. Leca, P. Boh, Mon and mmh pressure surges for a simplified propellant feed system, in: proceedings of 3rd international conference on spacecraft propulsion, Cannes, France, 2000.

[15] H. C. Hearn, Development and application of a priming surge analysis methodology, in: 41st AIAA/ASME/SAE/ASEE Joint Propulsion Conference & Exhibit, 2005.

[16] I. Gibek, Y. Maisonneuve, Waterhammer tests with real propellants, in: proceedings of 41st AIAA/ASME/SAE/ASEE Joint Propulsion Conference & Exhibit, Tucson (AZ), USA, 10-13 July, no. 2005–4081, 2005.

[17] R. Lecourt, J. Steelant, Experimental investigation of water hammer in simplified feed lines of satellite propulsion systems, Journal of Propulsion and Power 23(6) (2007) 1214–1224.
[18] J. Moral, R. Perez-Vara, J. Steelant, M. de Rosa, Espss simulation platform, in: proceedings of 2010 Space Propulsion conference, San Sebastian, Spain, 2010.
[19] A. K. Singhal, M. M. Athavale, H. Li, Y. Jiang, Mathematical basis and validation of the full cavitation model, Journal of Fluids Engineering 124 (2002) 617–624.
[20] E. Holmboe, W. Rouleau, The effect of viscous shear on transients in liquid lines, ASME Journal of Basic Engineering 1 (1967) 174–180.
[21] A. S. Elansary, W. Silva, M. H. Chaudhry, Numerical and experimental investigation of transient pipe flow, Journal of Hydraulic Research 32 (1994) 689–706.
[22] A. S. Tijsseling, Fluid-structure interaction in liquid-filled pipe systems: a review, Journal of Fluids and Structures 10 (1996) 109–146.

Numerical modeling and experimental investigation of fine particle coagulation and dispersion in dilute flows

Bart Janssens

Department of Mechanical Engineering, Royal Military Academy, Belgium, bart.janssens@rma.ac.be

Supervisor: Tony Arts

Professor, Turbomachinery and Propulsion Department, von Karman Institute for Fluid Dynamics, Belgium, arts@vki.ac.be

Supervisor: Walter Bosschaerts

Professor, Department of Mechanical Engineering, Royal Military Academy, Belgium, walter.bosschaerts@rma.ac.be

University Supervisor: Karim Limam

Professor, Laboratoire d'Étude des Phénomènes de Transfert et de l'Instantanéité, France, klimam01@univ-lr.fr

Abstract

In this work, a numerical model will be developed to study the behavior of fine and ultra fine particles under conditions typical for air pollution problems. The particles considered are much heavier than the surrounding fluid, and can have sizes ranging from 5 nm to 10 μm. Effects of inter-particle collisions and coagulation will be included in the model.

The current discussion focuses on the development of the solver for the incompressible Navier-Stokes equations, using the SUPG finite element technique and with an implementation that makes use of a Domain Specific Embedded Language.

Finally, some preliminary PIV measurements, to be used for validation of the simulated flow field, will also be presented.

Keywords: Multiphase flow, Disperse flow, coagulation, LES, nanoparticles

1. Introduction

One of the major factors in determining air quality is the level of pollution in the form of particles. In general, particles with an aerodynamic diameter inferior to 10 μm can penetrate into the human body, and constitute a potential health risk [1]. Recently, the additional risks of nanoparticles have received much attention [2], so we will study particles in a range from about 5 nm to 10 μm. The goal of the present work is to arrive at a contribution to the numerical modeling of particle-laden flow, where the behavior of ultra fine particles is taken into account, as well as inter-particle collision and coagulation. This will be done in two phases: a model development phase, followed by an application phase. The target applications include flows in confined spaces that can be modeled using CFD. Particle loading should be such that the flow can be considered dilute, i.e. particle dynamics are dominated by the flow rather than inter-particle collisions.

So far, we focused on the implementation of a Finite Element Method with SUPG stabilization [3]. This was done within the framework of a Domain Specific Embedded Language, which greatly simplifies the implementation of Petrov-Galerkin approximations. The method can be compared to FEniCS [4] and Life [5]. OpenFOAM also has a similar language to express finite volume problems [6]. The following paragraphs will show how our framework was used to implement the SUPG scheme.

Experimental work was also started with PIV measurements to be used for flow model validation. The

first results are presented in paragraph 3.

2. Numerical model

The numerical method for solving the basic flow equations uses a Finite Element discretization, stabilized using the SUPG scheme. This allows the use of a single grid for the pressure and velocity. The method is detailed in [3]. What follows is a brief overview of the procedure, followed by details of the implementation using a Domain Specific Embedded Language (DESL).

2.1. Finite Element discretization

We consider the incompressible Navier-Stokes equations for conservation of mass and momentum:

$$\nabla \cdot \mathbf{u} = 0 \tag{1}$$

$$\frac{\partial \mathbf{u}}{\partial t} + (\mathbf{u} \cdot \nabla)\,\mathbf{u} + \frac{\nabla p}{\rho} - \nu \nabla^2 \mathbf{u} = \mathbf{0} \tag{2}$$

The equations are transformed to the weak formulation and PSPG, SUPG and bulk stabilization terms are applied, weighted by the respective coefficients τ. For the time discretization, a forward Euler method is used here for clarity, yielding the following semi-discrete weak formulation:

$$\int_\Omega \omega \nabla \cdot \mathbf{u}^{n+1} \mathrm{d}\Omega + \int_\Omega \tau_{\text{PSPG}} \nabla\omega \cdot \left(\frac{\mathbf{u}^{n+1} - \mathbf{u}^n}{\Delta t} + \left(\mathbf{u}^{n+1} \cdot \nabla\right)\mathbf{u}^{n+1} + \frac{\nabla p^{n+1}}{\rho} \right) \mathrm{d}\Omega = 0 \tag{3}$$

$$\int_\Omega \left(\omega + \tau_{\text{SUPG}} \nabla\omega \cdot \mathbf{u}^{n+1}\right) \left(\frac{\mathbf{u}^{n+1} - \mathbf{u}^n}{\Delta t} + \left[(\mathbf{u} \cdot \nabla)\,\mathbf{u} + \frac{\nabla p}{\rho} - \nu \nabla^2 \mathbf{u} \right]^{n+1} \right) \mathrm{d}\Omega + \int_\Omega \tau_{\text{BULK}} \nabla\omega \left(\nabla \cdot \mathbf{u}^{n+1}\right) \mathrm{d}\Omega = \mathbf{0} \tag{4}$$

The superscripts n and $n+1$ indicate the solution at two subsequent time steps, ω represents the weight function and Ω is the problem domain.

A space discretization is now obtained by splitting the domain into a number of smaller elements Ω_k over which we define shape functions $\mathbf{N}$, which we write here as a row vector containing a weight for each element node. We can then multiply $\mathbf{N}$ with a column vector of nodal values to obtain an interpolated value for a variable. This interpolation scheme is applied to the unknowns $\mathbf{u}$ and p, resulting in an equation that depends on the unknown nodal values. Furthermore, the weight function ω is chosen to be equal to the shape function and is written in each node, resulting in a number of equations equal to the number of nodes. Applying this procedure to the weak forms (3) and (4) yields an equation that can be written in matrix form for each element, which we define as follows:

$$\frac{1}{\Delta t} T_e \left(\mathbf{x}_e^{n+1} - \mathbf{x}_e^n \right) + A_e \mathbf{x}_e^{n+1} = \mathbf{0} \tag{5}$$

The elemental vector of unknowns $\mathbf{x_e}$ is arranged as follows:

$$\mathbf{x_e}^n = \begin{bmatrix} p_0^n & \dots & p_m^n & \left(u_0^n\right)_0 & \dots & \left(u_0^n\right)_m & \left(u_1^n\right)_0 & \dots & \left(u_1^n\right)_m & \left(u_2^n\right)_0 & \dots & \left(u_2^n\right)_m \end{bmatrix}^\intercal \tag{6}$$

Here, m is the number of nodes for an element. The structuring of the vector of unknowns also allows us to subdivide the element matrices T_e and A_e as follows (showing only A_e and considering three velocity components):

$$A_e = \begin{bmatrix} A_{pp} & A_{pu_0} & A_{pu_1} & A_{pu_2} \\ A_{u_0 p} & A_{u_0 u_0} & A_{u_0 u_1} & A_{u_0 u_2} \\ A_{u_1 p} & A_{u_1 u_0} & A_{u_1 u_1} & A_{u_1 u_2} \\ A_{u_2 p} & A_{u_2 u_0} & A_{u_2 u_1} & A_{u_2 u_2} \end{bmatrix} \tag{7}$$

Each element of this matrix is an $m \times m$ sub matrix for which the rows correspond to the equations at each element node for the variable in the first subscript and the columns represent the nodal contributions for the variable in the second subscript. Comparing this structure with the weak forms (3) and (4) allows us to define each matrix, after applying the interpolation procedure:

$$A_{pu_i} = \int_{\Omega_k} \left(\mathbf{N}^\intercal \left(\nabla \mathbf{N}\right)_i + \tau_{\text{PSPG}} \left(\nabla \mathbf{N}\right)_i^\intercal \mathbf{u}_{\text{adv}} \nabla \mathbf{N} \right) \mathrm{d}\Omega_k \tag{8}$$

$$A_{pp} = \int_{\Omega_k} \tau_{\text{PSPG}} \frac{1}{\rho} \nabla \mathbf{N}^\intercal \nabla \mathbf{N} \mathrm{d}\Omega_k \tag{9}$$

$$A_{u_i u_i} = \int_{\Omega_k} \left(\nu \nabla \mathbf{N}^\intercal \nabla \mathbf{N} + (\mathbf{N} + \tau_{\text{SUPG}} \mathbf{u}_{\text{adv}} \nabla \mathbf{N})^\intercal \mathbf{u}_{\text{adv}} \nabla \mathbf{N} + \tau_{\text{BULK}} \left(\nabla \mathbf{N}\right)_i^\intercal \nabla \mathbf{N}_i \right) \mathrm{d}\Omega_k \tag{10}$$

$$A_{u_i u_j} = \int_{\Omega_k} \tau_{\text{BULK}} \left(\nabla \mathbf{N}\right)_i^\intercal \nabla \mathbf{N}_j \mathrm{d}\Omega_k \qquad (i \neq j) \tag{11}$$

$$A_{u_i p} = \int_{\Omega_k} \frac{1}{\rho} \left(\mathbf{N} + \tau_{\text{SUPG}} \mathbf{u}_{\text{adv}} \nabla \mathbf{N}\right)^{\intercal} (\nabla \mathbf{N})_i \, \mathrm{d}\Omega_k \tag{12}$$

$$T_{p u_i} = \int_{\Omega_k} \tau_{\text{PSPG}} \, (\nabla \mathbf{N})_i^{\intercal} \, \mathbf{N} \mathrm{d}\Omega_k \tag{13}$$

$$T_{u_i u_i} = \int_{\Omega_k} \left(\mathbf{N} + \tau_{\text{SUPG}} \mathbf{u}_{\text{adv}} \nabla \mathbf{N}\right)^{\intercal} \mathbf{N} \mathrm{d}\Omega_k \tag{14}$$

In these equations, the indices i and j refer to the i-th or j-th row of the gradient matrices of the shape functions and thus take values 0, 1 and 2 for three-dimensional problems. We note that the advective and SUPG terms contain an advection velocity $\mathbf{u}_{\text{adv}}$, which is introduced to obtain a linear system. The value of $\mathbf{u}_{\text{adv}}$ is obtained through a series expansion as detailed by [3].

In order to obtain the final discrete system, equation (5) is transformed, introducing a θ-method for the time discretization and solving for the difference $\Delta \mathbf{x}_e = \mathbf{x}_e^{n+1} - \mathbf{x}_e^n$ between two subsequent time steps::

$$\left(\frac{1}{\Delta t} T_e + \theta A_e\right) \Delta \mathbf{x}_e = -A_e \mathbf{x}_e^n \tag{15}$$

Setting $\theta = 1$ yields a backward Euler method, while setting $\theta = 0.5$ results in the second order accurate Crank-Nicolson scheme. We note that some flexibility in this choice is useful, since even though both methods are unconditionally stable in theory, numerical simulations show that some instability in the pressure solution may appear during the first time steps if the Crank-Nicolson scheme is applied from the start.

Finally, the element contributions need to be summed together over the domain, resulting in a global linear system. Because the shape functions $\mathbf{N}$ are defined locally, the system is sparse and can be solved using iterative techniques such as GMRES.

2.2. Implementation

The implementation is usually accomplished by writing out the element matrices A_e and T_e for each element type that needs to be considered, and then calling an assembly procedure. Due to the complexity of the code, the link with the mathematical formulation is lost, and adding support for new element types requires a lot of repetitive work. The method proposed here alleviates these concerns, by providing a higher level of abstraction that closely resembles the expressions (8) to (14).

Using the Boost Proto library [7], we implemented a "Domain Specific Embedded Language" (DSEL) for the construction of FEM discretizations. The use of C++ template metaprogramming techniques allows for a high level of abstraction with a minimal loss in runtime performance. Because the language is embedded, it just compiles along with the rest of the C++ code, without any need for external preprocessing. Let's introduce the DSEL by looking at the first contribution to the element matrix, A_{pu_i} from equation (8). It is written in code as:

```
1 _A(p, u[_i]) += transpose(N(p)) * nabla(u)[_i] +
2   c.tau_ps*transpose(nabla(p)[_i])*u_adv*nabla(u)
```

The resemblance with equation (8) is immediately obvious. In the above expression, p and u are variables that have been defined to be associated with a scalar and vector field, using the following declarations:

```
1 MeshTerm<0, VectorField> u("Velocity", Tags::
      solution());
2 MeshTerm<1, ScalarField> p("Pressure", Tags::
      solution());
```

These declarations indicate that u and p are so-called Proto terminals, which means that by deriving from a Boost Proto class, they have a full set of Proto overloads. The 0 and 1 in the declarations are needed to make sure that each variable can be identified at compile time. Likewise, the operations such as transpose and nabla that appear in the expressions are also terminals, but they have been predefined in the Coolfluid 3 framework. The `nabla` terminal represents $\nabla \mathbf{N}$, but in the code it takes a variable as a parameter, to allow for different shape functions for each variable. The appearance of the predefined index `_i` indicates that a loop over the number of physical dimensions should be made.

When applying operators to the terminals (plus-assign, function call, product, ...) the result is an expression tree object that is then executed in a loop over the mesh. In order to evaluate the expression, a data object is passed along to the evaluation function to give access to the nodal values and the geometric mesh data. Because the whole system relies on template meta programming, the data that is passed can use fixed-size matrix and vector types, which allows for better code optimization at compile time.

In order to apply the integration over the element, a second-order Gauss quadrature is applied. It is inserted into the expression tree by calling the function `element_quadrature`. The full code for the assembly procedure is shown in listing 1. Note that here we start by defining a list of admissible element types. By executing a Boost MPL loop, code for each of these element types is generated, and the selection of which code to use is automatically made at runtime, based on the type of mesh that is used. This also easily en-

ables the use of heterogeneous meshes that combine triangles and quadrilaterals, for example.

Care needs to be taken when calculating the values of the stabilization coefficients, and we use a procedure that calculates a unique value for each element, based on the local Reynolds number. Such special needs can be handled by implementing a user-defined function, ready for use inside an expression. Here, we have defined `compute_tau`, which is simply declared as:

```
struct ComputeTau
{
  typedef void result_type;

  template<typename UT>
  void operator()(const UT& u, SUPGCoeffs& c) const
  {
    // do calculation here
  }
};
static MakeSFOp<ComputeTau>::type const compute_tau
    = {};
```

All that is needed is a struct with a function call operator, templated by the variables that are used. In this case, `UT` represents the data associated with the velocity field, and it can be used to access the underlying geometry, the current values and gradients. The `SUPGCoeffs` class is simply a struct that holds the different coefficients as well as the density and viscosity. The implementation allows defining custom functions with any number of parameters of any type. The return type is specified using the "result of" protocol, which here reduces to a simple typedef. The user defined function is made available for use in expressions by constructing a `compute_tau` terminal.

Finally, the assembly is written using the + = operator for the system matrix and right hand side.

2.3. Validation

A first validation was performed on a 2D backward facing step. This problem was chosen because of its simple geometry and boundary conditions, and because of the abundance of reference data in the literature. We compared with experimental data from [8] up to a Reynolds number of 400. Meshing guidelines were obtained from a previous numerical study by [9]. Figure 1 shows good agreement with the measured data. At Reynolds numbers above 400, the flow becomes three dimensional. The case of Re = 648 was considered, resulting in a normalized reattachment length of 10.28, showing again excellent agreement with [8] and [9]. Performance for the 3D case was not satisfactory, due to the long solution times required for the linear system. An improved preconditioning of the linear system should go a long way towards improving the performance and scalability of the solver. The methods proposed in [10] and [11] seem very appropriate for our discretization scheme, and promise a substantial performance increase.

```
elements_expression
(
 boost::mpl::vector4<LagrangeP1::Triag2D,
      LagrangeP1::Quad2D, LagrangeP1::Tetra3D,
      LagrangeP1::Hexa3D>(),
 group
 (
  _A = _0, _T = _0,
  compute_tau(u, c),
  element_quadrature
  (
   _A(p, u[_i]) += transpose(N(p)) * nabla(u)[_i] +
        c.tau_ps * transpose(nabla(p)[_i]) * u_adv
       *nabla(u),
   _A(p, p) += c.tau_ps * transpose(nabla(p)) *
       nabla(p) * c.one_over_rho,
   _A(u[_i], u[_i]) += c.mu * transpose(nabla(u)) *
        nabla(u) * c.one_over_rho + transpose(N(u)
        + c.tau_su*u_adv*nabla(u)) * u_adv*nabla(u
       ),
   _A(u[_i], p) += c.one_over_rho * transpose(N(u)
       + c.tau_su*u_adv*nabla(u)) * nabla(p)[_i],
   _A(u[_i], u[_j]) += c.tau_bulk * transpose(nabla
       (u)[_i]) * nabla(u)[_j],
   _T(p , u[_i]) += c.tau_ps * transpose(nabla(p)[
       _i]) * N(u),
   _T(u[_i], u[_i]) += transpose(N(u) + c.tau_su*
       u_adv*nabla(u)) * N(u)
  ),
  system_matrix += invdt() * _T + _A,
  system_rhs += -_A * _x
 )
);
```

Listing 1: Matrix assembly

3. Experimental setup

A first experiment that is being developed is designed to measure concentration variations and the effect of particle coagulation in a flow field that should be reproducible using numerical simulation. Flow enters a cubic chamber through a narrow slot near the bottom, and exits near the top of the opposite wall (see Fig. 2). For the particle coagulation, a short burst of particles will be injected near the center of the circulation zone.

In order to get a reproducible result, the inlet conditions are controlled using a device similar to the inlet section of a subsonic wind tunnel, as shown in Fig. 3

3.1. First measurement results

To get a first look at the flow field, PIV measurements at the vertical center plane in the length-wise direction were made. Figure 4 shows the velocity vectors, confirming the existence of the circulation zone.

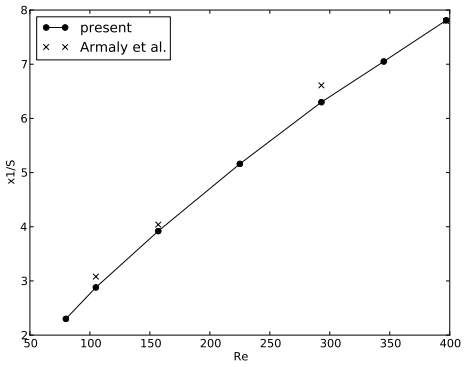

Figure 1: Normalized backward facing step reattachment length as a function of Reynolds number.

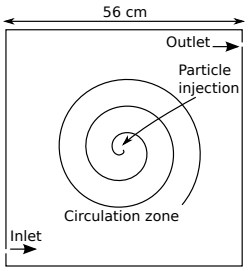

Figure 2: Schematic of the experimental test chamber.

Figure 5 shows the evolution of the X-velocity along the vertical center line for different fan settings indicated on the fan controller. As expected, the strength of the recirculation increases proportionally to the fan power. It should be noted that these are only preliminary results and an error analysis using synthetic images still needs to be performed, so for now the results are presented without any error indication. During the measurements, some practical problems were encountered with regard to the seeding of the flow. A Laskin tube was used to seed the flow with olive oil droplets at the inlet of the fan, on the left in figure 3. For any attainable particle flow, however, the test chamber was quickly filled with particles, resulting in a density far too high to correlate the PIV images. The problem was solved by turning off the seeding flow before the measurements, and take measurements while the box

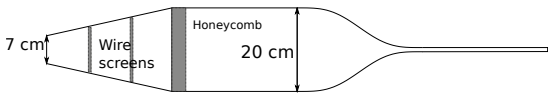

Figure 3: Conditioning of the test chamber inlet.

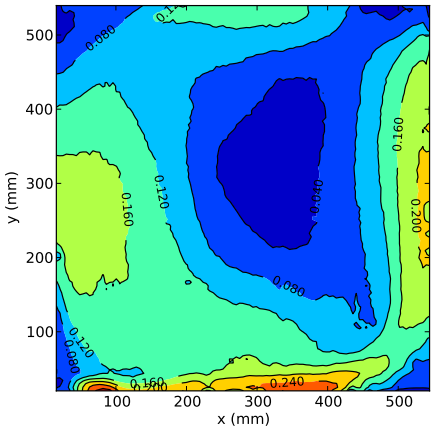

Figure 4: Contours of velocity magnitude, for a fan setting of 10.

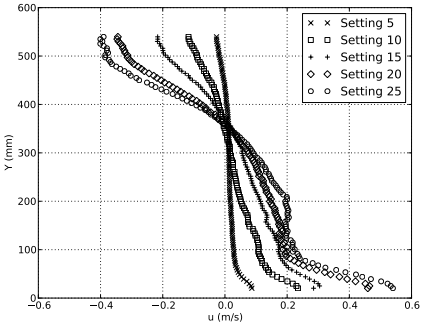

Figure 5: Evolution of the X-velocity along the vertical center line

was being cleared of particles. During these experiments, it was clear that a higher density of particles remained near the center of the box for long durations, exceeding 200s at fan setting 10. This observation is encouraging for the later particle coagulation experiments.

4. Conclusion and future work

The objective of the current work is to provide a meaningful contribution to the numerical modeling of dispersed phase flow. The inclusion of nanoparticles and coagulation effects constitute new challenges, and should extend the applicability of the method. Areas of application include for example indoor air quality or risk assessment when considering the behavior of chemical or biological agents, as well as the study of

pollutant aggregation in close proximity to the source.

Current work will be continued by extending the current flow solver with LES for turbulence modeling, which will be tested against the PIV data as well as channel DNS from i.e [12]. Once the flow field is validated, particle and coagulation modeling will be introduced, with validation against literature data, i.e. [13; 14; 15] as well as PDA measurements in the current test chamber.

Acknowledgements

The current implementation of the Navier-Stokes solver was realized thanks to the valuable assistance and comments of Tamás Bányai. For the PIV setup, the assistance from Elmar Recker was greatly appreciated.

References

[1] C. A. Pope, D. W. Dockery, Health Effects of Fine Particulate Air Pollution: Lines that Connect, J. Air & Waste Manage. Assoc. 56 (2006) 709–742.

[2] G. Oberdörster, E. Oberdörster, J. Oberdörster, Nanotoxicology: An Emerging Discipline Evolving from Studies of Ultrafine Particles, Environ Health Perspect 113 (2005) 823–839. doi:10.1289/ehp.7339.

[3] T. Bányai, D. Vanden Abeele, H. Deconinck, A fast fully-coupled solution algorithm for the unsteady incompressible Navier-Stokes equations, in: Conference on Modelling Fluid Flow (CMFF'06), Budapest, Hungary, 2006.

[4] M. S. Alnæs, K.-A. Mardal, On the efficiency of symbolic computations combined with code generation for finite element methods, ACM Transactions on Mathematical Software 37 (1) (2010) 1. doi:10.1145/1644001.1644007.

[5] C. Prud'homme, Life: Overview of a Unified C++ Implementation of the Finite and Spectral Element Methods in 1D, 2D and 3D 4699 (2007) 712.

[6] H. G. Weller, A tensorial approach to computational continuum mechanics using object-oriented techniques, Computers in Physics 12 (6) (1998) 620. doi:10.1063/1.168744.

[7] E. Niebler, Proto: a compiler construction toolkit for DSELs, in: Proceedings of the 2007 Symposium on Library-Centric Software Design - LCSD '07, LCSD '07, ACM, New York, NY, USA, 2007, pp. 42–51.

[8] B. F. Armaly, F. Durst, J. C. F. Pereira, B. Schönung, Experimental and theoretical investigation of backward-facing step flow, Journal of Fluid Mechanics 127 ( ) (1983) 473–496. doi:10.1017/S0022112083002839.

[9] P. T. Williams, A. J. Baker, Numerical simulations of laminar flow over a 3D backward-facing step, International Journal for Numerical Methods in Fluids 24 (11) (1997) 1159–1183.

[10] M. Benzi, M. A. Olshanskii, Z. Wang, Modified augmented Lagrangian preconditioners for the incompressible Navier-Stokes equations, International Journal for Numerical Methods in Fluids (2010) n/adoi:10.1002/fld.2267.

[11] T. Heister, G. Rapin, Efficient augmented Lagrangian-type preconditioning for the Oseen problem using Grad-Div stabilization, International Journal for Numerical Methods in Fluidsdoi:10.1002/fld.3654.
URL http://dx.doi.org/10.1002/fld.3654

[12] R. D. Moser, J. Kim, N. N. Mansour, Direct numerical simulation of turbulent channel flow up to $Re_\tau = 590$, Physics of Fluids 11 (4) (1999) 943–945. doi:10.1063/1.869966.

[13] M. Chen, K. Kontomaris, J. B. McLaughlin, Direct Numerical Simulation of Droplet Collisions in a Turbulent Channel Flow. Part II: collision rates, International Journal of Multiphase Flow 24 (November 1999) 1105–1138.

[14] J. R. Fessler, J. D. Kulick, J. K. Eaton, Preferential concentration of heavy particles in a turbulent channel flow, Physics of Fluids 6 (11) (1994) 3742. doi:10.1063/1.868445.

[15] M. Sommerfeld, Analysis of collision effects for turbulent gas-particle flow in a horizontal channel. Part II. Integral properties and validation, International Journal of Multiphase Flow 29 (4) (2003) 701. doi:10.1016/S0301-9322(03)00033-8.

Flow visualization and Planar Laser Induced Fluorescence (PLIF) measurements on horizontal shear-driven liquid films at the edge of a plate[☆]

Evangelos Bacharoudis[*]

Univ. Lille Nord de France, France, bacharoudis@vki.ac.be

Supervisor: Jean-Marie Buchlin

Professor, Head, Environmental and Applied Fluid Dynamics Department, von Karman Institute for Fluid Dynamics, Belgium, buchlin@vki.ac.be

University Supervisor: Larbi Labraga

Professor, Univ. Lille Nord de France, France, larbi.labraga@univ-valenciennes.fr

Industrial Partner: Hervé Bratec

Dr. Engineer, Robert Bosch Produktie N.V., Belgium, herve.bratec@be.bosch.com

Abstract

In this study a shear-driven liquid film on a horizontal plate of low surface energy approaching a sharp corner is investigated experimentally by means of high speed recording and Planar Laser Induced Fluorescence (PLIF). The liquid film is free to expand towards the spanwise direction of the test section. Different atomization regimes have been recognized and a map is proposed. The behavior of the liquid film under various flow conditions including the critical ones for the onset of separation is described. An empirical equation is given in order to define the onset of liquid film atomization.

Keywords: shear-driven film, PLIF, wave velocity, film thickness, critical conditions

1. Introduction

Liquid films driven by an external air flow are encountered very often in the industrial and natural environment. These films can flow over solid surfaces and depending on both the flow conditions and the geometry of the solid surface can be detached and atomized in small droplets. In the industrial domain, the generation of small droplets which usually follow the flow of the external air, can lead to either desirable or detrimental effects for the engineering applications. In all the cases, knowledge of the behavior of the liquid film in different flow conditions is necessary in order to predict the onset of these atomization phenomena and minimize or maximize their effects. On the other hand, optimization of the engineering applications can be accomplished from the understanding of the physics behind the liquid film and air flow interactions. A short review concerning mainly the experimental studies of shear-driven liquid films and their separation due to geometrical changes of the solid surfaces is given below.

Shear-driven films have been studied extensively for decades mainly in two configurations, the circular pipes and the rectangular channels. There is a vast bibliography concerning the study of liquid films encountered in annular flows dating back from the early experiments of Wallis and other researchers [1, 2, 3] to the more contemporary studies [4, 5, 6, 7]. Vertical, inclined and horizontal configurations have been used in combination with co-current and counter-current air-liquid mixtures in different flow conditions. In these studies the charac-

[☆] All rights of this paper owned by Robert Bosch Produktie N.V.

[*] Corresponding author

teristics of the mean shear-driven liquid film and the wavy interface have been measured in order to learn more about the mechanism of momentum, mass and heat transfer in annular flows and develop models able to predict the air-liquid interaction and specifically the interfacial shear.

Less in number studies have been conducted in rectangular channels. Jurman and McCready [8] studied experimentally the waves on a shear-driven liquid film and combined the measurements with predictions from the stability analysis. Wittig et al. [9] measured the thickness and wave velocity of a thin film on a flat plate inside a rectangular test section. The facility represents the configuration of a simplified prefilming air-blast atomizer. They showed that the laminar velocity profile fits better their experimental results for the liquid film flow. The investigation of the local characteristics of the liquid films in horizontal and vertical channels has been carried out by Kang and Kim [10] in order to develop a model for describing the interfacial shear stress. Recently, Friedrich et al. and Lan et al. [11, 12] measured and simulated with CFD the thickness and width of a shear-driven liquid film in rectangular channel which is free to expand in a spanwise direction. Finally, Lorencez et al. [13] investigated the local turbulent structures emerged from the air-liquid interaction on a stratified flow. It is one of the very few works on stratified flows conducted in open channel with relatively thin liquid media.

In all the above studies several experimental methods have been utilized in order to measure the liquid film thickness and extract useful information for the interface. Briefly, the capacity method, the conductivity method, the light absorption technique, the shadow method, the fluorescence method, the interferometric method are some of the methods used for the investigation of the shear-driven liquid films. The studies revealed that waves emerge on the interface due to the air-liquid interaction and become three dimensional very fast, especially, in higher air velocities. Concerning the characteristics of the liquid film, generally, the film thickness is increased with the liquid flow rate and is reduced with the increase of the air velocity. On the other hand, both, the liquid flow rate and the air flow above the film result in the increase of the wave velocity. Finally, when the liquid film is not restricted at its sides by the walls of the circular or rectangular channels, the film width seems to increase with the liquid flow rate and the air velocity.

The shear-driven liquid films when encounter a change in the geometry flowing above may separate from the wall surface depending on the flow conditions and the geometrical characteristics, resulting in the primary atomization of the liquid film into droplets. Very few studies have been conducted in order to determine the critical conditions in which the onset of the detachment and the primary atomization is taking place and even less to obtain sufficient experimental results in this limit. One of the early theoretical works on the liquid film detachment flowing over a smooth bent is the one of Owen and Ryley [14]. They presented many different factors that can affect the liquid film flow around the bent. They confirmed that the surface tension is the necessary force in order to hold the film on to the boundary wall, the inertia or centrifugal forces of the film cause the detachment from the wall and the gravitational forces may act either as adhesive forces or as repelling ones. They tried to support their analysis with few experiments, however their experimental results were very poor. Azzopardi and Sanaullah [15] have investigated the film separation in wave-plate mist eliminators. A model for the prediction of the critical conditions has been proposed based on the model of [14]. They supported their model with a number of experiments conducted by themselves and by collecting experimental data from other researchers in literature. A theoretical model for the determination of the critical conditions leading to liquid film detachment based on stability analysis has been developed by Maroteaux et al. [16]. According to their study the main reason for film separation is Rayleigh-Taylor instabilities growing when the film turns around a corner. They provided few experimental results using the PLIF method to verify their model. Finally, Firedrich et al. [17] and Wegener et al. [18] proposed a criterion for the onset of separation of shear driven films based on force balance as a function of local parameters of the flow. Their model is supported by a significant number of experimental results. However, they report that the experimental method for measuring the atomized mass is inaccurate close to the critical conditions and conclude that the identification of the critical conditions is an arbitrary process. Scrutinizing the literature, more detailed experiments are needed in order to understand the process of film detachment and determine the critical conditions for the onset of the atomization.

In this study a horizontal liquid film, free to expand towards the spanwise direction is sheared by a turbulent wall jet developed on the flat plate of an open channel. The liquid film is driven towards a sharp corner at the edge of the plate. Initially, the characteristics of this type of liquid film flow have been investigated using high speed recording in order to

gain understanding of the behavior of the film on the plate. Next, detailed measurements of the film thickness, width and velocity have been carried out with the PLIF method in order to identify the critical conditions for the onset of the film atomization. An empirical model is proposed from the experimental results.

2. Test facility and methods

The test facility used in this project in order to study the behavior of the shear-driven liquid film and its atomization in a sharp corner is presented in Figure 1. It is consisted mainly on three parts the wind tunnel, the hydraulic circuit and the test section.

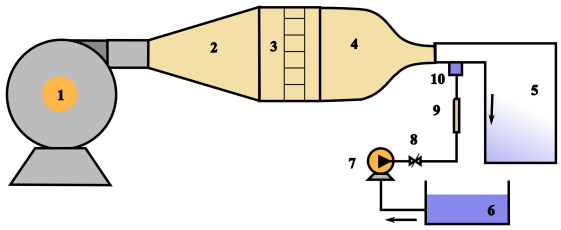

1. FAN
2. DIFUSSER
3. SETTLING CHAMBER
4. CONTRACTION
5. TEST SECTION
6. RESERVOIR
7. PUMP
8. BALL VALVE
9. ROTAMETER
10. CONTAINER

Figure 1: Experimental facility for the study of the shear-driven liquid film on a horizontal plate near a sharp corner.

An open circuit, blowing type, low speed wind tunnel has been manufactured in order to support different test section configurations. The wind tunnel is consisted of the fan of 11 kW, the diffuser, the settling chamber and the contraction. Special care has been given to the design of the 2D contraction in order to have an air flow of acceptable quality with minimum variations of the mean flow. The contraction ratio achieved at the design is 10.

The hydraulic circuit is mounted at the bottom of the test section and recirculates distilled water from the reservoir to the horizontal plate. A small container is fixed below the horizontal plate of the test section in order to collect the liquid and cut down significant disturbances generated by the system. The liquid enters the test section through a rectangular slit of spanwise length of 100 mm and opening of 1mm. The flow rate of the liquid introduced in the test section is measured by means of a rotameter with ±2 l/h uncertainty.

The test section is consisted of two plates one horizontal and one vertical comprising a sharp corner of 90°. The two plates made by Polycarbonate are restricted by two side walls from PMMA forming a short open channel. The side walls are used in order to avoid disturbances from the environment, especially at the region where liquid phase detachment occurs. The whole test section is transparent in order to apply different optical methods for the liquid film study. The test facility has been placed in a large room in order to avoid perturbations from the jet flow developing at the exit of the wind tunnel.

A detailed flow visualization study has been conducted using high speed recording. A side camera view with a backward light configuration has been realized in order to study the shear-driven film and its wavy interface on the plate while a top view with a front light setup has been utilized for the investigation of the liquid film atomization at the corner. The high speed camera works at 1000 fps for all the cases. Information concerning the wave velocity of the liquid film interface are extracted from the side view of the high speed recordings. A program based on the image analysis toolbox of Matlab has been developed in order to detect the interface from the shadow images and calculate the wave velocity cross-correlating the signal of the film thickness in two fixed positions of distance of 5 mm on the film. Though the film thickness is not calculated correctly due to the fact that all the waves which belong to the foreground or the background are projected as a shadow on the plane of the camera, however, their velocity is believed to be calculated with reasonable accuracy. The motion of the waves is independent on the precise calculation of their height. It depends on the distance of the two probes and the time needed for them to travel between the two probes. The overall uncertainty of the wave velocity calculation is estimated at ±0.05 m/s for low wave velocities and ±0.31 m/s for the maximum ones.

Planar Laser Induced Fluorescence (PLIF) has been used in order to detect the interface and extract the film thickness. Figure 2 shows the plane of measurements of the PLIF setup. Data have been measured at the edge of the corner in order to correlate them with the atomization occurring in that region especially for the critical conditions. With the PLIF method the liquid film is visualized and the resulting images are post processed with a Matlab program based on the interface detection through intensity variations. Fluorescein with maximum absorption wavelength at 490 nm and maximum emission wavelength at 518 nm is added in the reservoir as a fluorescent dye in a concentration of 100 mg/l. An Nd:YaG, green (532 nm), single pulse laser illumi-

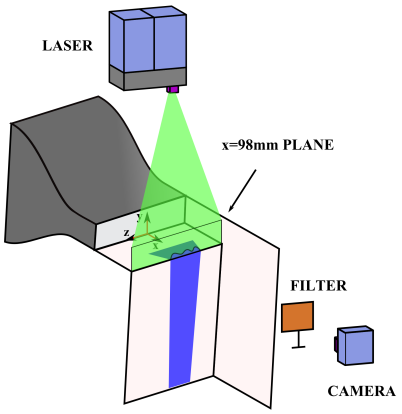

Figure 2: PLIF setup and film thickness plane of measurements.

nates the cross section of the film at the corner with a frequency of 7 Hz. The camera equipped with a lens of 105 mm captures a window of 145 mm length of the liquid film. A filter is used to suppress the laser light. The images collected are statistically independent and the average film thickness is calculated from the interface detection with a maximum overall uncertainty of ±0.21 mm.

Mass measurements have been carried out for the identification of the critical conditions. When the liquid film stops to be atomized at the sharp corner and no droplets are generated, the critical conditions have been captured. The atomized mass is collected with a small flat plate positioned downstream the corner in a distance of 5 mm from the vertical wall of the test section. From the high speed recording when the facility works close to the critical conditions the generated droplets possess enough inertia in order to be detached from the wall but at the same time their inertia is low in order to let them escape from the test section. Thus, all the droplets are collected in the plate and are weighed by means of a digital balance with overall uncertainty of ±0.01 gr. The method becomes inaccurate and stops working for high air velocities. Apart from the mass, the width of the film has been measured by placing a ruler below the transparent test section and taking pictures with a SLR digital camera from the top. The uncertainty of method is estimated at ±1 mm. From the measured magnitudes of the liquid film flow rate, the film thickness and the width, the mean film velocity has been calculated at the corner cross section with an overall maximum uncertainty of ±0.01 m/s.

3. Flow visualization

3.1. Atomization regimes

A liquid film on the order of 1-2 mm is formed on the horizontal polycarbonate surface of the test section. The critical surface energy of the polycarbonate surface is 30 mN/m and the working liquid is distilled water. The wetting of the solid surface from the working liquid is 'partial' according to Zisman's criterion [19] since the surface tension of water is quite higher than the critical energy of the surface. For this liquid-solid combination a detailed flow visualization study has been carried out and different atomization regimes have been identified. Figure 3 presents the atomization map that is proposed in order to describe the way a horizontal shear-driven liquid film is atomized at the edge of a low energy wall surface. The atomization regimes are expressed as a function of the air velocity and the liquid film Reynolds number which is based on the flow rate and the length of the slit.

Different patterns are formed on the free interface of the shear-driven liquid film and different ways of atomization are depicted by the film after the corner depending on the flow conditions. First, the atomization map can be separated in two parts, the part where there is no atomization and is located at the left of the critical curve and the part of the atomization which is at the right. The last part can be divided in regions and each region corresponds to a certain way of liquid film atomization at the sharp corner.

In Figure 3, region I is the area close to the critical conditions where low to moderate atomization occurs. A liquid film in that regime depicts regular 3D disturbances on its interface which evolute into ligaments at the corner traveling downwards on the vertical wall. Droplets are generated from these ligaments. The regime is encountered for either low air velocities or low film Reynolds numbers.

Increasing the speed of the air flow and the film Reynolds number the atomization regime of the region II occurs. In that regime the free interface of the film is dominated by 3D waves forming a kind of 'cellular' pattern. The atomization mass increases to moderate rates. The waves of the interface form ligaments when encounter the corner and break towards the streamwise direction into droplets due to the strong air flow. The bursts of these ligaments occur along a large part of the spanwise direction of the film. A transition zone exists between the regions I and II where both atomization regimes appear on the film simultaneously.

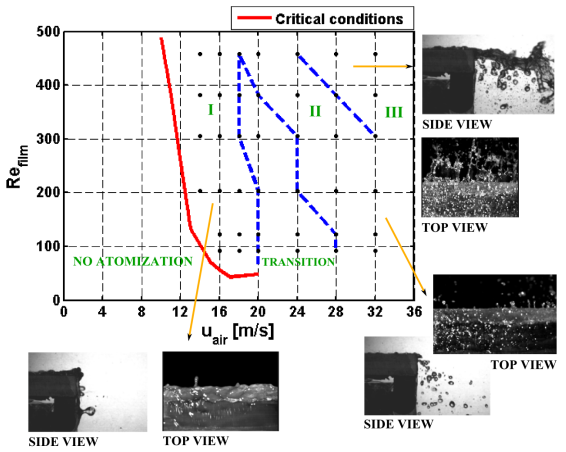

Figure 3: Atomization map for the horizontal shear-driven liquid film.

For the higher air velocities and liquid flow rates tested in this work a third regime is encountered in region III. The external shear is high enough in order to drift the liquid film downstream the corner and form a liquid sheet. The liquid sheet is divided in small cells which evolute into ligaments which break at the direction of the flow. This pattern is similar to the one identified in the studies on the prefilming atomizers [20] for high air and low liquid velocities. The free interface presents the same structure as in the region II with 3D waves of shorter wavelength. The atomization rate is very high.

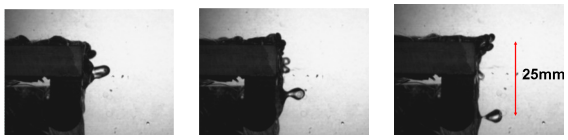

(a) t=0 sec (b) t=0.4 sec (c) t=1.2 sec

Figure 4: Different time instants for the droplet detachment from the film. The flow conditions belong to the region I

It is interesting to examine better the droplet generation in conditions very close to the critical ones shown in Figure 4. Three different instants of droplet detachment from the bulk of the film are presented. The ligament which is formed at the corner is deformed as it is moving downwards and develops a head. When this head grows enough a droplet is generated from the break-up of the ligament. In other cases, if the ligament is long enough, it can break in several droplets as it falls down. In all the cases the ligament break-up takes place quite far from the region of the corner. Another interesting point is the fact that the ligaments which produce droplets emerge sporadically and in an irregular manner along the width of the film. Summarizing, at the critical conditions, the onset of atomization of a horizontal, sher-driven liquid film is accompanied by the formation of few sporadic ligaments which break into droplets traveling downwards on the vertical wall. Neither detached film along the spanwise direction like a liquid sheet appear in these conditions nor spanwise ligaments occur.

3.2. *Wave velocity*

The images from the flow visualization with the back light configuration have been used in order to calculate the velocity of the waves traveling along the test section. Close to the critical conditions the calculation is not possible due to the limited number of disturbances on the interface. Figure 5 presents the wave velocity for different air velocity and liquid film Reynolds number (based on the flow rate and the width of the slit). The same trend is observed as reported in literature for this horizontal shear-driven film. Increasing the liquid Reynolds or the external shear the waves on the interface seem to accelerate. Direct comparison with data from the literature is not achieved due to the different range of flow conditions among this study and the other works in the literature and the different way the film is formed on the flat plate. In this study, the film is sheared by a turbulent jet and is free to expand towards the spanwise direction.

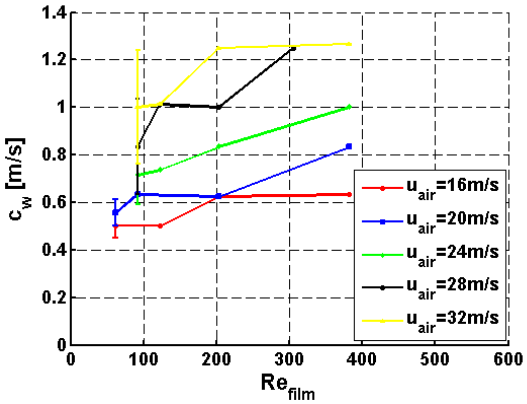

Figure 5: Wave velocity as a function of the Re_{film} and the air velocity.

4. PLIF measurements

4.1. Liquid film characteristics in region I

A liquid film can obtain different forms when it flows over a horizontal plate without restriction in expanding towards the spanwise direction. Consequently, the behavior of the liquid film and the primary atomization will change for every different film formation. The final form of the film on the plate depends on the initial conditions, the boundary conditions and the ambient conditions of the experiment. In this study, a considerable effort has been made in order to keep all the conditions constants or at least to minimize their variation. However, the ambient conditions, especially the temperature of the air and film flow, will vary in a short range of values due to the design of the experimental facility and the initial conditions, mainly due to the operation of the pump for the film formation will also slightly change among the tested cases. The results presented below represent this effort to maintain the conditions of the experiment invariable.

The liquid film characteristics of the shear-driven film developed on the horizontal plate are depicted in Figure 6 as a function of the air velocity and the liquid Reynolds number (based on the flow rate and the length of the slit). First, the efficiency of the liquid film in primary atomization is evaluated by measuring the atomized mass. In Figure 6a, the percentage of the total mass which is atomized at the sharp corner is presented. As expected, an increase of the liquid Reynolds number or the air velocity enhances the atomization.

The mean film velocity at the corner section is calculated from the measurements of the thickness, width and total flow rate of the liquid film at the same section. Raising both the inertia of the film or the external shear on the interface, Figure 6b, the mean film velocity increases.

The area of the liquid film cross section at the corner has been calculated from the film width and thickness as shown in Figure 6c. An increase of the external shear results in smaller cross sections which implies that the film is compressed. On the other hand, an increase of the film inertia is accompanied by an augmentation of the cross section area. The opposite trend is observed for the film sheared by the air velocity of 13 m/s. It has to do with the uncertainties of the film formation on the plate which is only partially controlled. The resulted film shows a steeper slope on the reduction of the thickness when the film inertia increases.

Figures 6d and 6e present the measurements of the film width and thickness at the edge of the corner. Concerning the width, raising the air velocity and the liquid Reynolds number the film is expanding on the flat plate towards the spanwise direction. Conversely, increasing the speed of the air and the liquid film flow results in films with lower thickness. The last shows that the behavior of the horizontal shear-driven liquid film depends on the wetting effects of the surface since the latter can determine how widely the liquid film is spread on the flat plate and consequently what will be the influence on the final film thickness and width.

Finally, Figure 6f presents the percentage of the root mean square of the film thickness comparing it to the value of the film thickness. This magnitude can be considered as a mean to measure the fluctuations emerging on the free interface of the film. Though there is a lot of uncertainty, it could be inferred that the fluctuations of the film grow with increasing liquid Reynolds. On the other hand, it is not clear what is happening with the increase of the air velocity, though, a trend of raising the RMS of the film thickness is observed fot higher velocities.

The results presented above signify a different tendency on the liquid film behavior comparing to the one reported in literature. Although there are no results for horizontal films, free to expand in any direction and flowing inside an open channel, there are many experimental data for annular flows [5, 6, 7] and flows inside rectangular ducts [9, 12]. In annular flows the shear-driven liquid film reduces its thickness with increasing shear, like it is reported here. However, the increase of the liquid Reynords number results in the development of the film thickness at the bottom wall of the circular pipes in contrast to what is mentioned in this study. This is explained by the fact that the liquid film generated in this work is expanding faster at the spanwise direction than the normal one resulting in wider liquid films with less thickness. The films inside the circular pipes have to overcome the action of gravity in order to expand towards their circumferential direction.

Inside the rectangular channels where the liquid film is expanding from one side of the channel to the other, the same trend is observed as for the annular flows. Again the same arguments are provided in order to explain the difference of the film behavior. It is interesting to notice that the experimental results presented from Lan et al. [12] concerning the film width and thickness for a shear-driven film without side restrictions in a channel agree well with the behavior of the film described here. In their study, in some cases

the film thickness is reduced with increasing liquid flow rate. Nevertheless, they do not explain the differences in the trend on the film thickness observed in their study, probably due to the high uncertainty of the measurement or the limited number of experimental evidence which would permit the drawing of a safe conclusion. They deduce conclusions similar to the one reported in the studies for the annular flows or the flows inside channels.

4.2. Critical conditions

The local characteristics of the horizontal shear-driven liquid film for the critical conditions have been investigated from the PLIF measurements. Before discussing the results, the term critical conditions has to be clarified and the way used to capture these conditions has to be presented.

The critical conditions have been determined by collecting and weighing the atomized mass ejected from the sharp corner, as mentioned in section 2. Figure 7 presents typical diagrams of mass measurements carried out in this study. The air velocity is fixed in a constant value and the inertia of the film is reduced by changing the flow rate of the liquid film. A total number of 20 acquisitions has been conducted and each acquisition has a duration of 2 min for every tested case.

In Figures 7a-7d the atomized mass collected after the corner is decreased with the liquid Reynolds number. For relatively high liquid Reynolds 7a, there is a significant amount of atomized mass captured downstream the corner. For lower liquid Reynolds first the atomized mass seem to be independent of the acquisition, Figure 7b. Then, the collection of the atomized mass is becoming irregular and intermittent until a minimum liquid film Reynolds below of which there is no atomization. Critical conditions are the flow conditions expressed as the pair of $We_{aerodynamic}$ and Re_{film} which cause a negligible amount of the mass of the film to be atomized at the corner. The limit for the negligible amount of atomized mass is when the latter start to become independent on the acquisition. This amount of mass is always less than the 0.05% of the total mass introduced inside the test section of the facility. For the case presented in Figure 7, any tested case which produce diagrams like presenting in Figures 7c and 7d would be consider as critical. Thus, the critical conditions are expected to obtain the form of a cloud in a diagram with axes the pair of the non-dimensional numbers of liquid Reynolds and Weber number.

The behavior of the local parameters of the shear-driven liquid film have been investigated extensively under critical conditions. After the pair of flow magnitudes is identified as critical, detailed measurements with the aid of the PLIF method are carried out in order to determine the liquid film thickness, width, mean velocity and RMS on these critical conditions. Experimental results for different critical conditions are presented in Figure 8.

The mean critical film velocity at the corner is calculated from the measured values of the liquid film thickness, width and flow rate. Increasing the external shear, the mean velocity of the film has to be decreased in order the liquid film to remain attached on the wall at the edge of the corner without being atomized. The trend of the mean critical film velocity is shown in Figure 8a.

It is important to notice that increase of the air velocity in the diagrams of Figure 8 signifies simultaneous reduction of the liquid flow rate in order to maintain the liquid film under critical conditions. Thus, the tendency of the critical film width, shown in Figure 8b, is to become more narrow with increasing air velocity since at the same time the liquid flow rate has been reduced.

Concerning the critical mean film thickness at the edge of the flat plate, generally, it is decreased when the shear on the liquid film is increased, Figure 8c. However, for low values of external shear, an opposite trend is observed. The liquid film thickness is decreasing with decreased shear. This is explained by the fact that as the external air velocity reduces the liquid flow rate is increased in order to keep the critical conditions resulting in a liquid film which develops towards the normal direction. However, after a certain amount of liquid film mass inserted inside the test section, the film seems to become heavy enough and the contact line at the sides of the film incapable to support the heavy film. The latter results in the spreading of the film towards the spanwise direction on the horizontal plate and thus triggering the reduction of the critical film thickness.

The percentage of the critical root mean square of the film thickness comparing it to the critical mean film thickness is depicted in Figure 8d. This ratio could be interpreted as a mean which records the fluctuations occurring on the interface of the film. Despite the large scattering of the experimental data which obscure the drawing of safe conclusions, a tendency can be recognized. It seems that for a liquid film at the critical conditions, the fluctuations are located at the zone with a mean value of 18% of the critical film

thickness. In other words, if the film is atomized the RMS of the film thickness should be above 18% of the mean film thickness. The peak observed for the air velocities in the range of 13-15 m/s is associated with inevitable vibrations of the test section transmitted by the fun during the experimental procedure.

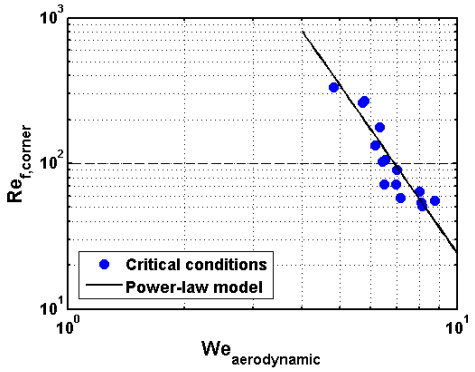

(a) Linear behavior of the critical conditions in a log-log plot.

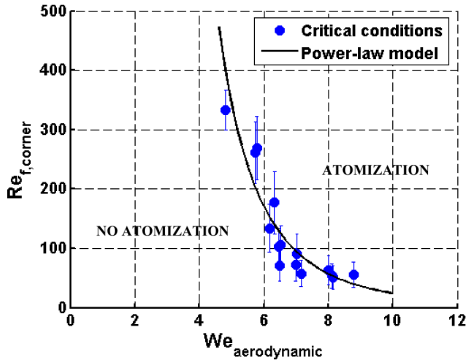

(b) Onset of atomization.

Figure 9: Critical conditions for liquid film detachment and power-law model fitted on the data.

Finally, the critical conditions for the onset of atomization of a shear-driven liquid film flowing over a horizontal plate of low surface energy, approaching a sharp corner of 90° are presented in Figure 9. They are expressed as a function of the aerodynamic Weber number ($We_{aerodynamic} = \rho_a \left(u_{air} - u_f\right)^2 h_f/\sigma_f$) which represents the ratio of the external shear to the surface tension of the film and the liquid film Reynolds number ($Re_{f,corner} = u_f h_f/\nu_f$) which expresses the inertia forces of the liquid film to the viscous ones. All the local parameters inserted in the non-dimensional numbers correspond to measurements at the edge of the flat plate. In the diagram of Figure 9b the flow conditions located at the right of the critical curve result in film atomization while tested cases at the left of the curve do not produce any atomization. A power-law model has been fitted to the experimental data in order to obtain the empirical equation of the critical curve. The formula is given below:

$$Re_{f,corner} = e^{12} \cdot We_{aerodynamic}^{-3.83} \tag{1}$$

The empirical equation is a function of the non dimensional numbers of the liquid film Reynolds and the aerodynamic Weber number. The choice of the power-law model has been dictated from the tendency observed on the experimental results in a logarithmic scale. Figure 9a shows this trend. The power-law model shows that for low external shear (low $We_{aerodynamic}$) the inertia of the liquid film has to be increased significantly in order to maintain the critical conditions while for high shear the film inertia has to become very small.

5. Conclusion

A detailed study of a horizontal shear-driven liquid film on a low energy surface approaching a sharp corner has been conducted using flow visualization techniques and PLIF measurements. The liquid film is free to expand towards the spanwise direction. The liquid film formation on the flat plate and its primary atomization depends on the ambient, initial and boundary conditions. For the conditions of this experimental work, the flow visualization study revealed different atomization regimes. An atomization map has been proposed as a function of liquid Reynolds number and air velocity. It is pointed out the way the liquid film is atomized close to the critical conditions. According to that, a disturbance created on the interface turns around the corner forming a ligament which is moving downwards and separates into a droplet after long distance from the corner.

The PLIF measurements brought light first on the characteristics of the developing film on the plate and second on the critical condition for the onset of atomization at the edge of the corner. A major difference of this horizontal film with the other ones existing in the literature is the ability to expand spanwisely. The latter influences the film formation and the atomization process at the edge of the corner. The atomization process is becoming a function of both the cross-section area of the film at the corner and the mean film velocity. Concerning the critical conditions, detailed measurements have been carried out on the liquid film.

A critical curve for the onset of liquid film separation and detachment has been determined. An empirical equation as a function of the liquid film Reynolds number and the aerodynamic Weber number fits the experimental data and describes the liquid phase detachment at the corner.

Acknowledgments

Robert Bosch Produktie in Tienen, Belgium is gratefully acknowledged by the author for the financial support of this work.

References

[1] G. B. Wallis, One-dimensional Two-phase Flow, McGraw Hill, New York, USA, 1969.

[2] N. S. Hall Taylor and G. F. Hewitt and P. M. C. Lacey, The motion and frequency of the large disturbance waves in annular two-phase flow of air-liquid mixtures, Chemical Engineering Science 18 (1963) 537–552.

[3] W. H. Henstock and T. G. Hanratty, The interfacial drag and the height of the wall layer in annular flows, AIChe Journal 22 (1976) 990–1000.

[4] J. S. Lioumbas and S. V. Paras and A. J. Karabelas, Co-current stratified gas-liquid downflow. Influence of the liquid flowfield on interfacial structure, International Journal of Multiphase Flow 31 (2005) 869–896.

[5] D. Schubring and A. C. Ashwood and T. A. Shedd and E. T. Hurlburt, Planar laser-induced fluorescence (PLIF) measurements of liquid film thickness in annular flow. Part I: Methods and data, International Journal of Multiphase Flow 36 (2010) 815–824.

[6] D. Schubring and A. C. Ashwood and T. A. Shedd and E. T. Hurlburt, Planar laser-induced fluorescence (PLIF) measurements of liquid film thickness in annular flow. Part II: Analysis and comparison to models, International Journal of Multiphase Flow 36 (2010) 825–835.

[7] P. S. C. Farias and F. J. W. Martins and L. E. B. Sampaio and R. Serfaty and L. F. A. Azevedo, Liquid film characterization in horizontal, annular, two-phase, gas-liquid flow using time-resolved laser-induced fluorescence, Experimetns in Fluids.

[8] L. A. Jurma and M. J. McCready, Study of waves on thin liquid films sheared by turbulent gas flow, Physics of Fluids A 1 (3) (1988) 522–536.

[9] S. Wittig and J. Himmelsbach and B. Noll and H. J. Feld and W. Samenfink, Motion and Evaporation of Shear-Driven Liquid Films in Turbulent Gases, Journal of Engineering for Gas Turbines and Power 114 (1992) 395–400.

[10] H. C. Kang and M. H. Kim , The relation between the interfacial shear stress and the wave motion in a stratified flow, International Journal of Multiphase Flow 19 (1) (1993) 35–49.

[11] M. A. Friedrich and H. Lan and N. E. Wilke and J. A. Drallmeier and B. F. Armaly , Measurement of the mean film thickness of dynamic shear-driven thin liquid films using optical interferometry, Atomization and Sprays 19 (7) (2009) 633–647.

[12] H. Lan and M. Friedrich and B. F. Armaly and J. A. Drallmeier, Simulation and measurement of 3D shear-driven thin liquid film flow in a duct, International Journal of Heat and Fluid Flow 29 (2008) 449–459.

[13] C. Lorencez and M. Nasr-Esfahany and M. Kawaji and M. Ojha, Liquid turbulence structure at a sheared and wavy gas-liquid interface, International Journal of Multiphase Flow 23 (2) (1997) 205–226.

[14] I. Owen and D. J. Ryley, The flow of thin liquid films around corners, International Journal of Multiphase Flow 11 (1) (1985) 51–62.

[15] B. J. Azzopardi and K. S. Sanaullah, Re-entrainment in wave-plate mist eliminators, International Journal of Multiphase Flow 11 (1) (1985) 51–62.

[16] F. Maroteaux and D. Llory and J-F. Le Coz and C. Habchi, Liquid Film Atomization on Wall Edges. Separation Criterion and Droplets Formation Model, Journals of Fluids Engineering 124 (2002) 565–575.

[17] M. A. Friedrich and H. Lan and J. L. Wegener and J. A. Drallmeier and B. F. Armaly , A Separation Criterion with Experimental Validation for Shear-Driven Films in Separated Flows, Journal of Fluids Engineering 130 (2008) 051301/1–9.

[18] J. L. Wegener and M. A. Friedrich and J. A. Drallmeier and B. F. Armaly, Experimental Evaluation of Film Separation Criterion, in: ICLASS 2009, 11th Triennial International Annual Conference on Liquid Atomization and Spray Systems, Vail, Colorado, USA, 2009.

[19] P.-G. de Gennes, F. Brochard-Wyart, D. Quéré, Capillarity an Wetting Phenomena. Drops, Bubbles, Pearls, Waves, Springer-Verlag New York Inc., 175 Fifth Avenue, New York, NY 10010, USA, 2004.

[20] I. S. Carvalho and M. V. Heitoyr and D. Santos , Liquid film disintegration regimes and proposed correlations, International Journal of Multiphase Flow 28 (2002) 773–789.

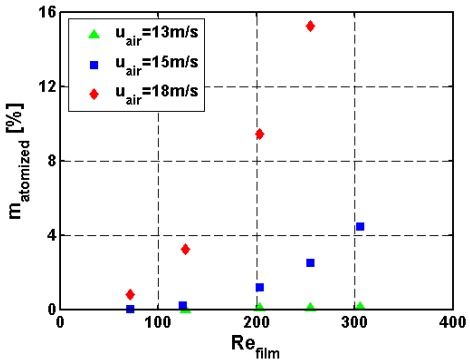

(a) Percentage of atomized mass

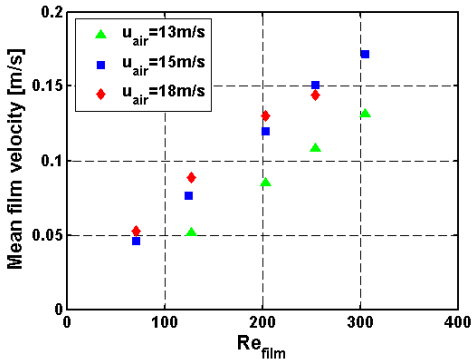

(b) Mean film velocity

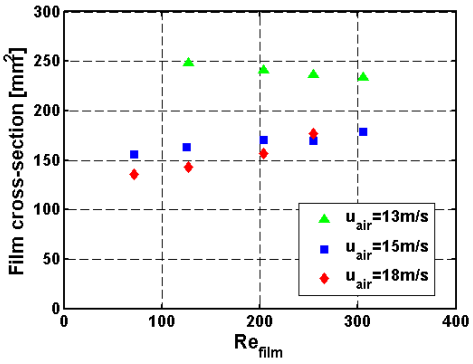

(c) Cross section of liquid film

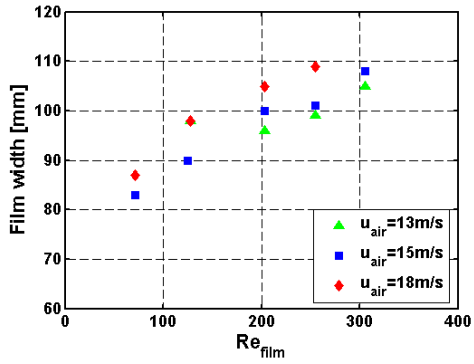

(d) Film width

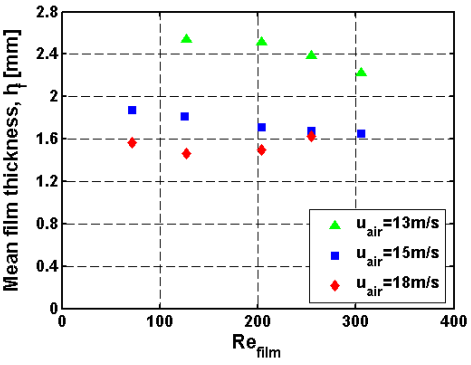

(e) Mean film thickness

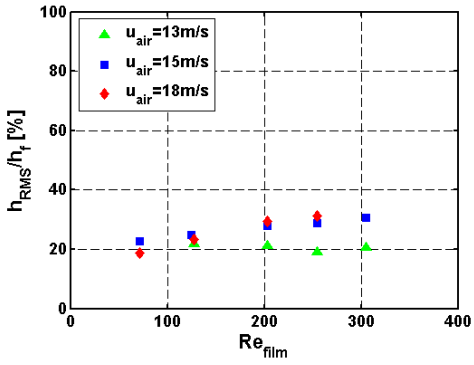

(f) Percentage of film thickness RMS

Figure 6: Atomized mass and local film characteristics measured at the edge of the corner. Case: Liquid film of region I

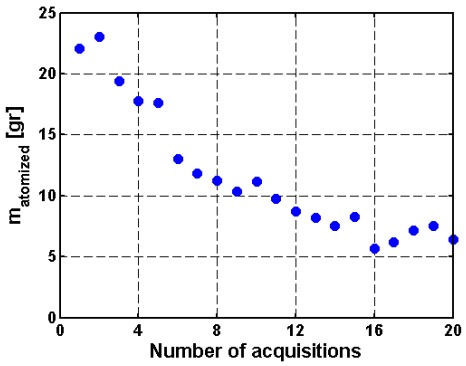

(a) Re_{film} = 254

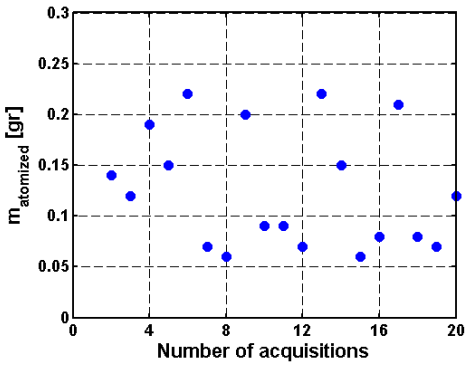

(b) Re_{film} = 117

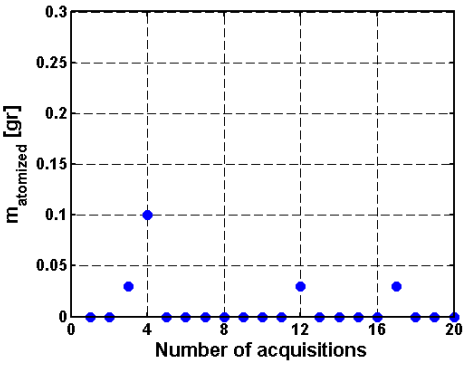

(c) Re_{film} = 97

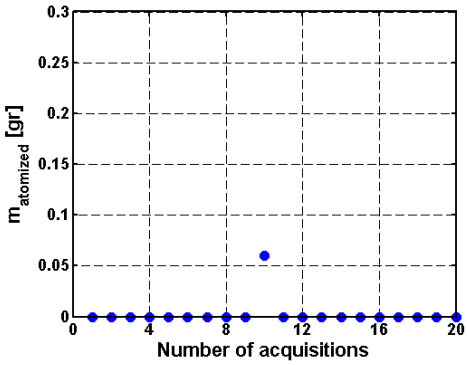

(d) Re_{film} = 86

Figure 7: Acquisitions of the atomized mass for constant air velocity u_a=15 m/s and different liquid Reynolds numbers.

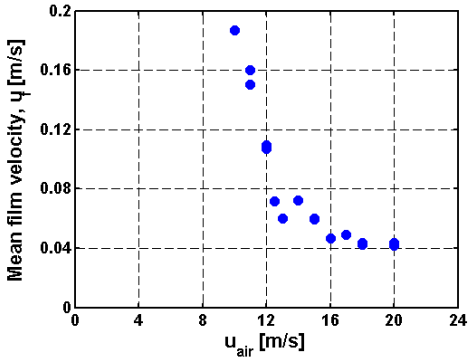

(a) Mean critical film velocity

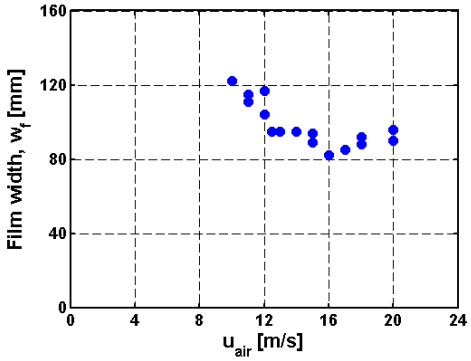

(b) Critical film width

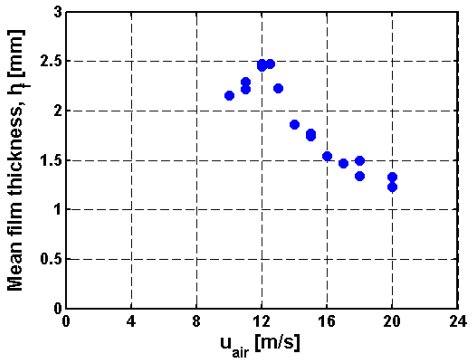

(c) Mean critical film thickness

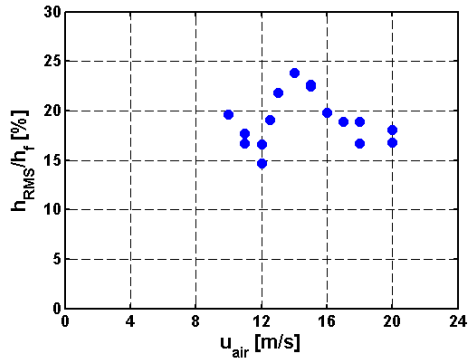

(d) Percentage of critical film thickness RMS

Figure 8: Liquid film parameters measured at the edge of the corner. Case: Critical conditions.

Development and application of the Multi Wavelength Light Extinction technique for the characterization of nano- and microparticles

Imre T. Horváth

Environmental and Applied Fluid Dynamics Department, von Karman Institute for Fluid Dynamics, Belgium, imre.horvath@vki.ac.be

Supervisor: Maria Rosaria Vetrano

Assistant Professor, Environmental and Applied Fluid Dynamics Department, von Karman Institute for Fluid Dynamics, Belgium, vetrano@vki.ac.be.

University Supervisor: Pierre Colinet

Professor, Transfers, Interfaces and Processes Department, ULB, pcolinet@ulb.ac.be

Abstract

Because of the large industrial and scientific interest in nanoparticles and nanoparticle flows, the requirement towards an online, submicron particle characterization technique is strongly expressed.

In the frame of the present PhD research a non-intrusive, optical measurement technique, the Multi Wavelength Light Extinction (MWLE) technique will be developed. It has several significant advantages compared to other existing measurement techniques. The MWLE technique is capable to measure the size distribution and concentration of the particles simultaneously, from several micrometres down to 30nm. The technique requires a simple and low-cost experimental apparatus and minimal optical access to the examined particles. These two properties make the technique suitable for online measurements in a large variety of situations. The shape of the investigated particles can be incorporated in the mathematical modeling, thus allowing the possibility for the qualitative evaluation of the particle shape, too.

The MWLE technique relies on relating the light transmittance spectrum of a particle cloud to the characteristics of the constituent particles.

The development was started with a bibliographic research on the field of light scattering by non-spherical particles. After the thorough understanding of the related theories, an appropriate mathematical model will be obtained. Two different cases will be considered; light scattering by airborne particles and particles deposited on a transparent substrate. Using the model, light scattering simulations will be carried out firstly to investigate the effect of the particle non-sphericity; secondly for the generation of the appropriate model parameters for the measurement of solid, metallic particles in both of the mentioned configurations. The retrieval of the particle size characteristics from the experimental data requires the solution of a Fredholm integral equation of the first kind, which is an ill-conditioned problem. Thus, the mathematical background of inverse problems will be studied. After, an inversion algorithm will be developed, which is robust, accurate and fast enough for the analysis of real measurement data.

After obtaining the necessary numerical and theoretical tools, the technique will be validated through the characterization of the size, concentration and fractal dimension of metallic nanoparticles and aggregates carried by a subsonic flow. The reference technique to be used will be the DMA-CPC (Differential Mobility Analyser Condensation Particle Counter) particle spectrometer. The latter investigation will be a preparation for the application of the technique in a nanoparticle production plasma facility. The aim will be to determine the particle characteristics as function of the operating parameters of the plasma facility.

The measurement technique will be further tested in the other mentioned configuration: particles deposited on a transparent substrate through the evaporation of a thin liquid layer will be examined. The prepared samples will be analysed by SEM (Scanning Electron Microscope), in order to provide a proper validation of the size analysis capabilities of the technique.

Keywords: nanoparticle, particle size distribution, light extinction, inverse problem, regularization

Experimental Study and Modeling of Two-phase Flow Cavitation and Flashing through Complex Valves

Jorge Pinho

Environmental and Applied Fluid Dynamics Department, von Karman Institute for Fluid Dynamics, Belgium, jorge.pinho@vki.ac.be

Supervisor: Patrick Rambaud

Associate Professor, Environmental and Applied Fluid Dynamics Department, von Karman Institute for Fluid Dynamics, Belgium, rambaud@vki.ac.be

Promotor: Jean-Marie Buchlin

Professor, Head, Environmental and Applied Fluid Dynamics, von Karman Institute for Fluid Dynamics, Belgium, buchlin@vki.ac.be

Industrial Supervisor: Saïd Chabane

CETIM, Centre Technique des Industries Mécaniques, France

Abstract

Two-phase flow are widely present in nuclear, chemical or mechanical engineering where different gas-liquid reactors, boilers, condensers, evaporators and/or combustion systems can be found. In these hydraulic systems the use of mechanical valves has a preponderant role for the security as it represents the ultimate protection before an accident. The complete understanding of the physics taking place in the flow through a valve becomes therefore crucial to guaranty this security of the protected process. In nuclear or thermal engineering systems the use of safety relief valves (SRV) is mandatory since it protects them against any over pressures. A careful design of the SRV is therefore essential. Reliable methods are available for SRV design in the cases of single phase flow such as liquid or gas discharge. When the static pressure through the valve falls below the liquid saturation pressure, vapor bubbles will form which tend to reduce the medium sound velocity. Similarly to compressible flow, this decrease of the speed of sound will be linked to limitation of the mass flow rate evacuated. In this two-phase flow, the single phase design methodology becomes inadequate. Currently, there are some calculation methods that attempt to predict the critical flow onset in SRV for two-phase systems knowing the inlet flow conditions and the outlet pressure; however none of them are acknowledged as being fully reliable as they make use of void fraction that is not currently measurable for flow experiencing cavitation.

This research project will be carried out at the von Karman Institute for Fluid Dynamics (VKI). A previous work carried out by Vasilis Kourakos focused on a two-phase flow through a SRV when air was injected upstream the valve. Several studies were performed and comparison with a transparent model was carried out at ambient temperature in an open loop. This previous work did not consider the case in which the fluid cavitates and/or flashes itself, being the reason why an external source of air was indeed needed to promote a two-phase flow.

The first part of the present research project is to update the VKI facility in order to increase the operational temperature and control the SRV back pressure. The new experimental facility will include a closed loop. Test conditions will be set through the control of a parallel pressurizing and vacuum system. Typically for water at 50C, cavitation will occur when the static pressure will fall below 12.3KPa.

Used measurement techniques will include; flow visualizations with a high-speed camera; unsteady pressure measurements upstream, inside and downstream the valve; temperature measurements; and void fraction measurement. This last technique will require a dedicated development. The proposed methodology consists in measuring the local sound velocity to retrieve the local void fraction. Proper calibration will have to be developed as well. Once knowing the void fraction in cavitation or flashing mode, the model predicting the mass flow rate such as the HNE-DS (2004) will be validated for the first time in this configuration.

Keywords: Two-phase flow, cavitation, flashing, safety relief valve, discharge coefficient

Experimental Study of Buoyant Plume and Thermal Stratification in a Liquid Metal Nuclear Reactor

Chiara Spaccapaniccia

Environmental and Applied Fluid Dynamics Department, von Karman Institute for Fluid Dynamics, Belgium, chiara.spaccapaniccia@vki.ac.be

Supervisor and University Supervisor: Jean-Marie Buchlin

Professor, Environmental and Applied Fluid Dynamics Department, von Karman Institute for Fluid Dynamics, Belgium, buchlin@vki.ac.be

Professor, Faculté de Sciences Appliquées, Université Libre de Bruxelles, Belgium, buchlin@vki.ac.be

Abstract

The development of new generation liquid metal cooled reactors leads to numerous advantages in the nuclear energy technology, such as a higher power density and improved operating safety.The Belgian nuclear research institute (SCK¢CEN) is developing MYRRHA, a subcritical liquid metal cooled reactor and commissioned at VKI the construction of a scaled water model.

One of the aspects to be tested is the formation of a stratified buoyant plume establishing during the reactor shut-down in the above core region that may influence the heat removal in natural convection working conditions and affect the integrity of the system. The thermal stratification of the plume anticipated in such a transient and the magnitude of the upper plenum thermal gradient should be assessed as a function of the core decay power.

The experimental techniques proposed for the analysis of the transient are the Particle Image Velocimetry and the Laser Induced Fluorescence: the PIV technique will be used for the measurement of the velocity field, while the thermal field will be measured by LIF.

The use of planar optical techniques for velocity and temperature measurements leads to numerous advantages. They can be used simultaneously, as required by the analysis of transient flows. They can picture complex phenomena like the thermal stratification of a buoyant plume . Furthermore the simultaneous measurements of the velocity and temperature fields allows the establishment of fine correlations between the buoyancy driven convective motion and the heat transfer mechanisms.

Before applying the proposed analysis to the water model of the whole MYRRHA reactor the combined PIV and LIF will be tested in step by step increasing complexity models.

The simultaneous application of PIV and LIF technique will be first assessed for natural convection cases by performing measurements on a vertical square enclosure uniformly heated in one side and uniformly cooled the other side thanks to the use of two Peltier elements. This model is chosen for the large availability of experimental and numerical data in literature. The aim is to determine which are the best seeding conditions for natural convection PIV test in water and the dye concentration that allows the highest temperature resolution obtainable through one color LIF.

A further step is the application of the proposed experimental study on the upper plenum of a small two dimensional natural convection model (Aquarium). The loop is designed in order to respect as much as possible the similarity with the MYRRHA hydraulic circuit working in natural convection conditions. The loop includes a heating section where a buoyancy plume develops and produces a thermal stratification in the upper plenum and a cooling section. The overall effect is a mass flow driven only by natural convection (Thermosyphon loop). The tests on the model will allow to validate the experimental techniques chosen and confirm the adequacy of their application for the analysis of stratification in the large scale model. Moreover they will allow to achieve a better understanding of the parameters that could influence the thermal stratification in the upper vessel region, such as the upper plenum geometry, the presence of obstacles in the above heat source region and the power distribution in the heat source.

Development of a Numerical Simulation Tool for the Aerothermal Flow through an Ablative Thermal Protection System for Atmospheric Entry

Pierre Schrooyen

Aeronautics and Aerospace Department, von Karman Institute for Fluid Dynamics, Belgium, pierre.schrooyen@vki.ac.be

Supervisor: Thierry Magin

Assistant Professor, Aeronautics and Aerospace Department, von Karman Institute for Fluid Dynamics, Belgium, magin@vki.ac.be

University Supervisor: Philippe Chatelain

Assistant Professor, Institute of Mechanics, Materials and Civil Engineering, Université Catholique de Louvain, philippe.chatelain@uclouvain.be

Keywords: atmospheric entry, thermal protection system, ablation, pyrolysis, laminar-turbulent flow transition.

1. Introduction

The challenge of atmospheric entry for a spacecraft has stimulated research on the aerothermal flow around the vehicle Thermal Protection System (TPS). During this phase, the spacecraft is strongly affected by aerodynamic heating due to the dissipation of its kinetic energy. Predicting an accurate heat-flux is a complex task, and especially modeling the following phenomena that are potential mission killers: the complex surface chemistry on the thermal protection material and the flow transition from laminar to turbulent. These difficulties are enhanced at higher entry velocities, typical of new missions to Mars or asteroids. To protect the payload or the astronauts onboard, engineers use safety factors to design the heat shield thickness leading to increased mass of the TPS.

The experimental investigation of entry aerothermal problems is still an extremely difficult endeavor which makes numerical methods crucial in advancing our understanding of these phenomena and in developing predictive design tools.

2. Problem statement

Reusable and ablative materials are the two main types of TPS in use today. While reusable protection materials are designed for low heat flux trajectories, ablative TPS are best suited for high entry velocity [1]. Requirements concerning mass efficiency for missions with very high entry velocities have led to the development of a new class of light carbon composite ablators. The components of these materials are carbon fibers and a filler matrix of phenolic resin. During atmospheric entry, a part of the heat flux is transferred inside the heat shield, leading to a gradual temperature increase of the material and to its transformation. One can separate the TPS in different zones: the virgin material, the pyrolysis zone and the char layer (see Fig. 1).

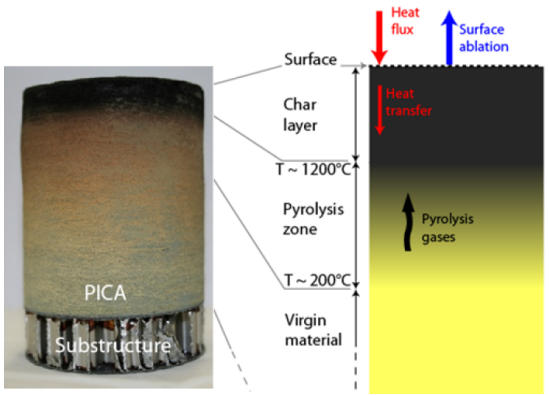

Figure 1: Picture of a core of Phenolic Impregnated Carbon Ablator (PICA) extracted from the TPS of Stardust [2] and schematic of the zones of degradation illustrating the material response to high-enthalpy flow

The virgin material is the unaltered part of the shield. In the pyrolysis zone, the phenolic resin is

progressively carbonized producing pyrolysis gases which are transported out of the material by diffusion and convection through the pores. The third zone is composed of the fibrous carbon preform and of the carbonized phenolic resin and is destroyed by ablation [3].

The models implemented until recently are well suited for dense ablative materials but for this new class of material, new design tools need to be developed. Our poor understanding of the coupled mechanisms of ablation and flow transition leads to difficulties in heat-flux prediction. More specifically, pyrolysis and ablation generate a mass flow and a surface roughness that interact with the flow in the boundary layer. Such perturbations can trigger transition of the flow from laminar to turbulent, leading to a strong increase of the convective heat-flux. This interaction between the type of flow and the roughness is illustrated in Fig. 2.

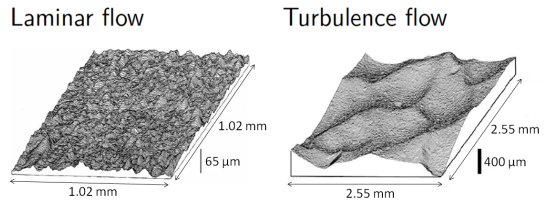

Figure 2: Surface topographies of polycrystalline graphite samples ablated under different flow regimes [4].

3. Method

The objective is to develop an integrated numerical tool for the high-fidelity prediction of the aerothermal performance of light carbon composite materials and their effects at the scale of the vehicle. This work focuses on the combined simulation and modeling of the flow and wall phenomena by means of a computational approach that can go seamlessly from a compressible flow to porous media and implements the most accurate physical models for non equilibrium flows and ablation. Accordingly, the goal is to capture the flow features away from the wall, the developing boundary layer, and the phenomena inside the TPS material. The challenges are many. Not only does one need to correctly resolve these two distinct media, the open flow and the wall but it is quite critical to capture their interactions and in particular the balance of the phenomena in the context of the transition of the boundary layer from laminar to turbulent regime.

The numerical tool will be implemented inside an existing code Argo developed in Cenaero. This platform is based on a Discontinuous Galerkin Method (DGM) which cumulates the advantages of finite volume and finite element discretization [5]. The approach will consider both the Direct Numerical Simulation (DNS) of the fluid flow equations for simplified geometry and their solution through modeling in a spatially filtered context (Large Eddy Simulation-LES). DGM is well suited for DNS and LES for complex geometry thanks to the use of unstructured meshes. Argo already possesses a formalism to solve convection-diffusion-reaction problem as well as an implicit temporal integration. This platform has already proven its capability to run DNS and LES computation in parallel for transitional flow at relatively high Reynolds number (60-100) [6].

The implementation strategy of the different models for the porous media follows the approach proposed by Lachaud to develop the Pyrolysis and Ablation Toolbox based on OpenFOAM (PATO) [7]. In a first step, we will consider the implementation of the model of Kendall et al [8] published in 1968 which has proved its validity for dense material. From the extremely complex phenomena occurring in a porous ablative material, they are only modeling Fourier's heat transfer and pyrolysis of the solid. Progressively more complex models will be introduced which take into account, for example, the identification of the species produced by pyrolysis, the transport and the chemical evolution of the pyrolysis gases inside or outside the material or the ablation as a volume phenomenon.

The verification and validation of the numerical tool developed will be gradual in its complexity and complementary by the different aspects tested. For instance, a milestone of the project is the comparison of the results with the work of Crocker and Dubief [9] which deals with a turbulent flow in a channel influenced by an eroding wall. Comparisons with simple geometry test cases studied at the Université catholique de Louvain in pyrolysis of the biomass and VKI experimental data will allow to validate the simulations inside the heat shield.

4. Ongoing work

Our current effort is twofold. On one hand, we focus on the implementation of diffusive and reaction

terms in a one dimensional DG code. On the other hand, we investigate immersed interface techniques for moving boundaries in a DG context in order to capture recession of the material. The results of the current 1D code are compared with the Aerotherm Charring Material Ablation (CMA) program developed by Kendall et al [8].

5. Perspectives

The numerical methods currently being implemented will be useful to compare against the results of Crocker and Dubief [9] . In this context, we envisioned to use immersed interface technique to model surface ablation. According to the assumptions of Kendall et al [8], the flow of pyrolysis gas through the TPS is considered normal to the heated surface and the drop in pressure through the char is supposed negligible. The next step will be to drop this hypothesis and solve Darcy's equation which models the gas flow inside the porous medium. Afterwards, the idea is to evolve towards 2D and 3D versions of the code describing the in-depth thermal response of the material.

Acknowledgments

The author acknowledges support through a fellowship from the "Fond pour la formation à la Recherche dans l'Industrie et dans l'Agriculture "and support of the Argo team from Cenaero.

References

[1] J. A. Dec, Three Dimensional Finite Element Ablative Thermal Response Analysis Applied To Heatshield Penetration Design, Ph.D. thesis, Georgia Institute of Technology (2010).

[2] M.Stackpoole and S. Sepka and I. Cozmuta and D. Kontinos, Post-flight evaluation of stardust sample return capsule forebody heat shield material, in: paper AIAA 1202, Aerospace Sciences Meeting and Exhibit, Washington, DC, 2008.

[3] J. Lachaud, T. Magin, C. I., N. Mansour, A short review of ablative material response models and simulation tools, in: 7th European Aerothermodynamics Symposium, Brugge, 2011.

[4] G. Vignoles, J. Lachaud, Y. Aspa, J. Goyhénèche, Ablation of carbon-based materials: Multisclae roughness modelling, Composites Science and Technology 69 (2008) 1470–1477.

[5] J. Hesthaven, T. Warburton, Nodal Discontinuous Galerkin Methods; Algorithms, Analysis and Applications, Text in Applied Mathematics, Springer Verlag, 2008.

[6] K. Hillewaert, Convergence analysis of higher-order discontinuous galerkin method for the direct numerical simulation of transitional flows, in: DEISA PRACE Symposium 2011, Stockholm, 2011.

[7] J. Lachaud, A pyrolysis and ablation toolbox based on openfoam, in: 5th OpenFOAM Workshop, Chalmers, Gothenburg, June 21-24, 2010.

[8] E. P. Bartlett, R. M. Kendall, An analysis of the coupled chemically reacting boundary layer and charring ablator. part 3 - nonsimilar solution of the multicomponent laminar boundary layer by an integral matrix method, Contractor Report CR-1062, NASA (1968).

[9] R. Crocker, Y. Dubief, Numerical study of turbulence over a receding wall by controlled and thermal ablation, in: Proceedings of the Summer Program 2010, Center for Turbulence Research, Stanford, USA, 2010.

ATMOSPHERIC FLOW

Experimental Parametric Study of the Influence of an Idealized Upstream Ridge on the Flow Characteristics over Alaiz Mountain

Boris Conan

Environmental and Applied Fluid Dynamics Department, von Karman Institute for Fluid Dynamics, Belgium, boris.conan@vki.ac.be

Supervisor: Jeroen van Beeck

Professor, Environmental and Applied Fluid Dynamics Department, von Karman Institute for Fluid Dynamics, Belgium, vanbeeck@vki.ac.be

University Supervisor: Sandrine Aubrun

HDR, PRISME Laboratory, Polytech'Orléans, France, sandrine.aubrun@univ-orleans.fr

Abstract

This paper presents a preliminary quantification of the influence of an upstream obstacle on the top of a main topography. Its influence is compared to the effect of changing inlet terrain roughness conditions. A simplified 2D model is built and several inlet conditions are coupled with different upstream relief distances. The velocity deficit and the turbulence increase are discussed. The main result is the higher influence of the inlet conditions compared to the obstacle position.

Keywords: atmospheric boundary layer, wind resource asessment, complex terrain, PIV, Alaiz hill.

1. Introduction

Physical modeling in a wind tunnel is a common tool for numerous applications like atmospheric dispersion investigations, wind comfort assessment or wind loads on buildings studies. In the booming wind energy sector, wind tunnel tests can be a suitable tool for the assessment of the wind resource, especially for wind turbine micro-siting in complex terrain.
The simulation of atmospheric flows in the wind tunnel requires the verification of a number of assumptions. Taking as implicit the similarity criteria (dimensionless numbers) described by Cermak [1], a certain number of parameters have to be taken into account: the Reynolds number dependence, the modelling of the local roughness on the mock-up, the reproduction of inflow conditions and the choice of the modelled area.
The latter is a major parameter that drives the choice of the scaling factor and influences all the other parameters. The choice of the area to model is the result of a compromise between: having a large area in order to reproduce closely the effects of the surroundings topographies, the limitation of the wind tunnel dimensions (blockage) and the difficulties to reproduce realistic flows at very high scaling factors (model roughness, reproduction of inflow conditions, measurements limitations).

The Alaiz site (Fig. 1) tested in the wind tunnel [2] illustrates this conflict. The terrain is a 1130m high mountain situated next to Pamplona (Spain); it is a very complex terrain stretching over 10km in the W-E direction and 8km in the N-S direction [3]. When the wind comes from the North, one of the dominant directions, it faces a ridge before reaching the mountain (position x = 0.75m in Fig. 1). The ridge is around 1/3 of the main mountain's height and 7km upstream. An influence is expected, it is then chosen to include it in the wind tunnel mock-up. Giving the test section size (2m x 3m), that leads to a very large scaling factor of 1/5300.
Experimental tests are realized at the von Karman Institute in the 2m x 3m x 15m wind engineering test section. Particle Image Velocimetry and hot-wire anemometry measurements are performed along a 2D plane parallel to the wind direction as described in Figure 1.

One of the main results of this study is the high influence of the upstream ridge on the flow field on the main mountain. Figure 1 shows the Fractional Speed-up Ratio (FSR) over the terrain and enlightens the important speed-down (almost -50% compared to the inlet conditions R1) at the foot of the mountain (R2) due to the disturbance of the upstream ridge (x = 0.75m). Measurements show the speed-up and the turbulence intensity at the top of the mountain very affected by the separation occurring at the ridge. It leads to the conclusion that the area of influence of the flow up to the mountain is vast and must be taken into account in the model.
On the other hand, the extreme scaling factor leads to some difficulties in reproducing the inflow conditions. The inlet turbulence profile provided by the VDI guidelines [4] is hard to match close to the surface for this scaling factor. Additionally, questions emerge concerning the relaxation of the Reynolds number and the surface roughness of the model.

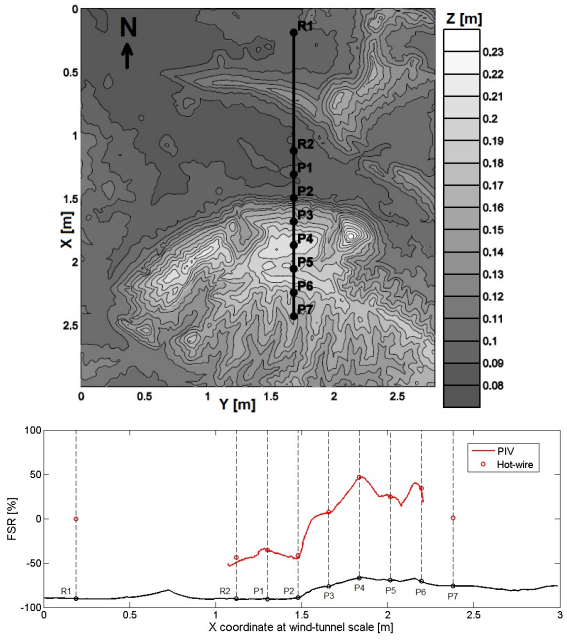

Figure 1: Top view of the Alaiz terrain at the wind tunnel scale 1/5300 (top). Fractionnal Speed-up Ratio (FSR) at 90m over the mountain (bottom).

Very high scales are difficult to work with, however, as shown by the study of the Alaiz mountain, the flow field over a mountain is influenced by an upstream ridge three times smaller and situated 7km upstream.

This study aims at illustrating the question of the modelled area size through a parametric study designed to evaluate the influence of an upstream hill on a major downstream mountain. Different configurations will be tested by changing the distance from the ridge to the mountain and inlet conditions.

2. Experimental conditions

2.1. Experimental set-up

For the parametric study, a suction-type wind tunnel is used with a 0.35m x 0.35m x 2m test section. The velocity can be adjusted up to 35 m/s. The use of a reduced size tunnel is an advantage for a parametric study so that several configurations can be tested in a short time and for limited costs.
To keep the blockage ratio below 10%, the model is scaled down to 1/19200. At that scale, the simulation of turbulence scales might not be respected. The objective of this model is a parametric study; results may not be used for direct application at full scale.
The mock-up is a two-dimensional model of the width of the test section representing the line shown in Figure 1 from point R1 to P7. The choice of a two dimensional model is supported by the comparison performed in a previous study showing a good agreement between the wind tunnel test and a 2D CFD computation on this very same line [5]. The front ridge is simplified to a triangular shape and can be displaced upstream and downstream for the parametric study. In the original configuration: H = 2.5*h; D = 24*h and h = 13 mm (Fig. 2). The wind tunnel is equipped for two-dimensional Particle Image Velocimetry (PIV) measurements. Three planes are necessary to measure all the topography but a reconstruction of the measurements is possible for average quantities: U, V, I_u and I_v. 500 images are acquired and averaged for each plane.

2.2. Flow conditions

The atmospheric inflow conditions are modeled thanks to a 1m fetch where roughness generators are placed to simulate an atmospheric boundary layer (ABL). Three different inlet conditions (Fig. 3) are tested in the wind tunnel by combining surface roughness (lego floor with $h_{lego-floor}$ = 2mm) and Counihan wings (h_{CW} = 90mm) in the following, they are named: FP = Flate plate, LF = Lego floor and CW = Counihan wings + Lego floor. (Fig. 3)
At the scale of 1/19200, the boundary layers represent three different terrain roughness (Fig. 3) from slightly rough to rough according to the VDI guidelines [4].

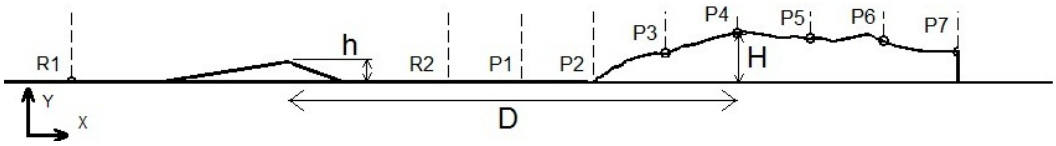

Figure 2: Mock-up in the wind tunnel.

The two-dimensionality of the flow is estimated by performing PIV planes at four locations in the Z direction around the middle measurement plane. In a +/- 20mm slice in the middle of the test section the velocity varies by less than 0.7% and the turbulence by less than 0.4%.
In the range of the wind tunnel velocities, measurements at three different Reynolds number are recorded at the top of the model. Taking as reference length the front ridge height (h), it gives Re = 8300; Re = 12400 and Re = 16600. The Reynolds number dependency decreases with increasing velocity, the maximum discrepancies are at around h = 400 m with less than 3% difference in speed. The very high scaling factor may explain this dependency. The highest velocity (20 m/s) is chosen for the tests.

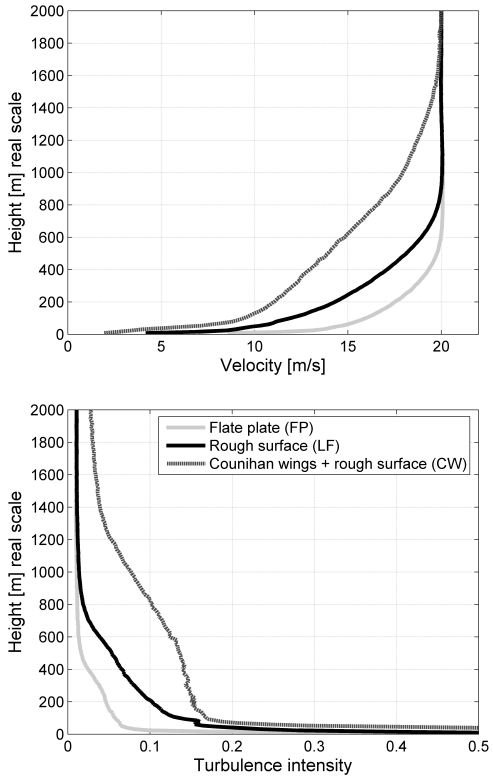

Figure 3: Boundary layer simulated in the test section.

3. Presentation of the results

3.1. Flow around the original configuration

When it reaches the front ridge, the velocity increases and creates an over-speed at its top. On the lee side, the flow separates and creates a recirculation bubble (Fig. 4). This separation is generating high turbulence and a very important velocity reduction at the height of the ridge. The velocity recovers after the perturbation but the flow is still disturbed, with lower velocities and higher turbulence, when it reaches the mountain. The behavior is very similar to the one described on the three-dimensional model [2].
Two local quantities are used in this study: the Fractional Speed-up Ratio (FSR) and the Turbulence Intensity Ratio (TIR), they represent the ratio of change compare to the inlet conditions:

$$FSR_i = \frac{U_i - U_{inlet}}{U_{inlet}} \quad (1)$$

$$TIR_i = \frac{Ti_i - Ti_{inlet}}{Ti_{inlet}} \quad (2)$$

The FSR is computed at 90m and compared with the study at scale 1/5357 presented in the introduction. It illustrates well the behavior of the flow around the ridge and the mountain (Fig. 5), the front ridge creates a speed-up followed by a strong speed-down in the recirculation, then the speed increases again until x = 1.25m, at this point the mountain creates a speed-down. On the mountain, the speed is rising until the top, where the speed-up is the highest. The mountain speed-up is nearly 100% front the foot to the top but due to the front ridge, it is reduced to around 50%.

Figure 5 shows the comparison between the test in the big wind tunnel at scale 1/5 357 with a three-dimensional model and the test presented above at 1/19 000 scale with a two-dimensional model. The two measurements are very comparable, both in terms of behavior (shape) and quantities; the speed-up at the top of the mountain is very well reproduced. Discrep-

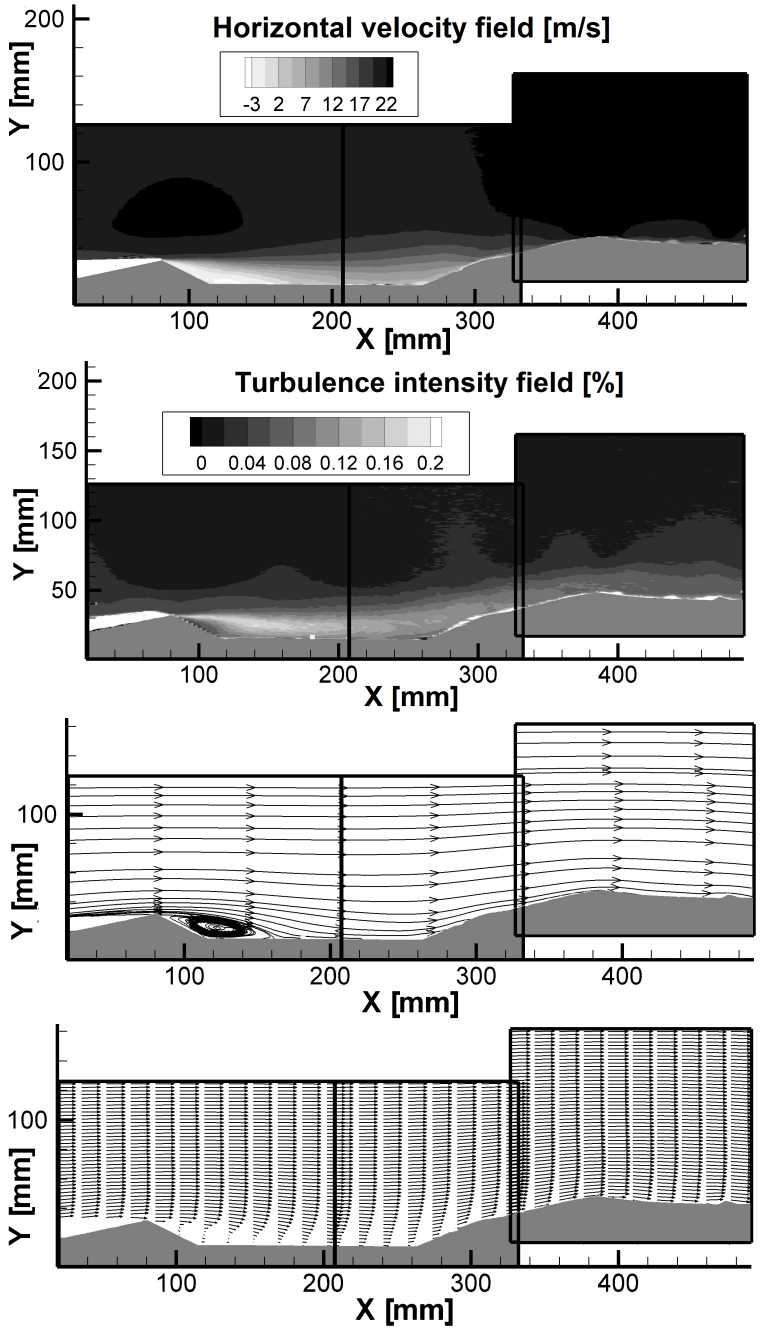

Figure 4: Velocity and turbulence intensity fields, velocity streamlines and velocity vector field in the original Alaiz configuration with low roughness inlet conditions (FP).

ancies appear in the recirculation after the ridge (x = 0.75m), this is most probably due to the simplification of the geometry (2D), therefore, 3D effects are not all reproduced. The two dimensionality of the flow in the measurement plane was already detected by the comparison of the wind tunnel tests with 2D CFD computation [5] and reinforces the validity of the choice of a two-dimensional model.

3.2. Profiles at the top of the mountain (position P4)

Figure 6 presents the results (PIV) from the parametric study with 5 ridge positions and three inlet

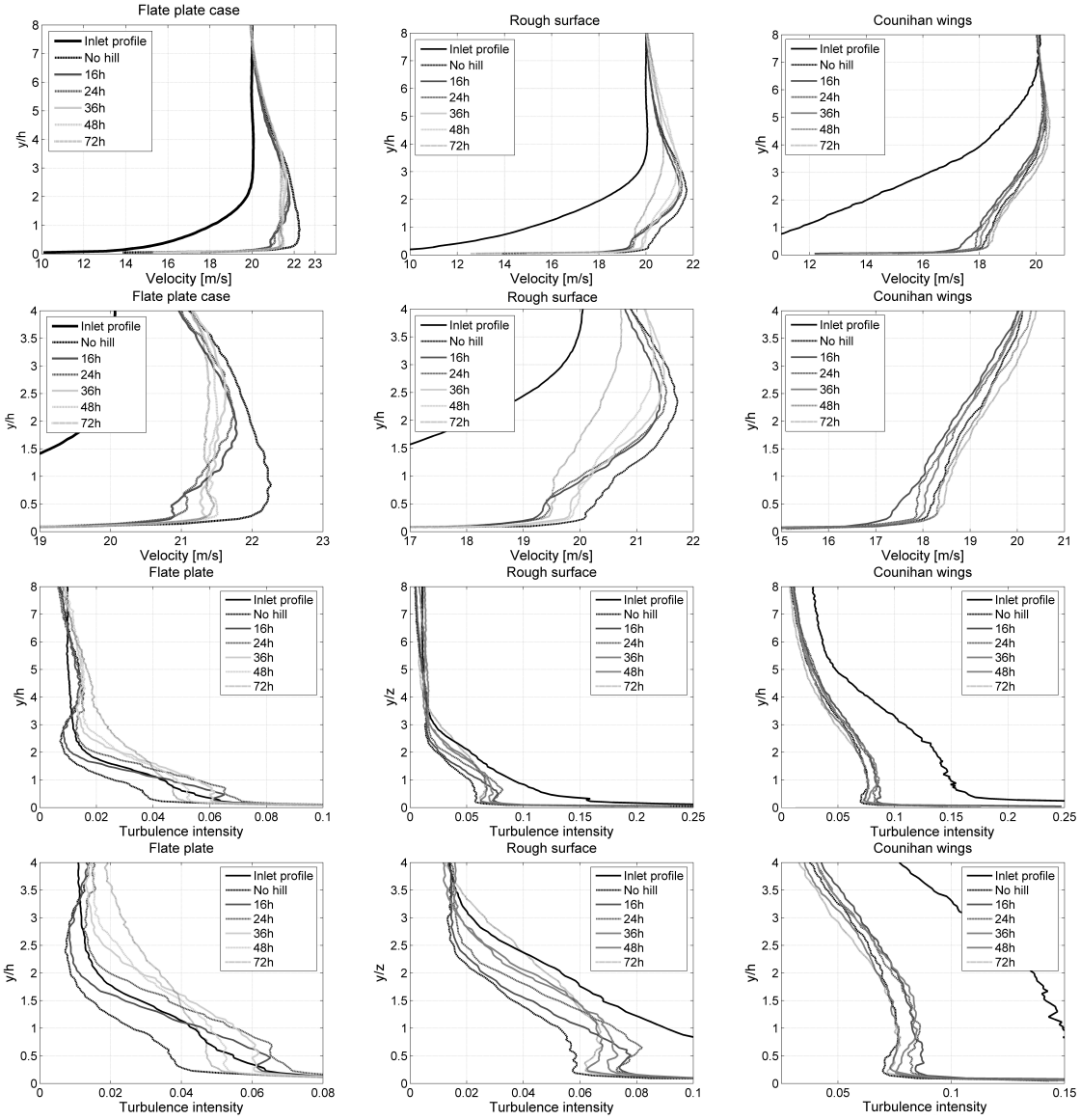

Figure 6: Velocity and turbulence profiles for five ridge distances: 16h, 24h, 36h, 48h and 72h, and three inlet conditions: left: ”flate plate” (FP), middle: ”rough surface” (LF) and right: ”Counihan wings + rough surface” (CW). Global views and clser look are proposed.

conditions (see section 2.2).

Two heights (a.l.g) are defined to describe the influence of the ridge on the flow at the top of the mountain: z = 2h and z = h/2.
The influence of the ridge is clearly enlightened by comparing the velocity profile for the ”no ridge” case with any of the ridge distances: the velocity is reduced and the turbulence increased at, below and above the ridge’s height. Concerning the Counihan wings case, the boundary layer is not completely measured in the PIV field so the normalization of the velocity profile can be a problem: the velocity of the ”no ridge” case might be underestimated.

Figure 7 presents the ratio of change in velocity and in turbulence intensity with the distance downstream of the ridge; the reference point is the case without front ridge. This is a great tool to describe the relative evolution of the values with the distance.

The effect of the ridge distance depends of the height of comparison, at z = h/2, for all inlet condi-

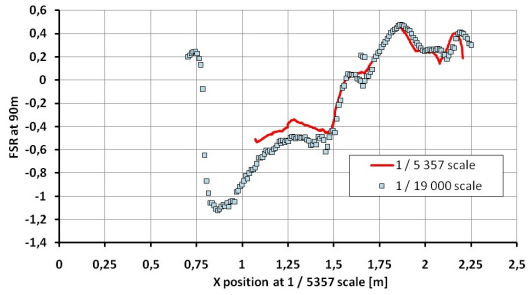

Figure 5: Comparison of the FSR at two scales.

tions, the velocity deficit, that is very high after the separation, gradually decreases with increasing distance. In the same time, the turbulence intensity decreases. It can be noticed from Figure 7 that the ratio of velocity is increasing equally for the flat-plate (FP) and the rough surface (LF) cases. With the Counihan wings, (CW), the velocity increases faster. Concerning turbulence levels, the ridge induces much higher perturbation for the flat-plate case than for the CW case. For both FP and LF configurations, the turbulence level decreases asymptotically to the initial value.

At z = 2h, observations for the FP and the LF inlet conditions are similar: the velocity decreases with increasing distance and the turbulence increases. This is the opposite behavior compared to the z = h/2 case. For the CW inlet conditions, the flow follows the same behavior as the z = h/2 case, the velocity is increasing and the turbulence intensity decreasing with increasing distance. As previously, the flow is much more affected with FP inlet conditions than with the CW.
At a distance of d = 72.h, for z = h/2, the velocity deficit is of the order of 3.4% for the FP and the LF cases, it is lower for the CW case. The relative turbulence increase is still important, especially for the FP case (+28% compare to the case without hill). At z = 2h, the velocity deficit is lower but the relative increase of turbulence much higher and very dependent on the inlet conditions.

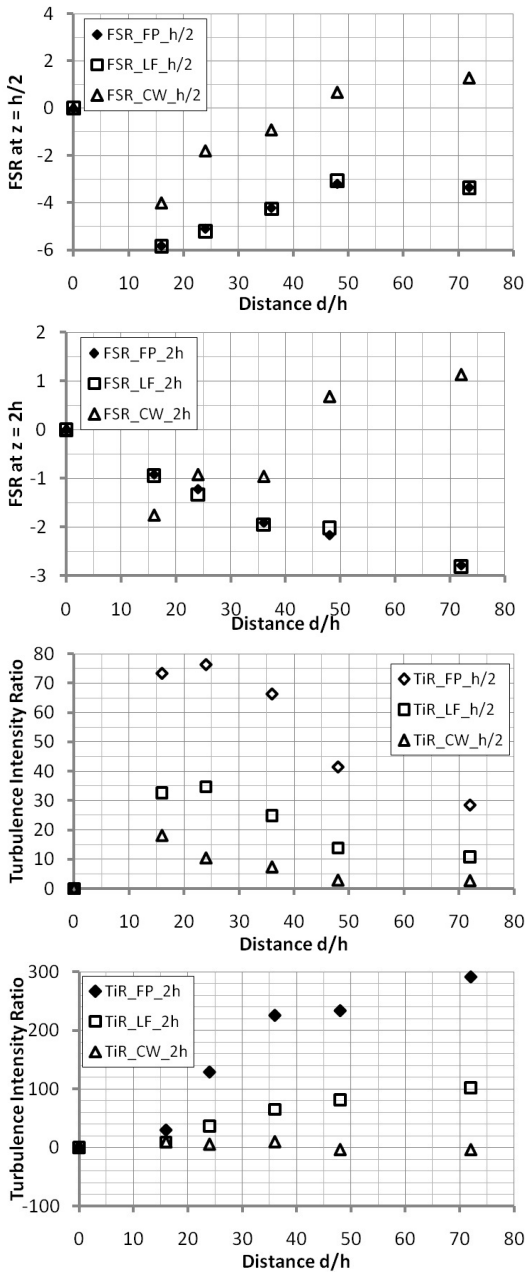

Figure 7: Fractionnal Speed-up Ratio [%] and turbulence intensity [%] evolution with the distance (FP = Flate Plate, LF = rough surface and CW = Counihan Wings).

4. Interpretation and discussions

The flow is highly affected by the ridge and a high velocity deficit is created together with a great turbulence increase. This happens at the ridge position, for z < h through a recirculation on the lee side of the ridge. After this, the flow recovers: the velocity and the turbulent level, affected by the separation, tend to come back to the inlet conditions. Flow conditions at the top of the mountain are then influenced by the distance of the ridge: the further the ridge, the more recovered is the flow when it reaches the mountain.

Above the ridge's height, the flow experiences a speed-up due to the relief, the wake propagates upward creating a velocity deficit and a turbulence

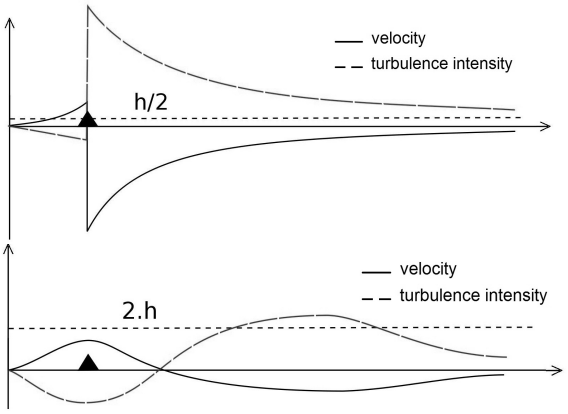

Figure 8: Tentative of a schematic representation of the evolution of the velocity and the turbulence intensity in the wake of a hill at two altitudes below and above the ridge's height.

increase for z > h. After a while, the velocity and turbulence level will then tend to come back to the inlet flow conditions. The observations are coherent with a recovery of the flow after the ridge separation (Fig.8).

From the observations, an important factor influencing the flow on the mountain's top is the inlet turbulence intensity; for the same distance, the influence of the ridge is lower for more turbulent inlet conditions. This parameter is, in this case, more important than the distance from the ridge to the mountain. The results summarized in Figure 8 presents clearly this effect: the FSR is much more affected by the inlet conditions than by the distance from the hill to the mountain. Indeed, the wake of the ridge dissipates faster in a turbulent flow.

5. Conclusions and perspectives

The study underlines the two-dimensionality of the flow around this part of the Alaiz mountain, the 1/19000 scale is a valid assumption for parametric study. However, limitation rises when reproducing the inlet conditions.

The parametric study shows the influence of the upstream ridge on the flow conditions on the top of the mountain, at 72 times the ridge height, the FSR at h/2 is influenced by -3.5% and the turbulence intensity is increased by 30% (ratio compare to inlet conditions). The turbulence is the most important quantity modified.

When changing the roughness of the inlet terrain simulated, the influence on the flow at the top of the mountain turns out to be more important than

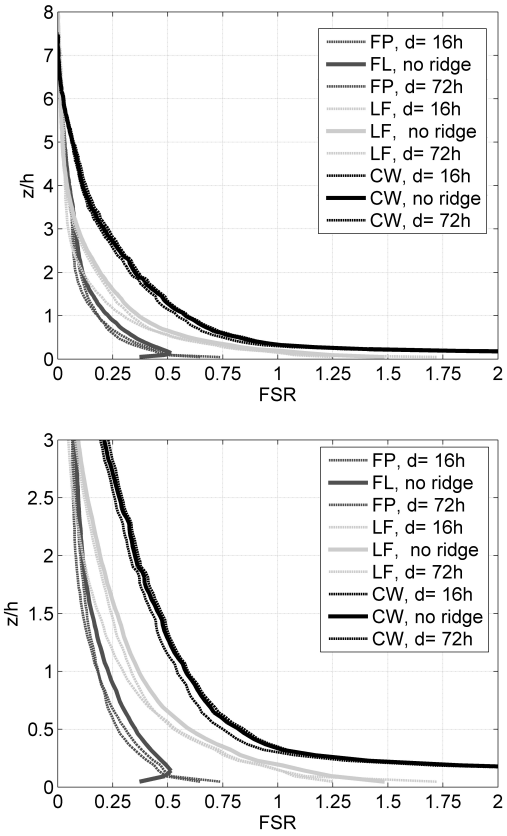

Figure 9: FSR at the mountain's top for the three inflow conditions and the two extreme ridge positions.

changing the ridge position. This is probably due to the faster wake recovery in more turbulent flows. The FSR is 37% for FP, 60% for LF and 80% for CW at h/2. The inlet condition, in this case, is a predominant parameter to consider compared to the ridge position.

For further studies, the investigation of the wake of simplified hills is planned with a particular focus on the far wake flow conditions and on the influence of the inlet flow conditions. Results can also be compared with available linear models.

Acknowledgments

This work is performed within the WAUDIT Marie-Curie Initial Training Network (Wind Resource Assessment Audit and Standardization) funded by the European Commission.

Fernando Carbajo, is greatfully acknoledge for his important participation in this work.

References

[1] J. Cermak, Applications of fluid mechanics to wind engineeringa freeman scholar lecture, Journal of Fluids Engineering 97 (1975) 9.

[2] B. Conan, S. Buckingham, , J. Van Beeck, S. Aubrun, J. Sanz, Feasibility of micro-siting in mountainous terrain by wind tunnel physical modelling, in: In: Sc. Proc. European Wind Energy Conf., March 2011, Brussels, 2011, pp. 136–140.

[3] D. Cabezón, J. Sanz, J. Van Beeck, Sensitivity analysis on turbulence models for the abl in complex terrain, in: In: Proc. Europ. Wind Energy Conf., May 2007, Milan, 2007.

[4] VDI-guidelines, Vdi guidelines 3783/12 - physical modellling of flows and dispersion processes in the atmospheric boundary layer - application of wind tunnels.

[5] D. Muñoz-Esparza, B. Conan, E. Croonenborghs, A. Parente, J. Van Beeck, J. Sanz, Sensitivity to inlet conditions of wind resourcce assessment over complex terrain using three cfd solvers and wind tunnel data, in: In: Sc. Proc. European Wind Energy Conf., March 2011, Brussels, 2011, pp. 200–204.

Mesoscale Modelling and On-site Measurements of the Offshore Boundary Layer in the North Sea

Domingo Muñoz Esparza

Environmental and Applied Fluid Dynamics Department, von Karman Institute for Fluid Dynamics, Belgium, domingo.munoz.esparza@vki.ac.be

Supervisor: Jeroen van Beeck

Professor, Environmental and Applied Fluid Dynamics Department, von Karman Institute for Fluid Dynamics, Belgium, vanbeeck@vki.ac.be

University Supervisor: Jean-Marie Buchlin

Professor, Faculté des sciences appliquées/Ecole Polytechnique, Université Libre de Bruxelles, Belgium, buchlin@vki.ac.be

Abstract

Nowadays, wind energy is increasing its contribution into the energy market. Because of that, accurate predictions of the power production are needed and thus, wind speeds need to be properly forecasted. This study thoroughly analyzes the ability of the WRF model to reprode Offshore Boundary Layer conditions under different stability scenarios. Results are validated against a comprehensive data base of field measurements from FINO1 platform, including turbulent fluxes calculated with sonic anemometry as well as LiDAR wind profiling.

Keywords: Mesoscale modelling, offshore boundary layer, turbulent fluxes, wind shear, atmospheric stability, tall wind profiles, FINO1 mast, wind energy

1. Introduction

The offshore wind capacity installed up to now in Europe is of almost 4 GW. Currently, almost 6 GW of offshore wind capacity are under construction, 17 GW have been consented by EU Member States and there are future plans for a further 114 GW. Therefore, it is expected that during this decade, offshore wind power capacity will grow tenfold to reach an estimated installed capacity of 40 GW for 2020 [1]. In order to make such a development feasible, mesoscale models play a key and promising position both for the optimization of the location of wind farms (wind resource assessment) and for the daily energy production once the wind farm will be in operation (short term forecasting).

Up to now, evaluation of wind resource assessment models at the offshore mast FINO1 was limited by the constraint in the height of the measurement mast (100 m). Nowadays, 5 MW wind turbines are typically operating in offshore wind farms, like is the case of the recently installed Alpha Ventus wind farm nearby FINO1. In that situation, the ability of mesoscale models to forecast "tall" wind profiles needs to be properly addressed as well as its applicability for wind energy purposes.

In the offshore environment, special attention has to be paid to the role of atmospheric stability. The atmospheric stability yields to notably different shear conditions and thus different velocity distributions across the rotor swept area, which dramatically influences, among others, the power production and fatigue loads on the wind turbine.

The effect of the vertical mixing due to turbulence in the planetary boundary layer (PBL) is not explicitly resolved by mesoscale models. Such models parameterize this effect employing the so-called closure techniques based on gradients of resolved quantities. For some applications, such as wind energy, where the near-surface atmospheric processes are crucial, the choice of PBL modelling becomes an important issue and thus, needs to be carefully analyzed.

In the present study, the ability of different turbulent flux parameterizations in the Weather Research



(a) (b)

Figure 1: Research platform FINO1. (a) General view of the mast. (b) Detailed view of a sonic anemometer.

and Forecasting model (WRF-ARW) to account for the atmospheric stratification is thoroughly evaluated at FINO1. For the first time, we took advance of the recent LiDAR measurement campaign carried out at FINO1 up to 250 m height, encompassing the rotor area of the tallest wind turbines, in order to accomplish this objective. All this information allowed us to perform a complete validation based on turbulent fluxes and surface stability parameters, as friction velocity, u_*, heat flux, $< w'\theta' >$, and Obukhov length, L (derived from sonic anemometry) and on tall wind profiles measured with LiDAR.

2. Field measurements

The German research platform FINO1 is located 45 km off the Borkum Island (lat. 54∘0.87'N, lon. 6∘35.24'E) in the North Sea and is in operation since 2003 (Fig. 1a). In the present work, measurements from one year period (Jan. 2010 - Dec. 2010) investigated by [2] are used. Sonic anemometer data (Fig. 1b) at 40 m, 60 m and 80 m were used to derive turbulent fluxes of momentum and heat (10 Hz sampling) while slow profile response sensors (10 min averages): wind speed (cup anemometers), wind direction, relative humidity, air pressure and temperature, are mainly used for data processing.

In addition, a ground-based pulsed LiDAR system, the so-called "WindCube", developed and manufactured by the French company Leosphere has been used in this study [3]. The LiDAR system was positioned on a container roof at approximately 10 m distance to the north-west of the offshore research mast FINO1 and performed continuous measurements from July 2009 to February 2010, scanning the wind profile up to a height of 250 m. This LiDAR has been proven to be applicable for wind speed and wind direction measurements by comparison against other velocity sensors [3; 4].

Once turbulence fluxes of heat and momentum are calculated, the atmospheric stability as described by the Monin-Obukhov Similarity Theory (MOST) was computed based on the Obukhov length, L (Eq. 1).

$$L = -\frac{\theta u_*^3}{g\kappa < w'\theta' >}, \quad (1)$$

where u_* is the friction velocity, $< w'\theta' >$ is the heat flux, g is the acceleration due to gravity, κ is the von Kármán constant (equal to 0.40) and θ is the potential temperature. Angle brackets denote ensemble averaged values.

Stability Regime	zL^{-1} [-]
Very Unstable	$-4 \leq zL^{-1} \leq -0.2$
Unstable	$-0.2 < zL^{-1} \leq -0.04$
Near Neutral	$-0.04 < zL^{-1} \leq 0.04$
Stable	$0.04 < zL^{-1} \leq 0.2$
Very Stable	$0.2 \leq zL^{-1} \leq 4$

Table 1: Limiting values of zL^{-1} for the four stability classes in which the data is grouped (for z=40 m).

According to the values of zL^{-1}, the data has been grouped into different stability classes according to [5] (Table 1). From the developed database, long periods corresponding to each stability class has been chosen and simulated with WRF, as is shown in the upcoming sections.

3. WRF model setup

In this study we use the Numerical Weather Prediction model of the National Center for Atmospheric Research in USA (NCAR): Advance Research WRF-ARW v3.2. WRF-ARW is a conservative finite differences model that solves the unsteady non-hydrostatic compressible Euler equations [6].

Our computational domain is composed by 4 domains centered over FINO1 platform. The parent domain has a horizontal grid spacing of 27 km and covers an approximate surface of 3000 km^2, including most of Europe. Grid spacing is refined progressively by a factor of 3 through three nested domains until 1 km resolution is achieved for the most inner one, which covers approximately 100 km^2. On the vertical coordinate, 46 levels are placed. Grid spacing is of

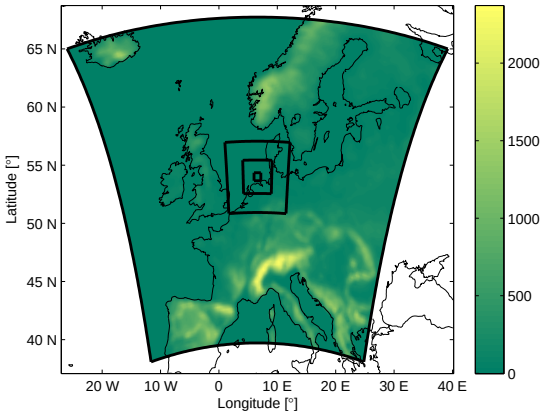

Figure 2: WRF domain configuration. The horizontal resolutions of the four domains are 27 km, 9 km, 3 km and 1 km, from the parent to the most inner domain, respectively. Color bar indicates surface elevation in meters.

10-20 m up to 300 m height to accurately resolve the lower part of the boundary layer. Above, grid spacing is progressively stretched in order to reduce the computational cost. Interactions of the meteorological fields between the domains are accounted for by two-way nesting. The domain configuration is shown in Fig. 2. The timestep is consistently reduced from the parent domain to the most inner domain in order to respect numerical stability constraints (CFL<1). WSM 3-class simple ice scheme microphysics, rapid radiative transfer in the longwave, the Dudhia shortwave scheme, NOAH surface scheme and cumulus Kain-Fritsch scheme (not applied into the two most inner domains) were used. Each PBL parameterization is tied to a particular surface layer scheme [6], all of them based on Monin-Obukhov similarity theory [7].

The parent domain is initialized and 6-hourly forced at the boundaries by meteorological fields derived from the NCEP Climate Forecast System Reanalysis data, CFSR [8], with a horizontal resolution of 0.5^o x 0.5^o. The first 24 hours are discarded as spin-up time of the model and subsequent forecasts are considered in order to devolop the proper mesoscale spectum [9].

Previous studies have already shown that the parameterization of the vertical mixing in the PBL plays a major role on the vertical structure of the wind profile [10]. To account for that, five different PBL schemes have been tested. One first order scheme: the Yonsey University (YSU [11]), and four one-and-a-half order (or TKE closure) schemes: Mellor-Yamada-Janić (MYJ [12]), Mellor-Yamada-Nakanishi-Niino (MYNN [13]), Quasi-normal Scale Elimination (QNSE [14]) and Bougeault-Lacarrère (BouLac [15]). The differences on the order of closure are briefly described in the next section. The effect of other model parameters as: number of nested domains, horizontal resolution, physical parameterizations, etc., was investigated so the setup proposed is optimized regarding the conditions at FINO1.

4. Turbulence closure techniques

The turbulent fluxes from momentum, heat and other species in both first and one-and-a-half order closure techniques are formulated similarly [16].

$$< w'\phi' >= -K_z \left(\frac{\partial \phi}{\partial z} - \gamma \right), \tag{2}$$

where ϕ is a prognostic variable. This kind of modelization is known as gradient transport theory or K-theory. The term γ represents the non-local mixing due to larger convective eddies and it is included or not depending on the scheme. K_z is the eddy diffusivity coefficient, which sometimes has different formulations for momentum and heat. The manner in which K_z is computed introduces the differences between first and one-and-a-half orders. In first order closure techniques (YSU) the eddy diffusivities are calculated in the following way:

$$K_z(z) = \psi\left(zL^{-1}\right) \cdot z \cdot \left(1 - \frac{z}{h}\right)^2, \tag{3}$$

where h is the boundary layer height, L is the Obukhov length and $\psi\left(zL^{-1}\right)$ is a function of stability based on the nondimensional profile functions of heat and momentum [17]. The one-and-a-half order schemes solve an additional prognostic equation for the turbulent kinetic energy, q, and the parameterization of fluxes depends on q, on the master length scale, l, and on the flux Richardson number, Ri.

$$K_z(z) = \chi(Ri) \cdot l \cdot q^{0.5}. \tag{4}$$

The diagnostic equations to obtain l and $\chi(Ri)$ differ from MYJ, MYNN and QNSE. In BouLac scheme the stability function is considered as a constant coefficient.

5. Surface fluxes

In the WRF model, turbulent fluxes for momentum, heat and moisture at the surface are computed based

on Monin-Obukhov Similarity Theory, as previously introduced. They represent the linkage between the surface and the atmosphere and provide lower boundary conditions for the integration of the PBL schemes. The momentum flux is parameterized based on the square of the friction velocity as showed by Eq. 5:

$$\tau_s = u_*^2 \rightarrow u_* = \frac{\kappa U_1}{\ln(z_1/z_{0m}) - \psi_m}, \qquad (5)$$

where the subscript 1 stands for the conditions at the first grid point in the vertical coordinate (~10 m) and z_{0m} is the roughness length for momentum (here modeled for offshore conditions using the Charnock's equation: $z_0 = \alpha_c u_*^2/g$). Regrouping the terms from Eq. 5 it can be easily shown that the momentum flux depends on the square of the wind speed at the first grid point. For the sensible heat flux, a similar expression is used.

$$< w'\theta' >_s = -C_H U_1 (\theta_1 - \theta_s)$$
$$\rightarrow C_H = \frac{\kappa u_*}{\ln(z_1/z_{0h}) - \psi_h}, \qquad (6)$$

where θ_s is the sea surface temperature and z_{0h} is the roughness length for heat. In this case the parameterization of the sensible heat flux depends on the product of wind speed and the $\Delta\theta$. Furthermore, there is a dependency on the momentum flux via the surface exchange coefficient for heat C_H.

Surface fluxes of momentum and heat are compared on Fig. 3. The numerical results correspond to MYNN scheme since similar conclusions are drawn for the other PBL parameterizations. Friction velocity (Fig. 3a) is overestimated by WRF for the whole range of measurements. Indeed, a decrease on the momentum flux with height is expected when being out of the surface layer. So this effect explains the lower level of u_* measured at 40 m. In the case of sensible heat flux, WRF predicts higher values both for unstable and stable conditions. The bias is not constant anymore and it grows with $< w'\theta' >$.

In order to evaluate the ability of WRF to forecast surface stability in offshore conditions it is worthy to compare the Obukhov length. This comparison is shown in Fig. 4. Despite of the fact that similar trends were obtained for u_* and $< w'\theta' >$, combination of the two trends could produce rather different results. Under unstable atmospheric stratification (L^{-1} <0), the overestimation of both momentum and heat fluxes by the numerical model have opposite effects on L^{-1}. Simulated values of u_* tend to reduce the magnitude of L^{-1} whereas $< w'\theta' >$ contributes

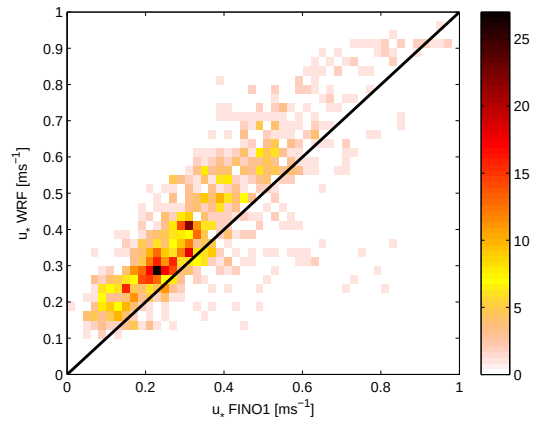

(a) Friction velocity, u_*.

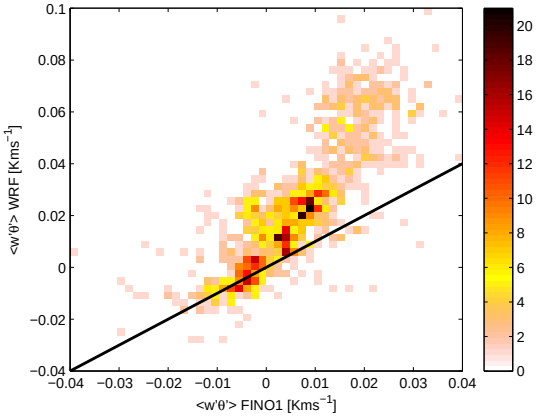

(b) Sensible heat flux, $< w'\theta' >$.

Figure 3: Two-dimensional histogram of FINO1 against WRF data (bar indicates number of data points). WRF values correspond to MYNN scheme and fluxes are 30 min averaged in all the cases.

to enhance it. For near-neutral conditions and moderate instabilities, competition of both effects yields to a slight overestimation of the inverse of the Obukhov length.

For stronger instabilities, the presence of higher values of heat flux dominates and the overestimation of L^{-1} grows. In the case of stable stability (L^{-1} >0), the values for the selected periods are lower compared to the ones measured for the convective scenarios. This gives more weight to u_* and thus, L^{-1} is underpredicted. For stable conditions the results from the five PBL parameterizations differ the most. It can be observed that QNSE (Fig. 4b) gives the best agreement with FINO1 measurements and, by contrary, BouLac (Fig. 4c) reproduce the lowest values of L^{-1}. For all the range of L^{-1} values, MYNN is the

scheme which produces closer results to the field data (Fig. 4d).

In general terms, it is confirmed that WRF forecast a neutralization of the stable stratification and a reinforcement of the instability for neutral and convective stability. Those effects create a displacement of the probability density function of L^{-1} from positive towards negative values.

6. Vertical structure of the wind profile

All the numerical results presented in the previous section in terms of surface fluxes are derived from Monin-Obukhov similarity theory. For the rest of the profile, the influence of turbulent mixing on the wind speed profile is determined by the PBL tendencies, briefly described in Sec. 4. In order to analyze the performance of the PBL schemes, FINO1 profiles obtained from a combination of sonic anemometers and LiDAR data up to 250 m are considered. The obtained results are shown in Fig. 5 in terms of mean shear (referenced to the wind speed at 40 m, U_{40m}). It can be noticed that, as expected, the shear increases dramatically from very unstable conditions, in which it is much reduced or non-existing (0.2 ms^{-1} at 250 m), up to stable stratification, where the shear reaches its maximum amplitude (3.5 ms^{-1} at 250 m). Most of the time, the PBL schemes are not able to reproduce as much shear as it occurs under stable conditions. QNSE outperforms the others and BouLac and YSU produce the highest bias. The difficulties of YSU and BouLac schemes to reproduce stable profiles of wind speed are due to an excessive mixing.

This enhancing of the turbulent mixing in the lower part of the boundary layer produces a important reduction of the wind shear. This problem of the BouLac scheme is due to the assumption of constant $\chi(Ri)$ in Eq. 4. The lack of link with stability, through the Richardson number, makes it fail under stable conditions. Better agreement was found under neutral and convective conditions most probably because the coefficient is more suited for such stability regimes [10]. The failure of YSU is attributed by [10; 18] to an excessive mixing during stable stratified conditions [19]. Similar behaviour was found for YSU in onshore studies carried out by [20], forecasting neutral conditions most of the time independently on the atmospheric stability. For neutral conditions (Fig. 5b), MYNN and QNSE match the FINO1 data up to 170 m. Above, MYNN deviates slightly. Again YSU and specially BouLac schemes are the most diffusive while MYJ does not show noticeable modification from stable stratification. For the convective atmosphere (Figs. 5c-d), WRF simulations generates higher shear and the bias decreases for larger values of L^{-1}. The root-mean-square error (RMSE) of the wind shear as a function of stability has been plotted in Fig. 6. These values correspond to the average over the rotor swept area of a 5 MW wind turbine, as the ones installed in the nearby wind farm Alpha Ventus. This allows us to obtain an equivalent shear RMSE which would be "seen" by the typical wind turbines operating offshore nowadays. The results from the mean shear profiles are reflected in Fig. 6. The shear RMSE is maximum for stable conditions and shows the largest spread among the five PBL schemes. BouLac has an error of almost 1.4 ms^{-1} and QNSE and MYNN drop up to about 0.9 ms^{-1}. There is a step reduction towards neutral conditions (~0.4 ms^{-1}) with higher errors for MYJ and BouLac. In convective conditions the errors continue decreasing and reach its minimum for very unstable stability (~0.2 ms^{-1}) except for MYJ, which has the highest errors for all the unstable range and remains almost constant (~0.35 ms^{-1}).

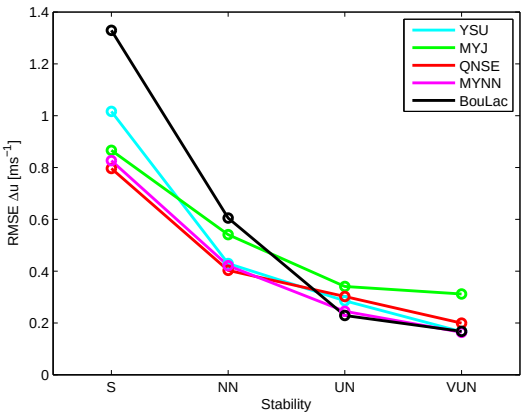

Figure 6: Averaged shear RMSE over the rotor swept area for a 5 MW wind turbine (40-160 m).

7. Conclusion

Five WRF Planetary Boundary Layer formulations were compared against field observations at FINO1 platform. Four nested domains allowed us to perform high resolution mesoscale simulations with grid spacing of 1 km in the most inner domain. Different stability scenarios were selected based on measurements of L^{-1} from the closest sonic anemometer to the surface. The observational database was composed of

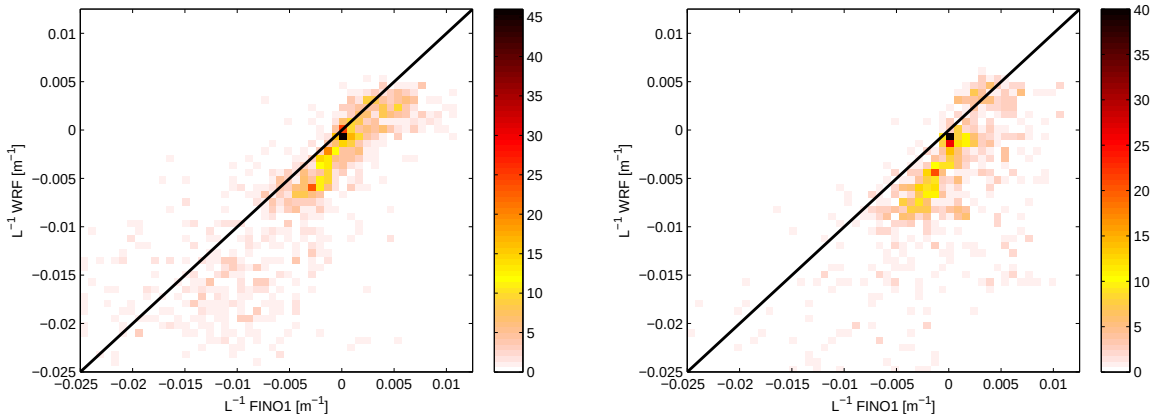

(a) YSU

(b) QNSE

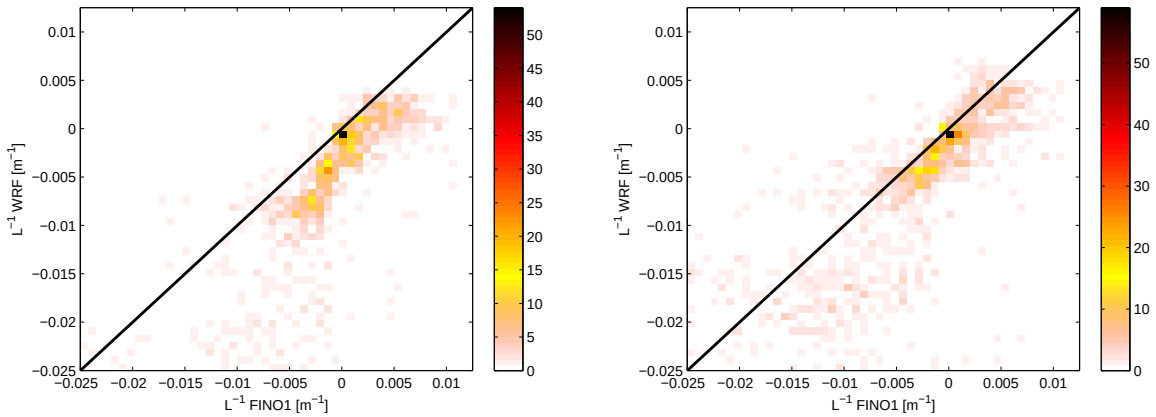

(c) BouLac

(d) MYNN

Figure 4: Two-dimensional histogram of FINO1 against WRF data for the inverse of the Obukhov length, L^{-1} (bar indicates number of data points).

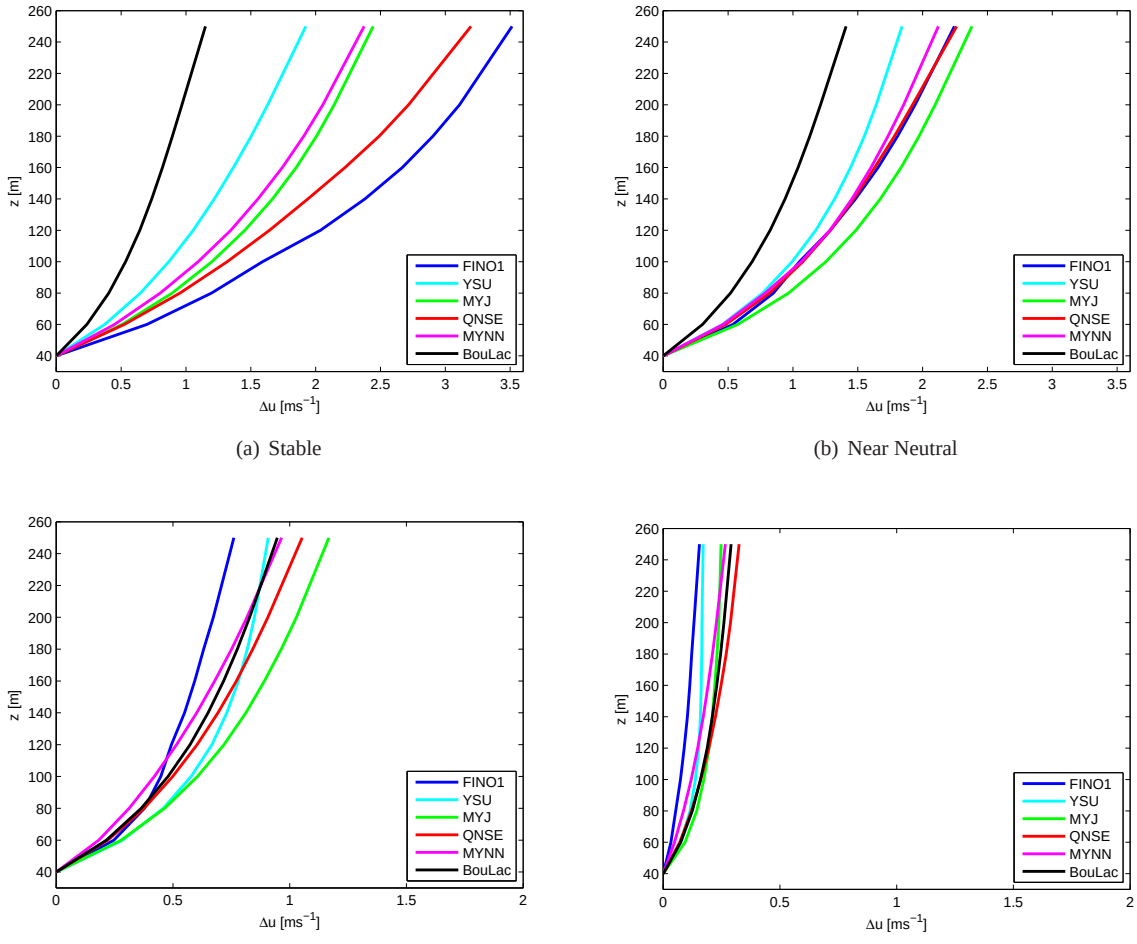

(a) Stable

(b) Near Neutral

(c) Unstable

(d) Very Unstable

Figure 5: Mean wind shear profiles, $\Delta u = U - U_{40}$, grouped by stability.

combined sonic anemometers and LiDAR wind measurements in order to have both the best spatial coverage possible and including turbulent flux information.

Results concerning turbulent fluxes showed a constant overestimation of u_*. For $< w'\theta' >$ the errors are larger for higher values of $< w'\theta' >$. In terms of L^{-1}, a displacement of the probability density function of L^{-1} from positive towards negative stabilities was found.

WRF wind shear was evaluated at tall heights where 5MW WT operates and beyond, by using a LiDAR measurement campaign carried out at FINO1. In general terms, convective boundary layers present lower errors which increase with L^{-1} and with height. The shear is underestimated for stable stratification, especially for YSU and BouLac schemes, which are too diffusive.

Some differences were found between surface and profile stability indicating that vertical mixing formulation can differ from surface forcing features. From all there results here presented, we conclude that MYNN and QNSE are optimum to reproduce the offshore environment corresponding to open sea conditions for wind energy purposes, having considered surface turbulent fluxes and tall wind speed profile data for validation.

Acknowledgments

DME has been supported by the European Commission through the Marie-Curie FP7 actions under the WAUDIT project and by the Deutsches-Windenergie Institute, DEWI GmbH. DME wants to specially thank Dr. B. Cañadillas and Dr. T. Neumann for their help and support conducting this research and also to thank the hospitality of all the staff members of DEWI Wilhelmshaven during his research stay. The FINO1 platform is one of three offshore platforms of the FINO Project.

References

[1] S. Azau, Z. Casey, Wind in our sails: the coming of Europe's offshore wind energy industry, EWEA Report, European Wind Energy Association (2011).

[2] B. Cañadillas, D. Muñoz Esparza, T. Neumann, Fluxes estimation and the derivation of the atmospheric stability at the offshore mast FINO1, no. EWEA OFFSHORE 2011, Amsterdam, TheNetherlands, 2011.

[3] B. Cañadillas, A. Westerhellweg, T. Neumann, Testing the performance of a ground-based wind LiDAR system: one year intercomparison at the offshore platform FINO1, DEWI Magazine 38 (2011) 58–64.

[4] B. Cañadillas, T. Neumann, D. Muñoz Esparza, First insight in offshore wind profiles up to 250 m under free and wind turbine wake flows, no. EWEA OFFSHORE 2011, Amsterdam, TheNetherlands, 2011.

[5] A. J. M. van Wijk, A. C. M. Beljaars, A. A. M. Holtslag, W. C. Turkenburg, Evaluation of stability corrections in wind speed profiles over the North Sea, Journal of Wind Engineering and Industrial Aerodynamics 33 (1990) 551–566.

[6] W. Skamarock, J. Klemp, J. Dudhia, D. Gill, D. Barker, M. Duda, X. Huang, W. Wang, J. Powers, A description of the advanced research WRF version 3, NCAR Tech. Note NCAR/TN-475+STR, 2008.

[7] A. S. Monin, A. M. Obukhov, Basic turbulence mixing laws in the atmospheric surface layer, Tr. Inst. Teor. Geofiz. Akad. SSSR 24 (1954) 163–187. (English translation available in V. N. Bespalyi, Ed., 2001: Turbulence and Atmospheric Dynamics, J.L. Lumley, 164–194.).

[8] S. Suranjana, et. al., The NCEP Climate Forecast System Reanalysis, Bulletin of the American Meteorological Society 91 (2010) 1015–1057.

[9] W. C. Skamarock, Evaluating mesoscale NWP models using kinetic energy spectra, Monthly Weather Review 132 (2004) 3019–3032.

[10] D. Muñoz Esparza, J. van Beeck, B. Cañadillas, Impact of turbulence modelling on the performance of WRF model for offshore short-term wind energy applications, in: 13th International Conference on Wind Engineering, Amsterdam, The Netherlands, 2011.

[11] S. Y. Hong, Y. Noh, J. Dudhia, A new vertical package with an explicit treatment of entrainment processes, Monthly Weather Review 134 (2006) 2318–2341.

[12] Z. I. Janić, Nonsingular implementation of the Mellor-Yamada level 2.5 scheme in the NCEP meso model, Office Note 437, National Centers for Environmental Prediction: Camp Springs, MD, USA, 2001.

[13] M. Nakanishi, Improvement of the Meyor-Yamada turbulence closure model based on Large-Eddy Simulation data, Boundary-Layer Meteorology 99 (2001) 349–378.

[14] S. Sukoransky, B. Galperin, A. V. Perov, Application of a new spectral theory of stably stratified tur-bulence to the atmospheric boundary layer over sea ice, Boundary-Layer Meteorology 117 (2005) 231–257.

[15] P. Bougeault, P. Lacarrère, Parameterization of orography-induced turbulence in a mesobeta-scale model, Monthly Weather Review 117 (1989) 1872–1890.

[16] R. B. Stull, An introduction to boundary layer meteorology, Kluwer Academic Publishers, Dordrecht, 1988.

[17] A. J. Dyer, A review of flux-profile relationships, Boundary-Layer Meteorology 7 (1974) 363–372.

[18] B. Storm, S. Basu, The WRF model forecast-derived low-level wind shear climatology over the United States Great Plains, Energies 3 (2010) 258–276.

[19] S. Y. Hong, S. W. Kim, Stable boundary layer mixing in a vertical diffusion scheme, in: 9th WRF Users' Workshop Proceedings, Boulder, Colorado, 2008.

[20] C. Draxl, A. Hahmann, A. Peña, J. Nissen, G. Giebel, Validation of boundary-layer winds from WRF mesoscale forecasts with application to wind energy forecasting, 19th Symposium on Boundary Layer and Turbulence, Keystone, USA, 2010.

FLOW WITH IMPORTANT HEAT TRANSFER AND/OR COMBUSTION

Experimental Characterization and Modeling of Hazards: BLEVE and Boilover
Small Scale Boilover Experiments

Delphine Laboureur

Environmental and Applied Fluid Dynamics Department, von Karman Institute for Fluid Dynamics, Belgium, laboureu@vki.ac.be

Supervisor & University Supervisor: Jean-Marie Buchlin

Professor, Head, Environmental and Applied Fluid Dynamics Department, von Karman Institute for Fluid Dynamics, Belgium, buchlin@vki.ac.be

Professor, Faculté des Sciences Appliquées, Université Libre de Bruxelles, buchlin@vki.ac.be

Co-Supervisor: Patrick Rambaud

Associate Professor, Environmental and Applied Fluid Dynamics Department, von Karman Institute for Fluid Dynamics, Belgium, rambaud@vki.ac.be

Abstract

Boilover is defined as a violent ejection of fuel due to the vaporization of a water sub-layer, resulting in an enormous fire enlargement and formation of fireball and ground fire. Small scale field and laboratory experiments are performed to allow a better understanding of the characteristics of the pool fire in steady conditions and at the boilover onset.

Keywords: boilover, flame, temperature, burning rate

1. Introduction

Most of the time, hydrocarbon storage reservoirs in process plant sites contain a water layer due to condensation effects, drilling and transport or from the natural composition of the oil. As the water density is higher than most of the hydrocarbons, the water always fall in the bottom of the tank where it is more difficult to remove. If by accident, a fire starts at the fuel surface, this fire progressively heats the fuel layer and therefore the water layer. As the water is heated it starts to vaporize and the vapor generated ejects the fuel from the reservoir. This phenomenon, called boilover, induces violent fuel ejections, flame enlargement and possible formation of fireballs.

In 1995, Hua divided the Boilover phenomenon in different steps, from the ignition of the fuel surface to the end of the fuel burning after the Boilover [1]. After ignition of the fuel surface and a small induction period, the pool fire is burning in a regular way, similar to a pool fire without any water sub-layer; the flame is stable and the fire properties like the burning rate or the flame size are constant. Therefore, Hua qualified this period as quasi-steady. During this period, the fuel layer is progressively heating the water layer under it. Once the water layer temperature is getting close to the boiling point, the boilover period starts. Water bubbles develop at the fuel - water interface, and some are ejected through the fuel layer in the flame, emitting a typical crackling sound. Once the water boiling is strong enough to

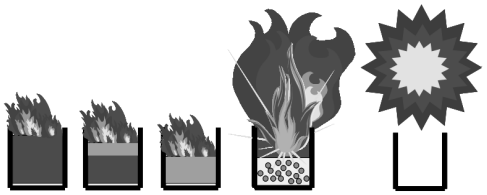

Figure 1: Boilover principle

push the fuel layer, the flame height increases quickly and burning fuel is sprayed out of the tank.

Boilover experiments with diesel as fuel, at large scales (reservoir diameter ranging from 1.5 to 6m) have been performed by Munoz and Ferrero [2; 3; 4]. They investigated the pool fire characteristics during the quasi-steady state, but also the change in characteristics from the quasi-steady to the boilover period. In an attempt to compare existing models of pool fire characteristics during the quasi-steady period with different scales of experiments, small scale experiments have been performed in this study.

Garo and Hua [5; 1] performed visualizations of the fuel and water layers and showed that bubbles appear at the fuel - water interface, and increase in scale and in generation rate with time up to Boilover apparition. But very few studies are dedicated to the characterization of the flame enlargement resulting from the piston effect. Therefore, high-speed visualization of the flame enlargement during small scale boilover experiments are also performed.



Figure 2: BABELs experimental facility

2. Experimental apparatus and technique

As boilover experiments include important flame dimensions and fuel projections, a dedicated boilover experimental setup, the BABELs facility, was constructed in beginning 2010 at the von Karman Institute. All the experiments presented in this study have been performed in this facility. After a more detailed description of BABELs, an instrumentation overview is presented.

2.1. Laboratory experimental facility

BABELs is an acronym for Bleve And Boilover ExperimentaL setup (see Fig. 2) and consists of a cylindrical chamber of 2m diameter, and 3m high, with round shape extremities, made out of steel with a rated pressure of 5 bar (hydraulic test). It has 3 series of 7 optical accesses of 0.15m in diameter, separated by 90°, and a door of $0.57m \times 0.77m$. The setup allows air venting through openings in its bottom and upper parts, the last one being ended by a vent that can be used after each test to remove smoke from the chamber. It also contains a ladder and a circumferential walking area at mid-height for better accessibility of the upper optical accesses.

2.2. Experiments overview

In these experiments, the influence of the fuel layer thickness and the ratio between water and fuel layer thicknesses were tested. The influence of the reservoir diameter and material were also investigated by using different reservoirs. Each configuration was performed twice for repeatability check. The fuel used was a mixture of Valvata Shell 460 oil (30% volume) and diesel (70% volume). Oil was added in order to increase the fuel viscosity (favorable condition for boilover apparition [6]). The dimensions and material of the reservoirs (i.e. diameter and height as the thickness is fixed to 2mm in all reservoirs) and the water and fuel layers are listed in Table 1. The glass reservoir was a DURAN crystallizing dish and the metal reservoir was made with steel.

Table 1: Laboratory tests configurations

D [m]	**H [m]**	**Material**	$H_f/D[-]$	H_w
0.08	0.045	glass	$0.1, 0.2, 0.4$	$H_f/H_w = 3$
0.08	0.045	glass	$0.1, 0.2, 0.4$	$H - H_w = 6$
0.08	0.045	metal	$0.1, 0.2, 0.4$	$H_f/H_w = 3$
0.08	0.045	metal	$0.1, 0.2, 0.4$	$H - H_w = 6$
0.15	0.065	metal	$0.1, 0.2, 0.4$	$H_f/H_w = 3$
0.15	0.065	metal	$0.1, 0.2, 0.4$	$H - H_w = 6$

The instrumentation that have been used for the small scale boilover experiments is presented in Fig. 3. For each experiment, mass loss, fuel and water layer temperatures, flame radiation and flame visualization were monitored.

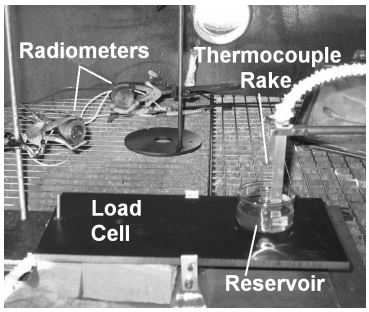

Figure 3: Schematic of boilover experimental setup

2.3. Temperature measurement

The time evolution of the fluid temperature was recorded at different heights from the fuel surface with a thermocouple rake inserted in the reservoir (see Fig. 3). The rake was composed of a series of 26 type K thermocouples of 1mm diameter, sheathed with stainless steel AISI310 and an isolated junction. They were placed together inside two steel clamps of 140mm high, 15mm long and 10mm large, with a thickness of 2mm, acting like a vice (see Fig. 4). The position of the thermocouples were chosen for the best space efficiency, considering the different configurations to be tested: with a space resolution ranging from 1 to 5mm. For the measured temperature to be independent from the clamps, the thermocouple junction were placed out of the support by 10mm length. The part of the 600mm long sheathed thermocouple that was not protected by the vice was surrounded by a silica fiber braided spaghetti from Omerin. The thermocouples were connected to extension thermocouple cables of 3m, that reached a NI9213 acquisition module, plugged in National Instrument Compact-DAQ NI9178 and sampled at 10Hz.

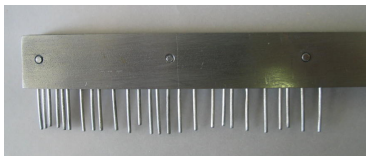

Figure 4: Thermocouple rake

2.4. Mass loss measurement

Simultaneously with the temperature, the mass loss due to the fuel combustion was monitored by a Futek LSB303 load cell with a maximum output of 5kg and a resolution of 0.2g and sampled at 10Hz by using a NI9205 acquisition module. The load cell was compensated on temperature in the $15 - 72°C$ range.
The load cell was fixed between two plates of 150mm large and 300mm long, linked together with a cone-point support. On one side of the cone, the load cell was inserted between the two plates and on the other side, the tested reservoir was placed on the upper plate, made out of Bakelite to reduce the heat transfer from the burning reservoir to the load cell.

2.5. Flame visualization and contours detection

For flame visualizations, a Panasonic NV-GS400 camera was used with a Raynox HD 3035 Pro Semi-Fisheye. The fisheye was needed because of the strong flame enlargement during boilover (up to 2-3m) compared to the distance between the flame and the optical accesses, as imposed by the design of BABELs (1.3m). The distortion created by the fisheye was corrected with Matlab algorithms of image spatial transformation, based on a calibration image representing a check-board (see Fig. 5). Flame visualizations at boilover apparition were also performed with a Phantom V7.1 high-speed camera and a 12mm objective, using an acquisition frequency of 900Hz and an exposure time of $10\mu s$. The fisheye was also used to widen the field of view.

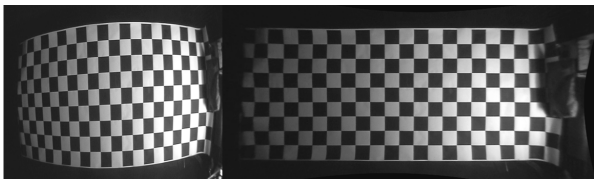

Figure 5: Image calibration: Original image (left) and distorted image (right) (distance between dot = 100mm)

A flame detection algorithm was developed with Matlab Image Processing Toolbox, consisting in several steps. First, a median filter is applied on the images for reduction of possible noise. Then, the image intensity values are adjusted such that only 1% is saturated at low and high intensities, which increases the image contrast. This step is specially needed at beginning of boilover when the flame is very intense, and can cause halo on the images. The resulting gray scale images are converted in binary image, using a global image thresholding based on Otsu method [7]. The pixels on the edges of the flame are extracted by means of the Moore-Neighbor tracing algorithm modified by Jacob's stopping criteria [8]. The computation of flame area, length or width is then straightfor-

ward. The definition of flame length differs, depending if the flame is taken from the steady period or during boilover apparition. Both situations are explained later in this article.

3. Steady burning analysis

The characteristics of a diesel pool fire during the quasi-steady period that lasts from ignition to the Boilover apparition are compared with models available in literature when existing. A parametric analysis is also performed, investigating the effect of parameters like the fuel layer thickness or the reservoir diameter on the quasi-steady burning characteristics.

3.1. Burning rate

After ignition of the diesel mixture and a small induction period needed to reach a quasi-steady state, the mass loss becomes constant with time as fuel is burning. The burning rate can then be computed from the slope of the mass loss measurements. A preliminary analysis of the results showed that the burning rate is influenced by the pool diameter, material and by the distance between the top of a vessel and the fuel surface (called lip height).

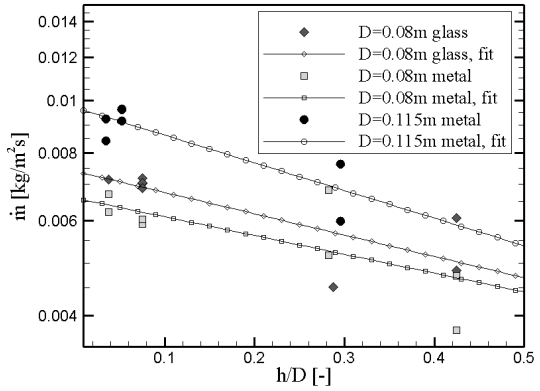

Figure 6: Influence of lip height on burning rate

While the pool diameter effect on the burning rate has been widely studied [9; 10; 11], few papers have dealt with the lip height effect. In 2000, based on an experimental campaign, Dlugogorski [12] has showed that the relationship between the fuel burning rate and the lip height initially follows an exponential decline, as expressed in Eq. 1.

$$\dot{m} = \dot{m}_t exp(-\alpha h^*) \quad (1)$$

where $\dot{m}_t$ is the burning rate when the liquid level corresponds to the burner rim, α is a fitted parameter and $h^* = h/D$ is the lip height ratio with the vessel diameter [12]. The experimental burning rates confirm the Dlugogorski correlation, as shown in Fig. 6.
A difference is also observed between the burning rates of metal and glass reservoirs. When the material conductivity increases, the burning rate decreases. Indeed, keeping the pool diameter constant, $\dot{m}_t = 7.4 \cdot 10^{-3} kg/m^2 s$ for glass reservoir against $6.6 \cdot 10^{-3} kg/m^2 s$ for metal reservoir, which gives approximately 10% decrease. This conclusion is in accordance with the previous studies, resumed in Hall [13].

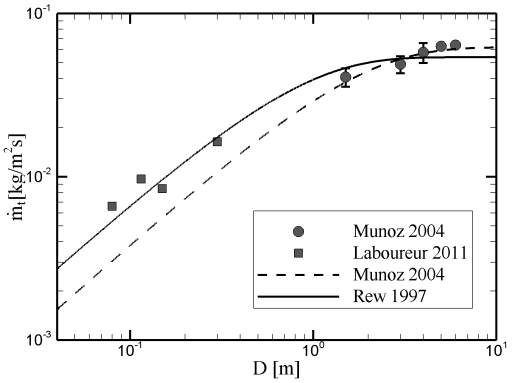

Figure 7: Diesel pool fire burning rate for different pool diameters

Following the Hottel classification of flame regimes, the experiments are ranged in the transition mode, characterized by an increase of the burning rate with the reservoir diameter [9]. The Fig. 7 presents the $\dot{m}_t$ values from the exponential fits of Fig. 6 for a metal reservoir, added with previous results using the same fuel but larger reservoir sizes (D=0.15m and 0.3m [14]). The data fit well the correlation given by Rew [11] (Fig. 7), expressed in Eq. 2, the values of the parameters being listed in Table 2.

$$\dot{m}_t = \dot{m}_\infty (1 - exp(-kD)) \quad (2)$$

In 2004, Munoz has measured the burning rates of diesel fires from 1.5 to 6m diameter, and proposed a new correlation based on these measurements [2] (see Table 2 for parameters values). But compared to the present experiments, the correlation of Munoz is underestimating the burning rate. This can be due to the oil addition in small scale experiments, or to the influence of conductivity due to the smaller size of reservoir. But putting aside these differences, the correlation of Rew shows a good agreement at the two scales

(small scale from the current results and large scale from Munoz [2]).

Table 2: Burning rate correlation coefficients (Diesel oil)

Author	m_∞ $[kg/m^2 s]$	k $[m^{-1}]$
Rew	0.054	1.3
Munoz	0.062	0.63

3.2. Temperature profiles

The experimental campaign allowed the measurement of the time evolution of a vertical profile at the center of the reservoir. The following paragraphs are investigating the effect of different parameters on the temperature evolution: the fuel layer thickness, the water layer thickness, the reservoir diameter and the reservoir material.

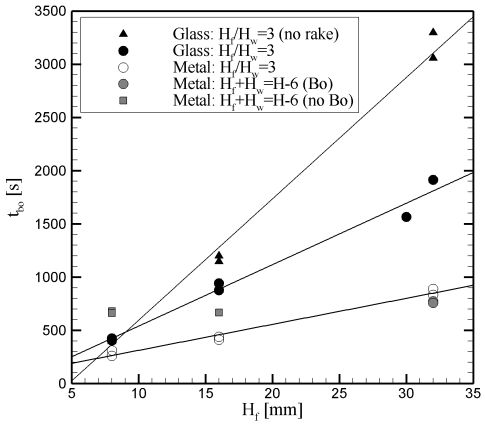

Figure 8: boilover apparition time D=80mm

The Figure 8 presents the boilover apparition time, calculated as the time interval between ignition of the fuel layer surface and the onset of fuel ejection by the water boiling. The presence of the thermocouple rake is clearly accelerating the heating of the fuel and water layers, especially in the glass reservoir. But as the rake is present in all the configurations, a parametric analysis is still possible.

3.2.1. Influence of fuel layer thickness

Figure 9 shows the vertical temperature profile at three fractions of the total time before boilover apparition, for three different fuel layer thicknesses. The fuel layer is more strongly heated as the thickness is decreasing. The influence of the fuel layer thickness on the boilover apparition time is linear, as observed in Fig. 8, which is consistent with previous studies

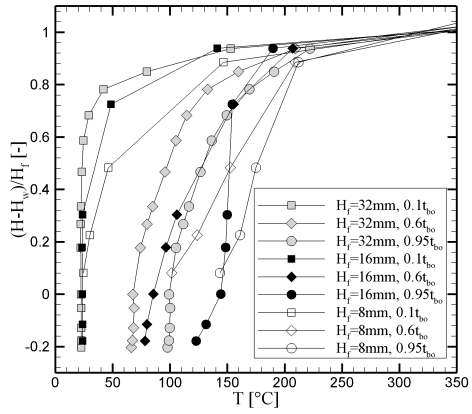

Figure 9: Influence of H_f: D=80mm, metal reservoir, $H_f/H_w = 3$

([15; 16]).

3.2.2. Influence of water layer thickness

The Fig. 10 shows vertical profiles at three different fractions of the time to boilover. The two experiments presented in Fig. 10 have a fuel layer thickness of 16mm and the water layer thickness is either 23mm or 6mm. The influence of the water layer thickness is negligible at the beginning of the combustion, and as the burning time increases, the cooling effect of a thicker water layer becomes more and more visible on the temperature profiles.

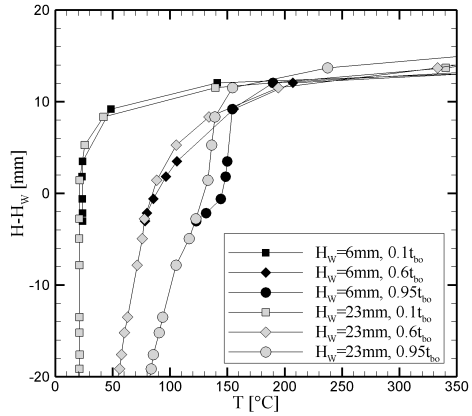

Figure 10: Influence of H_w: D=80mm, metal reservoir, $H_f = 16mm$

But in the case of the large water layer thickness ($H_w = 23mm$), the boilover did not occur; the water layer being too thick to generate the boiling front, causing the piston effect and therefore the flame enlargement. As observed in Fig. 11, if the water to fuel

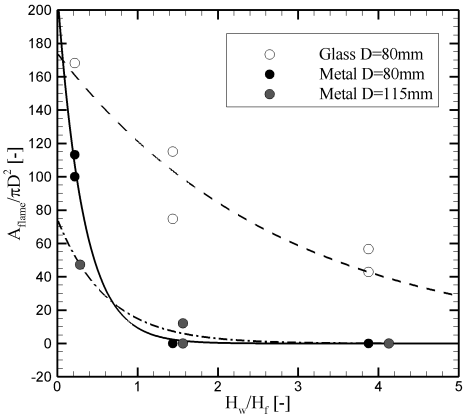

Figure 11: Maximum flame area during boilover occurence

layer thickness ratio is too large, the pool fire extinguishes before the boilover apparition (characterized here by the maximum flame area during boilover). The water layer thickness effect is also visible on the boilover apparition time (Fig. 8). For a small fuel layer thickness, if the water layer thickness is small, the boilover appears quite rapidly. If the water layer thickness is large, the fire extinguishes instead of a boilover apparition, and happens after a larger time. And for small water to fuel layer thickness ratio, a smaller water layer thickness decreases the boilover apparition time.

3.2.3. Influence of reservoir material

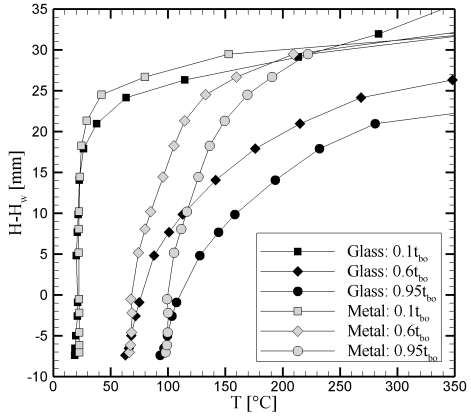

Figure 12: Influence of reservoir material: D=80mm, $H_f = 32mm$, $H_f/H_w = 3$

The Fig. 12 illustrates the influence of the reservoir material on the fuel heating. The heating of the water layer is similar for both materials, but the heating of the fuel layer is a lot stronger in the glass reservoir. This is due to the conduction inside the walls of the reservoir, which is more pronounced with a metal reservoir than with a glass. This can also explain the difference in the time for boilover apparition (see Fig. 8). As there is few conduction inside the walls of the glass reservoir, the water layer is heated only by the conduction and radiation propagated by the combustion, which takes more time than if there is conduction inside the walls (like with the metal reservoir).

3.2.4. Influence of reservoir diameter

The influence of the reservoir diameter on the temperature profiles can be observed in Fig. 13. The effect of the diameter on the fuel and water layers is similar than the effect of the material: there is almost no change on the heating of the water layer as the diameter increases, but the heating of the fuel layer is stronger for the larger reservoir.

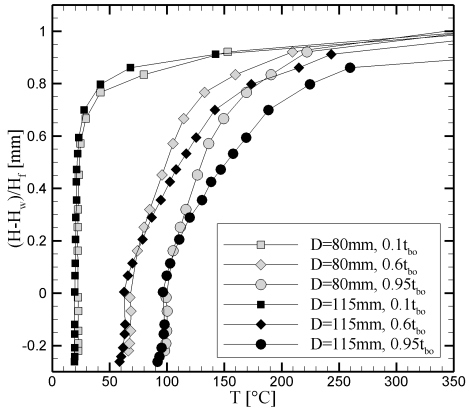

Figure 13: Influence of reservoir diameter: Metal reservoir, $H_f/D = 0.4$, $H_f/H_w = 3$

This is again due to the conduction inside the walls of the reservoir, which has a smaller effect on the liquid when the reservoir size increases. Concerning the boilover apparition time, for two diameters of $D = 80mm$ and $D = 115mm$, with the same fuel layer over diameter ratio ($H_f/D = 0.4$), the time increases from around 850sec to 1350sec. This means that, even if the burning rate increases with the diameter (as shown in the previous section), the conduction effect is less pronounced for a larger diameter and increase the boilover apparition time.

3.3. Flame shape

Numerous studies are available in literature concerning the pool fire flames characteristics; experi-

mental studies at different scales and fuel types, but also correlations. For each quantity, the main correlations available in literature are compared with experimental data extracted from the flame images recorded with the digital camera and the fish eye.



Figure 14: Mean flame D=115mm,H_f/D = 0.4, H_f/H_w = 3

Pool fire flames are diffusive and the flame time evolution is oscillatory. The flame can be decomposed in three regions: the base flame, the intermittent flame (where the flame oscillations are visible) and the plume region, at the top. In Fig. 14, representing the average flame during the steady burning, the two first regions are clearly visible. The base region is represented as the small white cone appearing in all images, and the intermittent flame is shown as the larger grey cone. The black line at the left of the flame is due to the presence of the thermocouple rake. The frequency of the oscillations, controlling the rate of air entrainment into the flame has been called the puffing frequency by Weckman [17]. The principal geometrical quantities that define flames from a pool fire are the flame length and tilt. The flame tilt is only function of the wind speed. As in this study the experiments are performed in a calm environment (without wind), only the flame length is investigated here.

3.3.1. Flame length

As explained before, pool fire flames oscillate; the flame length is changing with time. In this article, the approach developed by Zukoski [18], and followed by Ferrero [4] is applied. The average flame length is defined as the length at which the intermittency $I(L)$ (which is the fraction of time in which the flame is higher than L), is equal to 0.5. The calculation of flame length intermittency is carried out using MATLAB, based on the processing of 999 images in the steady part of the pool fire (recorded 1 to 2 minutes after ignition). For each image, the flame length is calculated as the distance between the reservoir edge and the upper pixel of the flame profile.

$$\frac{L}{D} = a(m^*)^b(u^*)^c \tag{3}$$

$$m^* = \frac{\dot{m}}{\rho_a \sqrt{gD}} \tag{4}$$

$$u^* = \frac{u}{(\frac{\rho_a}{g\dot{m}D})^{1/3}} \tag{5}$$

Among the correlations that predict the flame length, most of them show a dependency with the diameter, the burning rate and the wind speed, in the form of Eq. 3-5, each model having a specific set of values for the parameters a, b and c and are resumed in Table 3.

Table 3: Flame length correlation coefficients

Author	a	b	c
Thomas [19]	42	0.61	-
Moorhouse [20]	4.7	0.21	-0.044
Mangialavori [21]	31.6	0.58	-
Ferrero [4]	4.201	0.181	-0.082

The Fig. 15 compares the average flame length for the different configurations tested in this study, with previous experimental data showed by Mudan and Ferrero [22; 4] and the correlations of Thomas (considering no wind) [19], Moorhouse (with a conical flame shape) [20], Mangialavori [21] and Ferrero [4]. For the measurements of this study, the burning rates used in Eq. 4 are determined from the exponential fits following the Dlugogorski model (see Fig. 6). The correlation the closest to the experiments is the one of Mangialavori [21]; the correlation of Thomas [19] showing a similar trend, but with an overestimation.

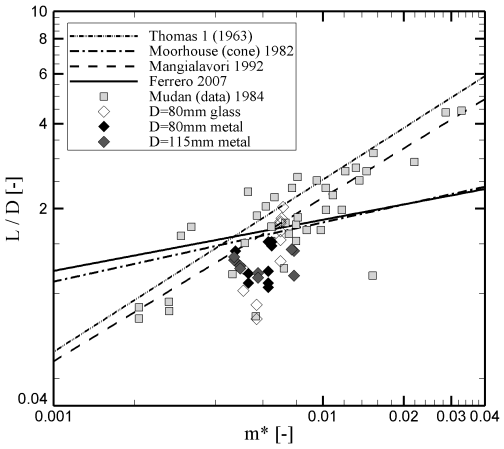

Figure 15: Flame length, compared with other data and correlations

3.3.2. Flame frequency

Following the approach of Ferrero [4], the flame frequency is calculated from the time evolution of the flame height. The approach of Ferrero [4] consists in first, to smooth the signal and then to calculate the puffing frequency as the ratio between the number of peaks in the flame length signal, divided by the average time duration of one oscillation. But as each pool fire configuration has its own set of 999 images, the length of the signal used here is too long to apply the procedure of Ferrero [4]. So another approach is to calculate the FFT of the signal. But Henriksen [23] has explained that, due to the turbulent nature of the flame, the FFT is too noisy to identify clearly the frequency peak. Therefore, the Burg implementation of the maximum entropy method to calculate the power spectrum is used, which gives a lot smoother results than the traditional FFT approach.

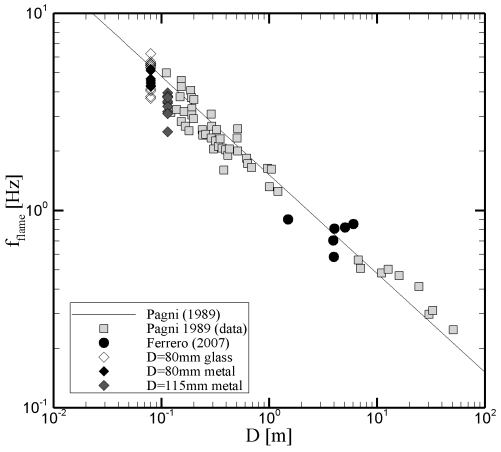

Figure 16: Flame flickering frequency, compared with other data and correlation of Pagni [24]

The Fig. 16 shows the resulting puffing frequencies, compared with the correlation of Pagni [24], which has the form of Eq. 6, the data presented by Pagni [24] in the same article, and the data of Ferrero [4]. The experiments of the present study show the same discrepancy as the previous experimental data, and follow the correlation.

$$f = \sqrt{\frac{2.3}{D}} \tag{6}$$

4. Boilover analysis

4.1. Pre-boilover burnt mass ratio

The ratio between the fuel mass burnt before the occurrence of boilover and the initial fuel mass is an important parameter since it provides information on the available quantity of fuel that can be ejected during the water boiling. In previous studies, Garo and Ferrero [5; 3] showed that the pre-boilover burned mass ratio (also called χ) depends both on the initial fuel thickness and on the pool diameter. They presented either an evolution of χ with the fuel thickness, or with the pool diameter, but no attempt to combine the effect of the two parameters was done.

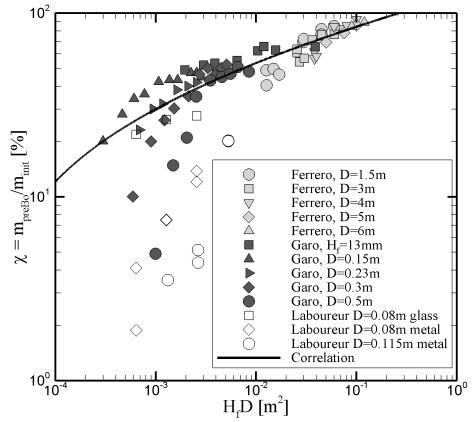

Figure 17: New correlation for the pre-boilover burnt mass ratio χ

The Fig. 17 presents the pre-boilover burnt mass ratio in function of the product of the initial fuel layer thickness and the pool diameter. The data of the present experiments (white points) are presented together with the previous results of Garo (using heating oil, dark grey points [5; 15]) and Ferrero (using diesel, light grey points [3]). The correlation in the form of a power law (see Eq. 7) follows well the large and middle scale. A discrepancy is observed only at smaller scale.

$$\chi = 170.3 \left(H_f D\right)^{0.1171} - 45.81 \tag{7}$$

This is probably due to the influence of the wall conduction in the heating process of the small scale reservoir, which is not present at larger scales. Indeed, the glass reservoir points of this study are following a lot better the correlation than the metal reservoir points, as glass is not a good heat conductor.

4.2. Flame enlargement

The major boilover hazard is the flame enlargement resulting from the piston effect induced by the water boiling, as observed from high-speed visualization performed in a previous study [25]. A typical flame

enlargement recorded with the high-speed camera is shown in Fig. 18. The water boiling front is first pushing the fuel in the flames, which enhances the combustion and increases the flame size to form a fireball shape which evolves into a column. Once the water boiling stops, the flame decreases and comes back to its original flame size or extinguishes, depending on the remaining quantity of fuel. If the whole fuel layer is not participating to the flame enlargement, several boilover can be observed.

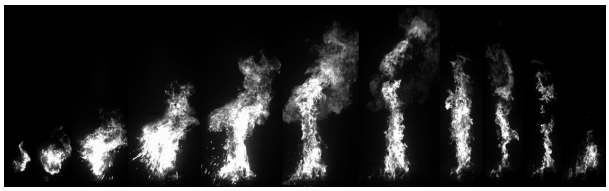

Figure 18: Flame enlargment during boilover apparition (D=115mm metal reservoir, $H_f/D = 0.2$), $\Delta t = 0.11s$ between images

The LS-PIV technique (Large Scale Particle Image Velocimetry) that calculates the flow velocity based on large structures instead of individual particles, can be used by processing the high-speed flame images with an algorithm for the interrogation of PIV images, based on cross-correlation [26].

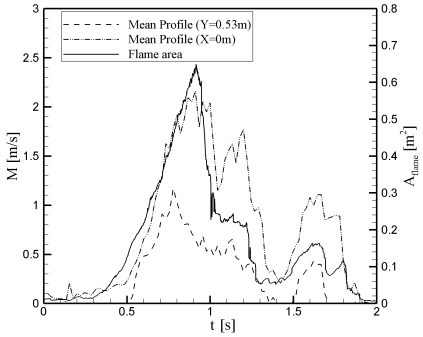

Figure 19: Flame velocity compared with total area (D=115mm metal reservoir, $H_f/D = 0.2$)

In Fig. 19, the time evolution of a vertical velocity profile at the center line of the reservoir is compared with the time evolution of an horizontal profile at about $4.6D$ above the reservoir, and with the total flame area calculated with the flame detection algorithm explained previously.

Once the fuel is ejected from the reservoir, both the flame size and velocity magnitude are increasing in a similar way until reaching a maximum flame size

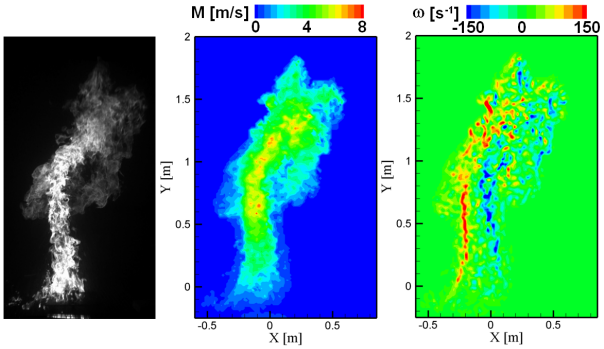

Figure 20: Max area (D=115mm metal reservoir, $H_f/D = 0.2$), t=0.91s after Boilover onset

around $t = 0.91s$. The Fig. 20 shows the velocity and vorticity fields at the time of the maximum flame area. It can be observed in the velocity field that the movement of the flame is mainly coming from the flame center line and from the vorticity field, shear is visible on the flame boundary.

After reaching the maximum area, the flame size is decreasing until reaching almost its original size. A second smaller peak is visible on the area and velocity plots (after $t = 1.5s$). This is not a second boilover but more a ground fire aside of the reservoir created by the ejection of fuel during the boilover. In Fig. 19, a second peak in the velocity evolution is visible, while the flame size is decreasing. The Fig. 21, representing the flame at the second velocity peak ($t = 1.2s$) shows that, even if the flame is smaller, the upper part is moving faster than the larger flame. In addition, the shear is increased.

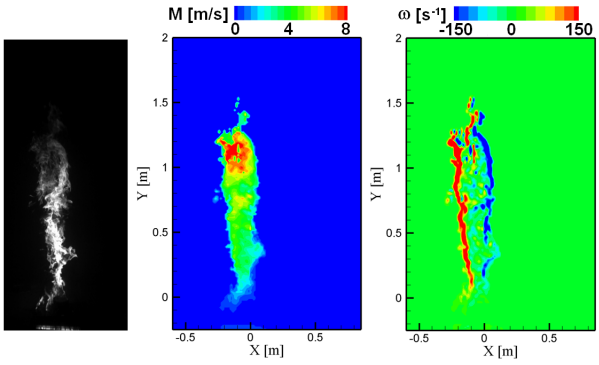

Figure 21: 2nd peak of velocity (D=115mm metal reservoir, $H_f/D = 0.2$), t=1.2s after Boilover onset

The general correlation between the flame size

and velocity has already been observed and different authors have proposed a relationship between the flame height and the Froude number which is a measure of the relative importance of inertia and buoyancy [27; 28; 29]. In an attempt to find a correlation independent on fuel type, Zukoski [27] have expressed the square root of a Froude number in terms of the heat release rate (see Eq. 8-9 [30]).

$$\dot{Q}_D = V \Delta H_c \rho_{fv} \left(\pi D^2 / 4 \right) \tag{8}$$

$$\dot{Q}_D^* = \frac{\dot{Q}_D}{\rho_a C_{p_a} T_a \sqrt{gD} D^2} \tag{9}$$

Depending on the value of $\dot{Q}_D^*$, the flame can be momentum or buoyancy dominated. The time evolution of $\dot{Q}_D^*$ is calculated for the boilover phenomenon, using as the velocity V, an average of the vertical velocity along the horizontal profile just above the reservoir.

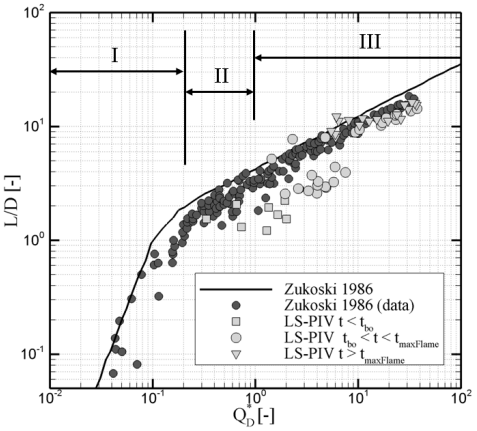

Figure 22: Flame length evolution with non dimensional Froude number

Before the apparition of the boilover (light grey squares in Fig. 22), the flame height is in the buoyancy dominated region II, dependent both on the heat release rate and the pool diameter [27]. Delichatsios defines also the interval $0.23 < \dot{Q}_D^* < 1.9$ as typical for intermediate scale pool fire [31]. During the boilover (light grey circles and diamonds in Fig. 22), the flame height increases to the region III, where the dependency on the pool diameter is negligible compared to the heat release rate. Delichatsios defines flames with $\dot{Q}_D^* > 1.9$ as buoyant jet flames [31]. This regime is consistent with the boilover phenomenon, since the velocity and the flame size are increasing while the reservoir size is kept constant. In addition, an increase of $\dot{Q}_D^*$ is similar to an increase of the Froude number, and therefore a stronger importance of the momentum, created by the piston effect of the water boiling, compared to the buoyancy, which is normally dominant for this pool fire configuration. And when the boilover ends, the flame comes back to the regime II, as before the boilover apparition.

5. Conclusion

A small scale experimental campaign have been performed, allowing the selection of the best correlation from the previous studies available in literature, for diesel pool fires of small to large scale. The fuel burning rate for a completely filled reservoir can be well predicted by Rew [11] and the influence of the lip height on the burning rate, first pointed by Duglogorski [12] has been proved. The temperature evolution of the fuel and water layer is influenced by the pool diameter and material, but also by the fuel and water layer thickness. Conduction through the walls of a metal reservoir is heating the fuel and water layers faster, which accelerates the boilover apparition. The conduction effect is decreased as the reservoir diameter increases. Conduction can also prevent boilover from happening when the water layer is at least two times bigger than the fuel layer, acting like a heat sink. As no hot-zone have been observed, the boilover apparition time is increasing with the fuel layer thickness, as already observed by Garo and Koseki [15; 16]. Finally, the best correlation for the average flame length is given by Mangialavori [21] and the flame puffing frequency during the steady period can be correctly modeled by Pagni [24].

The small scale experiments have also improved the understanding of the flame enlargement during the boilover period. A new model for the pre-boilover burnt mass ratio, which is directly linked to the boilover intensity, is proposed, which takes into account both the fuel thickness and the reservoir diameter. This new correlation works fine when the conduction through the reservoir wall is limited. The flame enlargement during boilover has been visualized by high-speed camera and processed with a PIV algorithm that allowed to compute the flame velocity. During a boilover, the flame velocity and size are increasing and decreasing with time with the shape of a Gaussian. By using a dimensionless parameter for the velocity (changed into a dimensionless heat release rate linked to the Froude number) and for the flame length (using the pool diameter), the buoyancy

dominated flame typical of medium size pool fire is turning during boilover into a jet flame, where only the velocity of the flame is influencing its height, before coming back to the steady pool fire flame after the boilover.

Nomenclature

Roman Symbols

A	Area $[m^2]$
a, b, c	Constants in flame length model
C_p	Specific heat $[kJ/kgK]$
D	Pool diameter $[m]$
ΔH_c	Heat of combustion $[kJ/kg]$
f	Puffing frequency $[Hz]$
g	Gravity $[m/s^2]$
h	Lip height $[m]$
H	Height $[mm]$
k	Extinction coefficient $[m^{-1}]$
L	Flame length $[m]$
m	Mass $[kg]$
$\dot{m}$	Burning rate $[kg/m^2 s]$
M	Velocity magnitude $[m/s]$
$\dot{Q}_D$	Heat release rate $[kW/m^2]$
t	time $[s]$
T	Temperature $[°C]$
u	Wind speed $[m/s]$
V	Vertical flame velocity $[m/s]$
X	Horizontal coordinate $[m]$
Y	Vertical coordinate $[m]$

Greek Symbols

α	Constant in Dlugogorski model [-]
Δt	Time interval $[s]$
ρ	Density $[kg/m^3]$
χ	Pre-boilover burnt mass ratio [%]
ω	Vorticity $[s^{-1}]$

Subscript

a	Air
bo	Boilover onset
f	Fuel
fv	Fuel vapor
$flame$	Flame
$init$	Before ignition
$preBo$	Before Boilover onset
t	No lip height
w	Water
∞	Infinite diameter
$*$	Dimensionless

Acknowledgments

The authors wish to thank the CEA of Gramat which is supporting this study and collaborating with the von Karman Institute and the Ecole des Mines d'Alès in this joint research project about source term characterization in major hazards.

References

[1] J. Hua, W. Fan, G. Liao, Study and prediction of boilover in liquid pool fires with a water sublayer using micro-explosion noise phenomena, Fire Safety Journal 30 (3) (1998) 269–291.

[2] M. Munoz, J. Arnaldos, J. Casal, E. Plana, Analysis of the geometric and radiative characteristics of hydrocarbon pool fires, Combustion and Flame 139 (3) (2004) 263–277.

[3] F. Ferrero, M. Munoz, B. Kozanoglu, J. Casal, J. Arnaldos, Experimental study of thin-layer boilover in large-scale pool fires, Journal of Hazardous Materials 137 (3) (2006) 1293–1302.

[4] F. Ferrero, M. Munoz, J. Arnaldos, Effects of thin-layer boilover on flame geometry and dynamics in large hydrocarbon pool fires, Fuel Processing Technology 88 (3) (2007) 227–235.

[5] J. Garo, Combustion d'hydrocarbures répandus en nappe sur un support aqueux. analyse du phénomène de boilover, Ph.D. thesis, Université de Poitiers, Faculté des Sciences fondamentales et appliquées (1996).

[6] K. Hasegawa, Experimental study on the mechanism of hot-zone formation in open tank fires, Proc. Fire Safety Science, 2nd Int. Symp. (1987) 221–230.

[7] N. Otsu, A threshold selection method from gray-level histograms, IEEE transactions on systems, Man and Cybernetics 9 (1) (1979) 62–66.

[8] R. Gonzalez, R. Woods, S. Eddins, Digital image processing using matlab, New Jersey, Pearson Prentice Hall.

[9] H. Hottel, Review: certain laws governing the diffusive burning of liquids, by blinov and khudiakov, Fire Res. Abstr. Rev. 1 (1959) 41–44.

[10] V. Babrauskas, Estimating large pool fire burning rates, Fire Technology 19 (1983) 251–261.

[11] P. Rew, W. Hulbert, D. Deaves, Modelling of thermal radiation from external hydrocarbon pool fires, Safety Environ. Protect. 75 (1997) 81–89.

[12] B. Dlugogorski, M. Wilson, Effect of ullage on properties of small-scale pool fires, Dev. Chem. Eng. Mineral Process. 8 (1/2) (2000) 149–166.

[13] A. Hall, Pool burning, Oxydation and Combustion Rev. 6 (1973) 169–225.

[14] D. Laboureur, Experimentation a petite echelle du phenomene de boilover, Actes du Congres Annuel de la SFT 18 (2) (2010) 345–350.

[15] J. Garo, H. Koseki, J. Vantelon, C. Fernandez-Pello, Combustion of liquid fuels floating on water, Thermal Science 11 (2) (2007) 119–140.

[16] H. Koseki, M. Kokkala, G. Mulholland, Experimental study of boilover in crude oil fires, Proceedings of the 3rd International Symposium of Fire Safety Science (1991) 865–874.

[17] E. Weckman, A. Sobiesiak, The oscillatory behavior of medium scale pool fires, 22nd Symposium (International) on Combustion 180 (4) (1988) 699–712.

[18] E. Zukoski, B. Cetegen, T. Kubota, Visible structure of buoyant diffusion flames, 20th Int. Symp. on Combustion 20 (1) (1985) 361–366.
[19] P. Thomas, The size of flame from natural fires, 9th Symposium on Combustion, Pittsburgh (1963) 844–859.
[20] J. Moorhouse, Scaling criteria for pool fires derived from large-scale experiments, IChemE Symposium Series 71 (1982) 165–179.
[21] G. Mangialavori, F. Rubino, Experimental tests on large hydrocarbon pool fires, 7th International Symposium on Loss Prevention and Safety Promotion in the Process Industries, Italy.
[22] K. Mudan, Thermal radiation hazards from hydrocarbon pool fires, Progress in Energy and Combustion Science 10 (1) (1984) 59–80.
[23] T. Henriksen, T. Ring, E. Eddings, G. Nathan, Puffing frequency and soor extinction correlation in jp-8 and heptane pool fires, Combustion science and Technology 22 (1) (2008) 1299–1310.
[24] P. Pagni, Pool fire vortex shedding frequencies, in some answered questions in fluid mechanics, Applied Mechanics Review 43 (8) (1989) 153–170.
[25] D. Laboureur, Experimental characterization and modeling of hazards: Bleve and boilover, Summaries of VKI's doctoral candidate research (2011) 145–151.
[26] F. Scarano, Iterative image deformation methods in piv, Measurement science and Technology 13 (1) (2002) R1–R19.
[27] E. Zukoski, Fluid dynamic aspects of room fires, Proc. Fire Safety Sicence, 1st Int. Symp. (1986) 1–30.
[28] G. Heskestad, Luminous heights of turbulent diffusion flames, Fire Safety Journal 5 (2) (1983) 103–108.
[29] M. Delichatsios, Transition from momentum to buoyancy-controlled turbulent jet diffusion flames and flame height relationships, Combustion and Flame 92 (4) (1993) 349–364.
[30] D. Drysdale, An introduction to Fire Dyanmics, second edition, John Wiley & Sons, West Sussex, England, 1999.
[31] M. Delichatsios, Air entrainment into buoyant jet flames and pool fires, Combustion and Flame 70 (1) (1987) 33–46.

Shape and Temperature Field Distortions Induced by Convective Effect on Hot Object in the Visible, near Infrared and Infrared Bands

Anthony Delmas

Environmental and Applied Fluid Dynamics Department, von Karman Institute for Fluid Dynamics, Belgium, anthony.delmas@vki.ac.be

Supervisor: Jean-Marie Buchlin

Professor, Environmental and Applied Fluid Dynamics Department, von Karman Institute for Fluid Dynamics, Belgium, buchlin@vki.ac.be

University Supervisor: Le Maoult Yannick

Doctor, Metrology, Identification, Control and Surveillance Department, Institut Clement Ader, France, yannick.lemaoult@mines-albi.fr

Abstract

The goal of this study is to point out the perturbation induced by convective effect (mirage effect) on shape and temperature measurement and to give an estimation of the error done. This work will explore the sensitivity of several spectral bands and single wavelengths. A numerical approach is carried out and an original set up has been build in order to investigate easily all the spectral bands of interest with the help of CCD camera (Si) or VisGaAs camera. We will give the displacement due to the perturbation for each spectral band and finally give some hints about how to correct it.

Keywords: high-temperature, mirage effect, natural convection, infrared, near infrared, visible, hot disk.

1. Introduction

In industries like in research center, non-contact measurements of the temperature and/or of the displacement are often necessary. A good way to do it is to use cameras and to observe the object whom we want to know size and temperature. Some studies has been done in order to use usual visible CCD cameras (Silicium detector 0.35μm-1.1μm) to make thermal-dimensional coupling measurements and merge usual video data with infrared data [1]. Several advantages to work in the near infrared to measure the temperature exist, for instance, we have a good sensibility and well resolute detector and we are less dependent on the unknown emissivity of metals. However, some investigations made in this specific domain have underlines some perturbations emphasized at high-temperature (T$\geq$800°C), the standard deviation of dimensional measurements is multiply by 5 [2]. Numerous works realized by means of camera to provide measurements have pointed out the problem of images pertubated by refractive index gradient in the air [3; 4; 5; 6]. We will focus in this study on perturbations which arise from convective effect present around hot objects. Such perturbation can induce a shape distortions in the visible band but also errors on shape and temperature measurements for near infrared and infrared bands. We choose first to focus on a simple geometry objects like a cylinder or a hot horizontal disk in order to generate a reproducible convective plume. We present here a numerical way (ray-tracing [7]) to obtain the displacement induced by the density variation and an experimental method to get quantitative values of displacements. Because of the recent emergence of new generations cameras with high resolution even in the infrared band, this work will be carry out for several spectral bands going from visible until infrared passing by near infrared. Finally, we will give some ideas about a strategy of correction of pertubated images.

2. Mirage effect: description and generation

The mirage effect appears as soon as we have a refractive index gradient. What we called mirage effect is when light beams do not arrive at the expected

destination (without temperature gradient). Usually this effect does not have a big influence on optic measurement. But, if we are in presence of a strong refractive index gradient, the information measured can be wrong enough to be taken into account. In our case, the refractive gradient is engendered by a temperature gradient coming from a natural convective plume. The convection is induced by the movement of molecules within fluids, here the air, due to temperature differences which affect the density, and thus relative buoyancy, of the fluid. More dense components will fall while less dense components rise, leading to bulk fluid movement. In the case of a hot object, the convective field around it will pilot the temperature field around the object. This temperature gradient around and above the object leads to a refractive index gradient which, if the deviation is important, can bring big aberrations. Light distortion induced by natural convection is very frequent and can be observed in numerous cases. The most famous one is the mirage effect which occurs over a road or in the desert when the sun is strongly hitting the ground (Fig. 1).

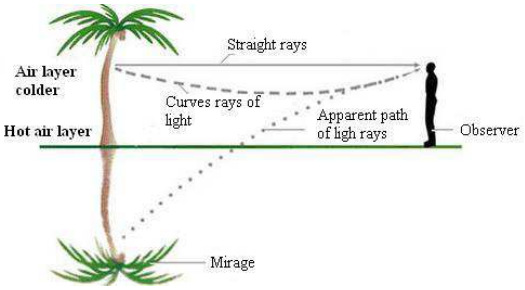

Figure 1: Mirage effect principle.

Either the observed object is far (hundreds of metres) and the deflection can be important even with small gradient (20°C of relative difference), see Fig. 2, or the object is close to the observer (few metres or centimetres) but the temperature gradient is much strong (500°C to ambiant temperature) like in the Fig. 3.

In our case, we will focus on mirage effect occurring within a short distance. It can be sometimes a real problem when we need to know with accuracy the shape or the temperature of a given point of the object. We give in this work a value of the error made when we are trying to make such measurement. In addition, the deflection induced by the temperature gradient varies with the wavelength. According to the Eq. 1 called Gladstone-Dale law [8], we can obtain for a given temperature field and wavelength, the refractive index distribution.



Figure 2: Mirage effect with far object.

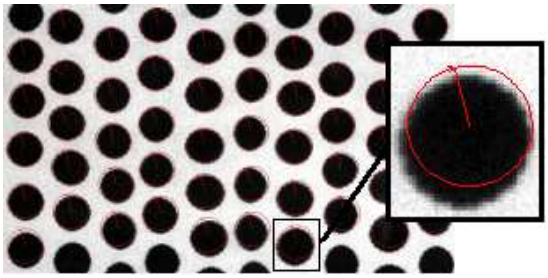

Figure 3: Mirage effect with object 1m far (circles are the original shape of the black disk).

$$n_\lambda - 1 = K_\lambda \cdot \rho(T) \quad (1)$$

$$\text{where } K_\lambda = (N \cdot \alpha_0)/(2 \cdot \epsilon_0) \quad (2)$$

The Gladstone-Dale parameter K is function of the wavelength λ (because α_0: polarizability of one molecule depends on λ), ϵ_0 is the vacuum permittivity and N is the Avogadro number. We choose to work first in the visible band, with the wavelength of the He-Ne laser: λ =632,8nm and K=0,2256.10^{-3} m^3/kg. In our case, air can be taken as an ideal gas, and so:

$$\rho(T) = 352.86/T \quad (3)$$

With combination of Eqs. 1 and 6, we establish for the specific wavelength of an He-Ne laser:

$$n - 1 = 0.079 \cdot T^{-1} \quad (4)$$

We can see in the Fig. 4 how the refractive index depends on the temperature and on the wavelength. The index of refraction decreases with the rise of temperature or wavelength. However, we see that the variation of the refractive index tends quickly to a constant value. The variation is the most important for the short wavelength (UV and visible). Knowing that the bigger the refractive index is, the more the light is deviated, if we look a mirage effect with a visible camera

(or by eyes), we will see only the biggest deviation corresponding to the shortest wavelength of the camera (≈400nm). It means that we dont need to use an effective refractive index for a spectral band (refractive index integrated index over the spectral band) to obtain the displacement observed in real but only the one corresponding to the shortest wavelength. Above 1000nm, it doesnt really matter anymore since the refractive index varies very slightly. We are now able to obtain directly from the temperature field, the refractive index distribution for a given wavelength.

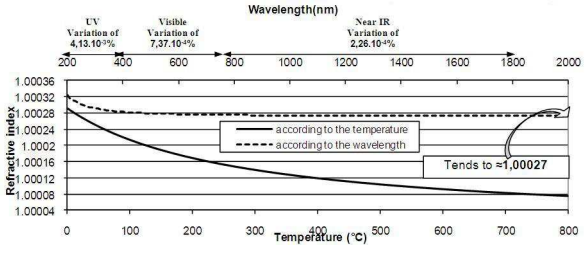

Figure 4: Refractive index evolution according to the wavelength (at 15°C) and to the temperature (at λ=632,8nm) [9].

The next step is now to choose a hot object able to generate a reproducible convective effect with an important temperature and refractive index field. We thought first to use a vertical hot plate but issues appear quite fast about a well homogenized hot plate and the generation of a stabilized boundary layer [10]. Our choice ended on the generation of a plume coming from a hot horizontal disk. This generation of the perturbation is interesting because is a free convection, in agreement with our context, and in addition, such system permits to obtain both a strong displacement of the lights through the perturbation and a heating element of small dimensions. Displacements expected and size of the heating element are both validated thanks to a ray-tracing method and a CFD software (cf. section 3). Moreover, since the heating element is much smaller than a vertical plate, its possible to generate very high temperature with a good homogeneity. We present now how the design of the set-up has been selected.

3. Numerical tool and experimental design

The heating element chosen is a hot horizontal disk generating an axisymmetric plume. We will discuss here which diameter it should have and the temperature necessary to have a displacement big enough to be measured. Firstly, before to start any computation or sizing, we should verify in which regime the flow in the plume will be. In free convection, a non-dimensional number is used as reference to predict the flow regime, its the Rayleigh number:

$$Ra = (g \cdot \beta \cdot \Delta T \cdot x^3)/(a \cdot \nu) \quad (5)$$

With g gravitational acceleration, β dilatation coefficient, ΔT difference of temperature between the air and the disk, x the characteristic length (diameter of the disk), a the thermal diffusion of the air and ν the cinematic viscosity. We want something small enough to be easily heat up and to have a good homogeneity. If we take a disk with a diameter of 10cm and heated up to 1200K (around the highest temperature of materials met in our laboratory) we obtain a Rayleigh number equal to $2{,}19.10^6$. This means that the flow will never reach a turbulent flow, cause the transition limit between laminar and turbulence is defined at $Ra=10^9$. With such laminar plume, we have something easily reproducible and well established. We can notice here that such laminar convective flow is the case of almost all the hot objects studied in laboratory (an images average can be needed in order to override external perturbations). In addition, the big advantage of a perturbation generated by such device is the displacement brought throw the plume. Indeed, an axisymmetric perturbation brings, just by its own curved shape, a light deviation (cf Eq. 10). Moreover, the temperature gradient in the plume is really strong (much stronger than a jet of hot air blowing from a pipe), and thus gives another way to deviate efficiently the rays of light. We can now start the numerical simulation of the deflection induced by the plume. The numerical method is described briefly in the Fig. 5. We first need to obtain the temperature field above the disk, to deduce the refractive index from the temperature and to include it in the ray-tracing code. We will present in this paper only the sizing case which gives best results. An insulator will be take into account in the simulation in order to avoid a gradient temperature on the disk surface during the experiment.

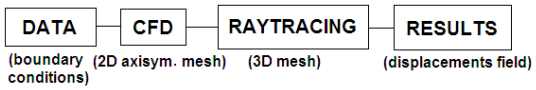

Figure 5: Diagram showing the main steps of the numerical method.

3.1. Computational fluids dynamics (CFD)

3.1.1. Simulation

The first step is to know the temperature field in the plume. We will compute it with the help of a CFD

software. The axisymmetric geometry is meshed with Gambit then introduced in FLUENT (Fig. 6). The computing is, as we showed it upper, realized in laminar flow. Often, in order to facilitate the computation, correlations are used to define the material properties (here the air) [11]. The different correlations used in our case are the followings:
About the density, we know that the air can be assimilate as a perfect gas. The error made compared to the exact values are in average about 0.16% in our temperature scale (300K to 1300K). Thus, the correlation used for the density is the perfect gas law:

$$\rho(T) = (P \cdot M)/(R/cdotT) \quad (6)$$

With ρ the density (kg/m^3), P the pression, M molecular mass, R the perfect gas constant, T the temperature. // For the viscosity, the correlation used is:

$$\mu(T) = 1,875.10^{-5} \cdot (T/273)^{0,6386} \quad (7)$$

For the specific heat:

$$Cp(T) = 975,3 + 0,0368 \cdot T + 2.10^{-4} \cdot T^2 \quad (8)$$

For the thermal conductivity:

$$\lambda(T) = 0,026(T/293)^{0,7231} \quad (9)$$

In this condition, we obtain the temperature field around and above the disk (Fig. 7)

The size of the domain has be taken big enough (50cmx100cm) in order to avoid any kind of border effect. The mesh is made in order to have smaller cells close to the disk. The number of cells in this simulation is 60000 (300 vertically by 200 horizontally).

3.1.2. Results validation

The validation of FLUENT results will be carried out in the section 4 and numerical results will be compared with the experimental ones.

3.2. Ray-tracing

The ray-tracing code has been initially developed to simulate the heating of plastic preform in the ICA. The code has been modified for our study to be able to make optic computations in an environment of inhomogeneous refractive index.

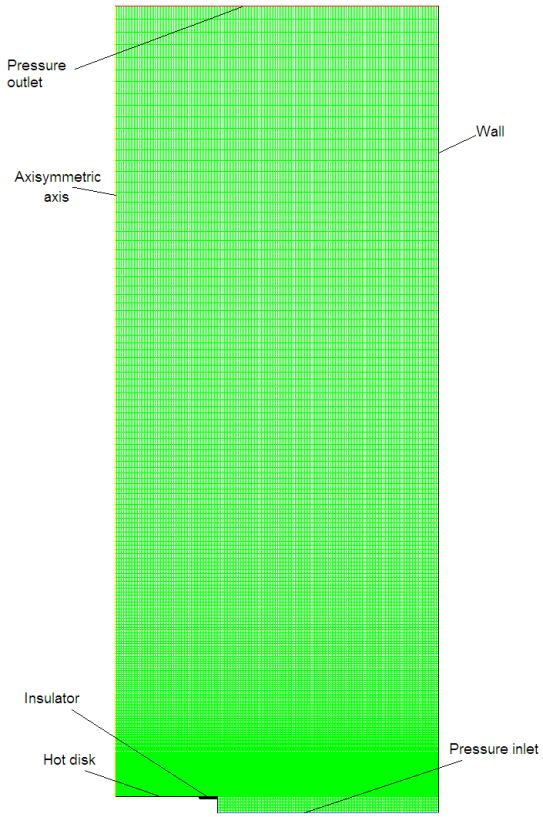

Figure 6: Mesh and boundary conditions used for the simulation.

3.2.1. Preliminary validation

In order to validate the ray-tracing code, we will use a simple geometry and we will compare the numerical result with an analytic one. The geometry used here is a vertical plate (see details in Fig. 8) with a uniform index of 3. In order to reduce a maximum errors due to approximation, the air index will be taken equal to 1 numerically and analytically. The ray will be throw from the original plan with a vertical angle α of 1° and 2°.

With this configuration, we find analytically a displacement Z of 4.654mm and 9.311mm respectively for 1° and 2°. The results obtained using the ray-tracing code are respectively 4.654mm and 9.309mm. The error made by the code is inferior to 0.02

3.2.2. Simulation

For the input data of the code, thanks to the Gladstone-Dale law (Eq. 4), we deduce from the temperature field, the refractive index field for a given wavelength (for the example we chose λ=632,8nm). Finally, we incorporate this refractive index field in

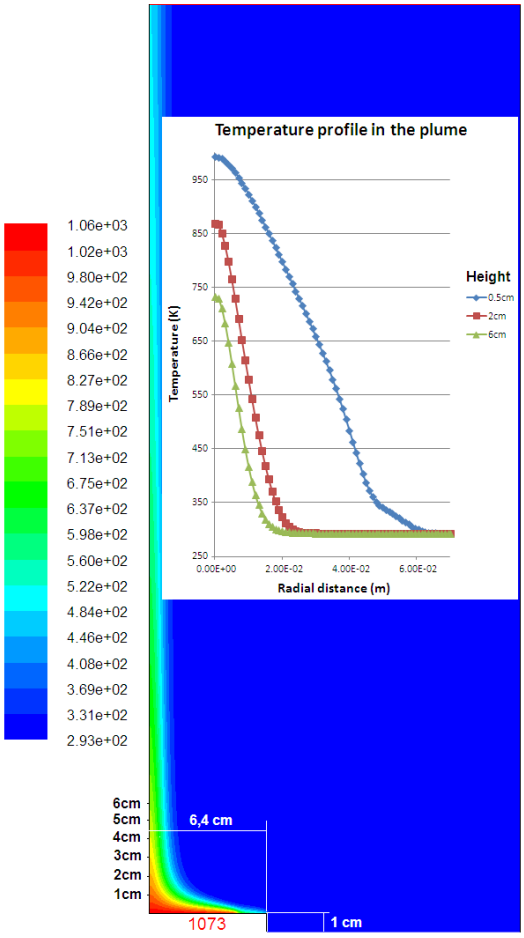

Figure 7: Temperature contours obtained with FLUENT and temperature profiles at different heights above the disk at 1073K.

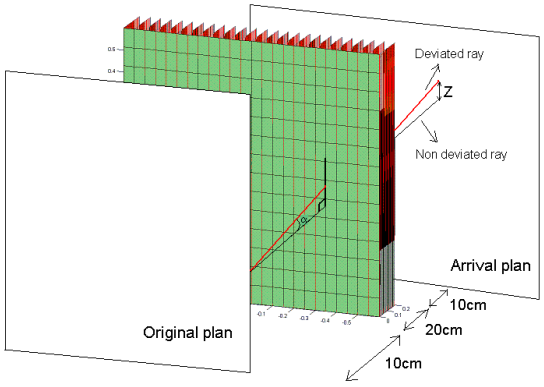

Figure 8: Geometry and distances used for the validation.

time saved is consequent.

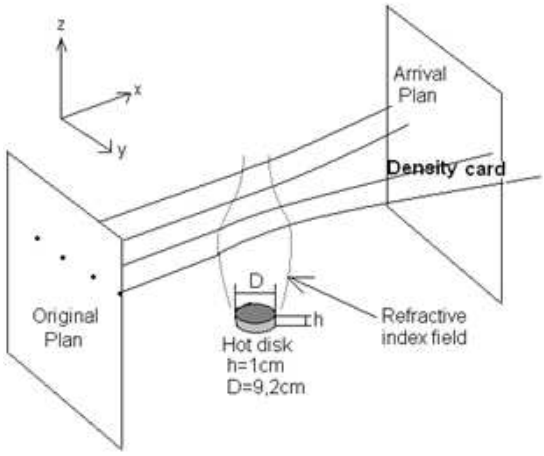

Figure 9: Diagram showing the functioning of the code and its geometry.

our ray-tracing code as the Fig. 9 illustrates it. The original plan is composed of radiating elements located with their y and z coordinates. Each element launches one ray perpendicularly to the original plan. The refractive index field around and above the disk is discretized according to the radial, circumferential and axial coordinates in order to create a large number of cells with constant refractive index (Fig. 10). A parametrical analysis on the mesh has been realized before in order to obtain good results within a time not too large (the creation of 1 000 000 cells (100x100x100) leads to several days of computation [15 days exactly on our computer]). We will choose here a mesh of 125 000 cells (50x50x50), giving a computing time of approximately 6h30 (AMD Opterion 2GHz, 1Mo cache, 2Go Ram, on Linux-Feodora). The error between a meshing of 1 000 000 cells and 125 000 cells is between 10 and 15% but the

The transition from one cell to another is governed by the Snell-Descartes law (transition between a cell i to a cell j with n and θ respectively the refractive index of the cell and the angle between the ray and the normal to the cell surface):

$$n_i \cdot sin(\theta_i) = n_j \cdot sin(\theta_j) \quad (10)$$

Then, when the ray goes out of the last cell, so from the thermal perturbation, it continues his path until the arrival plan, which the position according to x can be adjusted to accentuate the distortion effect. Indeed, the further the screen is, the more the deviation is. We will chose in our example a distance of 37cm. If we discretize sufficiently the original plan and thus enough rays are launched (around

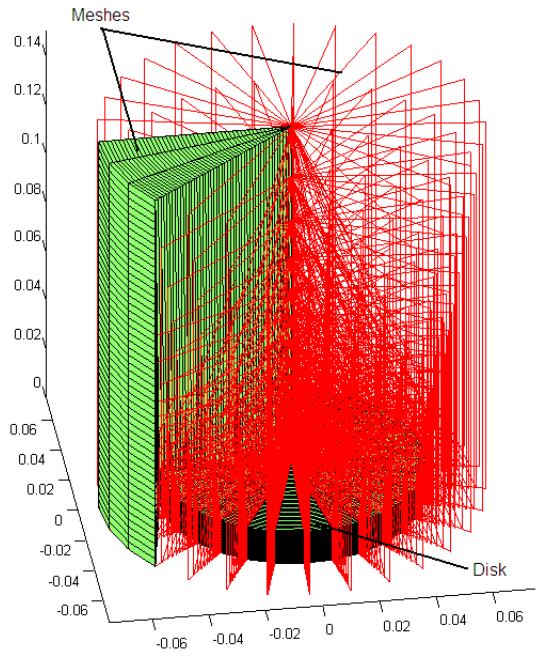

Figure 10: The volume discretisation in cells.

500 000 to obtain the Fig. 11) we obtain on the arrival a displacement map. The most important is to discretize sufficiently the arrival plan because it will affect directly the precision of the displacement. For example, if the arrival plan is 7cmx7cm, and if we discretize it by 1000x1000, the smallest displacement measurable is 0.07mm but thanks to mathematic interpolations we can reach much smaller displacement (0.0001mm). The discretization of the original plan matters mainly about the results visualization and result density. The displacement map obtained permits to quantify the displacement of each ray between the original plan and the arrival one. We can display either the displacement along y, z or the component of both $w=\sqrt{(y^2+z^2)}$. Results obtained are showed in Fig. 11.

The displacement map shows that the biggest displacements are located along the vertical edges of the disk, in the thermal boundary layer. These zones correspond to the strongest temperature gradient. The displacement on the vertical above the disk can reach around 0.3mm and 0.14mm in the plume. Moreover, in agreement with the Snell-Descartes law, we can notice that we dont have displacement in the center of the plume.

According to results obtained numerically with such set-up (Table 1), and using the proper objective on the camera in order to have a field of view

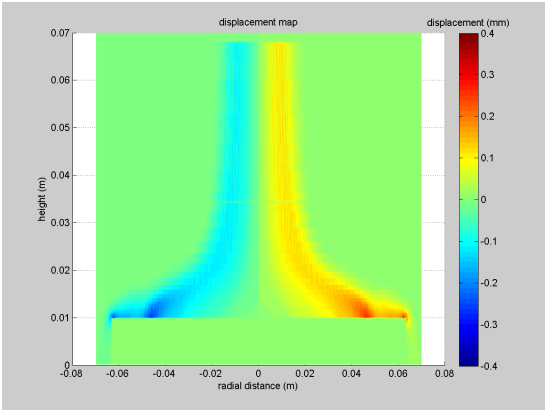

Figure 11: The volume discretisation in cells.

around 10cm, we will be able to obtain displacement big enough to be detected by the detector of the camera:

3.3. Set-up design

The disk selected for the experiment has a diameter of 9.2cm with 1cm of thickness. Its made of Inconel 600 and is heated up thanks to a resistance coiled and welded under it. The maximum temperature reachable (to dont deteriorate the welds) is 950°C with a power heating of 1300W. The heating element includes two embedded thermocouples used for regulation and security. The disk will be surrounded of an insulator made of mica paper impregnated with silicone resin under high pressure and temperature. This material has a poor conductivity (0.27W.m^{-1}.K^{-1}) and can resist to high temperature up to 800°C. Moreover, to avoid any perturbations coming from the surrounding environment, an enclosure is needed. We chose to realize an enclosure with metallic plates painted in black in order to avoid reflections on the walls (Fig. 12). Different holes are done on its face for future experiments. We can see in the Fig. 12 that the whole enclosure has been included in a second enclosure made of wood to avoid again perturbation coming from the room. The plume is VERY sensible to the out coming variation of pressure. Indeed the pressure variation in the plume is extremely small, around 1 or 2 Pa only.

4. Characterization and tests of the set-up

4.1. Disk characterization

The first test performs on the disk was done to verify the stability in time of the temperature and the homogeneity of the disk at the surface. In order to reg-

Type of cameras *Resolution*	**Classical Camera CCD** *1392x1036*				**NIR Camera** *320x256*	**IR Camera** *320x240*
Wavelengths	*200nm*	*400nm*	*632,8nm*	*750nm*	*1µm*	*8µm*
Maximum displacement in the plume (mm)	0,1482	0,1295	0,1267	0,1262	0,1257	0,1241
Maximum displacement above the disk (mm)	0,323	0,2822	0,2761	0,2751	0,2739	0,2705
Plume width 3cm aboce the disk (mm)	43,00	42,34	42,28	42,26	42,24	42,18

Table 1: Displacements expected for each wavelength and width of the plume.

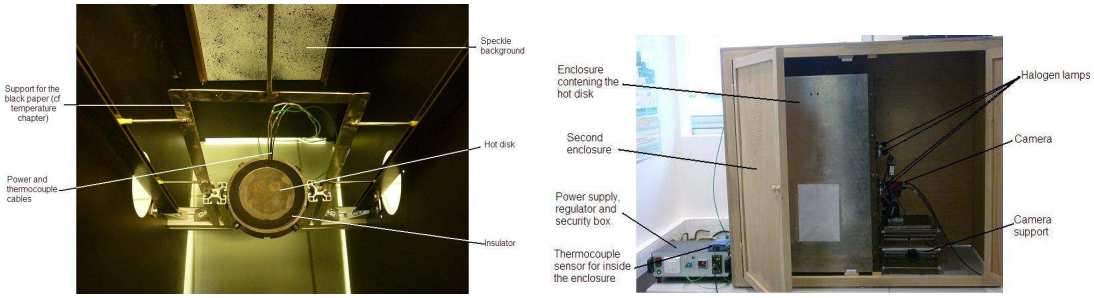

Figure 12: Pictures showing the set-up inside the enclosure and the whole equipment.

ulate the disk and to supply it in power, a PID regulator and a power supply unit are used (Fig. 12). A black paint for high-temperature is applied on the surface in order to have a uniform emissivity, then is observed with an infrared camera during the heating period (Fig. 13). We set the temperature of the resistance at 800°C. The heating element reaches the stability (within 0.1°C) after a slow increase of the temperature (20°C per min) and we get a surface temperature with an average of 800°C and a standard deviation of 18.4°C (if we take a zone of interest smaller than the whole disk, we can reach a much smaller standard deviation).

4.2. Plume characterization

4.2.1. Temperature

The plume obtained with this heating element is investigated by means of several methods and is compared with results obtained with FLUENT. The temperature inside the plume is measured by the aim of an infrared camera. We put vertically, in the exact middle of the plume, a sheet of paper painted in black (of known emissivity) and we measure the temperature taken by the paper itself. The paper can be considered as a thermally thin object (Paper Biot number $\approx 0.03 \ll 0.1$) which means that the paper will take, in all its depth, the temperature of the fluid in contact. However, the problem of the diffusion appears in this case. Indeed, we can see on the Fig. 16 that that width of the plume is lightly longer than the width of the numerical plume. This diffusion leads to a plume more width and thus a maximum temperature lower. The temperature of the disk has been fixed at 100°C. The numerical and experimental temperature

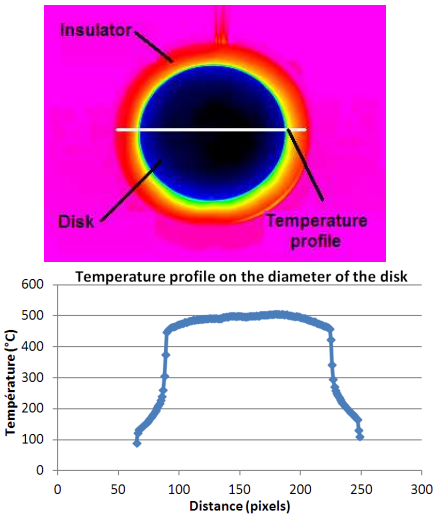

Figure 13: Thermogram and temperature profile of the disk and its insulator at 500°C.

fields are shown respectively in Fig. 14 and 15, and a profile done at a given height (20mm above the disk) is compared with a FLUENT profile in the Fig. 16.

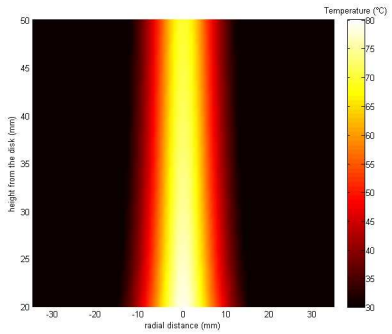

Figure 14: Temperature field obtained with FLUENT.

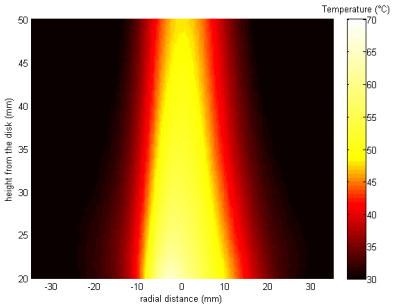

Figure 15: Temperature field obtained with the infrared camera.

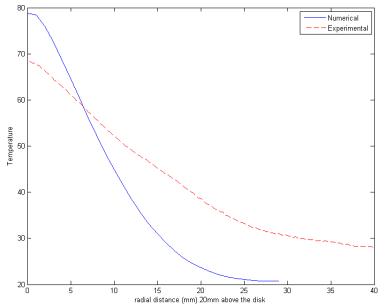

Figure 16: Temperature profiles 20mm above the disk obtained experimentally and numerically.

4.2.2. *Velocity in the plume*

Moreover, a PIV method [12] has been carried out in order to get the velocity field inside the plume and to validate once more FLUENT. The data comparison is displayed in the Fig. 18 and 17.

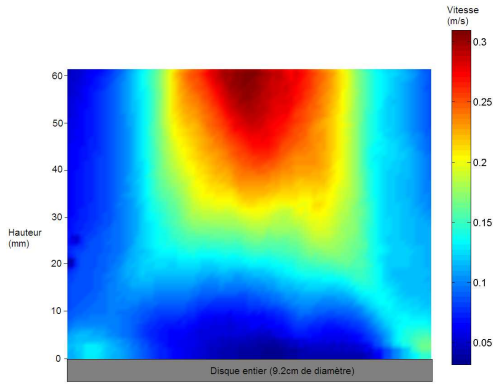

Figure 17: Velocity field obtained with FLUENT.

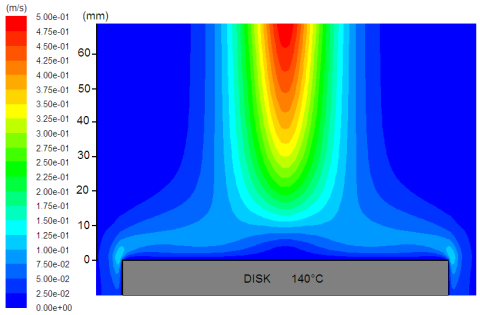

Figure 18: Velocity field obtained by PIV.

If we check in the middle of the plume at 6 cm above the disk, we can find the value of 0.32m/s and 0.45m/s respectively for the experimental and numerical results. The lower speed for the experimental result can be explained by the fact that we were measuring the speed of the seeding and not of the air itself. The ambient air was seeded with very thin drops of oil and its certainly possible that the velocity of the drops, cause of their weight, underestimates the velocity of the air. However, the results obtained (with quite difficulties) show that the order of magnitude remain the same and the velocity fields are similar (experimental results close to the disk are very hard to obtain, thats why the picture is sharper at the top).

4.2.3. *Schlieren photography*

The shape of the plume is explored as well with a schlieren photography technique. Schlieren photography is a visual process that is used to photograph the fluids flow of varying density. The basic optical schlieren system uses light from a single collimated source shining on a target object. Variations in refractive index causes by density gradients in the fluid distort the collimated light beam. the collimated light is

focused with a lens, and a knife-edge is placed at the focal point, positioned to block about half the light. In flow of uniform density this will simply make the photograph half as bright. However in flow with density variations the distorted beam focuses imperfectly and parts which have been focused in an area covered by the knife-edge are blocked. The result is a set of lighter and darker patches corresponding to positive and negative fluid density gradients in the direction normal to the knife-edge.
Several interferential filters has been used in order to see if it was possible to distinguish an enlargement of the diameter between several wavelength (cf Fig. 4) and then to compare it with the one calculated with the ray-tracing (Table 1). But as you can see in this table, the width changes only of 0.8mm in the visible band, too small to be clearly seen by the schlieren photography technique. However, if we check the average width of the plume itself over the different wavelengths with the numerical results we find a length in agreement with an error of few percent with the numerical results. If undisturbed, the plume will be a steady flow whose energy transport rate is equal to the heat transfer rate from the disk surface. Theoretically, the plume width (at a given elevation) should decrease with increased source strength [13]. A example of image taken with this method is shown in the Fig. 19.

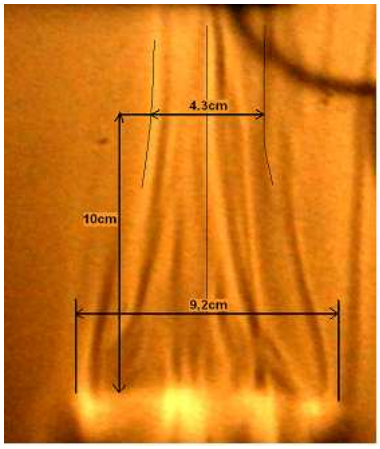

Figure 19: Image of the plume done with the Schlieren photography technique (disk temperature = 650K).

5. Displacements results

To measure the displacements induced by the plume we will use a technique called Background Oriented Schlieren (BOS) [14]. Background Oriented Schlieren is a novel technique for flow visualization of density gradients in fluids using the Gladstone-Dale relation between density and refractive index of the fluid. BOS simplifies the visualization process by eliminating the need for the use of expensive mirrors, lasers and knife-edges. In its simplest form, BOS makes use of simple background patterns of the form of a randomly generated dots, speckle image. In its initial stages of implementation, it was mostly being used as a qualitative visualization method. But in our case, thanks to a correlation software, we are able to obtain a quantitative displacement. The Fig. 20 gives the working of the BOS method:

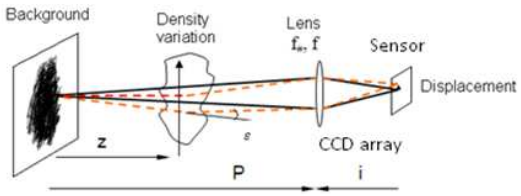

Figure 20: Diagram explaining the BOS technique.

To obtain result of displacement, two images of the background are recorded, one with perturbation and one without. Then, an analysis of these images is made in order to deduct the displacement of each element from the dot-pattern. This analyze is realized with the help of the software VIC2D [15]. It makes a correlation between the two pictures and gives as result the displacement of each element in pixel along the *x* direction and *y* direction. The displacement measured by the camera is directly linked to its distance with the plume. The distance **Z** is fixed at 30cm and **P+I** at 67cm (cf Fig. 20).

5.1. Visible

The camera used is a Pike F-145B/C with Sony ICX285 CCD sensor. The sensor resolution is 1388x1038 and works efficiently between 400nm and 800nm. We used an objective with a focal distance of 25mm which allowed us to explore around 10cm width in the plume few milimeters above the disk. With such set-up and with a disk heated up to 800°C, we obtained the following displacement field:

The Fig. 21 shows clearly the perturbation produced by the presence of the plume created by the hot disk. As expected, a deviation of rays of light occurs on the right side (displacement in the *x* direction) and left side (displacement inverse to the *emphx* direction) of the plume whereas the center of the plume

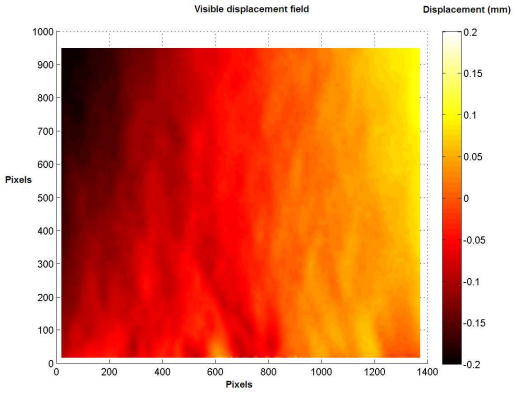

Figure 21: Displacement field in the visible band (average figure over 20 images.

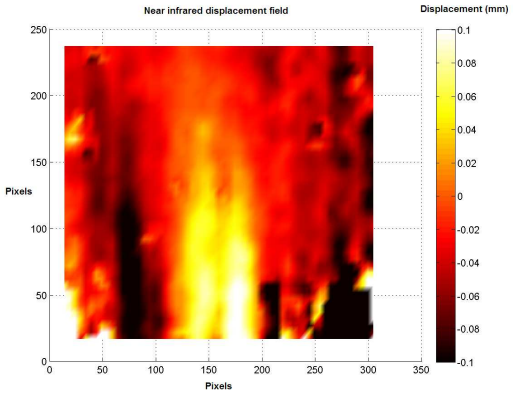

Figure 22: Displacement field in the NIR band (average figure over 10 images.

keeps a displacement very close to 0. If we compute the mean of the maximum displacement over all the pictures taken (600), we obtain a displacement of 0.27mm which is in good agreement with the numerical result (Table 1). The difference between the numerical and experimental results are lower than 5%.

5.2. Near infrared

For the near infrared band, we will use a XenICs camera XEVA-FOA-1.7-320, with a InGaAs Sensor. This sensor of 320x256 is working exceptionally in the range of 400nm - 1700nm. We had to insert between the objective and the density variation a filter in order to cut off the visible spectral band. The filter from Optosigma company cuts 100% of rays under 850nm. The focal length of the objective used in this case, cause of the lower resolution, is 50mm which permit to have 6cm of the plume in the field of view. The interest zone in pixel is 290x225.

In the Fig. 22 , we can still located the center of the plume between the two zones of positive and negative displacements (red and blue). The lowest displacement upper in the plume doesnt appear clearly with such camera because of the weak resolution of the sensor (even though we used a longer focal length). But we can still distinguish easily the perturbation occurring close of the disk. The two bottom corners of the figure have to be ignored because of correlation problems in this zone, as well as some blue and red points in the plume, corresponding with dead pixels. If we realize a window of interest on the plume itself and that we compute the average of the maximum displacement over 600 pictures, we obtain a value of 0.24mm. This result is in agreement with the numerical one, with 12% difference.

5.3. Infrared

For the infrared measurement, we used a FLIR SC325 camera. The microbolometric sensor working between 7.5 and 14μm (and -20°C up to +1200°C) has a resolution of 320x240 pixels. The objective used for the experiment has a focal length of 30mm, giving us the possibility to have 10cm (width) of field of view in the plume. The background observed with the camera in this case was different as before. We created a IR pattern [16] thanks to a copper plate painted in black and heated ($\approx$ 250°C) by a MICA resistance, and an aluminum plate pierced with holes (Fig. 23). The pattern is smaller than the field of view of the camera (to short focal length or to small pattern) and thats why the Fig. 24 is only a matrix of 175x140.

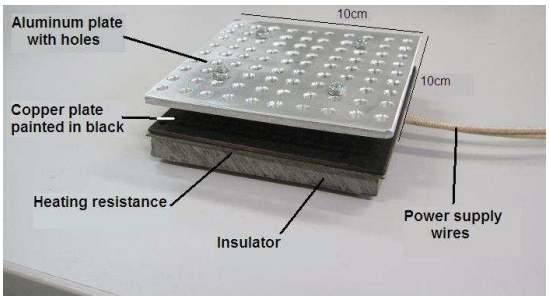

Figure 23: Pictures of the IR pattern created for the experiment.

As we can guess, the density results with such pattern is inferior than with a speckle image. Nevertheless, thanks to the interpolations made by the software VIC2D, we can obtain a result quite similar. We notice however somevertical bands on the pictures which actually correspond with zones without holes. We see on the Fig. 24 a part of the plume (around 5cmx4cm)

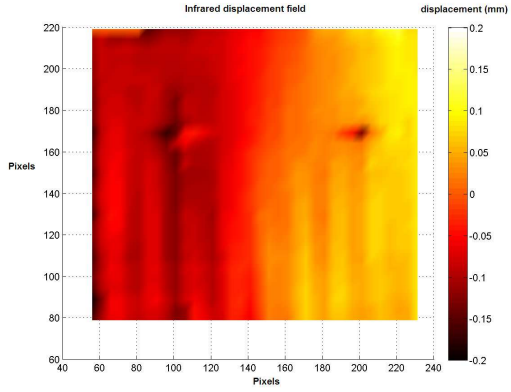

Figure 24: Displacement field in the NIR band (average figure over 10 images.

with no displacement in the center and respectively a positive and negative displacement on the right and left side of the plume. The displacement is slightly inferior than in the previous case because the picture has been taken a little upper in the plume. Indeed, the bottom of the pattern was loosing of contrast with time because it was getting more hot with the disk radiation. The average max displacement computed here is 0.153mm, still in agreement with the numerical results obtained in the plume. The two blue points on the picture correspond on the screws used to hold the aluminum plate with heating element.

6. Conclusion and perspectives

The work done here has pointed out the mirage effect phenomena in several spectral bands and we gave quantitative information about the displacement induced by the perturbation. We showed, thanks to an original set up allowing measurement in all the cameras spectral bands, that the displacement was around 0.26mm close to the disk and about half of it in the plume. The variation of the refractive index is essentially due to the temperature gradient (compare with the wavelength) and thus the displacements observed in any spectral bands are slightly the same. The main problem to be able to compare the experimental results is the weak resolution of sensor in the near infrared and infrared spectral bands. Indeed, the camera has to be far enough of the perturbation (or longer focal length should be used) to allow a measurement of the displacement. In our case, a strong temperature gradient and a focal length big enough gave us interesting results. We also brought out that the displacement generated by the axisymmetric plume was predictable by our ray-tracing tool (and by the preliminary use of a CFD software). Many experiments has be carried out in order to validate the numerical method such as infrared thermography, particle image velocimetry, schlieren photography. Although the preliminary experiences were tending to underestimate the Fluent results, the final measurements with background oriented schlieren are inclined to prove the accuracy of the numerical method.
The next step will be to correct pertubated images and to obtain images without perturbation coming from refractive index gradient. In the case of a laminar convection, the ray-tracing code can be used to predict the deviation of each point since we know the perturbation. If we don't know the perturbation but keeps axisymmetric proprieties, a method is in progress in order to retrieve the 2D index refractves field from the displacement given by the BOS [17; 18]. The 2D index refractives field is then transofrmed in 2D axisymmetric field thanks to the inverse Abel transform [19]. In the case of a turbulent flow, a statistical approach [20] and/or treatment of images by an algorithm [21; 22] seem to be more appropriate in an attempt to correct images.

References

[1] Healey G. E., Kondepudy R. - *Radiometric CCD Camera Calibration and Noise Estimation*, IEEE Transaction on pattern analysis and machine intelligence, vol.16, no.3, March 1994

[2] Claudinon S. - *Contribution l'tude des distorsions au traitement thermique*, Thse Ecolde des Mines de Paris, 2000

[3] Bing P., Dafang W., Yong X. - *Hight-temperature deformation field measurement by combining transient aerodynamic heating simulation system and reliability-guided digital image correlation*, Optics and Lasers in Engineering 48, pp 841-848, 2010

[4] De Strycker M., Schueremans L., Van Paepegem W., Debryne D. - *Measuring the thermal expansion coefficient of tubular steel specimens with digital image correlation techniques*, Optics and Lasers in Engineering 48, pp 978-986, 2010

[5] Lyons J.S., Liu J., Sutton M.A. - *High-temperature deformation measurements using digital image correlation*, Experimental Mechanics, March 1996

[6] Grant B.M.B., Stone H.J., Withers P.J., Preuss M. - *High-temperature strain field measurement using digital image correlation*, The Journal of Strain Analysis for Engineering Design May 1, 2009

[7] Cosson B., Schmidt F., Le Maoult Y., Bordival M. - *Infrared heating stage simulation of semi-transparent media (PET) using ray-tracing method*, International Journal of Material Forming, vol.4, n1, p1-10, 2011

[8] Mayinger F., Feldmann O. - *Optical measurements* 2nd *Edition*, Springer, 2001

[9] Lide D. R. - *Handbook of Chemistry and Physics* 88th, 10-253, 2007-2008

[10] Crespy C. - *Contribution la mesure de champs de temprature bi et tri-dimensionnels par Photographie de Speckle. Applica-*

tion lestimation des flux d chaleur paritaux, PhD thesis INSA Lyon, 2009

[11] El Motassadeq A., Chechouani H., Waqif M., Benet S. - *Simulation des effets de la rfraction dans la couche limite thermique au-dessus d'un disque horizontal*, Congrs franais de thermique, 2000

[12] Scarano F., Carlomagno G.M., Riethmuller M.L. - *Particle Image Velocimetry Development and Application.* Rhode Saint Genese: Von Karman Institute for Fluid Dynamics, 2000

[13] Robinson S. B., Liburdy J. A. - *Prediction of the natural convective heat transfer from a horizontal heated disk*, Journal of Heat Transfer, vol. 109, November 1987

[14] Klinge F. - *Investigation of background oriented schlieren towards a quantitative density measurement system*, Project report, von Karman Institute, 2001

[15] VIC-2D, Correlated Solutions Inc., http://correlatedsolutions.com.

[16] Saint Laurent L., Prvost D., Maldague X. - *Fast and accurate calibration-based thermal / colour sensors registration*, QIRT 2010-126.

[17] Klinge F. - *Investigation of background oriented schlieren towards a quantitative density measurement system*, project report 19, Von Karman Institute, 2001

[18] Sourgen F., Haerting J, Rey C. - *mesure de champ de masse volomique par Background Schlieren Displacement (BSD)*, Institut Franco-allemand de Recherches de Saint Luis, 2003

[19] Dibrinski V., Ossadtchi A., Mandelshtam V., Reisler H. - *Reconstruction of Able transformable images: the gaussian basis-set expansion Abel transform method*, Review of scientific instruments, Volume 73 number 7, 2002

[20] Rondeau X. - *Imagerie travers la turbulence : mesure inverse du front donde et centrage optimal*, PhD thesis, Lyon University, 2007

[21] Thorpe G., Fraser D. - *Correction and restoration of images obtained through turbulent media*, Digital signal processing applications, pp 415-420, 1996

[22] Lemaitre M., Lalignant O., Blanc-Talon J., Meriaudeau F. - *Local isoplanatism effects removal on infrared sequences*, Proceedings of SPIE, Quality Control by Artificial Vision (QCAV) Conference, France, Vol. 6356, 2007

AEROACOUSTICS

Beamforming in Non-ideal Acoustic Environments

(Grid Adaptation for L_1 Norm Generalized Inverse Beamforming)

Péter Tóth

Environmental and Applied Fluid Mechanics Department, von Karman Institute for Fluid Dynamics, Belgium, tothp@vki.ac.be
Fluid Mechanics Department of Budapest University of Technology and Economics, toth@ara.bme.hu

Supervisor: Christophe Schram

Associate Professor, Environmental and Applied Fluid Dynamics Department, Aeronautics and Aerospace Department, von Karman Institute for Fluid Dynamics, Belgium, schram@vki.ac.be

University Supervisor: Máté Márton Lohász

Assistant Professor, Department of Fluid Mechanics, Budapest University of Technology and Economics, Hungary, lohasz@ara.bme.hu

Abstract

This paper presents some advancement of the acoustics beamforming technique developed in the VKI. The development is focusing on the L_1 norm generalized inverse beamforming methodology. The algorithms are improved and the present study introduces an adaptive methodology to refine the source grid. The refinement gives a non-uniform, unstructured source plane grid. The method helps to achieve similar results compared to the uniform grid solution with reduced number of grid points. This is useful when the searching zone and the grid is relatively large compared to the extent of the true sources. With this method the required computational resources for the inversion procedure can be decreased. Results are promising, but still improvement of the adaptive refinement algorithm is advisable. The performance of the algorithm is presented in this paper on a numerical test case for the generalized inverse beamforming algorithm.

Keywords: acoustics, generalized inverse, beamforming, adaptive grid, condition number

1. Introduction

There is an increasing desire for acoustic noise reduction of machines, those principles of fluid mechanics nature. Along with the numerical aeroacoustic advancements of understanding the principles of aerodynamic noise sources the need for experimental testing is increased to quantify complex sources or provide validation database.

The aim of this PhD project is to develop quantitative acoustics measurement configuration for aeroacoustic source localization in non-ideal acoustics environments. In several cases it is desirable to preform aeroacoustic measurements in non-anechoic environments, such as aerodynamic wind tunnels or in situ industrial measurements. The beamforming technique would extend the use of advanced aeroacoustic testing in a cost efficient way in such environments. The beamforming method was first used in radio astronomy and radar technology to obtain a directionally sensitive antenna for the detection of the incoming signal direction [1]. The principle of this technique is to utilize the signal of several microphones in such a way that the directional sensitivity of device is adjustable. This is usually achieved with digital signal processing techniques on the simultaneously acquired data of the microphones. The acoustics field can be scanned point by point in order to find the unknown source positions by 'steering' the array sensitive 'spot' (main lobe) into different spatial directions, at a given frequency. The result is the so called the beamforming map, shows the source amplitude distribution in the spatial region that have been scanned. Today's this technique is widely used in different configuration for acoustics source identification. Many application dependent microphone arrangement exist, using advanced data processing algorithms, in order

to obtain high resolution and clean source maps [2]. One of the method is using the mathematical concept of generalized inverse of matrices [3]. This is the technique used in the VKI beamforming project.

After the description of the motivation of the study, first the theoretical background of the used generalized inverse method will be presented in the first section. This is followed by a description of the grid adaptation technique and the used numerical source model. Then the adapted grid results will be shown compared to a conventional uniform grid. This is followed by the discussion of the results. Finally the study is concluded in the last section.

1.1. The motivation

The previous investigations in the VKI of the generalized inverse beamforming (GIBF) technique has been showed that the method is sensitive to the source modeling error introduced by a source grid that is not includes all the significant sources of the measurement. This is often a situation when uniform source grid is used and the measurement contains disturbing sources far from the investigated model. This is a typical situation of a measurement in non-ideal acoustic environment. These errors decrease the robustness of the method. The uniform grid is usually extended only with a small amount beyond the expected location of the sources in order to reduce the computation resources and in this way this type if grid is not suitable for such measurement cases.

The current study gives an attempt to solve the problem by automatically adjust the model source grid in order to place many grid points close to the approximate location of the sources and remove the model sources where no source is expected. The approximate location of the sources is detected by the first iteration on a uniform coarse grid that can be chosen to include not only the investigated sources but other disturbing sources as well. The adaptation of the grid later gives sufficient source resolution for the final iterations.

2. Theory

Many different beam-forming methods have been developed in the past few years for aeroacoustic applications [2]. In this section the generalized inverse beamforming method is introduced based on the formulation of [3] with iteratively reweighed least squares (IRLS) method for the solution of the L_1 norm problem.

2.1. The microphone array data model

The microphone array data represents the sound field generated by physical sound sources. These sources are modeled with an appropriate source model and then this model problem is solved to retrieve the unknown model source amplitudes those are supposed to give a good estimation of the true physical sources. In this paper monopole representation of the sound sources is assumed. The transfer matrix involves each model source and each microphone can be written as:

$$V_{k,l} = \frac{e^{-ik|\mathbf{r}(\mathbf{y}_k^m, \mathbf{y}_l^s)|}}{4\pi|\mathbf{r}(\mathbf{y}_k^m, \mathbf{y}_l^s)|} \tag{1}$$

where the transfer matrix $\mathbf{V}$ is called the array manifold matrix in beamforming terminology. The distance between the microphone position $\mathbf{y}_k^m$, $k = 1..N_m$, and source position $\mathbf{y}_l^s$, $l = 1..N_s$ is $r = \mathbf{y}_k^m - \mathbf{y}_l^s$. The wave number is $k = c/\omega$ at a given circular frequency ω. The number of microphones and model sources denoted by N_m and N_s respectively.

The model sources can be represented by their cross correlation matrix $\mathbf{C_{ss}}$ of size $N_s \times N_s$ formed by the unknown complex source amplitudes $\mathbf{s}$. The source cross spectrum matrix is diagonal if the model sources are perfectly uncorrelated (they are incoherent) giving a full rank matrix. The matrix is singular with the rank of one, if the model sources are perfectly correlated (coherent sources). Finally, in case of partly correlated model sources the matrix has a full rank, with non-zero off diagonal elements.

During the measurement, the microphone array cross spectrum matrix $\mathbf{C_{xx}}$ can be computed from the measurement time data with the help of fast Fourier transformation. The elements of $\mathbf{C_{xx}}$ represents the amplitude and phase correlation between the acoustics signal sampled at different spatial points. The rank of the array cross spectrum matrix indicates the number of incoherent sources. The array cross spectrum matrix $\mathbf{C_{xx}}$ can be represented by its eigendecomposition since it is Hermitian.

$$\mathbf{C_{xx}} = \mathbf{U\Lambda U}^\dagger \tag{2}$$

Introducing the previous source reconstruction idea that the model sources with proper amplitude distribution can describe measured cross spectrum the following relation can be written:

$$\mathbf{U\Lambda U}^\dagger = \mathbf{V C_{ss} V}^\dagger \tag{3}$$

This equation is the basis of the GIBF formulation.

2.2. Generalized Inverse Beamforming algorithm

The GIBF algorithms are based on the inversion of the wave propagation problem relating the assumed possible source distribution and the measured acoustic field. The idea of the reconstruction is to treat one coherent source distribution at a time, meaning that a microphone array cross spectrum matrix $\mathbf{C_{xx}}$ can be constructed from the summation of $\mathbf{C^n_{xx}}$ for each eigenvalue λ_n of $\mathbf{C_{xx}}$, where $n = 1..N$. The problem is solved for the desired number of eigenvalues and the final source map is the squared sum of the resulting reconstructed source maps for each n. The problem of Eqn. 3 can be simplified with this idea as follows:

$$\mathbf{u}^n \sqrt{\lambda_n} = \mathbf{V}\mathbf{s}^n \tag{4}$$

Introducing the notation $\mathbf{b}^n = \mathbf{u}^n \sqrt{\lambda_n}$ for the eigenmode n the following inverse problem has to be solved to retrieve coherent source amplitudes $\mathbf{s}^n$:

$$\mathbf{s}^n = \mathbf{V}^{-1}\mathbf{b}^n \tag{5}$$

In order to retrieve the source amplitudes generalized inverse method has to be used, because of the propagation model can contain more sources than microphones or vice verse, therefore the coefficient matrix of the problem is non-square.

Non-square coefficient matrices represent underdetermined problems when the number of unknowns is larger than the number of available observations $N_s > N_m$. Overdetermined system is also possible when the number of unknowns is less than the number of observations $N_s < N_m$. The non square matrices arising in the beamforming problems are usually underdetermined since the number of measurement points are limited by the applied hardware (the number of microphones and acquisition channels) and the number of unknown model source amplitudes are user determined by taking into considerations the resolution of the algorithm (that depends on the frequency of interest and the microphone array size) and the scanning zone size.

2.3. Regularized solution methodology

If the problem is underdetermined a robust solution of Eqn. 5 can be obtained by imposing additional a priori information on the sources. Certain order of smoothness of the solution can be such an additional information. In the simplest case a constraint giving priority to the source distributions with smaller norm can be constructed. In order to allow this side constrain to have an effect on the solution, the residual of the solution in some p norm $R_p = \|\mathbf{V}\mathbf{s}^n - \mathbf{b}^n\|_p$ is allowed to be higher than zero. These requirements can be formulated as a minimization of the following cost function.

$$J_p = \epsilon\|\mathbf{s}^n\|_p + \|\mathbf{V}\mathbf{s}^n - \mathbf{b}^n\|_p \tag{6}$$

The solution of the inverse problem formulated as a minimization problem helps to overcome on the problem of the often badly conditioned $\mathbf{V}$. The cost function of Eqn. 6 with $p = 2$ represents the original Tikhonov regularization problem where the regularization parameter is ϵ. The regularization parameter can be considered here as a user definable parameter controlling the balance between the solution norm and the residual norm R_p. If $\epsilon = 0$ the residual norm is minimized leading to the unregularized solution. This can give meaning full result in numerical test cases when the condition number of the array manifold matrix $\mathbf{V}$ is small and there is no measurement error present in $\mathbf{b}^n$. When $\epsilon = \infty$ the effect of the constraint vanishes and only the solution norm is minimized. This would essentially lead to the $\mathbf{s} \equiv 0$ solution. Excessive regularization also decrease the resolution of the source maps, due to suppressing the effect of the smallest singular values of $\mathbf{V}$ [4] . Knowing that the small or zero regularization gives non-physical results, in real measurement cases the amount of the applied regularization should be carefully adjusted to the investigated case otherwise quantitative beamforming or desired resolution is not possible. In order to choose an optimal regularization parameter the L-curve analysis is used in this study, by defining the optimum at the corner of the curve [5]. This is automatically detected by the algorithm in the present L_p norm implementation.

The solution of the minimization of the cost function Eqn. 6 with a given ϵ and $p = 2$ can be written as:

$$\mathbf{s}^n = \mathbf{V}^\dagger(\mathbf{V}\mathbf{V}^\dagger + \epsilon\mathbf{I})^{-1}\mathbf{b}^n \tag{7}$$

The resolution of this method is only slightly better than the least squares beamformer, and as it is proposed by Suzuki [6; 3] the issue can be addressed by replacing the L_2 norm with L_1 norm in the cost function Eqn.:6 (means $p = 1$)

This cost function prevents the spreading of the amplitudes between grid points close to each other. Contrary to the $p = 2$ case when direct solution is exist with Eqn. 7 the minimization problem of the cost function Eqn.: 6 with ($p \neq 2$) can be solved only with iterative procedures. One solution, that is proposed

by [3], is to use the iteratively reweighed least squares approach to obtain a solution.

$$\mathbf{s}^n_{q+1} = \mathbf{W}_q \mathbf{V}^\dagger (\mathbf{V}\mathbf{W}_q\mathbf{V}^\dagger + \epsilon\mathbf{I})^{-1}\mathbf{b}^n \qquad (8)$$

Here $\mathbf{W}_q = \mathrm{diag}(|\mathbf{s}^n_q|^{2-p})$ is a weighting diagonal matrix, and the iteration counter is q. The iteration is stopped when the solution norm begin to increase, or the maximum number of iteration is reached, that is $q_{max} = 15$ in this study.

During this iteration procedure the number of the unknown model sources can be decreased by removing the smallest amplitude sources at each iteration. This is increasing the speed of the iteration and can also increase the final resolution of the algorithm. However it is complicating the stopping criteria of the algorithm since small level sources can be removed by the inappropriate stopping criterion. This procedure is proposed to use by [3]. In this paper an alternative solution methodology is proposed by using an adaptive grid technique to reduce the number of points therefore speed up the iteration and allow the proper resolution of every sources on the source map. It is worth to note that the problems presented here always falls into the category of the underdetermined system of equation.

2.4. Adaptive re-meshing of the model source domain

For the adaptive modification of the model source positions an unstructured grid is created with the help of the algorithm presented in [7]. The meshing algorithm takes the geometry and a distance function as an input and it is initialized with a uniform grid point distribution. This initial grid point distribution is defined by the user as well as the boundaries of the 2D domain where the source model have to be imposed. The distance function is prescribed by the result of an initial GIBF calculation on the user defined uniformly meshed domain. In the present case this involves only one iteratively reweighed least squares iterations ($q = 1$ in Eqn. 8). The resulted source map is smoothed with a moving average filter in order to have a smooth size control function and it is used with the help of a linear interpolation function to obtain the relative distances in the location of every unstructured grid points for the meshing algorithm.

The peaks on this map prescribes where the mesh should be fine and the valleys where it can be coarse. In real situations when the aeroacoustic source nature is of broadband type, this grid can be used to calculate source amplitudes for the close spectral lines also and therefore it is not needed to be recomputed often.

3. Application on a numerical test

In this section the application of the presented adaptive model source grid generation and GIBF algorithm is presented on a numerical test.

3.1. The model of the true sources with added noise

The used test case consist of two monopoles placed at x, y coordinates $[-2\lambda, -2\lambda]$, and $[2\lambda, 2\lambda]$ respectively. The wavelength is denoted by λ. The source plane is placed 11.66λ away from the plane of the microphone array (corresponds to 1m at $f = 4000$Hz with the defined sound speed). Both monopole source has an amplitude of 1 kg/s^2. The used microphone array layout is a multi-arm spiral layout of 32 microphone positions, depicted in Fig. 1. The origin of the reference coordinate system is defined in the center of the array as it is shown in the picture.

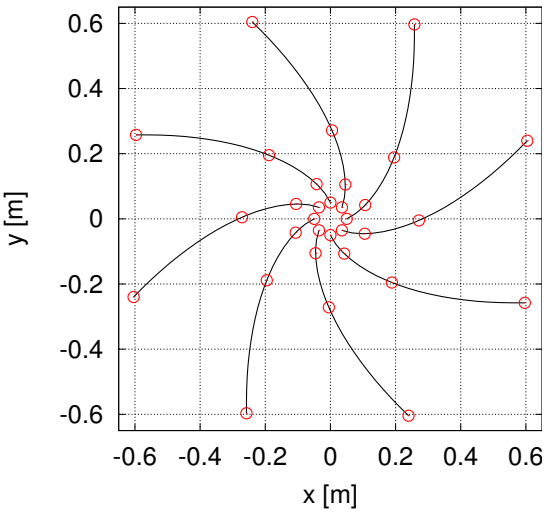

Figure 1: Optimized multi-arm spiral array geometry

In the presented test case the microphone array cross spectrum matrix $\mathbf{C_{xx}}$ is directly generated from the known position, frequency and amplitude of the imposed sources. In order to simulate realistic cross spectrum matrix additional noise is generated and introduced to this cross spectrum matrix. The sources are considered to be coherent.

3.1.1. Random noise cross spectrum model

The cross spectrum matrix is a positive semi definite Hermitian matrix. By introducing additional noise to simulate the real measurement scenario these

properties has to be respected. The array cross correlation is a transformation of the source cross correlation matrix with the array manifold matrix that is written for the true source locations. Since Eqn. 2 holds, each orthogonal eigenmode can be treated separately and their cross spectrum can be formed by the signal vectors $\mathbf{x}_s^n$.

$$\mathbf{C}_{\mathbf{xx}} = \sum_{n=1}^{N_m} \mathbf{C}_{\mathbf{xx}}^n = \sum_{n=1}^{N_m} \frac{1}{K} \sum_{m=1}^{K} \mathbf{x}_s^{n,m} \mathbf{x}_s^{n,m\dagger} \tag{9}$$

Averaging process is taken place for K samples of the microphones signal vector (length N_m) can be written:

$$\mathbf{x}_s^n = \mathbf{V}\mathbf{s}^n + \mathbf{x}_{noise}^n \tag{10}$$

where $\mathbf{x}_{noise}^n$ is the additive noise formed by introducing a signal with random phase and constant amplitude as a fraction of the monopole source amplitude computed for the array center.

$$\mathbf{x}_{noise}^n = \beta \frac{\|\mathbf{s}^n\|}{4\pi L} e^{i2\pi\mathbf{w}} \tag{11}$$

where $\mathbf{w} \in U(0,1)$ is a vector of N_m elements from a uniform random distribution $U(0,1)$. The L is the array source distance (L = 1m in the study), $\mathbf{s}^n$ is the imposed source amplitude vector and β is a user defined parameter controlling the level of the introduced noise. The number of averages K also has an effect on the generated cross spectrum. As the number of averages increase the noise in the cross spectrum decrease while the auto spectra in the diagonal still contains the averaged level of noise. In this way cross spectrum matrix with similar white noise representation as of the real measurement scenarios can be build. The present test case $\beta = 0.05$ and $K = 60$.

4. Results

The normalized ordered eigenmodes of the noisy microphone array cross spectrum matrix is illustrated in Fig. 2. It can be seen that all the eigenmodes are non-zero due to the added random noise, but the first one has a significantly larger value than the others. This is the expected coherent mode, corresponds to the defined sources and the associated noise in that mode. In the reconstruction of the sources therefore only this eigenmode desired to be considered.

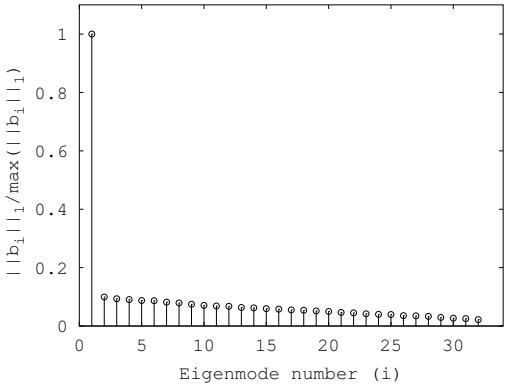

Figure 2: The normalized ordered eigenmodes for the test case

First the reconstruction is presented on a uniform grid without refinement. The grid size is chosen to be 6λ along which 101 grid points are placed in each directions. The reconstructed source map is presented in Fig. 3. Both sources are well retrieved. The source map spot size is about 0.3λ computed for the spot half width. The level of the spurious sources is small. The integrated source amplitude is approximately 0.5[kg/s^2] computed for the half width spot. In previous studies linear dependence of the source amplitude of the size parameters of integration region have been found, therefore the half width integrated value (size parameter 0.5) should correspond to approximately of the half of the true source amplitude. One should not forget that the added noise can cause some additional uncertainty. In the light of these considerations the reconstructed amplitude corresponds well to the true source amplitude as well as the position of the sources.

The reconstructed source field of the same microphone array cross spectrum matrix can be seen in Fig. 4 for the adapted grid. The distance function for the adaptive mesh generator was produced with one GIBF iteration on a 51×51 grid and the resulted source map is smoothed with a 19 point moving average filter. The final number of grid points is about 2930 in this adapted grid, and the model source distribution is plotted in Fig. 5. The model sources are strongly clustered around the true sources, while in the other regions of the source map few points are placed. The grid adaptation algorithm is used 20 retriangulations in order to obtain the present distribution of the points. The initial uniform distribution of the grid points for the grid generation algorithm is chosen in order to have approximately the same model source

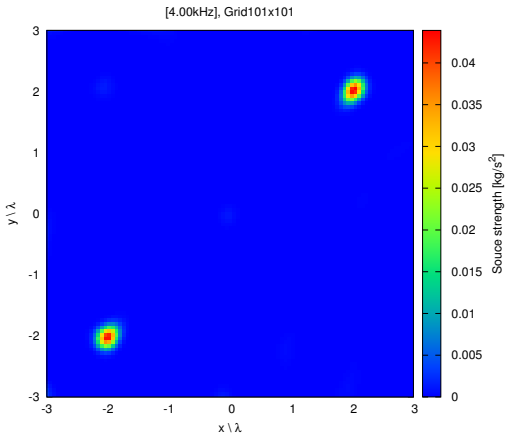

Figure 3: The reconstructed monopole source amplitude on the uniform source grid 101×101

density around the sources as in the 101×101 uniform grid. The source map spot size is about 0.3λ based on the spot half width. The spurious sources levels are higher than in the uniform model source distribution case. The integrated source amplitude is approximately $0.46[\mathrm{kg/s^2}]$ close to the values found on the uniform grid.

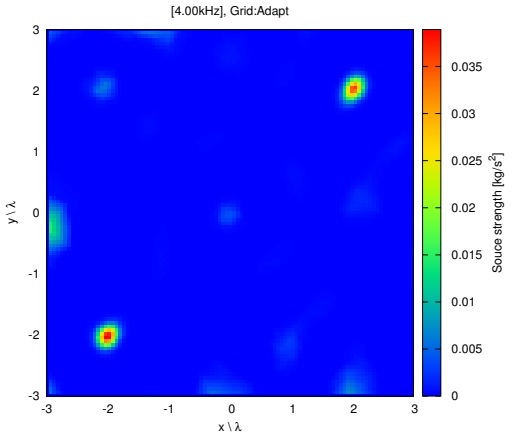

Figure 4: The reconstructed monopole sources on the adapted grid of approximately 2930 model sources. (The colour map is interpolated to a 101×101 grid)

The convergence of the IRLS iteration is plotted in Fig. 6. The plot shows the continuous decrease of the absolute value of solution summed for all grid points, that is the imposed constrain in the regularization method.

The effect of the non-uniform grid on the regularization method can be measured by comparing the

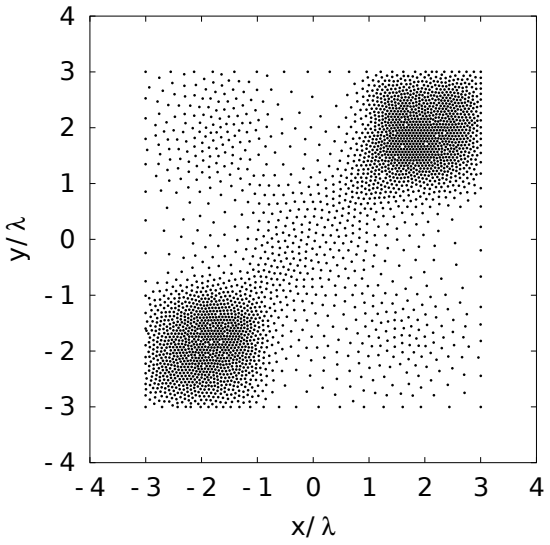

Figure 5: The adapted model source positions. $101x101$

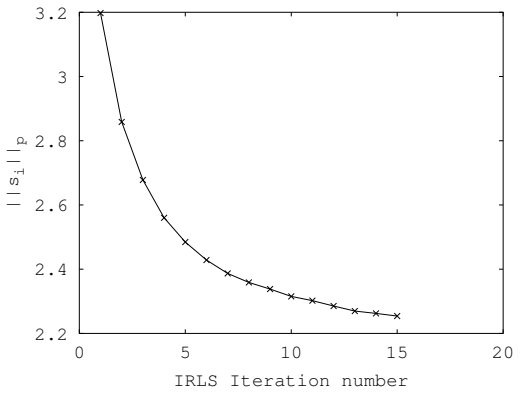

Figure 6: The convergence of the GIBF IRLS algorithm on the adapted grid.

singular value distribution of $\mathbf{V}$ (the spectrum of $\mathbf{V}$) in case of the uniform and the adapted grid [4]. The ratio of the highest and smallest singular values gives the condition number of the of the matrix. The value of the condition number indicates the level of ill-posedness of problem. The higher the condition number the more regularization should be used to overcome the amplification of the errors during the inversion process. The singular value distribution for the uniform grid and the adapted grid is shown in Fiq. 7.

The adaptation significantly changed the singular value distribution of $\mathbf{V}$. The singular values are significantly decreased. The condition number of the uniform grid model is 1225 while in the non-uniform grid model it is 1990. The adaptation of the grid is in-

creased the condition number, however this increase in not significant and it is not expected that it is changing the behavior of the inverse problem. The condition number of both cases can be considered as relatively small and the problem is not severely ill-posed.

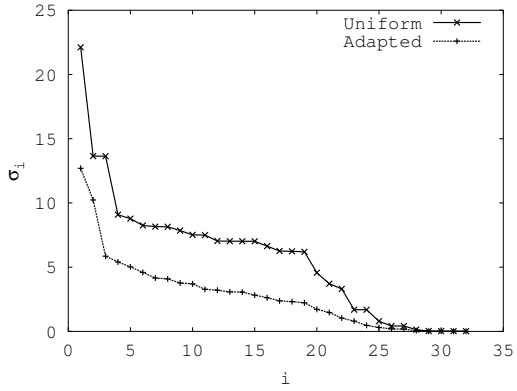

Figure 7: The distribution of the singular values of **V** for the two different meshes.

5. Discussion

Comparing the results obtained on the adapted and on the uniform grid both gives very similar source maps. The resolution and the source amplitudes are in good agreement. The uniform grid solution is a bit cleaner and the spurious sources are represented with smaller amplitude than in the case of the adapted grid solution. In this respect the uniform grid solution is slightly better than the non-uniform grid solution. The actual level of the spurious sources also depends on the used noise model. The applied random noise model significantly changed the distribution of the eigenmodes, that can be observed in Fig. 2. In case of the noiseless cross spectrum matrix only one non-zero eigenmode would exist. However in the present case all eigenmodes are non-zero and the second largest eigemode value is about 10% of the largest one. This implies the strong effect of the noise on the reconstruction and on the results. The test case shows that the algorithm handles well this level of random noise. The good resolution of the L_1 norm algorithm can be observed in both cases, that gives a resolution of approximately 0.3λ computed for the spot half width size on the source-map. This is very close to the $\lambda/4$ limit of the resolution. The usability of the L_1 norm generalized inverse beamforming method on arbitrary source map configuration is confirmed by the test, without the loss of the resolution or source amplitude prediction.

The convergence of the algorithm is good in the non-uniform grid also. The convergence characteristic shows that several additional iterations could be performed in order to further increase the accuracy. However it is not expected that the presented results changes significantly.

The inspection of the singular values draws an important behavior of the grid adaptation. The distribution of the singular values are significantly changed compared to the uniform grid, while the condition number, that is the ratio of the highest to smallest singular values, only slightly modified. Considering the fact that the number of model sources decreased by a factor of approximately 3.7 (from 10201 to approximately 2930) and their distribution changed to form two dense spots, suggest that the condition number cannot be significantly changed by varying the model source positions and number, in the same area, if the minimum distance between the points kept approximately unchanged. This is an interesting founding additionally to [8] where they found that the condition number is significantly affected by the microphone spacing, the source distances compared to the wavelength and the source array distance. They found also that the condition number of the problem is the smallest when the model source geometry is matching with the microphone array geometry (i.e. the distribution of the sources on the source plane are similar to the distribution of the microphones on the array plane). The fact that distributing the sources in an adaptive manner does not changed the condition number significantly, allows to prepare efficient adaptive grid techniques to resolve large source domains with the generalized beamforming method. These findings should be studied more precisely when efficient algorithms are intended to be created.

Concerning the required CPU time of the algorithm slightly better than linear speed-up have been found when considering the number of grid points used in the uniform and adapted grids. If the CPU time required for the uniform grid solution is denoted by T_u, then the solution of the same problem with the adaptive grid method is requires $\sim 0.27T_u$, from which the re-meshing is $\sim 0.04T_u$. The figures are measured on a 2.5Ghz Intel CPU with 6Mb cache and 2Gb of RAM. The numbers shows the required computational resource is reduced, and that can be still slightly improved by reducing the time required for the re-build of the source grid by using a faster implementation if the method of by using different technique. The used

method of [7] known to be a bit slow especially on large meshes.

The results emphasize that the appearance of the higher level of spurious sources depends on the model source grid. The distribution of the points has to be chosen carefully and low level of spurious sources can be achieved by using the uniform grid in the expense of higher computational cost. This results points out that the method to distribute the model source points is critical and can be the target of further improvements of the adaptive source grid beamforming technique.

6. Conclusion

In this paper the adaptive model source grid refinement technique is presented and evaluated with the help of a numerical test case. The generalized inverse beamforming method is used to retrieve the source positions and amplitudes with the L_1 norm formulation solved by the iteratively reweighed lest squares technique. For the regularization parameter choice the L-curve method is used. The retrieved source amplitudes and positions agree well with the imposed source parameters. The resolution is close to the $\lambda/4$ limit on the uniform as well as on the refined grid. The introduced significant level of random noise in the cross spectrum matrix of the microphone array does not prohibit the good quality reconstruction. On the other hand it causes the appearance of spurious sources on the source map especially in case of the adapted source grid. The level of these spurious sources can be possibly decreased with the careful choice of the grid size distribution function. This possibility has to be investigated when robust adaptation method is searched for.

The solution procedure with the mesh adaptation to the actual source geometry helped to reduce the CPU time of the computation with a factor of approximately 3.7. The reason is identified as the reduction of the model source points in the refined mesh. Roughly linear decrease of the computation time with the amount of source points in the final meshes can be achieved.

The condition number of the model problem is also investigated. It is observed that the condition number does not changed much between the uniform and refined mesh case. This is additionally supports the idea of using an adaptive model source distribution.

With the help of the adaptive model source grid technique the source domain size can be increased. Consequently one of the important source of error, the model error of the generalized inverse beamforming can be decreased. The grid adaptation algorithm therefore helps to extend the possibilities of the beamforming methodology for non-ideal acoustics environments.

Acknowledgments

This work is supported by the VALIANT project coordinated by the VKI.

References

[1] R. P. Dougherty, Noise source imaging by beamforming, in: Society of Automotive Engineers Brazil Noise and Vibration. Conference, Florianopolis SC, 2008.

[2] L. Koop, Beamforming methods in microphone array measurements theory, practice and limitations, in: M. L. Riethmuller, M. R. Lema (Eds.), Experimental Aeroacoustics, von Karman Institute, 2007.

[3] T. Suzuki, L1 generalized inverse beam-forming algorithm resolving coherent/incoherent, distributed and multipole sources, Journal of Sound and Vibration doi:10.1016/j.jsv.2011.05.021.

[4] P. C. Hansen, Rank-Deficient and Discrete Ill-Posed Problems, Society for Industrial and Applied Mathematics, 1998.

[5] P. C. Hansen, The L-Curve and its Use in the Numerical Treatment of Inverse Problems in Computational Inverse Problems in Electrocardiology, Advances in Computational Bioengineering, 2000.

[6] T. Suzuki, Generalized inverse beam-forming algorithm resolving coherent/incoherent, distributed and multipole sources, in: 14th AIAA/CEAS Aeroacoustics Conference (29th AIAA Aeroacoustics Conference), Vancouver, British Columbia Canada, 2008.

[7] P.-O. Persson, G. Strang, A simple mesh generator in matlab, SIAM Review 46 (2) (2004) 329–345.

[8] P. A. Nelson, S. H. Yoon, Estimation of acoustic source strength by inverse methods: Part i, conditioning of the inverse problem, Journal of Sound and Vibration 233 (4) (2000) 639–664. doi:10.1006/jsvi.1999.2837.

Prediction of Free and Scattered Acoustic Fields of Low-Speed Fans: Scattering of Tonal Fan Noise by a Rigid Corner

Korcan Kucukcoskun

École Centrale de Lyon, Laboratoire de Mécanique des Fluides et d'Acoustique, France, korcan.kucukcoskun@vki.ac.be

Supervisor: Christophe Schram

Associate Professor, Environmental and Applied Fluid Dynamics Department, von Karman Institute for Fluid Dynamics, Belgium, christophe.schram@vki.ac.be

University Supervisor: Michel Roger

Professor, Laboratoire de Mécanique des Fluides et d'Acoustique, École Centrale de Lyon, France, michel.roger@ec-lyon.fr.

Abstract

The exact analytical solution for the scattering of tonal fan noise by a rigid corner is addressed. The theory proposed for a monopole is first extended in order to compute the scattered field of a dipole. Combining the extended model with the dipole array approach, the scattered field of tonal fan noise by a corner is computed. Different blade forces and fan orientations are tested. A very good agreement is satisfied for all configurations in comparison with numerical simulations performed with a commercial BEM software.

Keywords: Aeroacoustics, tonal fan noise, scattering by a rigid corner.

1. Introduction

Exact analytical solutions addressing the acoustic free-field radiation from aerodynamic noise sources exist for many aeroacoustic problems. However, due to installation effects and presence of solid surfaces in radiation field, free-field propagation condition may become invalid. Scattering of acoustic waves by obstacles therefore needs being taken into account.

This paper deals with the analytical solution for the scattering of aerodynamic noise by a rigid corner and its application to tonal fan noise. One of the possible application areas is the cooling units of locomotives in parking position. The noise generated by a cooling unit located on the top of a locomotive and its scattered field by the corner of the locomotive-body may result in annoyance for passengers waiting on the platform. Noise generated by a small wind turbine located on the roof of a building and its effect on inhabitants can also be associated as another application area.

For low-frequency problems, numerical techniques such as Finite Element Method (FEM) and Boundary Element Method (BEM) are already in use to compute acoustic scattering by complex geometries [1]. However they are known to be dependent on the mesh resolution, such as the assumption of the requirement of 10 elements per wave length, λ [2; 3]. At higher frequencies, the number of elements required for an accurate prediction increases, hence the numerical solution becomes computationally demanding. Therefore, it is more convenient to use analytical solutions for high frequency problems if possible. For problems including simple geometries such as an infinite plane [4] or a semi-infinite plate [5], exact analytical scattering techniques can be used independent from the mesh resolution. An analytical method was proposed by MacDonald in order to deal with the acoustic scattering by a rigid wedge [6].

2. Scattering by a Rigid Corner

In the proposed analytical method, the scattering problem is treated as a boundary-value problem. A Green's function is derived for the Helmholtz equation with the exact boundary conditions. The rigid-wall boundary condition on the wedge surface and

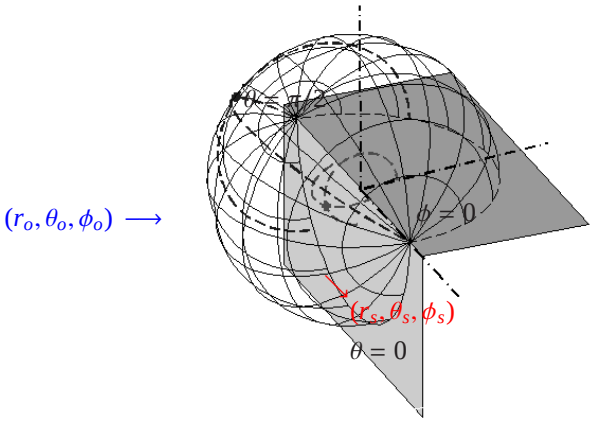

Figure 1: Sketch of the wedge, source-observer positions defined in polar coordinates

Sommerfeld radiation condition at large distances from the source are satisfied in the derivation.

MacDonald derived the Green's function for the Helmholtz equation around a wedge using polar coordinates [6]. The source and observer coordinates are (r_s, θ_s, ϕ_s) and (r_o, θ_o, ϕ_o), respectively shown in Figure 1. In MacDonald's formulation, the source is assumed to be located in the mid-plane of the rigid wedge, hence $\theta_s = \pi/2$.

For any wedge angle $0 < \phi < 2\pi$, the Green's function is defined as [6]

$$G(\mathbf{r}_s, \mathbf{r}_o) = \frac{2\pi}{\phi} \sum_{m=0}^{\infty} \varepsilon \cos(m'\phi_o)\ \cos(m'\phi_s) \sum_{k=0}^{\infty} 2^{m'}(2m' + 4k + 1) e^{(m'+2k+\frac{1}{2})\frac{1}{2}\pi \mathrm{i}} r_o^{-\frac{1}{2}} r_s^{-\frac{1}{2}} J_{m'+2k+\frac{1}{2}}(\kappa r_<) K_{m'+2k+\frac{1}{2}}(\mathrm{i}\kappa r_>) \cos(k\pi) \frac{\Pi(m' + k - 1/2)}{\Pi(k)\Pi(-1/2)} P^{-m'}_{m'+2k}(\cos\theta_o). \quad (1)$$

The parameter ε is 1 for $m = 0$ and 2 for $m > 1$ [7]. $P^{-m'}_{m'+2k}$ stands for the general Legendre function where $m' = m\pi/\phi$. J_υ and K_υ are the Bessel function of the first kind and of order υ and the modified Bessel function of order υ, respectively. Corresponding expressions with $r_>$ and $r_<$ interchange with the definition of the source and observer positions, $r_> = max(r_s, r_o)$ and $r_< = min(r_s, r_o)$. κ is equal to $2\pi/\lambda$.

Mel'nik and Podlipenko later proposed an expression for the scattering by a wedge containing soft walls for arbitrary source locations, as [8]

$$G(\mathbf{r}_s,\mathbf{r}_o) = \frac{\mathrm{i}\kappa}{\phi} \sum_{m=1}^{\infty} \sin(m'\phi_s)\ \sin(m'\phi_o) \sum_{n=0}^{\infty} (2n + 2m' + 1) j_{m'+n}(\kappa r_<) h^{(1)}_{m'+n}(\kappa r_>) \frac{\Gamma(n + 2m' + 1)}{\Gamma(n + 1)} P^{-m'}_{m'+n}(\cos\theta_s) P^{-m'}_{m'+n}(\cos\theta_o) \quad (2)$$

where j_υ and $h^{(1)}_\upsilon$ are the spherical Bessel and Hankel functions of the first kind and of order υ, respectively. The spherical functions are related to the cylindrical Bessel and Hankel functions via,

$$j_{m'+n}(\kappa r_<) = \sqrt{\frac{\pi}{2\kappa r_<}} J_{m'+n+1/2}(\kappa r_<) \quad (3)$$

$$h^{(1)}_{m'+n}(\kappa r_>) = \sqrt{\frac{\pi}{2\kappa r_>}} H^{(1)}_{m'+n+1/2}(\kappa r_>). \quad (4)$$

Combining formulations (1) and (2), the Green's function of a rigid wedge for arbitrary source and observer positions then becomes [14]

$$G(\mathbf{r}_s, \mathbf{r}_o) = \frac{-\pi\mathrm{i}}{4\phi\sqrt{r_s r_o}} \sum_{m=0}^{\infty} \varepsilon \cos(m'\phi_s) \cos(m'\phi_o) \sum_{k=0}^{\infty} (2m' + 4k + 1) \frac{\Gamma(2m' + 2k + 1)}{\Gamma(2k + 1)} P^{-m'}_{m'+2k}(\cos\theta_s) P^{-m'}_{m'+2k}(\cos\theta_o)\ J_{m'+2k+1/2}(\kappa r_<)\ H^{(1)}_{m'+2k+1/2}(\kappa r_>). \quad (5)$$

The trigonometric expansion of the Legendre function $P^{-m'}_{m'+k}(\cos\theta)$ employed in the computations [9] is

$$P^{-m'}_{m'+2k}(\cos\theta) = \frac{2^{1-m'}(\sin\theta)^{-m'}}{\sqrt{\pi}\Gamma(1/2 - m')} \sum_{n=0}^{\infty} \frac{\Gamma(n + 1/2 - m')\Gamma(2k + n + 1)}{\Gamma(n + 1)\Gamma(2k + n + m' + 3/2)} \sin[(2n + 1 + k)\theta]. \quad (6)$$

Formulation (5) is a general solution of acoustic diffraction by a wedge. Replacing the wedge angle ϕ by $3\pi/2$ results the specific case of a rigid corner. Equation (5) then becomes

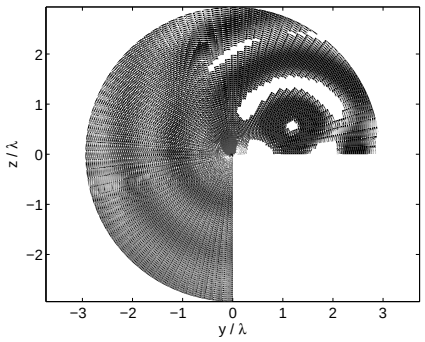

Figure 2: The map of acoustic potential of a point monopole nearby a rigid corner at $f = 10$ kHz. The point monopole is located at $(1.32\lambda, \pi/2, \pi/6.6)$.

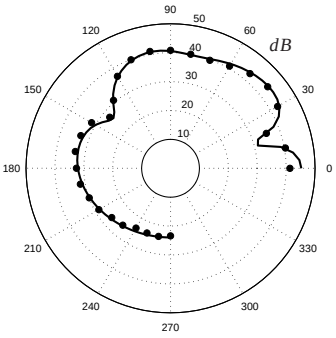

Figure 3: Directivity of a monopole located nearby of a rigid corner; analytical solution (line) and BEM results (symbols) at $f = 1$ kHz. The monopole is located at $(1.32\lambda, \pi/2, \pi/6.6)$ and observer distance is 3λ.

$$G(\mathbf{r}_s, \mathbf{r}_o) = \frac{-\mathrm{i}}{6\sqrt{r_s r_o}} \sum_{m=0}^{\infty} \varepsilon \cos(2m\phi_s/3)\cos(2m\phi_o/3)$$
$$\sum_{k=0}^{\infty} (4m/3 + 4k + 1) \frac{\Gamma(4m/3 + 2k + 1)}{\Gamma(2k+1)} P^{-2m/3}_{2m/3+2k}(\cos\theta_s)$$
$$P^{-2m/3}_{2m/3+2k}(\cos\theta_o)\, J_{2m/3+2k+1/2}(\kappa r_<)\, H^{(1)}_{2m/3+2k+1/2}(\kappa r_>). \tag{7}$$

Equation (7) is the exact solution for the acoustic waves scattered by a rigid corner. It will then be used to predict the scattered acoustic field of sources located in the vicinity of a rigid corner. For simplicity, a point monopole located nearby a corner will be investigated first. The theory will then be extended to a point dipole and finally it will be applied to a source representation of a fan.

2.1. Scattered field of a monopole

A first test is performed putting a point monopole at $(1.32\lambda, \pi/2, \pi/6.6)$ with respect to the origin of a rigid corner at $f = 10$ kHz. Figure 2 shows the map of the acoustic potential of a point monopole in the $\theta = \pi/2$ plane. Illuminated and shadow zones due to the corner can be seen clearly.

Once the Green's function is derived for a particular geometry, the acoustic field can then be computed for harmonic sources. The total acoustic field of a monopole is equal to

$$p(\omega, r) = G(\mathbf{r}_s, \mathbf{r}_o) q(\omega) \tag{8}$$

where $q(\omega)$ is the source strength of the point monopole.

A second test is performed in order to compare the analytical solution with numerical simulations. BEM is known to be able to handle scattered field problems for unbounded domains [3]. However, since at least 10 acoustical elements per wavelength is assumed to be required in an accurate BEM computation, in order to solve the BEM problem in a reasonable time, the tests are performed at lower frequencies. The computations are then performed at $f = 1$ kHz. A harmonic monopole source is located at $(1.32\lambda, \pi/2, \pi/6.6)$. The source strength of the monopole is selected as $q(\omega) = (0.01 + 0.01\mathrm{i})kg/s^2$. In order to minimize effects of the free edges, a corner containing two $7\lambda \times 7\lambda$ flat plates is built. The size of the quadrilateral elements, $l \approx 0.1\lambda$, are satisfying the BEM criteria [2]. The total number of acoustic elements is then equal to 7200.

Figure 3 shows the directivity of the monopole-corner configuration at $f = 1$ kHz computed with the analytical solution (line) and with BEM (symbols). The radius of the field point mesh is selected as 3λ. The sound pressure levels are plotted in dBs. A very good agreement is observed in comparison of the amplitudes with the analytical and numerical solutions. The difference for all the directions is not more than 1 dB. It may be related to the scattering of the waves from the free edges of the acoustic mesh.

It appears that the scattered field of a point monopole by a rigid infinite corner can be computed accurately with the analytical model. Multipole monopoles can be summed up if needed. However, for a point dipole a specific development is more appropriate which is derived in the following section.

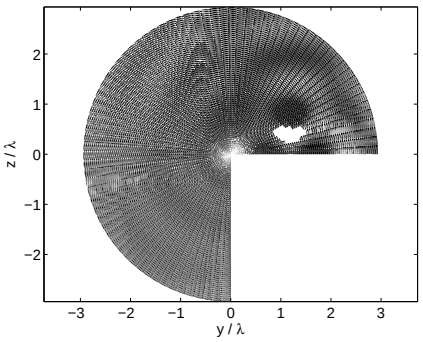

Figure 4: The map of acoustic potential of a point dipole nearby a rigid corner at $f = 10$ kHz. The point dipole is located at $(1.32\lambda, \pi/2, \pi/6.6)$.

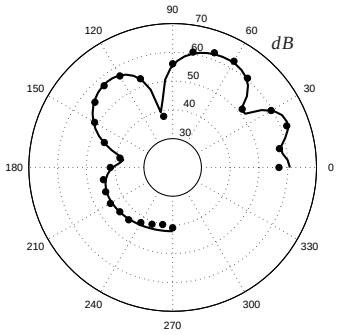

Figure 5: Directivity of a dipole located nearby a rigid corner; analytical solution (line) and BEM results (symbols) at $f = 1$ kHz. The dipole is located at $(1.32\lambda, \pi/2, \pi/6.6)$ perpendicular to $\phi = 0$ plane and observer distance is 3λ.

2.2. *Scattered field of a dipole*

The radiation field of a point dipole is related to the gradient of the Green's function with respect to the source coordinates. The acoustic pressure then becomes

$$p(\omega, r) = \nabla G(\mathbf{r}_s, \mathbf{r}_o) \cdot \mathbf{F}(\omega) \tag{9}$$

where $\mathbf{F}(\omega)$ is the source strength of the point dipole. Detailed derivations of the Green's function of a rigid corner for the dipole source can be found in the related reference [15].

A contour plot in the $\theta = \pi/2$ plane of the acoustic potential of a point dipole located nearby a corner is seen in Figure 4. The dipole is oriented at the same position as the monopole described in the previous section applying perpendicular to the $\phi = 0$ plane. The dipole-like behavior, reflected waves and shadow zone are clearly seen in the figure.

The analytical solution is again compared to the numerical model. A perpendicular dipole to $\phi = 0$ plane is again tested. The strength of the dipole is selected as $\mathbf{F}(\omega) = (0.01 + 0.01\mathrm{i})N$.

Figure 5 shows the directivity of the dipole-corner configurations at $f = 1$ kHz. The line and symbols represent the results obtained with the analytical solution and BEM model, respectively. A good agreement of the analytical and numerical solutions is again observed. The difference between the analytical and numerical results for a dipole is less than 1 dB.

Once validated for a single dipole, the theory is now extended to an equivalent distribution of a tonal fan noise source.

2.3. *Scattered field of tonal fan noise*

Several closed-form solutions addressing the free-field tonal fan noise exist in literature [11; 12; 13]. The exact closed-form analytical solution of free-field tonal fan noise is obtained by introducing the free-field Green's function into the solution of the inhomogeneous wave equation (see the related references [12; 13] for further derivation).

A tonal fan noise formulation taking near-field terms into account was derived by Roger [13]. The acoustic pressure at the nth harmonic of the blade passing frequency (BPF) at the observer is given as [13]

$$p'_{nB} = \frac{\mathrm{i}k_{nB}\Omega}{4\pi} \sum_{p=-\infty}^{\infty} \Big(-G^{(2)}_{nB-p} F^D_p x \sin\theta + G^{(3)}_{nB-p} F^R_p x \sin\theta + G^{(1)} (F^T_p (\zeta_3 - x\cos\theta) - F^{(R)}_p r') \Big) \tag{10}$$

for B equally spaced identical blades. F_R, F_D and F_T are the radial (R), drag (D) and thrust (T) forces acting

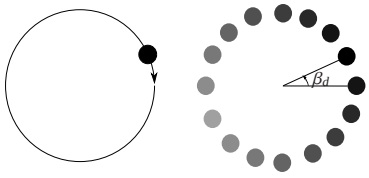

Figure 6: Equivalent fan source modeling strategies; (left) single rotating dipole, (right) continuous array of phase shifted dipoles.

on the blade, respectively. The applying forces are periodic with angular frequency Ω. $k_{nB} = nB\Omega/c_0$ is the wave number at the nBth harmonic. The geometrical parameters are shown in Figure 7.

Due to its periodicity, the sound field can be expanded as a Fourier series. G_m^N is the mth Fourier component of the auxiliary functions G_N (N=1,2,3). The auxiliary functions G_1, G_2 and G_3 are defined as

$$\begin{aligned} G_1(t) &= \frac{\mathrm{e}^{-\mathrm{i}k|\mathbf{R}|}}{|\mathbf{R}|^2}\left(1+\frac{1}{\mathrm{i}k|\mathbf{R}|}\right) \\ G_2(t) &= \sin(\Omega t+\varphi'-\varphi)\, G_1(t) \\ G_3(t) &= \cos(\Omega t+\varphi'-\varphi)\, G_1(t) \end{aligned} \tag{11}$$

with $k = \Omega/c_0$.

A common denominator of closed-form methods mentioned above is the consideration of a rotating dipole as shown in Figure 6 (left). However, introducing the gradient of the Green's function of a corner instead of the free-field one, it is not possible anymore to obtain an exact analytical solution for the scattered acoustic field of a fan operating next to a rigid corner. Still, an equivalent fan source can be obtained employing circular distribution of phase shifted dipoles as shown in Figure 6 (right). The phase difference of the dipoles is linked to the azimuthal position of the dipole, β_d. Using the dipole array, the equivalent free-field acoustic pressure of a B bladed fan at the nth harmonic of BPF then reads

$$p_{nB} = \frac{B}{N_d}\sum_{N_d} p_{nB,d} \tag{12}$$

where N_d is the number of dipoles in the azimuthal array.

Introducing Equation (9) into Equation (12), the total acoustic pressure field of the fan scattered by a rigid corner reads

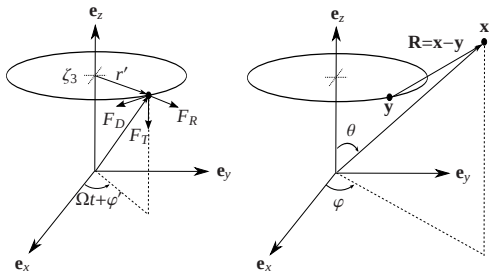

Figure 7: Source and listener coordinates

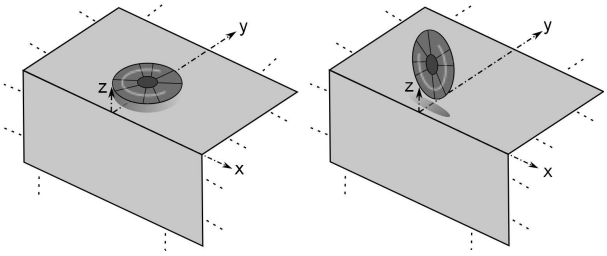

Figure 8: Sketches of fan-corner configurations; fans operating parallel to the *xy*-plane (left) and parallel to the *xz*-plane (right).

$$p_{nB}(\omega, r) = \frac{B}{N_d}\sum_{N_d} \nabla G(\mathbf{r}_s(\beta_d), \mathbf{r}_o)\cdot\mathbf{F}(\omega, \beta_d). \tag{13}$$

Since the Green's function of a rigid corner is extended for arbitrary positions of the source with respect to the wedge origin, it can now be used for any point dipole of the circular array. Equation (13) is a general solution for a fan operating out of a rigid corner. It can therefore be used for different fan-corner applications. The problem is first simplified to a fan operating parallel to the *xy*-plane. Figure 8 (left) shows the sketch of the simplified problem. A possible application area is the cooling units of locomotives in parking position as mentioned above. Only the scattering from the corner of the locomotive is addressed, neglecting other installation effects. Only one side of the locomotive is considered for the illustration.

The model fan employed has 10 equally spaced identical blades. The fan is rotating with 3000rpm making the blade loading frequency equal to $N/60$ = 50 Hz. Artificial blade forces are considered for the test case [15]. The blades are assumed acoustically compact and reduced to point dipoles. The radius of the fan source is selected as 0.15λ for the first BPF, f = 500 Hz. The center of the fan is located at $(0.6\lambda, \pi/2, \pi/12.8)$. The blade Mach number is then around 0.1, satisfying the low Mach number condition. The observers are located in the *yz*-plane with a radius of 1.5λ with respect to the origin of the corner.

Two low-speed axial fans are tested for comparison. The first test includes only the thrust force component, whereas the second one contains both drag and thrust force components as in a more realistic application. The radial forces are neglected for both configurations.

The problem is also dealt with the numerical approach combining Equation (10) with the BEM formulation. The same acoustic mesh and field points

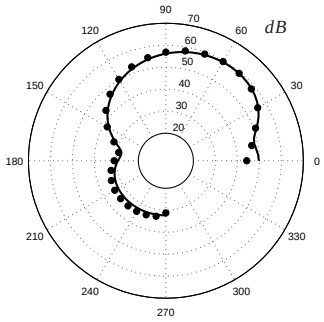

Figure 9: Directivity of a fan operating parallel to the *xy*-plane by a rigid corner; analytical solution (line) and BEM results (symbols) for test1. The fan center is located at $(0.6\lambda, \pi/2, \pi/12.8)$. Fan radius is 0.15λ. Observers are in the *yz*-plane at a radius of 1.5λ, at the first BPF, f = 500 Hz.

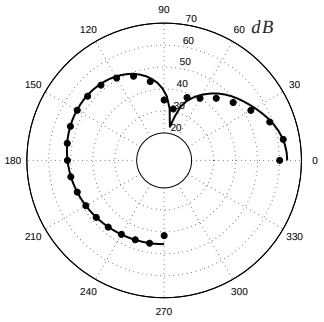

Figure 11: Directivity of a fan operating parallel to the *xz*-plane by a rigid corner; analytical solution (line) and BEM results (symbols) for test1. The fan center is located at $(0.66\lambda, \pi/2, \pi/6.6)$. Fan radius is 0.15λ. Observers are in the *yz*-plane at a radius of 1.5λ, at the first BPF, f = 500 Hz.

are used as in the dipole test case for the BEM model. The BEM problem is solved with LMS software Virtual Lab [3].

The scattered acoustic field directivities at the first BPF are seen for the first and the second tests in Figures 9 and 10, respectively. Line and symbols represent the analytical and numerical results, respectively. A good agreement is found between analytical and numerical solutions for both test fans. It is also seen that adding the drag component results higher acoustic pressure levels in the shadow zone.

A second fan orientation is selected where the rotation axis is perpendicular to the *xy*-plane, such as the example of small axial wind turbines located on the roof of buildings. A sketch of the problem is shown in Figure 8 (right). The problem can be dealt with the model described above only considering a new orientation of the fan. Same tests, one with only thrust and one with trust and drag forces, are selected for comparison. The rotation center is at $(0.66\lambda, \pi/2, \pi/6.6)$ and the fan is operating parallel to the *xz*-plane.

Figures 11 and 12 show the scattered-field directivities of the first and second tests, respectively. The line and symbols represent the analytical and BEM methods, respectively. It is seen that adding drag forces affects the acoustic field around the rotation plane. Finally, implementation of the proposed analytical model is validated against numerical simula-

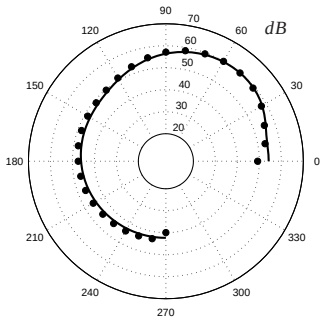

Figure 10: Directivity of a fan operating parallel to the *xy*-plane by a rigid corner; analytical solution (line) and BEM results (symbols) for test2. The fan center is located at $(0.6\lambda, \pi/2, \pi/12.8)$. Fan radius is 0.15λ. Observers are in the *yz*-plane at a radius of 1.5λ, at the first BPF, f = 500 Hz.

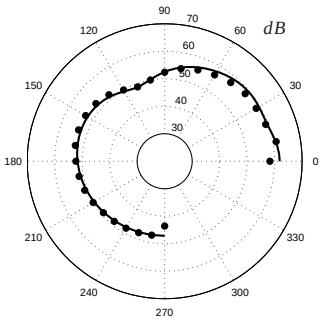

Figure 12: Directivity of a fan operating parallel to the *xz*-plane by a rigid corner; analytical solution (line) and BEM results (symbols) for test2. The fan center is located at $(0.66\lambda, \pi/2, \pi/6.6)$. Fan radius is 0.15λ. Observers are in the *yz*-plane at a radius of 1.5λ, at the first BPF, f = 500 Hz.

tions in all tested configurations.

As a result, extending the Green's function for arbitrary source positions and combining its gradient with the dipole array model, the scattered field of a low-speed axial fan by a rigid corner is computed accurately. For high frequency problems, where the numerical methods are demanding, the analytical solution can be useful irrespective of any mesh resolution issue.

3. Conclusion

The scattering of low-speed axial fan noise by a rigid corner is investigated numerically and analytically. It is seen that the scattered-field can be computed accurately with both numerical and analytical techniques. The numerical approach can be applied to more complex geometries for bounded and unbounded domains. On the other hand, for relatively simple configurations and where the numerical methods are computationally demanding, analytical solution can be useful independent from mesh resolution at any frequencies.

Acknowledgements

This work is supported by the FP7 Collaboration Project ECOQUEST (grant agreement no 233541).

References

[1] Desmet, W., Sas, P., "Introduction to numerical acoustics", In Lecture Notes of the ISAAC21 Course. K.U.Leuven, Leuven, Belgium, Sept. 23-24, 2010.

[2] Desmet, W., "Boundary element modeling for acoustics", In Lecture Notes of the ISAAC21 Course. K.U.Leuven, Leuven, Belgium, Sept. 23-24, 2010.

[3] Virtual Lab Rev 9: user manual, LMS International, 2009.

[4] Powell, A., "Aerodynamic noise and the plane boundary", J. Acoust. Soc. Am. 32 (8), 982:990, 1960.

[5] Ffowcs Williams, J., E., Hall, L., H., "Aerodynamic sound generation by turbulent flow in the vicinity of a scattering half plane", J. Fluid Mech. 40 (4), 657:670, 1970.

[6] Macdonald, H., M., "A class of diffraction problems", Proc. London Math. Soc. 14, 410:427, 1915.

[7] Pierce, A., "Acoustics: An introduction to its physical principles and applications", Ac. Soc. of America, 1989.

[8] Mel'nik, P., Podlipenko, Yu., K., "On Green's function for the Helmholtz equation in a wedge", Ukranian Mathematical Jou. 45 (9), 1471:1474, 1993.

[9] Abramowitz, M., Stegun, I., "Handbook of Mathematical Functions", Dover Publications, 1972.

[10] Crighton, D., G., Leppington, F., G., "On the scattering of aerodynamic noise", J. Fluid Mech. 46 (3), 577:597, 1971.

[11] Ffowcs Williams, J.E., Hawkins, D.L. "Sound generated by turbulence in arbitrary motion", Royal Society of London 264 (1151), 321:342, 1969.

[12] Goldstein, M.E. "Aeroacoustics", McGraw-Hill International Book Company, 1976.

[13] Roger, M., "Noise from moving surfaces", In advances in aeroacoustics and applications, VKI Lecture Series 2004-05, Rhode-St-Gense, 2004.

[14] Kucukcoskun, K., Roger, M., "On the scattering of aerodynamic noise by a rigid corner", AIAA paper, Accepted to the 18th AIAA/CEAS Aeroacoustics Conference, 2012.

[15] Kucukcoskun, K., "Prediction of free and scattered acoustic fields of low-speed fans", PhD Dissertation (in review), Ecole Centrale de Lyon, 2012.

Unsteady Panel Code for Airfoil Turbulence Interaction Computation

Leandro Dantas de Santana

Aeronautics and Aerospace Department, von Karman Institute for Fluid Dynamics, Belgium, leandro.santana@vki.ac.be

Supervisor: Christophe Schram

Associate Professor, Aeronautics and Aerospace Department, von Karman Institute for Fluid Dynamics, Belgium, christophe.schram@vki.ac.be

University Supervisor: Wim Desmet

Full Professor, KULeuven - Department of Mechanical Engineering, Belgium, wim.desmet@mech.kuleuven.be

Abstract

This paper describes the theoretical formulation of an unsteady panel code for the prediction of turbulence-airfoil interaction noise, valid for incompressible turbulent flows. This panel code formulation adopts the vorticity as elementary distributed singularity, in contrast with other approaches that use distributed sources and a constant intensity vortex sheet. Preliminary calculations present the quasi-steady and unsteady capabilities of this code to predict the response of a thin airfoil subjected to pitch oscillations and incoming vortical disturbances. The aerodynamic responses are compared with results obtained with the unsteady thin airfoil theory. The panel code is shown to predict with good accuracy unsteady response of an incompressible sinusoidal gust for reduced frequencies up to 8. This panel method advantages, from the traditional methods, for describing complex geometries with reasonable accuracy but very low computational cost, being attractive for conceptual design applications.

Keywords: unsteady panel code, incompressible turbulent flow, turbulence interaction noise, airfoil noise

1. Introduction

In turbofan engines and contra-rotating open rotors (CROR), airfoil-turbulence interaction typically considered as the main noise source generation mechanism. For an airfoil free of flow separation, the noise sources are mainly localized around the leading and trailing edges. The first is the main noise source when the incoming flow turbulence level exceeds a certain level. For lower levels of incoming turbulence, the scattering of self-generated boundary layer turbulence at the trailing edge dominates. The present work focuses on the incoming turbulence problem, relevant to the interaction between the wakes shed by the upstream rotor of a CROR and convected across the downstream rotor plane.

The problem has been already addressed by many authors since the seventies, and significant contributions to the field consist of semi-analytical approaches, mostly relying on thin-airfoil theory, based on a frequency-wavenumber representation of the incoming turbulence.[1; 2; 3; 4; 5] With the recent development of computational power, Large Eddy Simulation (LES) and Direct Numerical Simulation (DNS) techniques have been applied to obtain high accuracy flow descriptions [6; 7; 8] providing valuable input for prediction schemes based on the aeroacoustic analogy. These techniques have been proven to be powerful for simplified geometries, giving deep insight into complex physical phenomena. However, they still suffer from limited industrial applicability due to the large CPU effort involved in the flow calculation.

Discrete vortex boundary element methods are an interesting low-cost alternative to these expensive approaches, while offering more geometrical fidelity than the thin airfoil theories that linearize the airfoil shape as a flat plate with zero thickness, camber, and small angle of attack. The present work follows this alternative approach. Previous works in

this manner include Gennaretti et. al [9; 10] who proposed a unified boundary methodology for helicopter rotor aerodynamics and aeroacoustic predictions. Grace [11] discussed the respective merits of using time domain boundary element methods or harmonic gust analysis. Recently Glegg and Devenport [12] developed an unsteady vortex-based panel method and applied Amiet's theory to compute the far-field noise of turbulence-airfoil interaction. Their results are in good agreement with the flat plate analytical solution, nevertheless further comparison with experiments or high accuracy simulations of airfoils with realistic thickness, camber and angle of attack are still needed. Recently Zheng et al. [13] also used a discrete vortex method to predict the noise of a 3-elements high lift device. His panel method formulation, closer to the classical methods described by Cebeci et al. [14], shows a remarkable aerodynamic agreement with DNS simulations for the same geometry, with an angle of attack up to 8 degrees.

To reach its objective the present paper follows the Glegg and Devenport [12] unsteady vortex based panel method to predict the airfoil response to a turbulent inflow. In this paper, the aerodynamic unsteady response of this panel code is compared with analytical solutions obtained from the thin airfoil theory.

2. Panel method

Cebeci et al. [14] present a conventional two-dimensional panel method for the unsteady loading computation. This methodology is based on the Laplace's solution of a potential flow generated by the superposition of sources and vortex singularities, where the first is localized on each panel application point and the second is considered as a constant intensity sheet, placed along the airfoil chord. The system of equations is closed when the Kutta condition is applied to the trailing edge. The wake vortex sheet intensity is determined by Biot-Savart integration applied to the control surface in two dimensions. Conservation of the total circulation carried by the airfoil and wake is prescribed according to first principles.

While Cebeci's formulation has been extensively used in aeroelastic and wing morphing problems, it hasn't been as successful for aeroacoustic prediction. A more fruitful boundary element method for aeroacoustics, which applies the essence of the ideas described by Cebeci but with a different singularity distribution, has been presented by Glegg et. al [12]. In this approach the panel method adopts point vortices, instead of sources, as the base singularity. This singularity is distributed along each panel. This approach has been shown effective for predicting airfoil-turbulence interaction noise for reduced frequencies up to 10.

To describe the panel method used in this paper, the Howe [15] functional airfoil surface definition is adopted. In this formulation, for a given function f the region where $f(\boldsymbol{x}) = 0$ represents the body contour, $f(\boldsymbol{x}) < 0$ defines the airfoil interior region and $f(\boldsymbol{x}) > 0$ represents the exterior region. Using the Heaviside function $H(f(\boldsymbol{x}))$ it is possible to specify the non-penetration boundary condition to the velocity vector $\boldsymbol{v}$. Based on this definition, Howe proposes that the incompressible flow over a nonpermeable surface can be expressed as:

$$\begin{aligned}\nabla \times \nabla \times (H(f)\boldsymbol{v}) &= -\nabla^2 (H(f)\boldsymbol{v}) = \\ &= \nabla \times (H(f)\boldsymbol{\omega} + \boldsymbol{n} \times \boldsymbol{v}|\nabla f|\delta(f))\end{aligned} \tag{1}$$

with the following solution:

$$\begin{aligned}H(f)\boldsymbol{v}(\boldsymbol{x},t) = \nabla \times \int_D \frac{\boldsymbol{\omega}(\boldsymbol{y},t)}{4\pi|\boldsymbol{x}-\boldsymbol{y}|^3} dV(\boldsymbol{y}) + \\ + \nabla \times \int_S \frac{\boldsymbol{n} \times \boldsymbol{v}(\boldsymbol{y},t)}{4\pi|\boldsymbol{x}-\boldsymbol{y}|^3} dS(\boldsymbol{y})\end{aligned} \tag{2}$$

where D is the volume exterior to the airfoil surface S. The first term of Equation (2) represents the velocity induced by the wake vorticity computed by Biot-Savart integration. The second term of Equation (2) is the contribution of the bound vorticity to the airfoil surface velocity. Considering a right-handed coordinate system, where the indices 1, 2 and 3 represent the directions $\hat{\imath}$, $\hat{\jmath}$ and $\hat{k}$, respectively, the induced velocity by a vortex of intensity $\gamma(\boldsymbol{y})$ is represented as:

$$\boldsymbol{n} \times \boldsymbol{v}(\boldsymbol{y},t) = -\gamma(\boldsymbol{y})\hat{k} \tag{3}$$

where $\boldsymbol{n}$ is the unit vector normal to the airfoil surface. Substituting Equation (3) in Equation (2) leads to:

$$\begin{aligned}H(f)\boldsymbol{v}(\boldsymbol{x},t) = \int_D \frac{\boldsymbol{\omega}(\boldsymbol{y},t) \times (\boldsymbol{x}-\boldsymbol{y})}{4\pi|\boldsymbol{x}-\boldsymbol{y}|^3} dV(\boldsymbol{y}) + \\ - \int_S \frac{\gamma(\boldsymbol{y})\hat{k} \times (\boldsymbol{x}-\boldsymbol{y})}{4\pi|\boldsymbol{x}-\boldsymbol{y}|^3} dS(\boldsymbol{y})\end{aligned} \tag{4}$$

Since we consider a two-dimensional problem, Equation (4) can be simplified to:

$$\begin{aligned}H(f)\boldsymbol{v}(\boldsymbol{x},t) = \int_C \int_{-\infty}^{\infty} \frac{\boldsymbol{\omega}(\boldsymbol{y},t) \times (\boldsymbol{x}-\boldsymbol{y})}{4\pi|\boldsymbol{x}-\boldsymbol{y}|^3} dy_3 dy_1 dy_2 + \\ - \oint_A \int_{-\infty}^{\infty} \frac{\gamma(\boldsymbol{y})\hat{k} \times (\boldsymbol{x}-\boldsymbol{y})}{4\pi|\boldsymbol{x}-\boldsymbol{y}|^3} dy_3 dS(\boldsymbol{y})\end{aligned} \tag{5}$$

where C represents the contour of the plane which contains the airfoil and its wake vorticity. Integrating in y_3 we obtain:

$$H(f)\boldsymbol{v}(\boldsymbol{x},t) = -\int_C \frac{\boldsymbol{\omega}(\boldsymbol{y},t)\times(\boldsymbol{x}-\boldsymbol{y})}{2\pi|\boldsymbol{x}-\boldsymbol{y}|^2}dy_1dy_2 + \\ + \oint_A \frac{\gamma(\boldsymbol{y})\hat{k}\times(\boldsymbol{x}-\boldsymbol{y})}{2\pi|\boldsymbol{x}-\boldsymbol{y}|^2}dS(\boldsymbol{y}). \quad (6)$$

Equation (6) can be solved numerically for the bound vortex sheet strength $\gamma(\boldsymbol{y})$ with the imposition of the non-penetration boundary condition on the airfoil surface control and the Kutta condition at the airfoil trailing edge. The time domain is discretized in interval Δt and the wake vorticity is represented by a sum of elementary vorticity elements as:

$$\boldsymbol{\omega}(\boldsymbol{y},t) = \sum_m \Gamma_m\hat{k}\delta(y_1 - y_1^{(m)}(t))\delta(y_2 - y_2^{(m)}(t)), \quad (7)$$

where Γ_m represents each discretized vortex circulation and $y^{(m)}$ its position on the coordinate reference system. Equation (6) then simplifies into:

$$H(f)\boldsymbol{v}(\boldsymbol{x},t) = -\sum_m \frac{\Gamma\hat{k}\times(\boldsymbol{x}-\boldsymbol{y}^{(n)}(t))}{2\pi|\boldsymbol{x}-\boldsymbol{y}^{(m)}(t)|^2} + \\ + \oint_A \frac{\gamma(\boldsymbol{y}\hat{k}\times(\boldsymbol{x}-\boldsymbol{y}))}{2\pi|\boldsymbol{x}-\boldsymbol{y}|^2}dS(\boldsymbol{y}) \quad (8)$$

which can be numerically solved by a time-marching routine and applying the Biot-Savart law.

Through Bernoulli equation, the instantaneous lift per unit span is determined at each time step:

$$L = -\oint_A p dx_1 = \frac{1}{2}\rho\oint_C |\boldsymbol{v}|^2 dx_1 + \rho\oint_A \frac{\partial\phi}{\partial t}dx_1 \quad (9)$$

with ϕ defined as the velocity potential. The lift can be calculated from the vortex sheet strength as:

$$L = \frac{1}{2}\rho\oint_C \gamma^2 dx_1 + \rho\frac{\partial}{\partial t}\oint_A\int_0^s \gamma(s')ds'dx_1 \quad (10)$$

with all integrals performed along the airfoil blade contour.

3. Panel code validation

3.1. Steady lift

The following step is the unsteady panel code validation considering its static response verification. In order to validate its inviscid steady solution the developed code is verified against the XFOIL solution. The NACA 0012 pressure distribution is compared against the reference solution in Figure 1, along the airfoil chord, for angles of attack of 0°, 5° and 10°.

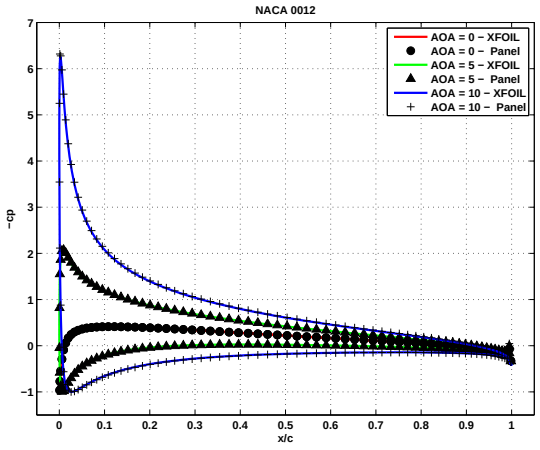

Figure 1: Steady cp comparison with XFOIL for the airfoils NACA 0001, NACA 0005, NACA 0012 and NACA 0024.

3.2. Unsteady response - The Wagner Function

Once the steady solution is verified, the next step is to compare the unsteady panel code response with a case with known analytical solution. A first verification case is the Wagner function. This solution is based on the linearized airfoil theory, valid for very thick airfoils subjected to small angles of attack. This function expresses the time domain airfoil lift, when subjected to an impulsive angle of attack variation. The impulsive change of the angle of attack generates a strong starting vortex, which by turns, influences the airfoil velocity. Immediately after the angle of attack impulse, the airfoil lift is considered as half of the steady lift. As the starting vortex is convected with the flow speed, its influence over the airfoil is reduced and, after enough time, its influence completely disappears and the flow becomes steady.

An approximation to the Wagner function is given by the equation:

$$\Psi(t) = 1 - \Phi_1 e^{-\epsilon_1 U_\infty t/b} - \Phi_2 e^{-\epsilon_2 U_\infty t/b} \quad (11)$$

where $\Phi_1 = 0.165$, $\Phi_2 = 0.335$, $\epsilon_1 = 0.0455$ and $\epsilon_2 = 0.3$, so that and the time domain lift coefficient is given by:

$$cl(t) = 2\pi\alpha\Psi(t) \quad (12)$$

and the lift force time variation becomes:

$$l(t) = \rho\pi U^2 c\alpha\Psi(t) = \rho\pi U c w\Psi(t) \quad (13)$$

where $w = U\alpha$ is the downwash velocity.

Figure 2 presents a comparison of the results obtained by the unsteady panel code and the airfoils NACA 0001, NACA 0005, NACA 0012 and NACA 0024. Here the airfoil NACA 0001 is considered as an airfoil which satisfies the thin airfoil theory due to its reduced thickness.

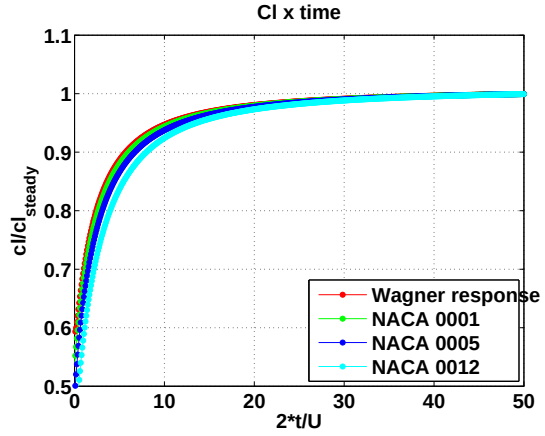

Figure 2: Airfoil lift response to an impulsive variation on angle of attack.

3.3. Unsteady response - The Sears Function

The Wagner function is an interesting first assessment of the unsteady panel code capabilities to predict the time domain unsteady lift, but, impulsive increases in angle of attack are not very common and generally speaking the the flow ingested by a lifting surface is not homogeneous, suffering variations of velocity module and angle of attack. In principal, these inhomogeneities can be decomposed by a series of trigonometric functions, which in turn can be representative as a sum of sinusoidal form gusts. A direct consequence of considering the airfoil impacting flow as an sum of sinusoidal gusts is that its time domain lift variation $F(t)$ can be directly represented in the frequency domain as $\tilde{F}(\omega)$.

In the Sears theory the flow inhomogeneities are considered to travel frozen along the airfoil chord, unaffected by its pressure field, which means that their decaying time is large, in comparison with the characteristic traveling time along the airfoil chord. Considering that the transverse disturbances are mostly responsible for the unsteady loads and considering that linearized airfoil theory is valid (the thickness, camber and angle of attack small) it is possible to affirm that the transverse gust component is predominant over the longitudinal one.

If steady inhomogeneous flow is assumed in a frame of reference moving with the flow, by means of a Fourier analysis of this flow, it can be decomposed into a series of transverse sinusoidal gusts, in the sense of unsteady aerodynamics, which can be characterized by the chord-wise wavenumber k_1 and its convection speed $U\infty$ as $\omega = k_1 U_\infty$. At a given value of ω or k_1 the Fourier coefficient $\tilde{F}(k_1)$ of the total unsteady lift force is determined by the Sears theory, in terms of transverse fluctuation amplitude $\tilde{w}(k_1)$. The connection between the lift and the upcoming gust is represented on Equation 14:

$$\tilde{F}(k_1) = \pi\rho c U\infty \tilde{w}(k_1)\bar{T} \tag{14}$$

where $\bar{T}$ is an additional aerodynamic transfer function.

In this way the local instantaneous lift fluctuation, per unit span, is given by:

$$l(k_1, y_1, t) = 2\rho_0 U_0 \tilde{w}(k_1) \sqrt{\frac{1-y_1^*}{1+y_1^*}} S^*(k_1^*) e^{-i\omega t} \tag{15}$$

where $y_1^* = 2y_1/c$ is the non-dimensional chord-wise coordinate, with reference to the mid chord, and $k_1^* = k_1 c/2$ is the non-dimensional aerodynamic wave number of the incident fluctuation, in the chord-wise direction. The theory applies to a given wavenumber and requires a Fourier analysis of the incident fluctuations. $S(k_1^*)$ is the known Sears function which is expressed in terms of Bessel functions as:

$$S(k_1^*) = \frac{2}{\pi k_1^*}\left([J_0(k_1^*) - Y_1(k_1^*)[- i\,[J_1(k_1^*) + Y_0(k_1^*)[\right)^{-1} \tag{16}$$

For the comparison of the developed code against the Sears function the airfoil NACA 0001 is considered as the flat plate, where the linearized airfoil theory is applicable. To assess the capabilities of the present code to compute the unsteady response of thicker airfoils to a sinusoidal type gust the NACA 0005, NACA 0012 and NACA 0024 are considered as well. The Figure 3 shows the panel's code obtained response compared with the analytical Sears function solution.

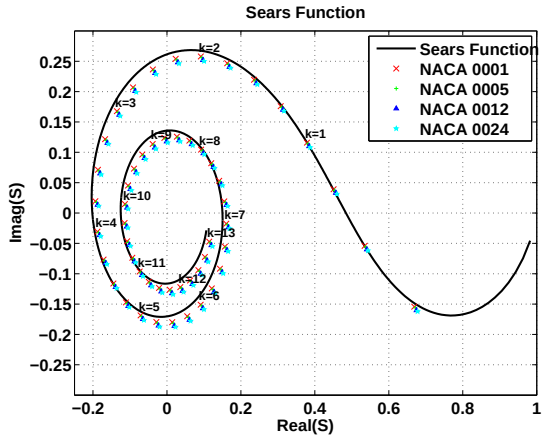

Figure 3: Airfoil lift response to a sinusoidal form impact gust.

4. Conclusions

This paper describes the aerodynamic part of validation of an unsteady panel code to be used for turbulence-airfoil interaction noise. This code is valid for incompressible flows and it is able to describe sinusoidal gusts with reduced frequency up to 8. The steady solution of this code perfectly matches with the results given by traditional panel codes. With regard to the unsteady solutions, for the case of an impulsive angle of attack variation, this code gives an overshoot of the lift for the initial time steps mainly, due to the intensity of the starting vortex, which influence is reduced as it is convected with the flow speed, and consequently the solution smoothly converges to the stationary one. The second unsteady testing case, where an sinusoidal gust impinges the airfoil surface it is seen that the thickness effects diverges the panel code solution from the analytical one. Based on this two unsteady analysis, it can be concluded that this unsteady panel code is suitable for airfoil surface forces prediction, which information is required for the turbulence-airfoil interaction noise prediction. Future works intend to present acoustic comparison against analytical solution cases, high precision simulations and experiments. The present results encourage further studies, because of the presently developed panel code presents very low computational cost when compared to traditional aeroacoustic codes, but shows potential to predict the airfoil with the reasonable precision necessary in conceptual design engineering applications.

5. Acknowledgments

Leandro D. Santana acknowledges the Brazilian Coordination for Improvement of Higher Education Personnel - CAPES - process number BEX-0520-10-1. The support of the European Commission, provided under the FP7 DINNO-CROR project (Grant Agreement no 255878), is gratefully acknowledged as well.

References

[1] R. Amiet, Acoustic radiation from an airfoil in a turbulent stream, Journal of Sound and Vibration 41 (4) (1975) 407 – 420. doi:10.1016/S0022-460X(75)80105-2.

[2] H. M. Atassi, The sears problem for a lifting airfoil revisited - new results, Journal of Fluid Mechanics 141 (1984) 109–122. doi:10.1017/S0022112084000768.

[3] H. M. Atassi, J. Grzedzinski, Unsteady disturbances of streaming motions around bodies, Journal of Fluid Mechanics 209 (1989) 385–403.

[4] M. Howe, Correlation of lift and thickness noise sources in vortex-airfoil interaction, Journal of Sound and Vibration 137 (1) (1990) 1 – 7. doi:10.1016/0022-460X(90)90713-A.

[5] M. R. Myers, E. J. Kerschen, Influence of incidence angle on sound generation by airfoils interacting with high-frequency gusts, Journal of Fluid Mechanics 292 (1995) 271–304. doi:10.1017/S0022112095001522.

[6] H. J. Kim, S. Lee, N. Fujisawa, Computation of unsteady flow and aerodynamic noise of naca0018 airfoil using large-eddy simulation, International Journal of Heat and Fluid Flow 27 (2006) 229–242.

[7] S. Moreau, J. Christophe, M. Roger, Les of the trailing-edge flow and noise of a naca0012 airfoil near stall, in: Center for Turbulence Research Proceedings of the Summer Program 2008, 2008.

[8] R. Sandberg, L. Jones, Direct numerical simulations of airfoil self-noise, Procedia Engineering 6 (2010) 274 – 282. doi:10.1016/j.proeng.2010.09.029.

[9] M. Gennaretti, L. Luceri, L. Morino, A unified boundary integral methodology for aerodynamics and aeroacoustics of rotors, Journal of Sound and Vibration 200 (4) (1997) 467 – 489. doi:10.1006/jsvi.1996.0713.

[10] M. Gennaretti, G. Bernardini, Novel boundary integral formulation for blade vortex interaction aerodynamics of helicopter rotors, AIAA Journal 45 (6) (2007) 1169–1176.

[11] S. M. Grace, Unsteady blade response: The bvi model vs. the gust model, in: 7th AIAA/CEAS Aeroacoustics Conference, 2001.

[12] S. A. Glegg, W. J. Devenport, Panel methods for airfoils in turbulent flow, Journal of Sound and Vibration 329 (18) (2010) 3709 – 3720. doi:10.1016/j.jsv.2010.03.007.

[13] Z. Zheng, B. Tan, Y. Xu, Near-field fluctuations and far-field noise of a three-element airfoil system by a discrete vortex method, Applied Mathematics and Computation 216 (4) (2010) 1072 – 1086. doi:DOI: 10.1016/j.amc.2010.01.129.

[14] T. Cebeci, M. Platzer, H. Chen, K.-C. Chang, J. P. Shao, Analysis of Low-Speed Unsteady Airfoil Flows, Horizons Publishing Inc., 2005.

[15] M. S. Howe, Acoustics of Fluid-Structure Interactions, Cambridge University Press, 1998.

PLASMA FLOW

Investigation of High Enthalpy Plasma Flow

Damien Le Quang

Aeronautics and Aerospace Department, von Karman Institute for Fluid Dynamics, Belgium, lequang@vki.ac.be

Supervisor: Olivier Chazot

Associate Professor, Head, Aeronautics and Aerospace Department, von Karman Institute for Fluid Dynamics, Belgium, chazot@vki.ac.be

Co-Supervisor: Yacine Babou

Research Engineer, Aeronautics and Aerospace Department, von Karman Institute for Fluid Dynamics, Belgium, babou@vki.ac.be

University Supervisor: Pascal André

Professor, Electric arc and thermal plasmas, France, Pascal.ANDRE@univ-bpclermont.fr

Abstract

A preliminary study of a supersonic air plasma jet produced in the VKI Plasmatron facility is presented. Plasma flow regimes corresponding to underexpanded and highly underexpanded situations are investigated by means of high speed camera imaging. Plasma characterization is performed using Optical Emission Spectroscopy (OES) technique. Several diagnostics allowing to evidence possible departure from thermodynamic equilibrium are presented. OES is performed on both molecular and atomic radiative contribution at the exit of the sonic throat of the convergent nozzle in the first expansion zone. Additionally to the investigation on supersonic air plasma jet, atmospheric pressure plasma jet produced in the Microwave Plasma Torch (MPT) facility is investigated. Using forwarded and reflected microwave power monitoring, electrical characterization of the torch is performed. Simultaneously, comprehensive characterization of the flow by means of high speed imaging evidences the effect of the oscillation of the delivered power on the plasma jet unsteadiness. Basic OES is performed to obtain air, N_2 and CO_2 typical radiative signature.

Keywords: Plasma, Optical Emission Spectroscopy

1. Introduction

During hypersonic atmospheric entries, the radiative heating experienced by a vehicle is a major issue for accurate prediction of thermal heat flux. Computational tools development requires experimental data to assess the the reliability of models. In particular, non equilibrium kinetic models need to be assessed in order to replicate the radiative contribution of the excited gas in the shock layer where collisional and radiative processes lead to thermodynamic non equilibrium situations. Due to the relatively large cost of missions and the difficulty of performing accurate measurements in flight, plasma source ground test facilities have been developed. The most common devices allowing electrodeless operations are the RF inductively coupled and microwave plasma sources where the discharge is ignited and sustained by high-frequency electromagnetic fields. In this study, experimental studies were carried out using the Plasmatron Inductively Coupled Plasma (ICP) and Microwave Plasma Torch (MPT) VKI facilities. Concerning the Plasmatron facility, the study is focused on the interpretation of spectroscopic measurements performed in the first expansion zone of a supersonic underexpanded air plasma jet. A sonic throat has been installed on VKI Plasmatron facility to obtain a strong expansion. In the literature, the use of supersonic plasma jets to investigate non equilibrium processes has been widely reported but most investigations deal with mono-atomic gases (Sember & al.[1], Selezneva & al.[2] and Sanden & al. [3]). Robin

& al.[4] have investigated a supersonic nitrogen arc plasma jet to examine the kinetic scheme of ionic recombination. Various technologies are used to obtain supersonic plasma jets. Yano & al. [5] have developed a facility to generate a supersonic high pressure glow discharge. High speed plasma flow can be generated from a magnetic nozzle [6] that reduces power losses occurring in solid nozzles. In our study, the expansion of the plasma is performed through a sonic throat into a low pressure chamber. In a such flow, the expansion of the plasma is accompanied by a rapid cooling and recombination which results in kinetic non equilibrium between electrons and heavy particles. In this situation, the plasma is recombining by collisional processes and a departure from Saha-Boltzmann equilibrium is observed. Non intrusive method based on Optical Emission Spectroscopy (OES) are commonly used to characterize supersonic plasma jets. They allow to get excited level densities of various species. Although OES studies are encouraged in supersonic plasma jets, characterization have to be carried using cautious assumptions. Sember & al. [1] have shown that spectroscopic analysis based on atomic lines, and hydrogen lineshape profiles might give questionable results if the plasma is out of thermodynamic equilibrium. In this study, proper diagnostics based on atomic and molecular contributions have been developed to evidence the non equilibrium state.

A detailed investigation of the plasma source performance is necessary to insure high quality measurements. Frequency analysis of electrical parameters and light emission are the most common ways to understand the nature of the plasma jet fluctuations. In the literature, much effort is devoted to the diagnostic of the arc plasma jet unsteadiness (Tu al. ([7]), Singh & al [8]). In RF plasma sources, the heating procedure may also induce oscillations in the emission. Performance of the Microwave Plasma Torch (MPT) producing atmospheric plasma is investigated. Electrical characterization of the source has been performed for some operating conditions using forwarded and reflected microwave power monitoring. Comprehensive characterization of the flow by means of high speed imaging has been performed to estimate the effect of the oscillation of the delivered power on plasma jet unsteadiness. Basic OES measurements are performed to get typical radiative signatures of air, N_2 and CO_2 atmospheric plasma jets.

Diagnostics adopted to examine the thermodynamic state present in the Plasmatron supersonic air plasma jet are described in section 2 and the results are presented in section 3. Performances of MPT will be discussed in section 4.

2. Spectroscopic plasma diagnostics

2.1. Plasma diagnostics using atomic lines

2.1.1. Atomic state distribution function

Measured emission ϵ_{ul} allows a straight probing of the upper (emitting) level n_u population density through the relation:

$$\epsilon_{ul} = n_u \frac{A_{ul}}{4\pi} \frac{hc}{\lambda_{ul}} \quad (W.m^{-3}.sr^{-1}), \tag{1}$$

where A_{ul} (s^{-1}) is the Einstein coefficient associated to spontaneous emission from level u to level l respectively of energy E_u and E_l (m^{-1}). $\lambda_{ul} = \frac{1}{(E_u - E_l)}$ (m) designates the line position. Assuming Local Thermodynamic Equilibrium (LTE), the internal level population density of a level u of energy E_u and degeneracy g_u follows the Boltzmann distribution ruled by a single temperature T_{LTE} given by:

$$n_u(T_{LTE}) = N(T_{LTE}) \frac{g_u exp\left(-\frac{hcE_u}{k_B T_{LTE}}\right)}{Q_{int}(T_{LTE})} \quad (m^{-3}), \tag{2}$$

where species concentration N (m^{-3}) and internal partition function Q_{int} are calculated at equilibrium.

In thermal plasmas, atomic state distribution function obeys Boltzmann equilibrium and the excitation temperature T_{exc} is evaluated on the basis of the Boltzmann diagram method. This approach is convenient as no assumption is made concerning the species concentration. The upper level density being straightly related to emission through relation 1, it is expressed in terms of T_{exc} combining equations (1) and (2) in the form:

$$ln\left(\frac{n_u}{g_u}\right) = -\left(\frac{hc}{k_b Tex}\right) E_u + ln\left(\frac{N}{Q_{int}}\right). \tag{3}$$

Excitation temperature T_{exc} is directly obtained from the slope of a straight line fitted on the set of experimental electronic excited states population logarithm values (left term of Equation 3).

Occasionally, the equilibrium distribution is not applicable to electronic states. In this case, experimental points in Boltzmann diagram do not comply with a single straight line. In order to qualitatively express the departure from equilibrium, it is convenient to defined two temperatures T_{exc}^{low} and T_{exc}^{high} corresponding respectively to the excitation temperature of lower and higher states. In such case, it is important to know

if ionizing or recombining state is prevailing in the plasma in order to determine the electron temperature T_e. For this purpose, the atomic state distribution function can be completed using the so-called Saha point n_∞ defined as:

$$\frac{n_\infty}{g_\infty} = \frac{n_2^2}{2g_0^i} \times \left(\frac{h^2}{2\pi m_e k T_e}\right)^{3/2} \quad (4)$$

Where g_0^i is the degeneracy of the ground state of the corresponding ion. In a situation of Partial Local Saha Equilibrium (pLSE), the Saha point will be within the line that fits the levels with populations conforming to the Saha Boltzmann equation. In a first approximation, the ground state n_0 can be evaluated using equation 5. Its position with regard to the pLSE fitted line will determine the pLSE ionizing or recombining state. Such investigation is not presented in the following as it requires missing information on the pressure inside the jet.

$$n_0 = P/kT_{gas} \quad (5)$$

2.1.2. Stark broadening of hydrogen lines

The determination of the electronic number density is executed though the fitting of calculated hydrogen Stark broadened lines onto experimental data. Calculation of the the Stark broadened line profiles have been reported in the literature for the first three Balmer lines of hydrogen (H_α, H_β and H_γ). Databases are elaborated using three different theoretical models named as quasi-static ion approximation model (VCS)[9], Model Microfield Method (MMM)[10] and Computer Simulation (CS)[11]. The available domains for each set of theoretical data are presented in table 1. The line half-profiles are available in the form of tables where values of intensity are tabulated against wavelengths for certain values of electron temperature T_e and density N_e. In order to obtain a profile for any couple (T_e,N_e), a bilinear interpolation is performed from theoretical data. The theoretical line profile is convoluted with the instrumental broadening of the apparatus accounting also for the doppler broadening using a gas temperature T_g. The program interpolates points from the theoretical line profile to match the grid of the experimental data set. Any background in the experimental data is zeroed so that the data is directly comparable to the theoretical profiles.

Model	Constraint on N_e (cm^{-3})	Constraint on T_e (K)
VCS	$10^{10} \leq N_e \leq 10^{18}$	$2500 \leq T_e \leq 1.610^5$
MMM	$10^{10} \leq N_e \leq 10^{19}$	$2500 \leq T_e \leq 1.310^6$
CS	$10^{14} \leq N_e \leq 10^{19}$	$1042 \leq T_e \leq 1.710^6$

Table 1: Plasma parameters validity range.

2.2. Plasma diagnostics using molecular spectra

Plasma characterization using molecular spectra is done on the basis of common fitting approaches consisting of the minimization of the functional defined by the Root Mean Square Error (RMSE) between the experimental spectrum and the spectrum calculated under various equilibrium assumptions. The theoretical spectra required to determine the RMSE are calculated on the basis of an advanced tool developed and available at the EM2C laboratory and so-called High Temperature Gas Radiation (HTGR) code [12]. Assuming thermal equilibrium, the temperature $T_{thermal}$ is obtained applying the fitting procedure on experimental spectra normalized to unity, which consist in the minimization of the functional expressed as:

$$RMSE\,(T_{thermal}) = \sqrt{\frac{1}{N}\sum_{i=1}^{N}\left(\bar{S}_{\lambda_i}^{exp} - \bar{S}_{\lambda i}^{theo}(T)\right)^2} \quad (6)$$

where $\bar{S}_{\lambda_i}^{exp}$ (resp. $\bar{S}_{\lambda_i}^{theo}$) designates the normalized experimental spectrum (resp. calculated spectrum) and N is the number of experimental points in the considered spectral range.

2.2.1. Vibrational non equilibrium assessment

The HTGR code can support various assumption concerning the distribution of emitting levels. Additionally to the thermal situation, an other assumption is considered to determine the population of the vibrational excited states from the vibrational band of a molecular system. In the frame of thermal equilibrium model, the population of an energy level (n,v,j) is expressed as:

$$n_{n,v,j} = N_{tot} g_s \frac{(2J+1)}{Q_{int}(T_{LTE})} \times exp\left(-\frac{E_{el}(n) + E_{vib}(n,v) + E_{rot}(n,v,J)}{kT_{LTE}}\right) \quad (7)$$

where $Q_{int}(T_{LTE})$ is the internal partition function, N_{tot} is the total population of the considered species and g_s is the nuclear spin statistical factor. Assuming rotational equilibrium, the population can be expressed as a function of the population of the vibrational levels n_v:

$$n_{n,v,j} = n_v g_s \frac{(2J+1)}{Q_{rot,v}(T_{rot})} \times exp\left(-\frac{E_{rot}(n,v,J)}{kT_{rot}}\right) \quad (8)$$

where $Q_{rot,v}(T_{rot})$ is the rotational partition function. The determination of the variables (T_{rot},$n_{v_{k=1,vmax}}$) consists in the minimization of the functional defined as:

$$RMSE\,(T_{rot}, n_{v_k}) = \sqrt{\frac{1}{N}\sum_{i=1}^{N}\left(\bar{S}_{\lambda_i}^{exp} - \bar{S}_{\lambda_i}^{theo}(T_{rot}, n_{v_{k=1,vmax}})\right)^2} \tag{9}$$

3. Supersonic air plasma jet in VKI Plasmatron facility

The VKI Plasmatron Inductively Coupled Plasma (ICP) source uses a high frequency, high power and high voltage generator (400 kHz, 1.2 MW, 11 kV), feeding a single-turn inductor [13]. For the present experiments, the Plasmatron is operating at 350 kW power and 1.8 g/s mass flow rate. Supersonic plasma jet is obtained by expanding the plasma through a convergent nozzle into a chamber maintained at low pressure. Multiple reflections of expansion waves originating from the throat of the nozzle gives rise to complex structures of compression and expansion zones in the jet. The presence of non monotonic pressure

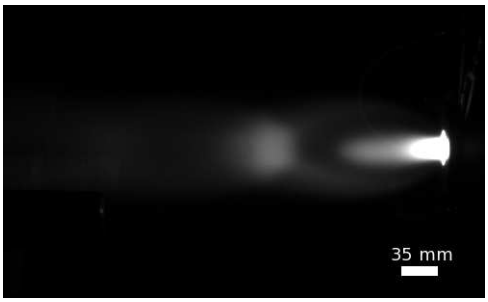

Figure 1: Supersonic air plasma jet (2 mbar chamber pressure).

and velocity gradients causes the plasma to propagate through various stage of equilibrium states along the axis of the jet. In the present study, the pressure in the chamber is maintained at 2 or 10 mbar corresponding respectively to a highly underexpanded figure 2 and underexpanded figure 1 situation while the pressure in the reservoir is maintained at 50 mbar. A basic analysis of the oscillation of the emission in the supersonic jet enables to evidence peaks at 600 and 1200 Hz induced by the three phase rectifier operating at 300 Hz. Lower frequency peaks were also observed at 170 and 340 Hz.

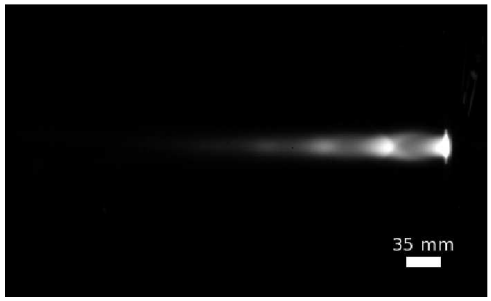

Figure 2: Supersonic air plasma jet (10 mbar chamber pressure).

3.1. Supersonic regime

The supersonic plasma flows encountered in this study evidence a pressure at the exit of the convergent being higher than in the chamber. In order to equilibrate the pressure difference at the exit of the convergent, expansion waves are created and directed towards the jet axis which are then reflected in the direction of the plasma jet boundaries. These expansion waves direct the flow towards the edge of the plasma jet, creating a radial expansion in addition to the axial expansion. The edges of the expansion zone are bright because of the reflection of the expanding flow by the cold dense surrounding gas, which gives rise to the so called barrel shocks. Reducing the chamber pressure, leads to the creation of a Mach disk downstream of the first expansion cell, leading to subsonic velocities downstream of this region with an increase of the local temperature and pressure.

3.2. Nonequilibrium diagnostics using OES

Optical Emission Spectroscopy (OES) allows to obtain information on excited states densities without disturbing the flow. Accurate measurements rely on stationary flow emission and low contamination of the jet. A conventional OES technique was set up and applied in a large spectral range on a supersonic underexpanded air plasma jet in the first expansion zone at 25 mm from the exit of the convergent throat. We focus our study on the spectral domain that includes the N_2^+ First negative system $\Delta v=+1$ and the H_β hydrogen line. The discharge is generated inside the torch and the plasma jet flows into the test chamber maintained at a constant pressure of 10 mbar through a 35 mm diameter nozzle exit. The line of sight plasma jet emission is collected through an aperture and then focused with a fused silica lens onto the entry of a Acton Series monochromator of 75 cm focal lengths. The spectrometer is combined with a ICCD PI-MAX

camera with a frame of 1024×1024 pixels of 12.8 μm side. Emission issued from the jet is spatially resolved in the radial direction. A radial slice of about 19 cm height was optically conjugated using a 100 mm focal lens onto an image with a magnification factor of 0.07. It allows to capture the whole radial profile of the jet onto the CCD screen of the camera with a spatial resolution of about 180 microns. The radiation from the N_2^+ First negative system was recorded using a 150 groves/mm grating as the hydrogen line H_β spectral resolution was improved by using a 1200 groves/mm grating in order to resolve Stark broadening contribution. The corresponding spectral resolutions were measured to be respectively 0.5 nm and 0.06 nm, setting the entrance slit of the monochromator to 3 microns. The recorded spectra were calibrated in absolute intensity combining a ribbon tungsten lamp and its documented absolute radiance and a deuterium source. At the conditions reported here, the air mixture is assumed to be optically thin and proper Abel inversion was applied on measured spectra allowing to rebuild the spectral emission ($W.m^{-3}.sr^{-1}.\lambda^{-1}$). Calibrated spectra at the plasma jet center line are shown in figure 3. The displayed radiative signature is dominated by oxygen and nitrogen atomic lines in the visible spectral range. The N_2^+ First Negative system is hardly detected.

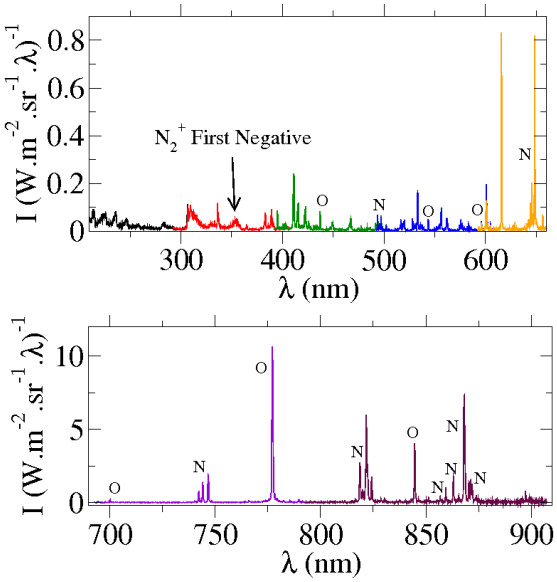

Figure 3: Typical radiative signature of supersonic air plasma jet in the first expansion zone (r = 0 mm, z = 25 mm).

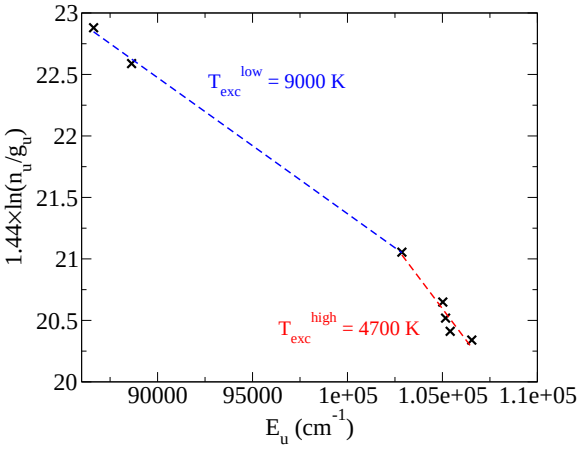

Figure 4: Boltzmann diagram at the center of the jet using oxygen atomic lines (r = 0 mm, z = 25 mm).

3.2.1. *Departure from equilibrium of the electronic excited states*

Boltzmann diagram as plotted in figure 4 using atomic oxygen lines at the center of the jet. The useful spectroscopic data are recalled in Appendix A. The diagram does not comply with a single straight line, indicating that departure from Boltzmann equilibrium occurs. Two straight lines are fitted on the experimental points to derive the excitation temperature of lower states T_{exc}^{low} at a temperature of about 9000 K and higher states T_{exc}^{high} at a temperature of about 4700 K. Provided pLSE starts at the higher excited states $T_e = T_{exc}^{high}$, the plasma is characterized by an underpopulation of lower excited states which is representative of a recombining plasma.

3.2.2. *Assessment of vibrational equilibrium*

Detailed energy distribution among the quantum states within the vibrational mode is essential to characterize non thermal plasmas issued from supersonic nozzle expansion. The fitting procedure is executed on Abel transformed spectra at 1.7 cm from the jet center line where molecular radiative contribution is not overlapped by atomic lines. Figure 5 exhibits the distribution of the vibrational bands of N_2^+ First Negative system $\Delta v=+1$ calculated at 9000 K with an apparatus function of 0.06 nm. Taking this spectral resolution, we can clearly distinguish bands from v=0 to v=4. For vibrational level higher than 5, we can notice vibrational band inversion which allows to execute the minimization procedure on a large amount of vibrational levels despite the small spectral win-

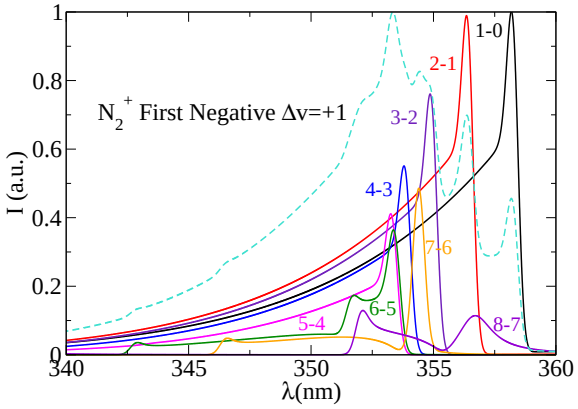

Figure 5: Vibrational bands distribution of N_2^+ First Negative system $\Delta v=+1$.

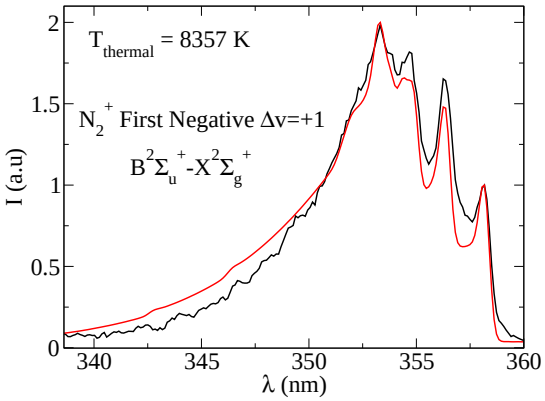

(a) Thermal equilibrium assumption.

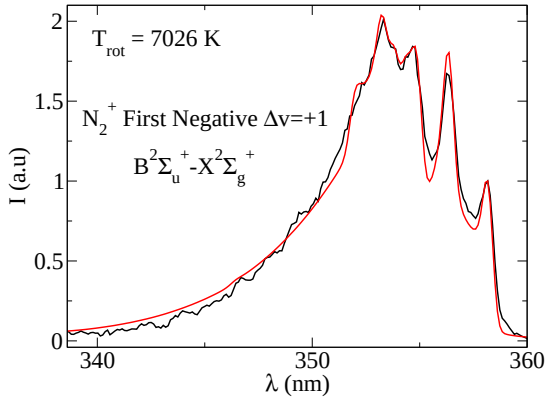

(b) Rotational equilibrium and vibrational nonequilibrium assumption.

Figure 6: Best fit between experimental spectrum (black) and calculated spectrum (red) (r = 17 mm, z = 25 mm).

dow. Assuming thermal equilibrium, best fit is obtained 1.7 cm from the jet center line with a temperature $T_{thermal}$= 8357 K. The calculated spectrum is in fairly good agreement with the experimental spectrum figure 6 (a), suggesting for proximity to rotational and vibrational equilibrium. Accounting for rotational equilibrium only, the vibrational distribution is determined. Best fit is presented in figure 6 (b). This method allows to improve the matching between experimental and calculated spectra. In this case, the RMSE is 2% lower than in the thermal equilibrium case. The rotational temperature is found to be T_{rot}=7026 K. Vibrational population is plotted on figure 7. Neglecting the weak contribution of the vibrational level v=8, a straight line can be fitted on the logarithm of the vibrational population and by using the energy of each level we obtain a vibrational temperature T_v= 8800 K.

3.2.3. Electronic density measurement

Fitting of experimental data is performed with MMM data at the center of the jet. Contamination in the wings of the hydrogen H_β line is excluded by the minimization procedure. The best fit obtained is presented in figure 8 corresponding to an electronic density of 3.0 10^{-20} m^{-3}. The MMM data tables have been calculated for an emitter-perturber reduced mass of 0.5 which corresponds to a pure hydrogen plasma and we take the electronic temperature T_e equal to the excitation temperature of high electronic excited states T_{exc}^{high} providing that pLSE is effective. CS data would permit to account for other perturbing species and also to account for non equilibrium between electrons and heavy particles. This study will be part

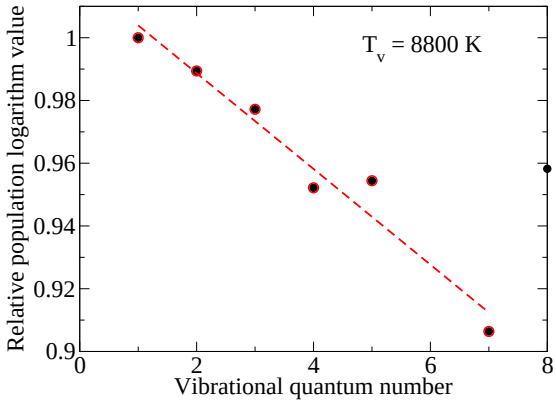

Figure 7: Relative population of vibrational energy levels for N_2^+ First Negative system $\Delta v=+1$ vibrational band (r = 17 mm, z = 25 mm).

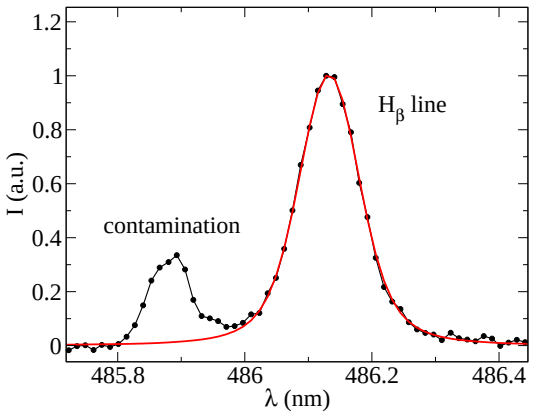

Figure 8: Best fit between experimental (black) and theoretical (red) hydrogen H_β line profile (r = 0 mm, z = 25 mm).

of further investigation. It should be noted that air plasma was not seeded with water or hydrogen. The intensity of the hydrogen lines was fluctuating which does not prevent from performing a diagnostic based on line broadening. The contamination in figure 8 might be caused by a Fe atomic line.

4. Investigation of microwave sustained plasma source

The MPT plasma source was built in VKI on the basis of a magnetron head (MH3.OW-S1 Richardson Electronics) operating at 2.45 GHz with a SM1150T power supply to produce microwave power in the kilowatt range transmitted through a rectangular waveguide (WR 340 adapted for λ =12.24 cm wavelength) to the gas flowing in a quartz tube of 30 mm inner diameter similarly to [14].

4.1. Plasma jet unsteadiness

The fluctuating part of the intensity has been investigated by means of high speed imaging measurements using a Phantom v7.0 8 bits CCD camera at an acquisition rate of 1 kHz. The examination of the unsteady feature of the flow emission provides useful information about the effect of microwave power oscillation on thermal inhomogeneity taking place in the plasma flow. Simple processing has been applied to high speed frame records to show the presence of regions inside the jet that are hotter or colder than the steady contribution. The FFT of optical emission fluctuation was executed to show the heating modulation at well defined frequencies. Figure 9(a,b) shows

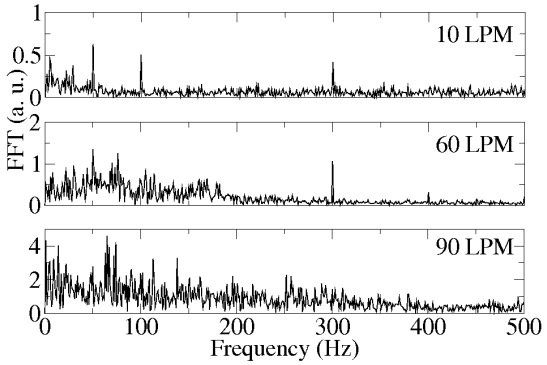

(a) 2kW air plasma jet.

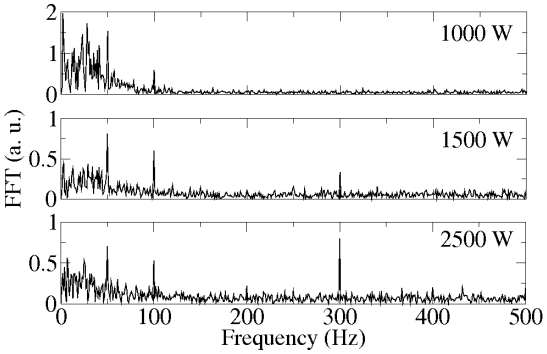

(b) 15 LPM air plasma jet.

Figure 9: FFT of an air plasma jet emission fluctuation on the axis at 1 cm from the waveguide.

the FFT operated on a spatial pixel located at 1 cm from the waveguide at the plasma center line for an air mixture at different power and flow rates. At 10 LPM, the spectrum is mainly composed of well defined frequencies above 50 Hz (50, 100 and 300 Hz) related to the coherent dynamic of the jet. Increasing the flow rate leads to the damping of these peaks vanishing into noisy background rising towards the low frequency range. These coherent peaks result from the modulated Joule heating of the feeding circuit. It has been observed that operating with a forwarded power slightly above the minimum threshold value required to sustain the plasma leads to a highly unstable plasma flow. The instability of the flow resulting from thermal inhomogeneities generated by the power modulation is damped by increasing the power. Figure 9(b) shows the effect of the input power on the plasma jet dynamics. As the power is increased, the spectral dynamics of the oscillations is mostly driven by peaks above 100 Hz as moderate frequencies contribution tends to fade.

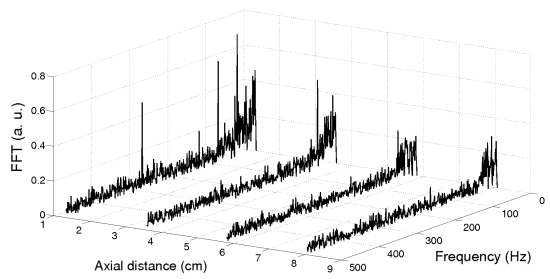

Figure 10: FFT of an air plasma jet emission fluctuation as a function of the distance from the waveguide.

4.2. Forwarded and reflected power monitoring

Forwarded and reflected microwave power were monitored at different flow rates and power in an air plasma. An Alter RD8400 power sensor is used to measure the microwave signal at 2.45 GHz previously attenuated at 60 dB by the circulator device. It allows to measure the maximum waveguide power with a full scale 0-10 Vdc output voltage. Alternative measurements have been performed on the forwarded and reflected signals. Temporal and frequential forwarded and reflected power signals are plotted in Figure 11(a,b). The effect of the flow rate variation on the reflected power is considerable. As the flow rate increases, the amplitude of the oscillations evolves from a coherent situation to random variation associated to noisy dynamic increasing towards low frequencies below 100 Hz. It is in agreement with plasma optical emission light dynamic oscillation. Coupling microwave power to the plasma requires the impedance between the discharge and the microwave power source to be matched. A common means to achieve this match is to insert a metallic element into the waveguide, which was performed here using screws. Since an impedance mismatch has phase and amplitude components, both position and depth of insertion of the matching element must be adjusted. Three screws, manually adjusted, are positioned inside the waveguide and the effect of the depth of the insertion was studied. For different configurations, the efficiency of the plasma source is illustrated on Figure 12, where the reflected RF power is plotted versus the forward RF power. We observe that the optimal configuration of the screws allows more than 90 % efficiency ($1 - \left(P_{reflected}/P_{forwarded}\right)$). Bad impedance matching can decrease the efficiency to about 75 % efficiency.

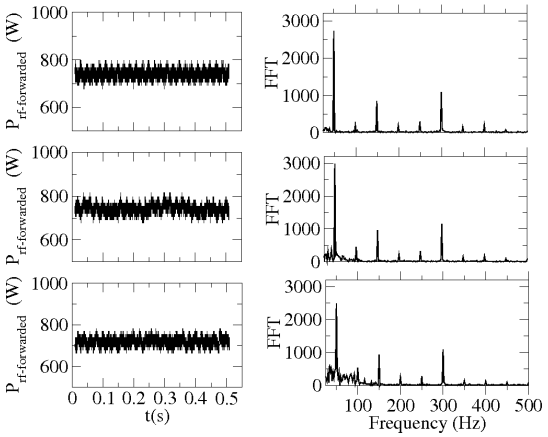

(a) Forwared power (top to bottom: 5, 10, 20 LPM).

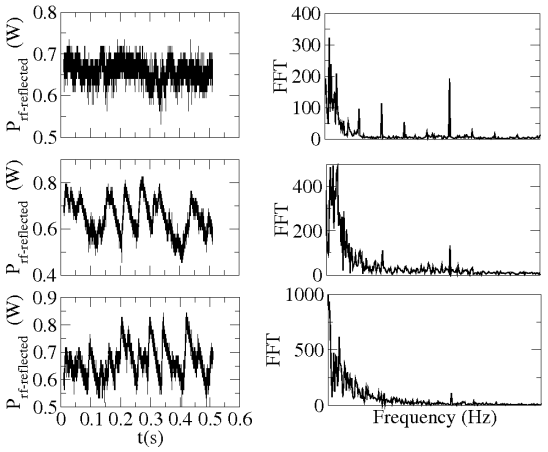

(b) Reflected power (top to bottom: 5, 10, 20 LPM).

Figure 11: Microwave power and associated FFT signal for air plasma at different flow rate.

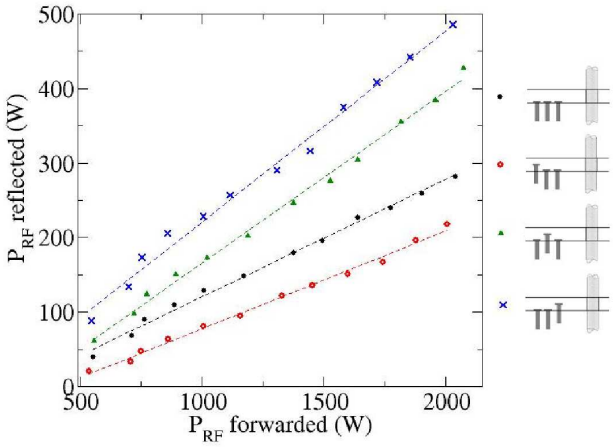

Figure 12: Reflected power versus forwarded power for different configurations of the impedance matching screws

4.3. Low resolution spectra examination

The examination of the radiative transitions of air, N_2 and CO_2 plasmas was performed by means of a low resolution OES bench at the jet center line. Acquired raw data are displayed in Figure 13(a) for various operating powers. The displayed spectra are characterized by significantly different contribution depending on the operating gas. Air radiative signature is mainly constituted of molecular emission of O_2 Schumann-Runge in the spectral domain below ~ 600 nm and of NO systems ($\beta, \gamma, \delta, \epsilon$) peaking at 250 nm. N_2^+ First Negative and N_2 Second Positive systems are the main contributors in pure N_2 plasma between 290 nm and 450 nm. CO_2 plasma emission is constituted of both molecular transitions from C_2 Swan system and atomic lines of Oxygen and Carbon. Air plasma emission spectrum is less appropriate for temperature determination by means of a spectra fitting approach in comparisons with N_2 and CO_2 radiative signatures. Indeed, air plasma emission in the visible range exhibit a poor dynamic detrimental for accurate fitting and the NO systems lying in the UV are self absorbed preventing a direct access to the local emission. In Figure 13(b), normalized radiative signatures of N_2 plasma are presented at different input powers. The poor dynamic change in the shape of the spectra indicates for a weak change in temperature. An additional microwave power contributes to the expansion of the plasma in the radial direction associated with an increase of the light emission intensity rather than a change in temperature. It is consistent with the observations in [15].

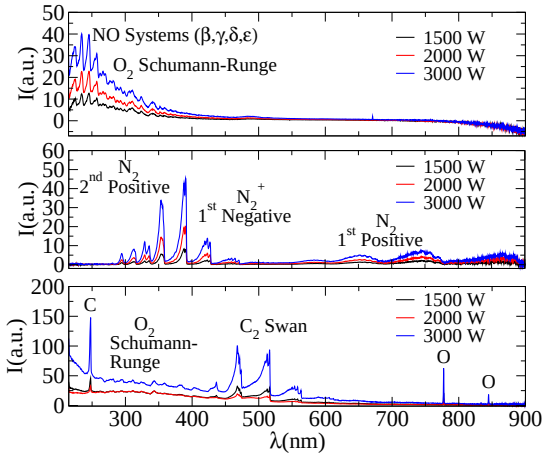

(a) Typical radiative signature of air, N_2 and CO_2 plasmas using different input power.

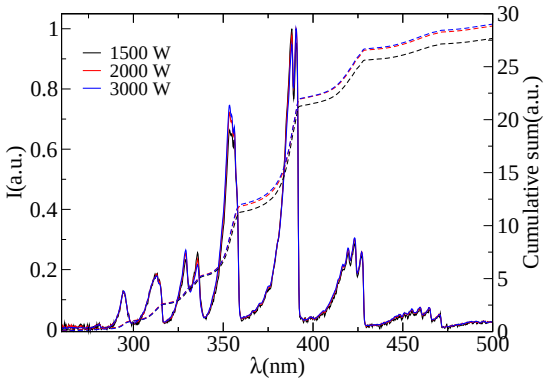

(b) Normalized N_2^+ First Negative system of pure N_2 plasma using different input power.

Figure 13: Low resolution spectra.

5. Conclusion

Various diagnostics have been used to characterize a supersonic air plasma jet in the first expansion zone. Plasma parameters have been derived at the center of the jet where diagnostic involve atomic contribution of oxygen species. Parameters derived from molecular radiation were studied at 1.7 cm from the jet center line where the contribution of N_2^+ First Negative system Δv=+1 is clearly defined. The lack of information about the static pressure and the non equilibrium distribution of oxygen atomic excited states make the determination of excitation temperature questionable leading to a temperature of the higher excited states of about T_{exc}^{high}= 3800 K. Assuming pLSE T_{exc}^{high} has been used to determine the electron number density by fitting experimental hydrogen H_β line onto theoretical lineshape. Despite weak contamination on the wing of the experimental hydrogen line, a good fit is obtained for an electron density corresponding to 3.0 10^{-20} m^{-3}. The presence of molecular radiation on the edge of the plasma jet allows us to probe rotational and vibrational levels and indicates a proximity to rotational and vibrational equilibrium. The rotational temperature has been determined by either assuming thermal equilibrium or assuming rotational equilibrium and vibrational non equilibrium. In the first case, T_{rot}=$T_{thermal}$= 8357 K, with a fairly good agreement between experimental and calculated spectra. In the second case, the fitting is improved and leads to a rotational temperature T_{rot}=7026 K. Vibrational temperature obtained by fitting the experimental vibrational levels with a straight line gives a temperature T_v= 8800 K. Description of microwave sustained plasma jet structures has been established within a large range of operating conditions (0-≈100 LPM, 1-≈3.5 kW) for

an air mixture at atmospheric pressure. Flow rate and input power contribute highly to the jet dynamics and shape. The fluctuating emission of the plasma jet has been monitored by means of high speed camera imaging. Plasma jet unsteadiness was clearly consistent with the powering circuit oscillations. The high efficiency of this source was measured at about 0.9 in best configuration for an air plasma jet. Although the dielectric properties of the plasma vary with changes in temperature and chemical composition, a single matching screws configuration corresponding to the highest efficiency will be retained and used for further experiments. Low resolution spectra were measured using air, N_2 and CO_2 gases. It indicates that increasing the microwave power contributes to the expansion of the plasma in the radial direction of the jet. Experimental campaigns, not presented here, have ensured that MPT might be considered as a valuable source to provide an appropriate reservoir of high temperature gas close to equilibrium.

Appendix A. Spectroscopic data

O lines			$D_e = 109837.02cm^{-1}$		
501.8782	4.2810^5	86 625.757	106 545.354	3	5
501.9291	7.1310^5	86 627.778	106 545.354	5	5
543.5178	$7.74\ 10^5$	86625.757	105019.307	3	5
543.5775	$1.29\ 10^6$	86627.778	105019.307	5	5
543.6862	$1.80\ 10^6$	86631.454	105019.307	7	5
595.8386	$6.80\ 10^5$	88630.587	105409.008	3	5
595.8386	$3.78\ 10^5$	88630.587	105409.008	3	3
595.8584	$2.27\ 10^5$	88631.146	105409.008	5	5
595.8584	$2.52\ 10^4$	88631.146	105409.008	5	3
595.8584	$9.06\ 10^5$	88631.146	105409.008	5	7
604.6233	$1.05\ 10^6$	88630.587	105165.232	3	3
604.6438	$1.75\ 10^6$	88631.146	105165.232	5	3
604.6495	$3.50\ 10^6$	88631.303	105165.232	1	3
615.5971	$5.72\ 10^6$	86625.757	102865.655	3	3
615.6778	$5.08\ 10^6$	86627.778	102865.547	5	7
615.8187	$7.62\ 10^6$	86631.454	102865.506	7	9
777.1944	$3.69\ 10^7$	73768.200	86631.454	5	7
777.4166	$3.69\ 10^7$	73768.200	86627.778	5	5
777.5388	$3.69\ 10^7$	73768.200	86625.757	5	3
844.6247	$3.22\ 10^7$	76794.978	88631.303	3	1
844.6359	$3.22\ 10^7$	76794.978	88631.146	3	5
844.6758	$3.22\ 10^7$	76794.978	88630.587	3	3

Table A.2: Spectroscopic data of the considered O emission lines used for air plasma [16].

Acknowledgments

The author would like to acknowledge the financial support of the European Commission within the frame of the 7th Frame Program Project FP7-SPACE209-242311: Planetary Entry Integrated Models.

References

[1] V.Sember, D.V.Gravelle, M.I.Boulos, Spectroscopic study of a supersonic plasma jet generated by an ICP torch with a convergent-divergent nozzle, Journal of Physics D: Applied Physics Vol.35 (2002) pp.1350–1361.

[2] S.E.Selezneva, M.Rajabian, D.Gravelle, M.I.Boulos, Study of the structure and deviation from equilibrium in direct current supersonic plasma jets, J. Phys. D: Appl. Phys. Vol.34 (2001) pp.2862–2874.

[3] M.C.M.van de Sanden, J.M.de Regt, D.C.Schram, Recombination of argon in an expanding plasma jet, Physical review E Vol.47-Number 4.

[4] L.Robin, P.Vervisch, B.G.Cheron, Experimental study of a supersonic low-pressure nitrogen plasma jet, Phys. Plasma Vol.1 - NO.2 (1994) pp.444–458.

[5] R.Yano, V.Contini, E.Plönjes, P.Palm, S.Merriman, S.Aithal, I.Adamovich, W.Lempert, V.Subramaniam, J.W.Rich, Supersonic nonequilibrium plasma wind-tunnel measurements of shock modification and flow vizualization, AIAA Journal Vol.38 (2000) No.10.

[6] M.Inutake, K.Yoshino, H.Tobari, H.Fukui, R.Sato, K.Hattori, A.Ando, Production of a Supersonic Plasma Flow through a Laval Magnetic Nozzle, Proc. of 26th Int. Conf. on Phenomena in Ionized Gases,1, (2003) pp.127–128.

[7] X. Tu, J. Yan, L. Yu, K. Cen and B. Cheron, The nature of the fluctuations in a double argon-nitrogen plasma jet, Applied Physics Letter Vol.91.

[8] Characterization of a DC plasma torch through its light and voltage fluctuations, N. Singh, M. Razafinimanana, J. Hlina, Journal of Physics D: Applied Physics Vol.33 (2000) pp.270–274.

[9] C. R. Vidal, J. Cooper, E. W. Smith, Hydrogen Stark-Broadening Tables, The Astrophysical Journal supplement Vol. 214.

[10] B. W. Acon, C. Stehle, H. Zhang, A. Montaser, Stark-broadened hydrogen line profiles predicted by the model microfield method for calculating electron number densities, Spectrochimica Acta Part B Vol. 56 (2001) pp. 527–539.

[11] M. A. Gigosos, M. A. Gonzalez, V. Cardenoso, Computer simulated Balmer-alpha, -beta and -gamma Stark line profiles for non-equilibrium plasmas diagnostics, Spectrochimica Acta Part B Vol. 58 (2003) pp. 14891504.

[12] M. Y. Perrin, P. Rivière, A. Soufiani, Radiation database for Earth and Mars entry, Von Karman Lecture Series RTO-EN-AVT-162.

[13] B. Bottin, M. Carbonaro , S. Zemsch and G. Degrez, Aerothermodynamic design of an inductively coupled plasma wind tunnel, 32nd AIAA Thermophysics Conference, Atlanta, USA AIAA paper 97-2498.

[14] Y. Babou, Transferts radiatifs dans les plasmas de mélange CO_2-N_2: base de données spectroscopiques, étude expérimentale et application aux rentrées atmosphèriques, Laboratoire d'Enèrgétique Moléculaire et Macroscopique, Combustion (EM2C) du CNRS et de l'ECP, Paris.

[15] A. V. Timofeev, Theory of microwave discharges at atmospheric pressures, Plasma Physics Reports Vol. 23, no. 72, pp. 158 164.

[16] NIST atomic spectra database , http://physics.nist.gov/PhysRefData/ASD/index.html.

Methodology for Ablation Investigations of Innovative Ablators in the VKI Plasmatron Facility Including First Results on a Carbon Fiber Preform

Bernd Helber

Aeronautics and Aerospace Department, von Karman Institute for Fluid Dynamics, Belgium, helber@vki.ac.be

Supervisor: Thierry Magin

Assistant Professor, Aeronautics and Aerospace Department, von Karman Institute for Fluid Dynamics, Belgium, magin@vki.ac.be

University Supervisor: Annick Hubin

Professor, Department of Electrochemical and Surface Engineering, Vrije Universiteit Brussel, Belgium, anhubin@vub.ac.be

Abstract

The continued interest in planetary entry probes, sample return missions, and the eventual extension to a manned mission to Mars demand ground testing of ablative materials as well as sophisticated modeling of their response to reentry environment. They are the only solution for such high speed reentries as no material is known to withstand the high thermal loads. Following the current developments of a new class of low-density, carbon/resin composite ablators, new efforts were initiated at the VKI on ablation research. This paper first summarizes the progress made on ablation testing in the VKI Plasmatron facility over the last years and presents a strategy for future investigations of innovative low-density ablators. Finally, preliminary results obtained on a carbon fiber preform are discussed, which is the basic material for new class ablators. Scanning-Electron-Microscopy was used to examine fiber ablation at microscale level and micrographs are shown revealing strong oxidation mechanisms.

Keywords: ablation, high enthalpy plasma flows, gas-surface interaction, emsission spectroscopy, scanning electron microscopy

1. Introduction

Motivation

On July 21, 2011, *Atlantis* landed safely back on earth after fulfilling the very last space shuttle mission, commencing the end of the first and so far only manned spacecraft with a reusable heat shield. The Russian *Soyuz* capsule, designed in the 1960s, is now exclusively serving the International Space Station (ISS) and is together with Chinese's *Shenzhou* (1992) the only transporter currently used for human spaceflight. ESA is developing an Advanced Reentry Vehicle (ARV) for crew and cargo transportation from the ISS, whereas NASA is planning a Multi-Purpose Crew Vehicle (MPCV) for deep space exploration with the final aim of a crewed Mars landing.

Following the launch of the Mars Science Laboratory (MSL) on November 26, 2011, with one of its scientific goals being a plan for human missions to Mars, the next steps will be to identify, develop and qualify required technologies for safely returning Martian samples. For such spacecraft entering a planet's atmosphere, high requirements are put on the thermal protection system (TPS) in order to shield crew and payload from the severe heating.

Problem statement

Since the strong efforts spent in the 1960's on the Apollo program [1; 2], ablative heat shields are the first choice for space capsules due to their efficiency and reliability (Fig. 1). Especially for very high reentry speeds exceeding 10km/s, typical for the new missions of ESA and NASA, ablators are the only solution as no known material is able to withstand the high thermal loads without degrading. Ablative heat shields take advantage of this property as they are able to dissipate the high heat fluxes through chemical and

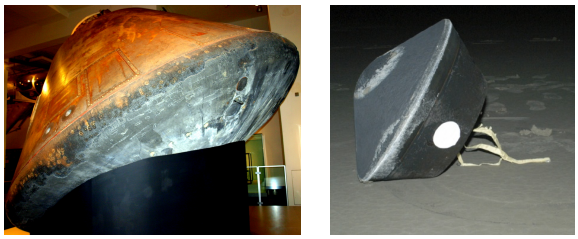

Figure 1: left: Apollo 10 with ablative heat shield after reentry (fastest manned reentry, 11.08 km/s, 1969), right: NASA Stardust probe after reentry (fastest man-made reentry object, 12.9 km/s, 2006)

physical decomposition, transforming the thermal energy into mass loss and recession, whilst the remaining solid material insulates the vehicle substructure. This makes selection of the TPS material and thickness design the two key performance parameters and inaccuracies in the prediction tools for TPS design can be fatal for the crew or the success of robotic missions.

The estimation of TPS sizing is a complex task and the prediction tools are still inherited from the Apollo program [3; 4]. Besides, a new generation of low density carbon/resin composite ablators is currently being developed. They are made of a carbon fiber preform impregnated in phenolic resin, such as PICA [5; 6] and ASTERM [7], developed by NASA and ESA, respectively, for high-speed entry missions. New high fidelity material response models are proposed [8] in order to take into account the micro-structure of the porous material. This calls for a sound methodology in numerical and experimental research to understand the complex gas-surface interaction and material response in plasma flows.

After first recalling the ablation process, this paper will review the efforts undertaken at the von Karman Institute on ablation testing during the last years and come up with a complementary approach for characterization of the performance of innovative ablators. This new methodology, existing of atmospheric plasma test in high enthalpy flows and microscale analysis, has been applied to a carbon fiber preform, which serves as basic material for new generation ablators. Preliminary results of carbon fiber preform ablation tests will be presented at the end of the paper.

2. Ablation of charring materials

2.1. The ablation process

The processes through which ablators are able to accommodate high heat fluxes are balanced between surface radiation, phase transitions (melting, sublimation) as well as chemical reactions (charring, oxidation) on the surface and inside the material. To achieve high performance characteristics of ablative materials mostly composite materials are used for the ablative heat shield. When subjected to increasing temperature, the virgin material successively transforms following two mechanisms (Fig. 2):

1. During ***pyrolysis*** the phenolic resin is progressively carbonized into a low density, porous char and loses around 50% of its mass producing pyrolysis gases by vaporization. The pyrolysis gases are transported out of the material by diffusion and convection and exhaust into the boundary layer, providing a further barrier for the heat exchange (blowing) and undergo additional chemical reactions, consuming more heat. Making usage of polymers such as phenolic resins for the matrix of the composite takes advantage of their endothermic degradation nature, thereby absorbing energy, and serving as a binder for the other components [9].

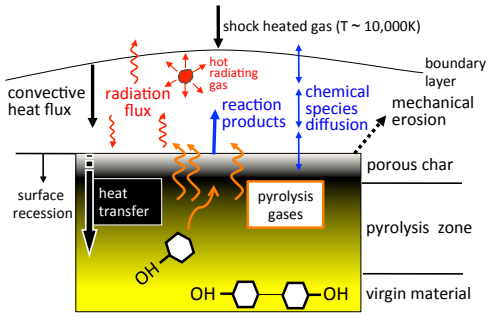

Figure 2: Ablation and pyrolysis processes of a charring material

2. ***Ablation*** of the char layer (composed of the carbonized resin and the remaining carbon fibers) is then promoted by heterogeneous chemical reactions, phase change and mechanical erosion (e.g. spallation), altogether leading to recession of the material. The rate at which an ablator recesses is therefore a functional consequence of its intended prevention of heat conduction and strongly coupled to the aerothermal conditions it encounters. In other words, the material will primarily respond with a higher ablation rate to increased heating whilst the heat conducted to the bondline will stay constant. This illustrates the great importance of material response models to accurately predict recession of the material. However, due to lacking good experimental data, this quantity remains as one of the largest uncertainties in material response analysis [10].

2.2. Existing modeling tools

During the Apollo program, strong efforts were invested to develop models for the prediction of complex gas surface interaction for thermal protection materials (TPMs). Those models, developed for dense ablative materials, are inspired from Kendall *et al.* published in 1968 [3; 11]. They rest on major assumptions and describe ablation as a surface phenomenon occurring on a homogeneous, dense material assuming equilibrium or finite-rate chemistry in a control volume close to the wall. The very complex thermochemical problem necessitates the generation of non-dimensional ablation tables, usually referred to as *B'*-tables, for pyrolysis-gas mass flux and char consumption rate (B'_g and B'_c). The coupling strategy with the flow environment is based on considering a thin control volume where the gas-surface interactions occur and where mass balance and equilibrium chemistry are satisfied. By this, the interaction of material and flow codes are approximated through the use of heat and mass transfer coefficients.

Weaknesses of this strategy are for example the model of mass transport due to diffusion into the control volume as well as negligence of blowing the pyrolysis products into the boundary layer, what will change the boundary layer condition. The efforts now focus on developing new flow solvers that can bypass the use of *B'*-tables and to couple them to in-depth, high fidelity material response solvers. For this task, innovative experiments are necessary on multicsale level for characterization of the material degradation in high enthalpy flows and subsequent model validation.

3. First efforts on ablation testing at the VKI

Graphite is widely used as exploratory material for basic research to narrow down the physics and thermochemistry to a non-charring, purely carbonic material. This enables to focus on the ablation phenomenon in the absence of pyrolysis. Ablation studies on graphite at the VKI were initiated by Fletcher and Vancrayenest in 2005, who started with investigations of the thermochemistry of ablating graphite by means of emission spectroscopy in the 15 kW inductively coupled plasma windtunnel Minitorch [12]. Due to the limited capabilities of the Minitorch windtunnel and the necessity of high enthalpy plasmas for ablation studies, the experiments were moved to the 1.2MW Plasmatron facility [13; 14]. The work of Vancrayenest and Fletcher showed the successful integration of emission spectroscopy, providing emission spectra as well as recession and mass loss rates of a 50 mm diameter, flat faced ablating graphite piece in air and nitrogen plasmas at heat flux levels between 500 $\mathrm{kW/m^2}$ and 1500 $\mathrm{kW/m^2}$

The knowledge gained throughout those ablation tests was translated into the development of a testing methodology for charring, low-density ablators. A cork compound provided by AMORIM (P50) was tested at varying heat flux and pressure levels [15] as well as the newly developed monolythic ablator *MonA* (Lockheed Martin Space Systems, distributed by LMUK) [16; 17]. This low-density ablator is a carbon-phenolic composite, structurally reinforced by a Flex-Core honeycomb, and was a considered TPM for the NASA Orion capsule. The heat flux levels for *MonA* ablation tests reached a maximum of 4500 $\mathrm{kW/m^2}$ and the experimental setup was extended by a high speed camera for surface recession measurements. This new technique enabled in-situ measurements of the degrading surface from which the assumption of a steady ablation rate was assessed. This is pointed out in Fig. 3 where a contour plot is presented, obtained by applying edge detection filters during post-processing of the HSC images. By conversion of pixel:millimeter, the rate of recession can be estimated in-situ, contrary to only absolute pre- and post-test measurements. Furthermore, a gas-front ahead of the ablating sample was identified, which is most likely an effect of the degassing pyrolysis products. Those help keeping away the hot plasma flow from the surface before burn-off in the boundary layer, what is visible as a bright flame.

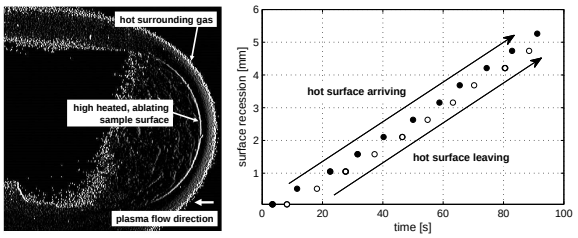

Figure 3: HSC snap-shot during ablation test showing the surface and gas-front (no shock wave); consequently the recession rate of *MonA* can be computed [16].

The radiation emitted by the reacting plasma flow can be captured by various spectroscopy tools. Time resolved emission spectroscopy was applied to ablation of *MonA* and indicative of electronically excited CN violet ($B^2\Sigma^+ \rightarrow X^2\Sigma^+$) and CN red ($A^2\Sigma_u^+ \rightarrow X^2\Sigma^+$), which was highly apparent in pure nitrogen plasma flows suggesting strong nitridation reactions.

In air plasma, the amount of CN significantly decreased pointing out dominant oxidation reactions (CO, CO_2, NO). Transient thermo-chemical mechanisms were found in nitrogen plasma, where electronically excited diatomic carbon (C_2 Swan system) was highly radiating after injection of the *MonA* sample but truncated after a few seconds. An illustrative emission spectrum recorded during sample injection into nitrogen plasma is shown in Fig. 4.

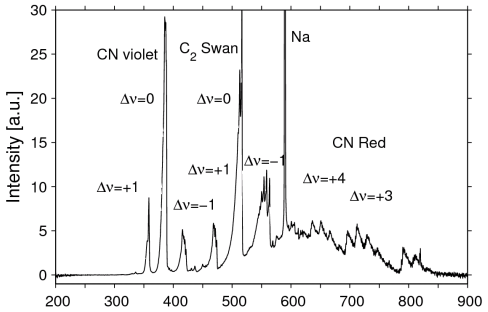

Figure 4: Emission spectrum ahead of ablating carbon resin composite sample in nitrogen test gas [16]

Utilizing combined measurements such as emission spectroscopy and high-speed-imaging illustrate the attempt of experimentally approaching the coupled physico-chemical problems, resulting from the evolution of pyrolysis products inside and outside the material, their reaction with gases coming from the freestream and the subsequent process of ablation.

It was further understood that a proper examination of tested samples has to be performed, especially at the surface and sub-surface. In this region, the char layer is subjected to ablation where for example the degradation of the carbon fibers can vary with pressure and surface temperature due to the changing diffusion mechanisms of oxygen. In particular, if oxygen is able to diffuse deep inside the material the internal structure can be weakened what leads to spallation and mechanical failure.

4. Methodology for ablator response characterization

To enable a proper design of heat shields based on porous, low-density composite ablators, a complete experimental analysis with parallel modeling is necessary. The following phenomena have to be analyzed and described accurately: **finite-rate chemistry** for pyrolysis gas, **transport phenomena in porous medium** as well as in the **boundary layer**, and **volume ablation** with an ablation zone (microscopic description of the carbon fibers).

Finally, the methodology has to be extended by an extrapolation strategy of the ground-testing conditions to real flight values, combining experimental data and numerical models. A flight extrapolation methodology was implemented at the VKI for application to reusable TPMs, which has to be approached and modified in order to be applied to the proposed work on ablative materials.

4.1. Ablation thermochemistry in high-enthalpy flows

The 1.2 MW Plasmatron facility [18] is extensively utilized at the VKI for ground-testing in atmospheric entry flows. In-situ measurements of a new generation of low density ablative materials will be performed for characterization of:

1. **Material response** to plasma exposure (temperature, heat transfer, ablation rate)
2. **Flow field** (surrounding gas phase, effect of "blowing" due to outgassing products)
3. **Radiation field** (identification and quantification of molecules and atoms such as C, C_2, CN, CO).

A schematic of the experimental setup comprising optical diagnostic bench for emission spectroscopy, high-speed-camera, and 2-color pyrometer can be found in Fig. 5. The successful application of emission spectroscopy encouraged the extend of the experimental setup by two more emission spectrometer in order to examine the ablation thermochemistry not only temporally but also spatially. The optical diagnostic bench consists of a light collection system, an optical fiber and the spectrometer. The light emitted by the plasma is collected through a variable aperture and focused by a converging lens (750 mm focal length, LA4745) via two mirrors to the entry of three 600 µm diameter optical fibers. The optics are aligned perpendicular to the flow and tangential to the test sample surface. By this, three points with variable distance (by the magnification and arrangement of the fibers) along the stagnation line through the boundary layer are imaged onto the three optical fibers. The fibers lead to three HR-4000 spectrometers which cover a broad spectrum in the desired range (200-1100 nm), suitable to rapidly determine radiating transitions of atoms and main molecular bands. The fixed entrance slit width of 5 µm and a 300 groove/mm grating lead to a typical resolution of approximately 0.6 nm (specification of supplier: 0.03-1.0 nm, depending on configuration). Calibration of the whole system in relative intensity, consisting of the light collection mechanism and spectrometer efficiencies, is

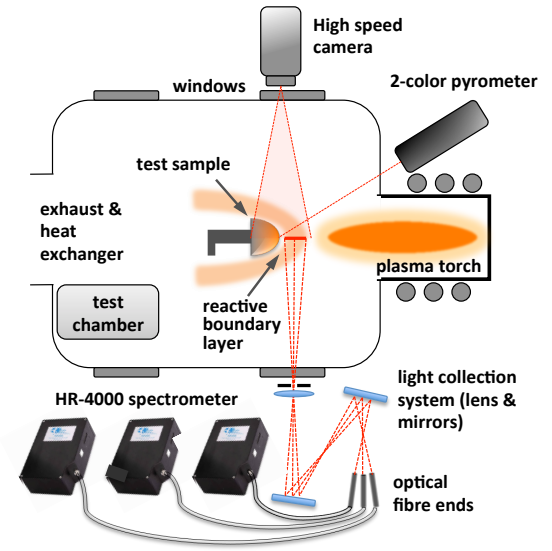

Figure 5: Emission spectroscopy setup applied to Plasmatron using three identical spectrometer focused on the reactive boundary layer ahead of the sample combined with HSC-imaging

performed using a deuterium lamp in the UV range (< 400 nm) and with a tungsten ribbon lamp (OSRAM WI 17G) in the visible range (> 400 nm), hence, obtained intensities are relatively comparable throughout the different tests.

Surface temperature measurements are carried out using a two-color Raytek Marathon MR1S-C pyrometer (0.75 − 1.1 µm, T_{max} = 3000°C). By using two separate narrow wavelength bands and under the assumption of an emissivity being independent of the wavelength, the surface temperature of a gray body can be measured independently of its emissivity. Calibration of the two-color pyrometer performed with a blackbody radiation source gave an uncertainty of $\delta T_S = \pm 10$ K.

4.2. *Multiscale analysis of porous & fibrous materials*

Tested and virgin samples will be analysed at the carbon fiber length scale of ∼1 µm. Microscopic and spectroscopic examination will be done at the research group on *Electrochemical and Surface Engineering* (SURF) of the *Vrije Universiteit Brussel* (VUB). Scanning Electron Microscopy (SEM) as well as spectroscopic tools, such as Energy-Dispersive X-ray spectroscopy (EDX) and Auger Electron Spectroscopy (AES), will be used to analyze the ablation phenomena of the carbon fibers and to evaluate the degradation inside the material. By doing so, a multiscale analysis in macro-, meso−, and microscale is being performed giving information about the depth of pyrolysis and char layer. The thinning and erosion of the carbonic fibers is of high interest [8; 19] as this helps in identifying the depth of the ablation zone and the susceptibility of the fibers to oxidation.

4.3. *Data integration and ablation model validation*

Physico-chemical models and material response codes will be developed in parallel, which will address the thermo-chemistry of the pyrolysis gases (e.g. identification of the species produced), their transport in the porous material as well as their evolution in the boundary layer. This will be done by coupling flow solvers with material response codes, at first, in a 1D 'stagnation line' description with a moving mesh to account for the recession of the surface [20]. This approach will then be able to be extended to a 3D description.

The extracted experimental data will be employed for comparison of observable data with model estimates. In fact, the functional integration of both experimental and numerical data is essential to identify the properties, physical processes and other factors required to fully characterize the ablation phenomenon.

As an illustrative example we refer to the surface recession rate of an ablating material, which is the result of complex thermo-chemistry and gas-surface interaction. Well defined boundary conditions are required for an adequate numerical simulation, which are inferred from experimental observations of the quantity of interest. For example, the recession of the material is dependent on surface temperature and pressure which can be taken from specific experiments for a certain flow condition. The numerical model will then present species-densities and mass fraction distributions at the stagnation line of a simulated Plasmatron experiment on an ablative carbon-phenolic surface as well as the temperature distribution throughout the boundary layer. Such data is then able to be compared to experimentally estimated concentration gradients and temperatures in the boundary layer, identified by means of emission spectroscopy.

4.4. *Flight extrapolation*

Duplication of the real hypersonic reentry condition in a ground-test facility can be achieved under the Local Thermochemical Equilibrium (LTE) assumption if the flight total enthalpy H_f, the total pressure p_f and the velocity gradient at the wall β_f are locally matched on the test sample. To inversely extrapolate the real flight condition from experiments, different steps are performed based on the Local Heat Transfer Simulation (LHTS) concept (Fig. 6). This methodology was

developed at the Institute for Problems in Mechanics of Moscow (IPM)[21] and applied to the Plasmatron facility [22]:

At first, heat flux and pitot pressure are intrusively determined during the experiment. The next step consists of numerically simulating the plasma flow using a Navier-Stokes-Solver characterizing the boundary layer geometry around the test sample under LTE and axisymmetric flow assumption (VKI ICP code [23]). Finally, the VKI Boundary Layer Code [24] is solving the chemically-reacting stagnation line boundary layer over a catalytic surface (the intrusively used calorimeter) under non-equilibrium conditions. The

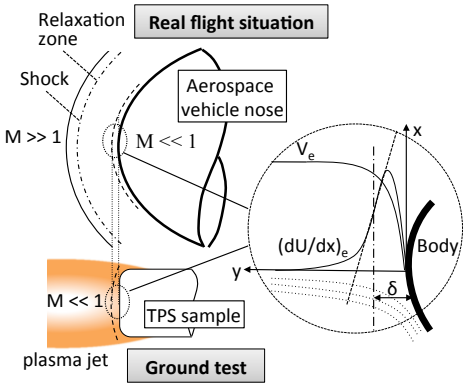

Figure 6: Local Heat Transfer Simulation (LHTS): Accurate duplication of the re-entry flight condition, existing at the stagnation point of an atmospheric entering vehicle, in a ground based plasma facility.

input boundary conditions for this tool are obtained from the experimentally determined heat flux and pitot pressure (step 1) as well as the so called five non-dimensional parameters (NDPs) coming from the flow solver (step 2). The code then iterates on the boundary layer outer edge temperature T_e, until experimental and numerical heat flux are matched, and provides outer edge enthalpy h_e and velocity v_e.

This procedure is up to now able to rebuild the freestream properties of the plasma jet and further, to extrapolate ground tests on reusable heat shields based on the principle of surface radiation to real flight conditions, such as for ceramic tiles and C-SiC compounds [25]. By flight conditions we mean a set of freestream conditions that will reproduce in the boundary layer of the space vehicle (near the stagnation point) the same kind of environment as found in the ground facility.

This methodology will be extended to ablative material testing with implementing new numerical models and validating them by means of comprehensive experiments. A complete analysis will be realized consisting of the plasma flow field, the reactive boundary layer (firstly in a stagnation line description), and brought to completion by coupling the decomposing material response. This will enable extrapolation of ground tests to real flight conditions, giving the material response of a specific material for selected points along the reentry trajectory. Such complex studies will allow for computation of the heat flux throughout the degrading material and, therefore, make TPS sizing possible.

5. Preliminary results on a carbon fiber preform

5.1. Atmospheric plasma tests

A low density, porous carbon fiber preform, obtained from Mersen Scottland Holytown LTD, was tested in the Plasmatron facility at sub-atmospheric conditions (15-200 mbar). The bulk carbon preform consists of 2D randomly oriented carbon fibers with their through-the-thickness (TTT) direction parallel to the flow direction. The fiber compound typically as a density of around 180 $\mathrm{kg/m^3}$, depending on the fabrication process and the nature of the precursor. The sample shape exposed to the flow was a flat faced cylinder of 45 mm length and 50 mm in diameter at a distance of 445 mm to the plasma-torch exit. Two type-K thermocouples were installed inside the sample at a distance of 10 mm and 20 mm downstream the initial stagnation point. Intrusively measured cold wall heat flux, surface temperatures as well as corresponding ablation quantities such as mass loss and recession are reported in Table 1.

Table 1: Test conditions (static pressure p_s, mean cold wall heat flux $\dot{q}_{cw}$) and comparison of surface temperatures at test end ($T_{S,end}$), mass loss ($\dot{m}$) and recession (r) in air plasma at a test time of 90 s.

p_s [mbar]	$\dot{q}_{cw}$ [$\mathrm{kW/m^2}$]	$T_{S,\,end}$ [K]	$\dot{m}$ [g/s]	r [mm]
(#1) 15	1021	2288	6.88/90	7.0
(#2) 100	946	1909	5.49/90	5.0
(#3) 200	1026	2228	5.11/90	5.5

The cold wall heat flux was constantly kept at 1 $\mathrm{MW/m^2}$ for the three test cases with static pressures in the test chamber varying between 15-200 mbar. Surface and internal temperature histories of low (#1) and high (#3) pressure case are presented in Fig. 7. A malfunction was recorded by thermocouple 10 mm /

15 mbar but is plotted for completeness. The internal temperatures still indicate material differences compared to a fully impregnated ablator, as both thermocouple outputs start rising quickly after sample injection. The protective endothermic pyrolysis processes of a fully compounded composite ablator would prevent penetration of the heat wave into the material.

For the flow conditions presented, the formation of CO due to atomic oxygen is expected to be the dominant reaction with the solid carbon of fibers (C_s). Reactions with nitrogen species as well as sublimation are neglected in this regime:

$$O + C_s \rightarrow CO \tag{1}$$

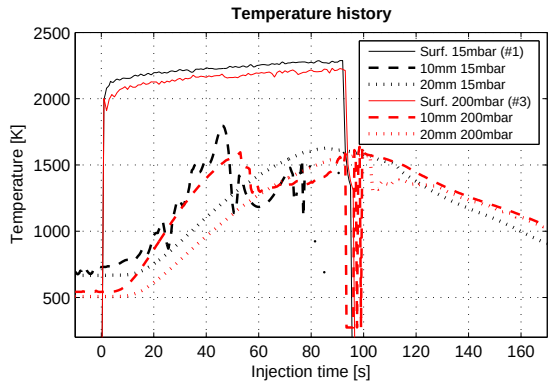

Figure 7: Surface and in-depth (10 mm & 20 mm from initial stagnation point) temperature history for carbon prefom ablation tests, mean surface temperature difference $\triangle\overline{T}$ = 70 K, thermocouples located 10 mm inside show malfunction (15 mbar) or break at T_{max} = 1500 K

However, the surface temperatures being in the order of 2200 K highly suggest a diffusion-controlled regime making surface kinetics insignificant [26]. In other words, the high thermal energy at the surface promotes total depletion of oxygen by oxidation and hence, reactions are only restricted by the ability of oxygen to diffuse through the boundary layer to the carbon surface.

The concentration change of atomic oxygen in the freestream for the various conditions can be found in Table 2, listing the boundary layer edge rebuilt values (free-stream enthalpy, density and oxygen concentrations, as well as the atomic oxygen diffusion coefficient (at edge temperature T_e), which will be discussed below. From this it can be seen that the freestream concentration of atomic oxygen for test #3 (200 mbar) exceeds that of test #1 (15 mbar) by a factor of almost 13 due to a strong density change (mass fractions are constant throughout the tests). Both recession and mass loss of test #1 at 15 mbar exceed that of test #3 (200mbar) by around 30%, as can be found in Table 1. This is somewhat counter-intuitive as a higher oxygen concentration would be assumed to lead to stronger oxidation mechanisms and, therefore, higher recession of the material.

Table 2: Boundary layer edge rebuilding: Free-stream enthalpy h_e, density ρ_e, atomic oxygen concentration c_O and atomic oxygen diffusion coefficient (at T_e) for each static pressure (p_s) condition.

	p_s [mbar]	h_e [MJ/kg]	ρ_e [kg/m^2]	c_O [mol/m^3]	$\mathcal{D}_O$ [m^2/s]
(#1)	15	22.65	0.6E-3	0.0087	0.52
(#2)	100	22.49	3.8E-3	0.0544	0.09
(#3)	200	20.42	7.9E-3	0.1121	0.04

A crucial period for tests of decomposing materials is the time during “start-up” of the facility, which is needed to operate the system to the target conditions. During this procedure, which contains adjustment of test gas, chamber pressure and heat flux, possible test specimens are hold on the injection mechanism close to the hot plasma flow. This is known to lead to additional errors in mass loss measurements as the hot environment can already lead to decomposition of phenolic compounds through pyrolysis. However, this not likely to be the case for the carbon preform as the bulk material is already fully carbonized. Furthermore, manufacturer specifications of thermal gravimetric analysis (TGA) claim that no considerable oxidation processes start below 770 K and that mass loss during a 6h analysis at 770 K resulted in only 0.35% mass loss. The thermal environment beside the plasma jet is not assumed to reach this temperatures, what can also be observed in Fig. 7 for the internal thermocouples. However, the internal temperatures of test #1 at 15 mbar exceed that of test #3 by around 140 K although the mean cold wall heat fluxes are almost identical.

In order to research into this problem we need to consider the carbon preform as a porous medium at microscale. In such a porous medium oxygen is able to diffuse into the deeper structure if its diffusivity is fast enough compared to oxidation reactions in the surface char layer. This is modeled by the Thiele number Φ, which is small if the diffusivity $\mathcal{D}$ is much

higher than the fiber reactivity k_f [m/s]:

$$\Phi = \frac{L}{\sqrt{\mathcal{D}_i / s_f k_f}} \tag{2}$$

with L being a characteristic length, e.g. the sample length and s_f the fiber volume surface [m^2/m^3]. Using Fick's law it is able to retrieve averaged species diffusion coefficients of a multi-component mixture for species i:

$$\mathcal{D}_i = \frac{1 - x_i}{\sum_{j \neq i} x_j / \mathscr{D}_{i,j}} \tag{3}$$

where $\mathscr{D}_{i,j}$ are the binary diffusion coefficients given by:

$$\mathscr{D}_{i,j} = \frac{3}{16} \sqrt{\frac{2\pi k_B T (m_i + m_j)}{m_i m_j}} \frac{k_B T}{p \Omega_{i,j}^{(1,1)}} \tag{4}$$

The atomic mass of the diffusing species i and j are m_i and m_j, k_B is the Boltzmann constant and $\Omega_{i,j}^{(1,1)}$ are the collision integrals at pressure p and temperature T, which can be computed from fitting expressions provided in ref. [27]. From Equation 4 we can see that at constant temperature but decreasing pressure the diffusivity will increase. This is also listed in Table 2, where the diffusion coefficient of oxygen based on the outer edge temperature T_e is given.

This brings us to the conclusion that in the case of low pressure, where diffusivity increases and atomic oxygen concentration decreases (leading to a lower fiber reactivity k_f), the Thiele number can decrease. As a consequence, oxygen would be able to penetrate deeper inside the material leading not only to ablation at the surface but also to degradation of fibers located further inside the material. This necessitates an examination of tested samples at microscale in order to be able to evaluate the degradation mechanisms of the carbon fibers, as presented in the following section.

5.2. Microscopic analysis

Virgin and tested carbon preform ablation samples were used to perform a microscale analysis by means of Scanning Electron Microscopy (SEM). Figure 8 presents micrographs of the virgin material exposing the carbon fibers at the surface of the test sample. Two glued fibers can be observed being indicative of an average fiber length of $l_f = 650\,\mu\text{m}$ and an average fiber diameter of $d_f = 6.5\,\mu\text{m}$.

Figure 9 presents ablated fibers at the preform surface after an ablation test at 100 mbar static pressure.

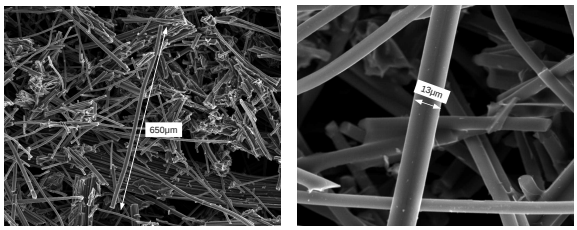

Figure 8: Surface of virgin carbon fiber preform showing two individual fibers glued together illustrating fiber length ($l_f = 650\,\mu\text{m}$) and doubled fiber diameter ($d_f = 6.5\,\mu\text{m}$).

On the first sight, a strong icicle shape of all fibers is visible due to their oxidation at the surface. It can also be said that the fibers shown in this micrographs are glued together to a fiber-bundle, which is a result of the manufacturing process of the preform. This leads to a certain percentage of all fibers being interconnected with a bunch of fibers to such bundles, embedded in between randomly oriented, individual carbon fibers. Several of such random fibers are shown in the micrograph to the right. Here, a thinning of the fiber is perfectly visible with the fiber diameter increasing from the top (inside the boundary layer) to the fiber-bottom (inside preform) reaching here almost the original fiber diameter of $d_f = 6.5\,\mu\text{m}$. A similar subject to thinning can be observed for the surrounding fibers. This implies an oxidation zone for this particular pressure case of $\sim 250\,\mu\text{m}$.

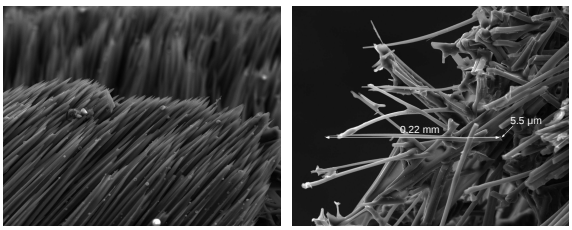

Figure 9: Ablated fibers at the preform surface (stagnation region, surface exposed frontal to the flow), thinning due to oxidation;
right: Fiber seems to be shortened due to ablation to a length of $\sim 220\,\mu\text{m}$ with its diameter increasing from fiber-top to fiber-bottom reaching almost the original fiber diameter of $d_f = 6.5\,\mu\text{m}$ $\rightarrow$ oxidation zone of $\sim 250\,\mu\text{m}$.

Comparing these results with micrographs taken after an ablation test at 15 mbar, reveals a few significant differences. Figure 10 presents such micrographs showing a fiber bundle at the surface of the preform being exposed to strong oxidation processes. However, compared to the micrographs shown before, a real icicle shape is not visible but rather strong degradation of the fibers over their whole length.

Such degradation in depth supports the assumptions

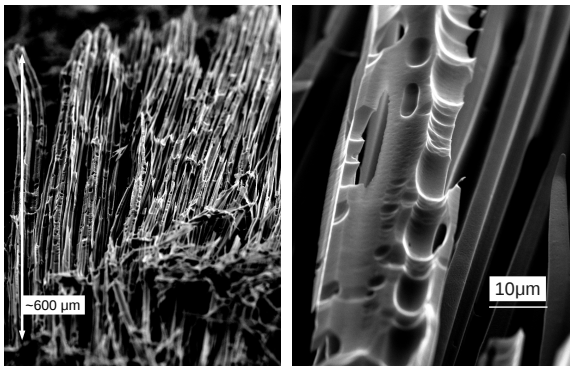

Figure 10: Fiber bundles exposed to the flow at the surface present strong corrosion of fibers throughout their whole length rather than a regular thinning from fiber-top to fiber-bottom.

found in the preceding section: A low pressure environment may lead to both increased oxygen diffusion along with decreased fiber reactivity, due to a lower oxygen concentration. With this, oxygen would be able to attack the fibers also in-depth rather than ablating only at the surface. This can weaken the substructure and for example lead to spallation, one mode of mechanical breakdown of the material, releasing small particles. Furthermore, fiber-bundels were identified in several micrographs of virgin but also ablated samples as mentioned before. As those bundles are embedded in-between individual fibers, they migh detach as soon as the surrounding fibers are ablated to a certain state, not able to retain a bundle anymore. Such mechanical failure could be the reason for an increased mass loss and recession of the material in various flow conditions.

An illustration of mechanical destruction of the material is given in Fig. 11, which shows two pictures taken by different instruments: A conventional reflex camera at comparable high exposure time (5 ms), exposing bright sparks during the ablation test, as well as a HSC image using a very short exposure time (5 µs). This reveals the flow being highly loaded with particles coming from the preform, what was constantly visible throughout the whole ablation test. This could be the result of what was said before: detaching fiber bundles as the preform ablates, releasing amounts of glued fibers at once to the flow, which then burn up in the hot plasma gas.

5.3. Comments

The preceding section briefly analyzed oxygen diffusion into the porous medium underlined by micrographs of ablated samples. However, although gas dynamics of the plasma flow are in continuum regime at

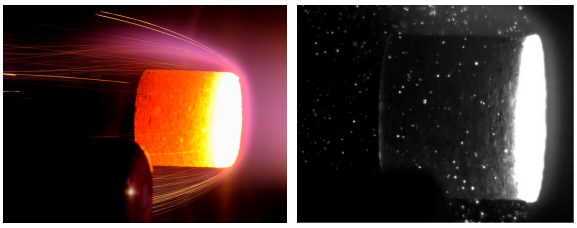

Figure 11: Images taken during a preform ablation test (p_s = 100 mbar); left: conventional picture taken with Nikon D5000, bright sparks visible (exposure time: 5 ms); right: taken with high speed camera, flow loaded with illuminated particles, probably assignable to spallation (exposure time: 5 µs)

the scale of the test sample, inside the porous preform the scale of interest is much smaller. Here, the Knudsen number is defined as the ratio of mean free path $\overline{\lambda}$ and pore diameter d_p:

$$Kn = \frac{\overline{\lambda}}{d_p} \tag{5}$$

Especially the fiber bundels, with a mean pore diameter of the order of 10 µm, a high Knudsen number of $Kn > 1$ can occur leading for low pressures to gas dynamics in the rarefied regime. This has to be kept in mind for any theoretical analysis of ablation in-depth of the material compared to pure surface ablation. Especially numerical models for mass transport at this small scale have to be adapted, e.g. using Boltzmann solvers as in the direct simulation Monte Carlo (DSMC), as the conventional macroscopic description using the Navier-Stokes equations is inappropriate in this regime.

6. Summary

The first part of this paper reviews the efforts undertaken at the VKI in ablation testing during the last years and concludes with an ablation testing strategy for future investigations of innovative low-density materials. This methodology will be followed to obtain crucial data for material response characterization, development and validation of new numerical models with final extension to real flight extrapolation.

The second part presents preliminary results of ablation experiments on a carbon fiber preform, which is the basic material for new class ablators before phenolic impregnation. The material was tested at a constant cold wall heat flux of 1 MW/m^2 with varying static pressures (15-200 mbar). A higher mass loss and recession of the sample was found at lower pressure level. SEM micrographs revealed strong degradation

of carbon fibers over their whole length (650 μm), especially for low static pressures. This raised the question in what extend oxygen is able to penetrate into the porous material. A first estimation of diffusion coefficients of atomic oxygen resulted in a rise of more than one order of magnitude from high (200 mbar) to low pressure (15 mbar) cases. More experiments along with numerical assistance are required to support those trends.

Acknowledgments

The authors are thankful to Mersen Scotland Holytow LTD for supplying the bulk carbon preform material. The research of B. Helber is funded by a Ph.D. grant of the Agency for Innovation by Science and Technology (IWT). Pascal Collins is acknowledged for his valuable help as Plasmatron operator.

References

[1] Sherman, M.M., NASA Space Vehicle Design Criteria, Entry Thermal Protection, NASA SP -8014, NASA Langley Research Center (1968).

[2] Pavlosky. J. E., Leger, L. G., Apollo Experience Report - Thermal Protection Subsystem, NASA TN D -7564 (1074).

[3] Kendall, R. M., An analysis of the coupled chemically reacting boundary layer and charring ablator: Part V, A General Approach to the Thermochemical Solution of Mixed Equilibrium-Nonequilibrium, Homogeneous or Heterogeneous Systems, NASA CR -1064 (1968).

[4] Milos, F. S., and Chen, Y.-K., Comprehensive model for multicomponent ablation thermochemistry, in: Aerospace Sciences Meeting & Exhibit, 35th, AIAA paper 1997-0141, Reno, NV, Jan. 1997.

[5] Tran, H. K., Johnson, C. E., Rasky, D. J., et al., Phenolic Impregnated Carbon Ablators (PICA) as Thermal Protection Systems for Discovery Missions, in: NASA, TM 110440, 1997.

[6] Tran H. K., Development of Lightweight Ceramic Ablators and Arc Jet Test Results, in: NASA TM-108798, Jan. 1994.

[7] Ritter, H., Portela, P., Keller, K., Bouilly, J. M., and Burnage, S., Development of a European Ablative Material for Heatshields of Sample Return Missions, in: 6th European Workshop on TPS and Hot structures, Stuttgart, Germany, 1-3 April 2009.

[8] Lachaud, J., Cozmuta, I., and Mansour, N. N., Multiscale approach to ablation modeling of phenolic impregnated carbon ablators, Journal of Spacecraft and Rockets 47 (6) (2010) 910–921.

[9] Torre, L., Kenny, J. M., and Maffezzoli, A. M., Degradation behaviour of a composite material for thermal protection systems Part I - Experimental characterization, Journal of Materials Science 33 (1998) 3137–3143.

[10] Cozmuta, I., Wright, M. J., and Willcockson, W. H., Defining Ablative Thermal Protection System Margins for Planetary Entry Vehicles, in: AIAA 2011-3757, 2011.

[11] Moyer, C. B., and Rindal, R. A., An analysis of the coupled chemically reacting boundary layer and charring ablator: Part II, Finite Difference Solution for the In-Depth Response of Charring Materials Considering Surface Chemical and Energy Balances, NASA CR 1061 (1968).

[12] Vancrayenest, B., and Fletcher, D. G., Investigation of the Thermochemistry of Ablation of Graphite for Planetary Entry Applications, in: AIAA 2005-5062, 2005.

[13] Vancrayenest, B., and Fletcher, D. G., Emission Spectroscopic Survey of Graphite Ablation in the VKI Plasmatron, in: AIAA 2006-2907, 2006.

[14] Vancrayenest, B., and Fletcher, D. G., Ablation of Carbonaceous Heatshields: Spectroscopic Emission Survey in a Subsonic ICP Flow, in: AIAA 2008-3911, 2008.

[15] Asma, C. O., Helber, B., Di Lello, L., Panerai, F., and Magin, T., Infrared thermography measurements on ablative thermal protection systems for interplanetary space vehicles, in: 10th Quantitative Infrared Thermography Conference, Quebec City, Canada, 2010.

[16] Helber, B., Asma, C. O., Babou, Y., Chazot, O. and Magin, T. E., Experimental Investigation of the Material Response of Carbon Composite Ablators in the VKI Plasmatron Facility, in: AIAA-2011-2302, 2011.

[17] Helber, B., Babou, Y., Panerai, F., Chazot, O., Hubin, A., and Magin, T. E., Investigation of the gas-surface interaction of innovative carbon composite ablators in the VKI Plasmatron, in: 7th European Aerothermodynamics Symposium, Brugge, Belgium, 9-12 May, 2011.

[18] Bottin, B., Chazot, O., Carbonaro, M., van der Haegen, V., Paris, S., The VKI Plasmatron Characteristics and Performance, in: RTO AVT Course on Measurement Techniques for High Enthalpy and Plasma Flows, published in RTO EN-8, Belgium, 1999.

[19] Lachaud, J., Mansour, N. N., Microscopic scale simulation of the ablation of fibrous materials, in: AIAA paper 2010-984, 2010.

[20] de Muelenaere, J., Lachaud, J., Mansour, N. N., and Magin, T. E., Stagnation line approximation for ablation thermochemistry, in: AIAA paper 2011-3616, 2011.

[21] Kolesnikov, A. F., Conditions of Simulation of Stagnation Point Heat Transfer from a High-enthalpy Flow, Fluid Dynamics 28 (1) (1993) 131–137.

[22] Barbante, P. F., and Chazot, O., Flight Extrapolation of Plasma Wind Tunnel Stagnation Region Floweld, Journal of Thermophysics and Heat Transfer 20 (3) (2006) 493–499.

[23] Degrez, G., Vanden Abeele, D. P., Barbante, P. F., and Bottin, B., Numerical Simulation of Inductively Coupled Plasma Flows under Chemical Non-equilibrium, International Journal of Numerical Methods for Heat and Fluid Flow 14 (4) (2004) 538–558.

[24] Barbante, P. F., Degrez, G., and Sarma, G. S. R., Computation of Nonequilibrium High Temperature Axisymmetric Boundary-Layer Flows, Journal of Thermophysics and Heat Transfer 16 (4) (2002) 490–497.

[25] Panerai, F., Aerothermochemistry Testing of Thermal Protection Systems, Ph.D. thesis, von Karman Institute for Fluid Dynamics / University of Perugia (2012).

[26] Park C., Effects of Atomic Oxygen on Graphite Ablation, AIAA Journal 14 (11) (1976) 1640–1642.

[27] Capitelli, M., Gorse, C., Longo, S., and Giordano, D., Collision Integrals of High-Temperature Air Species, Journal of Thermophysics and Heat Transfer 14 (2) (2000) 259–268.

Modeling of Inductively Coupled Plasma Reactor for Nanoparticles Production

Silvânia Lopes

Aeronautics and Aerospace Department, von Karman Institute for Fluid Dynamics, Belgium, lopes@vki.ac.be

Supervisor: Patrick Rambaud

Associate Professor, Aeronautics and Aerospace Department, von Karman Institute for Fluid Dynamics, Belgium, rambaud@vki.ac.be

University Supervisor: Jean-Marie Buchlin

Professor, Université Libre de Bruxelles, Belgium, buchlin@ulb.ac.be

Abstract

The general purpose of this thesis is to design an inductively coupled plasma (ICP) reactor for efficient production of nanoparticles at industrial scale. In the present work, a mathematical model has been developed for simulating the formation of nanoparticles in an ICP reactor. The model describes the evolution of the particle size distribution accounting for particle nucleation and growth by condensation and coagulation, using the method of moments. The effects of the quenching mechanism on the temperature fields and on the formation of the nanoparticles is investigated. The results show that the cooling efficiency has a strong impact on the final particle size.

Keywords: ICP plasmas, nanoparticles synthesis, CFD modeling

Nomenclature

d_1	Atomic size of the particle (m)
d_m	Particle mass diameter(m)
m_1	Mass of the atom
D_j	Diffusion coefficient of particle of size j
j	The size of the particle
j^*	Critical nucleus size
k_B	Boltzmann constant
m	Mass of particle
M_k	Moments of order k^{th}
n	Concentration of particle (m^{-3})
n_0	Initial concentration of monomers (m^{-3})
n_s	Vapor concentration at saturation (m^{-3})
S	Supersaturation ratio
T	Temperature
$\vec{u}$	flow velocity
w_1	Initial metal vapor concentration (m^{-3})
μ	Flow viscosity
λ	Mean free path
ρ	Density
Θ	Dimensionless surface energy
$slpm$	standard liter per minute

1. Introduction

Nanotechnologies, especially nanoparticles related applications, have recently received tremendous interest due to the great innovative potential they offer. Nanomaterials are usually produced by compaction of nanoparticles powder. They are characterized by a larger number of grain boundary interfaces in which the local atomic arrangements are different from those of the crystal lattice [1]. The small size of the nanoparticles is also responsible for many changes in the thermo-physical properties compared with the bulk materials, which makes them suitable for novel applications. Examples of these new properties include lower melting temperature, improved hardness and ductility, high self-diffusion coefficient, catalytic activity, and intriguing optical and electronic properties. However, the processes used to generate those nanoparticles play an important role in terms of particles size, morphology, crystalline phase and composition, which fundamentally determine the properties of the nanostructure material.

Thermal plasma processing, and in particular

high-frequency inductively coupled thermal plasmas (ICTP), have shown several distinctive advantages over other synthesis routes for nanoparticles. Due mainly to its high temperature and energy density, as well as the large plasma volume and long residence/reaction time, it is considered relatively easy, in principle, to evaporate all injected micro particles and then to quench and condensate the vapors to obtain the desired nanoparticles [2]. Additionally, an ICTP is generated without any internal electrodes and therefore inherently free of contamination and it offers the possibility to work under a controlled atmosphere.

In spite of all these advantages related to ICTP, neither the precise control of the particle size, distribution and morphology nor mass production has been successfully achieved in practice. The effects of the plasma torch and quenching parameters, including reactor design and configuration, on the flow field and on the formation of the nanoparticles appear to be of enormous importance [3].

Modeling studies can play an important role in the development and improvement of the nanoparticles synthesis processes, providing an insight into the phenomena involved and helping to identify the right operating conditions to employ. However, a full theoretical description of particles dynamics in plasma flows within an actual industrial environment is very complex. A complete model of such a system requires the solution of the fluid mechanics equations of continuity, momentum and energy, coupled with the electromagnetic field equations, which describe the generation of the plasma flow; with the description of micro particles evaporation in plasma flow; and with the aerosol dynamics equations, describing the nanoparticles formation. Nanoparticles are formed by numerous coexisting mechanisms, such as nucleation, condensation, coagulation, surface reaction, and coalescence or sintering. Several methods have been developed to represent the evolution of a population of particles, droplets or bubbles in a flow fields. These population balance methods often use statistical techniques based on moments of distribution. Among these methods of moments, the method developed by Frenklach [4] (MOMIC-Method of Moments with Interpolative Closure) has been one of the most used to represent the evolution of nanoparticle from a vapor phase. It remains still a simple, effective and easy method to implement. It can be used in a system within presence of nucleation, Brownian coagulation, condensation, thermophoresis, chemical reactions and aggregates which allows to describe the morphology of the powders produced.

In the previous study, an extended-field Computational Fluid Dynamic (CFD) model for simulating the behavior of inductively coupled plasma torches (ICPTS) had been implemented using the open source code, OpenFOAM. The model has been used to study the effects of operating conditions and torch design on the velocity and temperature fields in the ICP torch. Moreover, estimations of the particle residence time and accumulative heat for the different operating conditions has been done to evaluate the best conditions for particle evaporation. In this study, the plasma CFD model has been partially coupled with the nanoparticles model, which describes the formation of nanoparticles from a plasma vapor flow. The model is applied to the zone of the plasma reactor where nucleation and growth occurs, i.e, well below the hot plasma core, where the gases are cooled and the vapor can supersaturate and condense. Fig. 1 shows the schematic of the ICP reactor used in this study.

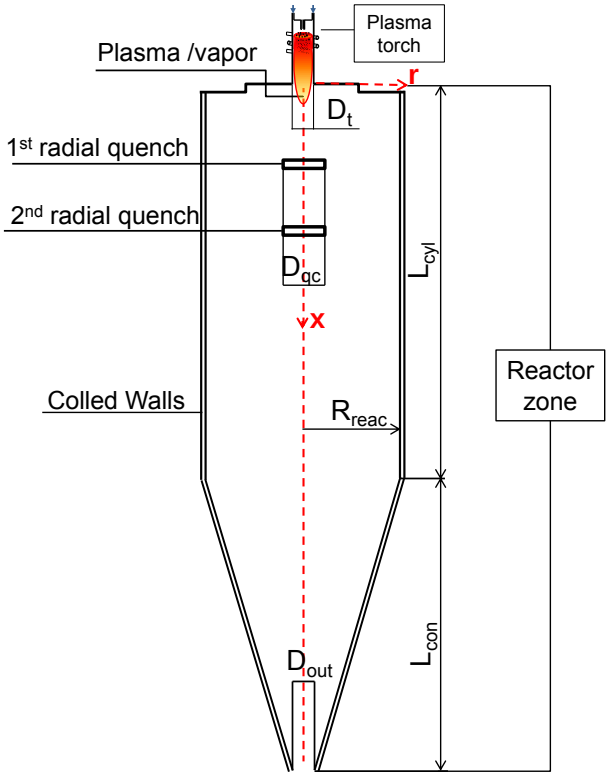

Figure 1: Schematic of the ICP plasma reactor

2. Model description

Up to this point, the overall model developed to optimize ICP reactor design consists of two parts. The

first part concerns the modeling and design of inductive argon plasma, used for synthesis of the nanoparticles. It essentially presents the fluid dynamics of the plasma flow in the presence of an electromagnetic field. Since on this work we focus on the nucleation and growth of metal vapor, the plasma flow itself is not included in the analysis. The second part deals with the formation of nanoparticles accounting for nucleation and growth by coagulation of the metal vapor in the reactor zone, considering different mechanisms of transport.

2.1. Nanoparticle Model

In the reactor zone, the metal vapor created in the plasma zone is quenched and converted in nanoparticles. To describe this phenomenon several assumptions are introduced:

- instantaneous homogeneous nucleation,
- the particles follow the fluid flow,
- the particles are spherical,
- Brownian coagulation in free molecular regime, because of the small size of the particles,
- nanoparticle size with a log-normal distribution,
- the only growth mechanism is coagulation.

The particle size distribution functions (PSDFs) of nanoparticles are obtainable by solving the general dynamic equation for aerosol growth (Eq. 1), taking into account the contribution of the different mechanisms (nucleation, coagulation, thermophoresis and diffusion).

$$\vec{\nabla}\cdot(\vec{u}n_j) = \overbrace{-\vec{\nabla}\cdot(\vec{u}_{th}n_j)}^{thermophoresis} + \overbrace{\vec{\nabla}\cdot(D_j\nabla n_j)}^{diffusion} + \overbrace{I j^{*}\delta_{j-j^{*}}}^{nucleation} + \underbrace{\frac{1}{2}\sum_{i=j^{*}}^{j-1}\beta_{i,j-1}n_i n_{j-1} - n_j\sum_{i=j^{*}}^{\infty}\beta_{i,j}n_i}_{coagulation} \quad (1)$$

2.1.1. Particle nucleation

According to the classical theory [5], homogeneous nucleation is the formation of particles from a supersaturated vapor, which is caused by the fast cooling of the gas. For the present model, the nucleation rate is given by the expression developed by Girshick [6]:

$$I = \frac{\beta_{11}n_s^2 S}{12}\sqrt{\frac{\Theta}{2\pi}}\left(\Theta - \frac{4\Theta^3}{27ln^2 S}\right) \quad (2)$$

where S is the supersaturation pressure, β_{11} is the Brownian coagulation coefficient between two manometers and Θ the dimensionless surface energy.

2.1.2. Particle Growth-Coagulation

Coagulation is the interparticle phenomenon wherein nanoparticles collide with one another, due to a relative motion between them and adhere to form a larger particle. After the instantaneous nucleation, the particles coalesce due to the brownian movement. Because most of the particles are smaller than the mean free path, the typical Knudsen numbers vary between 20 and 2000; therefore the Brownian motion is assumed in free molecular regime. It is characterized by $Kn >> 1$; in this case, the frequency of collision is expressed by the following expression presented by Frenklach [4]:

$$\beta_{i,j} = 2.2\sqrt{\frac{6k_BT}{4\rho}}\left(\frac{3m_1}{4\pi\rho}\right)^{\frac{1}{6}}\sqrt{\frac{1}{m_i}+\frac{1}{m_j}}\left(m_i^{\frac{1}{3}}+m_j^{\frac{1}{3}}\right)^2 \quad (3)$$

2.1.3. Thermophoresis

This phenomenon appears as a result of the gradient of temperature experienced by the particles in flow [5]. The thermophoresis velocity is independent of the particle size in the free molecular regime and is represented by:

$$\vec{u_{th}} = -\frac{0.55\mu}{\rho T}\vec{\nabla}T \quad (4)$$

2.1.4. Brownian Diffusion

In case of small particles flowing in the high temperature zones of the rector, the Brownian motion becomes important. The diffusion coefficient of particle of size d_j is then given by [7]:

$$D_j = \frac{k_BT}{3\pi\mu d_j}\left(1+\frac{3.31\lambda}{d_j}\right) \quad (5)$$

2.2. Method of Moment

It is generally difficult to solve Eq. 1 because of its nonlinearity. The method of moment reformulates the problem into a small set of differential equations describing the evolution of the moments of the PSDFs.

The *kth* moment M_k is defined as

$$M_k = \frac{1}{\rho n_0}\sum_{i=j^{*}}^{\infty} j^k n_j \qquad (k = 0, 1, 2, ...) \quad (6)$$

The moments of the size distribution are normalized with respect to the density ρ and the initial monomers concentration n_0 at the entrance of the reactor. The moments M of order 0 and 1 are the number concentration and mass of the particles in a given volume, respectively. The moment of order 2 is also known to be proportional to the light scattering by the nanoparticles when they have much smaller size than the wavelength of the incident light. Therefore, the definition of the moments of size distribution leads to the formulation of conservation equations (Eq. 1) in terms of moments (Eq. 7)

$$\frac{\partial(\rho M_k)}{\partial t} + \vec{\nabla}\cdot(\rho\vec{u}M_k) = -\vec{\nabla}\cdot(\rho\vec{u_{th}}M_k) + \vec{\nabla}\cdot(\rho\overline{D}\vec{\nabla}M_k) + \underbrace{\frac{I}{n_0}(j^*)^k}_{nucleation} + \underbrace{\frac{\rho^2 n_0}{4}\left[k^2+k-2\right]\Phi_{0,0}M_{k/2}^2}_{coagulation} \quad (7)$$

These conservation equations can be solved with the flow equation to describe the spatial distribution of the moments in the flow field.

The conservation of manometer in vapor phase is obtained by the mass balance over the aerosol and the vapor, as follow:

$$\frac{\partial(\rho\omega_1)}{\partial t} + \vec{\nabla}\cdot(\rho\vec{u}\omega_1) = \vec{\nabla}\cdot(\rho D_1\vec{\nabla}\omega_1) - Ij^*m_1 \quad (8)$$

For the moments of order k the contribution of nucleation and coagulation can be obtained directly by:

$$\frac{d(\rho M_k)}{dt}(nucl) = \frac{I}{n_0}(j^*)^k \quad (9)$$

and

$$\frac{d(\rho M_0)}{dt}(coag) = -\frac{\rho^2 n_0}{2}\phi_{0,0}M_0^2 \quad (10)$$

$$\frac{d(\rho M_1)}{dt}(coag) = 0 \quad (11)$$

$$\frac{d(\rho M_2)}{dt}(coag) = \rho^2 n_0 2\phi_{0,0}M_0^2 \quad (12)$$

In this study, the moment method is used for the first three moments of the PSDF. Using the hypothesis of log-normal particle size distribution, it is possible to calculate the different moments of the particle size distribution in a close form using only the first three moments of distribution. The collision coefficient $\phi_{0,0}$ is estimated by logarithmic interpolation of the reduced moments $\mu = M_r/M_0$ of fractional order. This method was proposed by Frenlach and Harris and it is detailed in Refs [4] [8].

Total concentration	M_0
Mass of particles	M_1
Mass diameter	$d_1 M_{1/3}/M_0$
Mean surface	$s_1 M_{2/3}/M_0$
Mean volume	$v_1 M_1/M_0$

Table 1: Principal physical properties of PSDFs

The principal physical properties of the PSDF (mass mean diameter, standard deviation) are obtained from the moments distributions, as defined on table 1 [5]. Therefore, a closed system of equation can be obtained to describe the evolution of the moments distribution in function of its own properties.

3. Model implementation

3.1. Reactor geometry and initial conditions

The nanoparticle model is applied to the reactor illustrated in Fig. 1 with the quenching mechanism. This ICP reactor has been developed in the von Karman Institute for nanoparticles production at industrial scale. The model is used to study the importance of the quenching on the final size of the particles. The quenching system consist of two quenching units, positioned perpendicularly to the plasma jet axis. This quench design type has been also simulated by [9]. The geometry is considered as 2D axisymmetric, specified as a wedge of a 5 degree angle and one cell thickness along the plane of symmetry (Fig. 2). The quenching inlet is therefore a uniform slot (which

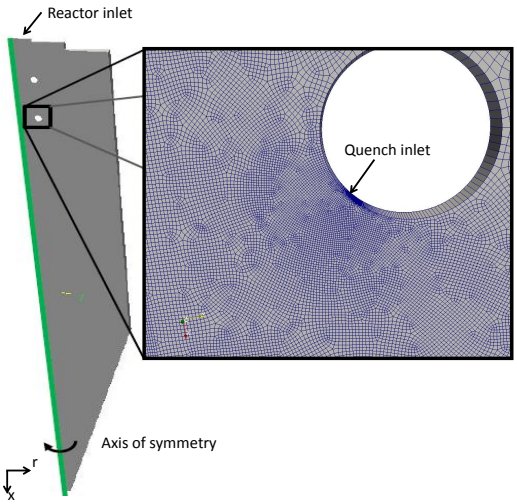

Figure 2: Axisymmetric geometry and reactor mesh.

corresponds to an annular injection around the quench

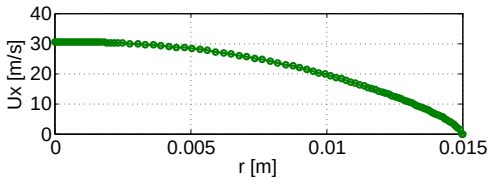

(a) Axial velocity

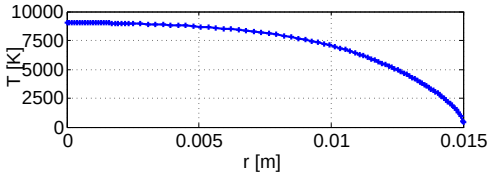

(b) Temperature

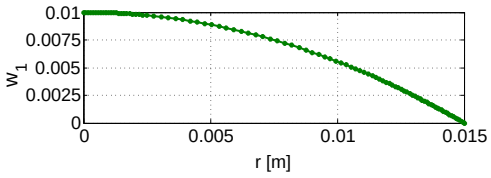

(c) vapor concentration

Figure 3: Inlet profiles at the entrance of the reactor.

unit) of equivalent diameter of the real radial quench inlets. The positions of the first and second quench units, and its respective intensity and injection angle had been previously study in order to determine the better conditions for fast cooling without a large perturbation of the flow.

In all the cases studied, the profiles at the entrance of the reactor are from the exit conditions of the inductive plasma torch solution for $5kW$ of dissipated power, $0.96g/s$ of argon mass flow and 1% of metal vapor (Fig. 3).

3.2. Simulations

Before analyzing the effects of the quench design on the nanoparticles formation, some numerical parameters has been investigated to obtain satisfactory convergence and stability. The grid size dependency has been analyzed, together with different numerical schemes and solver controls. The k-Omega SST and k-Epsilon models have been also implemented and analyzed for the expansion of the plasma jet into the reactor zone. The results obtained show that the k-Omega SST is more suitable, predicting satisfactory behavior for the plasma jet. In contrast, with the k-Epsilon models the plasma jet suddenly extinguishes after entering the reactor, as can be seen in Fig. 4.

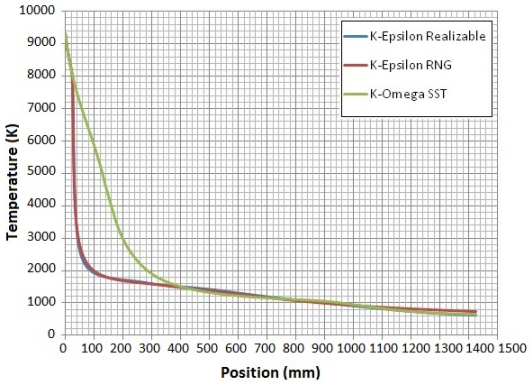

Figure 4: Static Temperature along the Axis for different turbulence models

The presence of strong turbulence in the particle formation zone is expected to affect the transport of the vapor and thus the trajectories of the nanoparticles. Shigeta and Nishiyama [10] have reported that turbulence must be accounted for even for relatively small overall Reynolds numbers. The plasma jet flame is often wavering and unstable accompanied with drastic heat/species transfer.

The gas flow temperature, velocity and concentration fields, together with the moments equations are then solved, in the reactor zone, assuming steady state, in turbulence regime modeled by k-Omega SST model and at atmospheric pressure. Thereafter, the effects of quenching rate, number position and angle are investigated.

4. Results and Discussion

Three different design conditions are presented. In the first case the reactor (No Quench) does not have any quench, only cold walls in the rector zone. In the second case (1 Quench) only one quench unity is considered, positioned at $95mm$ from the the reactor entrance, with 35 slpm of argon quenching gas injected with $45°$. The third reactor (2 Quench) uses a second similar quench units with $100mm$ distance from the first one and with 30 slpm of argon quenching gas. Figure 5 presents the temperature and the axial velocity contours for the three cases. As can be seen, the presence of the quenching units not only determines the cooling of the plasma jet but also has a strong effect on the flow trajectory, and therefore on the diffusion of the vapor in the reactor (Figure 7). The introduction of the first quench unit creates a shielded

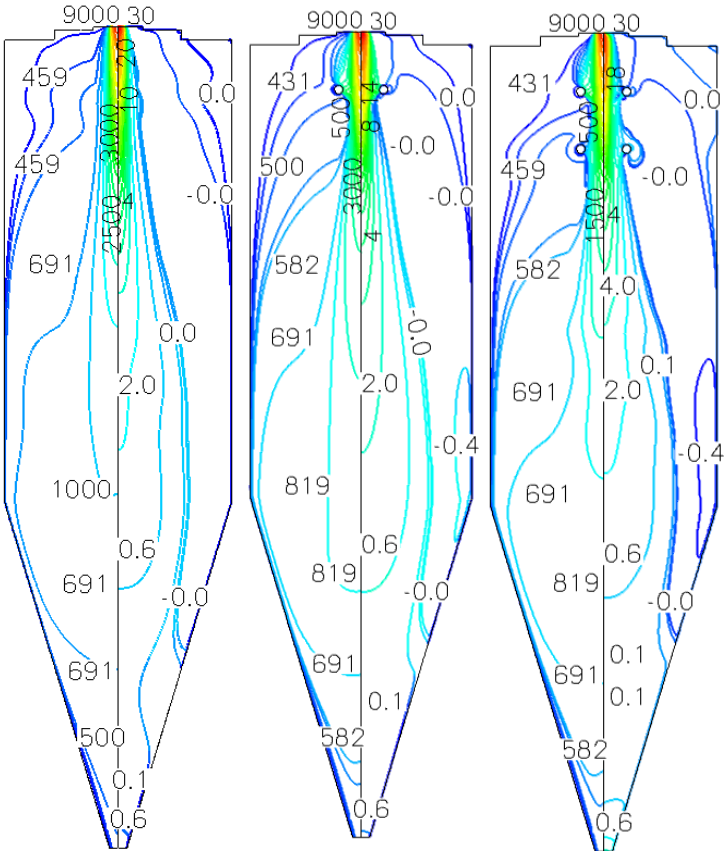

(a) No Quench (b) 1st Quench (c) 2nd Quench

Figure 5: Temperature contours [K] (left); Axial velocity [m/s] (right)

zone, keeping the vapor at the center of the reactor and favoring the stabilization of the flow. On the other hand, the second quench increases the cooling rate but also creates a small recirculation zone around its location. Fig. 6 shows the effects of the quench on the temperature fields in the reactor by plotting the axial profile of temperature at center line and the radial profile at $x = 0.4m$ for the cases of no quench, one stage and two stage quench, respectively. As expected, the injection of gas strongly affects the the temperature field by promoting a fast cooling of the flow. The concentration of vapor is reduced when the nucleation begins and also by dilution in case of quench injection. The temperature field and the vapor concentration indicate where the particles are formed or nucleation occurs. The temperature fields in the reactor establish the vapor pressure which influences the nucleation rate and strongly determines the coagulation and the thermophoresis terms.

Figure 8 shows the contours of the mean mass diameter with the concentration of particles for the three cases. The mean mass diameter is a physical property of PSDF in terms of moments, given by $d_m = d_1(M_{4/3}/M_0)$. Where d_1 is the atomic size of the particle, $M_{4/3}$ and M_0 are calculated moments. After the nucleation, the primary particles continue to grow due to the coagulation process. The effects of the quench design on the average mass diameter and particle concentration at the exit of the reactor can be seen in Fig. 8. The fast cooling introduced by the quenching units causes a decrease of the exit mean diameter. In case of no quench, large particles are formed near the walls ($\approx 50nm$) and the amount of formed particles is therefore lower. These results confirm the strong influence of quench design on the control of the particle size distribution. Similar results have been achieved by [7], [10] and [9], showing the dependence of the final particle size on the applied quenching.

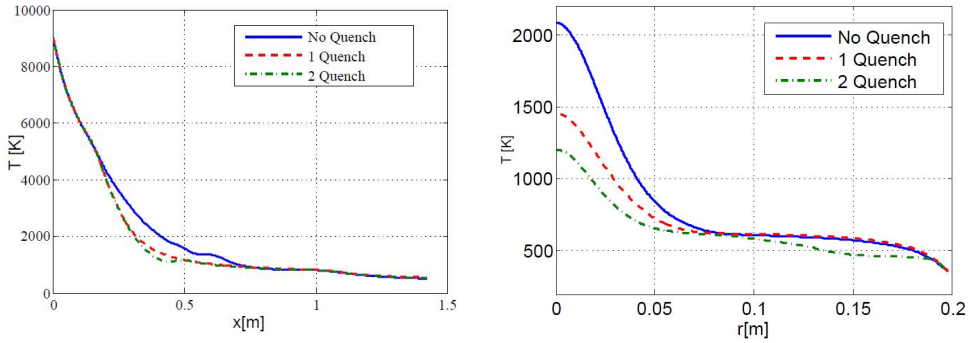

(a) at r= 0m (b) at x= 0.4m

Figure 6: Axial and radial temperature profiles

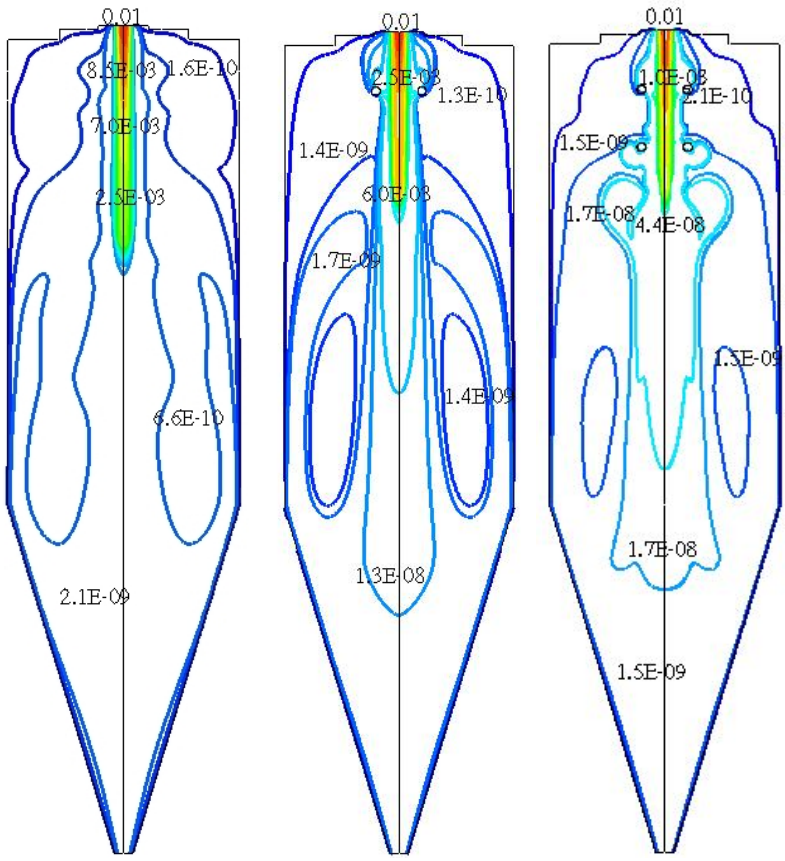

(a) No Quench (b) 1st Quench (c) 2nd Quench

Figure 7: Vapor mass fraction contours

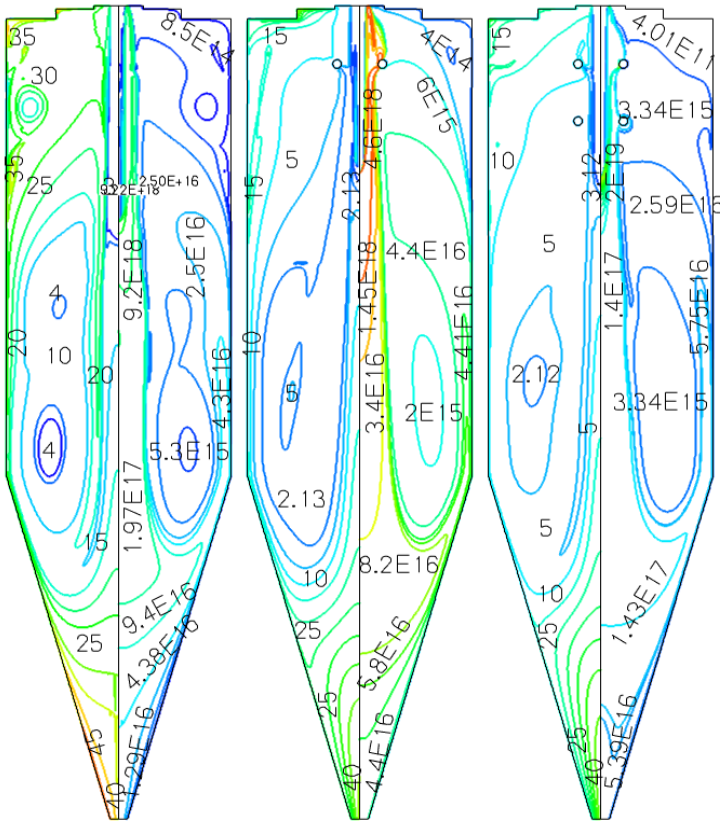

(a) No Quench (b) 1st Quench (c) 2nd Quench

Figure 8: Left: Average Mass Diameter [nm]; Right: Concentration of particles [m^{-3}]

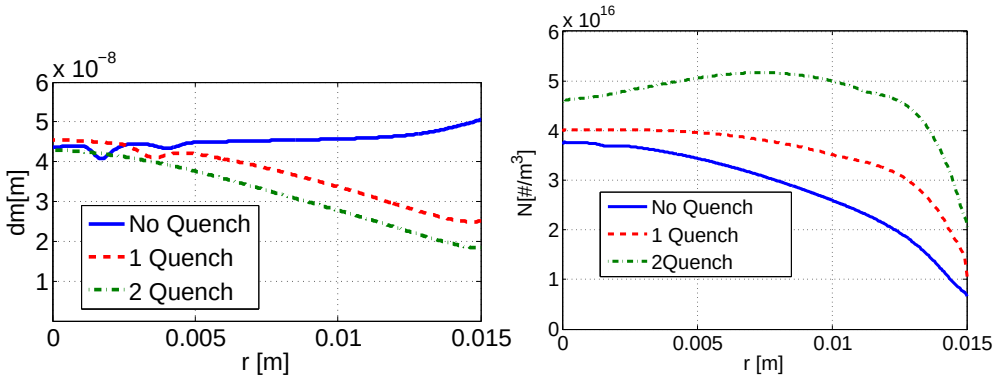

(a) Average Mass Diameter (m) (b) Concentration of particles (m^{-3})

Figure 9: Effects of the quench units at the exit of the reactor

5. Conclusion

The mathematical model was developed to simulate the formation of nanoparticles in an ICTP reactor. The model can be applied to study the importance of many parameters on the size distribution of the particles and morphology. In this present work, numerical investigation using the model was conducted to clarify the effects of the quenching flow. The results show that the quench strongly affects the temperature distribution in the reactor and consequently has a decisive impact on the final particle size. The diameters obtained at the exit of the reactor are between 40 and 50nm for the case without quench, 23 and 45nm using one quench unit and between 12 and 45nm using the double quench unit. This present model is limited to particles in free molecular regime and to nucleation and coagulation mechanism of growth. As reported by [7], the final size diameter does not change from considering only coagulation growth process. Although the condensation mechanism seems to have a dominant contribution in the growth, the overall growth mechanism is balanced.

The further extension of the model will include the condensation mechanism of growth, as well as a solid particle aggregation model. Different quench positions, intensities and injection angles will be also investigated in order to optimize the reactor design and the controlling of the final particle size.

Acknowledgments

I would like to thank my supervisor Patrick Rambaud, professor Pierre Proulx from the university of Sherbrooke and all the VKI NanoParticle project group for their help and support on this project. This work is supported by the Region Wallonne.

References

[1] S. L. Girshick, C. P. Chiu, R. Muno, C. Y. Wu, L. yang, S. Singh, P. McMurry, Thermal plasma synthesis of ultrafine iron particles, J. Aerosol Sci. vol. 24, No 3 (1993) pp– 367–382.

[2] E. Pfender, Y. C. Lee, Particle dynamic and particle heat and mass transfer in thermal plasmas. part i. the motion of a single particle without thermal effects, Plasma Chemistry and Plama Processing Vol.5, No 3 (1985) pp.211–237.

[3] N. Mendoza-Gonzalez, B. Goortani, P. Proulx, Numerical simulation of silica nanoparticles production in an rf plasma reactor: Effect of quench, Materials Science and Engineering C vol.27 (2007) pp.12651269.

[4] M. Frenklach, Method of moments with interpolative closure, Chemical Engineering science 57 (2002) 2229–2239.

[5] W. C. Hinds, Aerosol Techology, Wiley, 1999.

[6] S. L. Girshick, C. P. Chiu, Kinetic nucleation theory: A new expression for the rate of nucleation from an ideal supersatureted vapor, J. Chem. Phys. 93 (1990) 1273–1277.

[7] N. Mendoza-Gonzalez, M. E. Morsli, P. Proulx, Production of nanoparticles in thermal plasmas: A model including evaporation, nucleation, condensation and fractal aggregation, Journal of Thermal Spray Technology 17(4) (2008) 533–550.

[8] P. Proulx, J.-F. Bilodeau, A model for ultrafine powder production in a plasma reactor, Plasma Chemistry and Plama Processing vol.11 No 3 (1991) 371–385.

[9] C. Schreuders, Syntèse par plasma inductif de nanometriques de silicium optimization de la trempe, Ph.D. thesis, Universite de Limonges (2006).

[10] M. Shigeta, H. Nishiyama, Numerical analysis of metallic nanoparticle synthesis using rf inductively coupled plasma, Journal of Heat transfer - Transactions of the ASME vol.127 (November 2005) pp.1222–1229.

Ground Testing Methodologies Improvement in Plasma Wind Tunnels using Optical Emission Diagnostics

Alessio Cipullo

Aeronautics and Aerospace Department, von Karman Institute for Fluid Dynamics, Belgium, alessio.cipullo@vki.ac.be/alessio.cipullo@unina2.it

Supervisor: Olivier Chazot

Associate Professor, Aeronautics and Aerospace Department, von Karman Institute for Fluid Dynamics, Belgium, chazot@vki.ac.be

CIRA Supervisor: Federico De Filippis

Senior Research Engineer, Thermo-Structures Design and Experiments Department, CIRA, Italy, f.defilippis@cira.it

University Supervisor: Luigi Zeni

Professor, Information Engineering Department, Second University of Naples, Italy, luigi.zeni@unina2.it

Abstract

The characterization of the flow produced by CIRA SCIROCCO and VKI Plasmatron plasma wind tunnels was performed. The peculiar features of the two plasmas were addressed using optical emission spectroscopy, photomultiplier spectroscopy and high speed camera imaging. The temperature and total enthalpy were measured and compared to results from traditional diagnostics. Finally, the critical aspects and future perspectives are discussed.

Keywords: plasma, arc-jet, ICP, optical emission spectroscopy, photomultiplier spectroscopy, high speed camera imaging

1. Introduction

The development of new aerospace vehicles for future planetary exploration is a challenging task and involves a wide range of scientific and industrial expertise. One of the most important aspects is the appropriate design and implementation of Thermal Protection Systems (TPS). In this framework, the accurate reproduction of atmospheric entry phenomena in ground facilities for testing purposes is imperative. Nowadays, different technologies exist to produce plasma flows suitable for aerothermodynamic testings of TPS and the most popular are arc-jet wind tunnels and inductive coupled plasma (ICP) torches [1]. The technology adopted to get the plasma discharge is the key feature and it heavily influences the plasma flow aerothermochemistry. In arc-jets, the gas mixture is heated up by means of a DC discharge between two electrodes. Corrosion phenomena of the electrodes inner surface can introduce impurities in the flow. In ICPs, the gas is heated up by Joule effect inside a quartz tube, where a RF cylindrical discharge is generated. Because of the electrodeless design, the plasma is characterized by high purity. However, the power supply technology can be a source of undesirable unsteady heat and mass transfer phenomena in the flow.

The present work focuses on the experimental investigation of the flow produced by the two major European plasma facilities: SCIROCCO [2], [3] and Plasmatron [4], [5]. The first is a 70 MW arc-jet plasma wind tunnel and it is located at the Italian Aerospace Research Center (CIRA), the second is a 1.2 MW ICP torch and it is located at the von Karman Institute (VKI) for fluid dynamics. The peculiar features of the two types of plasma were addressed using optical emission diagnostics. In particular, Optical Emission Spectroscopy (OES) and Photomulti-

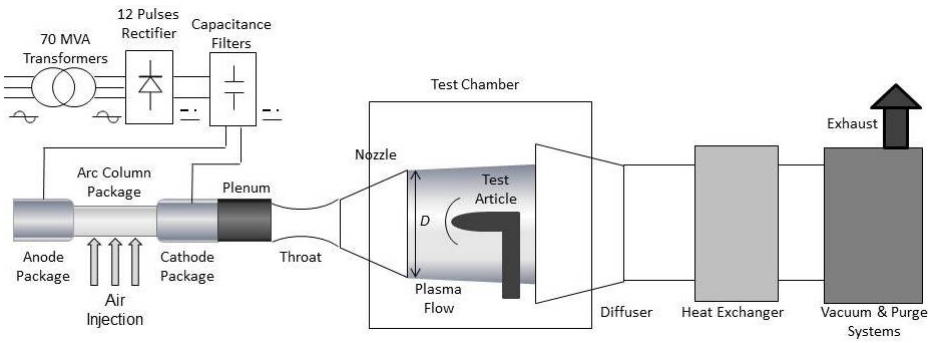

Figure 1: Simplified scheme of the CIRA SCIROCCO plasma wind tunnel with nozzle exit section diameter D=1150 mm. Side View.

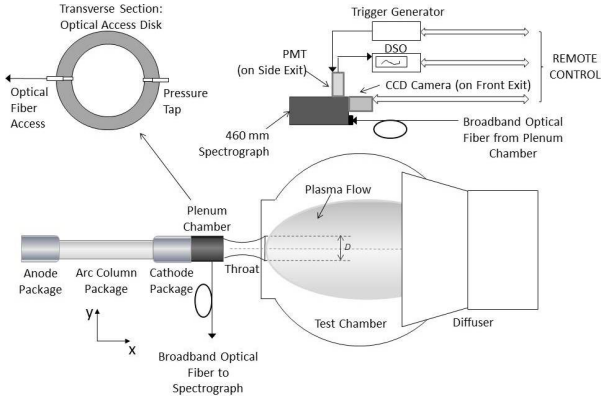

Figure 2: Simplified scheme of the experimental set-up for the CIRA SCIROCCO plasma wind tunnel (AURORA configuration, D=187 mm). View from the top.

plier Tube (PMT) spectroscopy were applied in the CIRA SCIROCCO plenum chamber for a set of conditions between 14.6 MW and 31.4 MW input electrical power. High Speed Camera (HSC) imaging and OES were applied to the VKI Plasmatron free-stream flow for a set of input electrical power between 120 kW and 300 kW. The above mentioned optical diagnostics were coupled to intrusive diagnostics in both cases. The final aim of the work is to investigate the total enthalpy determination methodologies in the two facilities.

Section II is dedicated to the experimental set-up. The description of the applied elaboration procedures is undertaken in section III. The experimental results are presented in section IV. The last part is dedicated to conclusions and future perspectives.

2. Experimental Set-up

2.1. CIRA SCIROCCO

SCIROCCO is the biggest and most powerful segmented constrictor type arc-jet facility worldwide. It uses a 70 MW DC power supply to ignite and sustain the electric arc into its 5500 mm long constricted-arc heater, between the anode and cathode packages (see Fig. 1). The constrictor internal diameter is 110 mm. The DC power is obtained through a cascade of high power transformers and a 12 pulses rectifier, fed by a dedicated high voltage AC line (50 Hz). After the rectification stage, a set of capacitance filters are used to smooth the conversion ripple. The nominal levels for DC voltage and current are V=30 kV and I=9000 A respectively. The cold gas mixture, made up of air and argon, is injected in the arc column in distributed locations using a swirling pattern. The maximum air mass flow rate is m_{air}=3.5 kg/s and the total pressure in the arc heater can reach P_0=17 bar. The gas is heated up by the arc and expanded through the nozzle. It then enters an evacuated test chamber, where the test article is placed. The nozzle exit diameter can be changed between D=187 mm and D=1950 mm, according to five different configurations. For the considered set of test conditions, two exit diameters were used: D=187 mm (AURORA configuration, where only the throat section is installed) and D=1150 mm. The pressure in the chamber is typically set to 0.10 mbar. The nominal flow Mach number is 12. Hot gas exits through a 50 m long diffuser and is cooled down by an active heat exchanger, before going to the 80 MW vacuum system and the purge unit to remove polluting products (such as NO_x). Although the nominal mass-averaged total enthalpy is H_0=45 MJ/kg, for typical test conditions H_0 is usually below 20 MJ/kg. Further details about SCIROCCO can be found in [2] and [3].

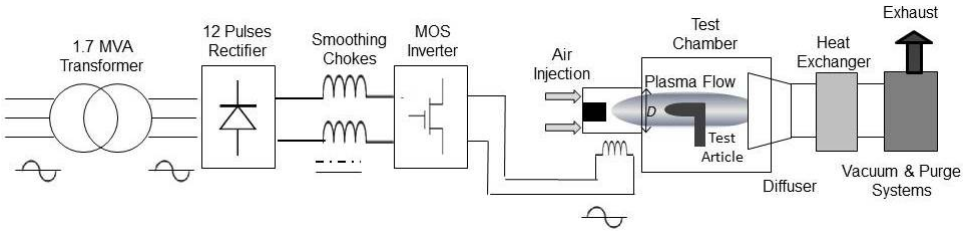

Figure 3: Simplified scheme of the VKI Plasmatron plasma wind tunnel with nozzle exit section diameter D=160 mm. Side View.

The experimental set-up is described in Fig. 2. The OES was performed using a silica optical fiber (200-1000 nm) looking directly at the internal part of the plenum chamber through an SMA connector and an integrated quartz window. The optical access disk is placed ~ 180 mm upstream the throat inlet section and its internal diameter is 172 mm. The diameter of the fiber core was 600 μm and the numerical aperture was 0.22 ± 0.02. The optical fiber was chosen to maximize the collected light intensity from the plasma. The light from the plasma was brought to the front entrance of a Jobin-Yvon HR460 spectrograph, having a focal length of 460 mm and a grating resolution of 1200 groves/mm. Spectral components were recorded using a Symphony CCD camera placed at the spectrograph front exit. It was characterized by a 1024×256 pixel matrix (with pixel dimensions of 26×26 μm). The entrance slit was set to 0.001 mm. Preliminary investigations in the wavelength range 200-1000 nm showed that N and O emission lines were dominant for the conditions of interest. Therefore, the analysis range was limited to 670-900 nm. The spectrum was calibrated in absolute intensity using a low power halogen source Avantes AvaLight-DHc. The wavelength calibration was performed using a low pressure mercury (Hg) lamp. The resolution was determined from the Hg lamp as well and it resulted in 0.1 nm Full Width Half Maximum (FWHM), which was not sufficient to resolve the single lines of the Oxygen triplet at 777 nm.

The PMT spectroscopy was applied to the plasma in the plenum chamber to investigate the temporal evolution of the emission signature. The optical fiber channel was used again to couple the light to the front entrance slit of the spectrograph (Fig. 2). A mirror was used inside the spectrograph to switch the diffracted light from the front exit (where the CCD camera was placed) to the side exit (where the PMT was placed). The grating was set to a central wavelength of 777 nm, to capture the temporal evolution of the light intensity associated to the O triplet. The spectral range was estimated to be about 20 nm. The entrance and exit slit were both set to 0.1 mm. The shutter was left open. The PMT was a Hamamatsu H7680 with a spectral range going from 400 nm to 900 nm and a bialkali photocathode. The gate/trigger signal to the PMT was provided through an Agilent 33120A 15 MHz waveform generator. Whereas, the output signal was acquired by means of an Agilent DSO6034A oscilloscope. The sampling frequency was set to 400 kHz and the acquisition interval to 2 s. The automatic control and acquisition were performed remotely using LabView.

The total pressure was measured using a Validyne P55A (0-22 bar range) connected to a pressure tap located on the optical access disk as well (Fig. 2). The mass-averaged total enthalpy (H_0) was measured applying a heat balance method, following the procedure outlined in [6] and [7]. In such method, H_0 is determined by dividing the total power input by the mass flow rate of the test gas. The total power input is the electrical power minus the Joule heating loss in the ballast resistors used for current regulation and the cooling water loss. The mass-averaged total enthalpy was also determined using an improved version of the ARCFLO code. Details about the code can be found in [8] and [9].

2.2. VKI Plasmatron

The VKI Plasmatron facility is the biggest and most powerful ICP torch worldwide. It uses a 1.2 MW RF power supply to ignite and sustain the plasma discharge. First of all, the 11 kV, 50 Hz voltage level coming from the network is adapted using a 1.7 MVA transformer (Fig. 3). The output signal is then rectified using a 12 pulses bridge and smoothed using chokes. The nominal values of DC voltage and current are 250 V and 5000 A respectively. A 1.2 MW, 400 kHz MOS inverter is then used to feed a single turn flat coil inductor. The RF cylindrical discharge is

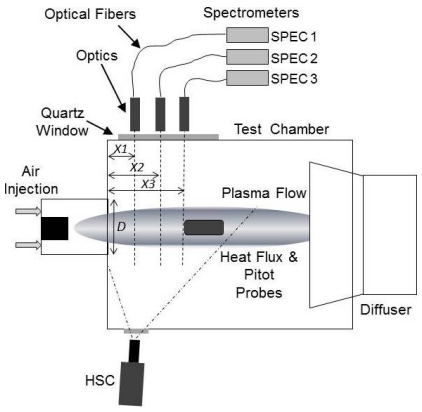

Figure 4: Simplified scheme of the experimental set-up for the VKI Plasmatron plasma wind tunnel. View from the top.

generated inside the torch composed of a quartz tube with an internal diameter of 200 mm and 5 mm thickness, and a cold-cage of D=160 mm internal diameter consisting of water-cooled copper segments inserted inside to prevent from severe overheating. The plasma discharge is ignited using a small amount of argon. The cold gas mixture (air at 16 g/s for the test conditions of interest) is then injected in an annular way into the quartz tube and heated up by Joule effect. The plasma enters the test chamber, where the test article is placed. In the case of interest no nozzle was installed (see Fig. 3) and the plasma jet was subsonic. The chamber is usually kept at a pressure between 15 mbar and 200 mbar, depending on the testing conditions. The plasma exits through a diffuser and it is cooled down by a water cooled heat exchanger. The vacuum system is composed by a roots pump and a set of three rotating vanes pumps. After proper dilution, the products are finally released to the atmosphere through an exhaust. The overall facility is equipped with a cooling system using a closed loop deionized water circuit coupled to fan coolers. See [4] and [5] for further details.

The experimental set-up is sketched in Fig. 4. The HSC imaging was performed using a Vision Research Phantom v7.0 CMOS camera (Fig. 4). The camera is characterized by a depth of 8 bit and the sensor is in black and white. The camera was equipped with a wide-angle VIS objective (12 mm focal length) to ensure the complete visualization of the plasma flow. The image resolution was set to 256×608 pixels and the acquisition rate was set to 13.16 kHz. The resulting acquisition interval was ~ 0.34 s for a total number of 4504 acquired frames.

Three Ocean Optics HR4000 spectrometers were looking at the plasma centerline for three different distances from the nozzle exit section: $x_1 = 19.5$ cm, $x_2 = 32$ cm and $x_3 = 44.5$ cm (1.2, 2 and 2.8 nozzle diameters D=160 mm respectively). The HR4000 spectrometer was characterized by a wavelength range of 200-1100 nm. The light was coupled to the spectrometer through a plano-convex fused silica lens and a quartz optical fiber (Ocean Optics QP600-SR/BX). The optical system was arranged according to the Newton's law for thin lenses to focus a collimated beam of light passing through the plasma centerline onto the fiber entrance. The beam of light had a diameter of ~ 2 cm, low enough to consider the emitted radiation at the three distances x_1, x_2 and x_3, uniform for the conditions of interest. The optical fibers were characterized by a 600 μm core diameter and an optimized numerical aperture to match the entrance slit of the spectrometer. The spectra were acquired using a 0.5 Hz repetition rate. The intensity calibration was performed in relative units combining a deuterium lamp in the UV (DH-2000 Mikropack) and a tungsten ribbon lamp in the VIS and NIR (OSRAM Wi 17/G). The wavelength calibration was performed using a low pressure Hg lamp (Oriel 6060). The Hg lamp was used to determine the spectral resolution as well and it resulted in ~ 0.9 nm FWHM. Each HSC movie was synchronized with the first spectrum acquired from the three spectrometers using a pulse generator.

The voltage output from the 12 pulses rectifier was monitored using a LeCroy LT584 oscilloscope at 100 kHz sampling frequency and 2 s acquisition interval. The oscilloscope was coupled with a calibrated 10× voltage probe. The heat flux (q_{cw}) was measured using a copper calorimeter embodied in a standard copper probe and the dynamic pressure (p_d) was measured by a Pitot probe [10]. Heat flux and pressure were the input for the VKI rebuilding code [11], which was used to retrieve the free stream temperature and enthalpy. Reference catalycity (γ_{ref}) and non-dimensional parameters were taken from [10]. Notice that both probes were injected 445 mm downstream the nozzle exit section, right at the location of the optical path at $x_3 = 445$ mm (see Fig. 4).

3. Elaboraton procedures

3.1. OES in the plenum chamber

The investigation of the thermodynamic state of the plasma flow produced by SCIROCCO is a challenging task. Due to the strong expansion through the

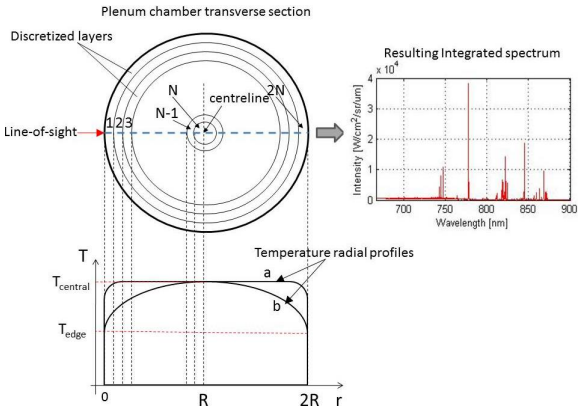

Figure 5: Simplified scheme of the procedure for the radial temperature profile extrapolation from line-of-sight measurements

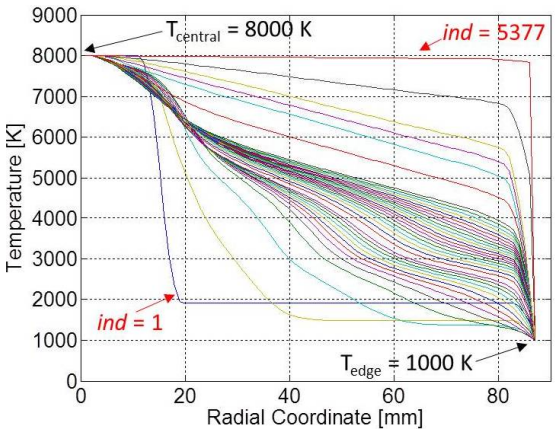

Figure 6: Example of radial temperature profiles extracted from ARCFLO. $T_{central}$ = 8000 K, T_{edge} = 1000 K

nozzle, the free-stream plasma is far from Local Thermodynamic Equilibrium (LTE) [12]. Therefore, the measurement of the total enthalpy using OES in free-stream is extremely difficult. However, before the plasma undergoes the compression-expansion phase (in the plenum chamber), it is still subsonic and the high P_0 (in the range 3.5 - 6.8 bar for the test cases of interest) promotes the thermalization of the energy level distributions according to the classical Boltzmann function. If the hypothesis holds true, the total enthalpy radial profile can be directly determined from the temperature profile. Furthermore, the mass averaged total enthalpy (i.e. one of the key parameters for ground testing) is known once temperature and velocity profiles are available. Of course, the LTE assumption is questionable. First of all, the effect of the electrical discharge located ~ 320 mm upstream the optical access disk in the cathode package could be non-negligible. Both the mere presence of the discharge and the arc root motion could promote non-equilibrium (NLTE). Moreover, there is the possibility that the thermodynamic conditions are non-uniform along the plenum chamber radius, as pointed out in [13]. Finally, the possibility of NLTE cannot be ruled out. Nevertheless, the elaboration procedure presented hereafter, which allowed to retrieve an estimation of the temperature and total enthalpy (h_0) profiles, is based on the assumption of LTE along the plenum chamber radial coordinate. The reliability of such assumption will be discussed together with the experimental results.

The chosen strategy consists of fitting the experimental calibrated spectrum with a theoretical spectrum, which is the result of the line-of-sight integration of simulated spectra according to a guessed parametric radial temperature profile. It is interesting to report that in similar works (such as [13]-[15]) the simplest approach was used regarding spectral emission: radial uniformity. A simplified scheme is presented in Fig. 5 to clarify the procedure. The transverse plane of the plenum chamber was discretized in $2N$=172 concentric disks. Because the plenum internal diameter is D_{pl}= 2 · R_{pl} =172 mm, the discretization step was 1 mm. The temperature profile was assumed axisymmetric with respect to the centerline. Furthermore, the thermodynamic features were assumed uniform within each single layer. The typical temperature radial profile shapes were extracted from ARCFLO and they were characterized by three parameters: central profile temperature i.e. temperature on the axis ($T_{central}$), temperature at the profile edges (T_{edge}) and a unique index associated to the particular shape of the profile (*ind*). In Fig. 5, two radial profiles are presented, just to show the difference between a fully developed profile (a) and a non-developed one (b). The developed profile corresponds to the uniform radial spectral emission case.

From Fig. 6 it is possible to appreciate a selection of temperature profiles (presented here for the sake of example) characterized by $T_{central}$ = 8000 K, T_{edge} = 1000 K and *ind* ranging from 1 to 5377. Indeed, the total number of profile shapes used for the spectral fittings was 5377. Index equal to 1 represents the case of starting profile, with the plasma condensed around the axis, where the electrical arc is located. Conversely, *ind* = 5377 represents the fully developed case and the example intermediate profiles represent the transition

between the two extremes. The set of 5377 profiles used for the fittings were considered representative of all the possible profiles the temperature can assume within the plenum chamber.

The spectral fitting was performed by minimizing the two parameters RMS error ($RMSE$) function, defined as in Eq. 1 [12]:

$$RMSE(T_{central}, ind) = \sqrt{\frac{\sum_{i=1}^{M}(S_{exp}(i) - S_{th}(i))^2}{M}}. \quad (1)$$

where M is the total number of spectral points, S_{exp} is the calibrated and normalized experimental spectrum and S_{th} is the normalized theoretical spectrum obtained from the integration of the theoretical spectra associated to each one of the discretized layers along the line-of-sight (see Fig.5), according to their own temperatures. T_{edge} was kept constant at 1000 K for the test cases of interest, following the approach outlined in [9]. The S_{th} which minimizes the the $RMSE$ function automatically gives back the resulting temperature radial profile. It is important to underline that the experimental calibrated spectrum is exactly the integrated light emission along the optical path. The theoretical spectra were obtained using the freeware Specair 2.2 [16] and the mole fractions for O and N species were obtained using the CEA code for LTE calculations [17].

A basic assumption of the aforementioned approach is that the optical fiber is collecting light along the optical path only, despite the fact that the numerical aperture is not 0 (i.e. 0.22 ± 0.02). However, between the plenum chamber wall surface and the fiber tip there is a 53 mm long cylindrical channel with opaque surfaces and 1.8 mm diameter. A test was performed using a VIS-NIR source coupled with the optical fiber, to ensure that the rays entering the hole with angles different from 0° did not reach the fiber acceptance cone. Conversely, the rays orthogonal to the plenum chamber internal surface were allowed to reach the fiber tip and to be guided to the spectrograph.

The radiation model took into account the NIR self-absorption [18]. The emission intensity at the $n-th$ discretized layer (refer to Fig. 5) and generic wavelength λ ($I_n(\lambda)$) was expressed as Eq. 2:

$$I_n(\lambda) = B_\lambda(T_n)[1 - exp(-k'_n(\lambda)L)] + I_{n-1}(\lambda)exp(-k'_n(\lambda)L). \quad n = 1, 2, ..., 2N. \quad (2)$$

where $B_\lambda(T_n)$ is the Planck blackbody function (depending on the temperature of the $n-th$ layer T_n), $k'_n(\lambda)$ is the absorption coefficient corrected for stimulated emission and L is the $n-th$ layer width (it was constant for the case of interest and equal to 1 mm). This is an iterative procedure: the emission from the $n-th$ layer depends on the emission from the layers between 0 and n-1. Additional details about the procedure can be found in [18].

3.2. PMT spectroscopy in the plenum chamber

The PMT spectroscopy was applied in the plenum chamber of the SCIROCCO facility to investigate the temporal evolution of the plasma flow optical emission. The time signal from the PMT was simply analyzed in the frequency domain applying a FFT transform [12]. Both arc root motion and power supply conversion ripple could induce unsteady heat and mass transfer in the flow, resulting in emission oscillations. In the first case, the random nature of the phenomenon will yield no specific spectral signature. Conversely, the 12 pulse rectifier introduces a frequency component at 600 Hz (the network frequency times the number of pulses: 50×12 Hz = 600 Hz) plus its harmonics. Additionally, the 50 Hz component itself (plus harmonics) could be found in the spectrum. The analysis of the FFT will tell how efficiently the capacitance filters and the high P_0 level in the plenum chamber damp the emission oscillations.

3.3. HSC imaging in free-stream

The investigation of the VIS optical emission field at high speed allowed to have a qualitative picture of the unsteady heat and mass transfer occurring in the plasma flow produced by VKI Plasmatron. The analysis of the acquired frames allowed to point out the effect of the test chamber pressure (p_{tc}) both in time and frequency domains [19]. Furthermore, the FFT analysis was applied to investigate the frequency components of the emission oscillations and a comparison was performed with the FFT of the voltage signal acquired by the oscilloscope at the output of the rectifier. The frequency analysis range was limited to 6.58 kHz (half of the acquisition rate 13.16 kHz, to fulfill the Nyquist criterion). However, it resulted sufficient to include the relevant frequency components for all the operating conditions of interest.

3.4. OES in free-stream

The temperature is one of the key physical quantities in plasma flow characterization and it is the starting point for the total enthalpy determination. The

peculiar features of the subsonic flow produced by the VKI Plasmatron facility make the task challenging. The unsteady heat and mass transfer induced by the RF power supply promotes intense mixing in the flow and a potential NLTE condition or a non-uniform thermodynamic state condition along the radial coordinate. Furthermore, the test chamber pressure and the power level could play a significant role in the definition of the boundary between LTE and NLTE conditions. The aforementioned issues were addressed by taking them from the other way around: the LTE assumption was taken for all the test cases of interest and the results were critically analyzed to check back the validity of the preliminary hypothesis.

The plasma flow temperature was measured by fitting the calibrated experimental spectra with theoretical spectra generated through Specair 2.2 [16] using the LTE approach. The best fit was obtained by minimizing the RMSE function defined in Eq. 1. In that case, S_{th} is the theoretical spectrum at the LTE temperature T_{LTE}. Of course, the RMSE is a function of T_{LTE} only in the present case. The attention was focused on the spectral region between 300 nm and 450 nm, where CN, N_2 and N_2+ mostly emit. The presence of the CN was due to carbonaceous impurities in the test gas. The mole fractions were generated using the VKI MUTATION library [20]-[22]. Preliminary investigations were performed including the self-absorption model offered by Specair 2.2 [16]. However, no significant difference was appreciated against the thin plasma case for the temperature range of interest.

Table 1: Test conditions matrix - CIRA SCIROCCO test campaign

Test	I	m_{air}	P_{el}	P_0	H_{0HB}	H_{0AF}
	A	kg s^{-1}	MW	bar	MJ kg^{-1}	MJ kg^{-1}
1	2014	0.70	14.8	3.5	11.6	11.63
2	2715	1.00	23.2	5.0	12.5	13.11
3	2806	1.30	27.0	6.3	11.7	13.00
4	2889	1.31	27.9	6.3	12.0	13.27
5	3801	1.29	36.0	6.8	14.1	15.50
6	3805	1.30	36.2	6.8	14.1	15.50
7	4024	0.84	31.3	4.7	16.6	17.08

An important aspect to be considered is that the presented experimental set-up only allowed to measure line-of-sight spectra at the plasma centerline. No deconvolution methods (such as Abel inversion) could be applied to retrieve the radial temperature profile. However, the two methodologies can be considered equivalent when the plasma is approximated by an uniform and homogeneous column. Therefore, if the temperature gradients along the radius are sufficiently low, while greatly simplifying the analysis procedure, the use of line-of-sight spectra would not produce any noticeable temperature difference with respect to the one obtained through de-convolution methods. To validate such hypothesis, the radial temperature profiles were obtained for one selected operating condition (P=200 kW and p_{tc}=100 mbar) at x_1 and x_3 distances. The spectra were acquired during a previous test campaign at the VKI Plasmatron and the temperature was retrieved by applying the same fitting procedure described in the present subsection. The maximum temperature difference found between the centerline and the plasma edges was $\sim$ 800 K ($\sim$ 10% of the centerline temperature), therefore the line-of-sight approach could be considered reliable. The detailed description of the experimental set-up and calibration process can be found in [23].

The second major issue is related to the unsteady nature of the plasma flow. The fluctuations in the plasma correspond to optical emission fluctuations and in turn to temperature fluctuations. Because of the spectrometers limited sampling frequency (i.e. 0.5 Hz), only stationary phenomena could be investigated. Indeed, the spectrometer acquires a spectrum which is the integration of all the spectral signatures emitted during the exposure time, according to the temperature evolution. Unfortunately, the integrated (i.e. averaged) spectrum does not correspond in general to the spectrum at the average plasma temperature. The distribution of the energy levels is influenced by the temperature of course, but it is not possible to establish any simple relation between the latter and the associated spectral signature. The issue will be further discussed in Section IV, along with the experimental results.

4. Experimental results

4.1. OES in the plenum chamber

The test campaign performed in the CIRA SCIROCCO facility consisted of seven operating conditions. The relevant parameters and the results from the fitting procedure are reported in Table 1. The test cases are listed for increasing values of arc current. The nominal conditions for test 5 and 6 were equal: the acquisitions were performed in the context of the same run within 2 minutes. That allowed to investigate the short term repeatability of the measurements.

P_{el} is the electrical power, H_{0HB} is the mass averaged total enthalpy obtained through heat balance method and H_{0AF} is the one from ARCFLO. The maximum measurement errors (combination of statistical,

Table 2: Results from fitting procedure - CIRA SCIROCCO test campaign

Test	$T_{central}$ K	$\Delta T_{central}$ K	ind -	Δind -	$RMS\,E_{min}$ -	$\Delta RMS\,E_{min}$ -	$h_0(r=0)$ MJ kg^{-1}	$\Delta h_0(r=0)$ MJ kg^{-1}
1	7780	117	5267	49	0.0125	1.7596e-4	29.6	1.45
2	7470	73	5336	15	0.0068	2.0172e-4	24.1	0.85
3	7590	134	5209	20	0.0065	1.1547e-4	24.4	1.54
4	7580	83	5235	31	0.0059	1.7650e-4	24.3	0.95
5	7820	75	5225	16	0.0068	2.0633e-4	26.6	0.87
6	7860	110	5202	12	0.0074	1.8974e-4	27.1	1.28
7	8360	88	5228	22	0.0164	1.9295e-4	34.6	1.06

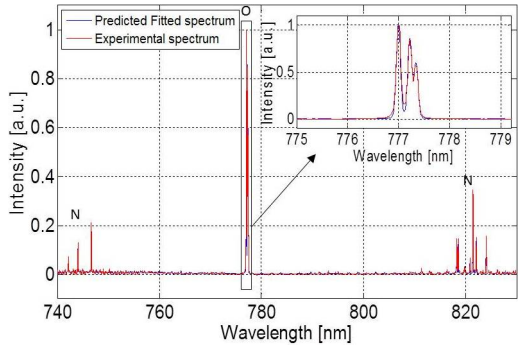

Figure 7: Fitting result for test 2 in the range 740-830 nm - CIRA SCIROCCO test campaign

instrumental and measurement chain errors) for the listed quantities were: ΔI = 100 A, Δm_{air} = 0.035 kg/s, ΔP_{el} = 21 kW, ΔP_0 = 0.11 bar and ΔH_{0HB} = 1.5 MJ/kg. It is extremely important to underline that the H_{0AF} is in the error band of H_{0HB} for all the test cases under investigation.

The spectral fitting was performed in the range 740 - 830 nm. The result from the spectral fitting for test 2 is reported in Fig. 7 as example. From the zoom, it is possible to observe the satisfactory fitting of the

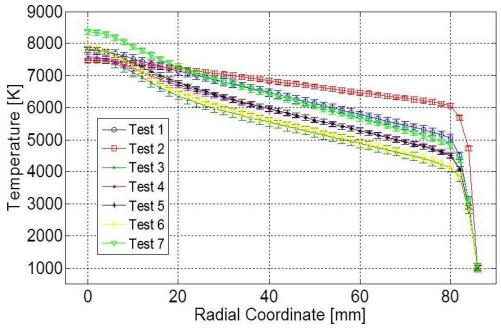

Figure 8: Temperature radial profiles in the plenum chamber - CIRA SCIROCCO test campaign

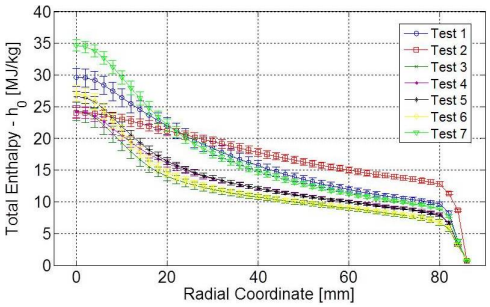

Figure 9: Total enthalpy radial profiles in the plenum chamber - CIRA SCIROCCO test campaign

oxygen triplet (although it is not completely resolved). The results of the fittings for the entire test matrix are reported in Table 2. $RMS\,E_{min}$ is the minimum of the RMSE function obtained from the fitting procedure, $h_0(r=0)$ is the total enthalpy at the centerline and it was determined from $T_{central}$ using CEA [17]. The measurement errors for $T_{central}$, ind and $RMS\,E_{min}$ (i.e. $\Delta T_{central}$, Δind and $\Delta RMS\,E_{min}$) were obtained in accordance to the procedure described in [12]. The sensitivity distribution [12] was computed for all the test cases. A unique absolute minimum was observed i.e. the fitting procedure results can be considered reliable.

The temperature radial profiles and the associated total enthalpy profiles for the test matrix are reported in Fig. 8 and Fig. 9 respectively. The profiles in test cases 5 and 6 were not in agreement within the error bar for the whole radius. Therefore, according to present results, temperature and total enthalpy were not fully repeatable in the short term.

Once the total enthalpy radial profile is known, it is possible to determine H_0 by applying Eq. 3 [24]:

$$H_0 = 1/m_{air} \cdot \int_0^{R_{pl}} 2\pi h_0(r)\rho(r)u_x(r)dr. \qquad (3)$$

where $\rho(r)$ is the plasma density in kg/m^3 and $u(r)$ is the velocity profile along the x axis in m/s (see Fig. 2). The plasma density profile was determined from CEA using the temperature profile as input. Conversely, the velocity profile could not be determined directly either from ARCFLO (it only provides the velocity in the arc column) or OES (because of the poor spectral resolution). Finally, H_0 cannot be determined from OES at the present stage.

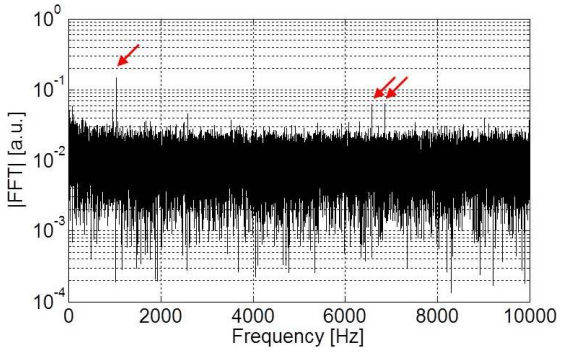

Figure 10: FFT modulus of the signal acquired from PMT - Test case 1

4.2. PMT spectroscopy in the plenum chamber

The PMT spectroscopy was applied only for test case 1 and 7 (the extremes) and the modulus of the FFT transform is presented in Fig. 10 for test case 1 as an example. The signal is normalized by the DC value and it is plotted only up to 10 kHz, because no relevant spectral features were observed for higher frequencies. The components indicated by the arrows were detected in the background signal as well (i.e. with plasma off): they were probably related to the electrical noise in the conditioning circuit. It is possible to observe that no 50 Hz or 600 Hz components (plus harmonics) were detected inside the plenum chamber (same conclusions for the test case 7), meaning that the capacitance filters damped them significantly. Furthermore, intensity was about ~ 2 order of magnitude lower than the DC for all the frequency components. Finally, the plasma can be considered temporally homogeneous within the plenum chamber and such conclusion is in accordance to the investigation performed in free-stream and reported in [25].

4.3. HSC imaging in free stream

The operating conditions and the results for the test campaign conducted in the VKI Plasmatron are summarized in Table 3. Heat flux (q_{cw}) and dynamic pressure (p_d) are included and their maximum measurement error is $\sim 10\%$. The mass flow rate was fixed to 16 g/s. The HSC imaging was applied to all the conditions and an example of normalized standard deviation (σ) distribution at 200 kW for the five pressure cases is reported in Fig. 11. At lower pressure (15 mbar) the emission oscillations were transported far in the flow. As the pressure rises, the oscillations were increasingly damped and most of the heat and mass transfer occurred close to the nozzle exit section. The distances at which the three spectrometers were looking at the plasma are indicated in Fig. 11 with dashed lines (lines 1, 2 and 3 correspond to x_1, x_2 and x_3 distances respectively). It is worth noting that, especially at 15 mbar, the spectrometer at x_1 was looking at a region with a significant fluctuations magnitude; i.e. the plasma could not be considered stationary in such region. In the subsection 4.4, the issue will be addressed. Furthermore, the mean radiation distribution (not presented here) showed that the plasma shrinks as the pressure rises. This resulted true for all the power settings. Although no analysis is presented here, the power level played a role as well: increasing the power, the heat and mass transfer was promoted. However, such effect was less marked than the one related to p_{tc}.

Table 3: Test conditions matrix and results - VKI Plasmatron test campaign

Test	P kW	p_{tc} mbar	m_{air} g s^{-1}	q_{cw} kW m^{-2}	P_d Pa	γ_{ref} -	$T(x_1)$ K	$T(x_2)$ K	$T(x_3)$ K	T_e K
1a	120	15	16	323.94	118.14	0.1	-	5986	-	3764
1b	160	15	16	559.40	143.59	0.1	6524	6270	5974	4902
1c	200	15	16	778.44	182.78	0.1	6709	6578	6454	5238
1d	250	15	16	1054.37	231.92	0.1	-	6868	6623	5538
1e	300	15	16	1346.71	264.47	0.1	-	-	-	5858
2a	120	50	16	216.15	22.66	0.1	-	-	-	3164
2b	160	50	16	594.22	37.51	0.1	6703	6454	6236	5135
2c	200	50	16	778.31	53.24	0.1	6980	6675	6477	5381
2d	250	50	16	1061.41	77.62	0.1	-	6907	6680	5652
2e	300	50	16	1582.33	95.05	0.1	-	-	-	6143
3a	120	100	16	134.73	9.63	0.01	-	-	-	2694
3b	160	100	16	384.14	13.92	0.01	6541	6388	5958	4714
3c	200	100	16	814.00	26.43	0.01	6853	6594	6465	5720
3d	250	100	16	-	-	-	7110	6959	6770	-
3e	300	100	16	-	-	-	-	7164	7041	-
4a	120	150	16	115.38	4.13	0.005	-	-	-	2911
4b	160	150	16	532.65	8.31	0.005	6490	6359	6108	5471
4c	200	150	16	844.09	14.80	0.005	6858	6576	6458	5933
4d	250	150	16	1175,44	29,04	0.005	6939	6792	6623	6190
4e	300	150	16	1704,80	42,29	0.005	7388	6908	6856	6761
5a	120	200	16	208.46	6.31	0.005	-	-	-	3342
5b	160	200	16	293.63	8.56	0.005	6500	6390	6290	3737
5c	200	200	16	859.58	13.58	0.005	6830	6628	6523	5910
5d	250	200	16	1195.20	20.94	0.005	7131	6940	6708	6241
5e	300	200	16	1696.01	37.20	0.005	7374	7198	7118	6623

The standard deviation represents a global quantity and does not allow to study the evolution of the different frequency components of the fluctuations. Therefore, the comparison between the modulus of the FFT (normalized with respect to the DC value) of the voltage signal and the FFT of the emission oscillations at x_1 was performed. The aim was to study the effect of the conversion ripple against the plasma emission oscillations. The comparison at 200 kW is presented in Fig. 12 for pressure cases 15, 100 and 200 mbar as example. The conversion ripple components (50 Hz plus harmonics and 600 Hz plus harmonics) were totally transmitted into the flow for the 15 mbar case and

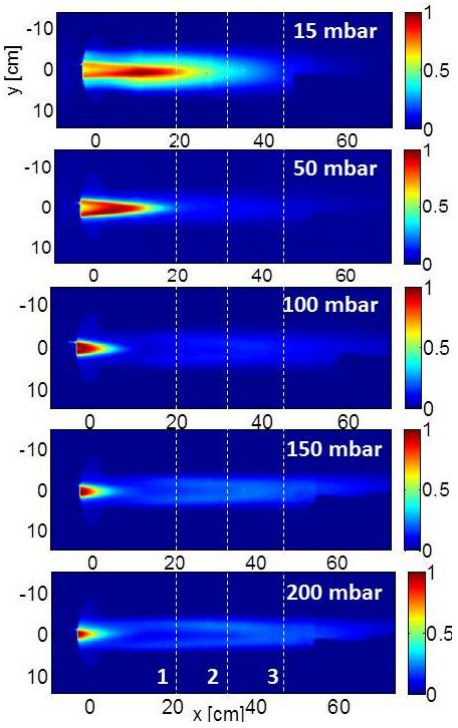

Figure 11: Standard Deviation distribution of the radiation oscillations for P=200 kW and m_{air}=16 g/s. Dashed lines 1,2 and 3 represent the distances x_1, x_2 and x_3.

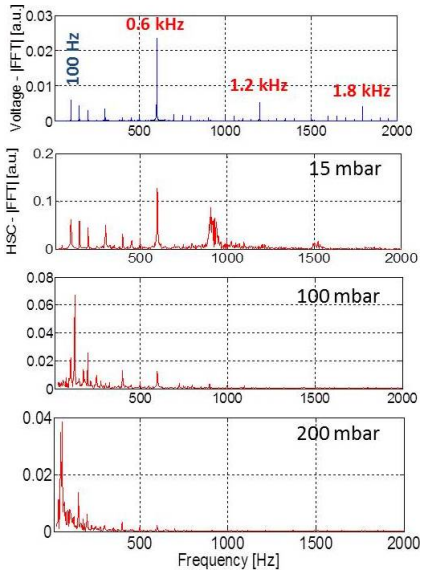

Figure 12: Comparison between voltage FFT and radiation oscillation FFT at x_1 for 15, 100 and 200 mbar cases. P = 200 kW

were clearly observable as emission radiation oscillations at x_1. The spectral content dramatically changed for higher pressures. The increase of pressure (i.e. inertia or matter) in the test chamber acted like a low pass filter with a decreasing cutoff frequency.

4.4. OES in free stream

The resulting temperatures at the positions x_1, x_2 and x_3 ($T(x_1)$, $T(x_2)$ and $T(x_3)$ respectively) are reported in Table 3 for all the test cases. The maximum error on the temperature was estimated to be $\sim$ 80 K. The free stream temperature (T_e) was rebuilt with the above mentioned VKI code [11] starting from the quantities in Table 3. It is important to underline that the probe was at 445 mm downstream the exit section of the nozzle, therefore T_e must be directly compared to $T(x_3)$.

An example of fitting result is presented in Fig. 13 for P= 200 kW and p_{tc}=100 mbar for the three spectrometers (test case 3c). The fitting was performed between 365 and 430 nm including the Δv=0 and -1 bands of the N_2+ first negative system and the Δv=0 band of the CN violet system. It is worth noting that the presence of the CN increased the fitting reliability: the relative weight between N_2+ first negative and CN violet Δv=0 bands is extremely sensitive to temperature. Figure 13 shows that the fitting quality was satisfactory for the three cases (and in general for all the test cases, although not presented here). However, it is important to underline that the quality increases with the pressure. It could be explained by a more efficient damping of the radiation oscillations at the spectrometers measuring point, inducing the plasma to go towards a stationary condition. Finally, the LTE assumption can be considered reasonable.

From Table 3, it is clear that no agreement exists between measured temperatures from OES and the ones from combined probe measurements and VKI rebuilding code. Such discrepancy is likely related to two main issues. The first one was the lack of knowledge regarding the γ_{ref} of the copper probes under different test conditions. Depending on the static pressure and power settings, T_e has a strong dependence on the value of γ_{ref} [10]. On the other hand, there was the effect of the radiation oscillations on the acquired spectra. As already mentioned, the experimental set-up allowed to record at a repetition rate (0.5 Hz) much lower than the typical frequency components of the plasma fluctuations. Therefore, the acquired spectra were in general not representative of the average temperature of the plasma flow. The resulting temperature from the fittings $T(x_3)$ could not directly compare to

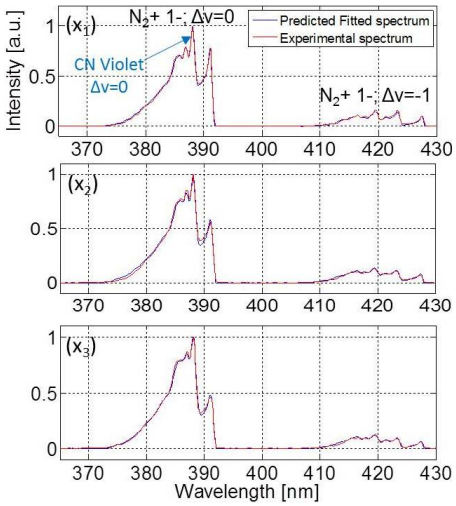

Figure 13: Spectral fitting results at x_1, x_2 and x_3 for P= 200 kW and p_{tc}=100 mbar

T_e, which was obtained by actual average measures of q_{cw} and p_d using the probes. Preliminary results from ongoing simulations (combining OES and HSC results) showed that the spectrometers could significantly overestimate the actual plasma temperature. In any case, the problem must be considered indeterminate at the present stage. The next step would be to use a time-resolved OES approach to capture the evolution of the spectral signature emitted from the plasma and measure the actual average temperature. Furthermore, such approach would allow to independently determine h_0 and the γ_{ref} of the copper probe for all the test conditions.

5. Conclusions

Optical emission diagnostics were applied for the flow characterization of the two major European plasma wind tunnels: CIRA SCIROCCO and VKI Plasmatron. The general aim of the work is to improve ground testing methodologies for Thermal Protection Systems (TPS) characterization. Seven operating conditions were tested in the SCIROCCO arc-jet facility, with a mass-averaged total enthalpy (H_0) ranging from 11.6 to 16.6 MJ/kg. H_0 was estimated using both a heat-balance method and an improved version of the ARCFLO simulation code. They resulted in agreement within error bars for all the test conditions. Furthermore, the radiation from the plenum chamber was analyzed using Optical Emission Spectroscopy (OES) and Photomultiplier (PMT) spectroscopy. Using an optical path reversal OES technique, the temperature and total enthalpy (h_0) radial profiles were obtained. The LTE assumption was adopted. Both profiles resulted non-uniform for all the test cases. Next step would be either to use simulations or absorption techniques, such as TDLAS (Tunable Laser Diode Absorption) or LIF (Laser Induced Fluorescence), to determine the velocity radial profile (u_x) in the plenum chamber. Knowing h_0 and u_x, it would be possible to determine H_0 by spectroscopy and finally validate both the optical path reversal technique and the LTE assumption against heat-balance method and ARCFLO results. The PMT spectroscopy was applied to the radiation from the plenum chamber as well. The attention was focused on the oxygen triplet (around 777 nm) and the repetition rate was 400 kHz. No significant frequency components were found in the spectrum, confirming the temporal homogeneity already pointed out for the free stream flow [25].

High Speed Camera (HSC) imaging and OES were applied to the free stream plasma produced by the VKI Plasmatron Inductive Coupled Plasma (ICP) torch. The operating conditions (25 in total) were characterized by an electrical power between 120 and 300 kW and a static pressure (p_{tc}) between 15 and 200 mbar. HSC imaging was used to point out the effect of the AC/DC ripple from the power supply on the plasma. The time domain analysis showed that p_{tc} is a driving parameter for the plasma instabilities. Furthermore, The FFT analysis showed that ripple components (50 and 600 Hz plus harmonics) were transported in the flow in different ways depending on the pressure. The facility acts like a low pass filter with cutoff frequency decreasing with increasing p_{tc}. Further investigations are ongoing. The spectra acquired from three positions along the centerline (1.2, 2 and 2.8 times the nozzle diameter D=160 mm) where used to measure the free-stream temperature. The LTE assumption was adopted and the fitting was performed on selected N_2+ first negative and CN violet bands. The quality of the fitting resulted satisfactory for the test cases, meaning that the LTE assumption can be considered reasonable. However, no agreement was found between OES and results obtained by combining heat flux and Pitot probe measurements with the VKI rebuilding code calculations [11]. The reason is likely due to both lack of knowledge regarding the reference catalycity (γ_{ref}) of the probes and the effect of the plasma oscillations on the spectral measurements. Due to the low repetition rate (0.5 Hz), the spectrometers were only able to acquire an integrated

spectrum over the radiation fluctuations occurring in the plasma. The resulting temperature could not be directly related to the average temperature obtained through the probe. The further step would be to use time-resolved spectroscopy techniques, such as intensified camera spectroscopy or TDLAS, to resolve the time evolution of the plasma temperature, determine h_0 and check back the γ_{ref} values.

Acknowledgments

The author would like to thank Campania Aerospace and CIRA for the Ph.D. grant; the VKI for the financial support during the Plasmatron test campaign; Bernd Helber and Francesco Panerai for their crucial contributions. Finally, thanks to both CIRA SCIROCCO and VKI Plasmatron groups.

References

[1] O. Chazot, R. Regnier and A. Garcia Munoz, Simulation Methodology in Plasmatron Facility and Hypersonic Wind Tunnels. Proceedings of the 12th International Conference on Method of Aerophysical Research, Novosibirsk, Russia, 2004. Published by "Nonparel", 2004, ISBN5-93089-005-6.

[2] G. Russo, F. De Filippis, S. Borrelli, M. Marini and S. Caristia, The SCIROCCO Plasma Wind Tunnel: a New Hypersonic Capability, Progress in Astronautics and Aeronautics 198 (2002) 315-351.

[3] S. Caristia, F. De Filippis, A. Del Vecchio and E. Graps, SCIROCCO PWT Facility for High Temperature Materials, Assembly Testing, Proceedings of 54th International Astronautical Congress, Bremen, Germany, 2003.

[4] B. Bottin, M. Carbonaro, S. Zemsch and G. Degrez, Aerothermodynamic Design of an Inductively Coupled Plasma Wind tunnel, no. AIAA 1997-2498, 32nd AIAA Thermophysics Conference, Atlanta, USA, 1997.

[5] B. Bottin, S. Paris, V. Van der Haegen and M. Carbonaro, Experimental and Computational Determination of the VKI Plasmatron Operating Envelope, no. AIAA 1999-3607, 30th AIAA Plasmadynamics and Lasers Conference, Norfolk, USA, 1999.

[6] C. Park, G. A. Raiche, II, D. M. Driver, J. Olejniczak, I. Terrazas-Salinas, T. M. Hightower and T. Sakai, Comparison of Enthalpy Determination Methods for Arc-Jet Facility, Journal of Thermophysics and Heat Transfer 20 (4) (2006) 672-679.

[7] T. M. Hightower, J. A. Balboni, C. L. Mac Donald, K. F. Anderson and E. R. Martinez, Enthalpy by Energy Balance for Aerodynamic Heating Facility at NASA Ames Research center Arc Jet Complex, Proceedings of 48th International Instrumentation Symposium, San Diego, CA, 2002.

[8] Aerotherm Corporation, ARCFLO Computer Code, Plasma Arc Heater Modeling, Aerotherm user manual 0713-93-011 (1993).

[9] K. H. Kim, O. H. Rho and C. Park, Navier-Stokes Computation of Flows in arc Heaters, Journal of Thermophysics and Heat Transfer, 14 (2) (2000) 250-258.

[10] F. Panerai, Aerothermochemistry Characterization of Thermal Protection Systems, PhD Thesis, von Karman Institute for Fluid Dynamics & University of Perugia (2011) (to be published).

[11] P. Barbante, G. Degrez, and G. S. R. Sarma, Computation of Nonequilibrium High Temperature Axisymmetric Boundary-layer Flows, Journal of Thermophysics and Heat Transfer, 16 (4) (2002) 490-497.

[12] A. Cipullo, L. Savino, E. Marenna and F. De Filippis, Thermodynamic State Investigation of the Hypersonic Air Plasma Flow Produced by the Arc-et Facility SCIROCCO, Aerospace Science and Technology (2011) (to be published. Available on line)

[13] D.G. Fletcher, Nonintrusive Diagnostic Strategies for Arcjet Stream Characterization, RTO AVT Course on Measurement Techniques for High Enthalpy and Plasma Flows, Rhode-Saint-Genese, Belgium, 1999 (published in RTO EN-8).

[14] M. A. Rob, L. H. Mack, S. Arepalli and C. D. Scott, Characterization of Plenum Spectra in an Arcjet Wind Tunnel, no. AIAA 95-2126, 30th AIAA Thermophysics Conference, San Diego, CA, 1995.

[15] J. M. Donohue, D. G. Fletcher and C. S. Park, Emission Spectral Measurements in the Plenum Chamber of an Arcjet Wind Tunnel, no. AIAA 98-2946, 7th AIAA/ASME Joint Thermophysics and Heat Transfer Conference, Albuquerque, NM, 1998.

[16] C. O. Laux, Radiation and Nonequilibrium Collisional-radiative Models. Physicochemical Modeling of High Enthalpy and Plasma Flows, von Karman Institute Lecture Series 2002-07, D. G. Fletcher, J.-M. Charbonnier, G. S. R. Sarma, T. Magin (Eds.), Rhode-Saint-Genese, Belgium (2002).

[17] B. J. McBride and S. Gordon, Computer Program for Calculation of Complex Chemical Equilibrium Compositions and Applications, NASA Users manual (1996).

[18] C. O. Laux, Optical diagnostics and radiative emission of air plasmas, Ph.D. thesis, Stanford University (1993).

[19] I. Benito, M. Aleo and Y. Babou, VKI Plasmatron Performances Investigations: I. Air Plasma Jet Time Dependant Behaviour, no. ESA SP-667, Proceedings of the 3rd International Workshop on Radiation of High Temperature Gases in Atmospheric Entry, Heraklion, Greece, 2008.

[20] T. E. Magin, A Model for Inductive Plasma Wind Tunnels, Ph.D. thesis, von Karman Institute for Fluid Dynamics, Belgium (2004).

[21] A. Munafo, M. Panesi, R. Jaffe, A. Lani and T. Magin, Vibrational State to State Kinetics in Expanding and Compressing Nitrogen Flows, no. AIAA 2010-4335, 10th AIAA/ASME Joint Thermophysics and Heat Transfer Conference, Chicago, IL, 2010.

[22] M. Panesi, Physical Models for Nonequilibrium Plasma Flow Simulations at High Speed Re-entry Conditions, Ph.D. thesis, von Karman Institute for Fluid Dynamics (2009).

[23] A. Cipullo, Plasma Flow Characterization by means of Optical Emission Diagnostics, Research Master project report, von Karman Institute for Fluid Dynamics (2010).

[24] A. B. Witte, Part I. Experimental Investigation of an Arc-Heated Supersonic Free Jet; Part Ii. Analysis of One-Dimensional Isentropic Flow for Partially Ionized Argon, Ph.D. Thesis, California Institute of Technology (1967).

[25] A. Cipullo, L. Savino, E. Graps, C. Purpura, L. Zeni and F. De Filippis, Investigation of Spatial and Temporal Flow Homogeneity in Arc-jet Plasmas using Intrusive and Non-intrusive Diagnostics, no. ESA SP-692, Proceedings of the 7th European Symposium on Aerothermodynamics for Space Vehicles, Bruges, Belgium, 2011.

NUMERICAL APPROACH FOR HYPERSONIC FLOW

Direct Simulation Monte Carlo in Reentry Flows

Erik Torres

Aeronautics and Aerospace Department, von Karman Institute for Fluid Dynamics, Belgium, erik.torres@vki.ac.be

Supervisor: Thierry Magin

Assistant Professor, Aeronautics and Aerospace Department, von Karman Institute for Fluid Dynamics, Belgium, thierry.magin@vki.ac.be

University Supervisor: Stefanos Fasoulas

Professor, Institute for Space Systems, University of Stuttgart, Germany, fasoulas@irs.uni-stuttgart.de

Abstract

The present project is focused on physical models applicable to the numerical simulation of rarefied gas flows. The main application considered in this work is the high-speed gas flow around vehicles returning from space at early stages of atmospheric entry. We to focus mainly on the improvement and extension of the physical models used with the most prevalent simulation technique for rarefied flows, the direct simulation Monte Carlo (DSMC) method. Specifically, the areas of interest include the high-fidelity modeling of internal energy exchange and chemical reaction processes occurring in the bulk gas, during its compression and heating in the bow shock region in front of the vehicle. The second topic to be studied is the influence of chemical reactions taking place at the surface of ablative materials on the gas flow.

Keywords: rarefied gas dynamics, RGD, reentry, hypersonics, direct simulation Monte Carlo, DSMC, non-equilibrium phenomena

1. Introduction

Taking into account rarefied gas effects is of importance in the correct prediction of the aerodynamic behavior of space vehicles entering a planetary atmosphere. A major factor in the success of such a mission is the correct determination of aerodynamic forces and moments affecting the stability of the vehicle. Under rarefied conditions the continuum description of the gas is no longer valid and traditional CFD techniques based on solving the Navier-Stokes equations produce inaccurate results. Nowadays, the preferred technique for the numerical simulation of rarefied flows is direct simulation Monte Carlo (DSMC). This is a particle-based method capable of describing the flow at a molecular level. It is very flexible in the sense that it can incorporate complex physical phenomena, such as excitation of internal energy modes and non-equilibrium chemistry directly into the collision algorithm.

As part of this doctoral project it was decided to implement a small DSMC code capable of handling simple one-dimensional flow problems, such as steady normal shock waves. After having used an existing DSMC software package (RGDAS) for preliminary studies in the previous year, it was concluded that restrictions in access to the sources and limited familiarity with the RGDAS code would prevent it from becoming a viable tool in the short term. This is the main reason for the development of the present code.

The first year of this project was dedicated to gaining familiarity with the subject matter of rarefied flows and with the DSMC technique. Several large-scale simulations of a classical reentry configuration (Apollo) were conducted to assess the capabilities of the method and to learn about properly setting the simulation parameters in order to obtain accurate results. The main effort in this second year of studies has been to go deeper into the details and implementation of already well-established models for inelastic collisions used in the DSMC method. For this purpose, a dedicated DSMC code has been written. It is capable of simulating simple one-dimensional, steady flow con-

figurations, such as normal shock waves, as well as the unsteady relaxation of internal energy modes in an adiabatic heat bath. It has also been adapted for modeling stagnation streamline, as well as Couette-type flows. At present, it is capable of simulating rotational and vibrational energy exchange using the standard Larsen-Borgnakke model. The implementation of the Total Collision Energy (TCE) method for modeling chemical reactions is still underway. In this paper, several of the preliminary results obtained with this code are presented and, when possible, compared to experimental results.

This summary is organized as follows: Section 2 outlines some basic features of the code. This includes the physical models implemented so far, but also some details of the code itself. Then, in section 3, results for three different test cases are presented. They serve to highlight the present-day capabilities of the code. Finally, section 4 draws some conclusions and gives an outline of the work still to come.

2. Development of DSMC code

The initial reason for writing this DSMC code was the difficulty of simulating a simple normal shock wave in RGDAS. The RGDAS package is very powerful when it comes to simulating two- or three-dimensional external flows around complex body shapes. However, it does not include the capability of applying arbitrary boundary and initial conditions. This makes it very difficult to simulate the normal shock wave problem. One way to circumvent this issue was to simulate the flow around a blunt body (e.g. a cylinder in 2D, or a sphere in 3D) and to extract the flow properties along the stagnation stream line. However, this approach represents a huge waste of computational resources, because one always has to simulate a full 2D or 3D flow, for only a small amount of information required. Additionally, the stagnation stream line always includes interaction of the gas with the wall and prevents slow relaxation phenomena (i.e. taking place over long distances behind the shock) to be analyzed without interference of the wall.

2.1. Collision routines

Most of the core functions that make up the DSMC method are concerned with modeling intermolecular collisions. The collision step itself can be divided into several sub-steps. At the beginning of a collision step, every collision cell contains those particles which ended up in the given cell after completing the free motion step. Determining the correct local collision frequency is the first task in the collision step. In the code this is done using the No Time Counter (NTC) method, proposed by Bird [1].

The second step is the formation of random collision pairs within the cell. In the code, this is accomplished by arranging all particles in a list with a randomized sequence. Then, consecutive particles (i.e. particle 1 and 2, 3 and 4, etc.) will form collision pairs. The standard DSMC routines used in this code make no distinction between particles because of their location within a cell or their relative pre-collision velocities [1].

The next step in the collision procedure is determining whether a collision actually occurs between the previously defined pairs. In the NTC method, the probability of collision for a given pair is calculated from the expression:

$$P_{\text{coll}} = \frac{\sigma_T \cdot c_r}{\{\sigma_T \cdot c_r\}_{\max}}$$

where the product of the total collision cross section σ_T and the relative speed for each pair c_r is used in the numerator, while the maximum value for the cell is used in the denominator. In order to calculate the total cross section, a model for the intermolecular potential needs to be defined. The most widely used ones today in DSMC are arguably the Variable Hard Sphere (VHS) and Variable Soft Sphere (VSS) models, introduced by Bird [4] and Koura [5] respectively. Both of these models have been implemented in the code.

2.2. Internal Energy model

One of the main reasons for developing the present code is the study of internal energy exchange and other inelastic collision processes, such as chemical reactions in highly non-equilibrium flows, e.g. behind normal shock waves. Over the years, a considerable amount of effort has been invested into the development of models for internal energy exchange in DSMC. See, for example, the work of Haas et al [6], [7]. These papers, along with a contributions by Lumpkin [8], Boyd [9; 10; 11] and Bergemann [12] helped to establish the Larsen-Borgnakke [13] model as the most widely used one in the DSMC community nowadays. Most of the details of the method are explained thoroughly in Bird's reference text [14]. It

[1] Several DSMC implementations use the relative distance between particles for selecting collision pairs, see [2], [3]

is worth mentioning that the current implementation in the code assumes a continuous distribution of energy in the rotational mode and a quantized energy distribution of the vibrational levels. These vibrational levels are based on the simple harmonic oscillator (SHO) model of vibration. So far, these models have only been implemented for diatomic species, such as molecular nitrogen.

2.3. Boundary conditions

Another important aspect in the implementation of a DSMC code is the treatment of the boundaries. The current code allows for the application of so-called stream boundaries (i.e. flow inlets/outlets) and solid walls with either fully diffuse or fully specular reflection at the domain boundaries.

The stream boundaries are implemented using so-called "buffer cells". These cells are located outside of the flow domain, but immediately adjacent to the regular cells. They simulate a reservoir of particles with the correct Maxwell-Boltzmann equilibrium distribution of velocities and internal energies so as to be consistent with the macroscopic flow parameters imposed at the boundary. At the beginning of every time step, these buffer cells are filled with new particles. These particles are then displaced along with the ones already present inside the regular domain. Afterward, all particles which have crossed the boundaries into the domain are kept, whereas all particles lying outside of the boundaries are discarded.

Since the present code only allows for flow field gradients in one spatial dimension, walls reduce to a single point at the domain boundary and are necessarily oriented normal to the coordinate direction. For now, only the two most basic wall boundary conditions in DSMC are implemented: fully specular and fully diffuse reflection. They can be viewed as the two extremes between which all gas-surface interactions lie.

2.4. Mesh

In the current 1D code, the flow domain is divided into a group of equally-spaced cells. In this implementation a two-level grid is used, where sampling of macroscopic flow variables (such as density and temperature) occurs at the coarser level, the so-called sampling grid. The collision routines are implemented on the second level, also called the collision grid. Usually, a sampling cell contains one or more collision cells and the reason for this arrangement lies in the different resolution requirements for collision and sampling. Collision cells need to be made smaller than the local mean free path in the gas. This is crucial for the correct prediction of the local collision rate during the collision step. The sampling cells, on the other hand, are usually comprised of more than one collision cell. Using the the particles contained in several contiguous collision cells helps to increase the sample size for obtaining average macroscopic properties and will result in smoother flow field profiles. It should be noted, that the sampling cell size has no influence of the accuracy of the underlying simulation, as sampling does not influence the behavior of the particles. The sampling cell size is, thus only a function of the desired spatial flow field resolution.

At present, the sampling and collision grids need to be set by the user at the beginning of a simulation. Their sizes remain unchanged until the end of the run. This simple set up has been enough for the test cases considered so far (see section 3), because in most of these flow configurations the local mean free path can be estimated with sufficient accuracy beforehand, so as to provide a lower bound on the collision cell size. This is generally not the case for flows including obstacles to the flow (such as general 2D or 3D flows around solid bodies or the stagnation line flow). As a consequence, some form of automatic grid adaptation may need to be added to the code in the future.

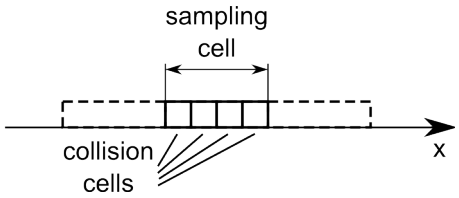

Figure 1: Two-level grid of sampling- and collision cells. There is always an integer number of collision cells, per sampling cell.

3. Results

In this section, the results of some simulations performed using the newly developed code, are presented. At the present time, the code is capable of simulating translational and internal energy relaxation in a cell, as well as in one-dimensional flows. Three test cases are mentioned in this paper, because of their relevance in testing several components of the code.

3.1. Normal shock wave in argon

One of the most simple flow configurations for studying non-equilibrium flow phenomena in gases, which can be simulated using a 1D code, is the normal shock wave. In order to be able to treat this phenomenon as a steady flow, it must be viewed in the shock frame of reference, i.e. the shock front remains stationary in space, while the incoming pre-shock equilibrium flow is supersonic and the post-shock equilibrium flow is subsonic. The relationship between pre-and post-shock flow conditions can be directly determined from the Rankine-Hugoniot normal shock relations. For non-reacting gas mixtures without vibrational excitation, these expressions have a closed, analytical form, allowing the calculation of post-shock density, temperature and velocity, as long as the pre-shock conditions are known.

Using the code, the simulations were set up as follows: The pre-shock flow conditions were taken to be equivalent to the ones studied by Alsmeyer [15]. In this paper, a number of density profiles were presented for normal shock waves in argon and nitrogen gas. These profiles were obtained from experimental investigations and are one of the few well-documented test cases to validate numerical simulations against. Alsmeyer reported profiles for argon at different Mach numbers, ranging from fairly low supersonic (M = 1.55) up to hypersonic (M = 9) speeds.

In the simulation set-up, both the pre- and post-shock conditions are imposed as boundary conditions at the left- and right-hand side of the flow domain. During the simulation, particles whose distribution functions conform to these conditions, are injected on both sides of the domain. At the beginning of the simulation, all the cells in the flow domain are already filled with particles. A specific location x_{step} separates two regions. To the left of it the flow is initialized at the pre-shock and to the right at the post-shock conditions. This initial condition fixes the initial shock location and "trips' the incoming supersonic flow to form the shock wave. After an initial transient phase, in which the shock structure is established, time-averaging of flow samples can begin. Time averaging is usually necessary in DSMC, because the number of particles in a given cell at a given time step is usually much too small to give accurate enough values for the macroscopic flow parameters. In order to obtain smooth profiles, the flow field samples need to be averaged over many time steps. Of course, this approach is only applicable to macroscopically steady flows.

A particularity of the normal shock wave problem is that, given the simulation set-up described before, the shock front location is not fixed in time. Since there is no solid obstacle holding the shock in place, it is possible for it to move from its initial position at x_{step} (sometimes referred to as random walk). This phenomenon has been observed in the present simulations and causes problems for time-averaging of flow samples. If such samples are taken over a large enough number of time steps, the shock front will have moved from its initial location. Consequently, the time averaged flow fields will be inaccurate, because of the "smearing out" of the shock front. There seems to be no direct solution to this problem. A way to minimize this effect is, of course to reduce the sampling time. Then, in order to compensate for the lower number of time-averaging steps, one may increase the number of particles per cell used in the simulation. This approach has been taken here and the number of particles per collision cell is on the order of several thousand, instead of the more usual ten to twenty particles per cell.

In the following, results for two different Mach numbers are shown. Figure 2(a) shows the density profile in a Mach 1.55 normal shock wave, with figure 2(b) presenting the corresponding profiles for the translational temperature components. The components of translational temperature in coordinate direction "i" is defined as:

$$T_{\text{t},i} = \frac{m}{\text{k}} \overline{(c_i - c_{0,i})^2}$$

where m is the mass of a single particle, k is the Boltzmann constant, c_i represents the i-component of velocity of a particle and $c_{0,i}$ the corresponding component of the hydrodynamic velocity. The over-bar symbolizes the average taken over all particles in the sample (i.e. the cell). The scalar translational temperature is then the average of all three components:

$$T_{\text{t}} = \frac{1}{3}\left(T_{\text{t},x} + T_{\text{t},y} + T_{\text{t},z}\right)$$

It can be seen in figure 2(b) that the different com-

ponents of translational temperature do not exactly lie on top of each other inside the shock wave, as expected. This shows the degree of translational non-equilibrium locally present in the flow. The x-component of translational temperature has a small overshoot over the post-shock equilibrium value, while the temperature components normal to the flow direction (i.e. $T_{t,y}$ and $T_{t,z}$) lag behind. The flow then "relaxes" to the post-shock equilibrium where all temperature components take on the same value.

The degree of translational nonequilibrium at a given position in the flow field can also be observed as a departure from the local equilibrium velocity distribution function (i.e. Maxwell VDF) f_0:

$$f_0\left(c_x, c_y, c_z\right) = \left(\frac{m}{2\pi k T}\right)^{3/2} \times \\ \times \exp\left[-\frac{m}{2kT}\left((c_x - u)^2 + \left(c_y - v\right)^2 + (c_z - w)^2\right)\right]$$

Here, c_x, c_y and c_z are the molecular velocities in the x-, y- and z-directions respectively, with u, v and w the corresponding average flow velocities. The shape of the velocity distribution also depends on the mass m of the molecules and the local temperature T. If the distribution is symmetric in the y- and z-directions (as is the case for all 1D flows considered here), one may integrate f_0 over these two velocity components to obtain a "reduced" expression dependent only on c_x:

$$\Phi\left(c_x\right) = \int_{-\infty}^{\infty}\int_{-\infty}^{\infty} f_0\left(c_x, c_y, c_z\right) dc_y\, dc_z \\ = \left(\frac{m}{2\pi k T}\right)^{1/2} \exp\left[-\frac{m}{2kT}\left(c_x - u\right)^2\right]$$

Figure 2(c) shows these reduced velocity distribution functions for the x-components of molecular velocity at three different locations in the flow. The lines represent the VDF's obtained from the simulation, while the symbols show the theoretical Maxwell equilibrium distribution functions at the pre-shock and post-shock temperatures respectively. It can be seen that they match up very well with the simulation results. A third curve (the long dashed line) shows the VDF at a location "inside" the shock wave, approximately at the center of the shock, i.e. where the density is halfway between pre- and post-shock. It can be seen that the VDF is somewhere "between" the two equilibrium values. The location of the maximum of the VDF curves on the velocity axis corresponds to the hydrodynamic velocity at that particular location in the flow. It can be seen that it shifts from its pre-shock value of $500\,\mathrm{m\,s^{-1}}$ to the post-shock $280\,\mathrm{m\,s^{-1}}$. The temperature is related to the "width" of the distribution and this too shifts from a "narrow" curve at 300K, pre-shock, to a "wider" one at the post-shock temperature of 464.32K. Overall, at this Mach number the degree of translational non-equilibrium in the flow is fairly mild, and the distribution seems to remain near equilibrium throughout the shock. This seems to be a reason why Navier-Stokes equations are able to provide reasonably accurate solutions to the shock wave problem at low supersonic Mach numbers.

The other extreme of the cases investigated is the flow with an incoming Mach = 9. From the density profile in figure 3(a), one can immediately notice that the density ratio (post- to pre-shock) is much higher in this case. However, the density profile shape does not appear to be very different from the one at $M = 1.55$. The shock thickness is of the same order of magnitude. The differences are more pronounced when comparing the temperature profiles. In figure 3(b), the degree of translational non-equilibrium is evident, with $T_{t,x}$ showing an overshoot of more than 2000 K over the post-shock equilibrium temperature. The contrast with the low-speed case considered before is even more noticeable in figure 3(c). Now, the pre- and post-shock temperatures differ widely from one another (300 K vs. 7856 K) and the velocity distribution behind the shock widens and flattens out considerably as a result. At the center of the shock wave, the velocity distribution is now far from the typical Maxwell form. It is almost a bimodal distribution, with one "maximum" in the curve located near the pre-shock velocity and another closer to the post-shock velocity.

Figures 4(a) and 4(b) show a comparison of the density profiles obtained with the code with those reported by Alsmeyer. In general, there appears to be good agreement between the two sets of data. In these plots, the density has been normalized:

$$\rho' = \frac{\rho - \rho_1}{\rho_2 - \rho_1}$$

where the number index refers to pre-shock (ρ_1) and post-shock (ρ_2) conditions respectively. The abscissa has been normalized by use of the pre-shock mean free path λ_1. This highlights an important point. For the simple cases where non-reacting monoatomic gases are used, normal shock wave profiles have a general shape, only dependent on the Mach number. If the previous normalization is used, the exact conditions of pressure and temperature in the experiment

should not affect the shape of the profiles. Thus, it is possible to match the results of experiments or simulations obtained at different free-stream densities.

From the two figures, one can argue that there is a good match between the experimental and DSMC results. It should be mentioned that the shape of shock wave obtained with DSMC is very sensitive to the viscosity model used and its dependence on temperature. In DSMC, the standard is to have a viscosity law such as:

$$\mu(T) = \mu_{\text{ref}} \left(\frac{T}{T_{\text{ref}}} \right)^{\omega}$$

where μ_{ref} is the viscosity of the gas known at a reference temperature T_{ref}. The exponent ω takes on values between 0.65 and 0.85 for most gases and is obtained from fitting this simple expression to experimental data. Depending on the temperature range of the fit, it can vary substantially, even for the same gas. In the simulations presented here, a value of $\omega = 0.72$ was used, which seems to give the best results for the "high" temperatures encountered in the post-shock regions. The value of $\omega = 0.81$ given by Bird in his book [14] is intended for low temperatures ($T_{\text{ref}} = 273$ K) and gives poor results in this case.

3.2. Self-diffusion coefficient of argon

In order to assess the behavior of the code when handling several species in the same flow, a simple test case was used. The details of the simulation parameters used can be found in section 12.5 of Bird's book [14]. Here, it is only important to mention that the flow set up consists of the domain bounded by two gas reservoirs. Both of these reservoirs are sources of argon gas at zero mean velocity and at the same temperature. The only difference between the two gases is that in the simulation they are labeled as different chemical species: "Argon blue" on the left and "Argon red" on the right. Besides this artificial difference, the molecules of both species behave exactly the same. The goal of this set up is to simulate the self-diffusion of argon and to determine the self-diffusion coefficient D_{11} from the results.

Figure 5(a) shows the species partial densities ρ_i of "Argon blue" and "Argon red", as well as the total density along the domain length. As expected, the concentration profiles are linear, with the highest concentration of each component near its "source". Due to the symmetry in the set up, at the center of the domain both components are present in exactly the same concentration. It can be seen that there is a small "concentration jump" at both boundaries for both components, i.e. the fraction of "Argon blue" is not exactly equal to 100 % at the left boundary and it does not drop to exactly 0 % at the other end. This is a result of the finite number of sampling cells used.

In figure 5(b) the diffusion velocities U_1 and U_2 are plotted for "Argon blue" and "Argon red" respectively. The diffusion velocity of species "i" is defined as:

$$U_i = \overline{u_i} - u_0$$

with $\overline{u_i}$ being the average over all particle velocities of species "i" in the sample and u_0 the momentum-average (i.e. hydrodynamic) velocity. The diffusion velocity for each species is nearly zero in the region where it is the main component of the mixture, but increases substantially at the other extreme of the domain. Again, since both "species" have exactly the same molecular properties, the picture is symmetric, i.e. the magnitudes of the diffusion velocities are mirrored along the x-axis.

The diffusion coefficient in a binary mixture, with concentration gradients in one dimension, can be determined from the expression:

$$D_{12} = -(U_1 - U_2) \frac{n_1 n_2}{n^2} \frac{dx}{d(n_1/n)}$$

where n_1 and n_2 are the number densities of "Argon blue" and "Argon red" respectively. Since both of these "species" have exactly the same molecular properties, this is also the self-diffusion coefficient D_{11}.

As indicated in figure 5(c), the average self-diffusion coefficient over the length of the domain is $2.89\,\text{m}^2\,\text{s}^{-1}$ (straight dashed line). This rather large value is a consequence of the low density specified in the simulation conditions. The diffusion coefficient is directly dependent on the number density and, converting it to standard conditions (i.e. $T = 273\,\text{K}$ and $p = 101325\,\text{K}$) gives a value of $1.51 \times 10^{-5}\text{m}^2\,\text{s}^{-1}$. This is in fairly good agreement with the value of $1.55 \times 10^{-5}\text{m}^2\,\text{s}^{-1}$ reported by Bird.

3.3. Normal shock waves in nitrogen

After being able to simulate a normal shock in a monoatomic gas such as argon, the next challenge is to move towards adding internal modes of energy, as is the case for molecular nitrogen. Before studying an actual shock wave, the internal energy exchange routines were tested in a single adiabatic cell (sometimes called a "0D" configuration). Unlike any of the other simulations presented in this summary, this is

the only situation, in which the time-dependent evolution of the system is considered, meaning that all samples taken at a given time step are instantaneous and not time-averaged. This fact implies that instead of the usual 10-20 particles per cell, now up to several million particles need to be used in the cell, in order to provide accurate enough statistics.

The simulation setup is fairly simple. All particles in the cell are initialized with their translational and internal energy distributions corresponding to different temperatures, i.e. the translational, rotational and vibrational temperatures are not the same at $t = 0$. This, clearly is a situation of thermal non-equilibrium and, given enough time, the intermolecular exchange processes should force the gas to "relax" towards thermal equilibrium, i.e. a common temperature: $T_\mathrm{t} = T_\mathrm{r} = T_\mathrm{v}$. Thus, the first requirement is that all temperatures reach a single value at some time long after the process has started, while conserving the sum of energy contained in the translational and internal modes. The second requirement is that this relaxation process take place at the correct rate. This relaxation rate is usually defined in terms of the characteristic numbers for rotation and vibration (Z_r and Z_v) respectively. These numbers are used both in DSMC and in CFD codes to calculate local relaxation rates. It is important that the numbers be defined in a mutually consistent manner between DSMC and CFD. (This is not always the case. In the early years of DSMC, the definitions of Z_r and Z_v differed from those used in continuum CFD at the same time. As a consequence, the results would show poor correspondence between each other. This issue was already addressed in two papers by Haas [7] and Lumpkin [8]).

In figures 6(a) and 6(b), the time evolution of the different temperatures is shown for two different initial conditions. In the first case, the initial translational temperature was set equal to 2000 K, while the rotational temperature was initialized at 300 K. At such low temperatures, the vibrational mode is barely excited and therefore not considered. One can see in figure 6(a) that the two curves representing translational and rotational temperature approach each other over time, until they merge at around $t = 2.5 \times 10^{-9}$ s. After this time, the temperature in the cell remains at 1320 K, the expected equilibrium temperature. Along with the lines representing the results of the DSMC calculations, symbols show the same information, but obtained with a Navier-Stokes code. The close correspondence of both sets of results confirms the correct implementation of the rotational collision number in the DSMC code. A second simulation was conducted at a higher overall energy level, which now made the inclusion of the vibrational mode necessary. Figure 6(b) shows the time evolution of a gas reservoir initially at $T_\mathrm{t} = 10000$ K and $T_\mathrm{r} = T_\mathrm{v} = 300$ K. Again, this simulation shows relaxation of all thermal modes to the equilibrium temperature and a close match between the DSMC and Navier-Stokes results. The behavior is typical of rotation-translation and vibration-translation relaxation processes in a gas, where the rotational mode reaches equilibrium with the translational mode much faster than the vibrational mode does. It should be mentioned that in all simulations presented in this section, the collision numbers for rotation and vibration have been set to constant values: $Z_r = 10$, $Z_v = 120$. It is known that in reality these numbers show a temperature dependence, especially Z_v can increase several orders of magnitude for higher temperatures. Therefore, the results shown here may not provide the correct relaxation times one would observe in experiment. In order to achieve this, the collision numbers must be calculated according to the well-known empirical correlations by Parker [16], Millikan & White [17] and Park [18]. Implementation of these correlations into the code is still ongoing.

Figure 7(a) shows the normalized density profile in a Mach 1.71 shock wave of molecular nitrogen. Again, the density profile is compared with the experimental data given by Alsmeyer and the correspondence is seen to be very good. In figure7(b), the temperature profile is plotted. The solid line represents the translational temperature, whereas the dashed line shows the rotational temperature lagging behind. Once again, the symbols represent results obtained with a Navier-Stokes code. For this relatively low Mach number of 1.71, the correspondence between the DSMC and CFD results is very good. However, this picture is expected to deteriorate for higher Mach numbers, as the Navier-Stokes equations are known to give inaccurate results for strong non-equilibrium flows.

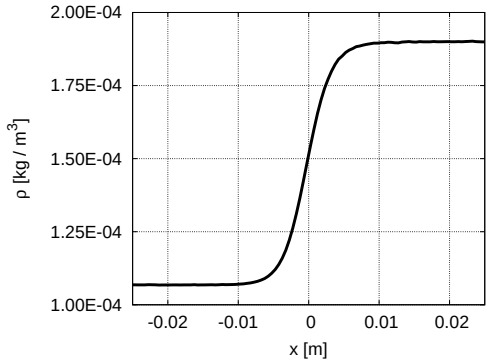

(a) Density profile

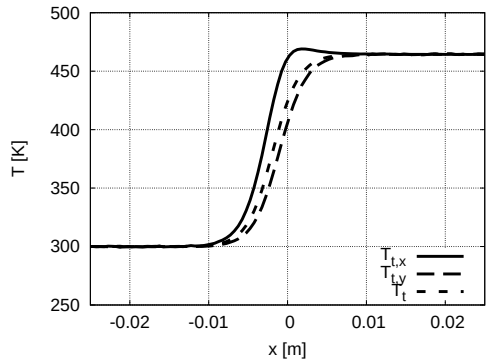

(b) Translational temperature profiles.
solid line: $T_{t,x}$,
dashed long: $T_{t,y}$,
dashed short: T_t

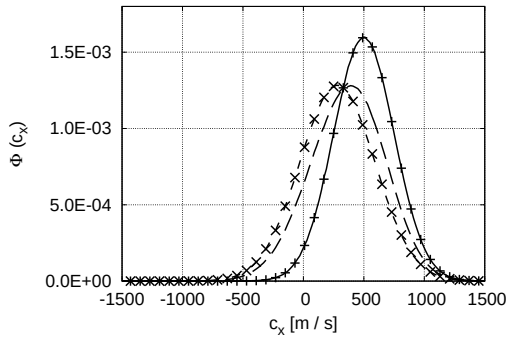

(c) Velocity distribution functions (VDF) for the x-velocity component.
solid line: DSMC at inlet (x = −0.05 m),
dashed long: DSMC at shock center (x = 0.0 m),
dashed short: DSMC at outlet (x = 0.05 m)
+: Maxwell for T = 300 K
×: Maxwell for T = 464.32 K

Figure 2: Macroscopic flow parameters and Velocity distribution functions for a normal shock wave in Argon, at Mach = 1.55

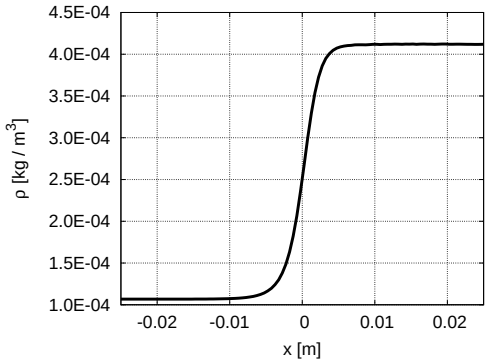

(a) Density profile

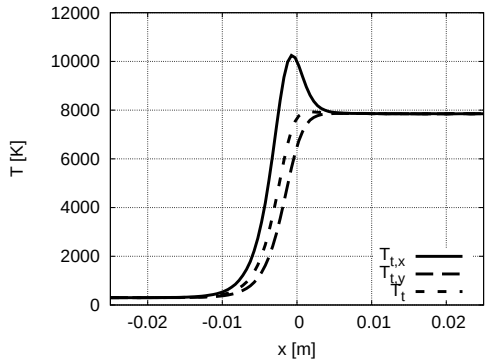

(b) Translational temperature profiles.
solid line: $T_{t,x}$,
dashed long: $T_{t,y}$,
dashed short: T_t

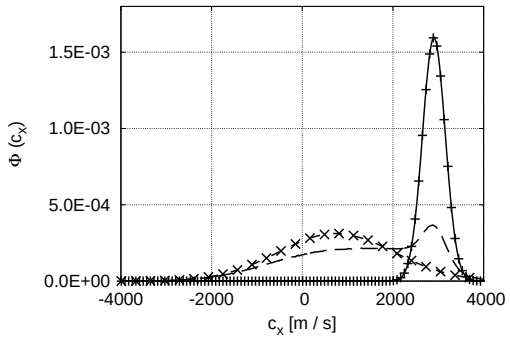

(c) Velocity distribution functions (VDF) for the x-velocity component.
solid line: DSMC at inlet (x = −0.05 m),
dashed long: DSMC at shock center (x = 0.0 m),
dashed short: DSMC at outlet (x = 0.05 m)
+: Maxwell for T = 300 K
×: Maxwell for T = 7855.56 K

Figure 3: Macroscopic flow parameters and Velocity distribution functions for a normal shock wave in Argon, at Mach = 9

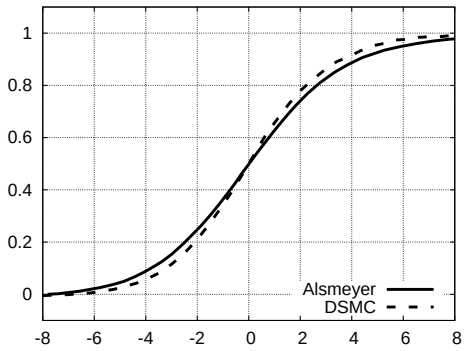

(a) Mach = 1.55

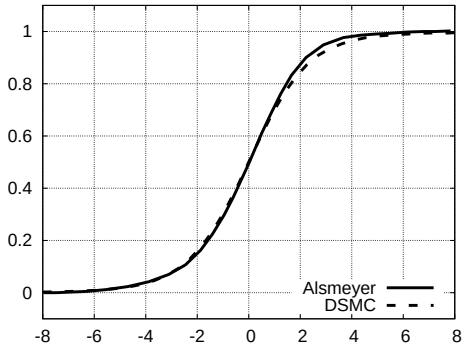

(b) Mach = 9

Figure 4: Comparison of normalized density $((\rho - \rho_1) / (\rho_2 - \rho_1))$ profiles between DSMC (dashed line) and experimental results obtained by Alsmeyer (solid line). The abscissa has been normalized with the free-stream mean free path λ_1

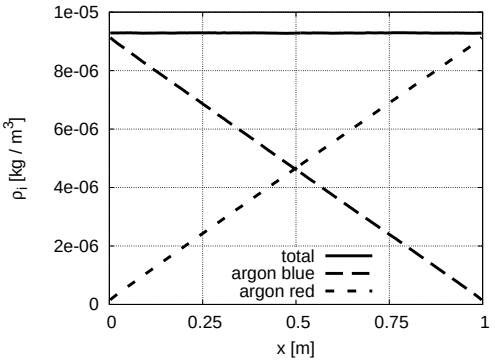

(a) Density profiles

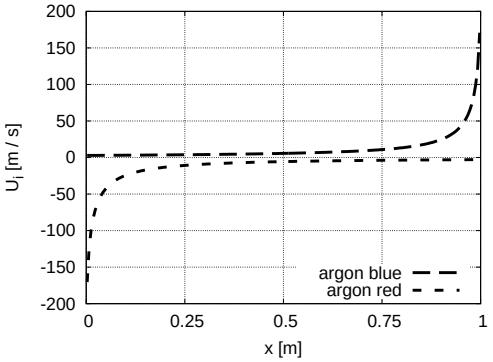

(b) Diffusion velocities

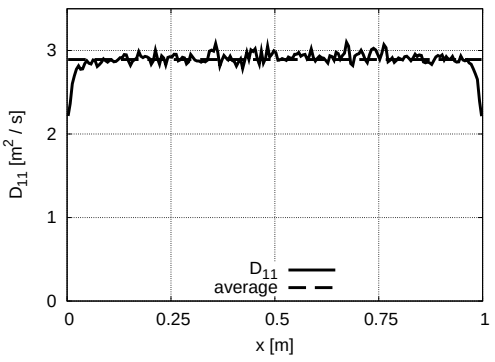

(c) Self diffusion coefficient

Figure 5: Profiles of density and diffusion velocity for a binary mixture of argon gas

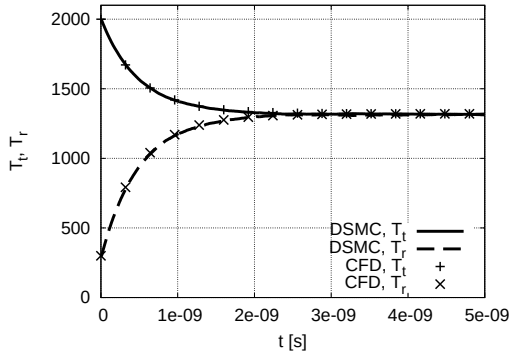

(a) R-T relaxation of N_2, time evolution of translational and rotational temperatures, comparison between DSMC and continuum CFD formulation

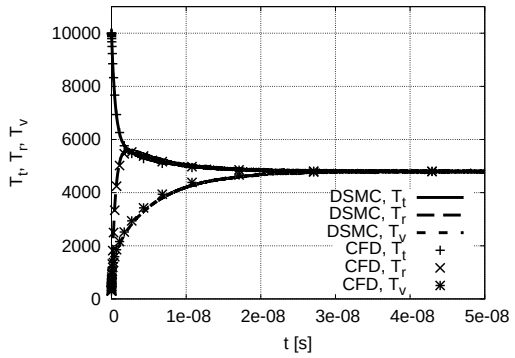

(b) R-T and V-T relaxation of N_2, time evolution of translational, rotational and vibrational temperatures, comparison between DSMC and continuum CFD formulation

Figure 6: Relaxation of internal energy modes of molecular nitrogen in an adiabatic heat bath for $Z_r = 10$ and $Z_v = 120$

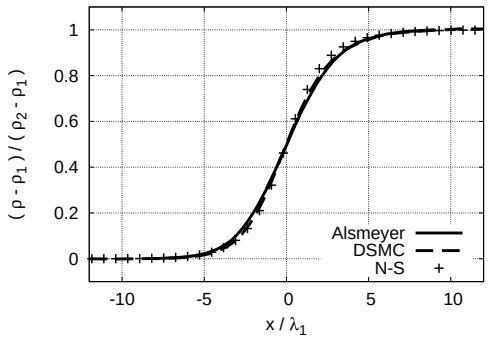

(a) Density

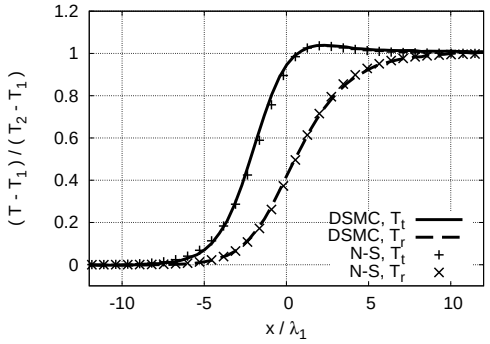

(b) Translational and rotational temperatures

Figure 7: Profiles of normalized density and temperature for a nitrogen Mach = 1.71, comparison between DSMC solution and continuum CFD based on Navier-Stokes

4. Conclusions and Future work

Some selected results obtained during the last year with a newly written DSMC code have been presented. The main elements of the code are functioning and it is possible to obtain accurate results with it for a number of test cases. Specifically, steady flow with a high degree of translational non-equilibrium, as in normal shock waves with monoatomic gases can be simulated. The treatment of internal energy exchange processes, present in all polyatomic gases, such as rotational-translational and vibrational-translational relaxation has been implemented using the standard model of DSMC [13].

However, work on the conventional models for internal energy exchange and especially for chemical reactions has not yet been completed. The inclusion of temperature-dependent rotational and vibrational collision numbers Z_r and Z_v, based on the empirical correlations of Parker, Millikan & White and Park has been implemented, but not yet thoroughly tested. The implementation of the TCE method for chemical reactions has yet to be started. Another topic, which will become relevant in reacting multi-species flows is the use of species-specific weighting factors. Instead of having a global value for the ratio of real to simulated particles F_{Num}, weighting factors result in individual F_{Num}'s for each component of the mixture. The inclusion of this feature should improve the treatment of trace species in the flow, which might often not be accounted for, due to the limited number of particles used.

So far, the computational performance of the code has been of secondary importance. The problems considered until now were rather manageable in terms of CPU run-time and memory usage, such that a serial implementation provided enough performance. However, it has been recognized, that as the problem size grows (specifically, the number of particles needed), significant improvements in speed and code efficiency have to be realized. This includes optimization of the code, as well as adding parallel processing capabilities. This work is underway.

Finally, it is important to mention that the main reason for the development of the code is still its future use with novel models for inelastic collision processes. In the future, the aim is to improve the existing models in DSMC for rotational and vibrational exchange by using a reduced model developed from a detailed chemical mechanism based on rovibrational cross sections for reactions in nitrogen. These models will be based on the cross sections for the N_2 + N system obtained from detailed quantum mechanical calculations obtained at NASA Ames Research Center. The N_2 + N system consists of approximately 10000 rovibrational levels and its implementation in DSMC, even for simple types of flows, becomes a challenge, due to the large number of particles needed for populating the possible states in a realistic fashion. Consequently, our efforts will be directed towards developing a model for lumping together energy states lying close to one another and thus reducing the total number of levels required. A similar effort is already underway in developing such reduced models for continuum CFD solvers [19]. The final goal will be again to compare simulations between consistent CFD and DSMC models.

Acknowledgments

I wish to thank Prof. Tom Schwartzentruber from the University of Minnesota for his advice and for providing reference material, which has been invaluable in developing the present DSMC code. Many thanks also to Alessandro Munafò for providing continuum CFD solutions for comparison.

References

[1] G. Bird, Perception of numerical methods in rarefied gasdynamics, in: 16th International Symposium on rarefied gas dynamics, 1988.

[2] G. LeBeau, K. Boyles, F. Lumpkin III, Virtual sub-cells for the direct simulation monte carlo method, in: 41st AIAA Aerospace Sciences Meeting and Exhibit, 2003.

[3] C. Su, K. Tseng, H. Cave, S. Wu, J, Y. Lian, T. Kuo, M. Jermy, Implementation of a transient adaptive sub-cell module for the parallel-dsmc code using unstructured grids, Computers & Fluids 39(7) (2010) 1136–1145.

[4] G. Bird, Monte-carlo simulation in an engineering context, in: 12 th International Symposium on rarefied gas dynamics, 1980.

[5] K. Koura, H. Matsumoto, Variable soft sphere molecular model for inverse-power-law or lennard-jones potential, Physics of Fluids A 3(10) (1991) 2459–2465.

[6] B. Haas, J. McDonald, L. Dagum, Models of thermal relaxation mechanics for particle simulation methods, Journal of Computational Physics 107 (1993) 348–358.

[7] B. Haas, D. Hash, G. Bird, E. I. Forrest, H. Hassan, Rates of thermal relaxation in direct simulation monte carlo methods, Physics of Fluids 6(6) (1994) 2191–2201.

[8] F. Lumpkin III, B. Haas, I. Boyd, Resolution of differences between collision number definitions in particle and continuum simulations, Physics of Fluids A 3(9) (1991) 2282–2284.

[9] I. Boyd, Rotational-translational energy transfer in rarefied nonequilibrium flows, Physics of Fluids A 2(3) (1990) 447–452.

[10] I. Boyd, Analysis of rotational nonequilibrium in standing shock waves of nitrogen, AIAA Journal 28(11) (1990) 1997–1999.

[11] B. Haas, I. Boyd, Models for vibrationally-favored dissociation applicable to a particle simulation, in: 29th Aerospace Sciences Meeting, 1991.

[12] F. Bergemann, I. Boyd, Rarefied Gas Dynamics: Experimental Techniques and Physical Systems (Progress in Aeronautics and Astronautics), American Institute of Aeronautics and Astronautics, 1994, Ch. 3. New Discrete Vibrational Energy Model for the Direct Simulation Monte Carlo Method, pp. 174–183.

[13] C. Borgnakke, P. Larsen, Statistical collision model for monte carlo simulation of polyatomic gas mixture, Journal of Computational Physics 18 (1975) 405–420.

[14] G. Bird, Molecular Gas Dynamics and the Direct Simulation of Gas Flows, Oxford University Press, 1994.

[15] H. Alsmeyer, Density profiles in argon and nitrogen shock waves measured by the absorption of an electron beam, Journal of Fluid Mechanics 74(3) (1976) 497–513.

[16] J. Parker, Rotational and vibrational relaxation in diatomic gases, Physics of Fluids 2(4) (1959) 449–462.

[17] R. Millikan, D. White, Systematics of vibrational relaxation, Journal of Chemical Physics 39(12) (1963) 3209–3214.

[18] C. Park, Nonequilibrium hypersonic aerothermodynamics, Wiley, New York, 1990.

[19] T. Magin, M. Panesi, A. Bourdon, R. Jaffe, D. Schwenke, Coarse-grain model for internal energy excitation and dissociation of molecular nitrogen, submitted to Chemical Physics.

In-flight Experiment Design and Ground Testing of a Re-Entry CubeSat

Işıl Şakraker

Aeronautics and Aerospace Department, von Karman Institute for Fluid Dynamics, Belgium, isil.sakraker@vki.ac.be

Supervisor: Olivier Chazot

Associate Professor, Aeronautics and Aerospace Department, von Karman Institute for Fluid Dynamics, Belgium, chazot@vki.ac.be

University Supervisor: Gaëtan Kerschen

Professor , Department of Aerospace and Mechanical Engineering, University of Liege, Belgium, g.kerschen@ulg.ac.be

Abstract

Spacecraft, returning back to Earth, experience a very harsh environment during the re-entry. One of the major issues of the re-entry is the extreme aerodynamic heating and the exothermic chemical reactions due to the gas-surface interaction at hypersonic free stream velocities. There is a constant effort by the space agencies to increase the understanding of the re-entry flight dynamics to optimize the spacecraft design. The re-entry phenomena are investigated using three powerful tools with their advantages and inconveniences: flight tests, numerical simulations and ground testing. The most valuable among all is the real flight testing however they come with very high costs and they have to be designed with ground tests. Different from low speed aerodynamics, high enthalpy flows cannot be fully simulated on ground but only partial simulations are possible. The approach at VKI is the Local Heat Transfer Simulation (LHTS) which says that the stagnation region behind the shock can be simulated only if the total pressure and the boundary layer edge enthalpy and velocity gradient are reproduced.

The first part of this study is to develop methods the **Plasmatron flow characteristics** eventually to make sure the boundary layer edge and velocity gradient are kept. Two methods are initially proposed: free stream temperature measurement by emission spectroscopy and direct enthalpy measurement. Subsequently an **Aerothermodynamic Database** will be built and an envelope, where the mission trajectory will later be imposed, will be defined to develop Gas-Surface Interaction models for further design steps. The last step is then called **Flight Extrapolation** where the ground test conditions are pinpointed to the mission flight trajectory. The reference mission of this study is VKI's QARMAN (QubeSat for Aerothermodynamic Research and Measurements on Ablation) in the framework of QB50. Different from the rest of the QB50 satellites, the Re-Entry CubeSat is a double CubeSat, with an extra ablative thermal protection system (TPS) unit, resulting in the external dimensions of a triple CubeSat.

The major scientific return of QARMAN project is the contribution of flight data on an Earth re-entry trajectory by a very low cost mission compared to other similar missions such as ARD, EXPERT, IXV, etc. The re-entry conditions of QARMAN are representative of a real spacecraft re-entry (starting altitude of 120 km, V=7.5 km/s and $q \geq 2MW/m^2$). It is the first time that such a low-resource vehicle will be used for re-entry studies.

Several important issues at different phases of the re-entry flight are the starting points of the scientific questions that will be answered through the PhD study. The phenomena under consideration are: Aerothermodynamic environment, thermal protection system, gas-surface interaction (mainly ablation), telecommunications blackout, different stability regimes, turbulence effects, radiation, rarefied flow aerodynamics, atmospheric effects, stability, attitude control and controlled re-entry, disintegration, subsystem functionality and safety aspects. Using the ground testing methodology developed in the first part, it is aimed to investigate how those phenomena can be measured during the flight on such a constraining platform. The goal is propose eventually a flight qualified payload for in-flight experiment.

Mission Analysis and Design of a CubeSat Network

Thorsten Scholz

Aeronautics and Aerospace Department, von Karman Institute for Fluid Dynamics, Belgium, scholz@vki.ac.be

Supervisor: Patrick Rambaud

Associate Professor, Aeronautics and Aerospace Department, von Karman Institute for Fluid Dynamics, Belgium, rambaud@vki.ac.be

Co-Supervisor: Cem O. Asma

Research Engineer, Aeronautics and Aerospace Department, von Karman Institute for Fluid Dynamics, Belgium, asma@vki.ac.be

Keywords: QB50, satellite network, CubeSat, thermosphere, orbital dynamics, atmospheric model, DSMC

1. Motivation & Objectives

In the framework of the QB50 project a network of 50 CubeSats will be launched to perform in-situ measurements of the spatial and temporal variation of atmospheric properties in the lower thermosphere at an altitude of 350 km to 150 km [1]. The project will demonstrate the possibility of using the small satellites as efficient and low-cost technology demonstrators. QB50 will be the first simultaneously launched CubeSat network and helps in gaining a better understanding of such complex missions.

The choice for conducting measurements in the lower thermosphere is influenced by several factors and constraints. The atmospheric properties in this region and their relationship to Earth's climate and space-weather like sun storms are yet not well known. This leads to larger uncertainties in lifetime and trajectory simulations, which the recently uncontrolled re-entries of UARS, Rosat or Phobos-Grunt have shown. Another influence factor is the mitigation of space debri creation and fulfillment of the 25 year lifetime requirement. The performance envelope of the chosen launch vehicle Shtil-1.2, which shall provide sustained and low-cost access to Earth orbit, restricts the reachable maximum altitude and a trade-off between number of satellites and altitude has to be performed.

The PhD main tasks will be the assessment of the atmospheric and aerodynamic input data, the mission design for QB50 with focus on the orbital dynamics of the network of 50 CubeSats and finally analyzing of concepts for deorbiting of satellites.

The first task deals with the aerodynamic characterization of the CubeSats. The flow-field around the satellite will be obtained with DSCM simulations using the software RGDAS. A database with the aerodynamic coefficient for different altitudes, attitudes and configurations will be generated. For the simulations a proper knowledge of the atmospheric conditions is mandatory. Therefore a detailed analysis of different existing atmospheric models will be made to assess the variations in the density distribution and the composition. Since the properties in the lower thermosphere are not well known, the uncertainty quantification is an important factor for the latter mission design.

The mission design of QB50 will be challenging and include several points to be looked at. First the development of an suitable deployment strategy for the 50 CubeSats is mandatory to reduce the collision risk to a minimum. The deployment also effects the spreading and therefore the global distribution of the satellites. This will be analyzed to obtain a suitable strategy and spreading for the distributed measurements in the thermosphere. Simultaneously 6 degree of freedom simulations of the 50 CubeSats will be performed using the software STK[1] or ASTOS[2] to obtain the trajectories and the behavior of the network. The

[1] Satellite Tool Kit, Analytical Graphics, Inc.

[2] AeroSpace Trajectory Optimization Software, Astos Solutions GmbH

network will be analyzed in terms of necessary number of satellites for global measurements. The results from the previous studies of the atmosphere and aerodynamics of the CubeSats will be used to predict the orbital life-time. The communication with the ground stations will be investigated in terms of coverage and communication time. A study of the collision risk with other satellites or debris could be performed.

The third task of the PhD deals with the effect of deorbiting concepts on the trajectory. These concepts like sails, fins or tethers are experiencing increasing popularity. DSMC simulations for different concepts and types mounted on a CubeSat demonstrator should be performed. In addition to that, 6 degree of freedom trajectory calculations will be performed to investigate their efficiency and effects on lifetime.

If the CubeSats will be launched in time during this PhD, the obtained measurements and trajectories will be analyzed and compared with the results from the atmospheric study and the mission design. This will help to further improve the atmospheric models for the lower thermosphere.

2. Challenges & Uncertainties

The challenge in the mission design of QB50 consists of the large number of parameters, the interconnection between them and their associated uncertainties. The proper prediction of the sun's activity for the launch time is difficult and only a crude statement according to the 11 year solar cycle can be made. Strong sun eruptions which are quite common during high activity periods can easily affect the lifetime of the CubeSats. Since the atmospheric models are based on the solar fluxes, the errors and uncertainties coming from the models will be amplified. Comparing different models, even with similar input, lead to discrepancies in terms of density values and global distribution. The inaccuracy for the density is still around 10 % to 15 % [2], even with the models improving over the last few years due to measurements obtained by the GRACE and CHAMP mission [3].

Since each CubeSat will be designed by a different university and the scientific payload will differ in terms of weight, size and external parts like additional sensors and communications links, the ballistic coefficient can not be assumed to be equal. The coefficient is also influenced by the satellite attitude and, most probably not all CubeSats will be perfectly aligned to the free-stream velocity direction. This results in varying atmospheric drag forces which have

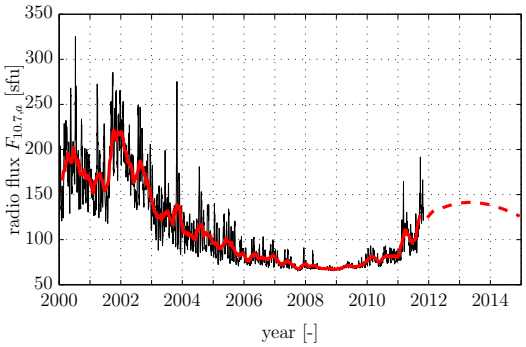

Figure 1: 10.7cm radio flux with prediction

to be considered during the mission planing and especially for the deployment strategy.

3. Comparison of atmospheric models

Currently the two experimental models JB2008 and NRLMSISE00 and the physical model TIEGCM have been analyzed. The launch of QB50 is scheduled for the summer 2014 and the input values have been chosen according to the prediction for this date, e.g. shown in Fig. 1. The deviation of the prediction has been coupled with the $1\,\sigma$ standard deviation of a comparable situation in the past.

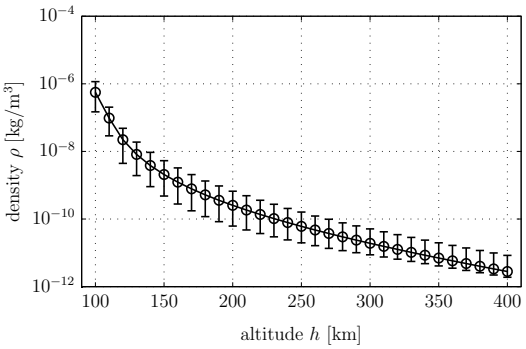

Figure 2: Density from US76 with obtained uncertainty

For the comparison all input parameters have been varied by the obtained deviations to simulate all realistic combinations. A horizontal grid resolution of 5° and vertical resolution of 5 km have been used. The mean, maximum, minimum and the values of the daylight and night side of the earth have been calculated for each horizontal layer and then afterwards compared to the U.S. Standard Atmosphere US76. Combining the results of all models a possible uncertainty

can be obtained for the density, shown in Fig. 2, or other values like neutral temperature.

Acknowledgments

The research leading to these results has received funding from the European Community's Seventh Framework Programme ([FP7/2007-2013]) under grant agreement n° 284427 for the QB50 Project.

References

[1] J. Muylaert, QB50, an international network of 50 double CubeSats for multi-point, in-situ measurements in the lower thermosphere and for re-entry research, 1st QB50 Workshop (2009).

[2] D. A. Vallado, D. Finkleman, A Critical Assessment of Satellite Drag and Atmospheric Density Modeling, Revision to paper AIAA-2008-6442.

[3] B. R. Bowman, W. K. Tobiska, F. A. Marcos, C. Y. Huang, C. S. Lin, W. J. Burke, A New Empirical Thermospheric Density Model JB2008 Using New Solar and Geomagnetic Indices.

Development of Multiphysics Numerical Methods to Study Coupled Flow, Radiation, and Ablation Phenomena for Planetary Entry Vehicles

James B. Scoggins

Aeronautics and Aerospace Department, von Karman Institute for Fluid Dynamics, Belgium, james.scoggins@vki.ac.be

Supervisor and University Supervisor: Thierry Magin

Assistant Professor, Aeronautics and Aerospace Department, von Karman Institute for Fluid Dynamics, Belgium, magin@vki.ac.be
EM2C Laboratory, École Centrale Paris, France

Abstract

This report briefly outlines the proposed research of developing numerical methods for the coupling of fluid flow, radiation, and ablation physics surrounding planetary entry vehicles.

Keywords: multiphysics coupling, numerical methods, hypersonics, radiation, ablation, planetary entry

1. Introduction and Motivation

Space exploration is one of the boldest and most exciting endeavors that humanity has undertaken, and it holds enormous promise for the future. After the successful manned missions to the Moon and many probe entries in the atmospheres of our outer planets, our next challenges for spatial conquest include bringing back samples to Earth by means of robotic missions and continued manned exploration, which aims at sending human beings to Mars and returning them safely home.

Of the many design challenges associated with these goals is the exceptionally difficult task of accurately predicting the heat-flux to the surface of the spacecraft thermal protection system (TPS) during planetary entry. An inaccurate prediction can be fatal for the crew or the success of robotic missions. Large safety factors are often added to vehicle TPS thicknesses to avoid such catastrophes at the expense of additional cost, weight, and reduced payload margins. Thus it is necessarily important to understand and accurately model the complex phenomena that affect the surface heat-flux such as the following potential "mission killers:" 1) Radiation of the plasma in the shock layer, and 2) Complex surface chemistry on the thermal protection system material (Fig. 1). However, current entry vehicle design paradigms largely decouple many of the physico-chemical processes due to numerical and modeling constraints, making it difficult to infer from current design tools the complex, coupled phenomena occurring for any given entry problem. Thus, our poor understanding of the coupled mechanisms of flow, radiation, and ablation leads to the difficulties in flux prediction.

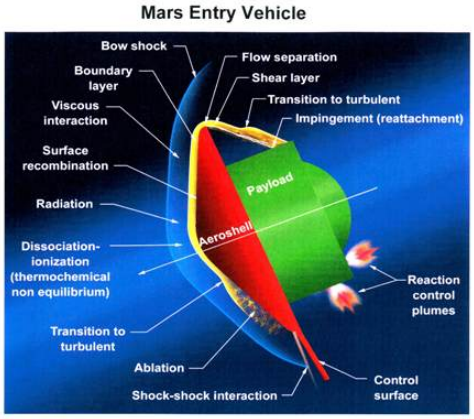

Figure 1: Diagram depicting physical phenomena surrounding a spacecraft during a Martian atmospheric entry. Credit: NASA Hypersonics Project [1]

2. Research Objectives

The AEROSPACEPHYS project is focused on improving our predictive capabilities by *"Integrating*

new advanced physico-chemical models and computational methods, based on a multidisciplinary approach developed together with physicists, chemists, and applied mathmaticians, to create a top-notch multiphysics and multiscale numerical platform for simulations of planetary atmosphere entries, crucial to the new challenges of the manned space exploration program. Experimental data will also be used for validation, following state-of-the-art uncertainty quantification methods." The proposed research project, aimed at developing a complete multiphysics tool which fully couples flow, radiation, and ablation models, will be an integral component of the overall objectives of the AEROSPACEPHYS project.

Currently, other researchers are working on state-of-the-art modeling capabilities for the various decoupled systems necessary for the accurate description of the flow physics associated with hypersonic flight [2]. These include the development of advanced collisional-radiative models for thermochemical nonequilibrium and radiation modeling via strong collaboration with the computational chemistry group at NASA Ames Research Center (ARC) [3; 4; 5], improved carbon-phenolic ablation models through Direct Simulation Monte Carlo methods [6], accurate and efficient modeling of atmospheric entry plasmas in the transition and continuum regimes, as well as a previously developed state-of-the-art treatment of transport properties for ionized plasmas [7; 8]. In addition to these advanced modeling efforts, an experimental investigation of various thermal protection materials is also under way with the use of the VKI Plasmatron facility [9; 10]. The next step in developing a complete multiphysics tool for studying hypersonic entries will be to couple these efforts, including contributions from outside VKI such as a new ablation code from NASA ARC (PATO [11]), into a comprehensive, 3-dimensional, multiphysics code which couples the various models being developed into a complete flow/radiation/ablation tool.

The development of this multiphysics framework will be completed through a series of important milestones during the research project at VKI. During the first phase, the Mutation library, which provides chemistry, transport, and equilibrium computations for ionized plasmas, will be upgraded to use C++ and incorporate improved algorithms and models for the transport and equilibrium calculations. The improved library will be designated Mutation++. Additionally, during the first phase of development, a 3-dimensional hypersonics CFD code will be implemented with the use of the OpenFOAM library. OpenFOAM is a natural choice because it offers extensive features to aid the development of a hypersonics solver including grid/mesh data structures, built-in parallel framework, and linear algebra routines. The flow solver will also make extensive use of Mutation++. Following this work, the task of coupling radiation into the flow solver will be completed alongside a detailed development of a general multiphysics framework for hypersonic problems. Next an ablation tool being developed by NASA ARC will be additionally coupled to the flow/radiation solver, finally allowing the computation of a fully coupled flow/radiation/ablation simulation.

Apart from improved simulation fidelity provided by the implementation of various physico-chemical models developed in the Aeronautics and Aerospace Department, the new multiphysics tool will finally allow a detailed study of the various coupled phenomena that have been largely overlooked due to lack of existing computational models. These include the coupled relationships between shock layer radiation and absorption by pyrolysis and ablation products in the boundary layer and gas-surface interactions and in-depth ablation due to boundary layer chemistry. The final goal of this research will be to study these effects as they pertain to specific experimental and flight test situations such as plasmatron simulations and post-flight analysis of the EXPERT mission (Fig. 2).

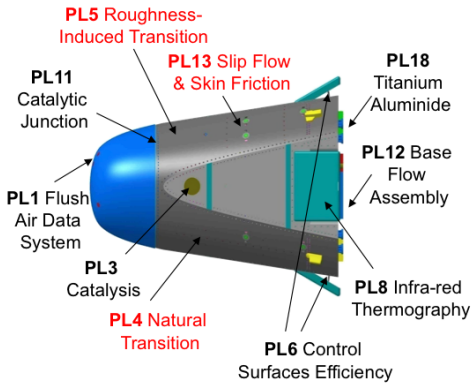

Figure 2: ESA Expert Vehicle & Payloads

3. Mutation++

As mentioned in Section 2, the first task in developing a complete multiphysics tool will be to update the Mutation library to a modern, object oriented library written in C++ which can be coupled to new or existing CFD tools. This effort is in fact

already underway. The MUTATION library provides **mu**lticomponent **t**ransport **a**nd **t**hermodynamic properties/chemistry for **ion**ized plasmas.

MUTATION++ will incorporate all of the same features as its predecessor, however a number of algorithmic changes will be made to improve the library's robustness and performance. In particular, the equilibrium composition solver in MUTATION can fail for some mixtures and thermodynamic states for which the nonlinear set of equations to be solved becomes numerically stiff. Such conditions have been encountered in certain pyrolysis gas mixtures making it impossible to solve some boundary layer problems with ablation and pyrolysis species. MUTATION currently employees the Newton-Raphson iterative procedure to solve the set of equilibrium equations with the fast Schur complement method for the linear update. This algorithm has proven to be very fast, however it does not handle numerical stiffness well. MUTATION++ will instead implement a method known as the Gibbs function continuation (GFC) method developed by Pope [12; 13], which is guaranteed to find the equilibrium composition for all well posed problems regardless of the numerical stiffness of the mixture.

To help increase the performance of the MUTATION++ over its predecessor, specialized lookup tables will be incorporated for the calculation of expensive model parameters such as Arrhenius rates laws, equilibrium constants, collision integrals, etc. This lookup table feature has already been incorporated into the MUTATION++ library and can compute lookup tables at start-up given a function and desired accuracy (error tolerance) or can be loaded from precomputed tables. More testing is still required to determine the exact speedup generated by using such lookup tables but initial tests with randomly generated functions shows that an order of magnitude decrease in computational time can be achieved for some model parameter calculations.

Additional features will also be added in MUTATION++ which will enable coupling to implicit CFD solvers such as the calculation of the species production rate Jacobian matrix for finite-rate chemistry.

4. Concluding Remarks

The focus of this research will be to develop state-of-the-art numerical methods that allow the coupling of fluid flow, radiation, and ablation modeling for planetary entry simulations that is computationally competitive with current uncoupled methodologies. To this extent, the basic ground work has been laid through planning and collaboration internal to VKI and abroad. However, this research is still in the preliminary phases, leaving much work left to be completed.

Acknowledgments

This research is funded through a Fellowship provided by the European Research Council Starting Grant #259354: "*Multiphysics models and simulations for reacting and plasma flows applied to the space exploration program.*"

References

[1] Depiction of Marsian atmospheric entry. Web address: `http://www.aeronautics.nasa.gov/fap/hypersonic.html`.

[2] T. E. Magin, O. Chazot, Review of the vki research on nonequilibrium phenomena in hypersonics, AIAA (2012-725).

[3] A. Munafó, M. Panesi, R. Jaffe, A. Lani, T. Magin, Vibrational state to state kinetics in expanding and compressing nitrogen flows, AIAA (2010-4335).

[4] A. Munafó, M. Panesi, R. Jaffe, A. Bourdon, T. Magin, Mechanism reduction for rovibrational energy excitation and dissociation of molecular nitrogen in hypersonic flows, AIAA (2010-3623).

[5] A. Munafó, M. Kapper, J. Cambier, T. Magin, Investigation of nonequilibrium effects in axisymmetric nozzle and blunt body nitrogen flows by means of a reduced rovibrational collisional model, AIAA (2010-0647).

[6] E. Torres, A. Munafó, T. Magin, Influence of internal energy excitation and molecular dissociation on normal shock structure, 7th European Aerothermodynamics Symposium, Brugge, Belgium.

[7] T. E. Magin, G. Degrez, Transport of partially ionized and unmagnetized plasmas, Physical Review E 70.

[8] T. E. Magin, G. Degrez, Transport algorithms for partially ionized and unmagnetized plasmas, Journal of Computational Physics 198 (2004) 424–449.

[9] B. Helber, C. O. Asma, Y. Babou, O. Chazot, T. Magin, Experimental investigation of the material response of carbon composite ablators in the vki plasmatron facility, AIAA (2011-2302).

[10] B. Helber, Methodology for ablation investigations of innovative ablators in the vki plasmatron facility: First results on a carbon fiber preform, Ph.d. symposium report, von Karman Institute for Fluid Dynamics (2012).

[11] J. Lachaud, H. Wong, I. Cozmuta, G. Reinisch, Develpment and validation of a physics-based multi-scale model for low-density carbon/phenolic ablators, Step 2 proposal - hyp1-2. 2.1.2: High fidelity modeling of low-density carbon/phenolic ablators (edl), NASA-NRA (2011).

[12] S. B. Pope, The computation of constrained and unconstrained equilibrium compositions of ideal gas mixtures using gibbs function continuation, Report FDA 03-02, Cornell University (2003).

[13] S. B. Pope, Gibbs function continuation for the stable computation of chemical equilibrium, Combustion and Flame 139 (2004) 222–226.

Multidisciplinary Gradient-Based Optimization of Turbomachinery Components using CAD Parameterization

Lasse Müller

Turbomachinery and Propulsion Department, von Karman Institute for Fluid Dynamics, Belgium, lasse.mueller@vki.ac.be

Supervisor: Tom Verstraete

Assistant Professor, Turbomachinery and Propulsion Department, von Karman Institute for Fluid Dynamics, Belgium, tom.verstraete@vki.ac.be.

Abstract

This PhD research aims to extend the VKI optimization system towards gradient-based algorithms to be utilized on turbomachinery components. Due to the industrial applicability, a CAD based parameterization will be used.

Keywords: Multidisciplinary Optimization, Gradient-Based Optimization, Turbomachinery Components, CAD

Over one decade of research has been conducted at the *von Karman Institute* (VKI) to develop a fully automatic multidisciplinary and multi-objective optimization system with focus on turbomachinery components (e.g. [1],[2],[3],[4],[5]). Evolutionary algorithms (EA), based on mechanisms found in nature according to the Darwinian theory such as mutation, crossover, and selection are used to find designs with minimal objective values ([6][7]). EA's have certain advantages [6] as they can handle non-differentiable, nonlinear, and multi-modal objective functions. These features make EA's particularly suitable to explore the complete design space without the risk of becoming trapped in a local minimum.

However, once the region of the global optimum within the design space is identified (see Fig. 1) gradient-based methods become attractive as they make directly use of the gradient of the objective function [8]. Moreover gradient-based methods provide the sensitivity of the gradients, i.e. the direction in which parameters need to be relocated to minimize the objective values. This is an important feed-back in the overall design process of turbomachinery components.

Regarding the terminology of CAD-based and CAD-free parameterization, a clear distinction is necessary. CAD-based parameterization refers to curves and surfaces defined by Bézier and B-Spline curves and surfaces [9], respectively. In CAD-free parameterization, surfaces are represented by the nodes of the surface mesh of the body. According to Fudge et al. [10] the CAD-free approach is intended for academic studies of relatively simple geometries, while the CAD-based system is suitable for geometries that are more complex and for industrial use. The CAD-based approach has certain advantages, e.g. it guarantees G2 continuity of the curves and surfaces and allows to use engineering parameters like lean, sweep, and stagger angle [11]. The main disadvantage is the inaccessibility of the source code of commercial CAD systems to compute the gradients. However, in recent years, great efforts were made to develop an in-house CAD system at VKI [12], hence being fully differentiable.

The main objective of this PhD research is to im-

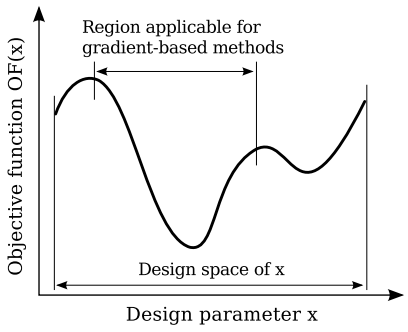

Figure 1: Feasible region of gradient-based methods for a single-objective function

plement gradient-based algorithms in the VKI optimization system based on CAD parameterization and to investigate the possible improvement as compared to evolutionary algorithms when applied to turbomachinery components. Computing the gradient of the objective function with respect to the design variables is an active field of research. Hence, many methods exist, e.g. the adjoint approach or automatic differentiation (AD). The feasibility of these methods will be assessed within the scope of this project and the most promising will be realized.

References

[1] S. Pierret, Designing Turbomachinery Blades by Means of the Function Approximation Concept Based on Artificial Neural Network, Genetic Algorithm and the Navier-Stokes Equations, Ph.D. thesis, von Karman Institute for Fluid Dynamics (1999).

[2] P. Rini, Z. Alsalihi, R. Van den Braembussche, Evaluation of a Design Method for Radial Impellers Based on Artificial Neural Network and Genetic Algorithm, in: Proceedings of the 5th ISAIF Conference, 2001, pp. 535–543.

[3] T. Verstraete, Z. Alsalihi, R. Van den Braembussche, Multidisciplinary Optimization of a Radial Compressor for Micro Gas Turbine Applications, in: ASME Turbo Expo 2007: Power for Land, Sea and Air, no. GT2007-27484, 2007.

[4] T. Verstraete, S. Amaral, R. A. Van den Braembussche, T. Arts, Design and Optimization of the Internal Cooling Channels of a HP Turbine Blade – Part II, Optimization, in: ASME Turbo Expo, Vol. GT2008-51080, 2008.

[5] T. Verstraete, Multidisciplinary Turbomachinery Component Optimization Considering Performance, Stress, and Internal Heat Transfer, Ph.D. thesis, Von Karman Institute for Fluid Dynamics - University of Gent (2008).

[6] R. Storn, K. Price, Differential Evolution - A Simple and Efficient Heuristic for Global Optimization over Continuous Spaces, Journal of Global Optimization 11 (1997) 341–359.

[7] G. Goldberg, Genetic Algorithms in Search, Optimization and Machine Learning, Addison-Wesley, 1989.

[8] A. Jameson, Gradient Based Optimization Methods, http://aero-comlab.stanford.edu/jameson/ (2005).

[9] G. Farin, Curves and Surfaces for Computer Aided Geometric Design, Academic Press. (1993).

[10] D. M. Fudge, D. W. Zingg, R. Haimes, A CAD-Free and a CAD-Based Geometry Control System for Aerodynamic Shape Optimization, American Institute of Aeronautics and Astronautics, 2005, 43.

[11] S. Shahpar, Challanges to Overcome for Routine Usage of Automatic Optimisation in Industry, in: VKI Lecture Series: Introduction to Optimization and Multidisciplinary Design in Aeronautics and Turbomachinery, 2011.

[12] T. Verstraete, CADO: a Computer Aided Design and Optimization Tool for Turbomachinery Applications, in: 2nd International Conference on Engineering Optimization, 2010.

Re-entry Platform for In-flight Demonstration and In-situ Measurement

Gilles Bailet

Aeronautics and Aerospace Department, von Karman Institute for Fluid Dynamics, Belgium,gilles.bailet@vki.ac.be

Supervisor: Jean Muylaert

Director, von Karman Institute for Fluid Dynamics, Belgium, jean.muylaert@vki.ac.be

University Supervisor: Christophe Laux

Professor, Laboratoire EM2C, Ecole Centrale Paris, France, christophe.laux@ecp.fr

Abstract

The von Karman Institute for fluid dynamics is aiming to develop and launch a re-entry vehicle by June 2015. Based on the CubeSat standard, with a highly constraining form factor (34x10x10cm), the vehicle will be developed in the frame of the PhD thesis and will represents a low-cost approach for the study of ablation and radiation in the harsh aerothermodynamics environment.

Keywords: re-entry, CubeSat, ablation, radiation, de-orbitation

1. Introduction

In the frame of the QB50 project led by the von Karman Institute for Fluid Dynamics (VKI) the paper exposes the preliminary results of the PhD thesis for the development of a re-entry CubeSat. More detailed data could be found in Bailet et al. (2011). The scientific objective of the QB50 project is to study the temporal and spatial variations of a number of key constituents and parameters in the lower thermosphere (50-320 km) with an international network of 50 double CubeSats (Fig. 1), miniaturized satellites weighing 2 kg in a 20x10x10 cm3 volume. The 50 CubeSats in a circular orbit will be separated by a few hundred kilometers and will carry identical sensors that will perform in-situ, long duration (~3 months) and multi- point measurements. QB50 will also study the re-entry process by measuring a number of key parameters during the re-entry process with the vehicle presented in this paper.

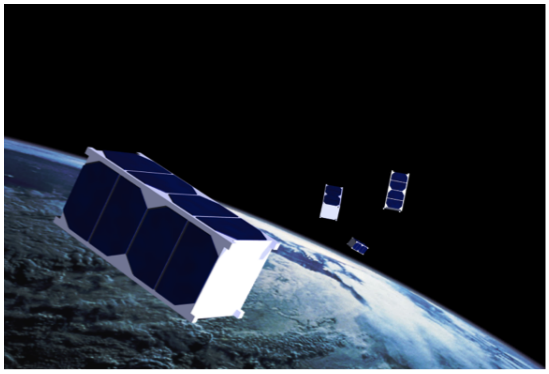

Figure 1: Artistic impression of few double-unit CubeSats of the QB50 constellation

2. Re-entry CubeSat concept

A low cost nano-size re-entry spacecraft for in-situ measurements and in-orbit demonstration will permit huge opportunities for independent research institutions and industries to test materials or subsystems in real flight conditions as it is not fully duplicable on ground. A very attractive part of such a mission is to provide an affordable low cost platform to validate ground testing and numerical simulations that are designed to understand the scientific background of the atmospheric re-entry of spacecraft.

The main difference between the proposed re-entry CubeSat platform and the 49 other QB50 CubeSats of the program is the need of an extra unit for the thermal protection system (TPS) to deal with the re-

entry constraints. Such CubeSat standard, a 3-Unit (3U) CubeSat, imposes a platform that does not exceed 34x10x10 cm in shape and 3 kg in mass. The challenging part of the re-entry is located below 120 km of altitude. The first step of the study has focused on a target minimum altitude expected between 50 and 70 km. A low altitude target is a challenge, because for every other re-entry vehicle, the payload is designed first and then the external shape of the spacecraft is defined such that it covers the integrity of the payload and permits a defined mission scenario to be executed. A major mission-constraint is to enforce the destruction of the vehicle before it reaches the ground thus avoiding any problem of collision with ground assets.

3. Feasibility analysis and conceptual design

After a shape definition by means of multi-criteria optimization (Bailet et al., 2011), it clearly appeared that the thermal protection system is one of the most crucial subsystems. Two different parts can be distinguished, the heat shield (first third of the vehicle) and the side panels. The heat shield part has been shown to be realistically feasible, through plasmatron tests and thermal response simulations. The Cork P50 has been chosen as TPS for its high thermal resistance capability and its affordability and availability. It appears in the second part that the thermal limitations would come from the side panels. In fact, the side panels in the standard concept (1.5 mm thick of aluminum) are not suitable at all to reach the most interesting part of the trajectory and should be two times and half the original size for an increased thermal protection of the sub-systems. This option is not desirable at all and a composite panel with the adjunction of a Nextel insulation layer has been selected as appropriate for the mass/volume budget and the thermal viability of the vehicle during the re-entry.

The proposed spacecraft design permits to carry out the experiment in-flight as expected. To provide these data as exploitable, the necessity to recover them without loss and with a suitable data rate according to the experiment sampling is needed. It has been shown that the most feasible system is to transmit the data up to the LEO/MEO orbit and then transmit it down to the ground stations. This methodology permits to avoid the re-entry black out and so have scientific return during the most interesting part of the trajectory hardly accessible otherwise. The choice of the scientific experiments in accordance with the available mass/volume capacity will permit in future studies to size the communication system in more details as applying new constrains on the power budget.

An adequate power budget is needed to avoid any incertitude in the orbital dynamic calculations. Actually, the re-entry will be extremely demanding for the power supply system. In only 10 minutes all flight experiments and subsystems of the vehicle will work in full regime and the antenna will need lots of energy to transmit the signal with an efficient gain. The next table presents the power budget with margins required to perform the experiments and transmit the data. A security margin equal to two is applied to the payload and the amplifier power budget to ensure that the designed equipment will be within this power consumption. The Communication system uses the HISPICO patch antenna (5 W) and the Iridium transceiver (¡1 W) to be the interface between the data acquisition system and the satellite relay communication system. A synthesis of the power budget is presented hereafter in Table 1.

Table 1: Power budget of the nano-size re-entry vehicle

Subsystem	*Power needed including margins W*
Functional unit (Avionic)	2
Telecommunication system	2
Payload + amplifier	6
Total	10

The available batteries are able to bring 10 Whr for each with a maximum of 30 Whr with three stackable batteries. The lifetime of the vehicle between 120 km (re-entry interface) and 50 km (targeted altitude) is 600 seconds but the power system have to be conceive in the optic to provide energy as soon as the solar panels stop their jobs. In the worst case, the Vehicle will have to spend a half of orbit before the re-entry (20 000 km at an altitude superior at 120 km) in the shadow of the earth and so the batteries should sustain the power supplement of the vehicle during this time estimate at 45 minutes. In reality, at an altitude above 120 km and so during this time, all subsystems will not be used. Actually, only the subsystems of the functional unit will consume some power and then, the real power budget will be lower. The most critical case (55 minutes of flight on the batteries) will consume 10 W of power. Considering this case, the power supply should have a capacity of at least 9 Whr. A single battery is at the limit of the needed power.

By adding a security margin, two batteries will be sufficient to perform the minimal experiments required and furnish 12.2 W of supplementary power for more demanding experiments. In the aim to add supplementary payloads a third battery (maximum a stackable batteries) could be needed to reach the limit of 33.3 W in total.

4. Conclusion

The feasibility study has shown the multi-disciplinary complexity of a nano-scale re-entry CubeSat and the necessity for each sub-system to be considered in a mass/volume optimization point of view, for the purpose of respecting the 3-unit CubeSat standard (3kg total weight limit and 3000cm3). Although the methodologies and results presented in this study have their limitations in both physical modeling and accuracy, the first approach permits to draw up the mass budget of the mission (Table 2).

All the work performed has been compiled to give the mass and power budgets for the vehicle and so demonstrate the interesting and feasibility of the proposed platform with a payload mass of minimum 0.612 kg. The mass available, associated to the payload mass, and the extra margins permits to be confident on the expected scientific return. Future studies within the PhD will permit to select the payloads according to the scientific objectives (ablation and radiation) through aerothermodynamics and line of sight simulations. The work presented in this paper has identified and treated the different critical challenges of the re-entry mission including the system view on the vehicle.

From the feasibility analysis to the final conceptual design every aspect of the mission have been covered and analyzed. The result of the study is promising for both system view and potential scientific return. For illustration purpose, Fig. 2 shows the proposed configuration for the re-entry CubeSat with external and internal composition.

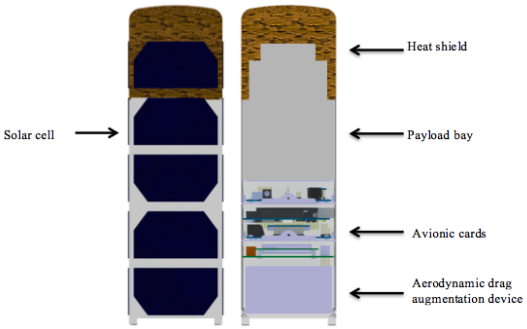

Figure 2: Re-entry CubeSat configuration external view (left) and internal view (right)

The nano-scale reentry vehicle remains an extraordinary opportunity for science and engineering in terms of in-situ experiment and in-flight demonstration capabilities and should be consider as the future low cost platform for in-flight experimentations.

Table 2: Mass budget of the nano-size re-entry vehicle

Subsystem	*Mass*	*Margins*	*Mass including margins*
	kg	*%*	*kg*
Heat shield	0.317	20	0.380
Functional unit	1008	0	
(Avionic, Structure,	+0.036 (nose support)	30	
Side panels,	+0.173(Nextel blanket)	10	1.248
(Telecommunication	+0.03 (transceiver)	10	
system			
Deorbiting system	0.400	30	520
Stability system	0.200	20	240
Total	1.937	-	2.388
		Payload	0.612-1.063

Acknowledgments

I would like to thank Mr. Jean-Marc Bouilly and his company EADS Astrium for their support and interest in this project.

References

[1] Bailet et al., Feasability Analysis and Preliminary Design of an Atmospheric Re-Entry Cubesat Demonstrator, 7th symposium on aerothermodynamics, ESA conference, Bruges, May 2011.

Multiscale Models and Computational Methods for Aerothermodynamics

Alessandro Munafò

Aeronautics and Aerospace Department, von Karman Institute for Fluid Dynamics, Belgium, munafo@vki.ac.be

Supervisor: Thierry Magin

Assistant Professor, Aeronautics and Aerospace Department, von Karman Institute for Fluid Dynamics, Belgium, magin@vki.ac.be

University Supervisor: Anne Bourdon

Chargée de recherche CNRS, Laboratoire EM2C CNRS UPR 288, École Central Paris, France, anne.bourdon@em2c.ecp.fr

Abstract

We propose to develop physical models and numerical methods for an accurate description of nonequilibrium physico-chemical phenomena in aerothermodynamics flows. Applications in aerospace range from space vehicle heat shield design to interpretation of experimental diagnostic measurements in high enthalpy facilities. In this work, we focus on the development of reduced collisional models for continuum nonequilibrium flows.

Keywords: Aerothermodynamics, Nonequilibrium, Collisional models, Coarse grain models, Finite volume method.

1. Introduction

Understanding nonequilibrium phenomena occurring in aerothermodynamic flows (such as the one around a spacecraft entering a planetary atmosphere) is of fundamental importance for many applications. Typical examples, taken from the aerospace domain, are the design of heat shields for space vehicles and interpretation of experiments carried out in high enthalpy wind tunnels. Nonequilibrium phenomena are also present in industrial processes making use of lasers, discharges and plasma torches. Progresses made in developing physical models and computational methods for aerospace applications, on which we focus here, could also be used in other areas (such as plasma enhanced combustion and electric propulsion) where the occurrence of nonequilibrium must be taken into account as well.

Before proceeding further, it is necessary to define nonequilibrium in aerospace applications. This concept can be introduced by recalling what occurs around a spacecraft entering a planetary atmosphere at hypersonic speeds. A strong bow shock is formed in front of the vehicle. The flow experiences a sudden compression. Pressure increases and, at the same time, most of the flow macroscopic kinetic energy is converted into thermal energy, leading to a steep temperature increase. The combined effects of pressure and temperature lead to higher values of collision frequencies between atoms and molecules and to more energetic collisions. These cause excitation of internal energy degrees of freedom and, if the collisions are energetic enough, breaking of chemical bonds can occur (molecular dissociation). If the entry speed is high enough ionization may also occur, and the gas becomes a partially ionized plasma where the presence of radiative transitions must be taken into account.

The description of these flows is extremely complicated because all collisional processes need a finite time to occur. If this time is very small compared to some macroscopic characteristic time scale (such as the time needed for a fluid particle to pass across a shock wave or through the boundary layer), the flow is in thermochemical equilibrium as it can immediately adapt to the varying conditions of pressure and temperature without any lag. If the inverse situation occurs, the flow is said to be frozen. The intermediate situation, where a finite lag exists, is that of nonequilibrium flows. In this case, a correct description of the flowfield can be achieved only if the finite rate nature

of collisional processes is taken into account in the flow governing equations.

The starting point for the description of nonequilibrium flows are the Navier-Stokes equations, where nonequilibrium effects can be taken into account by means of multi-temperature or collisional models [1; 2]. Multi-temperature are based on Boltzmann distributions of the internal energy levels at distinct temperatures and are valid only in case of small departure from equilibrium [3]. However, they are widely used outside of their range of validity because of the lack of more accurate physical models, their easy implementation and their reasonable computational cost for 3D simulations.

State-to-state or collisional models [4; 5; 6; 7; 8; 9; 10] treat each energy level as a separate pseudo-species. This approach provides more flexibility and accuracy, since effects of non-Boltzmann distributions are accounted for. However, a very large number of processes have to be considered and, for each one, rate coefficient values have to be obtained. Also, the number of equations to be solved rapidly increases with the number of internal energy levels. Applications of collisional models to 2D problems have become feasible as shown in [11; 12; 13].

A further complication in the study of nonequilibrium flows comes from the presence of rarefied gas effects [14]. These occur in flow regions (such as bow shocks and wakes) where the macroscopic spatial scales becomes of the same order of the local mean free path (average distance traveled by atoms/molecules between successive collisions). The main consequence of that is the failure of the Navier-Stokes equations where the shear stress tensor and heat flux vector are given by the Newton and Fourier laws (as it can be shown by means of the Kinetic theory of gases [15; 16]), respectively. If an accurate description of rarefied gas effects is wished, one should move towards numerical solutions of the Boltzmann equation for dilute gases. This equation expresses a balance in the phase space (velocity and position) for the species velocity distribution function and has a wider range of applications than the Navier-Stokes equations[1]. Stochastic numerical solutions of the Boltzmann equation can be obtained by means of DSMC (Direct-Simulation-Monte-Carlo) methods [17], the main reasons being (when aiming at a deterministic numerical solution) the necessity of solving an equation in a high dimensional space (the phase space) and the complicated mathematical structure of the elastic and inelastic collision operators. On the other hand, deterministic methods based on discrete velocity models [18] or on a spectral representation of the collision operator [19; 20] are gaining more and more popularity and have started to be used also for multi-dimensional flows [21].

We conclude this introduction by mentioning that nonequilibrium and rarefied gas effects are also present in recombining flows such as those occurring in nozzles. The latter are adopted in high enthalpy wind tunnels where understanding nonequilibrium is of crucial importance for a correct interpretation of experimental measurements.

2. Motivation

For the present doctoral period, it was decided to concentrate our research activity on the following topics:

- Development of reduced (coarse grain) collisional models for CFD applications. This activity will be performed within an innovative context at the interface between computational quantum chemistry and computational fluid dynamics.
- Development of computational methods for the numerical solution of the Boltzmann equation with chemical reactions and internal energy excitation. Applications will focus on flows out of the range of applicability of the Navier-Stokes equations (such as shock waves).

In this paper, the first topic is studied.

3. QCT-based coarse grain models for dissociation and internal energy excitation

3.1. The NASA Ames database

The development of coarse grain models for continuum nonequilibrium flows is based on the N + N_2 system database recently developed by the Computational Quantum Chemistry group at NASA Ames Research Center [4; 22; 5]. The NASA Ames database comprises 9390 (v, J) rovibrational levels for the electronic ground-state of nitrogen, where index v stands for the vibrational quantum number, and index J, the rotational quantum number. These levels can also be denoted by means of a global index i, sorting them by

[1] The Navier-Stokes equations are a first order perturbation solution to the Boltzmann equation as obtained independently by S. Chapman and D. Enskog [15].

increasing value of energy. The relation between the i and (v, J) notations is expressed as:

$$i = i(v, J),\ v = 0, \ldots, v_{\max},\ J = 0, \ldots, J_{\max}(v) \quad (1)$$

Conversely, the relation between the (v, J) and i notations is given by the relations:

$$v = v(i), \quad J = J(i), \quad i \in \mathrm{I_{BP}} \quad (2)$$

where $\mathrm{I_{BP}}$ is the set of global indices for the nitrogen energy levels. Most of these levels are truly bound, *i.e.*, their energy is lower than the dissociation energy relative to the level $(v = 0, J = 0)$, equal to 9.75 eV for the electronic ground-state of nitrogen, while some of the energy levels are predissociated, *i.e.*, their energy is higher than the dissociation energy relative to the level $(v = 0, J = 0)$.

The bound energy levels are denoted by the set $\mathrm{I_B}$, and the predissociated energy levels, by the set $\mathrm{I_P}$. The set for all the levels is then given by $\mathrm{I_{BP}} = \mathrm{I_B} \cup \mathrm{I_P}$. The database for the $\mathrm{N} + \mathrm{N_2}$ system comprises more than 23 million reactions, for the following collisional processes:

- Dissociation of truly bound states and predissociated states:

$$\mathrm{N_2}(i) + \mathrm{N} \underset{k_i^{Db}}{\overset{k_i^{Df}}{\rightleftharpoons}} \mathrm{N} + \mathrm{N} + \mathrm{N}, \quad i \in \mathrm{I_{BP}} \quad (3)$$

- Predissociation of the predissociated states:

$$\mathrm{N_2}(i) \underset{k_i^{Pb}}{\overset{k_i^{Pf}}{\rightleftharpoons}} \mathrm{N} + \mathrm{N}, \quad i \in \mathrm{I_P} \quad (4)$$

- Excitation between all states:

$$\mathrm{N_2}(i) + \mathrm{N} \underset{k_{ji}^{E}}{\overset{k_{ij}^{E}}{\rightleftharpoons}} \mathrm{N_2}(j) + \mathrm{N}, \quad i, j \in \mathrm{I_{BP}}, \quad j > i \quad (5)$$

The direct reaction rate coefficients k_i^{Df}, k_i^{Pf}, and k_{ij}^{E}, $j > i$, are obtained based on the reaction cross-sections for nine values of the gas translational temperature between 7,500 and 50,000 K. The reverse reaction rate coefficients k_i^{Db}, k_i^{Pb}, and k_{ij}^{E}, $j < i$, are computed based on micro reversibility.

3.2. Strategies for coarse grain model development

Different strategies have been considered for the development of coarse grain models for the quantitative description of nonequilibrium rovibrational dissociation and excitation.

3.2.1. Vibrational Collisional (VC) model

The development of a new Vibrational Collisional (VC) model for the $\mathrm{N} + \mathrm{N_2}$ system is the first step of coarse grain model development. The procedure employed for obtaining vibrationally averaged rate coefficients has been presented in [23; 24]. In [24] applications of the VC model to normal shock wave and quasi 1D nozzle flows have been shown and the results obtained have been compared with those obtained by means of multi-temperature (MT) models. Recently, rate coefficients for $\mathrm{N_2} + \mathrm{N_2}$ inelastic collisional processes among vibrational levels (VT and VV processes) have been added. Numerical values for them have been obtained by adapting the existing set of Billing data [25] to the vibrational energy levels of the NASA Ames database (the procedure is explained in [26]).

3.2.2. Boltzmann Rovibrational Collisional (BRVC) model

A new coarse grain approach has been proposed and investigated in parallel to the enrichment of the VC model recalled in the previous section. In this new coarse grain model, the energy levels of the $\mathrm{N_2}$ molecule are firstly sorted according to their values and then lumped into energy bins for which bin-averaged rate coefficients are obtained by means of the following procedure.

The energy E_i for level i within bin k is defined based on the energy $\hat{E}_k$ for the first level in the bin and the relative energy contribution with respect to this energy level:

$$E_i = \hat{E}_k + \Delta\hat{E}_k(i), \quad i \in \mathrm{I}_k. \quad (6)$$

The energy level populations are assumed to follow a Boltzmann distribution at the translational temperature T within the bin $k \in \mathrm{K_{BP}}$:

$$\frac{n_i}{\hat{n}_k} = \frac{1}{\hat{Q}_k(T)} g_i \exp\left(\frac{-\Delta\hat{E}_k(i)}{\mathrm{k_B}T}\right), \quad i \in \mathrm{I}_k \quad (7)$$

where the partition function $\hat{Q}_k(T)$ and number density for the bin $\hat{n}_k$ are defined as:

$$\hat{Q}_k(T) = \sum_{i \in \mathrm{I}_k} g_i \exp\left(\frac{-\Delta\hat{E}_k(i)}{\mathrm{k_B}T}\right), \quad \hat{n}_k = \sum_{i \in \mathrm{I}_k} n_i \quad (8)$$

where the symbols $\mathrm{k_B}$ stands for Boltzmann's constant and $g_i = g_i^{\mathrm{NS}}(2J(i) + 1)$ (with g_i^{NS} representing the nuclear and spin contributions to the degeneracy of the ground electronic state of the $\mathrm{N_2}$ molecule). As an alternative to Boltzmann Rovibrational Collisional

(BRVC) model presented in eq. (7), one could assume a uniform distribution within each bin leading to a Uniform Rovibrational Collisional (URVC) model that has successfully applied in [27]. This type of distribution does not allow to retrieve equilibrium when the number of bins is small.

The average rate coefficients for dissociation, predissociation and excitation for the BRVC model are:

$$\hat{k}_k^{Df}(T) = \frac{1}{\hat{Q}_k(T)} \sum_{i \in \mathrm{I}_k} g_i \exp\left(\frac{-\Delta \hat{E}_k(i)}{\mathrm{k_B} T}\right) k_i^{Df}(T), \quad (9)$$

$$\hat{k}_k^{Pf}(T) = \frac{1}{\hat{Q}_k(T)} \sum_{i \in \mathrm{I}_k} g_i \exp\left(\frac{-\Delta \hat{E}_k(i)}{\mathrm{k_B} T}\right) k_i^{Pf}(T), \quad (10)$$

$$\hat{k}_{kl}^{E}(T) = \frac{1}{\hat{Q}_k(T)} \sum_{i \in \mathrm{I}_k} g_i \exp\left(\frac{-\Delta \hat{E}_k(i)}{\mathrm{k_B} T}\right) \sum_{j \in \mathrm{I}_l} k_{ij}^{E}(T) \quad (11)$$

with $k \in \mathrm{K_B}$ in eq. (9), $k \in \mathrm{K_P}$ in eq. (10) and $k, l \in \mathrm{K_{BP}}$, $k < l$ in eq. (11). Reverse rate coefficients are computed by means of micro reversibility:

$$\frac{\hat{k}_k^{Db}}{\hat{k}_k^{Df}} = \frac{Q^t_{\mathrm{N_2}}(T)\, \hat{Q}_k(T) \exp(\frac{-(\hat{E}_k - 2E_\mathrm{N})}{\mathrm{k_B} T})}{[g_\mathrm{N} Q^t_\mathrm{N}(T)]^2}, \quad (12)$$

$$\frac{\hat{k}_k^{Pb}}{\hat{k}_k^{Pf}} = \frac{Q^t_{\mathrm{N_2}}(T) \hat{Q}_k(T) \exp(\frac{-(\hat{E}_k - 2E_\mathrm{N})}{\mathrm{k_B} T})}{[g_\mathrm{N} Q^t_\mathrm{N}(T)]^2}, \quad (13)$$

$$\frac{\hat{k}_{lk}^{E}}{\hat{k}_{kl}^{E}} = \frac{\hat{Q}_k(T) \exp(\frac{-(\hat{E}_k - \hat{E}_l)}{\mathrm{k_B} T})}{\hat{Q}_l(T)} \quad (14)$$

with $k \in \mathrm{K_B}$ in eq. (12), $k \in \mathrm{K_P}$ in eq. (13) and $k, l \in \mathrm{K_{BP}}$, $k < l$ in eq. (14). The quantity $g_\mathrm{N} = 12$ in eqs. (12) - (13) is the degeneracy of the N atom in the ground electronic state (N(^{4}S) nuclear and spin contributions) while $Q^t_\mathrm{N}(T)$ and $Q^t_{\mathrm{N_2}}(T)$ are the translational partition functions of the N atom and the N_2 molecule, respectively:

$$Q^t_\mathrm{N}(T) = \left(\frac{2\pi \mathrm{k_B} m_\mathrm{N} T}{\mathrm{h_P^2}}\right)^{3/2}, Q^t_{\mathrm{N_2}}(T) = \left(\frac{2\pi \mathrm{k_B} m_{\mathrm{N_2}} T}{\mathrm{h_P^2}}\right)^{3/2} \quad (15)$$

where the symbol $\mathrm{h_P}$ stands for Planck's constant.

3.3. Governing equations

The coarse grain models described in the previous sections have been applied to 1D/2D inviscid flows, for which, the governing equations can be written in the usual conservation law form:

$$\frac{\partial r^\epsilon \mathbf{U}}{\partial t} + \frac{\partial r^\epsilon \mathbf{F}}{\partial x} + \frac{\partial r^\epsilon \mathbf{G}}{\partial r} = r^\epsilon \mathbf{S}^{\mathrm{col}} + \epsilon\, \mathbf{S}^{\mathrm{axi}} \quad (16)$$

where $\epsilon = 0, 1$ for plane and axisymmetric flows, respectively. In eq. (16), $\mathbf{U}$ is the conservative variable vector, $\mathbf{F}$ and $\mathbf{G}$ are, respectively, the inviscid flux vectors along the x and r directions, $\mathbf{S}^{\mathrm{col}}$ is the source term vector due to collisional processes and $\mathbf{S}^{\mathrm{axi}}$ is an additional geometrical source term due to axial symmetry. The mathematical expressions for the quantities in eq. (16) change according to the physical model being used. If the BRVC model is considered, the following expressions are obtained:

$$\mathbf{U} = \left[\ \rho_\mathrm{N} \quad \tilde{\rho}_k \quad \rho u \quad \rho v \quad \rho E\ \right]^\mathrm{T}, \quad (17)$$

$$\mathbf{F} = \left[\ \rho_\mathrm{N} u \quad \tilde{\rho}_k u \quad p + \rho u^2 \quad \rho uv \quad \rho u H\ \right]^\mathrm{T}, \quad (18)$$

$$\mathbf{G} = \left[\ \rho_\mathrm{N} v \quad \tilde{\rho}_k v \quad \rho uv \quad p + \rho v^2 \quad \rho v H\ \right]^\mathrm{T}, \quad (19)$$

$$\mathbf{S}^{\mathrm{col}} = \left[\ \omega_\mathrm{N} \quad \tilde{\omega}_k \quad 0 \quad 0 \quad 0\ \right]^\mathrm{T}, \quad k \in \mathrm{K_{BP}}, \quad (20)$$

$$\mathbf{S}^{\mathrm{axi}} = \left[\ 0 \quad 0 \quad 0 \quad p \quad 0\ \right]^\mathrm{T} \quad (21)$$

In eq. (20), the components ω_N and $\tilde{\omega}_k$ of the source term vector $\mathbf{S}^{\mathrm{col}}$ represent the production rates for the N atom and the N_2 bins due to collisional excitation and dissociation and predissociation:

$$\omega_\mathrm{N} = 2M_\mathrm{N}[X_\mathrm{N}] \sum_{k \in \mathrm{K_B}} \left[\hat{k}_k^{Df}(T)\, X_k - \hat{k}_k^{Db}(T)\, [X_\mathrm{N}]^2\right] + 2M_\mathrm{N} \sum_{k \in \mathrm{K_P}} \left[\hat{k}_k^{Pf}(T)\, X_k - \hat{k}_k^{Pb}(T)\, [X_\mathrm{N}]^2\right], \quad (22)$$

$$\begin{aligned}\tilde{\omega}_k = &-M_{\mathrm{N_2}}[X_\mathrm{N}]\left[\hat{k}_k^{Df}(T)\, X_k - \hat{k}_k^{Db}(T)\, [X_\mathrm{N}]^2\right] \\ &- M_{\mathrm{N_2}}\left[\hat{k}_k^{Pf}(T)\, X_k - \hat{k}_k^{Pb}(T)\, [X_\mathrm{N}]^2\right] \\ &- M_{\mathrm{N_2}}[X_\mathrm{N}]\left\{\sum_{l \in \mathrm{K_{BP}}}^{k>l} \left[\hat{k}_{kl}^{E}(T)\, X_k - \hat{k}_{lk}^{E}(T)\, X_l\right]\right. \\ &\left. + \sum_{l \in \mathrm{K_{BP}}}^{k<l} \left[\hat{k}_{lk}^{E}(T)\, X_l - \hat{k}_{kl}^{E}(T)\, X_k\right]\right\}, \ k \in \mathrm{K_{BP}} \quad (23)\end{aligned}$$

For the VC model, the expressions for the vectors in eq. (16) and the production rates ω_N and $\tilde{\omega}_v$ for the N atom and N_2 vibrational levels are similar as given in [24; 26]. The only difference is that molecular energy exchange (VT and VV) and molecular impact dissociation processes are considered. Hence, their presence must be taken into account in the expression for ω_N and $\tilde{\omega}_v$ (see [26] for more details).

Eq. (16) can also be used for the investigation of nonequilibrium effects in quasi 1D nozzle flows. The only modification (after dropping all quantities relative to the r direction and setting $\epsilon = 0$) is the inclusion of a geometrical source term $\mathbf{S}^{\mathrm{area}}$ (due to cross sectional area variation) in the right-hand-side of eq.

(16):

$$\mathbf{S}^{\text{area}} = -\frac{\partial \ln A}{\partial x}\left[\begin{array}{cccc} \rho_{\text{N}} u & \tilde{\rho}_k u & \rho u^2 & \rho u H \end{array}\right]^{\text{T}}, k \in \text{K}_{\text{BP}} \tag{24}$$

3.4. Numerical method

Eq. (16) is discretized in space by means of the Finite volume method [28]. Roe's approximate Riemann solver [29] is used for inviscid fluxes. Roe's averaged state is computed by using the linearization proposed in [30]. Higher order spatial accuracy is reached through a polynomial reconstruction performed on primitive [31] or characteristic variables [12; 13]. The van Albada and minmod limiters [28] are used in order to preserve solution monotonicity close to discontinuities.

Time integration of the space discretized system of equations is performed by means of a fully implicit method for 1D/quasi 1D flows [31], while an operator splitting approach [12; 13; 26] is used for 2D flows.

3.5. Applications

3.5.1. VC model

The VC model of Sec. 3.2.1 has been used for investigating the 2D axisymmetric nonequilibrium flow within the nozzle of the EAST (Electric Arc Shock Tube) facility at NASA Ames Research Center (see Fig. 1).

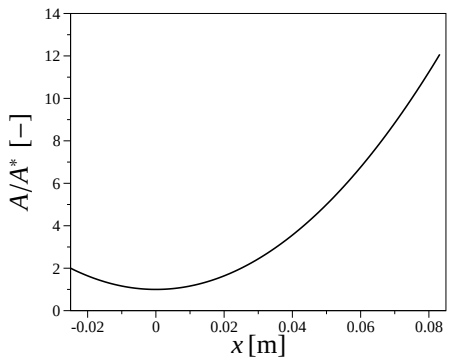

Figure 1: Normalized area distribution of the EAST facility nozzle (throat at $x = 0$ m).

Reservoir values of total pressure and temperature are 100 atm and 5,600 K, respectively. They correspond to operating conditions of the facility for which Raman spectroscopy measurements of the relative populations of vibrational levels are available [32]. Computations have been performed under the assumption of local thermodynamic equilibrium at the nozzle inlet. In order to get more physical insight from the simulation, a vibrational temperature T^{v} has been extracted from the vibrational energy level populations by solving the following algebraic non-linear equation:

$$\frac{\sum_{v=0}^{v_{\max}} \tilde{n}_v \tilde{E}_v}{n_{\text{N}_2}} = \frac{\sum_{v=0}^{v_{\max}} \tilde{E}_v \exp\left(-\frac{\tilde{E}_v}{k_{\text{B}} T^{\text{v}}}\right)}{\sum_{v=0}^{v_{\max}} \exp\left(-\frac{\tilde{E}_v}{k_{\text{B}} T^{\text{v}}}\right)} \tag{25}$$

at each mesh cell. Fig. 2 shows the temperatures together with the distribution of the same quantities along the nozzle axis.

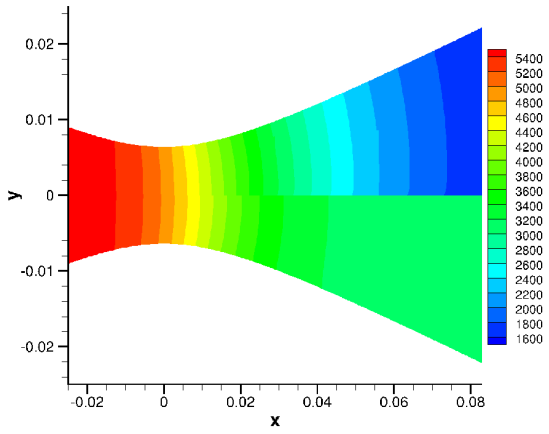

(a) Temperature distribution (upper part T - lower part T^{v}).

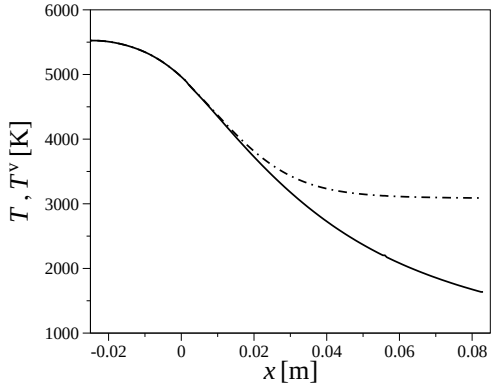

(b) Temperatures along the nozzle axis (—— T, –·– T^{v}).

Figure 2: Translational and vibrational temperatures.

The flow remains in thermal equilibrium for the entire converging part of the nozzle. Once it crosses the throat ($x = 0$ m), the expansion becomes significant and nonequilibrium effects start to appear. This is caused by a reduction of the flow macroscopic timescales due to the velocity increase. The translational

and vibrational temperatures start deviating from each other, with the latter becoming frozen around $x \simeq 0.04\,\mathrm{m}$. Downstream of this location, the flow further expands as if the inelastic collisional processes taken into account were not occurring.

The usage of a VC model allows for a detailed investigation of the energy level dynamics. Moreover, since no hypothesis is done on the population distribution, it is possible to check the approximation introduced by conventional multi-temperature models (where a Boltzmann distribution at its own temperature is supposed to exist for each species internal degree of freedom). Fig. 3 shows the evolution of the distribution along the nozzle axis.

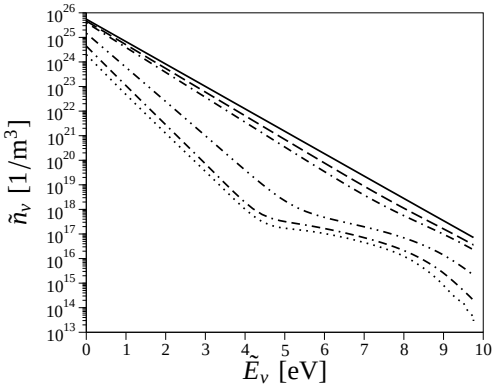

Figure 3: Population evolution along the nozzle axis (—— $x = -0.025\,\mathrm{m}$, – – – $x = -0.006\,\mathrm{m}$, – · – $x = 0\,\mathrm{m}$, – · · – $x = 0.024\,\mathrm{m}$, – – · – – $x = 0.054\,\mathrm{m}$, · · · · $x = 0.083\,\mathrm{m}$).

At the inlet, where equilibrium is imposed, all levels lie along a straight line. When the flow begins to expand in the converging part of the nozzle, the shape of the distribution remains the same. Only the slope changes as an effect of the cooling. A small overpopulation starts to appear (for high-lying levels) at the throat and this becomes more and more pronounced when the flow becomes supersonic. At the outlet, the ground state and low-lying levels are aligned along a straight line (whose slope is proportional to the inverse of the vibrational temperature T^{v} previously shown) while high-lying levels experience overpopulation. The latter is an indication that lumping all the levels within a Boltzmann distribution (as done within the context of multi-temperature models) is not possible (for the reservoir conditions adopted here).

The computed population distributions (for the first 9 vibrational levels) have been compared against experimental data acquired by means of Raman spectroscopy [32] at the locations $x = -0.006$, $x = 0.024$ and $x = 0.054\,\mathrm{m}$ (see Fig. 4). The agreement is excellent for the first location, where the flow is close to equilibrium. For the second and third locations, the agreement is good for the ground state and the first four excited levels, while discrepancies start to appear

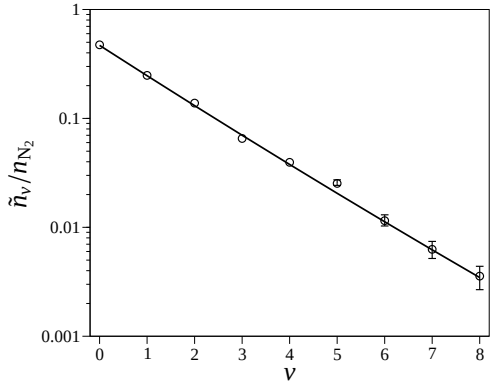

(a) Position 1 ($x = -0.006\,\mathrm{m}$).

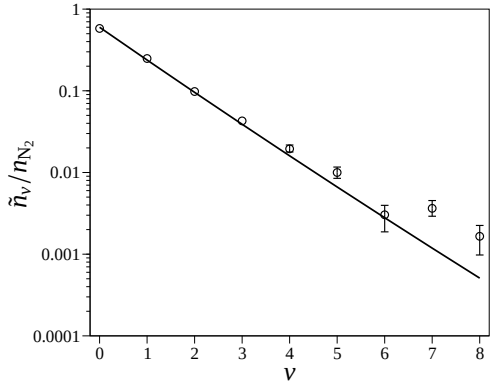

(b) Position 2 ($x = 0.024\,\mathrm{m}$).

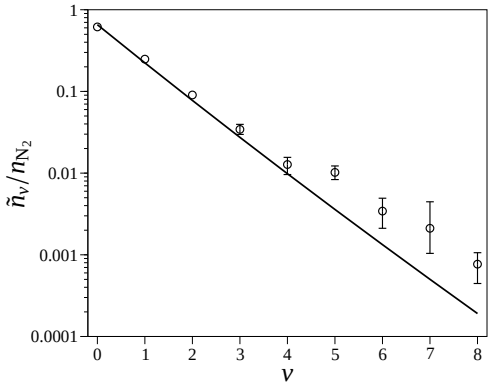

(c) Position 3 ($x = 0.054\,\mathrm{m}$).

Figure 4: Comparison between computed and experimental normalized vibrational energy level population distributions (—— Comp., ∘ Exp.).

for the higher states. In this zone (where measurement errors are more significant), the computational model adopted predicts a Boltzmann distribution at the temperature T^{v}, while an overpopulation appears in experimental data. The latter could be due to the presence of some nonequilibrium at the nozzle inlet (not accounted for in the computations). Moreover, the actual flow in the facility is characterized by the presence of viscous effects and unsteadiness. None of these factors has been taken into account within the computational model adopted. In view of that, the comparison between computational and experimental data can be considered satisfactory.

3.5.2. BRVC model

The BRVC model (see Sec. 3.2.2) has been applied to study nonequilibrium effects in simple flows, such as the flow downstream a normal shock wave and the quasi 1D flow within a nozzle. Computations have been performed by using different numbers of energy bins for the N_2 molecule for an estimation of how many bins are needed in order to get a flowfield description being both accurate (when compared with the Rovibrational Collisional (RVC) model) and computationally cheap. In this case, only N + N_2 collisions have been taken into account and computational results have been compared against the VC model of Sec. 3.2.1 and the classical Park MT model [33]. In all simulations, an internal temperature T^{int} has been extracted by solving the following non linear algebraic equation:

$$\frac{\sum_{k\in \mathrm{K_{BP}}} \hat{n}_k \hat{E}_k}{n_{\mathrm{N_2}}} = \frac{\sum_{k\in \mathrm{K_{BP}}} \hat{E}_k\, \hat{Q}_k(T)\, \exp(-\frac{\hat{E}_k}{\mathrm{k_B} T^{\mathrm{int}}})}{\sum_{k\in \mathrm{K_{BP}}} \hat{Q}_k(T)\, \exp(-\frac{\hat{E}_k}{\mathrm{k_B} T^{\mathrm{int}}})} \quad (26)$$

at each mesh cell in order to characterize macroscopically thermal nonequilibrium.

For the computation of nonequilibrium quasi 1D nozzle flow, the EAST nozzle shape (see Fig. 1) has been considered. In this case, the length of its diverging portion has been increased up to 0.15 m in order to enhance the gas expansion. The reservoir values of pressure and temperature have been artificially set to 1 atm and 10,000 K, respectively, in order to ensure N + N_2 collisions to be the dominant mechanism within the flow. Fig. 5 shows the temperature (translational, internal and vibrational) and N_2 molar fraction variations along the nozzle axis (75 bins for the BRVC model). The translation temperature for the VC and MT is not shown but it is very close to the one obtained by means of the BRVC model.

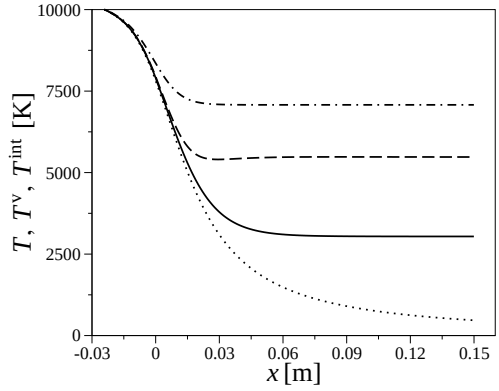

(a) Temperatures ($\cdots$ T BRVC, —— T^{int} BRVC, – – – T^{v} VC, – · – T^{v} MT.

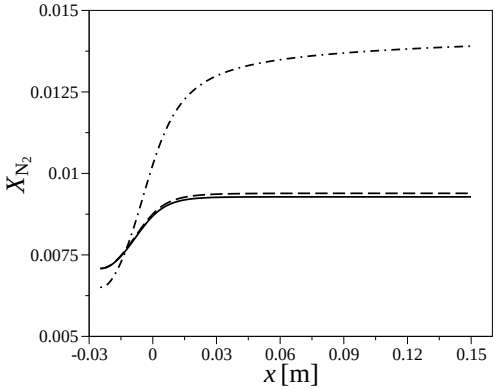

(b) N_2 molar fraction (—— BRVC, – – – VC, – · – MT).

Figure 5: Comparison between results provided by the BRVC (75 bins), VC and MT models (expanding flow).

The behavior of the vibrational and internal temperatures is very different for all models and this is due to the way the coupling between chemistry and internal energy (vibrational energy for VC and MT models) is realized in each model under consideration. In MT models, it is usually assumed that the average vibrational energy lost/gained during dissociation/recombination is equal to bulk vibrational energy of the flow (non preferential dissociation model [3]). However, the former does not take into account that molecules tend to preferentially recombine in high-lying states, as done by contrast by both VC and BRVC models. This inaccurate description has consequences not only on the temperatures, but also on the degree of recombination due to the coupling between chemistry and internal energy. This can be appreciated in Fig. 5, where it is shown that MT model provides the highest value. No appreciable differences (for the N_2 molar fraction) arise between the VC and

BRVC models. This fact could be explained by recalling that, for the conditions here adopted, rotational nonequilibrium effects (automatically taken into account in the BRVC) are negligible.

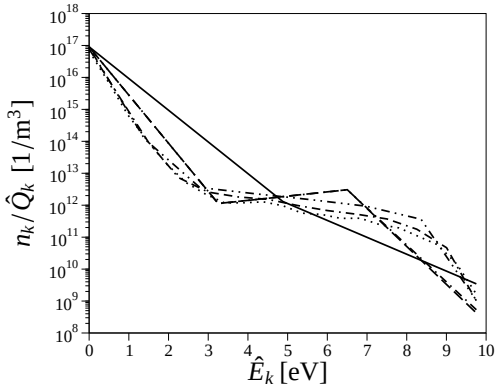

(a) —— 3 bins, – – – 4 bins, – · – 5 bins, – · · – 10 bins, – – · – – 20 bins, · · · · 30 bins.

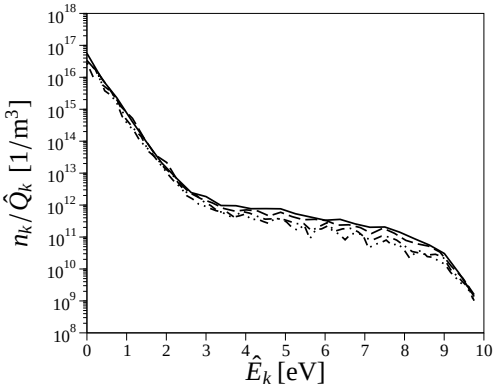

(b) —— 40 bins, – – – 50 bins, – · – 75 bins, – · · – 100 bins.

Figure 6: Bin number convergence study on the normalized population distribution at the nozzle outlet.

The same testcase has been run by using different number of bins (3, 4, 5, 10, 20, 30, 40, 50, 75 and 100) in order to understand its influence on the accuracy of the energy level dynamics. Fig. 6 shows the population distributions at the nozzle outlet with different number of bins. As already observed before for the VC model, the distributions experience in all cases departure from a Boltzmann distribution. In particular, heavy distortions due to overpopulation can be observed in the tail region. The former feature is common to all cases analyzed here. However, the accuracy of the description of the level dynamics is too poor when using 3-4 bins. The main features of the converged population distribution (straight line and plateau regions) are already retrieved with 10 bins. If the bin number is then increased, it is possible to obtain more accurate descriptions though the distributions look qualitatively the same. A good compromise between accuracy and computational efficiency (as suggested by the present testcase) would be to use 20-30 bins.

For the investigation of the nonequilibrium flow behind a normal shock wave, free-stream values of pressure, velocity and temperature have been set to 13.3 Pa, 10 km/s and 300 K, respectively. The free-stream has been seeded with 0.28 % of N since only N + N_2 collisions are taken into account.

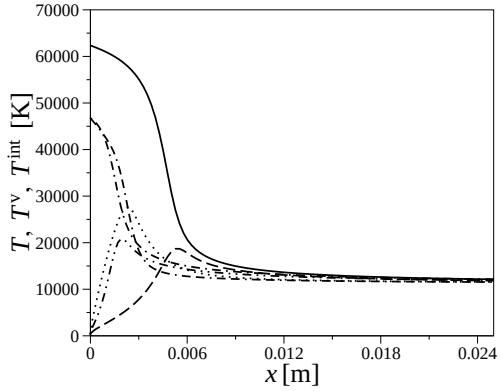

(a) Temperatures (—— T BRVC, – – – T^{int} BRVC, – · – T VC, – · · – T^v VC, – – · – – T MT, · · · · T^v MT).

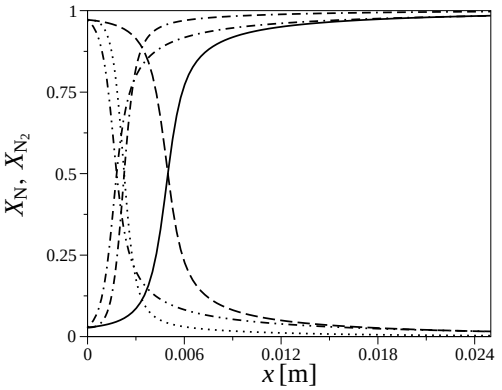

(b) Molar fractions (—— N BRVC, – – – N_2 BRVC, – · – N VC, – · · – N_2 VC, – – · – – N MT, · · · · N_2 MT).

Figure 7: Comparison between results provided by the BRVC (100 bins), VC and MT models (compressing flow).

A convergence study on the number of bins (see [31]), has allowed to retrieve the same conclusions as those found for the expansion case (i.e. only 20-30 bins are needed for a reasonably accurate description of the level dynamics).

Computational results have been compared with

those provided by the VC and MT models. Fig. 7 shows temperatures (translational, vibrational and internal) and N and N_2 molar fractions (100 bins for the BRVC model). The MT model leads to the fastest dissociation, while the BRVC is the slowest among the three models.

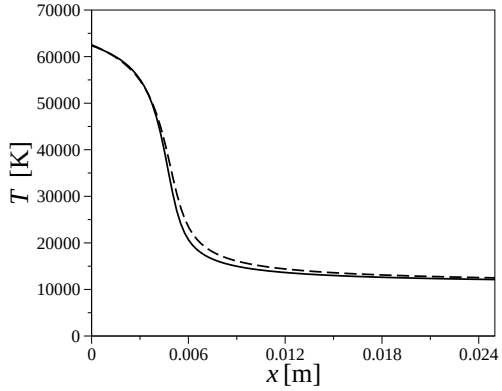

(a) Temperature (—— BRVC, – – – RVC).

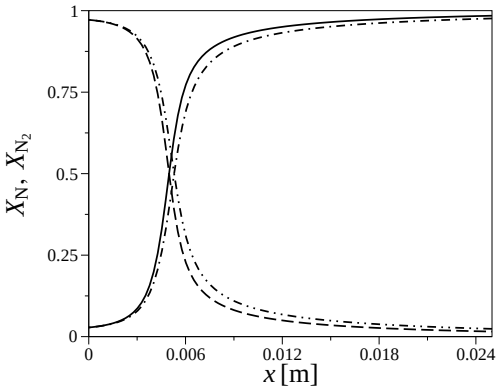

(b) Molar fractions (—— N BRVC, – – – N_2 BRVC, – · – N RVC, – · · – N_2 RVC).

Figure 8: Comparison between results provided by the BRVC (100 bins) and RVC models (compressing flow).

Differences between the BRVC and VC models arise now also for the chemical composition (while they are negligible in the expanding case). The faster dissociation obtained by means of the VC model is due to the hypothesis of rotational equilibrium. Indeed, in a previous work [34] it is has been shown that, for the free-stream conditions adopted here, the former hypothesis does not hold. On the other hand, the BRVC model does not make any assumption on the population of rotational levels. Hence, it automatically takes into account for rotational nonequilibrium effects. A confirmation is provided by the consistency observed for the translational temperature and N and N_2 molar fractions between the RVC and BRVC model solutions (see Fig. 8).

4. Conclusions

Coarse grain collisional models based on the NASA Ames Database for the N + N_2 system have been applied for the investigation of nonequilibrium effects in compressing and expanding flows. A VC model previously developed from the same database has been enriched in order to take into account for $N_2 + N_2$ inelastic collisions and been applied for computing the flow within the nozzle of the EAST facility. Computed vibrational energy level populations have been compared with experimental data. A good agreement has been observed. A new coarse grain BRVC model has been formulated and applied to 1D/quasi 1D flows. The results obtained have shown its higher flexibility (over the VC model) due to the possibility of taking into account for rotational nonequilibrium effects across shock waves.

Future work will focus on the multi-temperature reformulation of the BRVC and RVC models.

Acknowledgments

The research activity of the author is supported by the European Research Council Starting Grant #259354. The author would like to thank R. L. Jaffe and D. W. Schwenke, at NASA Ames Research Center, for providing the QCT rate coefficients used for obtaining the coarse grain models presented here, J. L. Cambier, at Edwards Air Force Base, and M. G. Kapper, at von Karman Institute, for their support and for providing the code used for the multi-dimensional simulations, and M. Panesi, at the University of Texas at Austin, for the help and the useful discussions while developing the Boltzmann Rovibrational Collisional model.

References

[1] C. Park, Nonequilibrium hypersonic aerothermodynamics, Wiley, New York, 1990.

[2] M. Capitelli, C. M. Ferreira, B. F. Gordiets, A. I. Osipov, Plasma kinetics in atmospheric gases, Springer, 2000.

[3] C. Park, The limits of two temperature model, AIAA Paper 2010–911, 48th AIAA Aerospace Sciences Meeting including the new Horizons Forum and Aerospace Exposition, Orlando, Florida (2010).

[4] R. L. Jaffe, D. W. Schwenke, G. Chaban, W. Huo, Vibrational and rotational excitation and relaxation of nitrogen from accurate theoretical calculations, AIAA Paper 2008-1208, 46th AIAA Aerospace Sciences Meeting and Exhibit, Reno, Nevada (2008).

[5] D. W. Schwenke, Dissociation cross-sections and rates for nitrogen, in: Non-equilibrium Gas Dynamics: from Physical Models to Hypersonic Flights, Lecture Series, von Karman Institute for Fluid Dynamics, 2008.
[6] F. Esposito, M. Capitelli, Quasi-classical molecular dynamic calculations of vibrationally and rotationally state selected dissociation cross sections: $N + N_2 \rightarrow 3N$, Chemical Physics Letters 302 (1) (1999) 49–54.
[7] J. G. Kim, O. J. Kwon, C. Park, Master equation study and nonequilibrium chemical reactions for $H + H_2$ and $He + H_2$, Journal of Thermophysics and Heat Transfer 23 (3) (2009) 443–453.
[8] A. Bultel, B. G. Chéron, A. Bourdon, O. Motapon, I. F. Schneider, Collisional-radiative model in air for earth re-entry problems, Physics of Plasmas 13 (4) (2006) 11.
[9] M. Panesi, T. E. Magin, A. Bourdon, A. Bultel, O. Chazot, Analysis of the fire II flight experiment by means of a collisional radiative model, Journal of Thermophysics and Heat Transfer 23 (2) (2009) 236–248.
[10] J. L. Cambier, S. Moreau, Simulation of a molecular plasma in collisional-radiative nonequilibrium, AIAA Paper 1993-3196, 24th AIAA Plasmadynamics & Lasers Conference, Orlando, Florida (1993).
[11] E. Josyula, W. F. Bailey, Vibration-dissociation coupling using master equations in nonequilibrium hypersonic blunt-body flow, Journal of Thermophysics and Heat Transfer 15 (2) (2001) 157–167.
[12] M. G. Kapper, J. Cambier, Ionizing shocks in argon. part I: Collisional-radiative model and steady-state structure, Journal of Applied Physics 109 (11) (2011) 113308.
[13] M. G. Kapper, J. Cambier, Ionizing shocks in argon. part II: Transient and multi-dimensional effects, Journal of Applied Physics 109 (11) (2011) 113309.
[14] C. Cercignani, Rarefied gasdynamics, Cambridge University Press, Cambridge, UK, 2000.
[15] S. Chapman, T. G. Cowling, The mathematical theory of non uniform gases, Cambridge University Press, Cambridge, UK, 1970.
[16] W. J. Vincenti, C. H. Kruger, Introduction to physical gasdynamics, Wiley, New York, 1965.
[17] G. A. Bird, Molecular Gas Dynamics and the Direct Simulation of Gas Flows, Clarendon press, Oxford, UK, 1994.
[18] F. G. Tcheremissine, Solution of the boltzmann equation for high-speed flows, Computational mathematics and mathematical physics 46 (2) (2006) 329–343.
[19] I. M. Gamba, S. H. Tharkabhushanam, Shock and boundary structure formation by spectral-lagrangian methods for the inhomogenesous boltzmann transport equation, Journal of Computational Mathematics 28 (4) (2010) 430–460.
[20] F. Filbet, G. Russo, High order numerical methods for the space non-homogeneous boltzmann equation, Journal of Computational Physics 186 (2) (2003) 457–480.
[21] L. Mieussens, Discrete-velocity models and numerical schemes for the boltzmann-bgk equation in plane and axisymmetric geometrieis, Journal of Computational physics 162 (2) (2000) 429–466.
[22] R. L. Jaffe, D. W. Schwenke, G. Chaban, Theoretical analysis of N_2 collisional dissociation and rotation-vibration energy transfer, AIAA Paper 2009–1569, 47th AIAA Aerospace Sciences Meeting and Exhibit, Orlando, Florida (2009).
[23] T. E. Magin, M. Panesi, A. Bourdon, R. L. Jaffe, D. W. Schwenke, Internal energy excitation and dissociation of molecular nitrogen in a compressing flow, AIAA Paper 2009–3837, 41st AIAA Thermophysics Conference, San Antonio, Texas (2009).
[24] A. Munafò, M. Panesi, R. L. Jaffe, A. Lani, T. E. Magin, Vibrational state to state kinetics in expanding and compressing nitrogen flows, AIAA Paper 2010–4335, 10th AIAA/ASME Joint Thermophysics and Heat Transfer Conference, Chicago, Illinois (2010).
[25] G. D. Billing, E. R. Fisher, VV and VT rate coefficients in N_2 by a quantum-classical mode, Chemical Physics 43 (3) (1979) 395–401.
[26] A. Munafò, M. G. Kapper, J. L. Cambier, T. E. Magin, Investigation of nonequolibrium effects in axisymmetric nozzle and blunt body nitrogen flows by means of a reduced rovibrational collisional model, AIAA Paper 2012-0647, 50th AIAA Aerospace Science Meeting, Nashville, Tennessee (2012).
[27] T. E. Magin, M. Panesi, A. Bourdon, R. L. Jaffe., D. W. Schwenke, Coarse-grain model for internal energy excitation and dissociation of molecular nitrogen, Chemical PhysicsIn press.
[28] C. Hirsch, Numerical computation of internal and external flows, John Wiley and Sons, Chichester, UK, 1988.
[29] P. L. Roe, Approximate riemann solvers, parameter vectors and difference schemes, Journal of Computational Physics 43 (2) (1981) 357–372.
[30] R. K. Prabhu, An implementation of a chemical and thermal nonequilibrium flow solver on unstructured meshes and application to blunt bodies:s, NASA CR 194867 (1994).
[31] A. Munafò, M. Panesi, R. L. Jaffe, A. Bourdon, T. E. Magin, Mechanism reduction for rovibrational energy excitation and dissociation of molecular nitrogen in hypersonic flows, AIAA Paper 2011-3623, 11th AIAA/ASME Joint Thermophysics and Heat Transfer Conference, Honolulu, Hawaii (2011).
[32] S. P. Sharma, M. R. Ruffin, W. D. Gillespie, S. A. Meyer, Vibrational relaxation measurements in an expanding flow using spontaneous raman scattering, Journal of Thermophysics and Heat Transfer 7 (4) (1993) 697–703.
[33] C. Park, Review of chemical-kinetic problems of future nasa mission, i: Earth entries, Journal of Thermophysics and Heat Transfer 7 (3) (1993) 385–398.
[34] T. E. Magin, M. Panesi, A. Bourdon, R. L. Jaffe, D. W. Schwenke, Rovibrational internal energy excitation and dissociation of molecular nitrogen in hypersonic flows, AIAA Paper 2010–4336, 10th AIAA/ASME Joint Thermophysics and Heat Transfer Conference, Chicago, Illinois (2010).

Arbitrary Lagrangian-Eulerian Simulation of a moving Piston in Hypersonic Ground Test Facility

Khalil Bensassi

von Karman Institute for fluid Dynamics, Aeronautics and Aerospace Department, bensassi@vki.ac.be

Supervisor: Patrick Rambaud

Associate Professor, Aeronautics and Aerospace Department, von Karman Institute for Fluid Dynamics, Belgium, rambaud@vki.ac.be

Co-Supervisor: Herman Deconinck

Associate Professor, Aeronautics and Aerospace Department, von Karman Institute for Fluid Dynamics, Belgium, deconinck@vki.ac.be

Abstract

Numerical simulation of a moving piston by means of an arbitrary Lagrangian-Eulerian solver in a two-dimensional field is performed in order to investigate the flow physics inside VKI-Longshot hypersonic ground test facility. The dynamics of the piston is coupled with the fluid using a moving boundaries. Rigid mesh strategy was used for the mesh adaptation algorithm. The numerical methods and time integration scheme are described. The space-time diagram shows the speed and the trajectory of the piston as well as the flow pattern involving expansion fan and shock waves in the driver-driven part of the facility.

Keywords: Unsteady Hypersonic flow, arbitrary Lagrangian-Eulerian, hypersonic facility

1. Introduction

The Development of future space vehicle requires hypersonic ground testing and extensive computations before the real flight. The success of a mission will depend on the reliability of the experimental data, the accuracy of the CFD and the methodology used to extrapolate these data from ground test to flight. The increase of the computational resources, the recent development in physical modeling and numerical schemes have gave the computational part much more important role in the space missions. The validation of the computational codes with experimental data is more than necessary , therefore accurate ground test conditions are needed. The free stream conditions in most hypersonic wind tunnel are very difficult to assess and remain on of the most challenging task even in the recent hypersonic facility. The uncertainties on their values could reach 20%. It's mostly due to a lack of experimental data on some part of the facility like inside the nozzle or the driven/driven tube and also to some technical difficulties to measure some main flow parameters. The full simulation of the facility is a complex task because it involves multi-physics and up to date it remains a challenging task.

In the current work we focus on the VKI-Longshot wind tunnel which is is a short duration facility (Fig.1) that can be operated with either nitrogen or carbon dioxide and it is designed to reach very high Reynolds number hypersonic flows. It is essentially based on two tubes (driver and driven tubes) and a nozzle which discharges into a test chamber. It has a Mach 14 contoured nozzle [5] of 0.42 m exit diameter and a 6° conical nozzle of 0.60 m exit diameter which can be used throughout a Mach number range from 15 to 20.

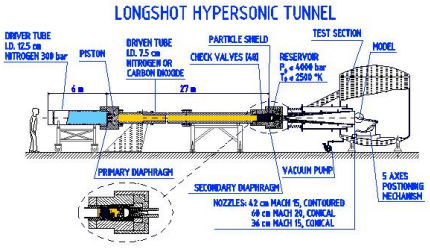

Figure 1: Schematic online of the Longshot tunnel

The driver gas, usually nitrogen operates at a pressure between 300 and 1000 bars at room temperature, in a 12.5 cm diameter tube which is 6 m long. The initial pressure of the gas in the driven tube can vary from 1 to 15 bars and its temperature is the room temperature. The nozzle and chamber are evacuated down to about 1 Pa pressure. In order to release the piston, a valve opens and applies the initial pressure on an extra surface of the piston front which is enough to break the diaphragm. The piston, then moves in the driven tube and it is accelerated at speeds of the order of 600 m/s, compressing the gas through a shock wave standing ahead at the end of the piston course there is a 48 check valves that allow the gas to be trapped. the gas expand through the nozzle into a $16m^3$vacuum vessel. A series of reflection occur between the piston head and the driver tube end which finally stops the piston. A decompression wave appears at the rear of the piston due to the rarefaction of the gas. It travels from the driver tube to eventually reach the rear part of the piston and causes the piston rebound. When the piston moves back in the driven tube, the pressure ahead of the piston decreases and finally becomes lower than in the reservoir. Therefore, in order to trap the gas in the $320cm^3$ reservoir, a plate check valves is installed at the end of the piston course which causes the closure of the 48 check valves. Once the gas is trapped, the second diaphragm breaks and this allows the gas to expand through the nozzle into a $16m^3$ vacuum vessel. In order to prevent the biggest particles caused by the rupture of the diaphragm from obstructing the nozzle or destroying the model, a particle shield has been placed just upstream the diaphragm.

2. Governing Equations

The conservative Navier-Stokes or Euler equations are usually solved on a computational domain $\Omega(t)$ that is constant in time, i.e $\Omega(t) = \Omega(t_0)$ for both steady and unsteady cases. the formulation used for those cases is called Eulerian form of the equations. In some cases, it is practical to use the velocity of the flow as a speed of the computational domain $\Omega(t)$, we then refer to a Lagrangian formulation. The formulation used for intermediate cases, in which the computational domain evolves and deforms independently, is called an Arbitrary Eulerian-Lagrangian formulation (ALE). The space discretization and time integration methods used in Eulerian framework were extended for Arbitrary Eulerian-Lagrangian formulation [2].

In the current work, Finite Volume method is used as a space discretization technique. The two-dimensional conservative Euler equations for a time dependent computational domain $\Omega(t)$ i.e in an Arbitrary Eulerian-Lagrangian formulation are:

$$\int_{\Omega(t)} \frac{\partial \mathbf{U}}{\partial t} d\Omega + \int_{\Omega(t)} \left(\frac{\partial \mathbf{F}_x}{\partial x} + \frac{\partial \mathbf{F}_y}{\partial y} \right) d\Omega = \int_{\Omega(t)} \mathbf{S} d\Omega \tag{1}$$

using Gauss theorem, we have:

$$\int_{\Omega(t)} \frac{\partial \mathbf{U}}{\partial t} d\Omega + \oint_{\partial\Omega(t)} \left(\mathbf{F}_x n_x + \mathbf{F}_y n_y \right) d\partial\Omega = \int_{\Omega(t)} \mathbf{S} d\Omega \tag{2}$$

where $\vec{n}$ is the outward normal to $\partial\Omega(t)$, and $\mathbf{F}_n$ is the normal flux defined as:

$$\mathbf{F}_n = \mathbf{F}_x n_x + \mathbf{F}_y n_y = (u n_x + v n_y)\mathbf{U} + \begin{pmatrix} 0 \\ p n_x \\ p n_y \\ p(\vec{v}_F \cdot \vec{n}) \end{pmatrix} \tag{3}$$

where $\vec{v}_F = (u, v)$ is the fluid velocity vector. Using Reynolds transport theorem to extract the time derivative:

$$\int_{\Omega(t)} \frac{\partial \mathbf{U}}{\partial t} d\Omega = \frac{d}{dt} \int_{\Omega(t)} \mathbf{U} d\Omega - \oint_{\partial\Omega(t)} \mathbf{U}(\vec{v}_G \cdot \vec{n}) d\partial\Omega \tag{4}$$

with $\vec{v}_G$ the velocity of $\partial\Omega(t)$ and we finally obtain :

$$\frac{d}{dt} \int_{\Omega(t)} \mathbf{U} d\Omega + \oint_{\partial\Omega(t)} \left[\mathbf{U}(\vec{v}_F - \vec{v}_G) \cdot \vec{n} \begin{pmatrix} 0 \\ p n_x \\ p n_y \\ p(\vec{v}_F \cdot \vec{n}) \end{pmatrix} \right]$$

$$d\partial\Omega = \int_{\Omega(t)} \mathbf{S} d\Omega \tag{5}$$

Eq. (5) shows that there are three contributions to the rate of change of $\mathbf{U}$ in $\Omega(t)$:

- Convection through $\partial\Omega(t)$ with speed $\vec{v}_r = (\vec{v}_F - \vec{v}_G)$
- Pressure surface terms
- Source terms

The domain $\Omega(t)$ is approximated by a set of N control volumes $\Omega_i(t)$. Thus, the second term of Eq. (5) is written as :

$$\oint_{\partial\Omega_i(t)} [\mathbf{F}_n - \mathbf{U}(\vec{v}_G \cdot \vec{n})]\, d\partial\Omega_i(t) = \sum_{m \in \partial\Omega_i(t)} F_m^{\perp} S_m \quad (6)$$

where $\Omega_i(t)$ is approximated by a sum of numerical fluxes. The numerical methods for the Arbitrary Lagrangian-Eulerian formulation are described in the next section.

3. Numerical Technique

3.1. Convective fluxes

AUSM scheme [4] was used this work. its Arbitrary Lagrangian Eulerian formulation have been described in [6], [1]. We have:

$$\mathbf{F} = \begin{bmatrix} \rho \cdot \vec{v}_r \cdot \vec{n} \\ \rho \cdot \vec{v}_F \cdot \vec{v}_r \cdot \vec{n} + p \cdot \vec{n} \\ \rho \cdot H \cdot \vec{v}_r \cdot \vec{n} + p \cdot \vec{v}_G \cdot \vec{n} \end{bmatrix} \quad (7)$$

where $\vec{v}_r = \vec{v}_F - \vec{v}_G$ is now the relative velocity.

As for the standard AUSM scheme, the convective ($\mathbf{F}^c$) and pressure ($\mathbf{F}^p$) fluxes are treated separately. The convective flux is written as:

$$\mathbf{F}^c = M_r \cdot a \cdot \Phi, \qquad \mathbf{\Phi} = \begin{bmatrix} \rho \\ \rho \vec{v}_F \\ \rho H \end{bmatrix} \quad (8)$$

where the local Mach number is now the relative local Mach number M_r. The flux $\mathbf{F}^p$ corresponding to the acoustic waves is described as:

$$\mathbf{F}^p = \begin{bmatrix} 0 \\ p \cdot \vec{n} \\ p \cdot \vec{v}_G \cdot \vec{n} \end{bmatrix} \quad (9)$$

in which we can note the appearance of an extra term $p \cdot \vec{v}_G \cdot \vec{n}$ depending on the mesh velocity $\vec{v}_G$.

where x_i denotes the centroid position of the control volume Ω_i. The linearly reconstructed state variables $\tilde{u}$ is calculated using least-squares method . In order to prevent the appearance of oscillations near discontinuities a flux limiter ϕ_i is needed on the reconstructed states. In the present work Venkatakrishnans limiter [7] is used.

3.2. Implicit Time integration

The time integration scheme proposed by Wuilbaut [8] which is a blending between a first-order positive time integration scheme (Backward Euler) and the 2nd order accurate Backward Differentiation scheme.

$$\frac{\mathbf{U}(\mathbf{P^{n+1}}) - \mathbf{U}(\mathbf{P}^n)}{\Delta t} + \theta\left(\frac{\mathbf{U}(\mathbf{P^{n+)}}) - 2\mathbf{U}(\mathbf{P}^n) + \mathbf{U}(\mathbf{P}^{n-1})}{\Delta t}\right) = -\mathbf{R}(\mathbf{P}^{n+1}) \quad (10)$$

where θ is a blending coefficient $\theta \in [0, 1]$. This blending is defined such that when $\theta = 1.$, the scheme is the 2nd order Backward Differentiation scheme while when $\theta = 0.$, the scheme transforms into a 1st order Backward Euler scheme. The resulting scheme is of order two in smooth flows ($\theta = 1.$) while reducing to 1st order at discontinuities ($\theta = 0$). This blending coefficient depends only on the evolution of the variable in time and acts like a time limiter defined as:

$$\theta_i = \begin{cases} \sqrt{\frac{\phi_i(r_i)}{max(1,|r_i|)}} & if\ |r_i| \geq \alpha \\ 1 & otherwise \end{cases} \quad (11)$$

Where ϕ_i is one of the space limiter function, in this work we use MINMOD limiter , α is a threshold parameter and r_i is the ratio of temporal slopes at any given point :

$$r_i = \frac{\frac{U_i^{n+1} - U_i^n}{\Delta t}}{\frac{U_i^n - U_i^{n-1}}{\Delta t}} \quad (12)$$

. This definition preserves the 2nd order accuracy for sufficiently smooth solution. At each time step, the system (10) is solved implicitly until convergence through a Newton iteration. At each of the inner time step iterations, the value of θ is updated using the solution $U^{n+1,k}$ where k is the inner iterations index. The GMRES algorithm with an Additive Schwartz preconditioner provided by the PETSC library serves to solve in parallel the corresponding linear systems arising from Newton linearization. The solution update is also performed in natural variables.

4. Flow prediction in the driver-driven tube

Numerical investigations of the flow in the diver-driven part the VKI-Longshot facility is performed using ALE solver in COOLFluiD framework [3] [8]. Fig. 2 shows a schematic of the driver-driven part of the VKI-Longshot facility. The driver tube has a

length of 6.095 m and an internal diameter of 127 mm. The driven tube is 27.50m long and an internal diameter of 76.2mm.

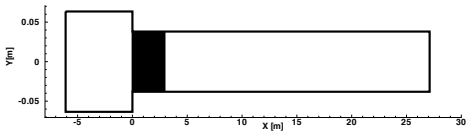

Figure 2: VKI-Longhost: driver-driven part

In the current work, the driver and the driven were considered as a one tube with the same diameter. The length of the driver tube was modified in order to keep the same volume of the gas as it is used in the real geometry. This approximation simplify the re-meshing algorithm, and eliminate the chamber effect.

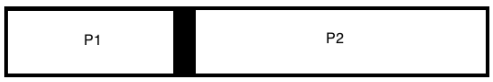

Figure 3: VKI-Longshot : simplified driver-driven geometry

The test condition concerning the pressures in the dirver and driven tubes are given un table 1 and the data related to the piston are given in table 2.

P_{driver} [Pa]	P_{driven} [Pa]
344.7	275800

Table 1: Initial driver-driven pressure for high Reynolds test conditions

Mass [kg]	Length [m]
4.592	0.355

Table 2: Piston Mass and length for high Reynolds test conditions

The numerical problem to be solved and the computational domain that is used are shown in Fig. 4.

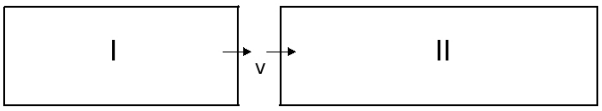

Figure 4: Computational domain

s

The physical domain (driver-driven tube) is divided into two subdomains, the left domain represents the driver tube and the right domain is the driven tube. The piston is simulated using moving boundaries of the two subdomains. The dynamic of the piston is implemented using Newton law. The only force (considered in this work) that apply on the piston are the sum of pressures on each face. Each time step, the displacement of the piston is computed allowing it advancement in time. Rigid mesh strategy is used to compute the mesh at each time steps, the nodes are equally redistributed on the boundaries allowing strong mesh deformation.

5. Results

Unsteady numerical simulation of the moving piston inside the driven tube has been performed. The initial conditions are given in table 1, the end of the driven tube is closed, and a wall is imposed as a boundary condition. This analysis is valid only during the first 5 ms of the full experimental test. In real conditions the diaphragm at the end of the driven tube beaks after the initial shock created by the piston strikes the end of the driven tube, then the dynamic of the piston depends also on what is happening outside the driven-driven tubes, i.e the flow in the nozzle.

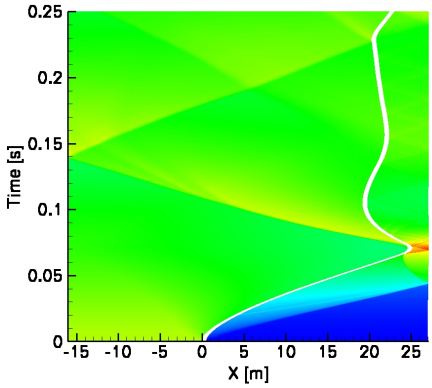

Figure 5: X-time Diagram : $Log[p]$ field

Fig. 5 shows pressure field in logarithmic scale, the white space in the filed shows the trajectory of the piston during the 25 ms. The expansion waves and the shock ahead of the piston before its rebound are shown in Fig. 6. After colliding with the reflected shock from the end of the driven tube, the piston is decelerated before a complete stop and changing its directions speed, thus creating anther compression wave

which is traveling to the driver tube. The primary shock hits the end of the driver tube after 4.3 ms, time at which the diaphragm breaks.

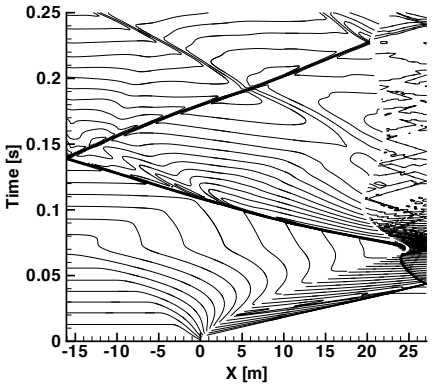

Figure 6: X-time Diagram : iso-pressure [Log_p] lines

Fig. 7 shows the pressure on the back face of the piston, It decreases due to the expansion fan behind the piston then it starts increasing when the piston decelerates. The pic conditions are reached when the piston changes its direction.

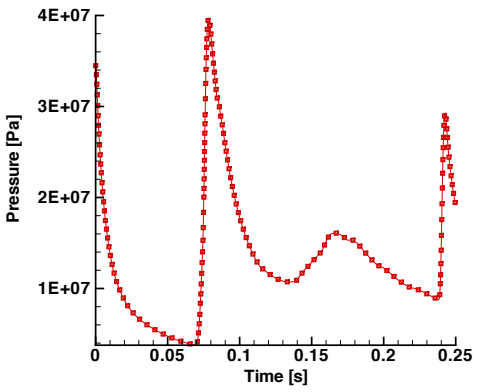

Figure 7: Pison: pressure at the back face

Fig. 8 shows the speed and the position of the piston along time. The maximum speed of 475 m/s is reached after 6ms. The piston stops at 24.75 m, goes back in the opposite direction and continue going back and forth driven by the pressure gradient on its back and front faces. There is no mechanism to stop the piston inside the facility, however a check valves are used in order to maintain the pressure in the reservoir when the piston starts going backward. These check valve were not taken into account in this current work.

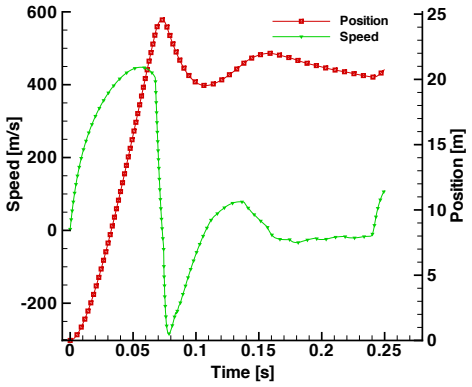

Figure 8: Piston: speed and position

6. Conclusions

Numerical simulation of a moving piston in VKI-Longshot hypersonic facility was performed using Arbitrary Lagrangian-Eulerian solver. This work was a first step throughout a complete simulation of the facility. It was necessary in order to understand the dynamic of the piston inside the driven-driver part of the facility before going any step further. The range of velocities and pressures involved in the first stage of the test were identified. The next step is a validation of the ALE solver with experimental data. Finally, diaphragm boundary condition has to be developed in order to couple the driver-driven tube with the hypersonic contoured nozzle and achieve the simulation the the full facility.

References

[1] D. Darracq, S. Champagneux, and A. Corjon. omputation of unsteady turbulent airfoils with an aeroelastic ausm+ implicit solver. *AIAA*, (98-2411), 1998.

[2] C.W Hirt. An arbitrary lagrangian-eulerian computing technique. volume 8. PHYSICS AND ASTRONOMY, 1971.

[3] Andrea Lani, Tiago Quintino, Dries Kimpe, and Herman Deconinck. The coolfluid framework - design solutions for high-performance object oriented scientific computing software. In *International Conference Computational Science 2005*, volume 1, pages 281–286, Atlanta, 2005. Springer-Verlag.

[4] M. S. Liou. A sequel to ausm, part ii: Ausm$^+$-up for all speeds. *Journal of Computational Physics*, 214:137–170, 2006.

[5] G. Simeonides. The contoured mach 15 longshot nozzle: final design parameters and construction. Internal note 87, von Karman Institute for Fluid Dynamics, September 1989.

[6] R. Smith. A geometrically conservative arbitrary lagrangian-eulerian flux splitting scheme. *Journal of computational physics*, 17(150):268–286, 1999.

[7] S. Venkateswaran and Ch. L. Merkle. Analysis of preconditioning methods for the Euler and Navier-Stokes equations.

VKI LS 1999-03, von Karman Institute for Fluid Dynamics, St.-Genesius-Rode, Belgium, March 1999.

[8] T. Wuilbaut. *Multi-Physics*. PhD thesis, Université Libre de Bruxelles, 2008.

Residual Distribution Methods For Atmospheric Entry Aerothermodynamics

Jesús Garicano Mena[1]

Aeronautics and Aerospace Department, von Karman Institute for Fluid Dynamics, Belgium, jesus.garicano.mena@vki.ac.be

Supervisor: Herman Deconinck

Professor, Aeronautics and Aerospace Department, von Karman Institute for Fluid Dynamics, Belgium, deconinck@vki.ac.be

Co-Supervisor: Andrea Lani

Research Engineer, Aeronautics and Aerospace Department, von Karman Institute for Fluid Dynamics, Belgium, lani@vki.ac.be

University Supervisor: Gérard Degrez

Professor, Service Aéro-Thermo-Mécanique, von Karman Institute for Fluid Dynamics, Belgium, Gerard.Degrez@ulb.ac.be

Abstract

In the present contribution the issue of simulating hypersonic flows by means of Residual Distribution Schemes is discussed. In particular, this discretization technique is briefly presented and its current capabilities reviewed. It turns out that certain aspects of the technique need some adjustments to deal with the very particular characteristics of the hypersonic regime. Extensive attention is given to the subject of enforcing conservation at the discrete level by means of a suitable conservative linearization.

Keywords: Residual distribution schemes, Conservative Linearization, Non-equilibrium Flow,Hypersonic flow, Compressible Flow.

1. Introduction

Numerical simulation of hypersonic flows is a challenging activity, since the complexities of compressible flow aerodynamics have to be addresed together with additional high-temperature effects due to thermal and chemical non equilibrium (or **TCNEQ**) phenomena (further details in [1]).

In the present contribution, we propose to use the Residual Distribution [2] (**RD**) framework for the discretization of the equations that govern the non-equilibrium hypersonic flow of air, as presented in [2]. The system of equations dealt with there expresses the conservation of mass, momentum and energy and can be cast in compact, vector form as:

$$\frac{\partial \vec{U}}{\partial t} + \nabla \cdot \bar{\bar{F}}^c = \nabla \cdot \bar{\bar{F}}^d + \vec{S}, \tag{1}$$

where $\vec{U}$ stands for the vector of conserved variables. For a two temperatures, N chemical species model, $\vec{U}$ includes the species densities ρ_s, the momentum ρu_j and the total ρE and electronic-vibrational energies ρe^v:

$$\vec{U} = \left[\rho_s, \quad \rho u_j, \quad \rho E, \quad \rho e^v\right]^t. \tag{2}$$

Tensors $\bar{\bar{F}}^c$ and $\bar{\bar{F}}^d$ describe the convective and diffusive fluxes of the conserved quantities, while vector $\vec{S}$ contains the chemical and internal energy modes source terms.

Several advantageous features of **RD** schemes justify our conviction of their suitability for the simulation of hypersonic flows. Among them, we stress the following:

- A maximum principle (Local Extrema Diminishing) borrowed from FVM, which allows to capture discontinuities monotonically on general unstructured grids;

[1]The author's research is funded by a *FRIA* fellowship provided by the FNRS.

[2]Sometimes **RD** methods are called fluctuation splitting (**FS**) as well.

- Being based on FE approximation theory, it is possible to obtain, on a compact stencil, 2nd order accurate solutions on unstructured grids;
- A better grid insensitivity on simplicial meshes, thanks to a built-in multidimensional dissipation property.

The reasons above encourage the application of **RD** schemes to the simulation of atmospheric entry flow problems. Nevertheless, the particular features of hypersonic flows prevent straightforward application of the method in its present form, since some details are not properly understood or still missing. This contribution focuses on how to enforce conservation at the discrete level, which is essential to capture accurately flow discontinuities.

In the following section, the problem found when trying to extend the Roe averaging procedure[3] (or its multidimensional counterpart[4]) to non-equilibrium flows is reported. Immediately after, a strategy to guarantee discrete conservation taken from the literature is presented and adapted for the N species, 2 temperatures thermo-chemical model we employ; its characteristics are then thoroughly detailed. After stating our conclusions, we close this contribution with a brief appendix containing the basics on **RD** schemes.

2. The importance of discrete conservation

The **RD** formalism has been applied to systems of equations structurally alike to that in Eq. 1, *e.g.*the Navier-Stokes equations for the turbulent flow of a Perfect Gas, as reported in [5] and [6].

For doing so, Eq. 1 is recast in quasilinear form before discretising it by means of **RD**:

$$\frac{\partial \vec{U}}{\partial t} + \bar{\bar{A}}^c_j \cdot \frac{\partial \vec{U}}{\partial x_j} = \nabla \cdot \bar{\bar{F}}^d + \vec{S}, \tag{3}$$

where $\bar{\bar{A}}^c_j$ stands for the Jacobian of the convective flux tensor with respect to the conserved variables $\vec{U}$:

$$\bar{\bar{A}}^c_j = \frac{\partial \vec{F}_j}{\partial \vec{U}}. \tag{4}$$

The steady state residual for cell Ω is defined as:

$$\vec{\Phi}^{\Omega} = \int_V \left(\bar{\bar{A}}^c_j \cdot \frac{\partial \vec{U}}{\partial x_j} - \frac{\partial \vec{F}^d_j}{\partial x_j} - \vec{S}^U \right) dV = \vec{\Phi}^{c,U} - \vec{\Phi}^{d,U} - \vec{\Phi}^{S,U}. \tag{5}$$

In the subsequent discussion we will consider only the convective contribution to the cell residual. Details on the dissipative and source terms discretization are given in the Appendix.

An essential ingredient for the applications reported in [5] and [6] is the possibility to represent the solution as a linear combination of nodal variables $\vec{Z}_j$, as in Eq. 34, such that an average state $\vec{\tilde{Z}}$ can be defined at every simplex, with the property that when the Jacobian matrices of the convective term in Eq. 4 are evaluated at it, the following relation is satisfied:

$$\begin{aligned}\vec{\Phi}^{\Omega,c} = \oint_{\delta\Omega} \bar{\bar{F}}^c \cdot \vec{n}\, ds = \int_\Omega \frac{\partial \vec{F}^c_j}{\partial x_j}\, dv = \int_\Omega \frac{\partial \vec{F}^c_j}{\partial \vec{Z}} \cdot \frac{\partial \vec{Z}}{\partial x_j}\, dv \\ = \left(\int_\Omega \frac{\partial \vec{F}^c_j}{\partial \vec{Z}}\, dv \right) \cdot \left. \frac{\partial \vec{Z}}{\partial x_j} \right|^h = \Omega \left. \frac{\partial \vec{F}^c_j}{\partial \vec{Z}} \left(\vec{\tilde{Z}} \right) \cdot \frac{\partial \vec{Z}}{\partial x_j} \right|^h = \\ \Omega\, \bar{\bar{A}}^c \left(\vec{\tilde{Z}} \right) \cdot \vec{n} \cdot \underbrace{\left. \frac{\partial \vec{U}}{\partial \vec{Z}} \left(\vec{\tilde{Z}} \right) \cdot \frac{\partial \vec{Z}}{\partial x_j} \right|^h}_{\left. \frac{\partial \vec{U}}{\partial x_j} \right|^{consistent}}. \end{aligned} \tag{6}$$

That is, Eq. 6 just states that evaluating the cell convective residual as the product of the Jacobian matrices and the consistent gradient of the conserved variables is equivalent to computing the contour integral of the fluxes across the boundaries of the simplex. This means that the numerical solution obtained respects a conservation principle, which is crucial when simulating flow fields including discontinuities.

For the Perfect Gas case, the variable $\vec{Z}$ is, as in [3]:

$$\vec{Z} = \left[\sqrt{\rho}, \quad \sqrt{\rho} u_j, \quad \sqrt{\rho} H \right]^t, \tag{7}$$

and the average state is -for the multidimensional case- the one corresponding to [4]:

$$\vec{\tilde{Z}} = \sum_{i=1}^{d+1} \frac{\vec{Z}_i}{d+1}, \tag{8}$$

where d is the physical dimensionality of the problem.

However, for the general N species, 2 temperatures model we intend to employ for non-equilibrium hypersonic flow computations, obtaining a single, physically meaningful average state is by no means trivial. The difficulty comes from the fact that the pressure, given by:

$$p = \sum_{i=1}^{N} \left(\frac{R}{M_s} \rho_s \right) T, \tag{9}$$

cannot be expressed explicitly in terms of the components of a corresponding $\vec{Z}$ vector.

A reformulation of **RD** schemes guaranteeing conservation (known as Contour Integration Based Residual Distribution or **CRD** scheme, see in [7]) is available; **CRD** schemes are unfortunately not applicable for general

hypersonic applications since they sometimes fail in providing monotone solutions across discontinuities, as reported in [8]. This event leads us to resort to the original Linearization Based **RD** approach, as described in [5], based on the multidimensional generalization of the Roe parameter vector described in [4].

In the following section we describe one possible strategy to uniquely define an average state which guarantees conservation at the discrete level.

3. Enforcing discrete conservation for non-equilibrium flow computations

Liu and Vinokur presented a strategy to guarantee discrete conservation when employing the Roe scheme to simulate the hypersonic flow of gas mixtures out of thermal and chemical equilibrium, in [9]. Degrez and van der Weide extended Liu and Vinokur's formulation, limited to dimensionally splitted solvers, to the multidimensional upwind context, though only for chemically reacting flows, in reference [10]. In what follows, we extend the results of Degrez and van der Weide for the case of a non-ionized gas in **TCNEQ** conditions.

Following the path traced by Degrez, we define the variable:

$$\vec{Z} = \left[\sqrt{\rho}\vec{Y}^t, \quad \sqrt{\rho}\vec{u}^t, \quad \sqrt{\rho}H, \quad \sqrt{\rho}e^v \right]^t. \tag{10}$$

The convective flux vector in Eq. 1 is, for the **TCNEQ** case:

$$\vec{F}_j^c = \left[\rho_s u_j, \quad \rho u_i u_j + p\vec{1}_j, \quad \rho H u_j, \quad \rho e^v u_j\right]^t, \tag{11}$$

and the following splitting is possible:

$$\vec{F}_j^c = \underbrace{\left(\vec{F}_j^c - [\vec{0}_{Nx1}, p\vec{1}_j, 0, 0]^t\right)}_{\vec{Q}} + \underbrace{[\vec{0}_{Nx1}, p\vec{1}_j, 0, 0]^t}_{\vec{\Pi}}. \tag{12}$$

It is evident that all terms in $\vec{Q}$ can be expressed as quadratic functions of the components of $\vec{Z}$, and thus entries in $\frac{\partial \vec{Q}}{\partial \vec{Z}}$ will simply be linear functions. On the other hand $\vec{\Pi}$ just contains the pressure. But more than in pressure itself, we are interested in its differential, which can be expressed -following reference [9]- as:

$$dp = \sum_{s=1}^{N} \alpha_s \, d\rho_s + \beta \, d\rho e^{tr}, \tag{13}$$

where terms α_s and β stand respectively for the partial derivatives of pressure with respect to the species densities and the translational-rotational energy, given by:

$$\begin{aligned} \alpha_s &= \frac{\partial p}{\partial \rho_s} = \frac{R}{M_s} T - \beta e_s^{tr}, \\ \beta &= \frac{\partial p}{\partial \rho e^{tr}} = \frac{\sum_{s=1}^{N} y_s \frac{R}{M_s}}{\sum_{s=1}^{N} y_s C_{v,s}^{tr}}, \end{aligned} \tag{14}$$

where e_s^{tr} is the s-th species contribution to the translational-rotational energy, $C_{v,s}^{tr}$ is the s-species translational-rotational specific heat at constant volume and y_s is the mass fraction.

In order to employ this principle in a multidimensional upwind framework, we consider:

$$\nabla p = \sum_{s=1}^{N} \alpha_s \, \nabla \rho_s + \beta \, \nabla \rho e^{tr}, \tag{15}$$

which can be immediately recast in terms of the components of parameter vector in Eq. 10 by using the relation:

$$\rho e^{tr} = \rho H - \frac{\rho \vec{u}^t \cdot \vec{u}}{2} - \rho e^v - p, \tag{16}$$

and considering:

$$\begin{aligned} \rho_s &= \left(\sum_{r=1}^{N} \sqrt{\rho} y_r \right) \sqrt{\rho} y_s, \\ \rho \vec{u}^t \cdot \vec{u} &= \sqrt{\rho}\vec{u}^t \cdot \sqrt{\rho}\vec{u}, \\ \rho H &= \left(\sum_{r=1}^{N} \sqrt{\rho} y_r \right) \sqrt{\rho} H, \\ \rho e^v &= \left(\sum_{r=1}^{N} \sqrt{\rho} y_r \right) \sqrt{\rho} e^v. \end{aligned} \tag{17}$$

At this point, if it is possible to find values for α_s and β for which Eq. 15 holds, then the gradient of pressure will be defined in terms of $\vec{Z}$, making in turn $\frac{\partial \vec{\Pi}}{\partial \vec{Z}}$ a linear function of the parameter vector as well, so that evaluating $\bar{\bar{A}}_j^c$ at an averaged state, as that in Eq. 8, would provide a conservative convective flux.

The problem is, however, that Eq. 15 provides as many equations as the dimensionality d of the problem (namely 1, 2 or 3) while $N + 1$ parameters have to be defined for the case of a non-ionized N species gas mixture.

In order to determine these $N + 1$ parameters, we can interpret Eq. 15 as d restrictions:

$$r_j \equiv \frac{\partial p}{\partial x_j} \beta - \sum_{s=1}^{N} \frac{\partial \rho_s}{\partial x_j} \alpha_s - \frac{\partial \rho e^{tr}}{\partial x_j}, \quad j = 1 \ldots d, \tag{18}$$

that the solution we seek for should respect. In that case, it would be sensible to look for a solution which, while fulfilling the aforementioned restrictions (guaranteeing thus conservation), is the closest one to a given a priori approximation, like for example the nodal averages:

$$\hat{\alpha}_s = \sum_{i=1}^{d+1} \frac{\alpha_s|_i}{d+1} \quad \hat{\beta} = \sum_{i=1}^{d+1} \frac{\beta|_i}{d+1}. \tag{19}$$

Under these hypotheses, we are faced with a constrained minimization problem. According to Liu [9], in order not

to obtain a solution dependent on the arbitrary reference enthalpy entering in the definition of the parameters α_s, it is better to work on the space $\{\xi_1, \ldots, \xi_N; \omega\}$, where:

$$\xi_s = \frac{\alpha_s}{\beta}, \; s = 1, \ldots, N; \quad \omega = \frac{1}{\beta} \tag{20}$$

We can define then the Lagrangian:

$$\mathcal{L} \equiv D - \lambda_{x_j} r_{x_j} = (\omega - \hat{\omega})^2 + \frac{1}{\hat{\sigma}^2} \sum_{s=1}^{N} \left(\xi_s - \hat{\xi}_s\right)^2 - \vec{\lambda}^t \cdot \left(\nabla p\, \omega - \sum_{s=1}^{N} \nabla \rho_s \xi_s - \nabla \rho e^{tr}\right), \tag{21}$$

where the factor $\frac{1}{\hat{\sigma}^2}$ is included for dimensional consistency, σ being typically of the order of the local speed of sound.

The corresponding stationary conditions are:

$$\begin{aligned} \frac{\partial \mathcal{L}}{\partial \xi_r} &= \frac{2}{\hat{\sigma}^2}\left(\xi_r - \hat{\xi}_r\right) + \vec{\lambda}^t \cdot \nabla \rho_r = 0, \quad r = 1 \ldots N, \\ \frac{\partial \mathcal{L}}{\partial \omega} &= 2\,(\omega - \hat{\omega}) - \vec{\lambda}^t \cdot \nabla p = 0, \\ \frac{\partial \mathcal{L}}{\partial \lambda_j} &= \frac{\partial p}{\partial x_j}\beta - \sum_{s=1}^{N} \frac{\partial \rho_s}{\partial x_j}\alpha_s - \frac{\partial \rho e^{tr}}{\partial x_j}, \quad j = 1 \ldots d. \end{aligned} \tag{22}$$

Fig. 1 shows the graphical interpretation of the minimization problem defined by the Lagrangian in Eq. 21 for a $2D$ computation and a 2 species mixture: starting from an approximation $\hat{P}$ in the space $\{\xi_r; \omega\}$, we look for the closest point $\tilde{P}$ which fulfills at the same time the $d = 2$ restrictions, that is, lies on the line where the blue and the green planes intersect.

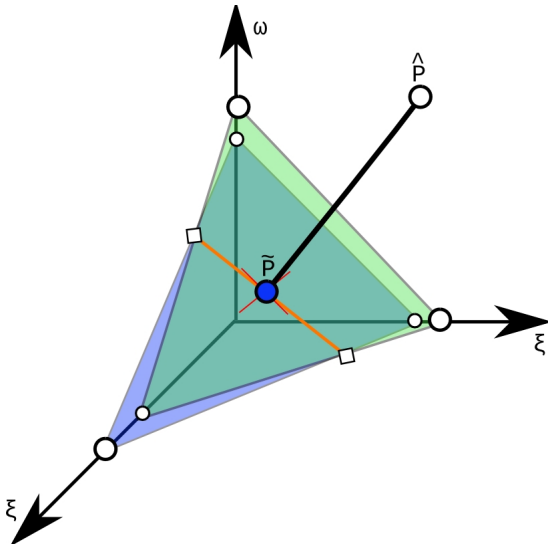

Figure 1: Constrained minimization problem: graphical interpretation.

Out of this stationary conditions, a linear system of equations is obtained:

$$\mathcal{A} \cdot \vec{x} = \vec{b}, \tag{23}$$

which consist, after application of elemental operations, of the coefficient matrix $\mathcal{A}$:

$$\mathcal{A} = \left[\begin{array}{c|c|cc} I_N & 0 & \frac{\hat{\sigma}^2}{2}\frac{\partial \rho \vec{y}}{\partial x} & \frac{\hat{\sigma}^2}{2}\frac{\partial \rho \vec{y}}{\partial y} \\ \hline \vec{0}_{1\times N} & 1 & -\frac{1}{2}\frac{\partial p}{\partial x} & -\frac{1}{2}\frac{\partial p}{\partial y} \\ \hline \vec{0}_{1\times N} & 0 & C_{xx} & C_{xy} \\ \vec{0}_{1\times N} & 0 & C_{xy} & C_{yy} \end{array}\right], \tag{24}$$

of the vector of unknowns $\vec{x}$:

$$\vec{x} = \left[\xi_1, \ldots, \xi_N; \omega; \lambda_{x_j}\right]^t, \tag{25}$$

and of the forcing vector $\vec{b}$:

$$\vec{b} = \left[\hat{\xi}_1, \ldots, \hat{\xi}_N; \hat{\omega}; -\hat{\omega}\,\delta p_{x_j}\right]^t, \tag{26}$$

where $C_{x_i x_j}$ stands for:

$$C_{x_i x_j} = \frac{1}{2}\left(\frac{\partial p}{\partial x_i}\frac{\partial p}{\partial x_j}\right) + \hat{\sigma}^2 \sum_{s=1}^{N}\left(\frac{\partial \rho_s}{\partial x_i}\frac{\partial \rho_s}{\partial x_j}\right), \tag{27}$$

while δp_{x_j} is:

$$\delta p_{x_j} = (1 + \hat{\omega})\frac{\partial p}{\partial x_j} - \sum_{s=1}^{N} \frac{\partial \rho_s}{\partial x_j}\hat{\xi}_s - \frac{\partial \rho e^{tr}}{\partial x_j}. \tag{28}$$

The structure of the linear system in Eq. 23 is such that a $d \times d$ subsystem:

$$\mathcal{B}\vec{\lambda} = -\omega\vec{\delta p}, \tag{29}$$

can be isolated, and once $\vec{\lambda}$ is determined (assuming that a solution exists), ξ_s and ω can be immediately obtained by back substitution.

Concerning the invertibility of $\mathcal{B}$, its determinant can be proven to be:

$$|\mathcal{B}| = \hat{\sigma}^2\left(\hat{\sigma}^2 \sum_{k,l=1,k\neq l}^{N}\left(\frac{\partial \rho_k}{\partial x}\frac{\partial \rho_l}{\partial y} - \frac{\partial \rho_k}{\partial y}\frac{\partial \rho_l}{\partial x}\right)^2 + \sum_{k=1}^{N}\left(\frac{\partial \rho_k}{\partial x}\frac{\partial p}{\partial y} - \frac{\partial \rho_k}{\partial y}\frac{\partial p}{\partial x}\right)^2\right) \geq 0, \tag{30}$$

being 0 only if planes r_j are coincident, but in that case we do not face a system of equations but rather a scalar equation, which poses no problem to invert.

The solution for the case $|\mathcal{B}| > 0$ is given by:

$$\lambda_x = \frac{C_{yy}\,\delta p_x - C_{xy}\,\delta p_y}{C_{xx}\,C_{yy} - C_{xy}\,C_{xy}}, \quad \lambda_y = \frac{C_{xx}\,\delta p_y - C_{xy}\,\delta p_x}{C_{xx}\,C_{yy} - C_{xy}\,C_{xy}}. \tag{31}$$

and the values of the pressure derivatives guaranteeing conservation are:

$$\begin{aligned} \tilde{\omega} &= \hat{\omega} + \frac{1}{2}\left(\lambda_x \frac{\partial p}{\partial x} + \lambda_y \frac{\partial p}{\partial y}\right), \\ \tilde{\xi}_s &= \hat{\xi}_s - \frac{\hat{\sigma}^2}{2}\left(\lambda_x \frac{\partial \rho_s}{\partial x} + \lambda_y \frac{\partial \rho_s}{\partial y}\right). \end{aligned} \tag{32}$$

The values that are actually employed in the computation are obtained in a straightforward manner from:

$$\tilde{\beta} = \frac{1}{\tilde{\omega}}, \quad \tilde{\alpha}_s = \tilde{\beta}\,\tilde{\xi}_s. \tag{33}$$

Now that the linearization procedure is well understood, and after testing it in a **FVM** framework, our next step will be to implement it in the non-equilibrium `COOLFluiD` **RD** solver .

4. Conclusions

In the present contribution the importance of having numerical schemes respecting conservation at the discrete level has been discussed. The reasons which make defining a conservative average state an involved task for flows out of equilibrium have been pointed out. A strategy to obtain a conservative linearization has been identified in the literature, and subsequently adapted to be applicable to the N chemical species, 2 temperatures model, and this into the multidimensional upwind framework of our interest. A theoretical analysis on the linearization procedure, and its limits of validity has been performed.

Residual Distribution Schemes: the basics.

A very short review of **RD** for the discretization of (1) is presented in this appendix. The interested reader will find extensive explanations in [5], [11] and [12].
The solution is expressed by means of a finite element representation on P1 linear triangles.

$$\vec{U}^h(\vec{x},t) = \sum_{j=1}^{\#DOF} \vec{U}_j(t)\, N_j(\vec{x}) \tag{34}$$

where the following property holds:

$$N_j(\vec{x}_k) = \delta_{jk} \tag{35}$$

The steady state residual for cell Ω is defined as:

$$\vec{\Phi}^{\Omega} = \int_{\Omega} \left(\frac{\partial \vec{F}_j^c}{\partial x_j} - \frac{\partial \vec{F}_j^d}{\partial x_j} - \vec{S}^U \right) dv = \vec{\Phi}^{c,U} - \vec{\Phi}^{d,U} - \vec{\Phi}^{S,U} \tag{36}$$

with contributions from the convective, dissipative and source terms.

The nodal system of equations is obtained by distributing fractions of the cell residuals $\vec{\Phi}^{\Omega}$ to the nodes forming part of the cell. The convective contribution to the nodal equation of the cell residual is expressed generically as:

$$\vec{\Phi}_l^{c,U} = \sum_{\Omega_i \in \Xi_l} B_l^{\Omega_i,U}(K^{\pm}) \cdot \vec{\Phi}_{\Omega_i}^{c,U}$$

in terms of the so called distribution matrices $B_l^{\Omega_i,U}$, which depend in turn on the nodal upwind parameters:

$$K_j = A_{j,x}\, n_{j,x} + A_{j,y}\, n_{j,y} + A_{j,z}\, n_{j,z} \tag{37}$$

where A_{j,x_d} is the Jacobian of the advective flux along direction x_d, and n_{j,x_d} are the components of the vectors normal to the element faces.

Different forms of the $B_l^{\Omega_i,U}$ matrices define different schemes. In this work, multidimensional, positive matrix N-scheme (further details in [5]) has been employed.

Distribution of diffusive contributions to the cell residual is done, when a $P1$ element mesh is used, by Galerkin discretization:

$$\vec{\Phi}_j^{d,U} = \int_{\Omega} \beta_j\, \nabla \cdot \bar{\bar{F}}^v\, dv \tag{38}$$

while source terms can be distributed either with the Galerkin method or together with the advective residual.

From the distribution process introduced before results a system of differential equation controlling the time evolution of the solution at the grid nodes. For l-th node, it is:

$$\Xi_l \frac{d\vec{U}_l}{dt} + \vec{\Phi}_l^{c,U} - \vec{\Phi}_l^{d,U} - \vec{\Phi}_l^{S,U} = \vec{0}, \tag{39}$$

where Ξ_l stands for the volume of the median dual cell around l-th node.

Acknowledgment

The author expresses his gratitude to his supervising team, Professors Deconinck and Degrez, and Dr. Lani for their continuous encouragement and support. The funding coming from von Karman Institute and FNRS, through a FRIA fellowship is gratefully acknowledged.

References

[1] J. D. Anderson, Hypersonic and High Temperature Gas Dynamics, McGraw Hill, New York, 1989.

[2] Gnoffo, P., Gupta, R. and Shinn, J., Conservation equations and physical models for hypersonic air flows in thermal and chemical non-equilibrium, TP 2867, NASA (1989).

[3] Roe, P.L., Approximate Riemann Solvers, Parameter Vectors, and Difference Schemes, Journal of Computational Physics 43 (1981) 357–372.

[4] Deconinck, H., Roe, P.L. and Struijs, R., A multidimensional generalization of Roe's flux difference splitter for the euler equations, Computers and Fluids 22 (2-3) (1993) 215–222.

[5] van der Weide, E., Compressible flow simulation on unstructured grids using multi-dimensiona upwind schemes, Ph.D. thesis, Technische Universitet Delft (1998).

[6] Sermeus, K. and Deconinck, H., Solution of steady euler and navier-stokes equations using residual distribution schemes, LS 2003-05, VKI (2003).

[7] Csik, A., Ricchiuto, M. and Deconinck, H., Conservative formulation of the multidimensional upwind residual distribution schemes for general nonlinear conservation laws, Journal of Computational Physics 179 (1) (2002) 286–312.

[8] Lani, A., Garicano Mena, J. and Deconick, H., A residual distribution method for symmetrized systems in thermochemical nonequilibrium, in: Proceedings of the 20th AIAA Computational Fluid Dynamics Conference, AIAA, Honolulu (Hawaii), 2011.

[9] Liu, Y. and Vinokur, M., Upwind algorithms for general thermo-chemical nonequilibrium flows, in: 46th AIAA Aerospace Sciences Meeting and Exhibit., Reno, 1989.

[10] G. Degrez, E. van der Weide, Upwind residual distribution schemes for chemical non-equilibrium flows, in: Collection of Technical Papers. Vol. 2, AIAA, 1999, pp. 978–987.

[11] Ricchiuto, M., Construction and analysis of compact residual distribution discretizations for conservation laws on unstructured meshes, Ph.D. thesis, Université Libre de Bruxelles (2005).

[12] Villedieu, N., High order discretisation by residual distribution schemes, Ph.D. thesis, Université Libre de Bruxelles (2009).

Stagnation Line Approximation for Ablation Thermochemistry

Julien de Mûelenaere

Aeronautics and Aerospace Department, von Karman Institute for Fluid Dynamics, Belgium, julien.demuelenaere@vki.ac.be

Supervisor: Thierry Magin

Assistant Professor, Aeronautics and Aerospace Department, von Karman Institute for Fluid Dynamics, Belgium, magin@vki.ac.be

Abstract

A stagnation line formulation is derived for ablation thermochemistry and used to solve for the distribution of species, density, and enthalpy in a chemically active boundary layer. The formulation is used to compute B'-tables that include the mass diffusion terms and the effects of wall blowing on the boundary layer. This formulation avoids the need of a blowing correction used in material response modeling. B'-tables are commonly used in ablative material response modeling to determine the consumption rate of material at the surface, B'_c, as a function of pyrolysis gas mass flux, B'_g, temperature and pressure. A thin control volume is considered where conservation of mass, equilibrium chemistry, and the transfer potential approximation to the diffusion transport terms are used to determine B'-tables as a function of temperature and pressure. The sensitivity of the tables to using equilibrium chemistry coefficients from JANAF fits, Gurvich fits and a rigid rotor/harmonic oscillator approximation is investigated. Little effect of the fits is found at temperatures below 2,250K. However, important differences at high temperatures have been identified. Differences at high temperatures were also found between B'-tables derived using the simplest mass transfer approximation and tables derived without the need to approximate the diffusion transport terms. This implies that estimates of the recession rate of ablative material in high enthalpy environments are sensitive to the approach used to build B'-tables.

Keywords: atmospheric entry flows, ablation, porous medium, chemical reactions, multi-physics coupling, Uncertainty Quantification.

1. Introduction

Exploration beyond low-earth orbit and sample-return missions require reentering the atmosphere at speeds above 10 km/s. In planning missions to planets with atmospheres, optimization of the mass of the fuel and the mass of the heat shield often results in high speed atmospheric entries. To achieve these missions, the mission designer relies on the availability of ablative materials. These specially designed materials harness interactions between the flow environment and the surface (gas-surface interactions) to protect the payload. They are designed to be an insulator that rejects heat by re-radiating and blowing the majority of the incident heat back into the environment. In this process, ablative materials lose mass and their surface recesses. A crucial tool in the design process of a thermal protection system is therefore a model that predicts the required thickness for the payload to remain protected during atmospheric entry.

A common strategy, first proposed by Kendall et al.[1] in 1968, is to run material and flow codes decoupled and approximate their interactions through the use of heat and mass transfer coefficients. The flow environment code uses "cold-wall" boundary conditions, i.e. independent of the material response code, but provides the heat transfer coefficients, density, pressure, enthalpy, and species mass fractions at the boundary layer edge. The material code, on the other hand, estimates the surface recession rate through the use of tables. Kendall et al.[1] generated non-dimensional pyrolysis-gas mass flux and char consumption rate, B'_g and B'_c, tables (commonly referred to as B'-tables) by considering a thin control volume where the gas-surface interactions occur and where mass balance and equilibrium chemistry are satisfied. To obtain the diffusive transport terms that appear in

the mass conservation equation, they used heat and mass transfer coefficients to relate the boundary layer edge quantities to the quantities in the control volume. Because of the efficiency of this strategy, it is still followed today.[2]

A weakness in this strategy is in the model of mass transport due to diffusion into the control volume. In addition, we expect that blowing the byproducts of the ablation process into the boundary layer will change the conditions in the boundary layer. Gnoffo et al. [3] have shown that coupling the byproducts of ablation to the fluid code has an important impact on the flow environment.

While flow solvers have now been developed[3] that can bypass the use of B'-tables, efforts to tightly couple them to an in-depth material response solver are still work-in-progress. These efforts will result in large codes that are designed for applications that require massive parallel computing capability. However, there is a need for approximate solvers that can be used on a personal computer. In this paper, we develop a stagnation line formulation and use it to test one of the approximations for the diffusion mass transport suggested by Kendall et al.[1] We solve for the distribution of species, density, and enthalpy in the boundary layer given conditions at the boundary layer edge. This new capability enables us to produce B'-tables that account for diffusion and blowing into the boundary layer, and we compare these to B'-tables generated using the approximations.

The present paper is organized as follows: in section (2), the thin control volume approach of Kendall et al.[1] is revisited. Their simplest approximation is used to compare B'-tables generated using CEA[4] fits, JANAF[5] fits, and a rigid rotor/harmonic oscillator approximation to the thermodynamics.[6] In section (3), the stagnation line approximation is derived without the use of self similar coordinates to represent the boundary layer at the stagnation line. In section (4), a new approach for the generation of B'-tables is developed by means of coupling the thin control volume formulation to the stagnation line solution. Summary and conclusions are presented in section (5).

2. Thin Control Volume

The B'-tables are built based on conservation of mass and equilibrium chemistry. They are essentially a means to impose a boundary condition on an ablation code without having to couple the flow environment. To compute the equilibrium mixture, the species equilibrium constants (functions of the Gibbs free energy) are obtained from fits to the species thermodynamic properties. Modifications to the equilibrium chemistry assumption may be added to account for heterogeneous finite-rate chemistry or material failure [1]; unfortunately, this methodology relies on rates and ablation mechanisms that are not well understood[7] and will not be considered in this paper. In a companion paper, the heterogeneous finite-rate chemistry of a carbon preform is analyzed[8]. In this section, we revisit the derivation of the open control volume [1] formulation to familiarize the reader with the details of the formulation and our choice of approximation for the diffusion transport terms.

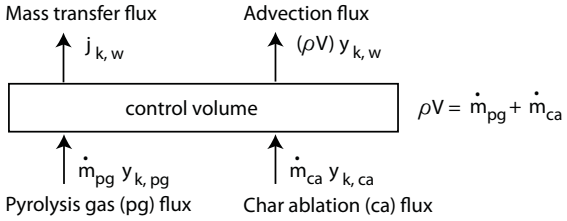

Figure 1: Mass fluxes and compositions at the wall

2.1. Mass Balance

We start with a *Thin Control Volume* (*TCV*), as shown in Fig. 1, that encloses the gas surface interface in the moving reference frame of the surface. We assume that: (1) the surface is chemically active with carbon char (C(gr)), assumed in equilibrium with the gas species, reacting with oxygen and sublimating; (2) the pyrolysis gas products and the gas from the flow environment get transported into the control volume at a rate slow compared to the chemistry time-scale, thus enabling equilibrium to be established for the mixture within the control volume. We further assume no accumulation of gas in the *TCV*. The mass balance of the elements in the control volume is given by,

$$\dot{m}_{pg} y_{k,pg} + \dot{m}_{ca} y_{k,ca} = (\rho V)_w y_{k,w} + j_{k,w} \tag{1}$$

where $y_{k,pg}$, $y_{k,ca}$, and $y_{k,w}$ are the mass fraction of the elements in the gas, the char, and the mixture, respectively; $\dot{m}_{pg}$ and $\dot{m}_{ca}$ are the pyrolysis gas mass flux and the char mass consumption rate $[kg\,m^{-2}s^{-1}]$; ρ is the density of the mixture $[kg/m^3]$; V is the velocity of the gas mixture, $[m/s]$; and $j_{k,w}$ is the diffusion flux of the elements of the mixture, $[kg\,m^{-2}s^{-1})]$ given by,

$$j_{k,w} = \sum_i \nu_k^j \frac{M_k}{M_i} J_{yi,w} \tag{2}$$

where ν_k^i are stoichiometric coefficients that are defined in Eq. 6, M_i is the molar mass of species i, and $J_{yi,w}$ is the mixture species diffusion flux.

By summing over the elements k in Eq. 1, we get the total mass conservation equation,

$$\dot{m}_{pg} + \dot{m}_{ca} = (\rho V)_w \tag{3}$$

Kendall et al.[1] considered several approximations to the species diffusion flux. The simplest of these approximations and the one we will adopt here is the transfer potential method that assumes equal mass diffusion coefficients for all species in the mixture:

$$j_{k,w} = \rho_e u_e C_M \left(y_{k,w} - y_{k,e}\right) \tag{4}$$

where ρ_e is the density of the gas at the boundary layer edge, u_e is the velocity at the boundary edge, $[m/s]$, and C_M is the Stanton number for mass transfer. Corrections to account for unequal diffusion coefficients have been proposed by Kendall et al. but are not currently used[9].

By substituting equations (3) and (4) into (1) and rearranging terms, we get the elemental composition of the mixture,

$$y_{k,w}(\dot{m}_{ca}) = \frac{\dot{m}_{pg} y_{k,pg} + \dot{m}_{ca} y_{k,ca} + \rho_e u_e C_M y_{k,e}}{\dot{m}_{pg} + \dot{m}_{ca} + \rho_e u_e C_M} \tag{5}$$

The mass fractions of the elements in the mixture, $y_{k,w}$, and the ablation mass loss rate, $\dot{m}_{ca}$, are the unknowns that we need to determine. These represent $n_c + 1$ unknowns, where n_c is the number of elements.

2.2. Chemistry for heterogeneous mixtures

The convention we will follow starts by expressing the formation reactions for n_s species as[9],

$$\sum_k \nu_k^j N_k \rightarrow \nu_j^j N_j \tag{6}$$

where N_k represents base species for the elements in the system, ν_k^j are the stoichiometric coefficients of the formation reactions, and N_j is the gaseous product species formed by the reaction.

2.2.1. Gaseous mixture

To compute the equilibrium composition of a gaseous mixture composed of n_s different chemical species, n_s independent equations are needed. We have $n_r = n_s - n_c$ independent equations obtained from the equilibrium of the formation reactions, Eq. 6, where n_c is the number of *base species* that are elements. Because of the adopted convention for the species formation reactions, n_c species formation reactions are trivial.

Equilibrium of the chemical reactions

Assuming that the species of the mixture are in chemical equilibrium, n_r equations are obtained from the definition of the equilibrium constants,

$$K_j = \left[\frac{Products}{Reactants}\right] = \frac{x_j^{\nu_j^j}}{\prod_k x_k^{\nu_k^j}} \tag{7}$$

From the above convention, the equilibrium constants are given by

$$\ln K_j(T,p) = -\frac{1}{RT}\left(\nu_j^j g_j\left(T, p_{ref}\right) - \sum_k \nu_k^j g_k\left(T, p_{ref}\right)\right) - \ln\left(\frac{p}{p_{ref}}\right)\left(\nu_j^j - \sum_k \nu_k^j\right) \tag{8}$$

where $g_i = h_i - T s_i$ is the species Gibbs free energy and p_{ref} is a reference pressure.

Mass conservation of the elements

The remaining, $n_c = n_s - n_r$, equations are obtained from the mass conservation of the nuclei,

$$\nu_k^k x_k + \sum_j \nu_k^j x_j = \nu_k^k M \frac{y_{k,w}}{M_k} \tag{9}$$

where M, the gas-phase average molecular weight ($M = \sum_i M_i x_i$), is an additional unknown in the system. At this point, we have n_s equations for $n_s + 2$ unknowns. We seek two additional relations.

Mole-Fraction definition

By definition, the mole fractions sum to one. This provides an additional equation:

$$\sum_i x_i = 1 \tag{10}$$

To summarize, for a gaseous mixture, the system of $n_s + 1$ independent equations reads:

$$\begin{cases} \nu_k^k x_k + \sum_j \nu_k^j x_j &= \nu_k^k M y_{k,w}(\dot{m}_{ca})/M_k \\ \sum_i x_i &= 1 \\ \nu_j^j \ln x_j - \sum_k \nu_k^j \ln x_k &= \ln K_j \end{cases} \tag{11}$$

The remaining constraint is obtained by considering the condensed phase reaction.

2.2.2. Condensed phase species chemistry

In the presence of solid reacting species (as is the case for ablating materials), solid species are added to the system. Therefore, heterogeneous equilibrium reactions are needed to close the system. Our current interest is in carbon-based materials, therefore, we will consider a char composed of a single element, $C(gr)$, formed by the following elementary reaction

$$C \rightarrow C(gr) \tag{12}$$

where C is carbon gas. In the case of ablative materials, it is assumed that the solid behaves as an infinite source of condensed species when present. Therefore, the activity of the solid (or its mole fraction), is taken equal to one, $x_{C(gr)} = 1$, in heterogeneous equilibrium reactions (it is equal to zero when not present). The following system is added to the gaseous species system,

$$\left\{ \begin{array}{rcl} x_{C(gr)} & = & 1 \\ -\ln x_C & = & \ln K_{C(gr)} \end{array} \right. \tag{13}$$

The equilibrium constant for condensed-phase species reads:

$$\ln K_{C(gr)}(T,p) = -\frac{1}{RT}\left(g_{C(gr)}(T) - g_C(T,p_{ref})\right) + \ln\left(\frac{p}{p_{ref}}\right) \tag{14}$$

Fits for the Gibbs free energy of carbon graphite $g_{C(gr)}(T)$ can be found in the literature [6].

2.2.3. Complete System

The complete homogeneous/heterogeneous equilibrium chemistry system coupled to mass transfer reads

$$\left\{ \begin{array}{rcl} \nu_k^k x_k + \sum_j \nu_k^j x_j & = & \nu_k^k M y_{k,w}(\dot{m}_{ca})/M_k \\ \sum_i x_i & = & 1 \\ -\ln x_C & = & \ln K_{C(gr)} \\ \nu_j^j \ln x_j - \sum_k \nu_k^j \ln x_k & = & \ln K_j \end{array} \right. \tag{15}$$

The system is closed: we have $(n_s + 2)$ unknowns and $(n_s + 2)$ equations; M and $\dot{m}_{ca}$ are 2 additional unknowns to the mole fractions of the mixture . The system is quadratic in these unknown quantities and an iterative procedure is used to solve it. It is interesting to note that only gaseous species mole fractions appear in the system. This is due to the fact that the mole fraction of gaseous carbon C is fixed by the heterogeneous equilibrium reaction $-\ln x_C = \ln K_{C(gr)}$ as long as graphite is present in the mixture. Carbon gas is carried out of the wall by diffusion and convection simultaneously, causing ablation.

Two intensive variables need to be fixed to solve the equilibrium chemistry problem. We choose the pressure and temperature as our state variables, because they are the available variables when coupling to a material response code. The input variables are $y_{k,pg}$, $\dot{m}_{pg}$ (given by the material response code), $\rho_e u_e C_M$, and $y_{k,e}$ (e for edge; these depend on the surrounding atmposphere), $y_{k,ca}$, T_w, and p_w. The current code implementation provides $\dot{m}_{ca}$ that is needed to compute the recession rate of the surface:

$$rr = \frac{\dot{m}_{ca}}{\rho_{ca}} = \frac{[kg/m^2/s]}{[kg/m^3]} \tag{16}$$

where ρ_{ca} is the density of the charred ablative material.

The computation also provides the species composition x_i, from which the total enthalpy of the gas in the control volume, h_w, can be evaluated.

The formulation has been implemented in the existing code MUTATION[10]. We refer to the code that implements the algorithm to solve the system given by Eq. 15 as MUTATION-B. The current code may be used to generate pre-computed B'-tables. It provides the dimensionless ablation mass-loss rate, $B'c = \dot{m}_{ca}/\rho_e u_e C_M$, and the wall enthalpy as a function of pressure, temperature, and the dimensionless pyrolysis-gas flow rate $B'_g = \dot{m}_{pg}/\rho_e u_e C_M$.

2.3. Representative B'-tables for carbon fibers with pyrolysis gas from phenolic

We have outlined a procedure where given $\dot{m}_{pg}$, T_w and p_w, and $\rho_e u_e C_M$, we can compute $\dot{m}_{ca}$. Kendall et al.[1] observed that by normalizing Eq. 5 using $\rho_e u_e C_M$, the system becomes independent of the conditions at the boundary layer edge and the Stanton number. Eq. 5 was then normalized and rearranged to read,

$$y_{k,w} = \frac{B'_g y_{k,pg} + B'_c y_{k,ca} + y_{k,e}}{B'_g + B'_c + 1} \tag{17}$$

Rewriting the above equation in terms of B'_c, we get,

$$B'_c = -\frac{B'_g(y_{k,pg} - y_{k,w}) + (y_{k,e} - y_{k,w})}{(y_{k,ca} - y_{k,w})} \tag{18}$$

where $B'_g = \dot{m}_{pg}/\rho_e u_e C_M$ and $B'_c = \dot{m}_{ca}/\rho_e u_e C_M$. We recall that B'_c is the key quantity extracted from the B'-tables to compute the recession rate.

MUTATION-B developed for the system of equations outlined in the previous sections was used to study an ex-phenolic pyrolysis-gas mixture in air. Starting from a mixture of about 150 species (corresponding to the species available in the JANAF [5] and Gurvich [6] tables containing C, H, O, N), we removed species from the mixture and checked that the B' obtained did not change in the temperature range of interest, $500K$ - $4000K$. With 4 elements (C, H, O, and N) included, we were able to reduce the mixture to 19 representative species: C, H, O, N, CH, CH_4, CO, CO_2, CN, C_2, C_2H, C_2H_2, C_3, C_4, C_5, HCN, H_2, H_2O, N_2.

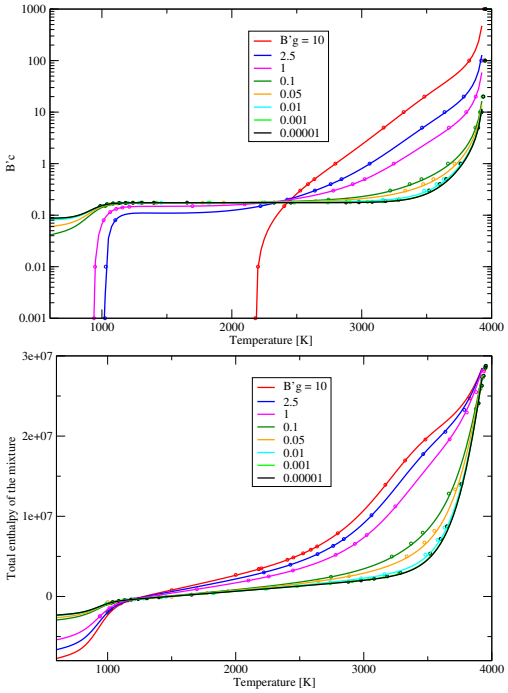

Figure 2: Char rate consumption rate as a function of temperature for a range gas injection rates. The mixture is assumed to be at $p = 1\ atm$. The solid lines are from MUTATION-B, the symbols are from MAT[9].

Figure 2 presents a typical B' table. B'_c is plotted on a logarithmic scale as a function of temperature for a range of pyrolysis-gas injection rates, B'_g. The most noticeable feature is the large plateau over a large temperature range, illustrating the fact that B'_c becomes independent of temperature at low pyrolysis gas injection rate. This illustrates the well known diffusion-limited regime where all of the oxygen transported from the boundary layer edge to the control volume is consumed at the surface. In other words, in this regime, the surface recesses at the same rate independently of the temperature. The gas composition at the wall is plotted in Fig. 3 as a function of temperature for small $\dot{m}_g$. It shows that the gas composition at the surface is independent of temperature in the diffusion-limited regime. At the surface, all of the oxygen available has been consumed by the carbon and is in the form of CO for intermediate temperatures. At lower temperatures, CO_2 is predominant at equilibrium (Boudouard equilibrium); therefore, two moles of oxygen are now necessary to remove one mole of carbon (this corresponds to the lower plateau on the left side of Fig. 2). At very high temperatures, the sublimation regime is observed leading to a sharp increase in the ablation rate.

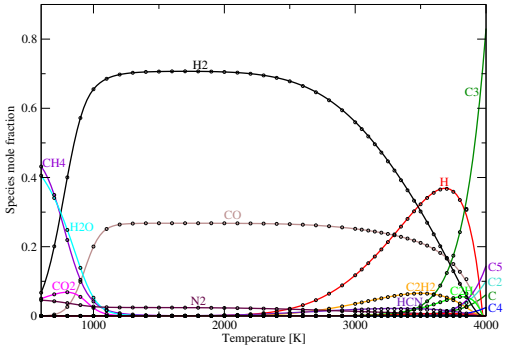

Figure 3: Species mole fractions over temperature for $p = 1 atm$ and given $\dot{m}_{pg}$

2.4. *Effects of the thermochemical tables on the B'-tables*

A key dataset for accurate estimates of ablation rates is the equilibrium constants needed to compute the equilibrium composition. The equilibrium constants are directly related to the value of the Gibbs free energy used for each species. At least three different databases are available to compute the Gibbs free energy, g_i, from equations (8) and (14). An option is to use polynomials with coefficients obtained from the CEA[4] or the JANAF [5] thermochemical tables. Another option is to re-compute the Gibbs free energy using a rigid-rotor/harmonic-oscillator approximation based on Gurvich spectroscopic constants.

Figure 4 compares B'-tables computed using the three methods. Significant differences are observed at high temperatures in the sublimation regime. These differences will impact the predictions of material response to high-enthalpy environments.[11] Further work is necessary to analyze and decide on the most appropriate database for use in material response

codes. An objective of the present work is to identify the parameters that impact the B'-tables by revisiting the original derivation and identify/verify the approximations used in the formulation.

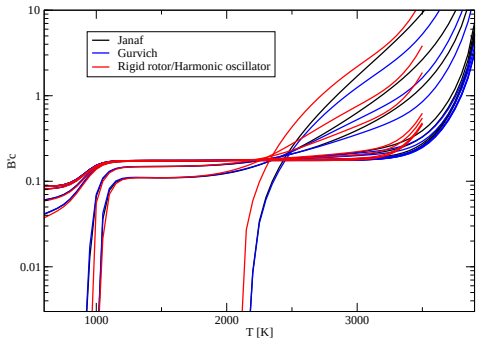

Figure 4: Comparison of Gurvich fit, JANAF fit and Rigid rotor/Harmonic oscillator

3. Stagnation Line Formulation

A major approximation in the previous B'-tables formulation is reliance on the transfer potential approximation, Eq. 4, to compute the diffusion transport. In the next section, we relax this approximation by solving the Navier-Stokes equations along the stagnation line and compute the species transport. The one-dimensional stagnation line equations are derived in this section from the boundary layer equations in cylindrical geometry. This simplification to the full Navier-Stokes equations enables us to have realistic chemistry transport models coupled to an equilibrium chemistry approximation at the boundary. We will show that this formulation will provide us with a powerful tool to develop B'-tables.

3.1. System of Equations

The governing equations written in conservative form read,

$$\frac{\partial \mathbf{Q}}{\partial t} + \frac{\partial \mathbf{G}(\mathbf{Q})}{\partial x} + \frac{\partial \mathbf{F}(\mathbf{Q})}{\partial y} = \mathbf{S} \tag{19}$$

where $\mathbf{Q}$ is the conservative variable vector, $\mathbf{G}$ and $\mathbf{F}$ are the flux vectors, $\mathbf{S}$ is the source term, x is the coordinate system along the body, and y is along the stagnation line (see Fig.5).

Starting with the 2D axisymetric boundary layer equations [12], we expand the dependent variables,

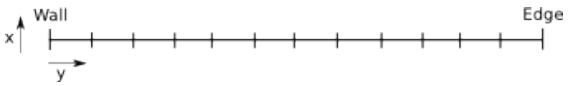

Figure 5: Coordinate system used where x is along the surface of the body and y is along the stagnation line

Q_i, in a Taylor series about the center line, $Q_i(x, y, t) = Q_i(0, y, t) + Q_{i,1}(0, y, t)x + Q_{i,2}(0, y, t)x^2/2 + ...$, where $Q_{i,j} = \partial^j Q_i/\partial x^j$. Substituting the expansion into the boundary layer equations and taking the limit $x \to 0$, we get

$$\frac{\partial}{\partial t}\begin{pmatrix} \rho \\ \rho_i \\ \rho u_{,1} \\ \rho e \end{pmatrix} + \frac{\partial}{\partial y}\begin{pmatrix} \rho v \\ \rho_i v + J_{yi} \\ \rho v u_{,1} - \mu \frac{\partial u_{,1}}{\partial y} \\ \rho v h + \phi \end{pmatrix}$$

$$= \begin{pmatrix} -2\rho u_{,1} \\ \omega_i - 2\rho_i u_{,1} \\ -\rho u_{,1e}^2 - \rho v_e \frac{\partial u_{,1}}{\partial y}|_e - 3\rho u_{,1}^2 \\ -2\rho u_{,1} h \end{pmatrix} \tag{20}$$

Where v is the velocity along the stagnation line direction y, $u_{,1} = \partial u/\partial x$ is the partial derivative with respect to the wall direction of the velocity in that direction,

$$J_{yi} = -\rho D_{im} \partial y_i/\partial y \tag{21}$$

is the diffusion flux,

$$\phi = -\lambda \partial T/\partial y + \sum_i J_{yi} h_i, \tag{22}$$

is the heat flux, and ρ_i is the mass density of species i. The mixture mass density is given by the expression $\rho = \sum_i \rho_i$. The mixture energy $e = \sum_i y_i e_i$. The mass fraction $y_i = \rho_i/\rho$, mixture enthalpy $h = e + p/\rho$, and pressure $p = \rho RT \sum_i y_i/M_i$, with M_i the molar mass of species i. The production term of species i is given by ω_i.

The properties of the species are computed assuming a rigid rotor and harmonic oscillator approximations; spectroscopic constants are taken from Gurvich[6]. The transport properties are computed following the Chapman-Enskog method. To estimate the viscosity and thermal conductivity, we solve the transport system using the conjugate gradient method. The collision integrals are computed using polynomials from Park[13]. This provide us only with $\Omega^{(1,1)}$ and $\Omega^{(2,2)}$; we have set $\Omega^{(1,2)}$ and $\Omega^{(2,1)}$ to zero. The

diffusion fluxes have been computed with the following approximation for Fick's law:

$$D_{im} = \frac{1 - x_i}{\sum_j x_j / \mathcal{D}_{ij}} \tag{23}$$

where $\mathcal{D}_{ij}$ is the binary diffusion coefficient.

3.2. Boundary Conditions for the Stagnation line formulation

To complete the system, boundary conditions need to be established for the stagnation line formulation. The boundary conditions of interest for coupling to the control volume formulation are as follows:

Boundary condition at the edge:

At the stagnation line, the height of the boundary layer cannot be defined in terms of the streamwise velocity, and the size of the domain can be arbitrary as long as the assumption of constant pressure holds. Magin[10] defines the edge of the boundary at the stagnation line to be the inflection point of the velocity gradient that is either measured or obtained from a simulation.

At the boundary edge, we specify the species density, $\rho_i|_e$, the normal (to the stagnation line) derivative of the normal velocity, $u_{,1}|_e$, the temperature, T_e, as well as, $\partial u_{,1}/\partial y|_e$. The last term provides information about the shape of the heat-shield in the stagnation line approximation.

The normal velocity at the edge, $v|_e$, is computed by integrating from the wall to the boundary edge using the continuity equation. This insures mass conservation under the constant pressure constraint.

The gas composition at the boundary layer edge, $\rho_i|_e$, is assumed to be in chemical equilibrium. This assumption is valid for large bodies or when the shock is far from the body.

Boundary condition at the wall:

At the wall, the blowing velocity is computed from the relation $v_w = (\dot{m}_{ca} + \dot{m}_{pg})/\rho_w$ and the species mass fraction, $y_i|_w$, is obtained from the *TCV* formulation for a fixed T_w. We set $u_{,1}|_w = 0$, i.e. the pyrolysis gas is injected normal to the wall.

3.3. Change of variables

A common problem in reacting flows is that the temperature is needed to compute the properties of the gas, such as the transport coefficients D_{im}, μ, λ, and the production term ω_i, but temperature is not a conserved variable and needs to be derived from the internal energy. In addition, the density, ρ, is computed using the equation of state to ensure that the pressure, p, is constant in the domain. The vector unknown of interest is then: $\mathbf{U} = \left[v, \rho_i, u_{,1}, T\right]^T$.

Because the natural unknowns in the integration procedure is the vector of conserved variables $\mathbf{Q} = \left[\rho, \rho_i, \rho u_{,1}, \rho e\right]^T$, the following change of variables is required: $\delta\mathbf{Q} = \mathbf{\Gamma}\delta\mathbf{U}$, where $\mathbf{\Gamma} = \partial\mathbf{Q}/\partial\mathbf{U}$. This will lead to a singular matrix, but this has no effect since we are only interested in the steady-state solution. Our equations are written as follows,

$$\mathbf{\Gamma}\frac{\partial \mathbf{U}}{\partial t} + \frac{\partial \mathbf{F}(\mathbf{Q})}{\partial y} = \mathbf{S} \tag{24}$$

3.4. Numerical procedure: time and space discretization

The governing equations in conservation law form are solved numerically by means of a finite volume method. The first-order implicit (backward) Euler scheme is use to discretize in time. Second-order differences on a staggered mesh are used to discretize space.[14] The fully discretized equation for cell i at time step n is:

$$A_i \delta U_{i-1} + B_i \delta U_i + C_i \delta U_{i+1} = R_i^n \tag{25}$$

where $\delta U_i = U_i^{n+1} - U_i^n$ and the matrices A_i, B_i, C_i and vector R_i^n are:

$$A_i = -\frac{1}{\Delta y}\left(\frac{\partial F_{i-1/2}}{\partial U_{i-1}}\right)^n \tag{26}$$

$$B_i = \frac{1}{\Delta t}\left(\Gamma_i\right)^n - \left(\frac{\partial S_i}{\partial U_i}\right)^n + \frac{1}{\Delta y}\left(\frac{\partial F_{i+1/2}}{\partial U_i} - \frac{\partial F_{i-1/2}}{\partial U_i}\right)^n \tag{27}$$

$$C_i = \frac{1}{\Delta y}\left(\frac{\partial F_{i+1/2}}{\partial U_{i+1}}\right)^n \tag{28}$$

$$R_i^n = S_i^n - \frac{1}{\Delta y}\left(F_{i+1/2}^n - F_{i-1/2}^n\right) \tag{29}$$

The variables within cell i are coupled to their neighbors $i-1$ and $i+1$. Writing Eq. 25 for each cell gives us a block tri-diagonal system which is inverted using the generalized Thomas algorithm. This can be solved for each δU_i^n so that the solution can be advanced in time: $U_i^{n+1} = U_i^n + \delta U_i$. We note that we are not interested in the time-accurate evolution of the solution, the time dependence being kept only for convergence purposes.

All variables are cell-centered except for v which is computed at the interface (staggered grid) to ensure pressure-velocity coupling at low speed. This would not be possible by means of a preconditioning technique, since p is constant inside the boundary layer.

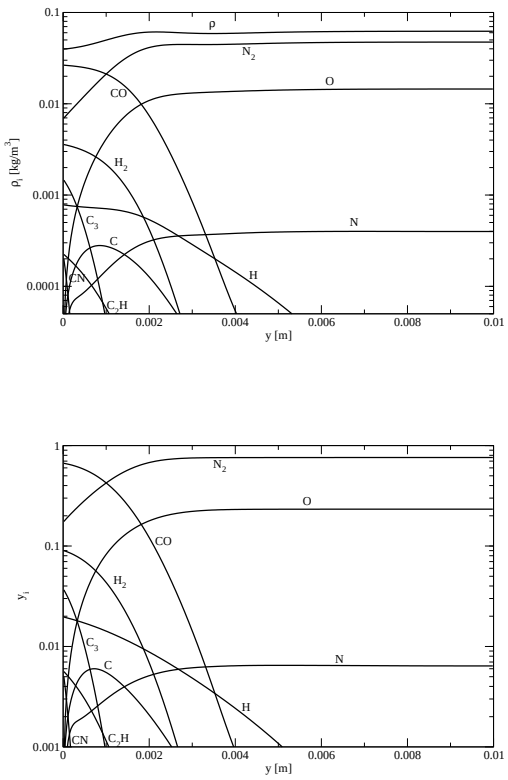

Figure 6: Species-density and mass fraction distribution at the stagnation line of a simulated VKI plasmatron[15] experiment on an ablative carbon-phenolic surface

3.5. Simulation of an ablating sample in the VKI plasmatron

We have implemented the stagnation-line formulation in a code that we call MUTATION-SL and have verified the implementation by comparing our results to results from the boundary layer code of Barbante [15]. In what follows, we present results for our simulation of the VKI "plasmatron" torch on an ablative material where we have set $p_e = 101325$ [Pa], $T_e = 4640$ [K], $u_{,1e} = 1143[\mathrm{s}^{-1}]$, $u_{,12}|_e = 82069.[\mathrm{m}^{-1}\mathrm{s}^{-1}]$. The wall was set at $T_w = 3200$ [K], with phenol mass injection of $m_{pg} = 0.1$ [Kg $\mathrm{m}^{-2}\mathrm{s}^{-1}$]. The velocity at the wall and at the boundary edge were computed to be $v_w = 2.21$ [ms^{-1}] and $v_e = 25.7$ [ms^{-1}] respectively.

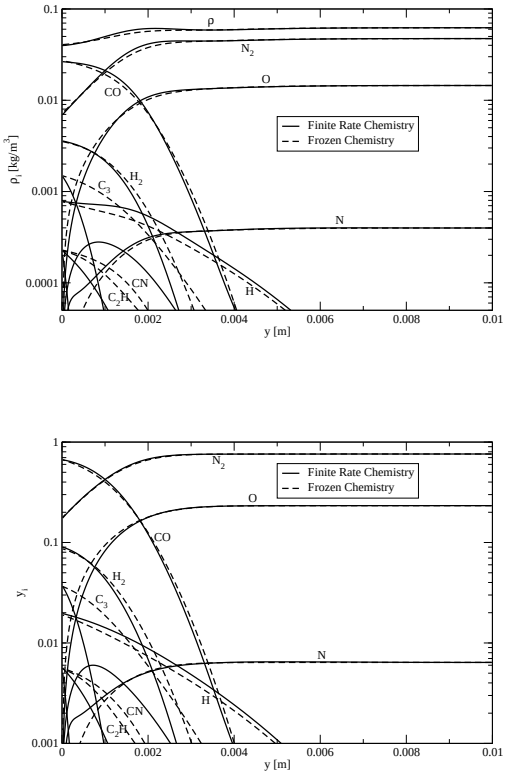

Figure 7: Effects of frozen chemistry compared to finite rate chemistry species-density and mass fraction distribution at the stagnation line of a simulated plasmatron [15] experiment on an ablative carbon-phenolic surface

Figure 6 shows the species mass fractions as a function of the distance from the wall. At the boundary layer edge we have mostly atomic oxygen and nitrogen entering the boundary layer. Some mass gets convected as seen in the total density of the N_2 profiles near the wall. It should be noted that it is hard to distinguish between convection and consumption of the species. However, we observe that the atomic species O and N become negligible at the wall. We have oxidation and nitridation as reflected in the profiles of CO and CN. All of the atomic oxygen, O, and atomic nitrogen, N, are consumed at the wall. The main reaction near the wall is the carbon oxidation reaction that produces CO: $C + O \rightarrow CO$. The second important species produced at the wall is hydrogen, H_2.

It observed in non-equilibrium Navier-Stokes simulations that frozen chemistry for air is a good approximation in the boundary layer. In Fig. 7 the composition profiles for frozen chemistry and finite rate chem-

istry (with and without the reaction term ω_i in Eq. 20) are compared. We find that frozen chemistry holds until the gas from the flow environment start to interact with the gas from the ablation products. We also observe that the slope of the two main species at the wall does not change. This is an indication that the concentrations of CO and H_2 are close to equilibrium, but the minor species, C_3 for example, is not. The implications of active chemistry near the wall may become important at high entry speeds where we expect high temperatures and higher blowing rates.

4. Computing B'-tables using the stagnation line formulation

The complete system of equations for the equilibrium boundary condition at the wall is given by Eq. 15; without the transfer potential approximation, the mass balance at the wall reads,

$$y_{k,w}(\dot{m}_{ca}) = \frac{\dot{m}_{pg} y_{k,pg} + \dot{m}_{ca} y_{k,ca} - j_{k,w}}{(\dot{m}_{pg} + \dot{m}_{ca})} \tag{30}$$

The strategy that we will follow is to compute the species diffusive flux at the wall $j_{k,w} = \sum_i \nu_k^i \frac{M_k}{M_i} J_{yi,w}$ from the stagnation line approximation.

4.1. Marching procedure

The boundary layer formulation as well as the *TCV* formulation require information from each other: the *Stagnation Line* requires v_w, y_{i_w}, and $j_{k,w}$; the *TCV* formulation requires $j_{k,w}$, as well as $\rho_e u_e C_M$.

To build a B'-table, we need to be able to fix B'_g and vary T_w. Our iteration strategy is shown schematically in Fig. 8,

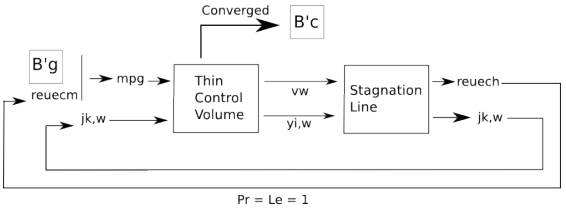

Figure 8: Marching strategy followed to compute the B'_c give B'_g

The simplest case to compare the formulation in MUTATION-B with the current formulation is for the case where $Le = Pr = 1$ is assumed to hold. In that case, the B'-table user assumes $\rho_e u_e C_M = \rho_e u_e C_H = \phi_w/(h_e - h_w)$. We start with the stagnation line approximation to compute the cold wall case. This gives us $r_e u_e C_M$. For a given B'_g, we compute $\dot{m}_{pg} = \rho_e u_e C_M B'_g$. Having $\dot{m}_{pg}$, we iterate to compute $y_{k,w}$ and $\dot{m}_{ca}$. Having, values for $\dot{m}_g$ and $\dot{m}_{ca}$, we can compute the velocity at the wall $v_w = (\dot{m}_{ca} + \dot{m}_{pg})/\rho_w$. The wall conditions are taken as input to the *Flow solver* which in turn gives us a new $\rho_e u_e C_M = \phi_w/(h_e - h_w)$ that needs to be iterated. Once the process has converged, we have $B'_c = \dot{m}_{ca}/\rho_e u_e C_M$. At this point we are ready to move to the next B'_g.

4.2. Preliminary B'-tables comparison

Because the transport properties are not known for all of the pairs of species present in the mixture that were used to produce Fig. 2, we have reduced the number of species to a set for which all the transport coefficients are available. We reduce the mixture of 19 species that we have discussed previously, to the 11 species set: C, H, O, N, CO, CN, C_2, C_2H, C_3, H_2, N_2.

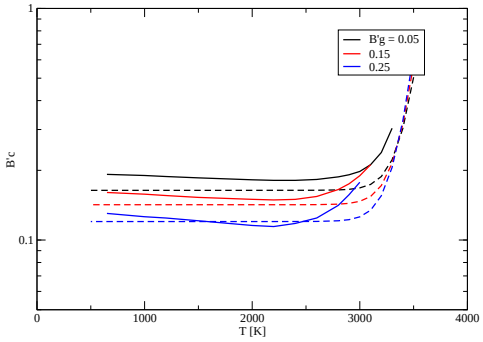

Figure 9: B'_c (char consumption rate) as a function of temperature for a range of B'_g (mass injection rate) rates for $p = 1atm$. The solid lines are from MUTATION-SL, the dashed lines are from MUTATION-B

Figure 9 shows a comparison between the stagnation line formulation in MUTATION-SL, and the formulation in MUTATION-B. We find surprising agreement between the two formulations given that the species profiles (shown in Fig. 6) show little similarity to each other. The B' generated by MUTATION-SL include the effects of blowing.

Figure 10 compares B'_c profiles computed using frozen chemistry to the profiles generated using finite-rate chemistry. These results are not surprising because we have seen that the effects of chemistry on the profiles of the major species are not strong, and that B'_c, in the diffusion limited regime, is a function of the atomic oxygen and atomic nitrogen supplied to the boundary, and these are the same for the frozen and equilibrium chemistry.

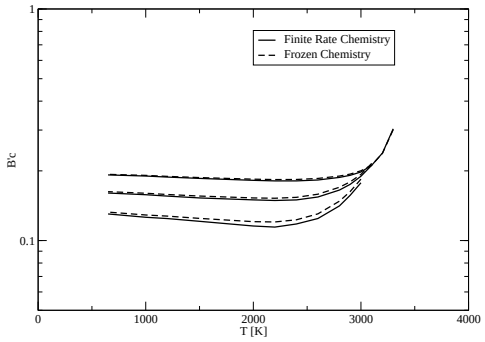

Figure 10: B'_c (char consumption rate) as a function of temperature for a range of B'_g (mass injection rate) rates for $p = 1atm$. Comparison between Finite Rate Chemistry and Frozen Chemistry

5. Summary and Conclusions

A stagnation line formulation has been developed to compute the gas surface interactions between an ablating surface and a chemically reactive flow. We find little effect of the treatment of chemistry on the species profiles for the conditions that we have considered. We also find that the frozen chemistry approximation yields reasonable results when compared to treating the chemistry with finite-rate reactions.

The classical *Thin Control Volume* formulation has been implemented in a way that easily couples to a stagnation line approximation (T, p, $\dot{m}_{pg}$ as input, $\dot{m}_{ca}$ as output). A procedure using the stagnation line approximation has been developed to evaluate the standard approximations used to build B'-tables. The new formulation builds into the B' tables the effects of blowing on the boundary layer transport.

We find that the tables are sensitive to the polynomials used to generate them. But at the conditions tested, the transfer potential approximation seems to hold surprisingly well.

Finally, comparing B'-tables using CEA data, JANAF data, and a rigid-rotor and harmonic-oscillator approximation, we find important differences at high-temperatures.

6. Acknowledgment

This research work will be sponsored by the European Research Council Starting Grant "*AEROSPACE-PHYS: Multiphysics models and simulations for reacting and plasma flows applied to the space exploration program,*". I also wish to gratefully thank Dr. Nagi N. Mansour and Dr. Jean Lachaud for their contribition and advises on this project.

References

[1] Kendall, R. M., Barlett, E. P., Rindal, A. R., and Moyer, C. B., "An Analysis of the Chemically Reacting Boundary Layer and Charring Ablator. Part V: A General Approach to the Thermochemical Solution of Mixed Equilibrium-Nonequilibrium, Homogeneous or Heterogeneous Systems," *NASA CR-1064*, 1968.

[2] Göķcen, T., Chen, Y.-K., Skokova, K., and Milos, F., "Computational Analysis of Arc-Jet Wedge Tests Including Ablation and Shape Change," *AIAA Paper 2010-4644*, 2010.

[3] Gnoffo, P. A., Johnston, C. O., and Thompson, R. A., "Implementation of Radiation, Ablation, and Free Energy Minimization Modules for Coupled Simulations of Hypersonic Flow," *AIAA 2009-1399*, 2009.

[4] Gordon, S. and McBride, B. J., "Computer Program for Calculation of Complex Chemical Equilibrium Compositions and Applications I. Analysis," NASA Reference Punblication 1311, NASA, 1994.

[5] Chase, M. W. e. a., "NIST-JANAF Thermochemical Tables (4th ed.)," *Journal of Physical Chemical Reference Data*, Vol. 14, 1985.

[6] Gurvich, L. V., Veyts, I., and Alcock, C., Thermochemical Properties of Individual Substances Fourth Edition.

[7] Lachaud, J., Cozmuta, I., and Mansour, N. N., "Multiscale Approach to Ablation Modeling of Phenolic Impregnated Carbon Ablators," *Journal of Spacecraft and Rockets*, Vol. 47, No. 6, NovemberDecember 2010, pp. 910–921.

[8] Lachaud, J., Mansour, N. N., Ceballos, A., Pejakovic, D., Zhang, L., and Marschall, J., "Validation of a volume-averaged fiber-scale model for the oxidation of a carbon-fiber preform," AIAA Paper 2011-2223, 2011.

[9] Milos, F. S. and Chen, Y.-K., "Comprehensive Model for Multi-Component Ablation Thermochemistry," *AIAA Paper 97-0141*, 1997.

[10] Magin, T. E., *A Model for Inductive Plasma Wind Tunnels*, Ph.D. thesis, von Karman Institute for Fluid Dynamics, Universite Libre de Bruxelles, 2004.

[11] Milos, F. S. and Chen, Y.-K., "Ablation Predictions for Carbonaceous Materials Using CEA and JANNAF-Based Species Thermodynamics," *42nd AIAA Thermophysics Conference*, 2011.

[12] Cousteix, J., Aérodynamique - Couche limite laminaire, *Cepadues, 1997.*

[13] Park, C., "Chemical-Kinetic Parameters of Hyperbolic Earth Entry," *Journal of Thermophysics and Heat Transfer*, 2001.

[14] Munafo, A., "Vibrational State to State Kinetics in Expanding and Compressing Nitrogen Flows," *American Institute of Aeronautics and Astronautics*, 2010.

[15] Barbante, P. F., Accurate and Efficient Modelling of High Temperature Nonequilibrium Air Flows, Ph.D. thesis, *von Karman Institute for Fluid Dynamics, 2001.*

DEVELOPMENT OF ADVANCED CFD

A Generalized Framework for Adjoint Error Estimation of PG Method Applied to Linear Problems

Stefano D'Angelo

Aeronautics and Aerospace Department, von Karman Institute for Fluid Dynamics, Belgium, dangelo@vki.ac.be

Supervisor: Herman Deconinck

Professor, Aeronautics and Aerospace Department, von Karman Institute for Fluid Dynamics, Belgium, deconinck@vki.ac.be

University Supervisor: Mario Ricchiuto

Research Engineer, INRIA Bordeaux - Sud-Ouest, France, mario.ricchiuto@inria.fr

Abstract

The current work concerns the study and the implementation of a modern algorithm for error estimation in Computational Fluid Dynamics (CFD) computations. This estimate involves the use of the adjoint argument. By solving the adjoint problem, it is possible to gain important information about the transport of the error related to the quantity of interest. The aim is to apply for the first time this procedure to the Petrov-Galerkin (PG) method. Some numerical schemes such as Streamline Upwind Petrov-Galerkin (SUPG), stabilized Residual Distribution (RD) and bubble method have been selected for implementation and tested. Scalar linear hyperbolic problems are used as basic demostration.

Keywords: error estimation, adjoint problem, hyperbolic problem, Petrov-Galerkin

1. Introduction

Over the last decade, much progress has been made in the area of error estimation. This theory provides a way to construct error indicators for CFD computations of PDE's. These indicators can be used to drive automatic mesh adaptation algorithms, by optimizing the mesh spacings or reducing the memory usage.
In this field, the *a posteriori* error analysis is one of the most used procedures to compute numerical error indicators. The relevance and generality of this estimation has been powerfully argued in the work of Johnson and his collaborators [1]. The *a posteriori* error bounds resulting from this analysis involve the numerical residual, obtained by inserting the computed solution into the current problem equations; this residual measures the extent to which the numerical approximation to the continuous solution fails to satisfy the current problem. From this study, the *Type II a posteriori* error bounds have been defined.
Becker and Rannacher worked also on this issue, developing the so-called weighted-residual-based, or *Type I*, *a posteriori* error estimation ([2] and [3]). Here, the error representation formula defines the error in the target functional for the numerical residual, weighted by the solution of an adjoint problem. The key ingredient is this auxiliary problem, involving the formal adjoint of the current partial differential operator. For computing this product, also the adjoint problem will be implemented and solved numerically. To solve this problem, added cost rises. However, it is paid back by important information which helps to identify the real source of the error. For example, Hartmann ([4]) shows the relevance and the advantages of *Type I* indicators over the *Type II* for the adaptive mesh design for a supersonic flow past an airfoil.
The data for the adjoint problem is a quantity of interest depending on the application. In engineering applications, this is typically a functional of the analytical solution such as a mean, point value or boundary flux. In fluid dynamics, it may be the pressure at the stagnation point, the pressure-drop between inflow and outflow or the drag or lift coefficients of a body immersed into the fluid.

2. Definition in continuous setting

2.1. Primal and adjoint problem

Primal problem model. Let Ω be a bounded open domain R^d with boundary Γ. Given the *primal problem* in strong form

$$Lu = f \quad \text{in} \quad \Omega \qquad Bu = g \quad \text{on} \quad \Gamma \tag{1}$$

where $f \in L^2(\Omega)$ and $g \in L^2(\Gamma)$, L denotes a linear differential operator on Ω and B a linear boundary operator on Γ.

The functional $J(\cdot)$. In many problems of physical interest the quantity of interest for the current problem is an output or target functional of the solution rather the solution itself. This target functional is defined as $J(\cdot)$. Depending on the problem, it can be a different quantity, for example the drag or the lift coefficient or a point value of the solution.
According to the theory, the linear functional is defined by

$$J(u) = (u, j_\Omega)_\Omega + (Cu, j_\Gamma)_\Gamma \tag{2}$$

where $j_\Omega \in L^2(\Omega)$ and $j_\Gamma \in L^2(\Gamma)$ and C is a differential boundary operator on Γ and $(\cdot,\cdot)_\Omega$ and $(\cdot,\cdot)_\Gamma$ denote the $L^2(\Omega)$ and $L^2(\Gamma)$ inner products respectively.

Associated adjoint problem. Following the theory of adjoint operators [5] we can write the (continuous) *compatibility equation*, for $\forall v \in H^1$

$$(Lu, v)_\Omega + (Bu, C^* v)_\Gamma = (u, L^* v)_\Omega + (Cu, B^* v)_\Gamma \tag{3}$$

where, L, B and C are the operators of the primal problem and L^*, B^* and C^* the corresponding adjoint counterparts. By these so-called *adjoint operators*, we build the adjoint problem associated to (1)

$$L^* z = j_\Omega \quad \text{in} \quad \Omega, \qquad B^* z = j_\Gamma \quad \text{on} \quad \Gamma. \tag{4}$$

Terms j_Ω and j_Γ on the right-hand side depend on the target quantity that we want to investigate. From the (3), we note that for given operators L and B associated with the primal problem (1) only some target functionals (2) with operator C are compatible whereas others are not. Moreover, in an adjoint-based optimization framework, [6], there ensures that

$$\begin{aligned} J(u) &= (u, j_\Omega)_\Omega + (Cu, j_\Gamma)_\Gamma = (u, L^* v)_\Omega + (Cu, B^* v)_\Gamma \\ &= (Lu, v)_\Omega + (Bu, C^* v)_\Gamma = (f, z)_\Omega + (g, C^* z)_\Gamma \end{aligned}$$

The associated adjoint problem describes how the information is transported towards the current quantity of interest. This is extremely useful to derive where and how the source of the error of the target quantity is carried over the domain. The error indicator derived by this information will allow to trace sources of the error of the quantity of interest.

3. Numerical discretization

Let Ω be subdivided into a shape-regular mesh $\mathcal{K} = \{\kappa\}$ consisting of elements κ. Let $\mathcal{V}_{h,p}$ be the standard finite element space of piecewise polynomials of complete degree p with C^0 continuity between elements

$$\mathcal{V}_{h,p} = \{v_h : v_h \in C^0(\Omega), v_h|_\kappa \in \mathcal{P}_p(\kappa), \forall \kappa \in \mathcal{K}\} \tag{5}$$

with $\mathcal{P}(\kappa)$ the space of polynomials of degree $\leq p$ defined on an element κ. Let then define a second space $\mathcal{V}^b_{h,q}$ which is the mesh dependent broken space of piecewise polynomials of complete degree q in each κ with no continuity between elements

$$\mathcal{V}^b_{h,q} = \{v_b : v_b|_\kappa \in \mathcal{P}_q(\kappa), \forall \kappa \in \mathcal{K}\} \tag{6}$$

We discretize both primal and adjoint problem and solve them numerically by using a *Petrov-Galerkin* (PG) method, where trial and test functions belong to $\mathcal{V}_{h,p}$ and $\mathcal{V}^b_{h,q}$, respectively, depending on the current problem.
According to (5) and (6), the boundary conditions are not imposed by the functional spaces, hence they have ti be added explcitly to the weak formulation of the problem.
Then following (3), the (discrete) compatibility condition holds as follows, for $\forall v_b \in \mathcal{V}^b_{h,p}$

$$\begin{aligned} (Lu_h, v_b)_\Omega + (Bu_h, C^* v_b)_\Gamma \quad = \\ (u_h, L^* v_b)_\Omega + (Cu_h, B^* v_b)_\Gamma + \sum_k (H(u_h, \boldsymbol{n}), v_b^+)_{\partial\kappa\setminus\Gamma} \end{aligned} \tag{7}$$

The additional terms in the RHS represents the effect of the broken test space when applying partial integration to the LHS, leading to jump terms over the element boundaries. Thus, for a conservation law, $H(w_h, \boldsymbol{n})$ is the numerical flux over $\partial\kappa$, which is unconditionally continuous because the $w_h \in \mathcal{V}_{h,p}$, $\boldsymbol{n}$ is the outward normal along the element boundary and v_b^+ the outward traces of v_b over $\partial\kappa$.
So we can define a bilinear operator $\mathcal{B}(\cdot,\cdot)$ as

$$\mathcal{B}(u_h, v_b) = (Lu_h, v_b)_\Omega + (Bu_h, C^* v_b)_\Gamma \tag{8}$$

Then, defining $F(\cdot)$ a linear form including the prescribed primal force and boundary data functions, f and g, the (discrete) primal problem is defined as

PRIMAL PROBLEM Find $u_h \in \mathcal{V}_{h,p}$ such that

$$\mathcal{B}(u_h, v_b) = F(v_b) \qquad \forall v \in \mathcal{V}^b_{h,q} \tag{9}$$

while the corresponding adjoint problem is given by

ADJOINT PROBLEM Find $z_b \in \mathcal{V}^b_{h,q}$ such that

$$\mathcal{B}(w_h, z_b) = J(w_h) \qquad \forall w_h \in \mathcal{V}_{h,p} \tag{10}$$

As we see, both problems use the same operator $\mathcal{B}(\cdot,\cdot)$, as in Discontinuous Galerkin (DG) methods. However due to the Galerkin properties, in the DG discretization test and trial space are identical, instead here, in the primal problem the solution $u_h \in \mathcal{V}_{h,p}$ and the test function v_b belongs to $\mathcal{V}^b_{h,p}$ while for the adjoint problem, the solution $z_b \in \mathcal{V}^b_{h,q}$ and the test function w_h is taken from $\mathcal{V}_{h,q}$.

3.1. Broken space $\mathcal{V}^b_{h,q}$

A plethora of possible Broken spaces $\mathcal{V}^b_{h,q}$ are available. Herebelow we list the three Petrov-Galerkin spaces that will be taken into account for the computations considered in section (5). Therefore, let remind that for a PG method, the broken spaces $\mathcal{V}^b_{h,q}$ can be always defined by a sum of two contributions

$$\mathcal{V}^b_{h,q} = \text{span}\{\Psi^0 + \Psi^1\}$$

where Ψ^0 is the "main" shape function of the space and Ψ^1 is a element stabilizer term.

Streamline Upwind Petrov-Galerkin method. In case of a Streamline Upwind Petrov-Galerkin (SUPG) method, the broken space $\mathcal{V}^b_{h,q}$ is the same as $\mathcal{V}_{h,p}$ except for the addition of a stabilizer term

$$\mathcal{V}^b_{h,q} = \text{span}\{\varphi^q_i + \tau_\kappa \boldsymbol{b} \cdot \nabla\varphi^q_i\} \tag{11}$$

where τ_κ is usually the size of the element κ and $\varphi^q_i \in \mathcal{V}_{h,q}$ the Lagrange interpolant polynomial of the degree of freedom, i, and order q; while, finally, $\boldsymbol{b}$ is the local advection speed of the current problem. So for this functional space $\Psi^0_j = \varphi^q_j$ and $\Psi^1_j = \tau_\kappa \boldsymbol{b} \cdot \nabla\varphi^q_j$.

Residual-Distribution Method. If the stabilised Residual Distribution (RD) space is chosen, the broken space, $\mathcal{V}^b_{h,q}$, is defined as

$$\mathcal{V}^b_{h,q} = \text{span}\{\beta_i + \tau_\kappa \boldsymbol{b} \cdot \nabla\varphi^q_i\} \quad \text{for} \quad q > 1 \tag{12}$$

where $\beta_i(x) = \beta^\kappa_i(\{k_i\}_{i\in\kappa}, u_h, \boldsymbol{b}, h, Lu_h|_\kappa)$ and $k_i = L\varphi_i$; while τ_κ is usually the size of the element κ and φ^q_i the Lagrange interpolant polynomial of the degree of freedom, i, and order q. So $\Psi^0_j = \chi^\kappa\beta^\kappa_j$ and $\Psi^1_j = \tau_\kappa \boldsymbol{b} \cdot \nabla\varphi^q_j$.

"Bubble" method. The "bubble" method comes out from the equivalence of the RD and SUPG method. Indeed, it takes the following broken space $\mathcal{V}^b_{h,q}$

$$\mathcal{V}^b_{h,q} = \text{span}\{\varphi^q_i + S^\kappa\alpha^\kappa_i\} \tag{13}$$

with φ^q_i the Lagrange interpolant polynomial of the degree of freedom, i, and order q, while S^κ is a bubble function vanishing along $\partial\kappa$. In this case, it is either a linear bubble, unary in the baricentric point $\boldsymbol{x}_g$, or a cubic one, coming out from the product of the three vertex linear functions. Finally α^κ_i is given by $\alpha^\kappa_i = \beta_i - \phi_i$, where β_i is the corresponding RD basis function. Then here $\Psi^0_j = \varphi^q_j$ and $\Psi^1_j = S^\kappa\alpha^\kappa_i$.

3.2. Numerical analysis

Consistency and adjoint consistency. All Petrov-Galerkin methods satisfy the *Galerkin orthogonality*

$$\mathcal{B}(u - u_h, v_b) = 0 \tag{14}$$

for $\forall v \in \mathcal{V}^b_{h,p}$ which means that the discretization error $e = u - u_h$ is orthogonal (with respect to the bilinear form $\mathcal{B}$) to the discrete test space $\mathcal{V}^b_{h,p}$. Hence, because $v \in \mathcal{V}^b_{h,p} \subset \mathcal{V}$, we find for $\forall v \in \mathcal{V}$

$$\mathcal{B}(u, v) = F(v) \tag{15}$$

This proves that a PG method is a *consistent* discretization of the primal problem (1). Furthermore, a numerical discretization is called also *adjoint consistent* [5], if the exact solution $z \in \mathcal{V}$ to the adjoint problem (4) satisfies, for $\forall w \in \mathcal{V}$

$$\mathcal{B}(w, z) = J(w) \tag{16}$$

In other words, the discrete adjoint problem is a consistent discretization of the continuous adjoint problem. Motivated by the identity (7) and replacing z_b by the exact solution z and because $w_h \in \mathcal{V}_{h,p} \subset \mathcal{V}$, we can state that the bilinear form $\mathcal{B}$ is also adjoint consistent.

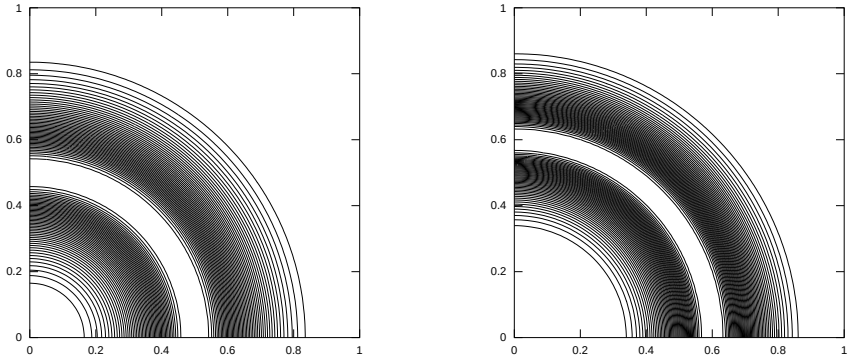

(a) (b)

Figure 1: Barth's problem : (a) primal; (b) adjoint

Method	h	$\|u-u_h\|_{L^2}$		$\|z-z_h\|_{L^2}$		$\|J(u)-J(u_h)\|$	
SUPG	.0312	3.8562e-03		5.3264e-03		5.8600e-05	
SUPG	.0156	8.9181e-04	(2.11)	1.8667e-03	(1.51)	8.9990e-06	(2.70)
SUPG	.0078	1.5552e-04	(2.52)	3.6204e-04	(2.37)	1.1747e-06	(2.94)
SUPG	.0039	2.5720e-05	(2.60)	6.2955e-05	(2.52)	1.4700e-07	(3.00)
RD-LDA	.0312	3.9011e-03		1.0118e-02		2.2153e-04	
RD-LDA	.0156	1.1269e-03	(1.79)	3.3506e-03	(1.59)	5.7671e-05	(1.94)
RD-LDA	.0078	2.9220e-04	(1.95)	9.7188e-04	(1.79)	1.5135e-05	(1.93)
RD-LDA	.0039	7.4076e-05	(1.98)	2.8564e-04	(1.77)	3.8672e-06	(1.97)
BUBBLE	.0312	2.6321e-03		5.0281e-03		9.6111e-05	
BUBBLE	.0156	6.0996e-04	(2.11)	1.5697e-03	(1.68)	2.5721e-05	(1.90)
BUBBLE	.0078	1.4730e-04	(2.05)	3.9956e-04	(1.97)	6.7168e-06	(1.94)
BUBBLE	.0039	3.5841e-05	(2.04)	1.1083e-04	(1.85)	1.7109e-06	(1.97)

Table 1: Convergence rates $p = 1$ order of SUPG, RD and BUBBLE methods for cicular advection problem [7].

Method	h	$\|u-u_h\|_{L^2}$		$\|z-z_h\|_{L^2}$		$\|J(u)-J(u_h)\|$	
SUPG	.0312	2.6300e-04		7.2814e-04		5.6795e-07	
SUPG	.0156	3.2645e-05	(3.01)	9.9617e-05	(2.87)	2.2024e-08	(4.69)
SUPG	.0078	2.8945e-06	(3.50)	1.0450e-05	(3.25)	7.4814e-10	(4.88)
SUPG	.0039	3.1390e-07	(3.20)	1.0542e-06	(3.31)	2.3627e-11	(4.98)
RD-LDA	.0312	3.7591e-04		5.8481e-03		2.1472e-06	
RD-LDA	.0156	8.1254e-05	(2.21)	3.1556e-03	(0.89)	2.7553e-07	(2.96)
RD-LDA	.0078	1.5478e-05	(2.39)	1.7036e-03	(0.89)	3.7701e-08	(2.87)
RD-LDA	.0039	2.5365e-06	(2.61)	9.1564e-04	(0.90)	4.7701e-09	(2.98)
BUBBLE	.0312	1.7989e-04		6.7172e-03		4.2105e-06	
BUBBLE	.0156	3.7848e-05	(2.25)	4.3264e-03	(0.63)	6.5782e-07	(2.68)
BUBBLE	.0078	8.3242e-06	(2.18)	2.5741e-03	(0.75)	8.9382e-08	(2.88)
BUBBLE	.0039	1.6420e-06	(2.34)	1.4398e-03	(0.84)	1.1594e-08	(2.95)

Table 2: Convergence rates $p = 2$ order of SUPG, RD and BUBBLE methods for cicular advection problem [7].

Convergence (order of convergence). Let $u \in H^{p+1}(\Omega)$ and $u_h \in \mathcal{V}_{h,p}$ be the solutions to (15) and (1), respectively. Then,

$$\|u - u_h\|_{L^2(\Omega)} \leq Ch^{p+1}|u|_{H^{p+1}(\Omega)} \tag{17}$$

Let $p \geq 0$ and $\mathcal{V}^b_{h,p}$ be the broken finite element space defined in (6). Then, by $P^b_{h,p}$ we denote the L^2-projection onto $\mathcal{V}^b_{h,p}$, i.e. given a $u \in L^2(\Omega)$ we define $P^b_{h,p}u \in \mathcal{V}^b_{h,p}$ by

$$\int_\Omega (u - P^b_{h,p}u)v_h \, d\boldsymbol{x} = 0 \quad \forall v_h \in \mathcal{V}^b_{h,p}$$

we use the short notation $P_h u$ instead of $P^b_{h,p}u$ when it is clear which projection is meant. Now, let $p \geq 0$ and $P_h v$ be the L^2-projection. Suppose $v \in H^{p+1}(\Omega)$, then

$$\|v - P_h v\|_{H^{p+1}(\Omega)} \leq Ch\|v\|_{L^2(\Omega)} \tag{18}$$

To numerically verify the convergence rate for smooth primal and adjoint data, numerical solutions of the following 2-D circular advection problem [7] were obtained

$$\begin{aligned} \boldsymbol{b} \cdot \nabla u &= 0 \quad \text{in } \Omega \\ u &= g \quad \text{on } \Gamma_- \end{aligned} \tag{19}$$

The target quantity is the weighted outflow flux functional

$$J(u) = \int_0^1 \delta_+(\boldsymbol{b} \cdot \boldsymbol{n})\psi_{\text{outflow}} u \, d\boldsymbol{x}$$

Figures 1a and 1b show primal and adjoint current solutions, respectively, while tables 1 and 2 tabulate values of the global solution error using a sequence of four nested meshes. Here, the $p + 1$ convergence rate for the u solution error is satisfied and so the rate for the adjoint solution. In this case, the latter rate is even better than the expected one from (22). The SUPG scheme keeps the same convergence rate for both solutions, while the other schemes RD-LDA and BUBBLE show a order 2 for $p = 1$ and 1 for $p > 1$.
Let now examinate the convergence rates for functionals. We consider the general linear problem (1) and its numerical discretization (9), where the bilinear form $\mathcal{B}(\cdot,\cdot)$ is continuous on $\mathcal{V}$ with respect to a specific $|||\cdot|||$-norm, i.e.

$$\mathcal{B}(w, v) \leq C_B |||w||| \, |||v||| \quad \forall w, v \in \mathcal{V} \tag{20}$$

Because the discretization is consistent and thus, the Galerkin orthogonality is satisfied, we assume that following *a priori* error estimate in the $|||\cdot|||$-norm holds: there are constants $C > 0$ and $r = r(p) > 0$ such that, for $\forall u \in H^{p+1}(\Omega)$

$$|||u - u_h||| \leq Ch^r |u|_{H^{p+1}(\Omega)} \tag{21}$$

Finally, we assume that the projection operator $P^b_{h,p}$ satisfies following approximation estimate in the $|||\cdot|||$-norm: there are constants $C > 0$ such that, for $\forall v \in L^2(\Omega)$

$$|||v - P^b_{h,p}v||| \leq Ch\|v\|_{L^2(\Omega)} \tag{22}$$

Let then assume that the target quantity as described in (2) with j_Ω and $\jmath_\Gamma$ smooth functions on Ω and Γ, respectively. Then we have following estimate

$$\begin{aligned} |J(u) - J(u_h)| &= |\mathcal{B}(u - u_h, z)| \\ &= |\mathcal{B}(u - u_h, z - P^b_{h,p}z)| \\ &\leq Ch^{r+1}|u|_{H^{p+1}(\Omega)}\|v\|_{L^2(\Omega)} \end{aligned} \tag{23}$$

Once again, to numerically verify the convergence rate of functionals for a Petrov-Galerkin scheme let consider the circular advection problem [7] whose results are tabulated on tables 1 and 2.
The $p + 1$ order for the functional error is satisfied by RD and BUBBLE schemes, while for SUPG a superconvergence rate $2p + 1$ is obtained. This behaviour seems to be strictly connected to the higher order of the corresponding adjoint solution of this scheme.

4. Error Representation Formula

Let consider the primal numerical problem (9) and that holds the *Galerkin orthogonality condition* (14). Let then notice that by the *compatibility condition* (3), using infinite-dimentional trial and test space, the adjoint problem can be redefined as

$$\mathcal{B}(w, z) = J(w) \qquad \forall w \in \mathcal{V}$$

So, an exact error representation formula for a given functional $J(\cdot)$ results from the following steps, where P_h denotes any suitable projection operator (i.e. interpolation, L_2 projection) into $\mathcal{V}^b_{h,p}$,

$$\begin{aligned} J(u) - J(u_h) &= J(u - u_h) \\ &= \mathcal{B}^*(z, u - u_h) \\ &= \mathcal{B}(u - u_h, z) \\ &= \mathcal{B}(u - u_h, z - P_h z) \\ &= \mathcal{B}(u, z - P_h z) - \mathcal{B}(u_h, z - P_h z) \\ &= F(z - P_h z) - \mathcal{B}(u_h, z - P_h z) \end{aligned} \tag{24}$$

so in summary

$$J(u) - J(u_h) = F(z - P_h z) - \mathcal{B}(u_h, z - P_h z) \qquad (25)$$

where no dependence on the exact solution u appears. Comptutationally, this error representation formula is not suitable for obtaing computable *a posteriori* error estimation unless the function $z - P_h z$ is unknown, since $z \in \mathcal{V}^b$ is a solution of the infinite-dimensional adjoint problem. So z has to be computed by the discrete adjoint problem (10). Since (7) holds, we can solve the adjoint problem by using the same bilinear operator, $\mathcal{B}(w_h, z)$, used for the primal problem. Due to the Galerkin orthogonality, the adjoint numerical problem must be approximated in a larger space of functions than that utilized in the primal numerical problem. Here, this is achieved by solving the adjoint problem using a polynomial space that is one polynomial degree higher than the primal numerical problem, i.e. if $v_b \in \mathcal{V}^b_{h,q}$ then $z \approx z_{b'} \in \mathcal{V}^b_{h,q+1}$.
The error representation formula written in the global abstract form of the (25) does not indicate which elements in the mesh should be refined to reduce the measured error in a functional. So, now the goal is to estimate the *local* contribution of each element in the mesh to the functional error. This local cell contribution will then be used as an error indicator for choosing which elements to refine or coarsen in the adaptive mesh procedure. By applying the *triangle inequality*, indeed, we have

$$\left|J(u) - J(u_h)\right| \leq \sum_{\kappa \in \mathcal{K}} \left|F_\kappa(z - P_h z) - \mathcal{B}_\kappa(u_h, z - P_h z)\right| \qquad (26)$$

where

$$F_\kappa(z - P_h z) - \mathcal{B}_\kappa(u_h, z - P_h z) = \mathcal{R}_\kappa(u_h, z - P_h z)$$

and

$$\mathcal{R}_\kappa(u, v) = (R(u), v)_\kappa + (r(u), C^* v)_{\partial\kappa \cap \Gamma}$$

with $R(u) = f - Lu$ and $r(u) = g - Bu$. This direct estimate let define for each partition element κ the *adaptation element indicator* η_κ

$$|\eta_\kappa| \equiv \left|\mathcal{R}_\kappa(u_h, z - P_h z)\right| \qquad (27)$$

Adaptive Meshing. Now, we consider the design of an adaptive algorithm to compute efficiently a given target quantity functional $J(\cdot)$. The simplest adaptation stopping criterion will be

$$|J(u) - J(u_h)| \leq \mathsf{TOL}$$

with TOL a given tolerance. To this aim, we employ the approximate error bound $\sum_{\kappa \in \mathcal{K}} |\eta_\kappa|$ to estimate when the desired level of accuracy has been achieved. Then, we practically enforce

$$\sum_{\kappa \in \mathcal{K}} |\eta_\kappa| \leq \mathsf{TOL}$$

Hence, a simple mesh adaptation strategy can be outlined as follows:

1. Construct an initial mesh $\mathcal{K}$.
2. Compute the numerical approximation $u_h \in \mathcal{V}_{h,p}$ on the current mesh $\mathcal{K}$.
3. Compute the numerical approximation $z_b \in \mathcal{V}^b_{h,q}$ on the same current mesh $\mathcal{K}$ and where $q > p$.
4. Evaluate the error indicators, η_κ, for all elements $\kappa \in \mathcal{K}$ and sum them all up.
5. If $\sum_{\kappa \in \mathcal{K}} |\eta_\kappa| \leq \mathsf{TOL}$ where TOL is a given tolerance, then STOP.
6. Otherwise, refine and coarsen a specified fraction of the total number of elements according to the size of $|\eta_\kappa|$, generate a new mesh $\mathcal{K}$ and GOTO 2.

5. Numerical Results

In this section, selected numerical examples are given for scalar advection (and/or reaction) problems. SUPG, RD and bubble schemes are the numerical schemes used for all cases. The following tables tabulate values of the functional error and the estimated error as given in (26) using numerically approximated adjoint problems.
In addition, an effictivity index is included to characterize the sharpness of the current estimates

$$\theta_{\text{eff}} = \frac{|\text{estimated error}|}{|J(u) - J(u_h)|} \qquad (28)$$

When the exact adjoint solution is used

$$|J(u) - J(u_h)| = \Big|\sum_{\kappa \in \mathcal{K}} \eta_\kappa\Big|$$

so the corresponding column in the following tables measures the effect of numerically approximating the adjoint problem. After application of the triangle inequality, the estimate

$$|J(u) - J(u_h)| \leq \sum_{\kappa \in \mathcal{K}} |\eta_\kappa|$$

is obtained. Mesh adaptation strategies are usually based on $|\eta_\kappa|$ and so they depend on this error estimation. As internal cancellations are precluded, the estimate can usually lose in accuracy. Hence, column six and seven of the following tables show the current estimate and its efficiency index.

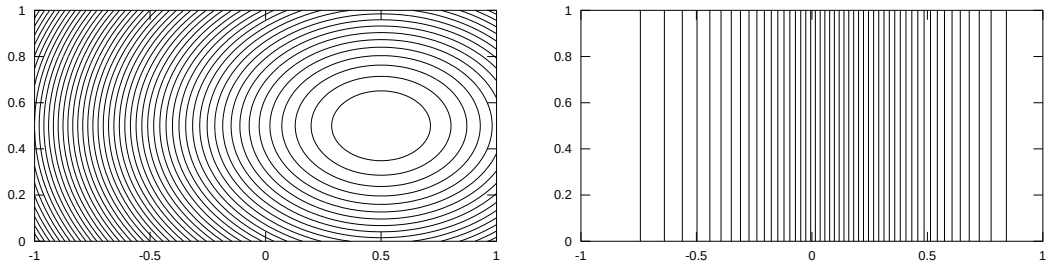

(a) (b)

Figure 2: Reaction problem : (a) primal; (b) adjoint

Method	h	$\lvert J(u) - J(u_h)\rvert$	$\lvert \sum_\kappa \eta_\kappa \rvert$	(θ_{eff})	$\sum_\kappa \lvert \eta_\kappa \rvert$	(θ_{eff})
SUPG	.0625	4.4835e-07	1.2320e-07	(0.27)	6.2854e-06	(14.0)
SUPG	.0312	4.8891e-08	1.2628e-08	(0.26)	1.4880e-06	(30.4)
SUPG	.0156	5.4553e-09	1.2829e-09	(0.24)	3.6255e-07	(66.5)
SUPG	.0078	6.3152e-10	1.3283e-10	(0.21)	8.9566e-08	(141)
RD-LDA	.0625	2.3770e-05	1.9639e-05	(0.83)	2.0265e-05	(0.85)
RD-LDA	.0312	5.9543e-06	4.9327e-06	(0.83)	5.0964e-06	(0.86)
RD-LDA	.0156	1.4910e-06	1.2368e-06	(0.83)	1.2757e-06	(0.86)
RD-LDA	.0078	3.7312e-07	3.0974e-07	(0.83)	3.1908e-07	(0.86)
BUBBLE	.0625	5.9175e-06	3.2404e-06	(0.55)	4.0190e-06	(0.68)
BUBBLE	.0312	1.4556e-06	7.9155e-07	(0.54)	9.7550e-07	(0.67)
BUBBLE	.0156	3.6096e-07	1.9585e-07	(0.54)	2.4039e-07	(0.67)
BUBBLE	.0078	8.9876e-08	4.8773e-08	(0.54)	5.9721e-08	(0.66)

Table 3: Efficiency rates $p_{\text{p}} = 1$ and $p_{\text{a}} = 2$ order of the SUPG, RD and BUBBLE methods error estimates for the advection reaction problem.

Method	h	$\lvert J(u) - J(u_h)\rvert$	$\lvert \sum_\kappa \eta_\kappa \rvert$	(θ_{eff})	$\sum_\kappa \lvert \eta_\kappa \rvert$	(θ_{eff})
SUPG	.0625	7.4432e-08	7.2144e-08	(0.97)	8.8806e-08	(1.19)
SUPG	.0312	1.0126e-08	9.8401e-09	(0.97)	1.1740e-08	(1.16)
SUPG	.0156	1.3178e-09	1.2815e-09	(0.97)	1.5062e-09	(1.14)
SUPG	.0078	1.6795e-10	1.6335e-10	(0.97)	1.9061e-10	(1.13)
RD-LDA	.0625	2.0983e-08	1.8213e-08	(0.87)	2.4471e-08	(1.17)
RD-LDA	.0312	2.6073e-09	2.2146e-09	(0.85)	3.0422e-09	(1.17)
RD-LDA	.0156	3.2153e-10	2.6966e-10	(0.84)	3.7474e-10	(1.17)
RD-LDA	.0078	3.9683e-11	3.3028e-11	(0.83)	4.5879e-11	(1.16)
BUBBLE	.0625	1.3311e-08	1.3106e-08	(0.98)	1.6135e-08	(1.21)
BUBBLE	.0312	1.5441e-09	1.4984e-09	(0.97)	1.9342e-09	(1.25)
BUBBLE	.0156	1.8277e-10	1.7538e-10	(0.96)	2.3381e-10	(1.28)
BUBBLE	.0078	2.1956e-11	2.0914e-11	(0.95)	2.9851e-11	(1.36)

Table 4: Efficiency rates $p_{\text{p}} = 2$ and $p_{\text{a}} = 3$ order of the SUPG, RD and BUBBLE methods error estimates for the advection reaction problem.

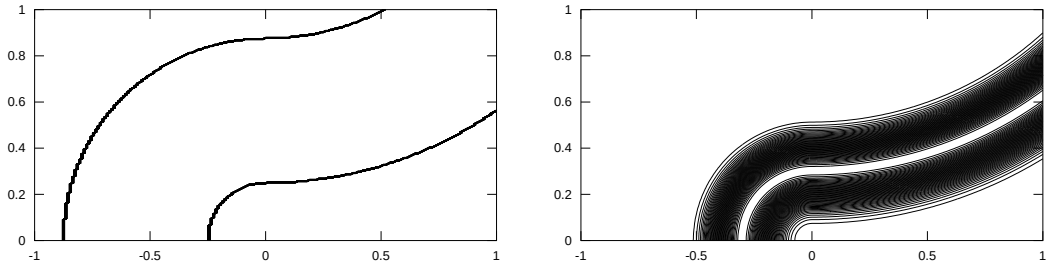

(a) (b)

Figure 3: Analytical solutions linear hyperbolic problem [4]: (a) primal; (b) adjoint

Advection-reaction. The advection-reaction case is defined by the following linear equation

$$\begin{aligned} \boldsymbol{b} \cdot \nabla u + cu &= f \quad \text{in } \Omega \\ u &= g \quad \text{on } \Gamma_- \end{aligned} \tag{29}$$

with $\boldsymbol{b} = (1, 0)$, $c = 1 - \text{sign}(x)x$. The source term f is given such that the analytical solution u^* of (29) is as follows

$$u^* = \alpha e^{-[a(x-x_0)^2 + b(y-y_0)^2]}$$

Finally, boundary conditions are consistent by the analytical solution. Once again the target quantity is an outflow functional such that the corresponding adjoint problem becomes

$$\begin{aligned} \boldsymbol{b} \cdot \nabla z + cz &= 0 \quad \text{in } \Omega \\ z &= 1 \quad \text{on } \Gamma_+ \end{aligned}$$

Figures 2a and 2b show primal and adjoint solutions, respectively, while error estimation data are tabulated on tables 3 and 4. Here, RD-LDA scheme seems to be the best scheme with all estimates which keep close to exact functional error. What sounds odd is the $p = 1$ SUPG estimate which seems out of control. This becomes even more weird by looking to the $p = 2$ estimate where both thetas converge to one.

Hartmann's problem. With the following example, we compare the efficiency of the adjoint based error estimation, in adaptive meshing, with respect to the *ad hoc* estimation procedure.
Let consider the linear hyperbolic problem ([4]):

$$\begin{aligned} \boldsymbol{b} \cdot \nabla u &= f \quad \text{in } \Omega \\ u &= g \quad \text{on } \Gamma_- \end{aligned} \tag{30}$$

with the advection $\boldsymbol{b} = \frac{\tilde{\boldsymbol{b}}}{|\tilde{\boldsymbol{b}}|}$, where

$$\tilde{\boldsymbol{b}} = \begin{cases} (y, -x), & \text{for } x < 1, \\ (2 - y, x) & \text{otherwise} \end{cases}$$

The analytical solution is shown in figure 3a, where the two discontinuites of the two inlet jumps are carried along the charactistic directions of the advection field. Let then suppose to be interested in the solution along the outlet boundary segment $1/4 \leq y \leq 1$. We solve numerically both problems by the SUPG scheme $p = 2$ and $p = 3$ order, respectively for primal and adjoint problem. Figure 4 shows the numerical solutions and the corresponding final adaptive meshes, generated by the *ad hoc* residual error indicators, $\eta_\kappa^{\text{ad hoc}}$, and the current adjoint weighted-ones, η_κ^{adj}, respectively. In figure 4c we see how the final mesh is refined along both discontinuites, giving a very good resolution for the both corresponding jumps, see figure 4a. Instead, the mesh coming out from the based adjoint error estimation refines only in the neighborhood of the lower jump, see figure 4d, the one which goes out through the target outlet. The other jump is then roughly solved but, as the adjoint solution over that zone is null, the error of the solution along the second jump do not affect the current target quantity. This is the reason why it is not refined during the adaptation.
Comparing the two procedures, the adjoint-based estimation proves to be more efficient, since it reaches a similar accuracy of the target quantity: $|J(e)| = 2.4697 \times 10^{-8}$ vs. $|J(e)| = 1.3100 \times 10^{-6}$, generating a final mesh with roughly half of the elements: 1771 instead of 3736. Moreover, figure 5 shows how the target quantity error of the adjoint refinement always remains inferior to the *ad hoc* one. However, we must remind to that this algorithm needs to solve two

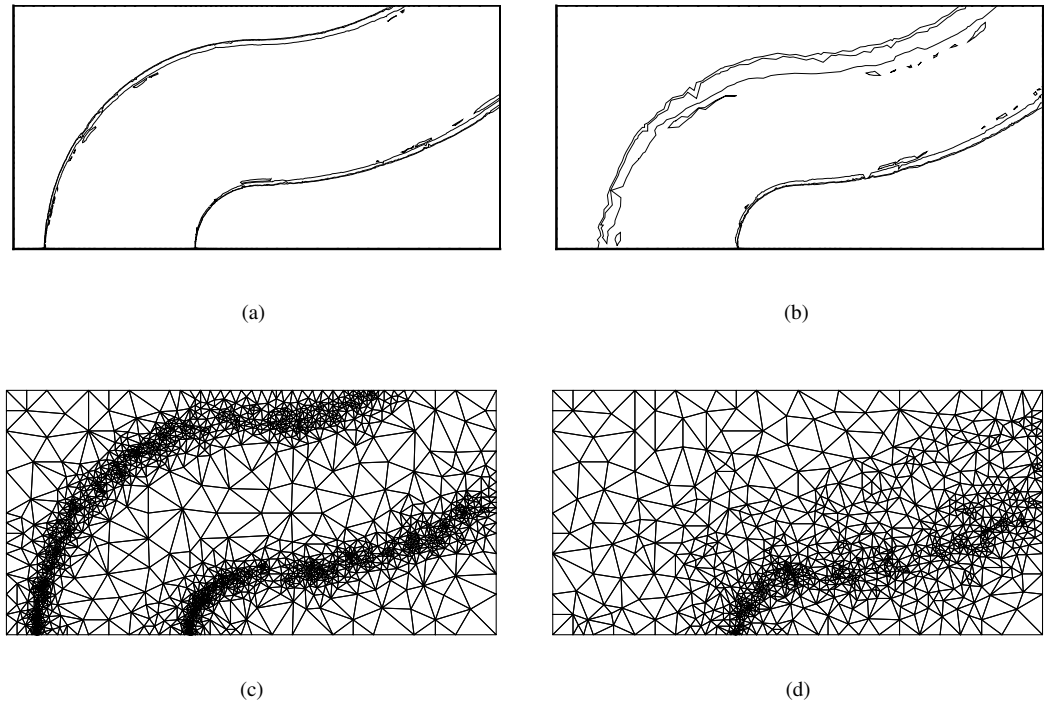

Figure 4: Adaptive refinement for the hyperbolic linear problem (30): (a) Numerical solution solved on the mesh (c), generated by a based-residual error estimation; (b) Numerical solution solved on the mesh (d), generated by the adjoint error estimation;

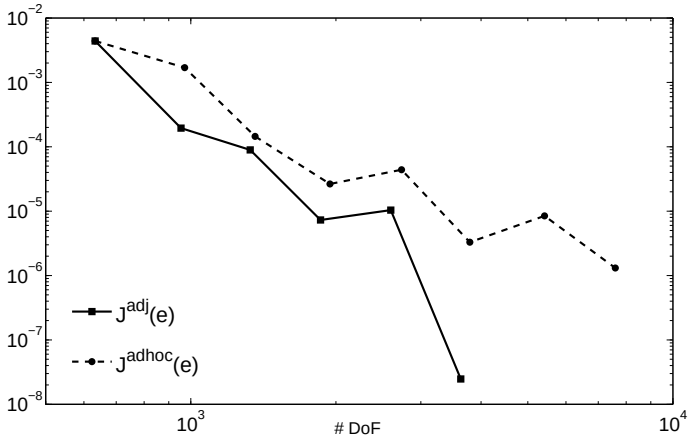

Figure 5: Convergence of the target quantity error, $J(e)$

problems, primal and adjoint, while the simple based-residual estimation solves the only primal one. Since, in this case, both problems are linear and the adjoint is solved with an higher order, the added computational cost can be remarkable. Anyway, this cost will become negligible for non-linear primal problem as the adjoint will be still linear.

6. Conclusions

Among different types of error representation formula, we were interested in Type I error indicator. Unlike Type II error bounds where the only local residual is taken into account, Type I involves also the solution of the associated adjoint problem. By it, we are able to obtain further information concerning the trasport of the error of computing the quantity of interest.
For the first time, we apply this to error analysis by using a Petrov-Galerkin discretization. Some schemes are then implemented: Streamline Upwind PG, Residual Distribution and a bubble scheme. Theory proves that the convergence rate of the target quantity error depends on the chosen scheme. Few linear problems have been employed to verify the behaviour of these schemes, while an hyperbolic problem has been used to test the efficiency of the current refinement with respect to the classical residual based estimation. Now, further extensions to non-linear hyperbolic problems are possible.

References

[1] P. H. K. Eriksson, D. Estep, C. Johnson, Introduction to adaptive methods for different equations, Acta Numerica (1995) 105–158.

[2] R. Becker, R. Rannacher, A feed-back approach to error control in finite element methods: basis analysis and examples, Journal Numerical Mathematics 4 (1996) 237–264.

[3] R. Becker, R. Rannacher, An optimal control approach to a-posteriori error estimation in finite element methods, Acta Numerica 10 (2001) 1–102.

[4] R. Hartmann, Adaptive finite element methods for the compressible euler equations, Ph.D. thesis, Universität Heidelberg (2002).

[5] R. Hartmann, Numerical analysis of higher order discountinuos galerkin finite element methods, in: 35th CFD VKI / ADIGMA, 2008.

[6] M. Giles, N. Pierce, Adjoint equations in cfd: duality, boundary conditions and solution behaviour, AIAA (1997) 97–1850.

[7] T. Barth, *A Posteriori* error estimation and mesh adaptivity for finite volume and finite element methods, Tech. rep., NASA Ames Research Center (2002).

High–order RDS and p-multigrid Solution Algorithms for Compressible Flow

Martin Vymazal

Aeronautics and Aerospace Department, von Karman Institute for Fluid Dynamics, Belgium, martin.vymazal@vki.ac.be

Supervisor: Herman Deconinck

Professor, Aeronautics and Aerospace Department, von Karman Institute for Fluid Dynamics, Belgium, deconinck@vki.ac.be

University Supervisor: Chris Lacor

Professor, Department of Mechanical Engineering, Faculty of Applied Sciences, Vrije Universiteit Brussel, Belgium, Chris.Lacor@vub.ac.be

Abstract

Residual distribution schemes are discussed in the context of higher order spatial discretization for hyperbolic conservation laws. The discrete solution is approximated by a finite element space based on triangular Lagrangian P_k elements. A natural subtriangulation of these elements allows the reuse of simple distribution formula previously developed for linear P_1 triangles. Curved elements with piecewise quadratic and cubic approximation of the boundaries of the domain are considered.

In the second part, a new variant of RD scheme is proposed. This particular formulation avoids the sub–triangulation procedure.

Keywords: residual distribution, multidimensional upwind, high order, curvilinear geometry

1. Introduction

The present work follows a Residual Distribution approach (1; 2; 3), which is close to continuous finite element methods, but allows the use of a maximum principle to construct nonlinear monotonicity preserving and truely multidimensional stabilizations. In previous papers (4) we have exploited the close relation with continuous finite element discretizations to present a class of higher order residual distribution methods defined on P_k Lagrangian triangular finite elements. Here we focus on the use of curved elements to allow for a higher order representation of the boundaries of the domain, using sub- or isoparametric transformation from physical space to a Cartesian parent element.

2. Notations

We consider the steady state solution of a conservation law on a two–dimensional spatial domain Ω:

$$\frac{\partial \boldsymbol{u}}{\partial t} + \nabla \cdot \boldsymbol{\mathcal{F}} = 0 \quad \forall (x, y) \in \Omega \subset \mathbb{R}^2, \quad \forall t \geq 0, \quad (1)$$

where $\boldsymbol{u}$ is the vector of conserved variables and $\boldsymbol{\mathcal{F}}$ is the inviscid flux vector, $\boldsymbol{\mathcal{F}}(\boldsymbol{u}) = (\mathbf{f}(\boldsymbol{u}), \mathbf{g}(\boldsymbol{u}))$. We denote by $\mathcal{T}_{h,k}$ a triangulation of the domain Ω, whereby each triangular element T of the triangulation $\mathcal{T}_{h,k}$ is a Lagrangian P_k finite element equipped with $K = \frac{(k+1)(k+2)}{2}$ degrees of freedom.

In the simplest case the geometry of the P_k triangle is considered to be linear, defined by its three corner nodes. Hence, the intermediate nodes on the boundary of the element are all located on the straight edges and therefore the boundary of the domain Ω is approximated by a polygone. Such a discretization will be denoted as a P_1P_k discretization (P_1 for geometry and P_k for the solution).

We work with elements whose edges are described by second- and third- order polynomials. Elements with quadratic geometry will be denoted as P_2P_k elements (P_2 for geometry and P_k for the solution). P_2P_2 elements are called isoparametric, while P_2P_k with $k > 2$ are called subparametric elements. The notation for P_3 elements is analogous.

The geometry of the curvilinear P_2 (P_3) element is transformed to a parent element in ξ–η space. In our

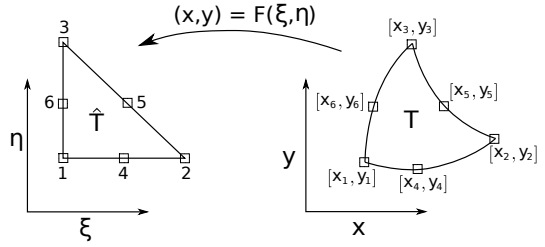

Figure 1: Transformation of triangle geometry from physical to reference space using Lagrange shape functions

case, we define $\mathbf{F}(\xi, \eta)$ from figure (1) as isoparametric mapping

$$\begin{bmatrix} x(\xi,\eta) \\ y(\xi,\eta) \end{bmatrix} = \sum_{i=1}^{N} \varphi_i^{h,k}(\xi,\eta) \cdot \begin{bmatrix} x_i \\ y_i \end{bmatrix} \tag{2}$$

where N is the number of degrees of freedom of P_2 or P_3 triangle, respectively. The number k refers to the order of shape functions φ_i and x_i, y_i denote the nodal coordinates of the triangle.

3. Residual Distribution method

For any triangulation $\mathcal{T}^{h,k}$ the cell residual for a given triangle is defined as the integral over the triangle of the spatial operator:

$$\begin{aligned} \phi^T &= \int_T \nabla \mathcal{F}(u^{h,k})\, d\Omega = \oint_{\partial T} \mathcal{F}(u^{h,k}) \cdot \vec{n}\, dl \\ &= \sum_{s=0}^{N_s} \int_{T_s} \vec{a}(u^{h,k}) \cdot \nabla u^{h,k}\, dx\, dy \\ &\qquad (N_s \ldots \text{number of sub–elements}) \end{aligned} \tag{3}$$

where we have used the expression for the Jacobian of the flux $\mathcal{F}(u)$ in (1),

$$\vec{a}(u) = \frac{\partial \mathcal{F}(u)}{\partial u} = \left(\frac{\partial f_1(u)}{\partial u}, \frac{\partial f_2(u)}{\partial u} \right) \tag{4}$$

We can also construct the residual over each P_1 sub-element of $\mathcal{T}^{h,k}$

$$\phi^{T_s} = \oint_{\partial T_s} \mathcal{F}(u^{h,k}) \cdot \vec{n}\, dl \tag{5a}$$

$$= \int_{T_s} \vec{a}(u^{h,k}) \cdot \nabla u^{h,k}\, dx\, dy \equiv \vec{a}^* \cdot \int_{T_s} \nabla u^{h,k}\, dx\, dy \tag{5b}$$

with $\vec{a}^*$ a properly defined local average of $\vec{a}(u)$ over the sub-triangle such that conservation is preserved (5). The existence of such local average for general nonlinear conservation law is not guaranteed, but in case of the conservation law (1) applied to the Euler equations considered in this work, a conservative linearisation is possible under the assumption that the vector of Roe variables changes linearly in each cell.

The basic idea of the residual distribution (RD) method consists of distributing fractions of this cell residual to the three nodes of the element T. The fraction sent to node $i \in T$ is denoted ϕ_i and we require

$$\sum_{i \in T} \phi_i = \phi^T \tag{6}$$

This requirement can be written in terms of *distribution coefficients* β_i which for consistency sum to unity

$$\sum_{i \in T} \beta_i = 1, \qquad \beta_i = \frac{\phi_i}{\phi^T} \tag{7}$$

After assembling all contributions in the nodes, the nodal equation for node i reads, with $\mathcal{D}_i$ the set of all triangles that share node i:

$$\sum_{T \in \mathcal{D}_i} \phi_i = 0 \tag{8}$$

Since the distribution is restricted to the nodes of the triangle itself, the stencil of the scheme remains compact. This equation can be solved by embedding in a pseudo–time iteration, i.e. by finding a steady state solution of

$$|S_i| \frac{du_i}{d\tau} + \sum_{T \in \mathcal{D}_i} \phi_i^T = 0, \tag{9}$$

where $|S_i|$ is the area of median dual cell.

3.1. Residual Distribution schemes on P_1 elements

For a given P_1 (both solution and geometry) triangle we consider the set of normal vectors $\{\vec{n}_j\}_{j \in T}$, defined by the inward normals to the edges of T facing each node $j \in T$ (see figure 2 left). The norm of $\vec{n}_i$ is equal to the length of the edge. Let us define the upwind parameter

$$k_j = \frac{1}{2} \vec{a}^* \cdot \vec{n}_j \quad \text{implying} \quad \sum_{i \in T_s} k_i = 0 \tag{10}$$

In this case, using a conservative linearisation (eq. 5b, 10), we can express the cell residual as follows:

$$\phi^T = \oint_{\partial T} \mathcal{F}(u^{h,1}) \cdot \vec{n}\, dl = \int_T \nabla \mathcal{F}(u^{h,1})\, d\Omega = \sum_{i \in T} k_i u_i \tag{11}$$

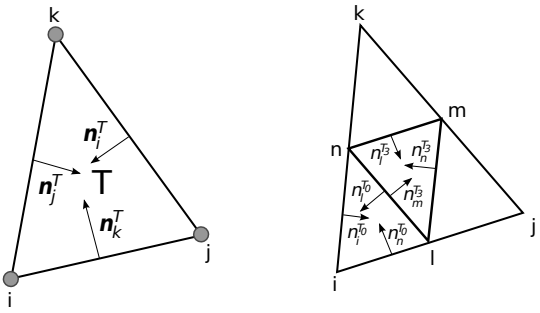

Figure 2: Definition of the normal vectors $\vec{n}_i$ in P_1 and P_2 elements

When all contributions for a given node are assembled, we end up with the following system of nodal equations, similar to equation (9), to be solved using explicit or implicit pseudo-time iterations. For example, using forward Euler method, we get:

$$|S_i|\frac{u_i^{n+1}-u_i^n}{\Delta\tau}+\sum_{T_s,\ i\in T_s}\phi_{i,n}^{T_s}=0 \tag{12}$$

Many distribution schemes (defining the split residuals ϕ_i) for P_1 elements have been developed in the past (4; 6; 7). A particular class satisfies a multidimensional upwinding property (MU). Such distributions satisfy the requirement that a node in a triangle does not receive a contribution if its opposed face is an outflow face. The condition is easily imposed by requiring $\phi_i = 0$ whenever $k_i < 0$. Within this work, we limited ourselves to the use of the LDA (Low Diffusion A) scheme. Denoting by k_i^+ and k_i^- the positive and negative part of the upwind parameter, $k^\pm = \frac{k\pm|k|}{2}$, the distribution coefficients of the LDA scheme can be written as

$$\beta_i^{LDA}=\frac{k_i^+}{\sum_{m=1}^3 k_m^+} \tag{13}$$

This scheme is of order $O(k+1)$ (k being the order of interpolating polynomial), but not strictly monotone. We refer the reader interested in detailed description of the LDA scheme to other literature (1; 8; 4; 6; 9).

3.2. Residual distribution schemes on P_1P_k elements

Consider now the extension of multidimensional upwind (MU) schemes to high order P_1P_k elements. We will assume that the inward normals $\vec{n}_j$'s are defined on the local P_1 sub-elements $T_s \in T$, as shown on figure 2 (right) for $k = 2$. Note that if we consider a P_1P_k element (P_k element for the solution but only P_1 triangles for the geometry, defined by the 3 corner nodes), the inward normals of the sub-elements can be deduced easily from the ones of the parent element by a simple rescaling. We compute the residual on each sub-element:

$$\phi^{T_s}=\int_{T_s}\nabla\mathcal{F}(u^{h,k})\,d\Omega=\oint_{\partial T_s}\mathcal{F}(u^{h,k})\cdot\hat{n}\,dl \tag{14}$$

Then, this residual is distributed to the 3 nodes of the sub-element, using the LDA distribution scheme (13) developed for P_1 triangles:

$$\phi_i^{T_s,LDA}=\beta_i\phi^{T_s} \tag{15}$$

The linearization used to compute the parameters k_i can be based on any linearized state over the sub-triangle, without affecting accuracy nor conservation.

Remark. *This is not the only strategy to achieve residual distribution schemes on P_k elements. In particular, we refer to Lax Friedrichs distribution schemes of Abgrall and collaborators (10), (11). In this case the residual is computed on the complete P_k element and then distributed to the N nodes of the element without making use of a sub-triangulation.*

3.3. Curvilinear P_2P_k and P_3P_k elements

We consider elements where the geometry is either piecewise quadratic or cubic. The geometry and numerical solution can be discretized independently so in general the solution can have any order k. However, we focus on isoparametric (P_2P_2 or P_3P_3) high–order elements.

To ensure conservation of fluxes, we compute the sub-element residual from equation (14) as a contour integral:

$$\phi^{T_s}=\oint_{\partial T_s}\mathcal{F}(u^{h,k})\cdot\vec{n}\,dl \tag{16}$$

The boundary ∂T_s is described by transformation (2). For every face on ∂T_s, this transformation is a function of only one parameter ζ:

$$\begin{aligned}x&=x(\zeta)\\ y&=y(\zeta)\end{aligned} \tag{17}$$

We integrate numerical the fluxes of (16) using Gauss quadrature: 3 points per face f of the sub–element for P_2 and 5 points for P_3:

$$\oint_f\mathcal{F}(u^{h,k})\cdot\vec{n}\,dl\simeq\sum_{q=1}^{N}w_q[\mathcal{F}(u_q)\cdot\vec{n}_q]J_q, \tag{18}$$

$$J_q=\sqrt{\dot{x}^2(\zeta_q)+\dot{y}^2(\zeta_q)} \tag{19}$$

where J_q is the Jacobian of transformation (17) at quadrature point q. We use the transformation also to compute the normal $\vec{n}_q$.

The integral over f in equation (18) is approximated:

- by three-point Gauss quadrature for each face of P_1P_1 triangle
- by the same quadrature for each face of each *sub–triangle* in the case of P_1P_2 and P_2P_2 elements
- by five–point Gauss quadrature on each sub–face of the P_3P_3 element

The quadrature nodes and weights on the biunit interval are given in table 1.

	Quadrature points	*Weights*
P_1P_1, $P_{1(2)}P_2$	0.0	$\frac{8}{9}$
	$\pm\sqrt{\frac{3}{5}}$	$\frac{5}{9}$
P_3P_3	0.0	0.5688888889
	±0.5384693101	0.4786286705
	±0.9061798459	0.2369268850

Table 1: Gauss quadrature used to approximate the residuals $\phi^{T,in}$.

3.4. Subsonic flow around a cylinder

We present results for a test case with stagnation point, namely the flow around a circular cylinder at $M_\infty = 0.38$. We consider four O–meshes with 16×5 (M1), 32×9 (M2), 64×17 (M3) and 128×33 (M4) points as described in (12). The first number indicates the number of nodes in the circular direction of the mesh, the second number refers to the number of nodes in the radial direction (figure 3). The radii of the circles in each mesh follow a geometric series

$$r_j = r_0\left(1 + \frac{2\pi}{128}\sum_{k=0}^{j-1}\alpha^k\right),\ j = 1, 2, \ldots 32, \qquad (20)$$

where $\alpha = 1.1648336$ and $r_0 = 0.5$ is the radius of the cylinder. The farfield boundary is located at 20 diameters from the center. To have the same number of degrees of freedom and make a fair comparison between the P_1P_1 and P_2P_2 schemes, we create a P_1 sub-triangulation of each P_2 triangle. The P_3P_3 meshes were created independently such that the number of *elements* is equal for P_1P_2, P_2P_2 and P_3P_3 meshes. We plot the P_1 solutions on all four meshes

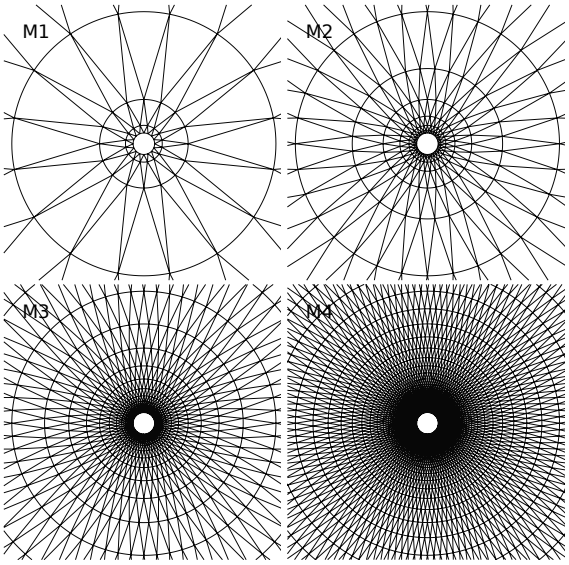

Figure 3: 16×5, 32×9, 64×17 and 128×33 meshes for subsonic cylinder test case.

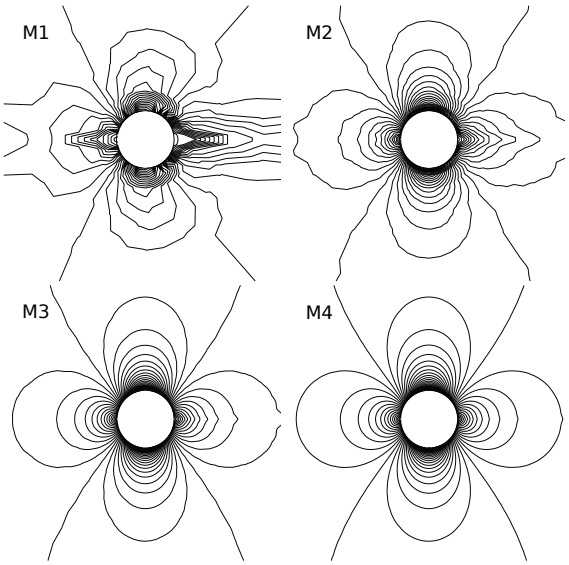

Figure 4: Mach isolines plotted for Ma $\in \langle 0, 1\rangle$, $\Delta Ma = 0.025$ on mesh with P_1P_1 elements.

(figure 4). Higher–order solution is shown in figure 5 for M2 and M3. Figure 6 presents the pressure coefficient on the cylinder wall and the entropy deviation on mesh M1. We measure the rate of convergence again by computing the relative decrease of the L_2 norm of entropy error Σ as the mesh is refined. The measured order is reported in figure 7. We did not include the entropy error on M1 in the computation of the convergence order of P_1P_2 discretization, since

this error is very large (all values are listed table 2). As a result, the convergence rate measured on all four meshes seems to be very high due to rapid decrease of the entropy error as the element size becomes small compared to the curvature of the cylinder.

		P_1P_1	P_1P_2
Mesh	NDOF	$\|\|\Sigma\|\|_{L_2}$	$\|\|\Sigma\|\|_{L_2}$
M1	288	4.87E -02	6.03E-02
M2	1088	7.64E -03	1.78E-03
M3	4224	1.13E -03	1.57E-04
M4	16640	1.78E -04	2.04E-05
Order		*1.99*	*3.05*

		P_2P_2	P_3P_3
Mesh	NDOF	$\|\|\Sigma\|\|_{L_2}$	$\|\|\Sigma\|\|_{L_2}$
M1	624	1.00E-02	1.46E-03
M2	2400	1.78E-03	5.62E-05
M3	9408	1.27E-04	5.35E-06
M4	37248	2.76E-05	5.33E-07
Order		*2.98*	*3.84*

Table 2: L_2 norm of entropy error (Σ): subsonic cylinder test case.

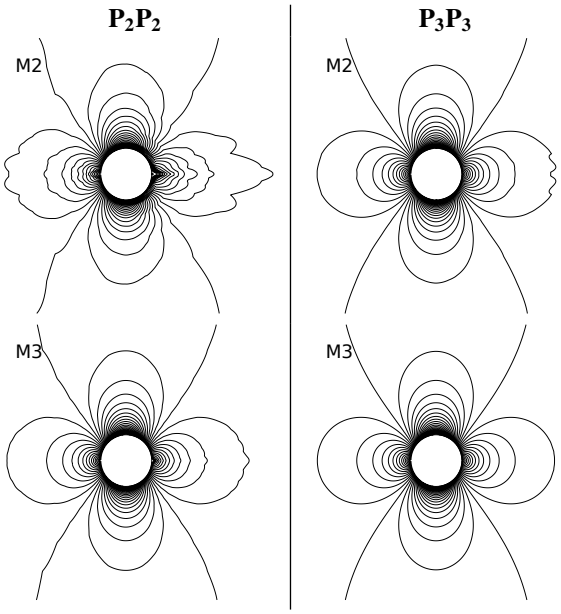

Figure 5: Mach number isolines plotted for $Ma \in \langle 0, 1\rangle$, $\Delta Ma = 0.025$ on meshes M_2 and M_3. Left: P_2 elements, right: P_3 elements.

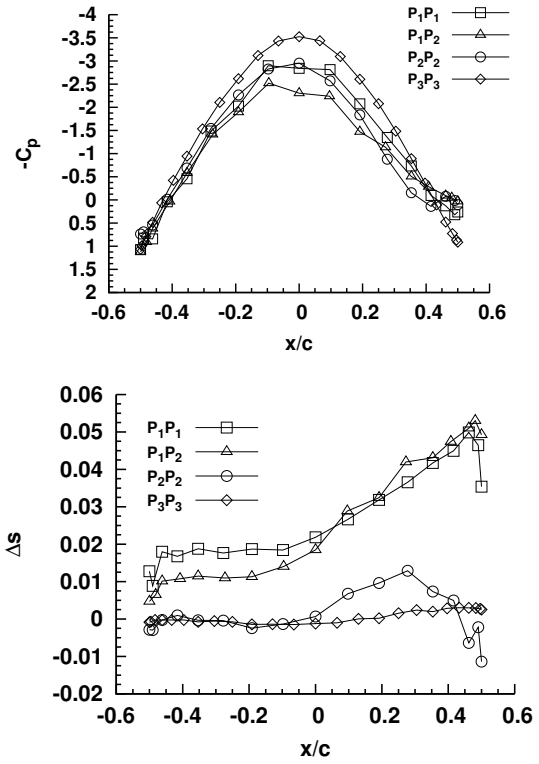

Figure 6: Pressure coefficient (left) and entropy deviation $s - s_{in}$ (right) on the cylinder wall on mesh M1

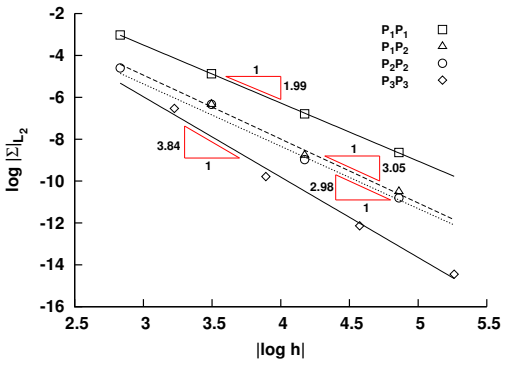

Figure 7: Subsonic cylinder test case; L_2 norm of the entropy error as a function of the mesh size h.

4. Residual distribution schemes with variable distribution coefficient

We consider a linear differential problem

$$\mathcal{L}u = f,$$

with for example $\mathcal{L} = \boldsymbol{\lambda} \cdot \nabla$ or $\mathcal{L} = \boldsymbol{\lambda} \cdot \nabla - \nu\Delta$. The numerical solution $u^{h,k}$, is a FE representation polynomial of the discrete solution:

$$u_h = \sum_{T \in \text{mesh}} \sum_{j \in T} \varphi_j u_j^{h,k}$$

When $k = 1$ ($u^{h,k}$ is a linear polynomial), RDS proceeds as follows

1. *Compute residual:*

$$\begin{aligned} \Phi^T &= \int_T \mathcal{L}u^h dX = \sum_{j \in T} \left(\int_T \mathcal{L}\varphi_j \, dX \right) u_j \qquad (21) \\ &= \sum_{j \in T} u_j \int_T k_j \, dX \end{aligned}$$

   defining k_j as

$$k_j = \mathcal{L}\varphi_j$$

2. *Distribution:* achieved eventually via the definition of coefficients $\beta_i^T = \beta_i^T(\{k_j\}_{j \in T}, u_h, \boldsymbol{\lambda}, h, \Phi^T)$
3. *Assembly/resolution:* obtain the values $\{u_j\}_{j \in \text{mesh}}$ as a solution of $\sum_{T | j \in T} \beta_j^T \Phi^T = 0$

In the linear case the derivatives of the basis functions are constants. This allows the following reinterpretation of the above scheme as a Petrov–Galerkin scheme with particular test functions.

1. Definition of the test function β:

$$k_j = \mathcal{L}\varphi_j, \quad \beta_j(x) = \beta_j^T(\{k_j\}_{j \in T}, u_h, \boldsymbol{\lambda}, h, r^T) \quad \text{with } r^T = \mathcal{L}u_h|_T$$

2. Integrate: $\Phi_i^T = \int_T \beta_i(x) r^T$
3. Assembly/resolution: get the values $\{u_j\}_{j \in \text{mesh}}$ by solving $0 = \sum_{T | j \in T} \Phi_i^T = \sum_{T | j \in T} \int_T \beta_i(x) r^K$

Since all the known definitions of β_i^T depend on the definition of k_j (i.e. on the derivatives of the shape functions), the two schemes are identical in the P^1 case. The schemes are not the same anymore for P^k interpolation, $k > 1$.

4.1. Conservation issues

In case we need apply the method to nonlinear conservation law

$$\nabla \cdot \boldsymbol{\mathcal{F}} = 0$$

a necessary condition for the scheme to converge to some weak solution is that

$$\sum_{j \in K} \varphi_j = \oint_{\partial K} \boldsymbol{\mathcal{F}}(u^{h,k}) \cdot \boldsymbol{n}$$

is satisfied for some approximation of the *physical* flux $\boldsymbol{\mathcal{F}}$ which is continuous across element edges. One possible approach to satisfy this requirement is a suitable volume integration.

Suppose that the flux is approximated by Finite Element shape functions φ^F:

$$\boldsymbol{\mathcal{F}}(u^{h,k}) = \sum_{j \in K} \boldsymbol{\mathcal{F}}_j(u^{h,k}) \varphi_j^F \qquad (22)$$

The Finite Element space which interpolates the discrete flux need not be the same as the Finite Element space used for the solution variable. However, it should be richer to account for the nonlinearity of the flux $\boldsymbol{\mathcal{F}} = \boldsymbol{\mathcal{F}}(u)$. Assuming the continuity of the flux function, the following relation is satisfied for exact integration

$$\int_K \nabla \cdot \boldsymbol{\mathcal{F}}(u^{h,k}) = \oint_K \boldsymbol{\mathcal{F}}(u^{h,k}) \cdot \boldsymbol{n}$$

Since the flux is interpolated as described in equation (22), the following identity holds

$$\begin{aligned} \int_K \nabla \cdot \boldsymbol{\mathcal{F}}(u^{h,k}) &= \sum_{j \in K} \boldsymbol{\mathcal{F}}_j(u^{h,k}) \cdot \int_K \nabla \varphi_j^F \\ &= \sum_{j \in K} \boldsymbol{\mathcal{F}}_j(u^{h,k}) \cdot \sum_{q \in K} |K| w_q \nabla \varphi_j^F(x_q) \end{aligned}$$

The quadrature points x_q and weights w_q are chosen such that the gradients of flux shape functions are integrated exactly. The nodal residual is then evaluated as

$$\int_K \beta_i(x) \nabla \cdot \boldsymbol{\mathcal{F}}(u^{h,k}) = \sum_{j \in K} \sum_{q \in K} |K| w_q \beta_i(x_q) \boldsymbol{\mathcal{F}}_j(u^{h,k}) \cdot \nabla \varphi_j^F(x_q)$$

4.2. Advantages of RD formulation with variable β

The RD schemes with variable distribution coefficient β work without any substantial modification not only on simplex elements, but also on tensor-product

elements (quadrilaterals in 2D). The construction of sub–elements used previously for the RD method becomes an important issue as the polynomial order of the underlying FE interpolation space becomes high (number of quadrature points per element quickly increases) and as we go to three dimensions (division into sub–elements becomes rather complex to implement in computer codes).

The generic formulation (21) avoids these problems and at the same time, it preserves the upwind nature of the original formulation of the RD schemes.

4.3. Examples of schemes

LDA

For the LDA scheme, we set

$$k_i = L\varphi_i = \boldsymbol{\lambda} \cdot \nabla \varphi_i, \qquad \beta_i^T = \frac{k_i^+}{\sum\limits_{j \in T} k_j^+}$$

and the nodal residual becomes

$$\Phi_i^T = \int\limits_T \frac{(L\varphi_i)^+}{\sum\limits_{j \in T} (L\varphi_j)^+} Lu_h \, dX$$

SUPG

Using the notation above, the SUPG residual can be written as

$$\Phi_i^T = \int\limits_T (\varphi_i + \tau L\varphi_i) Lu_h \, dX$$

with the upwind stabilization parameter $\tau = (\sum\limits_{i \in T} k_i^+)^{-1}$.

5. Scalar advection test case

Given a rectangular domain, we consider a steady advection equation

$$\lambda \cdot \nabla u = 0 \text{ with } \boldsymbol{\lambda} = (y, -x)$$

A cosinus profile is imposed at the inlet. The advection field is supposed to rotate this profile in the direction indicated in figure 8. The solution obtained with the LDA and SUPG schemes on a mesh consisting of P_2 triangles is depicted in figure 9.

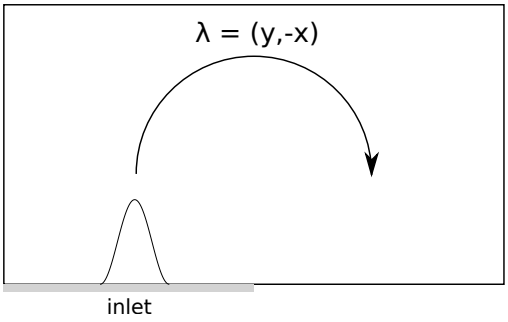

Figure 8: Setup for linear advection test case

6. Euler 2D test case

The extension of the scheme to a (nonlinear) system of equations was tested on a simple test case for Euler equations in 2D dimensions. Two supersonic states $\mathbf{u}_{L/R} = (\rho, \rho u, \rho v, E)_{L,R}$ are prescribed at the left and right half of the inlet (inlet boundary condition), and also in the left and right half of the whole domain as initial conditions (see figure 10). This test case was chosen because it does not require wall boundary condition, which are not implemented at this moment. The solution eventually forms an expansion fan (figure 11).

Acknowledgments

The presented results were obtained in collaboration with Tiago Quintino, Mario Ricchiuto and Nadège Villedieu. The construction of residual distribution schemes with variable β-coefficients as described in section 4 is due to an original idea of Mario Ricchiuto. No papers on this topic have been published so far.

References

[1] H. Deconinck, R. Abgrall, Introduction to residual distribution methods, VKI Lecture Series, Comput. Fluid Dynam., 2005.

[2] M. Ricchiuto, N. Villedieu, R. Abgrall, H. Deconinck, On uniformly high–order accurate residual distribution schemes for advection-diffusion, J. Comput. Appl. Math. 215 (2008) 547–556.

[3] H. Deconinck, K. Sermeus, R. Abgrall, Status of multidimensional upwind residual distribution schemes and applications in aeronautics, AIAA paper 2000-2328, AIAA CFD Conference, Denver (USA), June 2000.

[4] M. Ricchiuto, N. Villedieu, R. Abgrall, H. Deconinck, High–order residual distribution schemes: discontinuity capturing crosswind and extension to advection–diffusion, VKI Lecture Series, Comput. Fluid Dynam., 2005.

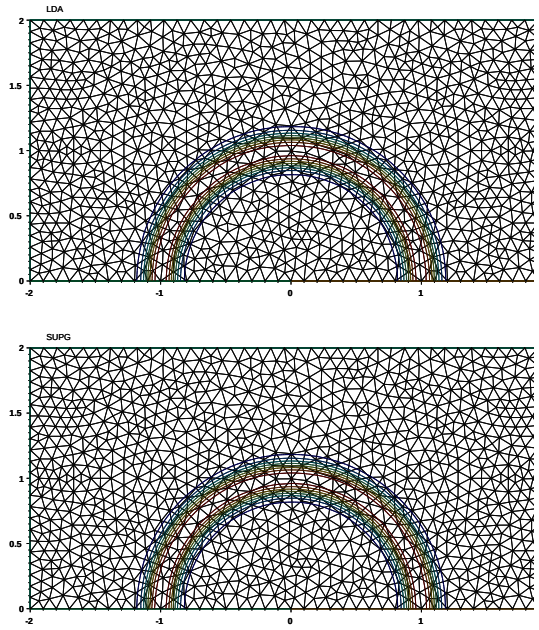

Figure 9: Linear advection test case - isolines of solution obtained with the LDA (top) and SUPG (bottom) schemes

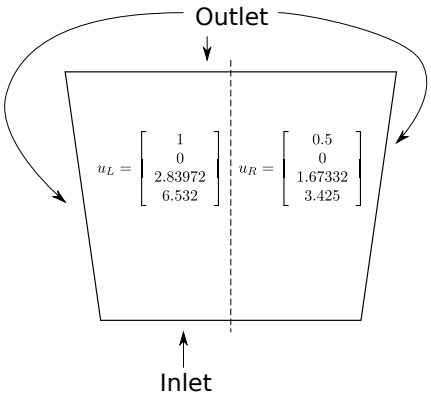

Figure 10: Initial and boundary conditions for the Euler 2D test case

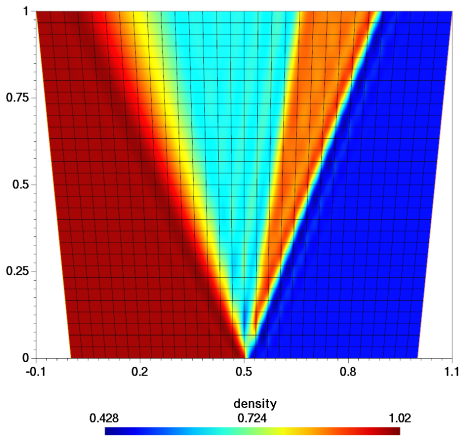

Figure 11: Solution of the Euler test case with LDA scheme on Q_2 elements

[5] H. Deconinck, P. L. Roe, R. Struijs, A multidimensional generalization of Roe's difference splitter for the Euler equations, Computers and Fluids 22(2/3) (1993) 215–222.

[6] H. Paillere, Multidimensional upwind residual distribution schemes for the Euler and Navier–Stokes equations on unstructured grids, Ph.D. thesis, Von Karman Institute for Fluid Dynamics and Université Libre de Bruxelles, Faculté des Sciences Appliquées (1995).

[7] E. van der Weide, H. Deconinck, Positive matrix distribution schemes for hyperbolic systems, with application to the Euler equations, Computational Fluid Dynamics (1996) 747–753.

[8] E. van der Weide, Compressible flow simulation on unstructured grids using multi–dimensional upwind schemes, Ph.D. thesis, Von Karman Institute for Fluid Dynamics and TU Delft (1998).

[9] N. Villedieu, T. Quintino, M. Vymazal, H. Deconinck, High-order residual distribution schemes: Unsteady and viscous terms, 35th Computational Fluid Dynamics Lecture Series, VKI/ADIGMA Course on High order Discretization Methods, Von Karman Institute for Fluid Dynamics, 2008.

[10] R. Abgrall, A. Lerat, M. Ricchiuto, C. Tavé, A simple construction of very high order non-oscillatory compact schemes on unstructured meshes, Computers and Fluids 38(7) (2009) 1314–1323.

[11] R. Abgrall, Residual distribution schemes: Current status and future trends, Computers and Fluids 35(7) (2006) 641–669.

[12] F. Bassi, S. Rebay, High–order accurate discontinuous finite element solution of the 2D Euler equations, J. Comput. Phys. 138 (1997) 251–285.